Proceedings

International Conference on Nuclear Science and Technology

Nuclear Society Of Iran | Atomic Energy Organization of Iran | Nuclear Sciences and Technologies Research Institute

Papers on:

Nuclear Fuel Cycle

*In this booklet, you will find the selected papers presented at the **First International Conference on Nuclear Science and Technology**, held from May 6-8, 2024, in Isfahan, Iran.*
We hope you find it informative and enjoyable!

ICNST 2024

Contact and Accessibility

icnst2024.com
registration@icnst2024.com


بسم الله الرحمن الرحيم

The Conference President's Message
ICNST 2024

Attendees, guests, and colleagues

I would like to warmly welcome you to the first International Conference on Nuclear Science and Technology (ICNST 2024). It has been a real honor and privilege to serve as the president of this conference. The conference this year has brought together an incredible diversity of authors and speakers from universities, government, and industry to share ideas and new perspectives on a wide range of radiation applications, nuclear reactors, particle accelerators, radiation measurements, fusion and plasma, stable and radioactive isotopes, radiation safety and security, nuclear agriculture, fuel cycle, lasers, education and training and nuclear governance.

Climate change, a new topic which has been added to this year's agenda as an important worldwide issue. a matter that has been brought up as a critical concern at the majority of IAEA conferences and nuclear scientific assemblies in recent years.

Panel discussions and exhibitions are being introduced as side activities in an attempt to keep this scientific meeting from becoming one-dimensional and increase its effectiveness.

More than 520 complete papers have been approved for this conference; when combined with the additional panels, get-togethers, and side activities, it is anticipated that over 1000 people will attend in person in the historical and touristic city of Isfahan. We look forward to welcoming participants to share their practical ideas and to enjoy an academical and cultural three days in Isfahan.

I'll close by wishing you everyone an incredible, instructive, and transformative experience during ICNST2024 and I hope that this conference can pave the route for academic materials to be used in industry and everyday life.

Prof. Javad Karimi-Sabet
President of ICNST2024
Javad Karimi-Sabet

welcome statment of scientific secretary ICNST 2024

"In the name of God, the Merciful,

Prior to giving the stage to address this distinguished forum, let me take this opportunity to express our deep gratitude, on behalf of all attendees, for His Excellency Mr. Islami's scientific, educational, and motivational remarks, as well as for his excellent organization of this conference.

I would also like to express our appreciation to His Excellency Dr. Mortazavi, Governor-General of Isfahan Province, for his constructive and useful support in enabling this meeting to take place.

This is a great pleasure and honor to extend a warm greeting to each and every one of you for the International Conference on Nuclear Science and Technology, scheduled from May 6th to May 8th, 2024, in the historic city of Isfahan, Iran.

With the aim of advancing our knowledge of nuclear science and technology, this conference is a major global convergence of experts, researchers, and practitioners. It is a platform for the sharing of creative concepts, the presentation of state-of-the-art research, and the formation of cooperative alliances.

As the scientific secretary of this prestigious event, I am particularly excited about the diverse array of participants expected to grace us with their presence. From the esteemed scientists and engineers of Russian universities and research centers to representatives from Islamic countries, friendly nations, and beyond, this conference promises to be a melting pot of perspectives, experiences, and expertise.

The extensive coverage of this conference is another aspect of its uniqueness. We have nearly 900 participants representing 22 countries around the world. Of the 900 participants, 620 are authors covering 13 major topics. There are 421 papers for oral and poster presentations, with additional documents for publication in ISC journals. There will be 3 plenary sessions, 16 panel discussions, 20 parallel oral presentation sessions, and 3 poster sessions.

Prof. Hosein Afarideh
Scientific Secretariat of ICNST2024

Organizers

Nuclear Society Of Iran (NSI)

Atomic Energy Organization of Iran (AEOI)

Nuclear Science and Technology Research Institute (NSTRI)

Scientific Partnership

IAEA

International Atomic Energy Agency (IAEA)

Isfahan University

Isfahan University

Sharif University of Technology

Sharif University

Kurchatov Institute

Amirkabir University of Technology

Amirkabir University of Technology (Tehran Polytechnique)

Shahid Beheshti University

Shahid Beheshti University

Isfahan University of Technology

Isfahan University of Technology

Shiraz University

Shiraz University

دانشگاه آزاد اسلامی
Islamic Azad University

Islamic Azad University

K. N. Toosi University of Technology

K. N. Toosi University of Technology

FERDOWSI UNIVERSITY OF MASHHAD

Ferdowsi University of Mashhad

Ministry of Science Research and Technology
Graduate University of Advanced Technology

Kerman Graduate University of Technology

Sahand University of Technology

University of Tabriz

ISC
Islamic World Science Citation Center

Islamic World Scieence Citation Center

Journal of Nuclear Science and Technology (JonSat)

Radiation Physics and Engineering

Radiation Physics and Engineering journal

nuclear watch
NETWORK

Nuclear Watch

Cooperative Organization

Isfahan Governorate

Isfahan Municipality

Abbasi Hotel

Iran Atomic Energy Production & Development Co.

Iran's Nuclear Raw Materials & Fuel Production Co.

Radiation Application Development Co.

Ofogh Consulting Engineers Co.

Nuclear Power Plant Safety Development & Promotion Co.

Nuclear Power Plant Engineering & Construction Co.

Engineering & Design of Industrial Simulator Co.

Energy Industry Development Engineering Co

Atomic Power Plant Pepair & support

Nuclear Reactors Fuel Co.

Iran Radioactive Waste Management Co.

Mesbah Energy Co.

Iran Gharb Industrial, Mining and Energy Co.

Pars Isotope Co.

Center for Laser Science & Technology of Iran

Centrifuge Production of Iran Co.

Plasma Technology Development Co.

Rasa Technology and Innovation Center

Behyaar Sanaat Sepahan Co.

Nuclear Data Base of Iran (NDB)

Parto think tank (strategic studies of nuclear industry development)

International Conference Alerts

Local Scientific Board

RAW	NAME	ROLE	AFFILIATION
1	**Prof. Hossein Afarideh**	**Chairman of Local Scientific Board**	**Amirkabir University of Technology (Tehran Polytechnique)(AUT)**
2	**Prof. Mohammad Ghanadi Maragheh**	**Member of The Local Scientific Board**	**Nuclear Science and Technology Research Institute of Iran (NSTRI)**
3	**Prof. Mohammad Lamei Rashti**	**Member of The Local Scientific Board**	**Nuclear Science and Technology Research Institute of Iran (NSTRI)**
4	**Prof. Mohammad Bagher Ghofrani**	**Member of The Local Scientific Board**	**Sharif University of Technology (SUT)**
5	**Prof. Hosein Faghihian**	**Member of The Local Scientific Board**	**University of Isfahan (UI)**
6	**Prof. Javad Rahighi**	**Member of The Local Scientific Board**	**Institute for Research in Fundamental Sciences (IPM)**
7	**Prof. Seyed Amirhossein Feghhi**	**Member of The Local Scientific Board**	**Shahid Beheshti University (SBU)**

Scientific Committee

RAW	NAME	ROLE	AFFILIATION
1	**Prof. Ali Akbar Salehi**	**Member of The Scientific Committe**	**Sharif University of Technology (SUT)**
2	**Prof. Seyyed Javad Ahmadi**	**Member of The Scientific Committe**	**Nuclear Science and Technology Research Institute of Iran (NSTRI)**
3	**Prof. Farhoud Ziaee**	**Member of The Scientific Committe**	**Nuclear Science and Technology Research Institute of Iran (NSTRI)**
4	**Prof. Saeed Hamidi**	**Member of The Scientific Committe**	**University of Arak**
5	**Prof. Seyedzafarollah Kalantari**	**Member of The Scientific Committe**	**Isfahan University of Technology (IUT)**
6	**Prof. Naser Bagheri Moghaddam**	**Member of The Scientific Committe**	**National Research Institute for Science Policy (NRISP)**
7	**Prof. Naser Vosoghi**	**Member of The Scientific Committe**	**Sharif University of Technology (SUT)**
8	**Prof. Seied Rabi Mahdavi**	**Member of The Scientific Committe**	**Iran University of Medical Sciences**
9	**Prof. Meisam Torab Mostaedi**	**Member of The Scientific Committe**	**Nuclear Science and Technology Research Institute of Iran (NSTRI)**
10	**Prof. Fereydoun Abbasi Davani**	**Member of The Scientific Committe**	**Shahid Beheshti University (SBU)**
11	**Prof. Seyed Farhad Masoudi**	**Member of The Scientific Committe**	**K.N.Toosi University of Technology**
12	**Prof. Rasool Ruknizadeh**	**Member of The Scientific Committe**	**University of Isfahan (UI)**
13	**Prof. Gholamreza Raeesali**	**Member of The Scientific Committe**	**Nuclear Science and Technology Research Institute of Iran (NSTRI)**
14	**Prof. Asghar Sedighzadeh**	**Member of The Scientific Committe**	
15	**Prof. Hossein Kazeminejad**	**Member of The Scientific Committe**	**Nuclear Science and Technology Research Institute of Iran (NSTRI)**

RAW	Name	role	Affiliation
17	**Prof. Seyyed Jaber Safdari**	**Member of The Scientific Committe**	**Nuclear Science and Technology Research Institute of Iran (NSTRI)**
18	**Prof. Omid Reza Kakuee**	**Member of The Scientific Committe**	**Nuclear Science and Technology Research Institute of Iran (NSTRI)**
19	**Prof. Alireza Keshtkar**	**Member of The Scientific Committe**	**Nuclear Science and Technology Research Institute of Iran (NSTRI)**
20	**Prof. Fereshte Haj esmail Beigi**	**Member of The Scientific Committe**	**Nuclear Science and Technology Research Institute of Iran (NSTRI)**
21	**Prof. Masoud Mahjour-shafiei**	**Member of The Scientific Committe**	**Nuclear Science and Technology Research Institute of Iran (NSTRI)**
22	**Prof. Mahmoud Payami Shabestar**	**Member of The Scientific Committe**	**Nuclear Science and Technology Research Institute of Iran (NSTRI)**
23	**Prof. Ali Bahrami Samani**	**Member of The Scientific Committe**	**Nuclear Science and Technology Research Institute of Iran (NSTRI)**
24	**Dr. Farhanaz Motamedi**	**Member of The Scientific Committe**	**Nuclear Science and Technology Research Institute of Iran (NSTRI)**
25	**Dr. Faezeh Rahmani**	**Member of The Scientific Committe**	**K.N.Toosi University of Technology**
26	**Dr. Ebrahim Moghiseh**	**Member of The Scientific Committe**	**Nuclear Science and Technology Research Institute of Iran (NSTRI)**
27	**Dr. Iraj Jabari**	**Member of The Scientific Committe**	**University of Isfahan (UI)**
28	**Dr. Nima Ghal-Eh**	**Member of The Scientific Committe**	**Ferdowsi University of Mashhad**
29	**Dr. Mitra Athari Alaf**	**Member of The Scientific Committe**	**Islamic Azad University Science and Research Branch**
30	**Dr. Gholamreza Etaati**	**Member of The Scientific Committe**	
31	**Dr. Amir Movafeghi**	**Member of The Scientific Committe**	**Nuclear Science and Technology Research Institute of Iran (NSTRI)**

Executive Committee

RAW	NAME	ROLE
1	Dr. Farshad Ghasemi	Chairman of the Executive Committee
2	Dr. Ehsan Molazadeh	Member of The Executive Committee
3	Dr. Seyyed Ghasem Biniaz	Member of The Executive Committee
4	Mr. Aliakbar Aminidoust	Member of The Executive Committee
5	Ms. Fatemeh Zamani	Member of The Executive Committee
6	Ms. Mahya Pazoki	Member of The Executive Committee
7	Mr. Hosein Maleki	Member of The Executive Committee
8	Mr. Maziar Dalili	Member of The Executive Committee
9	Mr. Shojaei	Member of The Executive Committee
10	Ms. Fatemeh Rezaei	Member of The Executive Committee
11	Mr. Reza Rafiei	Member of The Executive Committee
12	Ms. Seyyedeh Elham Ebrahimi	Member of The Executive Committee

Nuclear Fuel Cycle

Nuclear Fuel Cycle

Preparation of mixed nanofiltration membranes containing polyethersulfone and graphene oxide to investigate the removal of zinc-65 ions from the water of the first circuit of power reactors (Paper ID : 1005)

S. A. H. M .Zeinali1,2 , R. Yavari2* , M. A. Aroon1 , T. Yousefi2

Membrane Research Laboratory, Caspian Faculty of Engineering, College of Engineering, University of Tehran, Tehran, Iran

Nuclear Fuel School, Nuclear science and technology institute (NSTRI), P.O.BOX. 11365-8486, Tehran, Iran

Abstract

In this research, mixed polymer membranes containing Polyethersulfone (PES) and different percentages of graphene oxide (GO) were prepared to investigate the removal of zinc-65 ions from the water of the first circuit of power reactors using the nanofiltration process. These flat membranes, which contain 0.01 to 0.05% by weight of GO synthesized by the Hoffmann-Hammer method, were prepared by the wet phase inversion and conventional casting methods. The structural properties of GO as well as the morphology and hydrophilic properties of the synthesized mixed membranes were investigated using Fourier transform infrared spectroscopy, scanning electron microscope and contact angle test, respectively. The characterization results showed that the functionalization of graphene surface with hydrophilic functional groups such as epoxy, carbonyl, and hydroxyl is well done. Also, by increasing the amount of GO in the mixed membrane structure, the thickness of the active layer of the membrane decreases and the hydrophilic property of the membrane increases. On the other hand, the results of the permeation test showed that by increasing the amount of GO in the membrane containing 16% by weight of Polyethersulfone and under the laboratory conditions (pressure = 12 bar, temperature 25 °C, pH = 5 and time 60 min), the percentage amount of zinc ion rejection and permeate flux increases from 81.58 to 89.63 and 9.22 to 15.75 (Lm^2/h), respectively.

Keywords: Zinc-65, Nanofiltration, Polyethersulfone, Graphene Oxide, Power Reactors

* Email: ryavari@aeoi.org.ir

Introduction

Nuclear energy plays a major role in providing energy for various countries, especially in advanced countries. Today, more than 7% of the world's energy consumption is supplied by nuclear reactors. Nuclear energy is primarily used for electricity generation, and approximately 16% of the world's electricity is produced from nuclear energy. Consequently, about 50,000 tons of natural uranium are consumed annually, and about 11,000 tons of used fuel are produced as waste. The increasing demand for energy, the possibility of depletion of non-renewable oil and gas resources, environmental concerns, the need to reduce greenhouse gas emissions, population growth, and economic development are all driving forces for the development of nuclear energy and addressing global energy challenges [1]. Despite the numerous advantages of nuclear energy, its use in various sectors such as medicine, agriculture and industries generates a relatively large volume of radioactive waste which cannot be directly disposed of in the environment. Therefore, serious actions must be taken to prevent the release of the produced hazardous and toxic radioactive materials into the environment.

One of the sources where radioactive materials can exist and must be treated is the first circuit water in of nuclear power reactors. The first circuit water in nuclear power plants acts as a coolant and/or as a retardant. Therefore, in addition of fission fragments, some radioactive materials such as ^{55}Fe, ^{63}Ni, ^{54}Mn, ^{65}Zn etc. are present in this media as neutron activation products which should be removed and prevented from entering the environment. Among them, ^{65}Zn are formed by neutron activation reaction of stable zinc which are exist in the media due to the corrosion of steel equipment and metallic materials used in the water of reactors. It has a half-life of 245 days and decays to stable ^{65}Cu through a β^+ emitter and Auger electrons. On the other hand, zinc as one of the toxic heavy metals are found in wastewater of various industries such as metal plating and textile and can enters the environment and causes soil and groundwater pollution. If zinc enters the food cycle, this element accumulates in body tissues and can cause problems such as abdominal muscle cramps, skin inflammation, itching, vomiting, nausea, anemia, diabetes, dysfunction of the pancreas and protein metabolism, and ultimately cancer. Therefore, the removal of this toxic and hazardous contaminant from wastewater is very important. According to the regulations of the United States Environmental Protection Agency (EPA), the permissible amount of zinc in drinking water is 5 mg/liter. Up to now, conventional cationic and anionic organic resins have been used to remove these radioactive materials form the first circuit water of nuclear power reactors. However, these resins containing radioactive materials must be stored and eventually processed for final

disposal. Since the volume of these materials will be very large, nuclear power plant purification units have focused on using membrane processes for safe and effective removal of these materials [2]. Among various membrane processes, nanofiltration has found widespread use especially in the nuclear industry due to its low energy consumption, high efficiency in removing multivalent ions, ease of operation, and high reliability [3]. Nevertheless, the selection of a suitable material for membrane fabrication with both filtration and high permeability capabilities is crucial for the success of nanofiltration processes in removing pollutants from aqueous solutions [4]. Currently, polymeric materials found a special important in the construction of membranes in order to remove pollutants from wastewater. These types of membranes exhibit less stability against pH variations and are prone to fouling, with lower chemical stability and mechanical strength. Despite these drawbacks, their high porosity, lower cost, and easy production of them have led to their extensive use in commercial membrane applications[5, 6]. The commonly used polymers for the production of these membranes include cellulose acetate (CA), polyvinylidene fluoride (PVDF), polyethersulfone (PES), polysulfone (PSU), and polypropylene (PP). Among them, Polyethersulfone (PES) is a significant polymer used in separation processes, known for its resistance to oxidation and good thermal and mechanical stability. These asymmetric membranes are usually prepared using phase inversion and conventional casting methods [7]. However, the primary challenge in using these membranes lies in their hydrophobic nature leading to their inherent fouling. To address this issue, many researchers have been recently focusing on enhancing the performance of these membranes via nanoparticles (NPs) incorporation in the structure of them. Graphene oxide as a member of the graphite family and a nanostructure material, due to its strong hydrophilic properties and the presence of functional groups (carboxyl and hydroxyl) can help the absorption of various materials in the membrane and increasing the rejection and permeability of membrane. The literature survey indicates that no studies have been yet performed on the removal of zinc by nanofiltration membrane containing PES and graphene oxide nanoparticles. Therefore, in this study, graphene oxide nanosheets were used as hydrophilic additives in the fabrication of flat sheet nanofiltration membranes from PES to investigate the influence of different percentages of it on the removal of zinc ions from aqueous solution.

Experimental

Materials

The polymer PES with a molecular weight of 75000 g/mol which has been manufactured by BASF Germany was used. N-Methyl-2-pyrrolidone (NMP) with a molecular weight of 99.13 g/mol served as the solvent is purchased from Merck Germany. Polyvinylpyrrolidone (PVP) with a molecular weight of 25000 g/mol, obtained from Merck Germany, was employed as the hydrophilic agent. Graphite with particle size less than 50 micrometers and purity of 99.5% from Tianjin, China, was used for graphene oxide synthesis. Other chemical substances such as zinc nitrate, acids, and bases were all procured from Merck or Fluka company.

Membrane Fabrication

In this study, the phase inversion method was employed for the preparation of flat polymer membranes. In this approach, a homogeneous and transparent solution with varying weight percentages of polymer and graphene oxide nanosheets in NMP solvent was prepared using mechanical stirring. Subsequently, to eliminate the formed bubbles, the solution was subjected to 30 minutes of ultrasonic bath treatment. And for complete bubble removal, the solution was allowed to rest for one night. Finally, to produce the membrane, a uniform layer of the bubble-free solution was drawn onto a glass surface using a casting film. The mentioned film was transferred into a bath containing distilled water, and after membrane formation the desired membrane was airried for 24 hours in room temperature. Ultimately, the membrane system as illustrated in Fig. 1 below was utilized for permeability tests.

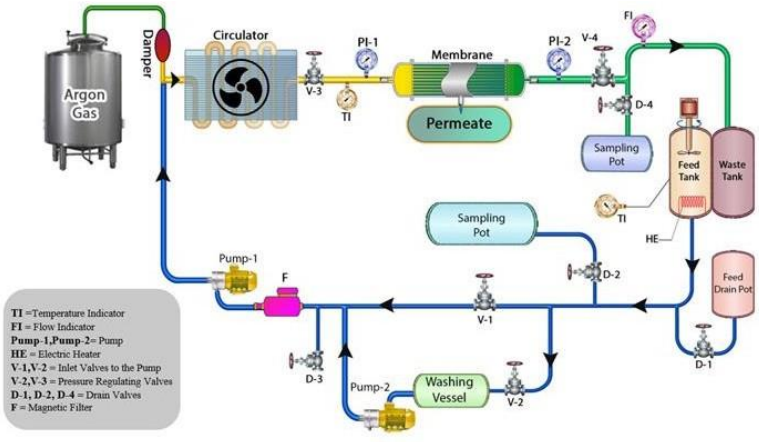

Fig 1: Schematic of membrane filtration system

Measurement of permeate flux

The flux passing through the membrane is calculated by measuring the volume of water exiting the effective surface of the membrane per unit of time from Equation (1) [8]:

$$J = \frac{V}{A.Dt} \quad (1)$$

where V is the volume of the permeate solution in (L), Δt is the time of passage through the membrane in (Sec) and A is the effective surface of the membrane in (m^2).

After determining the concentration of the samples using a spectrophotometer device, the percentage of zinc ion removal from the aqueous solution by the membrane is calculated from Equation (2) [8]:

$$R\% = 1 - \frac{CP}{CF} \times 100 \quad (2)$$

where in the above relationship, CP and CF represent the concentration of zinc ion in solution before and after experiments, respectively.

Membrane porosity, mean pore size

Membrane porosity is an important parameter for membrane description and has a significant effect on membrane permeability, which is defined as the volume of pores divided by the total volume of the porous membrane and is calculated from Equation (3) [8]:

$$e(\%) = \frac{w1 - w2}{A.l.dw} \times 100 \quad (3)$$

where Ɛ is the membrane porosity, ω1 and ω2 are the wet and dry membrane weight in (kg), dw is the density of water in, dw = 998 (kg/m^3), L is the membrane thickness in (m) and A is the effective surface area of the membrane in (m^2).

The porosity of the manufactured membranes was measured by gravimetric method, in which the membranes were first dried in an oven at 80°C for 24 hours, then weighed, and then immersed in water for 24 hours until the pores were filled with water. To estimate the average size of membrane pores, Equation

(4) (Guerout-Elford-Ferry) was used based on the pure water flux of modified membranes [8]:

$$r = \sqrt{\frac{(2.9 - 1.75e)8hlQ}{e.A.DP}}\,)4($$

m

where η and Q are the water viscosity of 9.8×10^{-4} in (Pa.s) and the volume of pure water leaving the membrane in (m^3/s).

Oxidation of graphite using Huffman Hummers method

Graphite powder is treated in a strong oxidizing environment such as nitric acid or sulfuric acid. The mixture is then placed in a water bath and sonicated. Sodium nitrate and potassium permanganate (KMnO4) are gradually added to the mixture, followed by cooling for 2 hours. The solution temperature is raised to 70°C, and distilled water is slowly added. The mixture is stirred vigorously outside the water bath at room temperature for 3 hours. The color of the solution changes from green to dark brown and finally to brick- red. Distilled water is added to reach a total volume of 400 mL. After 12 hours, the upper phase is discarded, and about 200 mL of deionized water is added to the settled residue and mixed. The solution is filtered, washed with 10% hydrochloric acid, and filtered again. After several washes with distilled water, the solution undergoes ultrasonic treatment for 30 minutes and is filtered once more. Finally, it is dried in an oven at 80°C for 24 hours [9].

Result and discussion

characterization

Fourier-transform infrared spectroscopy (FT-IR) has been used for the identification of various chemical bonds and functional groups. Figure (2) shows the FT-IR spectra for the synthesized graphene oxide nanosheets. As evident in the graph, peaks at 1064, 1230, and 1280 cm^{-1}correspond to the epoxy group (C- O-C) and skeletal vibrations of the nonoxidized graphite domains, indicating carbon atoms in the graphene oxide structure that have not reacted with oxygen yet. Peaks at 1450 to 1520 cm^{-1} are related to the bending vibrations of the hydroxyl group (C-OH) that has undergone deformation. In the wavelength range of 1600 cm^{-1}, it corresponds to aromatic groups (C=C), and the peak at 1730 cm^{-1} is attributed to the vibrations of the carbonyl functional group (C=O). Peaks at 3300 to 3500 $cm^{-1}$are associated with the stretching vibrations of the hydroxyl group (OH). According to the obtained results

from infrared spectroscopy, the graphene oxide synthesized by the Huffman Hummers method is in agreement with the research of other scientists [9, 10].

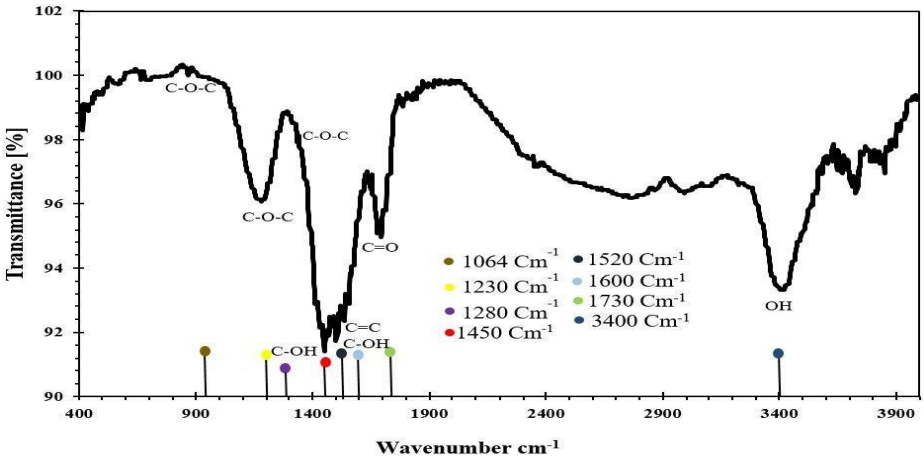

Fig 2: Infrared spectrum of GO

To evaluate the structure of the mixed matrix membranes containing PES (16%) and various amount of graphene oxide on their morphology, SEM images of three composite membranes with magnification of 1500 times were prepared with weight percentages of 0.01%, 0.025%, and 0.05% graphene oxide. Fig. 3 illustrates the morphology of these three membranes.

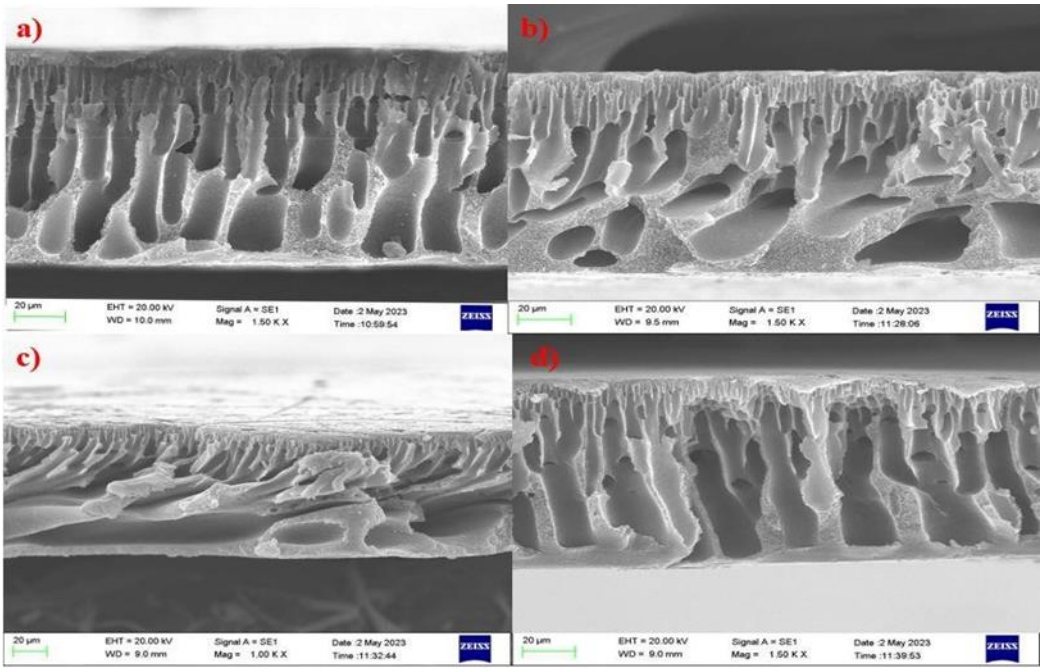

Fig 3: SEM images of the cross section of pure PES and the mixed matrix membrane containing PES (16%) and various amount of GO a) 0%, b) 0.01%, c) 0.025%, d) 0.05%

As can be seen in Fig. 3, the formation of longer channels and larger pore sizes in the sub-layers of the membrane are observed by increasing the amount of graphene oxide in PES membrane (16%). This can be attributed to the increased speed of solvent and non-solvent exchange during the phase inversion process. Additionally, measuring the active layer thickness using scanning electron microscope images indicates that with an increase in the amount of graphene oxide from 0.01% to 0.05%, the thickness of the active layer decreases. This reduction in thickness may be due to the increased mass transfer rate during the phase inversion process which could lead to an increase in the size of membrane pores, potentially affecting both permeate flux, and membrane fouling [11].

Fig. 4 shows the amount of contact angle for pure PES and mixed matrix membranes containing PES (16%) and different percentages of GO. As observed in Fig. 4, with an increase in the amount of graphene oxide, the amount of contact angle decreases suggesting that these hydrophilic nanomaterials enhance the membrane's wettability. The addition of graphene oxide due to the presence of hydroxide (OH) and carboxylic acid (COOH) functional groups leads to a reduction in the contact angle. Moreover, the layered structure of graphene oxide containing multiple oxygen functional groups acts as a hydrophilic center on the membrane surface, and increase the interactions between the membrane surface and water droplets. Therefore, the contact angle of these fabricated mixed matrix membranes increases [12, 13].

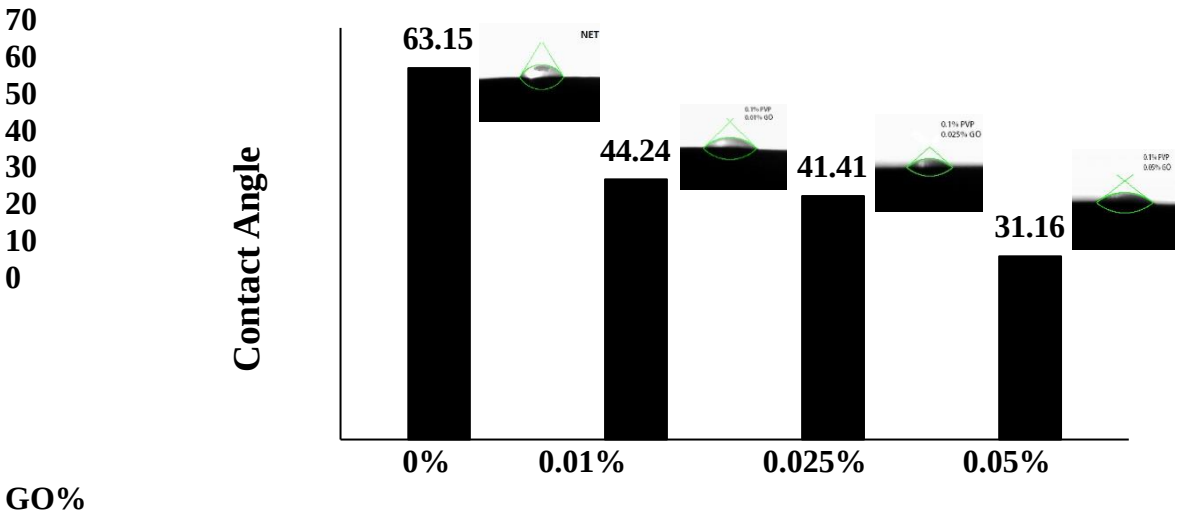

Fig. 4: the amount of contact angle for mixed matrix membranes containing PES (16%) and different percentages of GO.

Permeate tests

To investigate the effect of the graphene oxide content on rejection properties, mixed matrix membranes containing 0.01%, 0.025%, and 0.05% by weight of graphene oxide and PES (16%) were prepared and the obtained results from the permeate test were depicted in Fig. 5. As seen in Figure 5, the permeate flux increases with an increment of the graphene oxide content. This phenomenon can be attributed to the increasing in hydrophilic nature of membranes as a result of graphene oxide nature and the type of porosity in the fabricated membranes. This observation is consistent with the measured contact angle values. In fact, the presence of functional groups such as carboxylic acid, hydroxyl, and epoxy on the graphene oxide structure results in changes in pore size, the displacement of solvents and non-solvents in the phase inversion process, and permeate flux. Therefore, it leads to an increase in the membrane permeate flux [14]. Additionally, zinc ion rejection also increases with increasing the graphene oxide content. The reason for this phenomenon can be attributed to the presence of anionic functional groups on the surface of fabricated mixed matrix membrane which increase electrostatic repulsion between the presence anion in the solution (nitrate ion) and membrane surface. This increases the rejection of nitrate ions and consequently, the rejection of zinc ion increases due to Donnan effect.

On the other hand, the presence of these functional groups on the surface of graphene oxide can leads to the adsorption of zinc ions on the surfaces of the composite membranes and the decrease of them through the membrane.

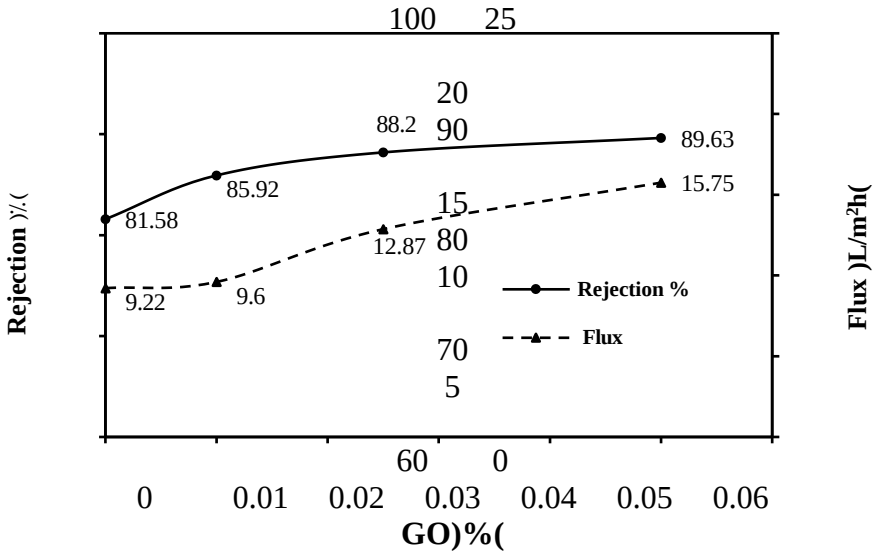

Fig. 5: The effect of GO on rejection of zinc ion and Flux ([PES%]= 16%, pH=5, T=25 °C, t=30 min, p=12 bar, $[Zn^{2+}]$= 10 ppm)

Conclusions

In this research, the process of nanofiltration and the use of the flat-sheet mixed matrix membranes containing graphene oxide nanosheets and PES were employed for the removal of zinc ions from aqueous solutions. The morphology, hydrophilicity, and the effect of the amount of graphene oxide nanosheets were investigated. The results indicate that the amount of graphene oxide nanosheets plays a crucial role in shaping the membrane morphology and forming a porous structure. Consequently, these factors directly affect zinc ion rejection and permeability of the membrane. It was also revealed that with an increase in the amount of graphene oxide, due to the presence of functional groups such as carboxylic, hydroxyl, and epoxy in the graphene oxide structure, the hydrophilic properties of the membrane increase. And this leads to a change in the size of membrane pores, the displacement of solvents and non-solvents in the phase inversion process, ultimately resulting in an increase in permeability and ion rejection of the membrane.

Reference

Caurant, D., et al., *Glasses, glass-ceramics and ceramics for immobilization of highly radioactive nuclear wastes*. 2007: Nova Science Hauppauge.

Siyavash Madaeini, A.R., Kasra Pirzadeh, *Polymeric membrane, Application, The method of making and modifying them*, ed. F. Edition. 1394, Babol noshirvani university of technology.

Ahmad, N.N.R., et al., *Nanofiltration membrane processes for water recycling, reuse and product recovery within various industries: A review*. Journal of Water Process Engineering, 2022. 45: p. 102478.

Shu, L., et al., *A thin and high loading two-dimensional MOF nanosheet based mixed-matrix membrane for high permeance nanofiltration.* Journal of Membrane Science, 2020. 603: p. 118049.

Dunleavy, M., *Polymeric membranes. A review of applications.* Medical device technology, 1996. 7(4): p. 14-6, 18.

Ng, L.Y., et al., *Polymeric membranes incorporated with metal/metal oxide nanoparticles: A comprehensive review.* Desalination, 2013. 308: p. 15-33.

Huang, J., et al., *Fabrication of polyethersulfone-mesoporous silica nanocomposite ultrafiltration membranes with antifouling properties.* Journal of membrane science, 2012. 423: p. 362-370.

Hosseini, S., et al., *Mixed matrix PES-based nanofiltration membrane decorated by (Fe3O4–polyvinylpyrrolidone) composite nanoparticles with intensified antifouling and separation characteristics.* Chemical Engineering Research and Design, 2019. 147: p. 390-398.

Muniyalakshmi, M., K. Sethuraman, and D. Silambarasan, *Synthesis and characterization of graphene oxide nanosheets.* Materials Today: Proceedings, 2020. 21: p. 408-410.

Al-Gaashani, R., et al., *XPS and structural studies of high quality graphene oxide and reduced graphene oxide prepared by different chemical oxidation methods.* Ceramics International, 2019. 45(11): p. 14439-14448.

Kiran, S.A., et al., *Impact of graphene oxide embedded polyethersulfone membranes for the effective treatment of distillery effluent.* Chemical Engineering Journal, 2016. 286: p. 528-537.

Kadhim, R.J., et al., *Removal of dyes using graphene oxide (GO) mixed matrix membranes.* Membranes, 2020. 10(12): p. 366.

Vatanpour, V., et al., *Novel antibifouling nanofiltration polyethersulfone membrane fabricated from embedding TiO2 coated multiwalled carbon nanotubes.* Separation and purification technology, 2012. 90: p. 69-82.

Zinadini, S., et al., *Preparation of a novel antifouling mixed matrix PES membrane by embedding graphene oxide nanoplates.* Journal of Membrane Science, 2014. 453: p. 292-301.

ICNST 2024
International Conference on Nuclear Science and Technology
6- 8 MAY 2024 | Isfahan, Iran

Evaluation of the effect of functionalized multi-walled carbon nanotubes in the structure of polyethersulfone membrane for the removal of Zn-65 from aqueous solutions using nanofiltration process. (Paper ID : 1006)

S. A. H. M. Zeinali[1,2], R. Yavari[2*], M. A. Aroon[1], T. Yousefi[2]

1. Membrane Research Laboratory, Caspian Faculty of Engineering, College of Engineering, University of Tehran, Tehran, Iran

2. Nuclear Fuel School, Nuclear science and technology institute (NSTRI), P.O.BOX. 11365-8486, Tehran, Iran

Abstract

In this study, we evaluated the hybrid membranes containing polyether sulfone and different percentages of functionalized multi-walled carbon nanotubes (FMWCNTs) for the removal of Zn-65 from aqueous solutions using the nanofiltration process. These flat sheet membranes were prepared using the phase inversion method and conventional casting methods. The morphological properties of prepared membrane and their hydrophilicity were investigated using transmission electron microscope and contact angle test respectively. The structure of FMWCNTs was also investigated using fourier transform infrared spectroscopy. The results of these investigations showed that during the oxidation process of nanotubes, hydrophilic groups such as carboxylic, ketone and phenol were introduced in the structure of these compounds. Also, the thickness of the active layer decreased with the increasing in the percentage of FMWCNTs in the membrane containing 16% by weight Polyethersulfone. On the other hand, the results of the permeation tests under the experimental conditions of P= 12 bar, T= 25 °C, pH= 5 and t= 60 min showed that the percentage of zinc ion rejection and the amount of permeate flux increase from 81.6 to 95.6 and 9.22 to 16.36 (Lm^2/h), respectively, which show the high ability of these hybrid membranes in zinc ion rejection and also increasing the permeate flux.

Keywords: Multi-Walled Carbon Nanotubes, Functionalized, Polyethersulfone, Zinc-65,Aqueous [1] Solutions, Nanofiltration

Introduction

Today, environmental pollution is one of the fundamental concerns of human societies. The presence of heavy metals in industrial wastewater creates a significant problem when discharging them into surface waters. Due to the presence of some heavy metals such as mercury, lead, cadmium, copper, zinc and nickel in water, even in very small amounts, they can lead to water toxicity. [1]. Zinc is a toxic metal used in industrial processes like metal plating and textile manufacturing. It can pollute soil and

*Email: ryavari@aeoi.org.ir

groundwater when it enters the environment through wastewater [2]. If zinc becomes radioactive, its presence in nature can cause even greater issues. Nuclear activities generate a significant amount of various waste, with a substantial portion being liquid waste. Radioactive liquid waste is produced in large volumes in nuclear and laboratory activities, but it cannot be stored for long periods. Various methods exist for treating and disposing of radioactive liquid waste to ensure its safe management. One of the radioisotopes present in the nuclear industry is zinc-65, which is indirectly produced in the primary circuit water of a reactor through the neutron activation of the zinc element, as indicated by reaction (1). Zinc-64 occurs in this media due to the corrosion of steel equipment and metallic materials used in reactors.

$$^{64}Zn\ (n, \gamma)\ ^{65}Zn \qquad (1)$$

The presence of this radioisotope in the reactor water increases the radioactivity level of the reactor water, impacting the performance of the system. Additionally, the potential presence of this radioisotope in the environment poses numerous challenges due to its radiotoxicity, attributed to its relatively long half-life (245 days) and gamma-ray emission. Therefore, removing it from the primary circuit water of the reactor and nuclear wastes containing this radioactive isotope is crucial [3]. There are various methods for removing zinc from aqueous solutions. Among these methods, membrane processes based on the driving force of pressure have distinct advantages. These advantages include reduced energy consumption due to no phase change, compact size, diversity in shape and size, minimal operational challenges, reduced radiation exposure for operators, no need for additives and solvents, simple construction, design simplicity, and ease of industrial-scale application. Membrane processes, especially Nanofiltration, have rapidly gained popularity for wastewater treatment. Nanofiltration has recently found extensive applications in nuclear industries, due to its ability to remove multivalent ions with high pollutant rejection coefficients [4]. Therefore, the aim of this research is to utilize this process for the removal of zinc-65 from the primary circuit water of the nuclear reactor and its wastes. Membrane processes can be classified into three categories based on their material and structure: organic membranes, inorganic membranes, and hybrid membranes. Organic membranes are made of polymers, while inorganic membranes are composed of metallic, ceramic, and carbon materials. Hybrid membranes are a combination of mineral and organic components, which can include a mineral base with an organic active layer, an organic base with a mineral active layer, or hybrid membranes that blend mineral materials within a polymer matrix. These different membrane types offer a range of options for

various applications in removing contaminants from aqueous solutions. [5]. Among the various types of membranes, polymer membranes due to their widespread availability are the most widely used and common. However, they have a drawback of high fouling and less stability against pH variations. Polysulfone (PS), polyethersulfone (PES), polyvinylidene fluoride (PVDF), polypropylene (PP), and polyvinyl alcohol (PVA) are commonly used polymers. PES-based membranes show good thermal and mechanical stability but it can also suffer from hydrophobicity-related fouling. Modifying the surface of the membrane can overcome this issue [6]. In recent years, research has focused on enhancing membrane performance by incorporating nanoparticles into polymer membranes to create hybrid membranes. Dispersed nanoparticles in the polymer matrix can control fouling, improve membrane structure, and enhance fouling resistance. Common fillers for hybrid membranes include zeolites, silicas, carbon nanotubes, graphene oxide nanosheets, and metal oxides. Among them, carbon nanotubes are significant due to their ability to create nanometer-scale porous membranes with excellent separation capabilities and selective permeation paths. Incorporating carbon nanotubes can regulate membrane selectivity and improve permeability and fouling resistance in polymeric nanofiltration membranes.[7].

Currently only few studies have been done for incorporation of nanoparticles into PES membranes to remove some heavy metals and the literature is silent on the preparation of hybrid membrane containing PES and oxidized multi-walled carbon nanotubes (FMWCNTs) for the removal of zinc ions from wastewater. Therefore, the aim of this research work was the preparation of the flat sheet membranes including PES and FMWCNTs to evaluation of the removal of zinc ions from water by nanofiltration process.

Experimental

Materials

The polymer PES from BASF, Germany, with a molecular weight of 75000 g/mol, N-methyl-2-pyrrolidone (NMP) as the solvent with a molecular weight of 99.13 g/mol, polyvinylpyrrolidone (PVP) as the hydrophilic agent with a molecular weight of 25000 g/mol from Merck, Germany, and multi-walled carbon nanotubes (MWCNTs) with a diameter ranging from 10 to 20 nanometers, an average length of 30 nanometers, and 95% purity from Changzhou, China, were used in this study. Other chemicals, such as zinc nitrate, acids, and bases, were all purchased with analytical grade purity from Merck or Fluka.

Purification and functionalization of MWCNTs

In order to remove impurities from the purchased MWCNTs, a treatment process was carried out as following:

The pristine MWCNTs were immersed in a 3M nitric acid solution and subjected to ultrasonic shaking for 24 hours at room temperature. After that, 1.5 g of the processed MWCNTs along with 100 mL of concentrated nitric acid were placed in a distillation flask and refluxed for 3 hours at 140°C. The resulting mixture was cooled, the excess acid was removed, and distilled water was added. The mixture was then filtered using a cellulose acetate filter membrane with a pore size of 0.45 μm. It was washed several times with deionized water and dried in an oven at 50°C for 24 hours.[8].

Membrane Fabrication

In this research, flat membranes were prepared using the phase inversion method. In this method, a uniform and transparent solution with different weight percentages of polymer, PVP, and FMWCNTs in NMP solvent was prepared using mechanical stirring. To eliminate the created bubbles, the solution was subjected to ultrasonic bath treatment for 30 minutes, and for complete bubble removal, the solution was allowed to rest for one night. Finally, to prepare the membrane from the bubble-free solution, a uniform layer of the solution was drawn onto the surface of a glass plate using a casting film, and the film was transferred into a bath containing distilled water. After membrane formation in the mentioned bath and detachment from the glass surface, the desired membrane was air-dried for 24 hours. The membrane, as shown in the schematic diagram Figure 1, was then used for permeability tests.

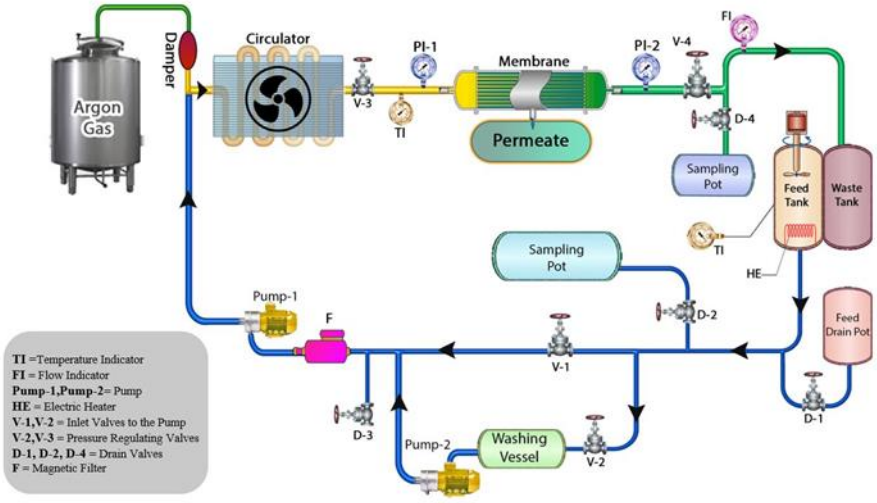

Fig 1: Schematic of membrane filtration Device

Measurement of passing flux and quantification determination of zinc ion

The flux passing through the membrane is calculated by measuring the volume of water exiting the effective surface of the membrane per unit of time from Equation (2) [9].

$$J_v = \frac{V}{A.\Delta t} \quad (2)$$

where V is the volume of the permeate solution in (L), Δt is the time of passage through the membrane in (Sec) and A is the effective surface of the membrane in (m^2).

The quantity determination of zinc concentration in the samples was done using a UV spectrophotometer. To do this, the specific amount of samples containing sufficient zinc ions was added to the 10 mL of borate buffer (pH=8). This was followed by 1 mL of the 4-(2-Pyridylazo) resorcinol (PAR) solution (0.1 %). After mixing the solution, the absorbance was measured at 495 nm in matched cuvettes against a blank prepared in a similar manner. A calibration curve of absorbance versus zinc ion concentration was constructed using standard solutions in the above procedures. The detection limit based on 3σ/b was 0.0143 and the dynamic linear range was 0.05-10 ppm. At the end, the percentage of zinc ion removal from the aqueous solution by the membrane was calculated from Equation 3 [9].

$$R\% = 1 - \frac{C_P}{C_F} \times 100 \quad (3)$$

where in the above relationship, C_P and C_F represent the concentration of zinc ions in solution and feed, respectively.

1. Result and discussion

Characterization

Fourier-transform infrared spectroscopy (FT-IR) has been used for the identification of various chemical bonds and functional groups. The FT-IR wavelengths diagram for FMWCNTs is shown in Figure (2). The initial wavenumbers in the FT-IR diagram of FMWCNTs in Figure (2) (873, 1037, and 1158 cm^{-1}) correspond to the vibrations of the carboxylic acid groups (COOH-) and phenolic hydroxyl (OH) groups. The peak at 1380 cm^{-1} in this diagram can be attributed to lactone groups in the infrared spectrum of carboxylic acid groups, and the peaks at 1626 and 1733 cm^{-1} indicate the stretching vibrations of carboxylate and carboxylic acid anions (COO-). Additionally, at the end of the diagram, a broad and intense peak is observed in the range of 3250 cm^{-1}, related to the stretching vibrations of hydroxyl (OH) functional groups. This can be attributed to the presence of these substances on the surface of FMWCNTs or the presence of water molecules absorbed by FMWCNTs during measurement [10, 11]. FT-IR spectroscopy analysis revealed that various polar groups such as phenolic,

carboxylic acid, and lactone groups are created on the surfaces of the nanotubes during the functionalization process of carbon nanotubes with nitric acid. These groups enhance the dispersibility and solubility of the nanotubes in polar solvents, such as water. Additionally, the introduction of these sorption sites increases the adsorption capacity of the nanotubes and allows for interaction with other compounds.

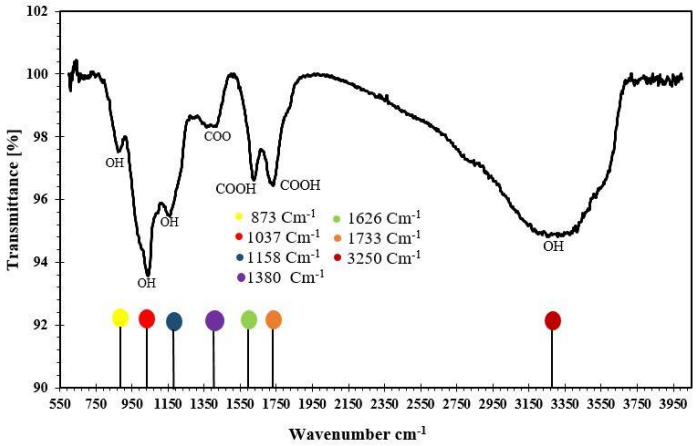

Fig 2: Infrared spectrum of FMWCNTs

To investigate the structure of the hybrid membranes prepared from PES and the effect of the amount of FMWCNTs on their morphology, SEM images of pure PES and three composite membranes with a magnification of 1500 times were prepared and evaluated. These membranes had weight percentages of 0.01%, 0.025%, and 0.05% FMWCNTs. Figure 3 illustrates the morphology of these three membranes.

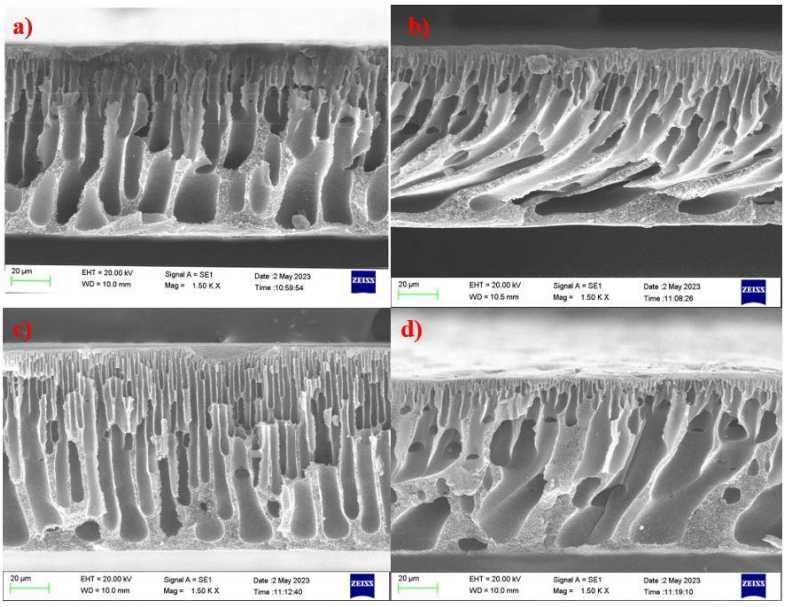

Fig 3: SEM images of the cross section of pure PES and the hybrid membrane containing PES (16%) and various amount of FMWCNTs a) 0%, b) 0.01%, c) 0.025%, d) 0.05%

As can be seen in Fig. 3, all membranes have an asymmetric cross sectional structure in which sponge-like porous substrates support the dense active layer. The comparison between these figures shows that the finger-like macrovoids are shorter in the pure PES compared with hybrid membrane and these finger-like defects don't continue to the surface of the membrane. This phenomenon is probably due to the rapid exchange of solvent and non-solvent in the phase inversion process, considering the hydrophilic nature of FMWCNTs and the mutual effect between components in the polymer solution and the kinetics of phase inversion. Also, as shown, when the amount of FMWCNTs increases, cavity walls begin to form beneath the layer, and the size of the cavities decreases. Additionally, an increase in the viscosity of the PES/FMWCNTs solution delays the exchange of solvent and non-solvent, where both factors (increased hydrophilicity and increased viscosity by adding FMWCNTs) mutually affect the formation of composite membranes [12, 13].

Fig 4 shows the amount of contact angle for pure PES and hybrid membranes containing PES (16%) and different percentages of FMWCNTs. As observed in Fig 4, with an increase in the amount of these nanoparticles in PES (16%), the contact angle decreases, indicating an enhancement in the hydrophilic properties of the membrane due to the increased presence of materials containing hydroxyl (OH), phenol, and carboxylic acid (COOH) functional groups in their structure [14].

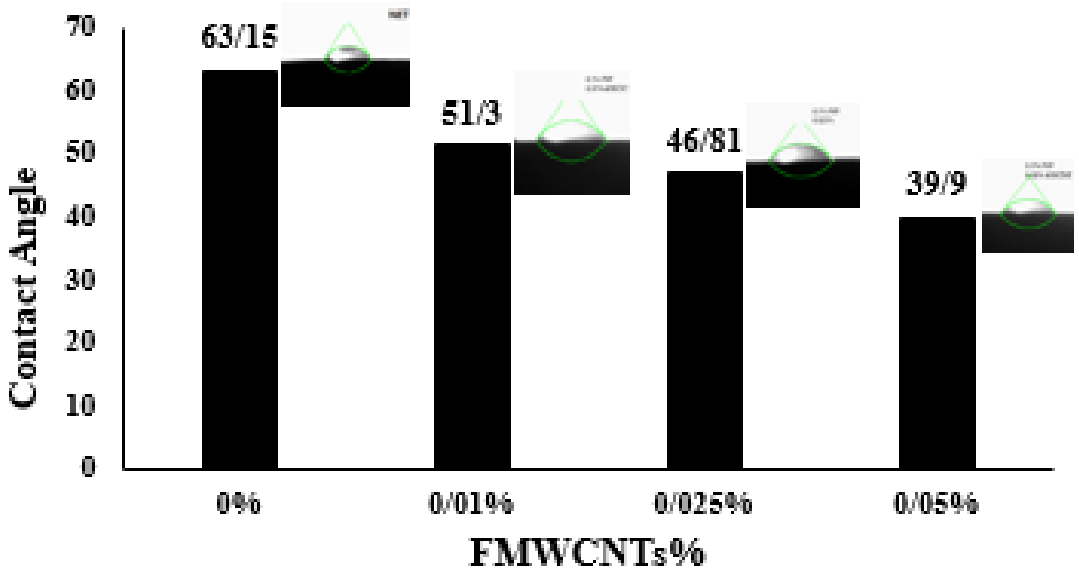

Fig 4: Contact angle images for hybrid membranes containing PES (16%) and different percentages of FMWCNTs

Permeate test

In this experiment, the influence of the amount of FMWCNTs (0.01%, 0.025%, and 0.05% by weight) on the rejection properties and permeate flux of hybrid membranes was investigated. As observed in the contact angle measurement experiment, by adding FMWCNTs to the membrane, the hydrophilic properties of the membrane increase. In fact, the addition of MWCNTs containing functional groups and the hydrogen bonding present in them increase the affinity of the hybrid membrane with water, leading to a faster exchange of solvent and non-solvent during the phase inversion process. Consequently, this results in an increase in pore size and thinning of the active layer in the membrane. Additionally, as shown in Fig. 5, it can be inferred that with an increase in the amount of FMWCNTs in the hybrid membrane, zinc ion rejection increases. Regarding this phenomenon, it can be stated that the negative charge created on the surface of the hybrid membrane, due to the dissociation of functional groups on the surface of FMWCNTs, can cause the electrostatic repulsion of nitrate anions present in the solution (dissolved zinc nitrate), and consequently they don't allow to pass through the membrane. In order to maintain the electrical charge of the solution, zinc ions in the solution are also not allowed to pass through the membrane and remain in the feed solution (based on Donnan effect). Therefore, it leads to an increase in the rejection of zinc ions from the solution[12]. Furthermore, due to anionic functional groups on the surface of FMWCNTs, they have a high ability to sorption various cations, preventing the passage of ions. This factor contributes to increased zinc ion rejection, also.

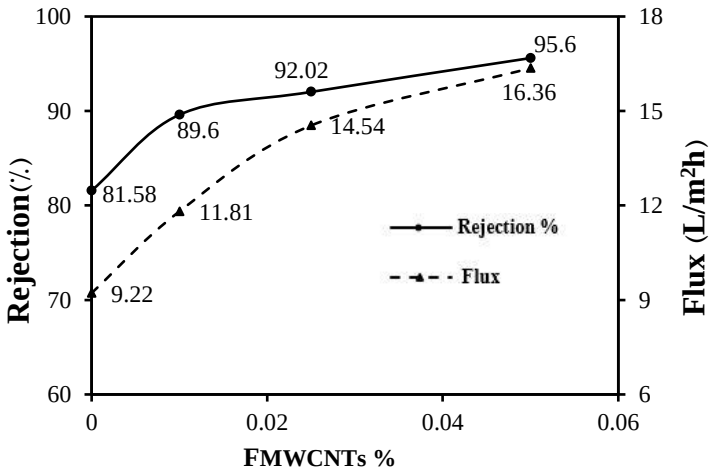

Fig 5: The effect of FMWCNTs on rejection of zinc ion and Flux (In condition [PES%]= 16%, pH=5, T=25 °C, t=30 min, p=12, $[Zn^{2+}]$= 10 ppm

Conclusions

In this study, the process of nanofiltration and the use of flat hybrid membranes containing FMWCNTs were employed for the removal of zinc from the first circuit water of nuclear reactor. The morphology, hydrophilicity,

and the effect of the amount of FMWCNTs on the membrane properties and its performance to removal zinc ions from aqueous solution were investigated. The results indicate that the amount of FMWCNTs plays a crucial role in shaping the membrane morphology and forming a porous structure. As a result, these factors directly affect the ion rejection and permeate flux of the membrane. It was also found that with an increase in the amount of FMWCNTs in membrane, the hydrophilicity of the membranes increases due to the presence of functional groups such as carboxylic, ketone, and phenol. The addition of carbon nanotubes containing functional groups due to the hydrogen bonding present in them, enhances the affinity of the hybrid membrane with water. This leads to an increase in the rate of exchange of solvents and non-solvents during the phase inversion process and an increase in pore size, thinning of the active layer in the membrane, and ultimately, a significant increase in permeate flux. Consequently, zinc ion rejection also increases due to these changes.

References

1. Briffa, J., E. Sinagra, and R. Blundell, *Heavy metal pollution in the environment and their toxicological effects on humans.* Heliyon, 2020. **6**(9).

2. Ferraro, G., et al., *Zinc removal by Chlorella sp. biomass and harvesting with low cost magnetic particles.* Algal research, 2018. **33**: p. 266-276.

3. Tsai, T.-L., et al., *Chemical and radiochemical analysis of corrosion products on BWR fuel surfaces.* Journal of Radioanalytical and Nuclear Chemistry, 2013. **295**: p. 289-296.

4. Ahmad, N.N.R., et al., *Nanofiltration membrane processes for water recycling, reuse and product recovery within various industries: A review.* Journal of Water Process Engineering, 2022. **45**: p. 102478.

5. Pan, Z., et al., *Membrane technology coupled with electrochemical advanced oxidation processes for organic wastewater treatment: Recent advances and future prospects.* Chemical Engineering Journal, 2019. **376**: p. 120909.

6. Huang, J., et al., *Fabrication of polyethersulfone-mesoporous silica nanocomposite ultrafiltration membranes with antifouling properties.* Journal of membrane science, 2012. **423**: p. 362-370.

7. Gugliuzza, A. and A. Basile, *Membrane processes for biofuel separation: An introduction*, in *Membranes for clean and renewable power applications*. 2014, Elsevier. p. 65-103.

8. Yavari, R. and R. Davarkhah, *Application of modified multiwall carbon nanotubes as a sorbent for zirconium (IV) adsorption from aqueous solution.* Journal of Radioanalytical and Nuclear Chemistry, 2013. **298**: p. 835-845.

9. Hosseini, S., et al., *Mixed matrix PES-based nanofiltration membrane decorated by (Fe3O4–polyvinylpyrrolidone) composite nanoparticles with intensified antifouling and separation characteristics.* Chemical Engineering Research and Design, 2019. **147**: p. 390-398.

10. Addo Ntim, S. and S. Mitra, *Removal of trace arsenic to meet drinking water standards using iron oxide coated multiwall carbon nanotubes.* Journal of Chemical & Engineering Data, 2011.

11. Atieh, M.A., et al., *Effect of carboxylic functional group functionalized on carbon nanotubes surface on the removal of lead from water.* Bioinorganic chemistry and applications, 2010. **2010**.

12. Vatanpour, V., et al., *Fabrication and characterization of novel antifouling nanofiltration membrane prepared from oxidized multiwalled carbon nanotube/polyethersulfone nanocomposite.* Journal of membrane science, 2011. **375**(1-2): p. 284-294.

13. Wong, K.K., Z.A. Jawad, and B.L.F. Chin, *A polyethylene glycol (PEG)–polyethersulfone (PES)/multi-walled carbon nanotubes (MWCNTs) polymer blend mixed matrix membrane for CO2/N2 separation.* Journal of Polymer Research, 2021. **28**(1): p. 6.

14. Vatanpour, V., et al., *Novel antibifouling nanofiltration polyethersulfone membrane fabricated from embedding TiO2 coated multiwalled carbon nanotubes.* Separation and purification technology, 2012. **90**: p. 69-82.

ICNST 2024
International Conference on Nuclear Science and Technology
6- 8 MAY 2024 | Isfahan, Iran

Characterization of ThO2 powder at various oxalate precipitation temperatures (Paper ID : 1060)

Narges Bagheri[1], Feryal Nosratinia[1*], Fazel Zahakifar[2*], Taher Yousefi[2]

1. Department of Chemical Engineering, South Tehran Branch, Islamic Azad University, Tehran, Iran.
2. Nuclear Fuel Cycle Research School, Nuclear Science and Technology Research Institute, AEOI, P.O. Box: 11365-8486, Tehran- Iran.

Abstract

Thorium oxide seems to be the most promising nuclear fuel in the near future. Determining its numerous physical and chemical properties is therefore critical. These properties are greatly affected by different preparation conditions. The most common method of producing this fuel is the thermal decomposition of precipitated thorium oxalate. The precipitation temperature is the most significant factor influencing the produced powder and particle characteristics, including the morphology and surface area of the particles, the size of the crystals, and the sinterability of the thorium oxide powder. The synthesis of thorium oxide using the oxalate precipitation method and the analysis of the precipitation temperature impact on ThO_2 have been covered in this work. XRD, SEM, and BET analyses were used for characterization. The particle size varied from 400 nm at low temperature to 1.5 µm at high temperature. As the temperature increased, the morphology of the particles became thinner, larger, and squarer.

Keywords: Thorium oxide powder; Oxalate; Precipitation; Temperature; Nuclear fuel cycle; Characterization.

Introduction

The overall knowledge of the world's thorium resources (reliable, reasonable, and recoverable sources) is significantly lower than that of uranium resources [1]. The nuclear fuel cycle based on thorium dioxide (ThO_2) applies the Th-232 isotope, which produces the fissile nuclide U-233, when thermal neutrons are captured. The present nuclear power industry puts great importance on thorium nuclear fuel and offers it as a U-235 substitute. This is because thorium has a lower coefficient of thermal expansion, a higher melting point, higher thermophysical characteristics, and is more readily available. Compared to UO_2, ThO_2 is more radiation resistant and has greater oxidation stability. When ThO_2 is utilized in conventional light-water reactors, fewer transuranic elements are produced, which results in the non-proliferation of nuclear weapons [2].

Like uranium, thorium is oxidized to be used in nuclear reactors, then converted into pellets and finally used as the fuel [3]. The most common method of producing thorium dioxide from thorium nitrate

solution is the thermal decomposition of its oxalate. Thorium oxalate is precipitated by adding oxalic acid to a solution of thorium nitrate during the following reaction [4]:

$$Th(NO_3)_4 + 2H_2C_2O_4.2H_2O \rightarrow Th(C_2O_4)_2.2H_2O + 4HNO_3 + 2H_2O \quad (1)$$

Thorium oxalate is converted to thorium oxide by thermal decomposition. Although thorium oxide is a resistant material, properties such as its density, chemical activity, morphology, and particle size are dependent on the precipitation conditions of its production unit [5]. The precipitation temperature is one parameter that has a great effect on the properties of the produced powder. Kinoshita and his colleague Aoki [6] investigated the effect of reaction temperature (6, 23, and 50 °C) on the particle size distribution of thorium oxalate powder. It was observed that with increasing precipitation temperature, the size of large particles and the difference in particle size increase. Allred et al. [7] showed that temperature has a very important effect on the size, shape, and specific surface of particles. At low temperatures (10 °C), the size of the crystals is smaller, the specific surface area is larger, and the thickness of the particles increases. At higher temperatures, the particles are larger and thinner. As a result, it is very necessary to investigate and optimize the precipitation temperature affecting the properties of thorium oxide powder, which is also the subject of this article.

Experimental procedure and materials

First, thorium nitrate and oxalic acid (Merck) were weighed to the required amount. Thorium nitrate was mixed with 1.5 M nitric acid to a concentration of 150 g/L, and oxalic acid was mixed with demineralized water to a concentration of 0.8 M. Precipitation was done by dropping oxalic acid solution into thorium nitrate solution slowly, at a rate of 1 mL/min, while it was stirring at 300 rpm. Oxalic acid was used in an additional amount of 20%. The temperature of the digest was set at the same reaction temperature and stirred for 2 hours. The precipitate was separated by filter paper, and the formed cake was washed more times with distilled water. Then it was dried in the oven at 70 ^{o}C for 24 hours. The resulting powder (thorium oxalate) was calcined in air at 5 ^{o}C/min to 700 ^{o}C, with a 4 h dwell in the calcination furnace. Thermal decomposition was performed and thorium oxide powder was obtained.

Characterization

Calcination temperature was determined by thermal gravimetric analysis (TGA) using a Rheometric Scientific model STA-1500 instrument. In order to identify and check the structure of the powder, XRD patterns were performed on a STOE STADI MP diffractometer. Specific surface area, size, and

percentage of powder porosity were determined by BET using a Quantachrome NOVA 2200 analyzer. Scanning electron microscopy (SEM) and energy dispersive X-ray (EDX) analyses were used to determine the elemental composition, structure, and morphology using the ZEISS EVO 18.

Results and discussion

In order to investigate the effect of the precipitation temperature parameter on the thorium oxide powder properties, the precipitation was performed at three temperature levels: 10, 25, and 60 ^{o}C. In order to determine the powder structure, XRD analysis was performed. Figure 1 shows the comparison of the X-ray diffraction pattern of the prepared thorium oxide powder and the reference (Ref. Pattern: thoria, 00-004-0556). A comparison of two spectra shows that the material made is thorium oxide.

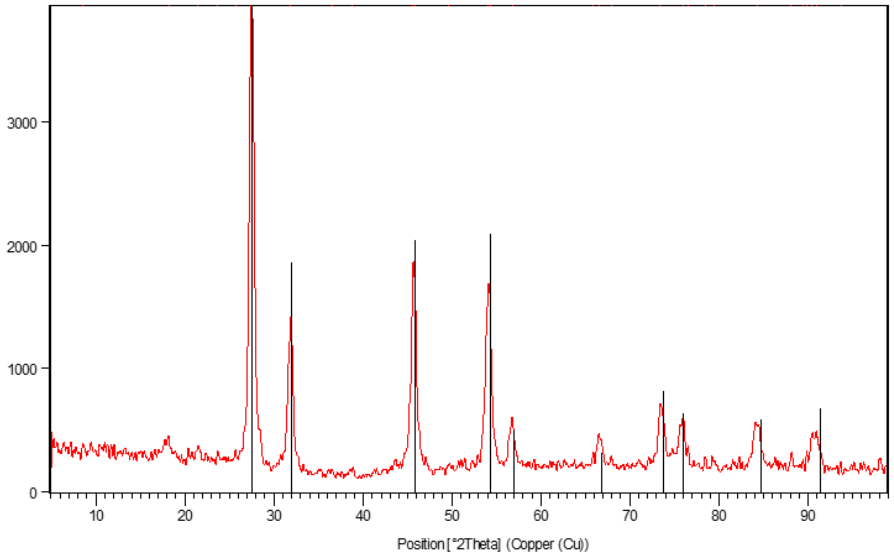

Fig. 1. Comparison of the X-ray diffraction pattern of thorium oxide powder made and reference

SEM images of the prepared powders are shown in Figure 2. The size of the formed thorium oxide crystals decreases with decreasing temperature. The results are shown in Table 1. The average size of particles at temperatures of 10, 25, and 60 ^{o}C is 0.4, 0.7, and 1.5 µm, respectively. The uniformity and thickness of the particles also increase with decreasing temperature. In general, at lower temperatures, the shape of the particles tends to be spherical, which is part of the improving properties of the powder. But agglomeration increases as the particle size becomes smaller. These results were similar to the results presented by Kinoshita and his colleague Aoki [6] and Allred et al. [7].

The porosity measurement of the manufactured samples showed that the specific surface area of particles at temperatures of 10, 25, and 60 ^{o}C was 28.5, 82, and 16.8 m^2/g, respectively. The reason for the

decrease in surface area at high temperatures is the increase in particle size. But the decrease in surface area at low temperatures is due to increased particle agglomeration. The highest surface area was obtained at ambient temperature. This is different from the results presented by Khani et al. [8].

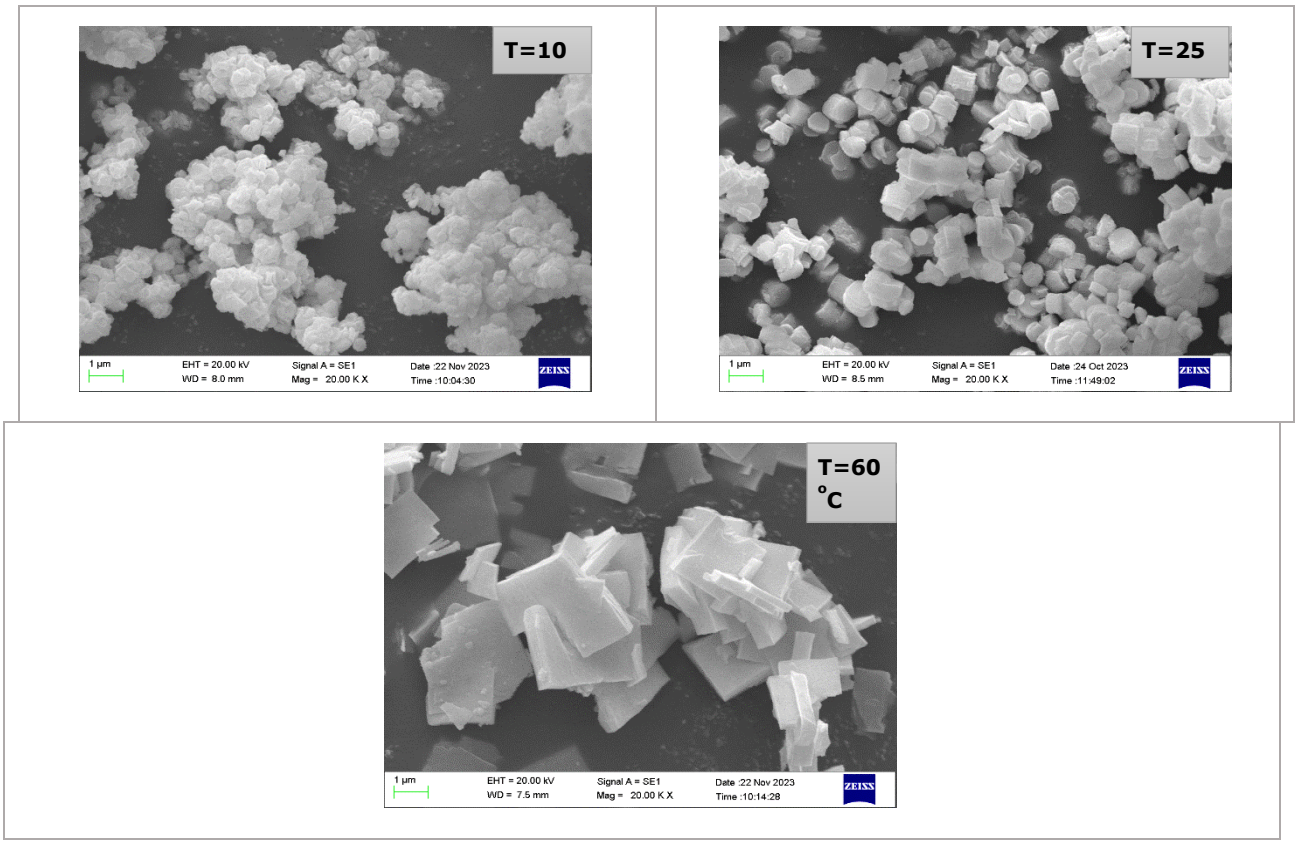

Fig. 2. The morphologies of thorium oxide particles made at different temperatures

Table 1. Characteristics of thorium oxide powder at different temperatures

Average particle size (µm)	Surface area (m^2/g)	Precipitation temperature (°C)
0.4	28.5	10
0.7	82	25
1.5	16.8	60

Conclusions

The synthesis of thorium oxide was done by thermal decomposition of thorium oxalate. In order to investigate the effect of the precipitation temperature parameter, this process was carried out at three temperature levels of 10, 25, and 60 °C. Several analyses' findings indicated that while average particle size decreases with decreasing temperature, but agglomeration increases. Therefore, the maximum surface area was obtained at an ambient temperature equal to 82 m^2/g. It is also observed that with

decreasing temperature, the particle thickness increased and the shape of the particles changed from flat and cubic to spherical.

References

[1] P. Hart, C. Griffin, K. Hsieh, R. Matthews, and G. White, (1979), "ThO_2-based pellet fuels-their properties, methods of fabrication, and irradiation performance: a critical assessment of the state of the technology and recommendations for further work,".

[2] O. Shichalin et al., (2020), "Synthesis and spark plasma sintering of microcrystalline thorium dioxide for nuclear fuel products," Russian Journal of Inorganic Chemistry, vol. 65, pp. 1245-1252.

[3] S. A. AllahYari, "Experimental investigation and modeling of thorium (IV) extraction process by hollow fiber liquid membrane (HFRLM)," Ph.D, Beheshti, 2016.

[4] R. d'Eye and P. Sellman, (1955), "The thermal decomposition of thorium oxalate," Journal of Inorganic and Nuclear Chemistry, vol. 1, no. 1-2, pp. 143-148.

[5] T. Wangle et al., (2017), "The effect of precipitation and calcination parameters on oxalate derived ThO_2 pellets," Journal of Nuclear Materials, vol. 495, pp. 128-137.

[6] H. Kinoshita and S. Aoki, (1964), "FABRICATION OF THORIUM OXIDE FUEL ELEMENT. I. THERMAL DECOMPOSITION OF THORIUM OXALATE AND PARTICLE SIZE GROWTH OF THORIUM OXIDE BY HEATING," Furukawa Electric Co., Ltd., Japan.

[7] V. Allred, S. Buxton, and J. McBride, (1957), "Characteristic Properties of Thorium. Oxide Particles," The Journal of Physical Chemistry, vol. 61, no. 1, pp. 117-120.

[8] A. A. G. K. M.H. Khani, (2018) "Investigating parameters affecting the size and size distribution of thorium oxalate precipitate particles in a stirred reactor," Iranian Chemical Engineering Journal, vol. 17, no. 99, p. 10.

ICNST 2024
International Conference on Nuclear Science and Technology
6- 8 MAY 2024 | Isfahan, Iran

The effect of processes parameter on thorium oxide powder properties: a case study of metal concentration (Paper ID : 1061)

Narges Bagheri[1], Feryal Nosratinia[1*], Fazel Zahakifar[2*], Taher Yousefi[2]
1. Department of Chemical Engineering, South Tehran Branch, Islamic Azad University, Tehran, Iran.
2. Nuclear Fuel Cycle Research School, Nuclear Science and Technology Research Institute, AEOI, P.O. Box: 11365-8486, Tehran- Iran.

Abstract

Despite the numerous benefits of thorium oxide over uranium oxide as a nuclear fuel, much less attention has been paid to it, and therefore the nuclear data published about it is very limited. Recently, the tendency to use this fuel has increased. The conditions of synthesis have a significant impact on the properties of thorium oxide. In this study, the effect of metal concentration on thorium oxide has been investigated using the oxalate precipitation method. The size, surface area, and morphology of the powder particles were determined by XRD (X-ray diffraction), SEM (scanning electron microscopy), and BET (Brunauer-Emmett-Teller) analyses. At low metal concentrations, the particles were in the form of thin hexagons, and the particle size was large. With the increase in metal concentration, the thickness of the particles increased and became close to spherical, and the size of the particles decreased. Also, the specific surface area rose with increasing concentrations of thorium nitrate.

Keywords: Nuclear fuel; Thorium Oxide; Characterization; Concentration; Synthesis.

Introduction

Since the beginning of the discovery and use of nuclear energy, uranium has been the primary material used. [1]. In recent years, the use of thorium has significantly increased due to its advantages over uranium, including 3 to 4 times more abundance, higher thermal-chemical properties and chemical resistance, less production of nuclear waste, no application in making nuclear weapons, and no requirement for complex and costly enrichment and separations [2].

The main method of preparing thorium oxide from aqueous solutions is the thermal decomposition of oxalate [3]. The crystalline thorium oxalate that precipitates from thorium nitrate solution is easily washed, filtered, and distributed as a slurry. Particle properties are determined by precipitation conditions [4]. Kanno et al. [5] used the two techniques of thorium hydroxide and thorium oxalate precipitation to create ThO_2 fuel powder. Both precipitates were filtered and calcined. They reported that ThO_2 produced from oxalate has better properties, including higher sinterability [6].

ThO_2 production by the method of thorium oxalate precipitation generally includes the following units [7,8]:

1. Precipitation (thorium oxalate production by the reaction of thorium nitrate with oxalic acid)

2. Digest

3. Filtration and drying

4. Calcination or thermal decomposition (thorium oxide production) [9]

Every step mentioned has its own effect on the quality of the produced oxide [10]. The properties of thorium oxide powder vary depending on the different control parameters during the primary stages of precipitation and decomposition [4]. One of the important factors is the initial thorium nitrate concentration. Tyrpekl et al. [11] showed that the metal concentration in the feed solutions affects the morphology, especially in very dilute cases where low saturation and atomic diffusion are expected to control crystal growth. According to Khani et al.'s report [12], the effect of thorium nitrate concentration and flow rate on thorium powder obtained from oxalate precipitation is the same, and with the increase of these two variables, the particle size decreases and uniformity increases. Hart et al. [4] showed that increasing the concentration of thorium nitrate decreases the particle size and increases the surface area. In general, increasing the concentration of thorium solution has been introduced as a favorable parameter to reduce the particle size, increase the surface area, and approach the spherical shape of the particles. In this article, the effect of thorium nitrate concentration on the final properties of thorium oxide produced by thermal decomposition of thorium oxalates has been investigated and examined.

Experimental

2.1. Materials

The materials used included thorium nitrate and oxalic acid, purchased from Merck, Germany.

2.2. Laboratory equipment

A digital scale, stirrer, furnace, oven, Eppendorf sampler, and other laboratory glassware such as a pipette, beaker, Erlenmeyer flask, graduated cylinder, burette, balloon, etc. were among the tools utilized in the lab.

2.3. Characterization

Calcination temperature was determined by thermal gravimetric analysis (TGA) using a Rheometric Scientific model STA-1500 instrument. In order to identify and check the structure of the powder, XRD patterns were performed on a STOE STADI MP diffractometer. Specific surface area, size, and percentage of powder porosity were determined by BET using a Quantachrome NOVA 2200 analyzer. Scanning electron microscopy (SEM) and energy dispersive X-ray (EDX) analyses were used to determine the elemental composition, structure, and morphology using the ZEISS EVO 18.

Experimental procedure

First, thorium nitrate was prepared at a determined concentration and with an acidity of 1.5 M. Precipitation was done by dropping oxalic acid solution (0.8 M) into thorium nitrate solution slowly, at a rate of 1 mL/min, while it was stirring at 300 rpm. Oxalic acid was used in an additional amount of 20%. The resulting slurry stirred for 2 hours. Then precipitate was separated by filter paper, and the formed cake was washed more times with distilled water. Then it was dried in the oven at 70 ^{o}C for 24 hours. The resulting powder (thorium oxalate) was calcined in air at 5 ^{o}C/min to 700 ^{o}C, with a 4 h dwell in the calcination furnace. Thermal decomposition was performed and thorium oxide powder was obtained.

Results and discussion

In order to investigate the effect of thorium nitrate concentration on the produced thorium oxide, precipitation was done with three different concentrations of thorium nitrate: 6, 75, and 150 g/L. According to XRD analysis and comparison with the reference range, the product is thorium oxide. SEM images showed the difference in morphology, particle size, and particle thickness, which is shown in Figure 1.

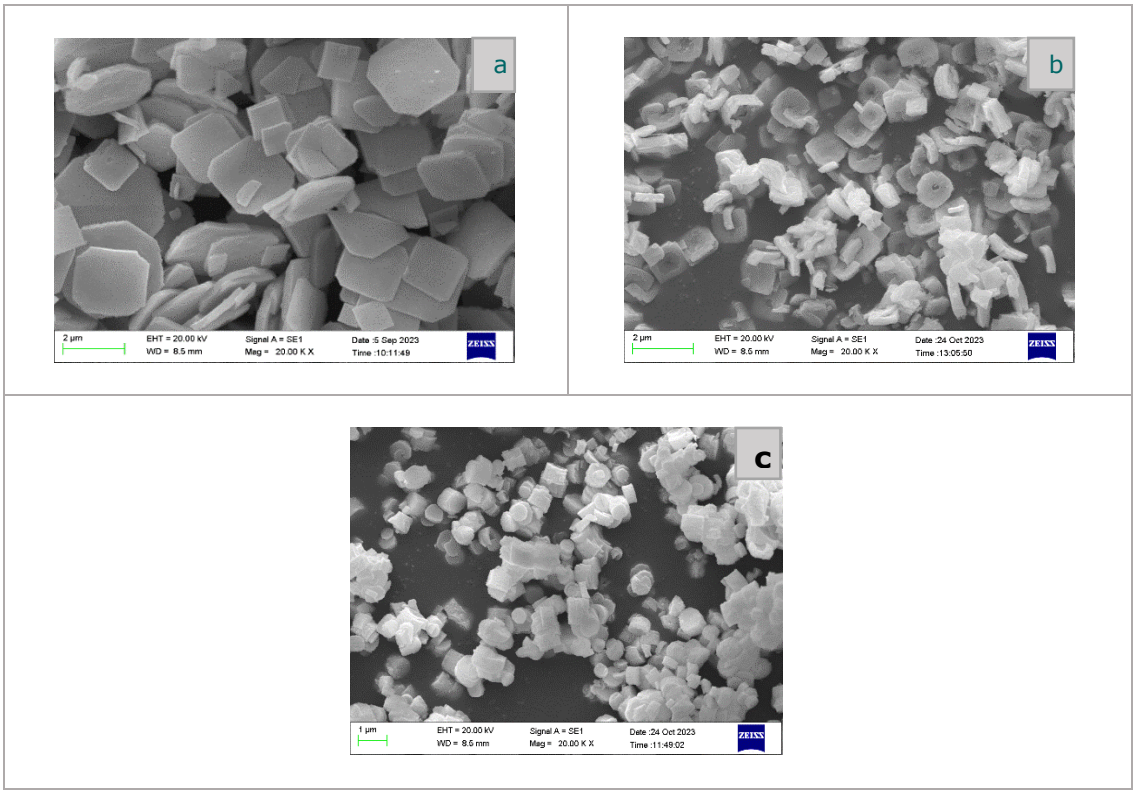

Fig. 1. Images from scanning electron microscope of thorium oxide produced at three different thorium nitrate concentrations: a: 6 g/L, b: 75 g/L, and c: 150 g/L.

As shown in Figure 1, with increasing thorium nitrate concentration, the average size of the thorium oxide particles decreases while the particle uniformity increases. According to Table 1, the average particle size increases from 2 µm in low concentrations to 0.7 µm in high concentrations. The thickness of the particles also increases with the increase in metal concentration, and their shape changes from plates to spherical cylinders. Spherical particles move more easily and fill the molds. This improves the flowability of the powder.

The powder's porosity measurement (BET) indicates that the surface area of the thorium oxide particles increases as the concentration of thorium nitrate increases. The surface area increases from 34 m^2/g at low concentrations to 82 m^2/g at high concentrations, as Table 1 illustrates. Along with the increase in concentration came an increase in the pores' diameter and volume. These findings confirm the results of Tyrpekl et al. [11] and Hart et al. [4] research.

Table 1. Characteristics of produced thorium oxide powders

Thorium nitrate concentration (g/L)	Surface area (m^2/g)	Average particle size (µm)	Pore diameter (nm)	Pore volume (cc/g)
6	34	2	2.456	0.041
75	63	1	2.73	0.083
150	82	0.7	3.06	0.109

Conclusions

In order to investigate the effect of thorium nitrate concentration on the thorium oxide, the metal concentration was determined at three levels of 6, 75, and 150 g/L using the method of oxalate thermal decomposition. The characterization results demonstrated that increasing the thorium nitrate concentration can reduce the size of the particles, increase the thickness, and change the shape of the particles from flat to spherical. The particle size changed from 2 microns in low concentrations to 0.7 microns in high concentrations. These changes caused an increase in the specific surface area, size pore, and diameter pore of the particles.

References

[1] J. Belle and R. Berman, (1984), "Thorium dioxide: properties and nuclear applications," USDOE Assistant Secretary for Nuclear Energy, Washington, DC. Office of ….

[2] V. K. Manchanda, (2023), "Thorium as an abundant source of nuclear energy and challenges in separation science," Radiochimica Acta, vol. 111, no. 4, pp. 243-263.

[3] V. Tyrpekl, J.-F. Vigier, D. Manara, T. Wiss, O. D. Blanco, and J. Somers, (2015), "Low temperature decomposition of U (IV) and Th (IV) oxalates to nanograined oxide powders," Journal of Nuclear Materials, vol. 460, pp. 200-208.

[4] P. Hart, C. Griffin, K. Hsieh, R. Matthews, and G. White, (1979), "ThO_2-based pellet fuels-their properties, methods of fabrication, and irradiation performance: a critical assessment of the state of the technology and recommendations for further work".

[5] M. Kanno, S. Kokubo, and H. Furuya, (1982), "Preparation of thorium-uranium mixed oxide pellets," Journal of Nuclear Science and Technology, vol. 19, no. 11, pp. 956-958.

[6] S. Mishra, J. Banerjee, and J. P. Panakkal, "Fabrication of Nuclear Fuel Elements, (2023)," in Nuclear Fuel Cycle: Springer, pp. 81-116.

[7] A. Alemayehu, A. Zakharanka, and V. Tyrpekl, (2022), "Homogeneous Precipitation of Lanthanide Oxalates," ACS omega, vol. 7, no. 14, pp. 12288-12295.

[8] T. Wangle, (2020), "Morphology dependent sintering path of nanocrystalline ThO_2," Journal of Nuclear Materials, vol. 533, p. 152081.

[9] K. Johnsson and R. Winget, (1959), "Pilot Plant Preparation of Thorium-And Thorium-Uranium Oxides," Oak Ridge National Lab., Tenn.

[10] L. Argo, (2003), "Experimental determination of the dry oxidation behavior of a compositional range of Uranium-Thorium mixed-oxide pellet fragments," University of Florida.

[11] V. Tyrpekl, M. Beliš, T. Wangle, J. Vleugels, and M. Verwerft, (2017), "Alterations of thorium oxalate morphology by changing elementary precipitation conditions," Journal of Nuclear Materials, vol. 493, pp. 255-263.

[12] A. A. G. K. M.H. Khani, (2018), "Investigating parameters affecting the size and size distribution of thorium oxalate precipitate particles in a stirred reactor," Iranian Chemical Engineering Journal, vol. 17, no. 99, p. 10.

ICNST 2024
International Conference on Nuclear Science and Technology
6- 8 MAY 2024 | Isfahan, Iran

The reduction of uranium (VI) to (IV) for uranium oxalate precipitation (Paper ID : 1062)

Narges Bagheri[1], Feryal Nosratinia[1*], Fazel Zahakifar[2*], Taher Yousefi[2]

1. Department of Chemical Engineering, South Tehran Branch, Islamic Azad University, Tehran, Iran.
2. Nuclear Fuel Cycle Research School, Nuclear Science and Technology Research Institute, AEOI, P.O. Box: 11365-8486, Tehran- Iran.

Abstract

Oxalate precipitation is a conventional and accepted method for the production of actinide oxides. In this method, oxalic acid is added to tetravalent actinide nitrate, and oxalate is precipitated. After filtration, washing, and drying, the resulting precipitate is calcined at a suitable temperature, and actinide oxide is obtained. But its use for the synthesis of non-tetravalent actinides such as uranium (VI) requires a reduction step as well. For this reason, despite its many advantages, including high efficiency, no need for advanced equipment, and making a desirable product, this method has received less attention in uranium oxide production. In this research, uranium oxide was synthesized using this method. Hydrazine and platinum oxide are used for the reduction of uranium (VI) to (IV). SEM and BET analyses showed that the morphology of the particles was cubic without agglomeration. The size of the particle was 1 µm, and the specific surface area was 70 m^2/g.

Keywords: Uranium oxide; Nuclear fuel cycle; Powder; Oxalate; Characterization; Hydrazine.

Introduction

The behavior of the nuclear fuel is determined by the sintered pellet's density, grain size, and porosity structure. Grain structure affects both the mechanical properties and the rate of fission products exit the nuclear fuel pellet during reactor operation. The pellet quality obviously depends on the characteristics of the powder, which are determined by the powder preparation process [1]. Therefore, choosing the correct method of powder synthesis will be very effective on the quality of nuclear fuel.

Although inorganic or metal-organic precursors have long been used to prepare actinide oxides, recent studies have looked at the advantages of using oxalate precursors [2]. One commonly used technique in this field is the synthesis of oxides by metal ion precipitation using oxalic acid, followed by calcination of the precipitate produced. One of the primary benefits of this process is that it allows for precise control over the final oxide's physical properties by optimizing heat treatment and precipitation [3]. In actuality, a wide range of operating parameters, including temperature, ionic strength, impurity presence, hydrodynamics, and others, have a significant impact on precipitation reactions [4]. This process allows

actinides with various oxidations to be combined simultaneously and precipitates cations from aqueous mixtures quickly and uniformly. Furthermore, the corresponding oxides are easily obtained through a thermal conversion step. In addition, the limited number of steps in this method leads to easy implementation on an industrial scale [5].

Precipitation of uranium oxalate $U(C_2O_4)_2.6H_2O$ is done by mixing uranium nitrate solution, nitric acid, and hydrazine with oxalic acid solution:

$$U^{4+} + 2C_2O_4^{2-} \rightarrow U(C_2O_4)_2.6H_2O \quad (1)$$

Aqueous solutions of tetravalent hydrated U(IV) uranium are stable if their acidity is high enough (for example, HNO_3 with a concentration of 0.5 M) to prevent the formation of U(VI), and if reducing agents (such as hydrazine) are added, they can be stable effectively [2].

After the precipitation step, the resulting uranium oxalate is converted to uranium oxide by thermal decomposition. Desfougeres et al. [3] studied and investigated the decomposition of hexahydrate uranium oxalate $U(C_2O_4)_2 \cdot 6H_2O$ under an oxidizing atmosphere (a He/O_2 mixture with a volume ratio of 75/25). They showed that the physical and chemical changes that take place during the thermal decomposition of metal oxalates can be significantly influenced by the type and oxidation state of the metal cation, the calcination atmosphere (involved gas), and the physical properties of the precursor powder (especially particle size and porosity). Martinez et al. [6], prepared UO_2 powders from $U(C_2O_4)_2 \cdot 2H_2O$ in order to study the effect of several parameters related to the precursor on the sintering process and subsequently on the pellet structure. Manaud et al. [5] also investigated the hydrothermal conversion of uranium oxalate $U(C_2O_4)_2.nH_2O$ to uranium oxides. The synthesis, characterization, and property description of uranium oxide powder were covered in this study using the thermal decomposition of uranium oxalates method.

Experimental

2.1. Materials

The materials used included uranium nitrate, nitric acid, hydrazine, platinum oxide, and oxalic acid, products of Merck, Germany.

2.2. Laboratory equipment

A digital scale, stirrer, furnace, oven, pH meter, Eppendorf sampler, and other laboratory glassware such as a pipette, beaker, Erlenmeyer flask, graduated cylinder, burette, balloon, etc. were among the tools utilized in the lab.

2.3. Characterization

Calcination temperature was determined by thermal gravimetric analysis (TGA) using a Rheometric Scientific model STA-1500 instrument. In order to identify and check the structure of the powder, XRD patterns were performed on a STOE STADI MP diffractometer. Specific surface area, size, and percentage of powder porosity were determined by BET using a Quantachrome NOVA 2200 analyzer. Scanning electron microscopy (SEM) and energy dispersive X-ray (EDX) analyses were used to determine the elemental composition, structure, and morphology using the ZEISS EVO 18.

2.4. Experimental procedure

First, solutions of uranium nitrate with a concentration of 100 g/L and oxalic acid with a concentration of 0.8 M were prepared. The reduction of U(VI) to U(IV) was done by adding hydrazine and nitric acid to uranium nitrate solution and using platinum oxide as a catalyst. The solution is allowed time before precipitation to finish the uranium reduction step. After 24 hours, platinum oxide was separated from the solution by filtration. Precipitation was done by dropping oxalic acid solution into uranium nitrate solution slowly, at a rate of 1 mL/min, while it was stirring at 300 rpm. Oxalic acid was used in an additional amount of 20%. The resulting slurry stirred for 2 hours. Then precipitate was separated by filter paper, and the formed cake was washed more times with distilled water. Then it was dried in the oven at 70 ^{o}C for 24 hours. The resulting powder (uranium oxalate) was calcined in air at 5 ^{o}C/min to 700 ^{o}C, with a 4 h dwell in the calcination furnace. Thermal decomposition was performed and uranium oxide powder was obtained.

Results and Discussion

TG analysis was used to determine the calcination temperature. The corresponding curve is shown in Figure 1. The process of uranium oxalate decomposition occurs in three stages. First, free water molecules are evaporated at a temperature of 50 to 100 ^{o}C, and dihydrate is produced. At a temperature of 100 to 200 °C, two water molecules are released, and anhydrous oxalate is formed. In the last stage,

CO and CO_2 are released, and UO_2 is produced. The total mass reduction of uranium nitrate in thermal decomposition is about 30%. According to Figure 1, thermal decomposition is completed at 700 °C, so this temperature was chosen for calcination.

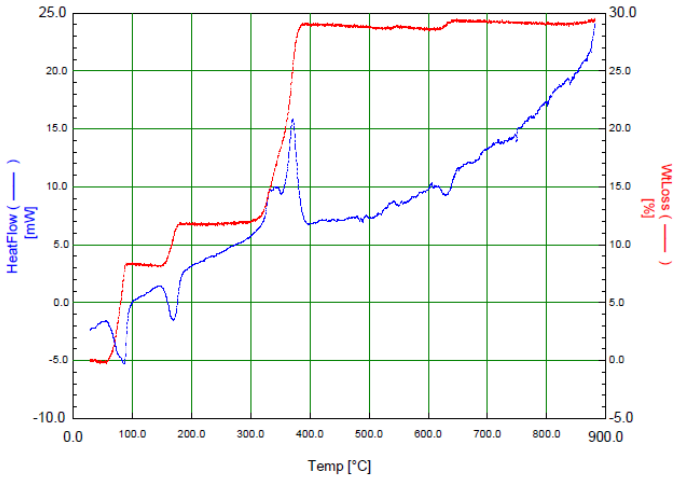

Fig. 1. TGA curve of uranium oxalate powder

XRD analysis of uranium oxide powder and comparison with the reference spectrum showed that the production material is uranium oxide. The results of SEM analysis (Figure 2) showed that a homogeneous product with cubic particles and an average particle size of 1 micron was produced.

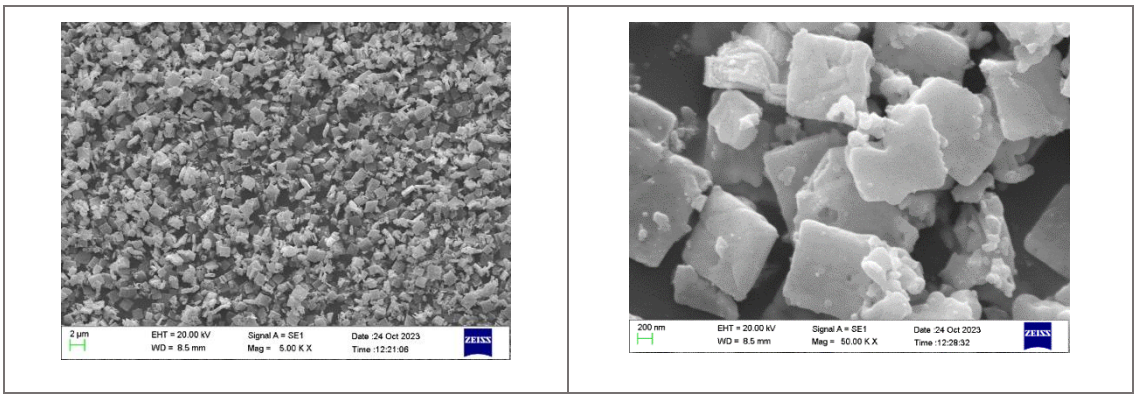

Fig. 2. SEM images of manufactured uranium oxide powder

The powder porosity was measured by BET analysis and showed that the particles have low agglomeration, the specific surface area is 70 m^2/g, the pore volume is 0.082 cc/g, and the pore diameter is 2.455 nm. The properties of the produced powder are presented in Table 1.

Table 1. Characteristics of produced uranium oxide powders

Average particle size (µm)	Surface area (m2/g)	Pore diameter (nm)	Pore volume (cc/g)
1	70	2.455	0.082

Conclusions

Uranium was precipitated from nitrate solution by oxalic acid, and uranium oxide powder was obtained using thermal decomposition of the formed precipitate. In this method, in order to react and precipitate uranium with oxalic acid, it is necessary to reduce U(VI) to U (IV). For this purpose, hydrazine and platinum oxide were used. The produced product is a homogeneous powder with a particle size of 1 micron, without agglomeration, a surface area of 70 m^2/g, and a cubic morphology. These results show the high quality of the oxide powder produced by the oxalate precursor.

References

[1] S. Beigi, M. A. Sobati, and A. Charkhi, (2016), "Drying kinetics of thorium oxalate: experimental investigation and modeling," Progress in Nuclear Energy, vol. 88, pp. 240-244.

[2] F. Abraham, B. Arab-Chapelet, M. Rivenet, C. Tamain, and S. Grandjean, (2014), "Actinide oxalates, solid state structures and applications," Coordination Chemistry Reviews, vol. 266, pp. 28-68.

[3] L. Desfougeres et al., (2020), "Oxidation as an early stage in the multistep thermal decomposition of uranium (IV) oxalate into U3O8," Inorganic Chemistry, vol. 59, no. 12, pp. 8589-8602.

[4] M. Bertrand, E. Plasari, O. Lebaigue, P. Baron, N. Lamarque, and F. Ducros, (2012), "Hybrid LES–multizonal modelling of the uranium oxalate precipitation," Chemical engineering science, vol. 77, pp. 95-104.

[5] J. Manaud et al., (2020), "Hydrothermal conversion of uranium (IV) oxalate into oxides: a comprehensive study," Inorganic Chemistry, vol. 59, no. 5, pp. 3260-3273.

[6] J. Martinez et al., (2015), "From uranium (IV) oxalate to sintered UO2: Consequences of the powders' thermal history on the microstructure," Journal of the European Ceramic Society, vol. 35, no. 16, pp. 4535-4546.

ICNST 2024
International Conference on Nuclear Science and Technology
6- 8 MAY 2024 | Isfahan, Iran

Production of uranium-thorium mixed oxide by co-precipitation method (Paper ID : 1063)

Narges Bagheri[1], Feryal Nosratinia[1*], Fazel Zahakifar[2*], Taher Yousefi[2]

1. Department of Chemical Engineering, South Tehran Branch, Islamic Azad University, Tehran, Iran.
2. Nuclear Fuel Cycle Research School, Nuclear Science and Technology Research Institute, AEOI, P.O. Box: 11365-8486, Tehran- Iran.

Abstract

Thorium fuels are typically used as mixed fuels with uranium or plutonium due to their characteristics and the requirement for a fissile element nearby. The main problem in the production of mixed fuels is the lack of homogeneity. One beneficial method for creating homogenous mixed fuels is co-precipitation. The main advantage of this method is the very high quality of the produced nanomaterials. It does not require advanced equipment, and its mechanism is simple. At first, mineral salts such as nitrate or sulfate of metals are combined in the desired ratio, and then the precipitating agent (such as oxalic acid, ammonia, or ammonium hydroxide) is added for simultaneous precipitation. The mixed oxide is obtained after the calcination of the resulting precipitation. Information about uranium-thorium mixed oxide using this method is limited. In this study, using the co-precipitation method of mixed oxalates, ThO_2-30%UO_2 (wt%) was produced. XRD, SEM, and BET analyses were used to characterize the properties of the produced powder, which indicated a specific surface area of 21 m^2/g and a particle size of 1 µm.

Keywords: Mixed oxide; Uranium; Thorium; Co-precipitation; Hydrazine; Characterization.

Introduction

The homogenous distribution of the constituent metals is an important point to be studied in the manufacture of mixed oxide (MOX) fuels, such as (Pu,U)O_2 and (Th,^{233}U)O_2, because it relates to fuel safety and reliability [1, 2]. (Th-U)O_2 pellets are traditionally made by the powder metallurgy method, which is obtained by combining ThO_2 and UO_2 powders, followed by grinding, compression, and sintering at a temperature of about 1700°C [3]. The presence of fissile-rich regions in a pellet affects fuel performance because these regions act as hot spots, increasing the temperature and releasing more fission gases at that point [4]. Among the various methods, co-precipitation provides an excellent method for creating a mixture that is highly homogeneous. This method has several advantages: it produces very little radioactive dust due to its wet process, homogeneous component distribution, small and uniform

particle size, weak particle agglomeration, low cost, industrial method, and easy access to inexpensive reagents that restrict access to pure plutonium or other fissile actinides [1, 5, 6].

Argo [7] prepared pellets of ThO_2-20%UO_2, ThO_2-35%UO_2, and ThO_2-50%UO_2 (wt%) by the co-precipitation method. Kutty et al. [6] synthesized ThO_2-30%UO_2 and ThO_2-50%UO_2 (wt%) powders by this method and characterized them in terms of particle size, particle shape, surface area, phase content, O/M ratio, etc. Atlas et al. [8] prepared ThO_2-20wt%UO_2 pellets by co-precipitating mixed oxalate from nitrate solutions with the addition of oxalic acid. Various parameters that might affect the powder's properties were investigated.

In this study, co-precipitation method was used to synthesize and characterize ThO_2-30%UO_2 (wt%) powder and to determine its properties.

Experimental

2.1. Materials

The materials used included uranium nitrate, thorium nitrate, nitric acid, hydrazine, platinum oxide, and oxalic acid, products of Merck, Germany.

2.2. Laboratory equipment

A digital scale, stirrer, furnace, oven, Eppendorf sampler, and other laboratory glassware such as a pipette, beaker, Erlenmeyer flask, graduated cylinder, burette, balloon, etc. were among the tools utilized in the lab.

2.3. Characterization

Calcination temperature was determined by thermal gravimetric analysis (TGA) using a Rheometric Scientific model STA-1500 instrument. In order to identify and check the structure of the powder, XRD patterns were performed on a STOE STADI MP diffractometer. Specific surface area, size, and percentage of powder porosity were determined by BET using a Quantachrome NOVA 2200 analyzer. Scanning electron microscopy (SEM) and energy dispersive X-ray (EDX) analyses were used to determine the elemental composition, structure, and morphology using the ZEISS EVO 18.

2.4. Experimental procedure

In the initial step, a solution of uranium nitrate with a concentration of 100 g/L and an acidity of 1.5 M was made using nitric acid. The reduction of U(VI) to U(IV) was done by adding hydrazine and using platinum oxide as a catalyst. After 24 hours, platinum oxide was separated from the solution by filtration. Next, equal volumes of uranium nitrate solution and thorium nitrate solution were combined. The thorium nitrate solution had an acidity of 1.5 M and a concentration of 150 g/L.

Precipitation was done by dropping oxalic acid (0.8 M) solution into uranium-thorium nitrate solution slowly, at a rate of 1 mL/min, while it was stirring at 300 rpm. Oxalic acid was used in an additional amount of 20%. The resulting slurry stirred for 2 hours. Then precipitate was separated by filter paper, and the formed cake was washed more times with distilled water. Then it was dried in the oven at 70 ^{o}C for 24 hours. The resulting powder (uranium-thorium oxalate) was calcined in air at 5 ^{o}C/min to 700 ^{o}C, with a 4 h dwell in the calcination furnace. Thermal decomposition was performed and uranium-thorium oxide powder was obtained.

Results and discussion

The co-precipitation technique was used to synthesize uranium-thorium mixed oxide. TG analysis was used to determine the calcination temperature. XRD analysis showed the presence of the dominant phase (Th-U)O_2 and a small amount of U_3O_8. (Figure 1). This was similar to the results presented by Kutty et al. [6]. The results of EDX analysis indicated the presence of uranium to thorium oxide in a 30% weight ratio (Figure 2).

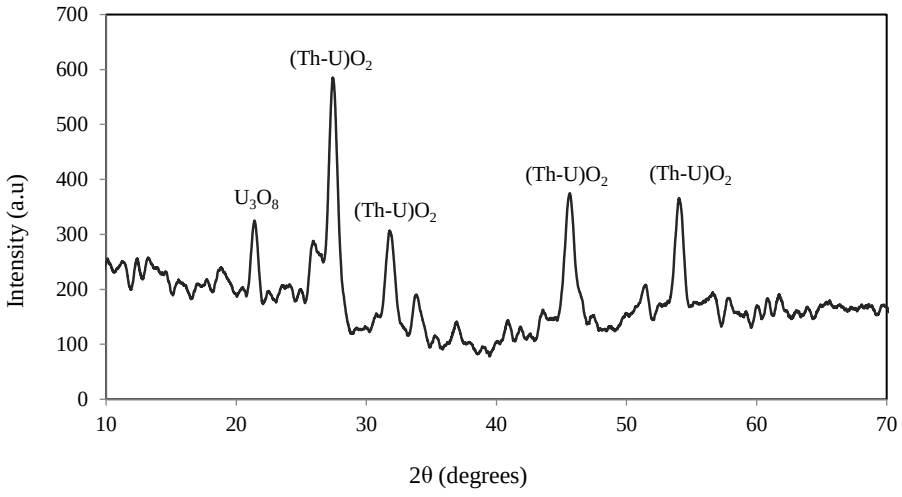

Fig. 1. XRD analysis results of produced uranium-thorium oxide powder

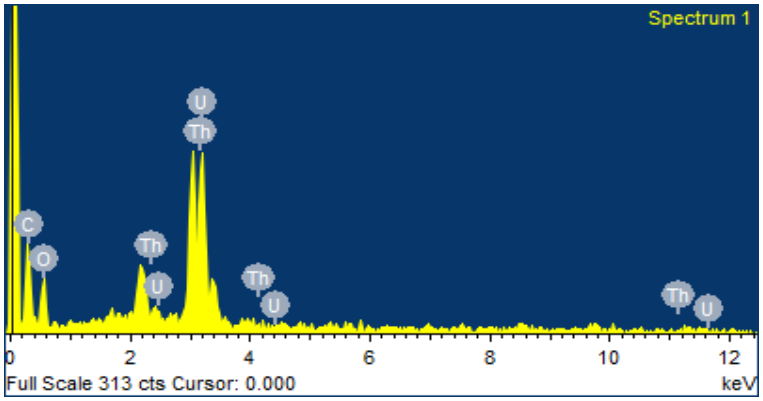

Fig. 2. EDX analysis results of produced uranium-thorium oxide powder

According to the SEM analysis results (Table 1 and Figure 3), the average particle size was 1 micron, and their average thickness was 200 nm. Particle morphology was cubic and relatively uniform. Based on the powder porosity measurement results, particle agglomeration was found to be minimal, with a specific surface area of 21 m^2/g, a pore volume of 0.04 cc/g, and a pore diameter of 6.1 nm.

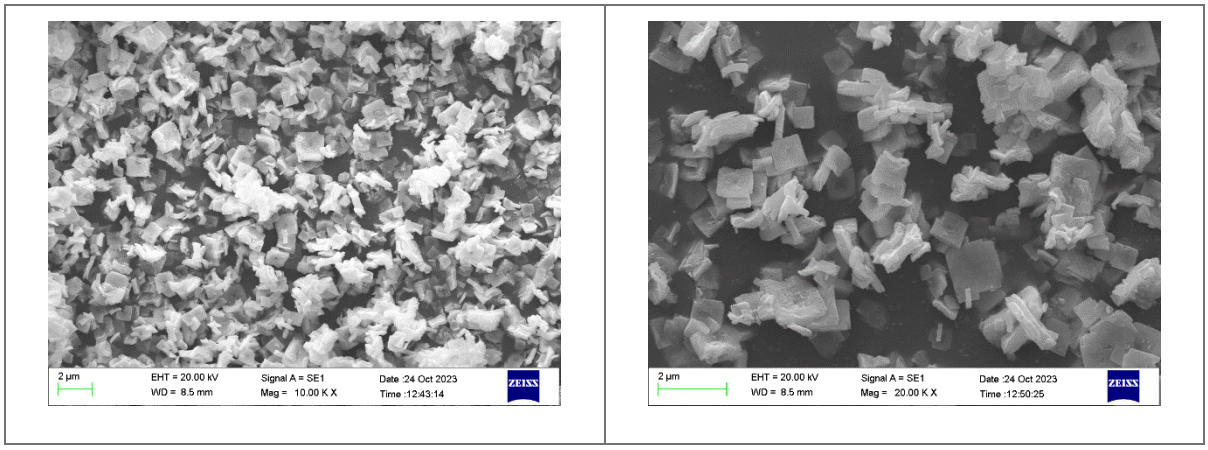

Fig. 3. SEM images of produced uranium-thorium oxide powder

Table 1. Characteristics of produced uranium-oxide powder

Average particle size (µm)	Surface area (m^2/g)	Pore diameter (nm)	Pore volume (cc/g)
1	21	6.1	0.04

Conclusions

ThO_2-30%UO_2 (wt%) powder was synthesized using the co-precipitation method, which has many advantages for producing mixed oxide powder fuels. In order to react and precipitate uranium with oxalic acid, it is necessary to reduce U(VI) to U (IV). For this purpose, hydrazine and platinum oxide were used. Finally, uranium-thorium oxide powder was obtained using the thermal decomposition of the precipitate oxalates. Characterization and analysis results demonstrated the production of a

homogeneous powder with a low agglomeration percentage, a cubic and relatively regular morphology, relatively small particles (size of 1 micron), and a specific surface area of 21 m^2/g. The production of very little radiotoxic dust and the precipitation reaction at ambient temperature were the main advantages of this method.

References

[1] P. D. Wilson, (1996), "The nuclear fuel cycle from ore to wastes,".

[2] J. Kennedy, D. Keiser, M. Lambregts, and S. Frank, (2004), "Advances for Future Nuclear Fuel Cycles," Atalante, France, June, pp. 21-24.

[3] D. R. Olander, (1976), "Fundamental aspects of nuclear reactor fuel elements: solutions to problems," California Univ., Berkeley (USA). Dept. of Nuclear Engineering.

[4] B. Lee, Y. Koo, and D. Sohn, (2001), "Nuclear Fuel Behaviour Modelling at High Burnup and its Experimental Support," IAEA-TECHDOC-1233, IAEA, Vienna.

[5] H. Bairiot et al., (2003), "Status and advances in mox fuel technology," Technical Report Series-International Atomic Energy Agency, vol. 415, pp. 1-179.

[6] T. Kutty et al., (2009), "Characterization of ThO2–UO2 pellets made by co-precipitation process," Journal of Nuclear Materials, vol. 389, no. 3, pp. 351-358.

[7] L. Argo, (2003), "Experimental determination of the dry oxidation behavior of a compositional range of Uranium-Thorium mixed-oxide pellet fragments," University of Florida.

[8] Y. Atlas, M. Eral, and H. Tel, (1997), "Preparation of homogeneous (Th 0.8 U 0.2) O 2 pellets via coprecipitation of (Th, U)(C 2 O 4) 2· nH 2 O powders," J Nucl Mater, vol. 249, pp. 46-51.

ICNST 2024
International Conference on Nuclear Science and Technology
6- 8 MAY 2024 | Isfahan, Iran

The effect of time and stirring speed on the extraction of thorium using the emulsion liquid membrane containing Cyanex 272 as carrier (Paper ID : 1091)

Ehyaie D.[1], Zaheri P.[2*], Samadfam M.[1], Zahakifar F.[2]

[1]Department of Energy Engineering, Sharif University of Technology, P.O. Box 11365-8639, Iran
[2]*Nuclear Fuel Cycle Research School, Nuclear Science and Technology Research Institute, P.O. Box: 11365-8486, Tehran, Iran*

Abstract

Significant features of the emulsion liquid membrane (ELM) as an innovative trend in traditional solvent extraction such as simple operation, fast processing, and low consumption of extractant have gained extensive responsiveness in recent years. This work reports, for the first time, the extraction of thorium from aqueous nitrate solution using the ELM process. The liquid membrane phase is composed of kerosene as a diluent, Span 80 as a surfactant, bis(2,4,4-trimethylpentyl)phosphinic acid (cyanex272) as extractant, and H_2SO_4 solution as an internal reagent. This paper comprises studies of extraction and stripping efficiency through time and stirring speed. The results confirm that ELM is a very effective technique to extract more than 99% of thorium without significant emulsion breakage and swelling after a contact time of 10 min. The stirring speed of 300 rpm was also appropriate for the efficacious transfer of thorium through the ELM with a swelling of 7.5% and the breakage of less than 0.2%.

Keywords: Thorium, Extraction, Emulsion liquid membrane, Cyanex272, Time, Stirring speed.

Introduction

Considering the limited reserves of uranium, the abundance of thorium compared to uranium, the lack of use in the proliferation of nuclear weapons, the development of the thorium fuel cycle in is of interest [1].

Liquid membrane (LM) separation technology is a relatively new approach that has always been the focus of many researchers due to lower operating costs, lower energy consumption, economical use of expensive extractants and high separation factor. This method can be 40% cheaper compared to the solvent extraction (SX) method [2]. The LM consists of two homogeneous and completely miscible phases called the feed phase (F) and the recovery phase (S), which is formed by the third phase (membrane phase, M), which is insoluble in the other two phases, are separated. In most cases, the feed and recovery phases are aqueous solutions. Due to the favorable thermodynamic conditions created on the surface between the feed phase and the membrane phase, some components are extracted from the feed phase and transferred to the membrane phase. At the same time, the conditions at the interface

between the membrane phase and the regenerator enable the transfer of these components from the membrane phase to the recovery phase [3].

Among the LM methods, the emulsion liquid membrane (ELM) method can be suitable for the extraction and separation of thorium due to its high surface-to-volume ratio and simplicity of operation.

In this research work, important operational parameters affecting thorium transfer rate such as contact time of feed phase and emulsion containing Cyanex 272 and stirring speed will be evaluated. Emulsion breaking and swelling will also be measured.

Experimental

Materials

To make the emulsion membrane phase from industrial kerosene made by Alfa-Aesar as an organic phase, surfactant sorbitan monolaurate with the commercial name Span 80, bis4,4,2-trimethylpentyl extractant (Cyanex 272) with the chemical formula C16H35O2P, stabilizer Polyisobutylene (PIB) from Sigma Aldrich, and distilled water was used. Distilled water, nitric acid, and thorium nitrate salt with the chemical formula Th(NO3)4.6H2O were used to prepare the feed phase. Sulfuric acid was used as stripping agent.

Experimental method

To make the emulsion, first the extractant, surfactant, and kerosene were mixed together, and then sulfuric acid was added and mixed by a homogenizer at 11,000 rpm for 20 minutes. After the feed (containing 200 ppm thorium ions) and emulsion were prepared, the two aqueous and organic phases were contacted and mixed by a glass stirrer to carry out ion transfer. Eq. 1 shows thorium ions extraction reaction in the emulsion liquid membrane.

$$Th(OH)_2(NO_3)^{+1} + (HA)_2 \leftrightarrow Th(OH)_2(NO_3)A, HA + H^+ \quad (1)$$

After 25 minutes, the contents were separated by decanter. The aqueous phase exiting the decanter was sampled to measure the extraction percentage for ICP analysis. To determine the breaking rate of the emulsion, the emulsion was completely broken by 1.5 mL of normal butanol and then a sample was taken from the internal aqueous phase to measure potassium concentration. The volume of the emulsion

was also measured to calculate the amount of swelling value. Calculations of extraction, recovery and breakage and swelling were performed with Eqs. 2-5.

$$\text{Extraction } (\%) = \frac{C_t - C_0}{C_0} * 100 \quad (2)$$

$$Swelling\ (\%) = \frac{V_{em\,t} - V_{em\,0}}{V_{em\,0}} * 100 \quad (3)$$

$$Breakage\ (\%) = \frac{C_{K\,ex\,t} V_{ex}}{C_{K\,int\,0} V_{int}} * 100 \quad (4)$$

$$\text{Stripping } (\%) = \frac{C_s V_s}{C_0 V_f} * 100 \quad (5)$$

C_0, C_t, C_s are the initial concentration of thorium, thorium concentration in the feed phase and stripping phase, respectively. $V_{em\ t}$ and $V_{em\ 0}$ are the emulsion volume at time t and t=0, respectively. Potassium concentration in the extranal phase and internal phase are presented by $C_{K\ ex}$ and $C_{K\ int}$, respectively.

Results and Disscusion

Effect of stirring time

It is evident from Fig. 1 that there are insufficient opportunities to collect and transmit thorium at low contact times. By increasing the contact time up to 25 minutes, the amount of thorium transfer increases and then decreases. Because extending the period that two phases are in contact gives water molecules enough chance to enter the emulsion, causing the emulsion to swell. The incidence of swelling rises sharply to 37.5% as the contact period extends from 25 to 35 minutes (Fig. 2). This effect has also been reported by Rouhani et al. in the transfer of molybdenum ions by an emulsion liquid membrane containing Cyanex 272 extractant [3].

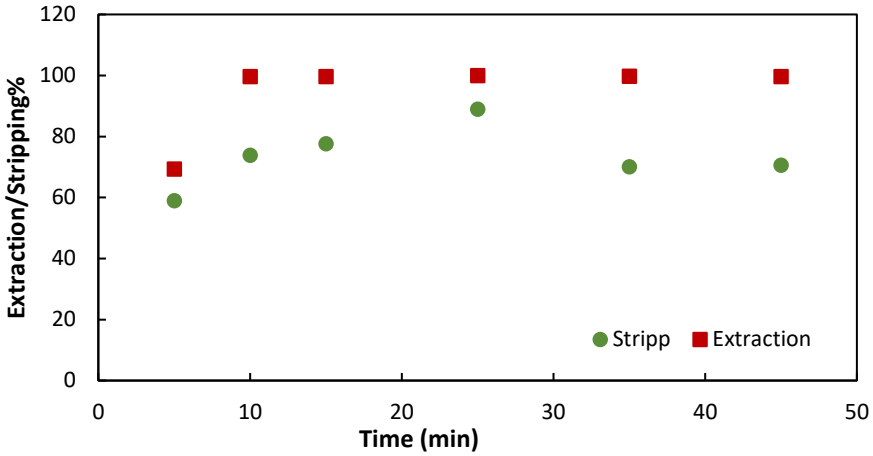

Fig. 2. The effect of stirring time on the extraction and stripping of thorium (feed phase pH: 1.05, cyanex 272 concentration: 0.11 mol/l, stripping phase concentration: 0.65 mol/l)

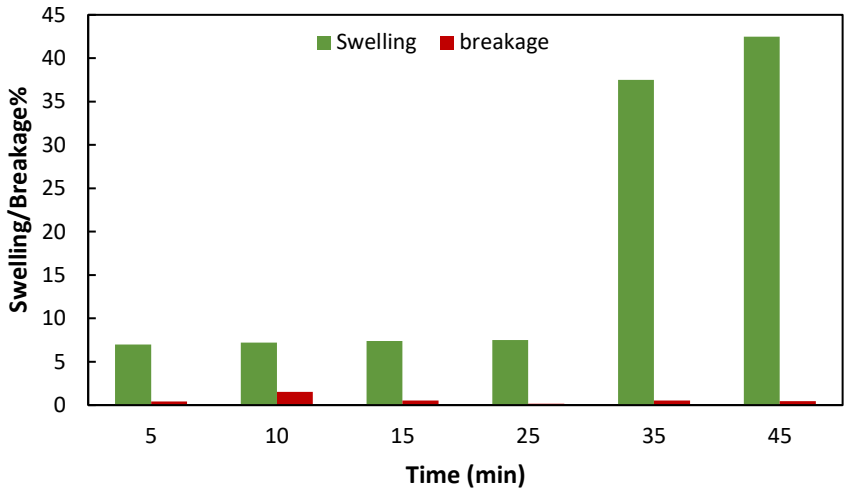

Fig. 3. The effect of stirring time on the swelling and breakage of emulsion (feed phase pH: 1.05, cyanex 272 concentration: 0.11 mol/l, stripping phase concentration: 0.65 mol/l).

Effect of stirring speed

The intensity, and speed of stirring have a significant impact on the size of emulsion globules. The stirring speed should not be so high that it breaks the emulsion, nor should it be so low that mixing does not take place and the emulsion globules do not turn into smaller droplets [4]. An analysis of the effect of stirring speed in Fig. 3 revealed that increasing turbulence and speed will improve mass transfer between the emulsion globules and feed phase, which will boost extraction. The extraction percentage went from 20.33 to 99.94% when the speed was raised from 100 to 200 rpm. The extraction rate is then unaffected by raising the stirring speed after that. Nonetheless, the transmission rate in speeds larger

than 300 rpm has dropped dramatically to less than 60%. This phenomenon can be explained by the emulsion's notable swelling that increases with increasing speed (Fig. 4).

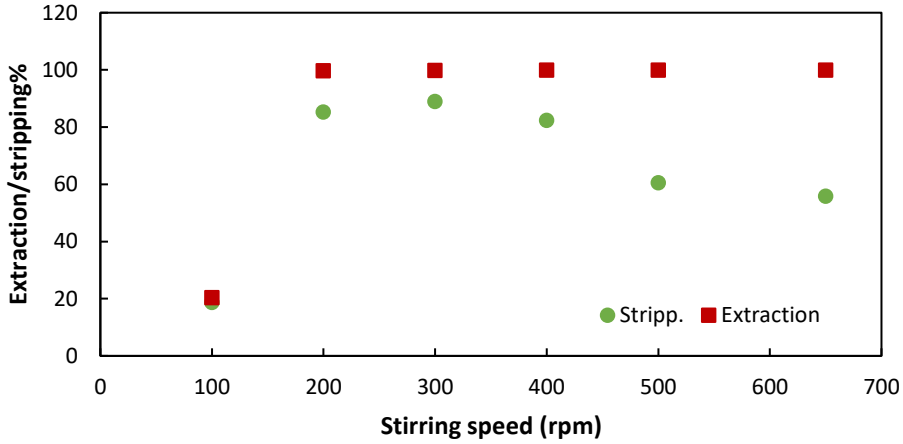

Fig. 4. The effect of stirring speed on the extraction and stripping of thorium (feed phase pH: 1.05, cyanex 272 concentration: 0.11 mol/l, stripping phase concentration: 0.65 mol/l).

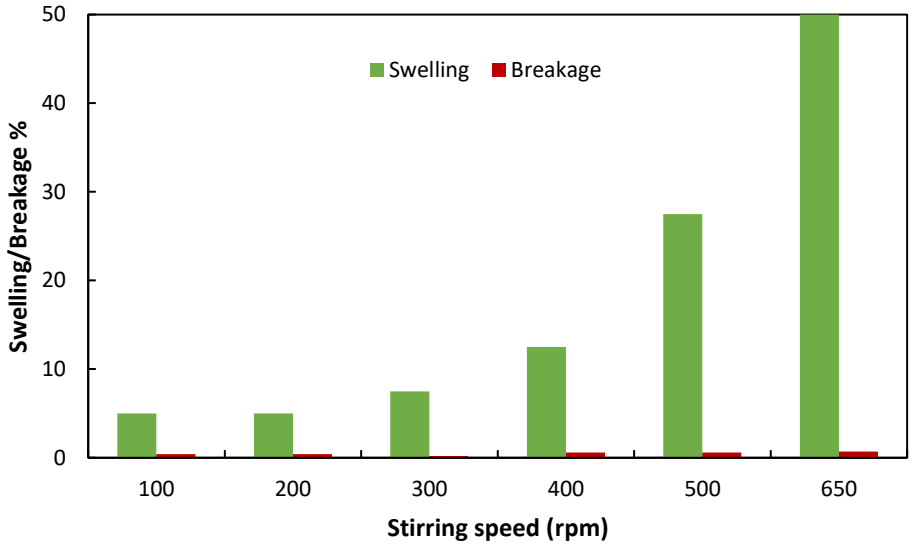

Fig. 5. The effect of stirring speed on the swelling and breakage of emulsion (feed phase pH: 1.05, cyanex 272 concentration: 0.11 mol/l, stripping phase concentration: 0.65 mol/l).

Conclutions

In the current work, an emulsion liquid membrane (ELM) system was used to investigate the extraction of thorium from aqueous solution. The components of the ELM were sorbitan monolete (Span-80) as a surfactant to stabilize the emulsion phase, kerosene as an organic diluent, and bis(2,4,4-trimethylpentyl)

phosphinic acid (cyanex272) as a carrier. The results validate that ELM is a very successful approach to extract 99.94% and to strip 88.99% of thorium at contact time of 25 min and stirring speed of 300 rpm. In these conditions, the ELM swelling and breakage were 7.5% and 0.2%, respectively.

References

1. Sokolov, F., K. Fukuda, and H. Nawada, *Thorium fuel cycle-Potential benefits and challenges.* IAEA TECDOC, 2005. 1450.

2. Kislik, V.S., *Liquid membranes: principles and applications in chemical separations and wastewater treatment*. 2009: Elsevier.

3. Rouhani, S.H.R., et al., *Separation of molybdenum from spent HDS catalysts using emulsion liquid membrane system.* Chemical Engineering and Processing-Process Intensification, 2020. 153: p. 107958.

4. Chakraborty, M., C. Bhattacharya, and S. Datta, *Emulsion liquid membranes: Definitions and classification, theories, module design, applications, new directions and perspectives*, in *Liquid membranes*. 2010, Elsevier. p. 141-199.

ICNST 2024
International Conference on Nuclear Science and Technology
6- 8 MAY 2024 | Isfahan, Iran

The effect of feed acidity and stripping phase concentration on the extraction of thorium using the emulsion liquid membrane system (Paper ID : 1093)

Ehyaie D.[1], Samadfam M.[1], Zaheri P.[2*], Zahakifar F.[2]

[1]Department of Energy Engineering, Sharif University of Technology, P.O. Box 11365-8639, Iran
[2]*Nuclear Fuel Cycle Research School, Nuclear Science and Technology Research Institute, P.O. Box: 11365-8486, Tehran, Iran*

Abstract

In the current study, the extraction of thorium from aqueous solution was studied using an emulsion liquid membrane (ELM) system. The ELM was made up of bis(2,4,4-trimethylpentyl) phosphinic acid (cyanex272) as a carrier, kerosene as an organic diluent, H_2SO_4 as a stripping solution, and sorbitan monolete (Span-80) as a surfactant for stabilizing the emulsion phase. The effect of feed acidity and stripping phase concentration was evaluated on the thorium transfer from the feed phase to the stripping phase. Besides, the stability of the emulsion was determined by specifying the emulsion breakage and swelling at each stage. The results revealed that increasing the stripping phase concentration improves the transfer efficiency, but on the other hand, it causes emulsion swelling. Investigating the influence of feed acidity showed that the appropriate pH for the recovery process of thorium from nitrate solution is 1.05. The outcomes of this study can be extended to the extraction of thorium from industrial leach solutions.

Keywords: Thorium, Extraction, Emulsion liquid membrane, Cyanex272, Feed acidity, Stripping phase concentration

Introduction

Due to the growing use of nuclear energy in various sectors of industry, agriculture and medicine, providing the fuel needed for nuclear power plants is very important. Since the mines that supply the required fuel are limited and their extraction takes place with an increasing trend, it is necessary to pay attention to the development of reserves and the discovery of alternative sources of fuel. Among the alternative deposits are thorium deposits, which have attracted a lot of attention due to thorium being 3 to 4 times more abundant than uranium and its suitable properties as a fuel for the thorium fuel cycle [1].

Liquid membrane (LM) separation technology is a relatively new approach that has always been the focus of many researchers due to lower investment and operating costs, lower energy consumption, economical use of expensive extractors and high separation factor. In this method, ion transfer is performed through various configurations of bulk liquid membrane (BLM), emulsion liquid membrane

(ELM) and supported liquid membrane (SLM). The LM consists of two homogeneous and completely miscible phases, namely the feed phase (F) and the recovery phase (S), which are separated by the third phase (membrane phase, M), which is insoluble in the other two phases. In most cases, the feed and recovery phases are aqueous solutions [2].

In the ELM method, the membrane is made by dispersing a recovery phase (receiving) inside an immiscible LM to form an emulsion. ELM has a large mass transfer surface per unit volume and as a result the separation process is fast in it. Research has shown that the Cyanex 272 extractant has a good efficiency for thorium extraction using the emulsion liquid membrane method.

In this research, the ELM formed by the Cyanex 272 extractant was used to extract and transfer thorium. In this research work, the important and effective operating parameters on the extraction and transfer of thorium, including the pH of the feed phase and the concentration of the internal phase, have been investigated. Emulsion breaking and swelling rates have also been measured.

Experimental

Materials

Distilled water was used as the aqueous phase in making emulsion and preparing feed. Kerosene made by Alpha Acer was used as an organic phase in making the emulsion. Surfactant Span 80 was obtained from Merck. Cyanex 272 extractant, sulfuric acid as a recovery agent in the internal phase, polyisobutylene stabilizer (PIB) for emulsion stability from Sigma Aldrich Company, nitric acid to adjust the pH of the feed phase, thorium nitrate salt with the chemical formula $Th(NO_3)_4.6H_2O$ for making Feed solution was purchased from Merck, Germany.

Experimental method

To make the emulsion, first the extractant, surfactant, and kerosene were mixed together, and then sulfuric acid in which KCl was dissolved was added and mixed by a homogenizer at 11,000 rpm for 20 minutes. After the feed (containing 200 ppm thorium ions) and emulsion were prepared, the two aqueous and organic phases (with the ratio of 50:20) were contacted and mixed by a stirrer to carry out ion transfer. After 25 minutes, the contents were separated by decanter. The aqueous phase exiting the decanter was sampled to measure the extraction percentage for ICP analysis. To determine the breaking rate of the emulsion, the emulsion was completely broken by 1.5 mL of normal butanol and then a sample

was taken from the internal aqueous phase to measure potassium concentration. The volume of the emulsion was also measured to calculate the amount of swelling value. Calculations of extraction, recovery and breakage and swelling were performed with formulas 1-4.

$$Extraction\ (\%) = \frac{C_t - C_0}{C_0} * 100 \quad (1)$$

$$Swelling\ (\%) = \frac{V_{em\,t} - V_{em\,0}}{V_{em\,0}} * 100 \quad (2)$$

$$Breakage\ (\%) = \frac{C_{K\,ex\,t} V_{ex}}{C_{K\,int\,0} V_{int}} * 100 \quad (3)$$

$$Stripping\ (\%) = \frac{C_s V_s}{C_0 V_f} * 100 \quad (4)$$

C_0, C_t, C_s are the initial concentration of thorium, thorium concentration in the feed phase and stripping phase, respectively. $V_{em\ t}$ and $V_{em\ 0}$ are the emulsion volume at time t and t=0, respectively. Potassium concentration in the extranal phase and internal phase are presented by $C_{K\ ex}$ and $C_{K\ int}$, respectively.

Results and Disscusion

Effect of feed acidity

Since Cyanex 272 extractant is an acidic ligand, the pH of the feed solution will affect its extractive qualities. Thus, the impact of the feed phase's pH value on the effectiveness of thorium extraction and transfer has been examined in this section. The findings displayed in Fig. 1 demonstrate that the extraction rate of thorium remains relatively unaffected by varying the pH of the feed phase within the range of 0.1 to 3. Put otherwise, it is feasible to extract thorium almost entirely (over 99%) in this pH range. Additionally, as the figure makes clear, thorium transfer increases from 74.76 to 88.99% when the pH is raised to 1.05. The driving power necessary for thorium transfer rises as a result of the rising pH, which also causes an increase in the gradient of proton concentration in the feed and stripping phases [3]. Furthermore, thorium transfer dropped and reached 71.84% with a pH increase of up to 3%.

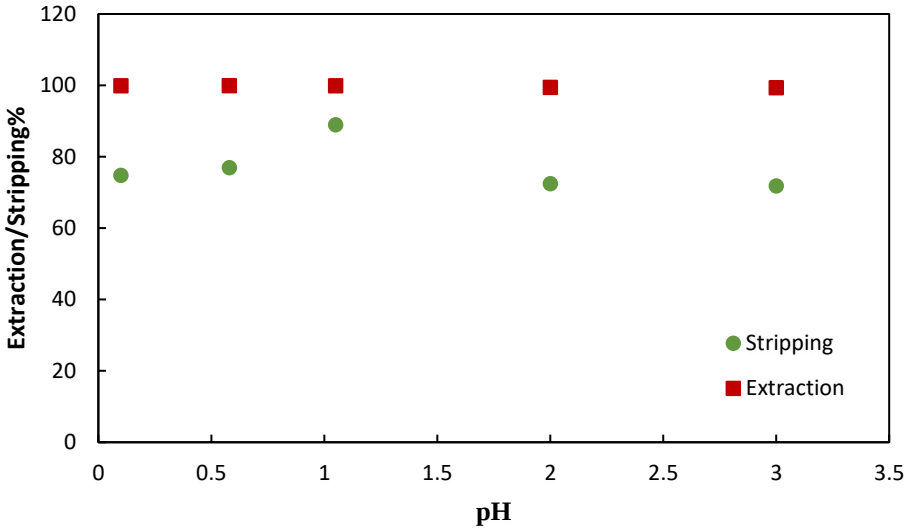

Fig. 6. The effect of feed acidity on the extraction and stripping of thorium (cyanex 272 concentration: 0.11 mol/l, stripping phase concentration: 0.65 mol/l).

Effect of stripping phase concentration

The movement of thorium ions from the membrane into the internal phase droplets is significantly influenced by the stripping process that occurs at the interface between the internal phase and the organic phase. At various sulfuric acid concentrations, the impact of stripping phase concentration on the extraction and transfer of thorium ions was examined. Fig. 2 shows more stripping agent is supplied for the thorium transfer when sulfuric acid concentration is raised to 0.65 mol/L, boosting extraction efficiency from 3 to 99.85% and transfer efficiency from 3.09 to 88.99%. After that, increasing the concentration of sulfuric acid has little effect on the thorium extraction rate, while it decreases the transfer rate. The cause of this phenomenon can be attributed to the instability of the emulsion in high concentrations of sulfuric acid.

The swelling measurements in Fig. 3 demonstrate that the emulsion's volume grows as the sulfuric acid concentration rises. Stated differently, the emulsion swells more. The difference in osmotic pressure between the feed phase and the internal phase, which facilitates the transfer of water molecules, appears to be the cause of the emulsion's swelling [4]. The internal phase is diluted as a result of the emulsion swelling, which lowers the transfer rate [5].

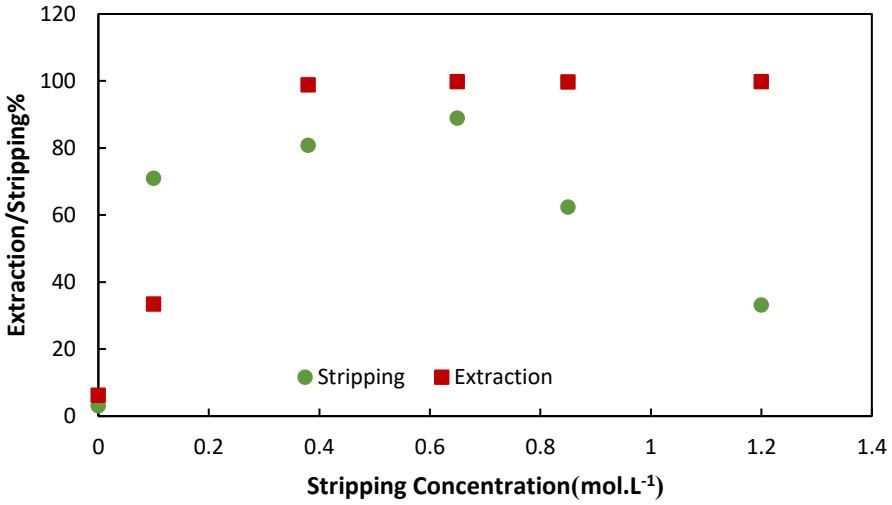

Fig. 7. The effect of stripping concentration on the extraction and stripping of thorium (feed phase pH: 1.05, cyanex 272 concentration: 0.11 mol/l).

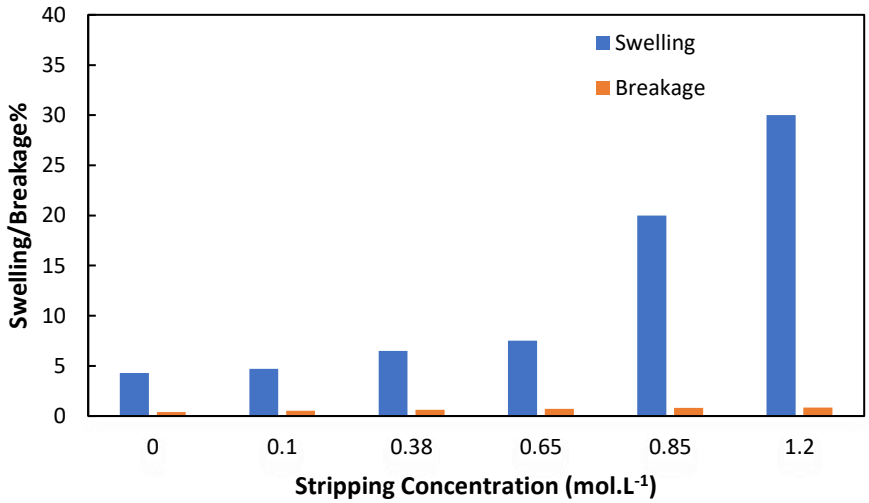

Fig. 8. The effect of stripping concentration on the swelling and breakage of emulsion (feed phase pH: 1.05, cyanex 272 concentration: 0.11 mol/l).

Conclutions

In the current work, an emulsion liquid membrane (ELM) system was used to investigate the extraction of thorium from aqueous solution. The components of the ELM were sorbitan monolete (Span-80) as a surfactant to stabilize the emulsion phase, kerosene as an organic diluent, and bis(2,4,4-trimethylpentyl) phosphinic acid (cyanex272) as a carrier. The findings showed that while the transfer efficiency is improved by increasing the stripping phase concentration up to 0.65 mol/l, the transfer rate falls after

that point. Because it results in emulsion swelling. The impact of feed acidity revealed that a pH of 1.05 is suitable for the thorium recovery procedure from nitrate solution.

References

1. Sokolov, F., K. Fukuda, and H. Nawada, *Thorium fuel cycle-Potential benefits and challenges.* IAEA TECDOC, 2005. 1450.

.٢ Kislik, V.S., *Liquid membranes: principles and applications in chemical separations and wastewater treatment*. 2009: Elsevier.

.٣ Rouhani, S.H.R., et al., *Separation of molybdenum from spent HDS catalysts using emulsion liquid membrane system.* Chemical Engineering and Processing-Process Intensification, 2020. 153: p. 107958.

.٤ Othman, N., et al., *Emulsion liquid membrane extraction of silver from photographic waste using tetramethylthiuram disulfide (TMTDS) as a mobile carrier.* Journal of Applied Membrane Science & Technology, 2006. 3(1).

.٥ Kulkarni, P.S. and V.V. Mahajani, *Application of liquid emulsion membrane (LEM) process for enrichment of molybdenum from aqueous solutions.* Journal of Membrane Science, 2002. 201(1-2): p. 123-135.

ICNST 2024
International Conference on Nuclear Science and Technology
6- 8 MAY 2024 | Isfahan, Iran

Separation of minor actinides and lanthanides using the phenanthroline-based polymeric organic frameworks (PhenTAPB-POF, PhenTAPT-POF, and PhenTAPE-POF) (Paper ID : 1101)

Afshin Khayambashi[1,2 *], Long Chen[2], Shuao Wang[2]

[1] Department of Energy Engineering, Sharif University of Technology, Tehran, Iran.

[2] State Key Laboratory of Radiation Medicine and Protection, School for Radiological and Interdisciplinary Sciences (RAD- X) and Collaborative Innovation Center of Radiation Medicine of Jiangsu Higher Education Institutions, Soochow University, Suzhou, China.

*Corresponding Author: a.khayambashi@sharif.edu

Abstract

Separation of the minor actinides (Am and Cm) from lanthanides in high-level liquid wastes (HLLW) is one of the most challenging chemical separation tasks known owing to their chemical similarities but is highly significant in nuclear fuel reprocessing plants because it could practically lead to sustainable nuclear energy by closing the nuclear fuel cycle. The solid phase extraction is proposed to be a possible strategy but all reported sorbent materials severely suffer from limited stability and/or efficiency caused by the harsh conditions of high acidity coupled with intense irradiation. This research aims to synthesize an acid and gamma irradiation-resistant polymeric organic frameworks (POFs) for actinides and lanthanides separation. The target materials would have a fast kinetics and high selectivity of americium (^{243}Am) towards europium (^{152}Eu). Herein, three phenanthroline-based polymeric organic frameworks (PhenTAPB-POF, PhenTAPT-POF, and PhenTAPE-POF) were synthesized for the separation of trivalent americium from lanthanides. Due to its fully conjugated structure, all three adsorbents exhibit previously unachieved stability under the combined extreme condition of strong acids and high irradiation field. In contrast to PhenTAPB-POF, the americium partitioning experiment indicates that PhenTAPB-POF and PhenTAPE-POF possess a high adsorption selectivity towards Am(III) over lanthanides in highly acidic simulated HLLW and relatively fast adsorption kinetics. The high stability and superior separation performance endow the PhenTAPE-POF and PhenTAPB-POF with a promising alternative for separating minor actinides over lanthanides.

Keywords: porous organic framework, americium, lanthanides, separation, stability

Introduction

Nuclear energy with an advanced nuclear fuel cycle is a primary clean energy source as a sustainable solution for the increasing global electricity demand [1, 2]. These issues have prompted many countries to develop their nuclear industries, and China is known as the most ambitious country to promote the nuclear energy which accounts 36% of the world's new nuclear power plants. Therefore, the close nuclear fuel cycle strategy is considered in some countries as China to reuse the spent nuclear fuels for the advanced nuclear reactors by reprocessing of spent nuclear fuels. However, environmental issues such as nuclear waste handling and disposal associated with the used fuel reprocessing have been of significant concerns [3, 4]. The advanced nuclear fuel cycles advocate the partitioning & transmutation strategy (P&T), which separates the long-lived MA and FP from HLLW and then transmutes them to stable or short-lived radionuclides as the partitioning scenraio is shown in Fig. 1 [5].

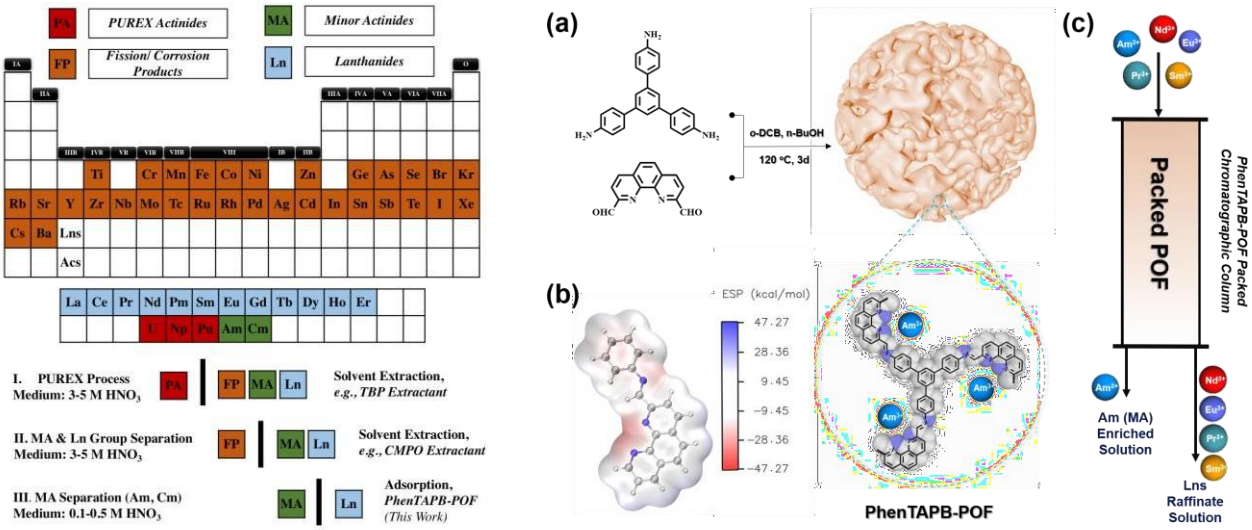

Fig. 1 Advance separation scenario for nuclear spent fuel, (a) The synthetic route for PhenTAPB-POF. (b) The simulation of the electrostatic potential (ESP) distribution of the 1,10-phenanthroline units in the synthesized POF framework. (c) The schematic of the chromatography column separation system packed by PhenTAPB- POF for MA and Lns separation [6].

The oxygen donor ligands such as CMPO [7], and TRPO [8] using solvent extraction (SE) can sequestrate MA(III) and Ln(III) together from fission products in HLLW. Minor actinides also need to be partitioned from the lanthanides before the transmutation process due to certain lanthanides' high

neutron absorption cross-sections such as Sm, Eu, and Gd [4]. However, the MA(III) and Ln(III) separation is still a significant challenge because of their similar ionic radii, charge density, and coordination modes, in addition to the large excess of Ln(III) compared with MA(III) in HLLW [7, 9].

The idea of introducing a simple phenanthroline-based ligand as the building blocks of imine- linked microporous polymer organic frameworks (POFs) came up due to the proposed potential of Phen- POF materials for MA/Ln separation under extreme conditions as well as its simple synthesis procedure for an industrial scale with no post-synthetic modification or functionalization energy as shown in Fig. 1 [6, 10]. It has been well-documented that Schiff-base reaction as a high-yielding approach is a versatile tool in synthesizing porous organic architectures that the process is a one-pot condensation reaction and does not involve expensive catalysts [11, 12]. Note that Phen-POFs are only composed of C, H, O, and N, which are advantageous to nuclear waste management based on the CHON principle since they are entirely combustible to gaseous products, resulting in less secondary radioactive waste [13]. In this study, we demonstrate the introduction of three POF materials for MA/Ln separation, which was synthesized by the imine condensation of 1,10-phenanthroline-2,9-dicarbaldehyde with 1,3,5-tris(4- aminophenyl)benzene (Fig. 1a for PhenTAPB-POF). The resultant POF adsorbents show significant chemical stability against irradiation and highly acidic conditions and demonstrate selective adsorption for Am(III) over lanthanides.

Experimental

Materials

^{243}Am(III) solutions were prepared from a laboratory stock solution with the concentration of 0.1 mM in the Center of Nuclear Environmental Chemistry at Soochow University. The stock solutions of ^{241}Am and ^{152}Eu were provided by Tsinghua University for the static Am/Eu separation experiments. Phenanthroline-2,9-dicarbaldehyde and 1,3,5-tris(4-aminophenyl) benzene were procured from Jinlin Province In-depth Research Technology Co., Ltd. Co. in China. All common chemicals and reagents used in this work were procured as analytical grades without further purification.

Synthesis and Characterization of PhenTAPB-POF, PhenTAPT-POF, and PhenTAPE-POF

The PhenTAPB-POF was synthesized using Schiff-base reaction of 1,10-phenanthroline-2,9-dicarbaldehyde (0.3 mmol, 70.8 mg) with 1,3,5-tris(4-aminophenyl)benzene (0.2 mmol, 70.3 mg), in the presence of 1-butanol and 1,2-dichlorobenzene with the solvent combination of 2 mL:2 mL, accompanying 0.2 mL of 6 M aqueous acetic acid in a solvothermal process. The reactants in in a 10 mL

Pyrex tube were degassed by three cycles of freeze-pump-thaw technique, and then was heated at 120℃ for 3 days. The precipitate was filtered and washed thrice with tetrahydrofuran (THF) to remove the unreacted ligands and residual oligomers. Then the red brown PhenTAPB-POF was gained after being dried at 50 oC under vacuum for 12 h. The obtained adsorbent has been characterized by means of different techniques. The PhenTAPT-POF was also synthesized using the same reaction and procedure but with different building block as 4,4',4''-(1,3,5-Triazine-2,4,6-triyl)trianiline (TAPT).

The PhenTAPE-POF was synthesized using Schiff-base reaction of 1,10-phenanthroline-2,9-dicarbaldehyde (0.3 mmol, 70.8 mg) with Tetrakis(4-aminophenyl)ethylene (TAPE) (0.15 mmol, 58.8 mg), in the presence of 1-butanol and 1,2-dichlorobenzene with the solvent combination of 2 mL:2 mL, accompanying 0.2 mL of 6 M aqueous acetic acid in a solvothermal process as explained in the previous section.

Results and discussion

PhenTAPB-POF

The effect of nitric acid concentration on the adsorption of americium into the POF material is illustrated in Fig. 2. Adsorption efficiency of americium gradually decreases with increasing the acidity from 0.01 to 0.5 M HNO_3 and subsequently decreased sharply with a further increase of acidity to 3 M. The reason is that the adsorption sites are likely to be protonated in a higher level of acidity, resulting in the decrease of available N-donor sites. From another perspective, the adsorption mechanism towards Am(III) and HNO_3 can be described in Eq. (1) and (2), respectively, which are derived from the extraction mechanism of the N-donor ligands [14].

$$Am^{3+} + 3NO^{-} + \text{PhenTAPB-POF} \rightarrow Am(\text{PhenTAPB-POF})(NO^{-}) \quad (1)$$

$$xH^{+} + xNO^{-} + \text{PhenTAPB-POF} \rightarrow \text{PhenTAPB-POF}\cdot xHNO \quad (2)$$

Due to the americium's trivalent oxidation state, three NO_3^- ions are incorporated into the coordination sphere of Am(III) to maintain the neutral POF as the chemisorption shown in Eq. 1. Further increase in HNO_3 concentration may support the sorption of nitric acid as illustrated in Eq. 2, which decelerates the rate and efficiency of Am adsorption by lowering the concentration of free adsorption sites on PhenTAPB-POF[15, 16].

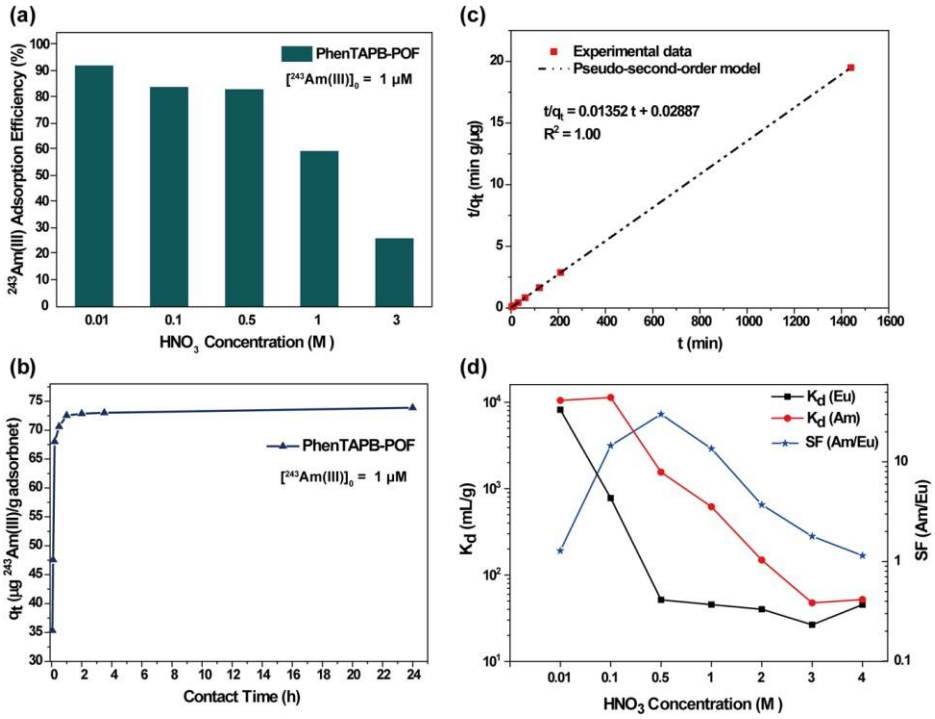

Fig. 2 (a) Variations of the americium adsorption efficiency of PhenTAPB-POF versus the nitric acid concentrations (M) in a pure americium system. (b) Effect of contact time on americium adsorption onto PhenTAPB-POF in 0.5 M nitric acid medium. (c) Pseudo-second order plot used for kinetics study of the americium adsorption process. (d) Influence of HNO_3 concentration on the adsorption and separation of ^{241}Am(III) and Eu(III) using PhenTAPB-POF[6].

The obtained results reveal that Am(III) adsorption using the PhenTAPB-POF in nitric acid media with a concentration less than 0.5 M is practically acceptable since the obtained adsorption efficiency is higher than 80%. Such a high adsorption efficiency for the americium extraction with a very low concentration (1 µM) might be received by a highly negative enthalpy of adsorption (ΔH_{ads}) caused by the multiple chemical interactions between the americium ions and the binding sites [17].

PhenTAPT-POF

To validate the formation of PhenTAPT-POF, the obtained red-brown POF material and its two reactants were characterized by FT-IR spectrometry, as shown in Fig. 3b. The characteristic peaks of TAPT at 3458,

3319, and 3200 cm−1 represent the stretching vibration of the N-H bond in amino functional group, and the peak at 1696 cm−1 for 10-phenanthroline-2,9-dicarbaldehyde is attributed to the C=O stretching band (aldehyde). In the IR spectra of PhenTAPB-POF, a characteristic peak of C=N stretching vibration appearing at 1669 cm−1 indicates the formation of an imine linkage which was accompanied by the absence of the peaks from the aldehyde and amino stretching vibrations [12]. The obtained results confirm a successful conversion of those two monomers into a Schiff-base POF polymer through a condensation reaction.

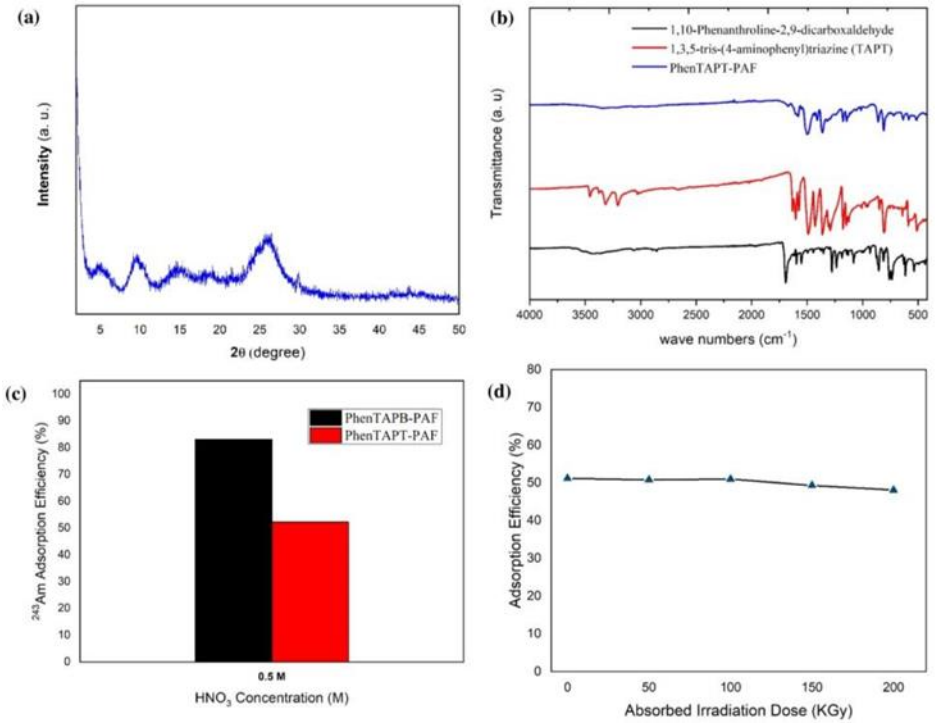

Fig. 3 (a) PXRD spectra of PhenTAPT-POF. (b) FT-IR spectra of 1,10-Phenanthroline-2,9-dicarbaldehyde (Phen), TAPT, and synthesized PhenTAPT-POF. (c) Americium adsorption efficiency of PhenTAPT-POF and PhenTAPB-POF in 0.5M nitric acid solution. (d) Effect of gamma irradiation on PhenTAPT-POF with the adsorbed doses of 50, 100, 150, and 200 KGy in a 0.5 M HNO_3 medium towards the adsorption efficiency of americium ($[^{243}Am(III)]_0$ = 1 µM).

Fig 3a shows the PXRD pattern of the PhenTAPT-POF in which indicates the poor crystallined structure of the POF material. Americium adsorption efficiency of PhenTAPT-POF in 0.5M nitric acid solution with the initial concentration of $^{243}Am(III)$ = 1 µM has been illustrated in Fig. 3c, in comparison with the one of PhenTAPB-POF in our preliminary experiment, which indicates the higher adsorption efficiency for PhenTAPB-POF towards americium in the same conditions.

PhenTAPE-POF

PhenTAPE-POF has been employed to indicate its separation properties towards Am and Eu and the results approved it can be a promising alternative for PhenTAPB-POF in this project. Characterization, adsorption and hydrolysis studies are listed as below to further introduce the capabilities of the synthesized adsorbent. To validate the formation of POF adsorbent, the obtained material was characterized by Fourier transform infrared (FT-IR) spectrometry, as shown in Fig. 4a. In the IR spectra of PhenTAPE-POF, a characteristic peak of C=N stretching vibration appearing at 1663 cm^{-1} indicates the formation of an imine linkage which was accompanied by the absence of the peaks from the aldehyde and amino stretching vibrations which confirm a successful conversion of those two monomers into a Schiff-base POF polymer through a condensation reaction [12].

Americium adsorption efficiency of PhenTAPE-POF and PhenTAPB-POF in a range of nitric acid solution**s** with initial concentration of $^{243}Am(III)$ = 1 µM were examined and the results are shown in Fig. 4**b**. Adsorption efficiency of americium gradually decreases with increasing the acidity from 0.01 to

0.5 M HNO_3 for both PhenTAPE-POF and PhenTAPB-POF, and subsequently decreased sharply with a further increase of acidity to 3 M. The reason is that the adsorption sites are likely to be protonated in a higher level of acidity, resulting in the decrease of available N-donor sites. the adsorption mechanism towards Am(III) and HNO_3 can be described in Eq. (3) and (4), respectively, which are derived from the extraction mechanism of the N-donor ligands [14].

$$\mathbf{Am^{3+} + 3NO^{-} + PhenTAPE\text{-}POF \rightarrow Am(PhenTAPE\text{-}POF)(NO^{-})} \quad \mathbf{(3)}$$

$$\mathbf{xH^{+} + xNO^{-} + PhenTAPE\text{-}POF \rightarrow PhenTAPE\text{-}POF \cdot xHNO} \quad \mathbf{(4)}$$

As it can be seen the Am adsoprtion efficiency of PhenTAPE-POF is almost 10% higher than that of PhenTAPB-POF in each acidity in which reveal the better adsorption performance of the PhenTAPE- POF among all the synthesized ones in this article [17]. The static adsorption study was carried out to investigate the feasibility of PhenTAPE-POF material for the selective adsorption of 241Am(III) towards Eu(III) in a range of nitric acid concentrations, as shown in Fig. 4c. The static results reveal the optimum point of separation at 0.5 M HNO3 that the adsorbent exhibits significant adsorption towards Am(III) with the distribution coefficient of more than 1400 mL g-1 and the Am(III)/Eu(III) separation factor over

30. The selective adsorption of Am(III) over Eu(III) might be caused by the greater covalency in complexes between Am (as a 5f element) and ligand than that in complexes of Eu (as a 4f element) [18].

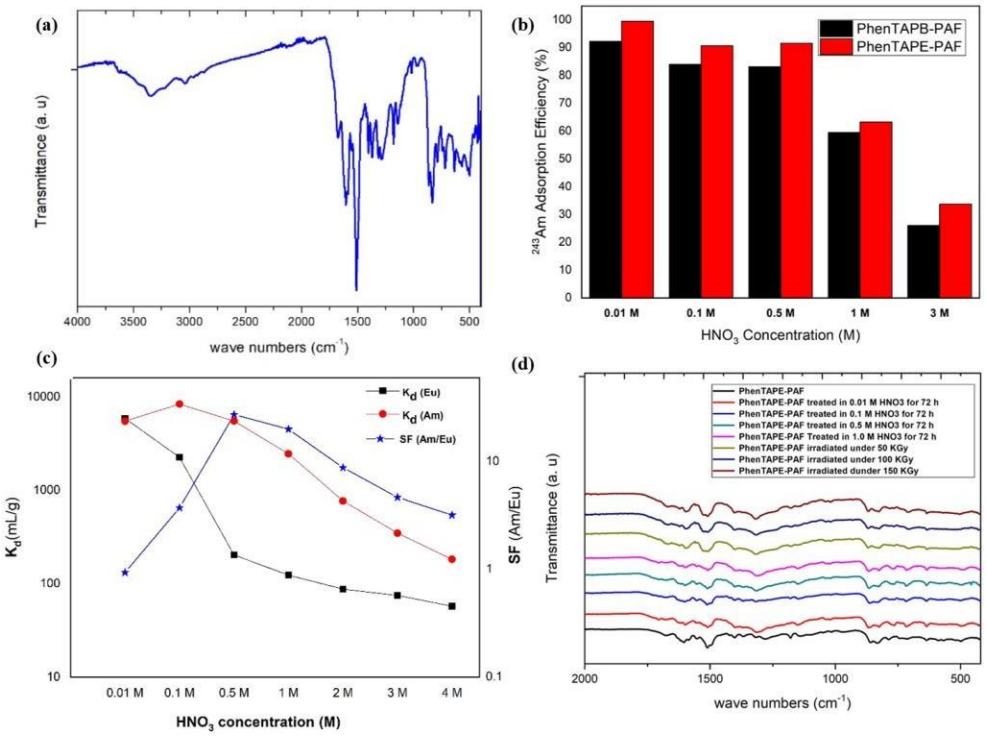

Fig. 4 a) FT-IR spectra of synthesized PhenTAPE-POF. **b)** Americium adsorption efficiency of PhenTAPE-POF and PhenTAPB-POF in different nitric acid solution. **c)** Influence of HNO_3 concentration on adsorption and separation of ^{241}Am(III) and Eu(III) using PhenTAPE-POF. **d)** The FT-IR spectra of soaked PhenTAPE-POF adsorbents in different media after 7 days in comparison with the FT-IR spectrum of as-synthesized one.

Fresh samples were dispersed in nitric acid solutions with various levels of acidities for 7 days to evaluate the chemical stability of PhenTAPE-POF. The characteristic peaks, including the C=N stretching vibration in IR spectra of the treated samples in Fig. 4d, almost kept similar as those of the as- synthesized sample. Furthermore, the structure of adsorbent protects the chemical bonds from the strong doses of γ irradiation

from a ^{60}Co radiation source (92.42 PBq, dose rate of 3.125 KGy/h) as shown in Fig. 4d. In addition, the vibrational bands of the HNO_3 adsorbed on polymer appear at 1316 cm^{-1}, which further confirms HNO_3 adsorption onto PhenTAPT-POF.

In Table 1, the optimization results for the adsorbent dose in separation of Am/Eu are reported and it clearly shows that the Am and Eu adsorption efficiency increase with the increase in adsorbent amount while the maximum Am/Eu separation factor first increased with the increase of S/L ratio to 3/2 and then decrease gradually. From the optained results we can consider the best adsorbent dose as 1.5 as the optimized ratio for this process.

Table 1 adsorption solid/liquid ratio optimization

Solid/Liquid ratio (mg/mL)	***2/2***	***3/2***	***4/2***	***5/2***
Eu Removal Efficiency (%)	17.9	22.0	28.9	31.9
Am Removal Efficiency (%)	89.7	92.3	93.7	94.4
Am/Eu Separation Factor	40.2	42.1	36.8	35.8

Conclusions

Herein, three phenanthroline-based polymeric organic frameworks (PhenTAPB-POF, PhenTAPT-POF, and PhenTAPE-POF) were synthesized and emploted for the separation of trivalent americium from lanthanides. In summary, the phenanthroline-based polymeric organic adsorbents were constructed with rigid aromatic ligands using Schiff-base reaction and comprehensively characterized. The synthesized adsorbents are all sufficiently stable in contact with nitric acid in a gamma source's radiation field and thermally stable up to 300^oC in the O_2 atmosphere The foregoing static adsorption results signify the extensive potential of PhenTAPB-POF and PhenTAPE-POF as nitrogen donor frameworks for the separation of minor actinides over lanthanide from the simulated HLLW in a highly acidic solution (0.5 M HNO_3) under robust gamma-ray irradiation (200 KGy). Moreover, this novel POF material can completely degrade into gaseous products in 550^oC, easing the waste management of the contaminated sorbents after use based on CHON principle. These merits together cannot be achieved by any of the previously reported adsorbents such as the silica-based solid-phase extractants and other inorganic or polymeric materials and frameworks. A POF adsorbent with these outstanding advantages endows the family of POF, PAF, and COF materials with the promising potentials to solve the most severe issues in nuclear fuel cycles, such as

the minor actinides and lanthanide separation, technetium removal, as well as the cesium and strontium recovery.

References

[1] Abu-Khader, M.M., Recent advances in nuclear power: A review. Progress in Nuclear Energy, 2009. 51(2): p. 225-235.

[2] Sun, X., H. Luo, and S. Dai, Ionic Liquids-Based Extraction: A Promising Strategy for the Advanced Nuclear Fuel Cycle. Chemical Reviews, 2012. 112(4): p. 2100-2128.

[3] Xiao, C.-L., et al., Excellent Selectivity for Actinides with a Tetradentate 2,9-Diamide-1,10-Phenanthroline Ligand in Highly Acidic Solution: A Hard–Soft Donor Combined Strategy. Inorganic Chemistry, 2014. 53(3): p. 1712-1720.

[4] Veliscek-Carolan, J., Separation of actinides from spent nuclear fuel: A review. Journal of Hazardous Materials, 2016. 318: p. 266-281.

[5] Cochran, R.G., et al., The nuclear fuel cycle: analysis and management. 1990: American Nuclear Society.

[6] Khayambashi, A., et al., Efficient separation between trivalent americium and lanthanides enabled by a phenanthroline-based polymeric organic framework. Chinese Chemical Letters, 2022. 33(7): p. 3429-3434.

[7] Ansari, S.A., et al., Aqueous Partitioning of Minor Actinides by Different Processes. Separation & Purification Reviews, 2011. 40(1): p. 43-76.

[8] Jianchen, W. and S. Chongli, HOT TEST OF TRIALKYL PHOSPHINE OXIDE (TRPO) FOR REMOVING ACTINIDES FROM HIGHLY SALINE HIGH-LEVEL LIQUID WASTE (HLLW).

[9] Solvent Extraction and Ion Exchange, 2001. 19(2): p. 231-242.

[10] Edelstein, N.M., et al., Summary and Comparison of Properties of the Actinide and Transactinide Elements, in The Chemistry of the Actinide and Transactinide Elements, L.R. Morss, N.M. Edelstein, and J. Fuger, Editors. 2011, Springer Netherlands: Dordrecht. p. 1753-1835.

[11] Zhang, S., et al., "Stereoscopic" 2D super-microporous phosphazene-based covalent organic framework: Design, synthesis and selective sorption towards uranium at high acidic condition. J Hazard Mater, 2016. 314: p. 95-104.

[12] Jin, Y., Y. Zhu, and W. Zhang, Development of organic porous materials through Schiff-base chemistry. CrystEngComm, 2013. 15(8): p. 1484-1499.

[13] Sun, X., et al., In-situ anchoring bimetallic nanoparticles on covalent organic framework as an ultrasensitive electrochemical sensor for levodopa detection. Talanta, 2021. 225: p. 122072.

[14] Khayambashi, A., et al., HDEHP-CMPO/SiO 2-P: a promising solid-phase extractant for uranium recovery from different acidic media. Journal of Radioanalytical and Nuclear Chemistry, 2018. 316: p. 221-231.

[15] Trumm, S., et al., An Improved Hydrolytically-Stable Bis-Triazinyl-Pyridine (BTP) for Selective Actinide Extraction. Solvent Extraction and Ion Exchange, 2011. 29(2): p. 213-229.

[16] Wei, Y.-Z., et al., Separation of Am (III) and Cm (III) from trivalent lanthanides by 2, 6-bistriazinylpyridine extraction chromatography for radioactive waste management. Journal of alloys and compounds, 2004. 374(1): p. 447-450.

[17] Hoshi, H., et al., Group separation of trivalent minor actinides and lanthanides by TODGA extraction chromatography for radioactive waste management. Journal of alloys and compounds, 2004. 374(1): p. 451-455.

[18] Demir, S., et al., Extraction of Lanthanide and Actinide Ions from Aqueous Mixtures Using a Carboxylic Acid-Functionalized Porous Aromatic Framework. ACS Central Science, 2016. 2(4):

[19] p. 253-265.

[20] Karslyan, Y., et al., Sequestration of trivalent americium and lanthanide nitrates with bis-lactam- 1,10-phenanthroline ligand in a hydrocarbon solvent. RSC Advances, 2019. 9(46): p. 26537- 26541.

ICNST 2024 International Conference on Nuclear Science and Technology
6- 8 MAY 2024 | Isfahan, Iran

Evaluation of the mass and activity of 241Am radionuclide production from different reactors using ORIGEN code (Paper ID : 1107)

Sareh Ammari Allahyari1*,Mohammad Ghannadi Maragheh1, Ehsan boustani2, Amir Charkhi1, Ali Yadollahi1

1. Nuclear fuel cycle research school, Nuclear Science and Technology Research Institute, P.O.BOX: 1439955933, Tehran, Iran
2. Reactor and nuclear safety research school, Nuclear Science and Technology Research Institute, P.O.BOX: 1439955933, Tehran, Iran

Abstract

^{241}Am is one of the transuranic elements that is used in measuring and controlling the thickness of various industrial materials, diagnosing thyroid disorders, smoke detectors production, designing neutron sources for well logging, etc. Therefore, due to the wide applications of this isotope, research and development for its production, separation, and purification are of great importance. Nowadays, the commercial production of this isotope is done in the United States and Russia. Since the production of ^{241}Am is carried out from irradiated fuel of power reactors or irradiation targets in research reactors, in this work, the possibility of production and activity of this radionuclide from the irradiated fuel of a typical MW1000 and MW 360 reactors has been investigated using the ORIGEN code. Results indicate the highest production of ^{241}Am in a MW 1000 reactor. Therefore, the irradiated fuel of the MW 1000 reactor can be a suitable source for the extraction of this isotope.

Keywords: Am-241, ORIGEN code, Irradiated fuel, 1000 and 360 MW Nuclear power reactors

Introduction

Americium is one of the synthetic actinide elements with the atomic number 95, without any stable isotopes. All isotopes of this element are radioactive. Among the 15 identified isotopes and isomers of americium, the longest half-life is attributed to ^{243}Am. The most important isotopes of americium, ^{241}Am and ^{243}Am, are significant due to their long half-lives of 433 and 7380 years, respectively. These isotopes have been produced in kilogram quantities with high purity. ^{242}Am, with a half-life of 141 years, can be produced in small amounts by the neutron absorption of ^{241}Am.

Due to the low price, accessibility, and suitable half-life, ^{241}Am, this element is considered as a low-energy gamma-ray source compared to all competing radionuclides [1,2].

The production of ^{241}Am through the (n, γ) interaction with plutonium proceeds as follows:

$$^{239}Pu(n\ \gamma)^{240}Pu(n\ \gamma)^{241}Pu \xrightarrow{-\beta^-} {}^{241}Am \quad (1)$$

This reaction is presently considered the best method for producing pure ^{241}Am. ^{241}Am has a long half-life and emits predominant 5.59 keV gamma radiation, which makes it useful for a wide range of industrial measurement applications and for detecting certain thyroid diseases [3]. Additionally, americium is a strong alpha emitter and is used in the industry as a neutron source, emitting 486.5 MeV energy in 85% of its decays.

The most widespread application of americium is in smoke detectors. One gram of americium dioxide, AmO_2, provides enough active material for over 5000 smoke detectors. In the 1980s, annual sales of smoke detectors reached 12 million units. This radionuclide, when combined with beryllium, emits 10^^17 neutrons per gram per second. This mixture is used in the design of neutron sources. ^{241}Am is used as a neutron source in radiography, tomography, and other radiochemical studies. Neutron sources are used in various industries for measurements of density, moisture, and hydrocarbon content. The most extensive use of neutron sources is in well logging operations. The cost of these operations is estimated between 60-70 million dollars annually. The weight of a neutron source is approximately 6 grams, and its activity is 30 Ci. Due to the high half-life of ^{241}Am compared to ^{238}Pu, this isotope is used in radioisotope thermoelectric generators (RTGs) in spacecraft. This isotope can also be used to produce other isotopes such as ^{242}Cm and ^{238}Pu. ^{242}Cm is used in RTGs due to its high specific thermal capacity (120 W/g), while ^{238}Pu is used in medical applications, such as long-term power supply for artificial hearts. In 1962, ^{241}Am was first introduced to the market with a current price of $1500 per gram [4-6].

While several kilograms of ^{241}Am are produced annually, this is the only commercially applicable isotope of americium. Though the exact amount of americium production is not well defined, the inventory of ^{243}Am has been reported between 10 to 100 grams [3]. ^{241}Am and ^{243}Am can be produced through the neutron activation of ^{239}U or ^{239}Pu in a high flux nuclear reactor.

The content of americium after irradiation of standard PWR and BWR fuel assemblies is approximately 600 grams (0.09%) and 220 grams (0. 07%) respectively. Commercial nuclear reactors produce kilogram quantities of the two americium isotopes, americium-241 and americium-243, with the specific isotope ratios being dependent on the reactor burn-up. The DOE Savannah River reactors in the United States produced approximately 9 kilograms of a 243Am-244Cm mixture over a period of 10 years. About 1 kilogram mixture of ^{241}Am and ^{243}Am was also recovered during the reprocessing of Shippingport blanket fuel at the Hanford DOE site in the United States. Approximately 30 kilograms of americium remain as

waste at the Hanford DOE site, while liquid wastes from the Plutonium Uranium Extraction (Purex) process are also considered as potential sources of americium [7].

Until now, there has been a lack of research in our country regarding the production of these valuable and extensively utilized radioisotopes, despite the considerable technological significance in their production, separation, and purification processes. This study has evaluated the feasibility of these elements production and their activity from irradiated fuel of a typical 1000 MW and 360 Mwe light water reactors to optimize the production of these elements using the ORIGEN code.

Research theories

The research was conducted by taking into account certain approximations and simplifications which should be considered in the interpretation and use of the results obtained. The ORIGEN computational code which has been used for calculations, developed for fuel consumption, decay, and radiation dose rate calculations. Key code outputs include isotopes mass in grams, total radiation and alpha radiation in curies, thermal power in watts, neutron absorption, fission, instantaneous fission, (α,n) reactions, and photon counts in 18 energy groups [8-11].

Results & Discussion

Mass and activity calculations of produced americium-241 in MW 1000 reactor: Calculations were carried out for a fuel assembly based on its irradiation history in a typical MW 1000 reactor and considering irradiation periods of 1091 days and cooling periods of 4, 10, 25, and 50 years. The mass and activity of the produced americium from a fuel assembly with a fuel burnup of 43000 megawatt-days per ton in a typical 1000 Mwe reactor are presented in Tables 1 and 2.

Table 1. The quantity of Americium production for one standard FA (g)

Radionuclide	Cooling(yr)				
	0	4	10	25	50
Am^{241}	1.331E+01	1.065E+02	2.155E+02	3.779E+02	4.727E+02
Am^{243}	3.808E+01	3.813E+01	3.811E+01	3.806E+01	3.797E+01
Am	5.175E+01	1.449E+02	2.539E+02	4.162E+02	5.109E+02

Table 2. The activity of Americium isotopes for one standard FA (Ci)

Radionuclide	Cooling(yr)				
	0	4	10	25	50
Am^{241}	4.57E+01	3.657E+02	7.399E+02	1.298E+03	1.623E+03
Am^{243}	7.594E+00	7.604E+00	7.600E+00	7.589E+00	7.571E+00
Am	9.335E+04	3.791E+02	7.532E+02	1.310E+03	1.635E+03

Calculations of mass and activity of Amersim-241 produced in a typical MW 360 reactor assuming 50% fuel consumption:

This reactor has a thermal power of 1130 megawatts, which produces this power from ceramic uranium with three different enrichments: 2.44%, 2.78% and 3.48%. The fuel characteristics of this reactor are considered similar to MW 1000 reactor. The weight percentage of uranium isotopes in the fuel cannot be more than 88%. According to this article, some of the most important specifications of this reactor are listed in Table 3.

Table 3. the specifications of a typical 360 Mwe reactor

Parameter	amount
Components of a FA with an average enrichment of 3% (kg)	^{235}U (9.91) / ^{238}U (320.33) / O (44.61)
Weight of a standard fuel assembly (kg)	374.8
The number of fuel assemblies	121
The total weight of Uranium 235 in the core(kg)	1199
Total core weight (kg)	45351
The duration of reactor operation in one cycle	354 days

For a fuel assembly operating during 354 days at a power of 1130 megawatts, the amount of 4066 grams of uranium-235 is consumed, which is equivalent to 41.04% of its fuel consumption. In the process of operation during 510 days, the fuel consumption will reach 59.13%, which is the maximum fuel consumption of the assembly. Calculations for the operation during 510 days, has also been done. The mass and activity of amersium produced for one fuel assembly out of 121 core fuel assemblies are shown in Tables 4 and 5, respectively.

Table 4. The quantity of Americium production for one standard FA (g)

Radionuclide	Cooling(yr)				
	0	4	10	25	50
Am۲۴۱	2.69E+00	2.99E+01	6.09E+01	1.07E+02	1.34E+02
Am۲۴۳	1.60E+00	1.60E+00	1.60E+00	1.60E+00	1.59E+00
Am	4.34E+00	3.16E+01	6.26E+01	1.09E+02	1.36E+02

Table 5. The activity of Americium isotopes for one standard FA (Ci)

Radionuclide	Cooling(yr)				
	0	4	10	25	50
$Am^{۲۴۱}$	9.23E+00	1.03E+02	2.09E+02	3.68E+02	4.60E+02
$Am^{۲۴۳}$	3.18E-01	3.19E-01	3.19E-01	3.19E-01	3.18E-01
Am	6.27E+03	1.04E+02	2.10E+02	3.69E+02	4.61E+02

Comparison of Americium-241 Production per Unit Mass

In this section, a comparison is made of the production and activity of americium per kilogram of spent uranium in MW 1000 and 360 reactors. The results are presented in figures below. As seen, the amount of americium production in the MW 1000 reactor is higher, as expected, compared to the MW 360 reactor.

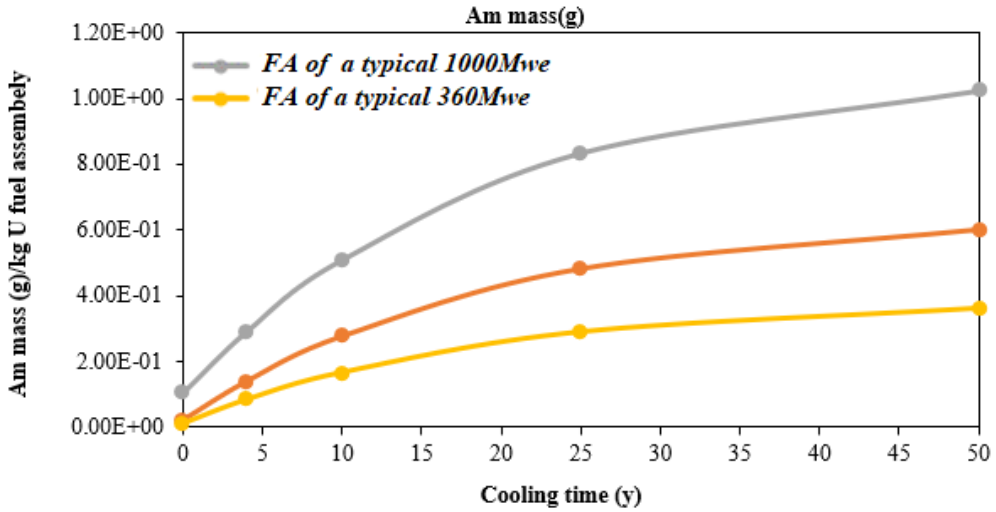

Fig. 1. Americium production

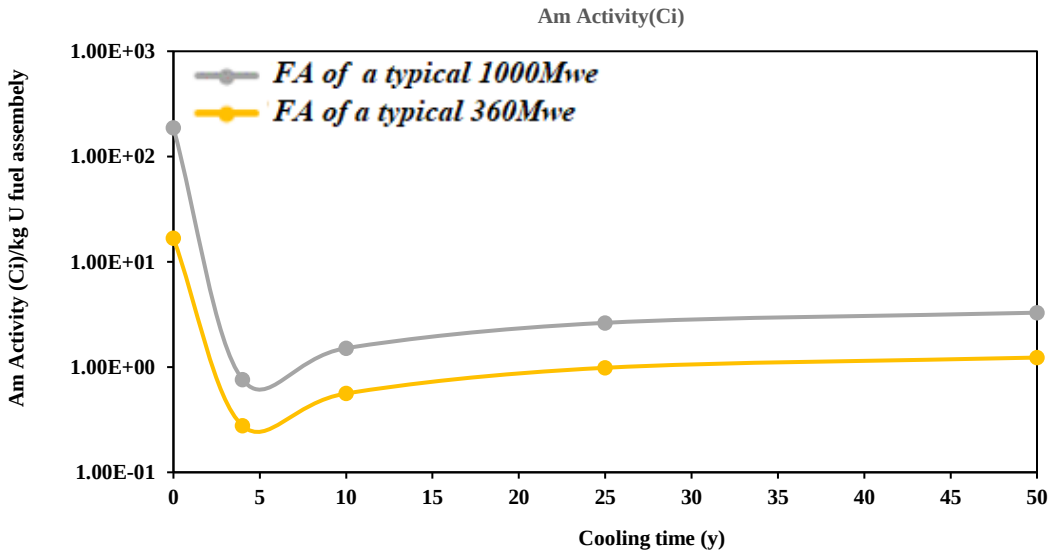

Fig. 2. Americium activity

Conclusion

In the present work, calculations related to the production and activity of the radioisotope americium-241 from irradiated fuel in the MW 1000 and 360 reactors have been conducted and the results have been compared. The results indicate that the amount of americium increases with cooling time. Additionally, the

production of 241Am per one kg of consumed uranium in the MW 1000 reactors is approximately 2.85-8.97 times higher than that of the MW 360, and 1.71-4.64 times higher than the target irradiation in the Tehran research reactor, depending on the cooling period. Regarding the activity, the corresponding values range from 11.2-2.67 and from 1.61-5.75, respectively. Hence, irradiated fuel from the MW 1000 reactor can be a suitable source for the extraction of this isotope.

References

[1] Crandall, J. L. (1971) Applications of Transplutonium Elements, Savannah River Laboratory.

[2] Morss, L.R., Edelstein, N.M, Fuger. (2006) Americium in: The Chemistry of the Actinide and Transactinide Elements (third edition), pp: 1265-1395.

[3] Seaborg, G.T. and Loveland, W.D. (1990) Elements beyond uranium.

[4] Americium, in Toxicological Profile for Americium, (2004) US department of health and human servicer. p. 104-113

[5] Ambrosi, R.M., Williams, H., Watkinson, E.J., Barco, A., Mesalam, R., Crawford, T., Bicknell, C., Samara-Ratna, P., Vernon, D., Bannister, N. and Ross, D., 2019. European radioisotope thermoelectric generators (RTGs) and radioisotope heater units (RHUs) for space science and exploration. Space Science Reviews, 215(8), pp.1-41.

[6] Parrington, J.R., Knox, H.D., Breneman, S.L., Baum, E.M. and Feiner, F. (1996) Nuclides and Isotopes: wall chart information booklet. General Electric, Schenectady, NY.

[7] Miguirditchian, M., Vanel, V., Marie, C., Pacary, V., Charbonnel, M.C., Berthon, L., Hérès, X., Montuir, M., Sorel, C., Bollesteros, M.J. and Costenoble, S. (2020). americium recovery from highly active PUREX raffinate by solvent extraction: the EXAm process. A review of 10 years of R&D. Solvent Extraction and Ion Exchange, 38(4), pp.365-387.

[8] Waters, L.S., 2002. MCNPX user's manual. Los Alamos National Laboratory, 124.

[9] IM J, B., ORIGEN-The ORNL Isotope Generation and Depletion Code. ORNL-7628, Oak Ridge National Laboratory, 1973.

[10] Wilson, W. B., T. R. England, M. Herman, R. E. MacFarlane, and D. W. Muir. "CINDER'90 code for transmutation calculations." In CONFERENCE PROCEEDINGS-ITALIAN PHYSICAL SOCIETY, vol. 59, pp. 1454-1457.

[11] IM J, B., ORIGEN-The ORNL Isotope Generation and Depletion Code. ORNL-7628, Oak Ridge National Laboratory, 1973.

ICNST 2024 International Conference on Nuclear Science and Technology
6- 8 MAY 2024 | Isfahan, Iran

Investigation of Crucial Aspects in the Removal of Vanadium Ions from Wastewater through the Utilization of a Membrane Bioreactor (Paper ID : 1126)

Mehdi Asadollahzadeh, Rezvan Torkaman*

Nuclear Fuel Cycle Research School, Nuclear Science and Technology Research Institute, P.O. Box: 11365-8486, Tehran, Iran

Abstract

Treating nuclear wastewater with high efficiency is crucial due to the significance of environmental pollution and water scarcity. The membrane bioreactor, comprised of a biological reactor equipped with suspended biomass and microfiltration membranes, plays a main role in this process. In the present investigation, the focus was on studying the removal of vanadium ions using the membrane bioreactor. Additionally, the study examined various environmental factors, such as the chemical oxygen demand. Interestingly, no significant changes were observed in the removal percentage of wastewater pollution when the vanadium ion concentrations were altered. The organic loading of the wastewater dropped from 1230 mg/L to 75 mg/L. The results indicated that the highest removal percentage, reaching 99.6%, was achieved in the experiments. Acidic conditions resulted in a decrease in the removal of organic loading, leading to a minimum organic load output of 790 mg/L. This study validated the feasibility of vanadium removal using the membrane bioreactor.

Keywords: Membrane Bioreactor, Vanadium Ions, Activated Sludge, Biosorption, Nuclear Wastewater Treatment

Introduction

Industries such as glass, textile, ceramic, photography, metallurgy, rubber, and plants that produce industrial inorganic chemicals and pigments discharge vanadium and its compounds into water bodies [1]. Furthermore, vanadium is present in the effluent of nuclear industries as it is an accompanying element in the extraction of uranium and thorium from minerals [2]. V(IV) and V(V) are the dominant valence states of vanadium in aquatic environments. The toxicity of vanadium increases with a higher valence state, making V(V) a more toxic form [3]. Its presence in groundwater results in greater pollution. Various physical and chemical treatments have been explored for vanadium removal, but their cost-effectiveness and potential for secondary pollution need further examination. Biological treatment, particularly microbial V(V) reduction, holds promise for remediating V(V) pollution due to its low cost and potential applications

for in situ remediation. It could be combined with other methods such as microbial electrochemistry to efficiently remove metal ions from groundwater [4].

The human body is exposed to heavy metals like vanadium, which can lead to various problems due to their accumulation and inability to break down. As a result, there is a global need for a solution to extract these heavy metals from urban and industrial wastewater [5]. Currently, membrane-based separation methods are widely utilized in daily activities, showing their simplicity and cost effectiveness compared to other conventional processes like adsorption. These membrane processes offer numerous advantages, including low energy consumption, scalability, compatibility with other techniques, continuous operation, high intensity, efficiency, automatic functioning, and the absence of chemical additives [6]. One specific technology, membrane bioreactors (MBRs), combines biological treatment using activated sludge with membrane filtration, either through microfiltration or ultrafiltration stages, creating a compact and economical system [7-8]. Zhang and co-workers stated that autotrophic microorganisms convert elemental sulfur S (0) and zerovalent iron Fe (0) into sulfate and ferrous iron Fe(II), respectively. The byproducts of this process, known as volatile fatty acids (VFAs), act as the main sources of nutrients for V(V) reducers [9]. Wang and co-workers provided evidence for the ability of Shewanella loihica PV-4 to reduce V(V) both inside and outside of cells [10]. The elimination of V(V) ions from individual metal water solutions through nanofiltration in a commercial spiral wound unit was examined by Lazaridis et al. The process was influenced by the pH level, and it was found that V(V) was highly rejected (90-100%) in the higher pH range due to the presence of different vanadium species [11]. Shang et al. conducted a study on the vanadium rejection and permeate flux using two commercial membranes, DK and DL, in the nanofiltration process. They discovered that both membranes were successful in effectively rejecting vanadium, with rejection rates exceeding 96%. They recommended the DL membrane for practical use due to its higher permeate flux [12].

This study focuses on investigating the key factors affecting the elimination of vanadium ions from synthetic nuclear wastewater using a membrane bioreactor.

Experimental

Membrane Bioreactor and Characteristics of Synthetic Feed

The aim of this research was to examine the effectiveness of a 120-liter membrane bioreactor in the removal of vanadium ions from wastewater. Fig.1 illustrates the design of the submerged membrane bioreactor.

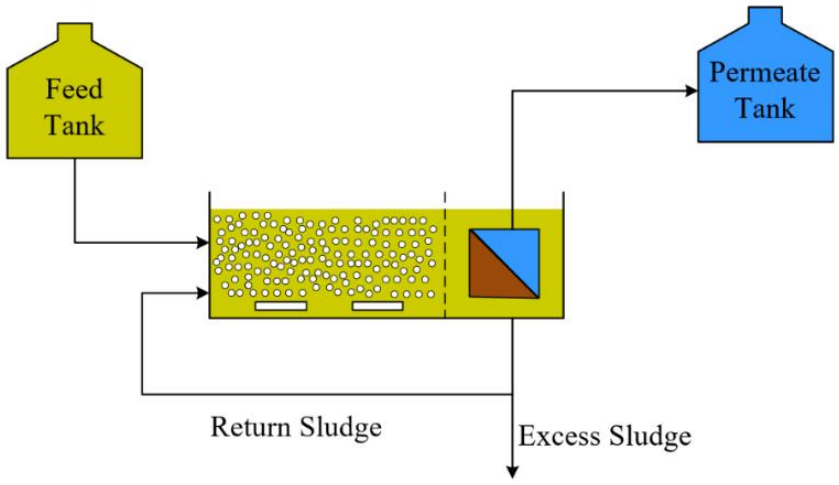

Fig.1. Schematic of the submerged membrane bioreactor

The proportion of carbon, nitrogen, and phosphorus in the treated effluent was maintained at a ratio of 100/5/1. To achieve this, glucose was utilized as the main source of carbon, potassium dihydrogen phosphate was used as the primary source of phosphate, and ammonium chloride served as the main source of nitrate. The effluent obtained from the South Tehran sewage treatment plant had a total concentration of 1000 mg/L.

Experimental Procedure

The most frequently employed technique for purifying wastewater is the use of activated sludge in a membrane bioreactor. Within these bioreactors, the microorganisms that exist degrade the organic contaminants found in both urban and industrial wastewaters, transforming them into carbon dioxide, sewage, and sludge. The measurement of chemical oxygen demand (COD) and biological oxygen demand (BOD) can be used to determine the degradation rates of these pollutants.

The growth and activity of microorganisms in the bioreactor system depend on factors such as appropriate aeration, temperature, pH levels, and suitable feed. Several factors, including bioreactor operating conditions, the requirements of activated sludge, and membrane structure, affect the capability of the membrane bioreactor system to eliminate heavy metals.

The main objective of this research was to investigate the elimination of vanadium ions by utilizing the membrane bioreactor system. Various factors related to operation and processes such as mixed liquor suspended solids (MLSS), mixed liquor volatile suspended solids (MLVSS), chemical oxygen demand (COD), dissolved oxygen (DO), and hydraulic retention time (HRT) were investigated in this study.

The quality of activated sludge is assessed by measuring MLSS and MLVSS. MLSS indicates the concentration of solid particles, such as cells and other solid particles, in the sludge mixture. This measurement helps determine the amount of suspended solids and soluble substances, both organic and inorganic, in the aeration tank of the wastewater treatment system. Regular measurement of MLSS and MLVSS is essential for evaluating the functionality of the wastewater treatment system. To determine the quantity of suspended particles in the system, 55 mm diameter filter paper was employed. Equation (1) was utilized to calculate MLSS values.

$$MLSS = \frac{M_2 - M_1}{V} \times 10^6 \quad (1)$$

The given equation represents the MLSS concentration in milligrams per liter. The masses of the filter paper before and after testing, M_1 and M_2 respectively, are utilized. The measured amount of sludge is denoted as V. An elevation in the volatile suspended solids within the MLVSS mixture indicates a growth in the bacterial population. The secondary filter paper is subjected to a temperature of 550 °C in the furnace for a period of 2 hours until it is completely burnt, and subsequently, it is transferred to the desiccator. One hour later, its weight is determined using the following formula:

$$MLVSS = \frac{M_3 - M_2}{V} \times 10^6 \quad (2)$$

In the equation mentioned above, M_3 denotes the mass of the filter paper after undergoing combustion in the furnace. The unit of MLVSS in this equation is expressed in milligrams per liter. Factors such as the type of air diffuser and aeration model, as well as water temperature, affect the concentration of dissolved oxygen in the system. Lower water temperatures lead to higher levels of dissolved oxygen. The amount of dissolved oxygen can be adjusted in the system by using a control valve. An oxygen meter was used to measure the DO value.

The pressure gradient within the transmembrane pressure (TMP), also known as the pressure at both ends, is determined by the average difference between the input and output pressures from the membrane. The hydraulic retention time is defined as a function of the reactor volume and the duration of reactor discharge, measured in minutes. Chemical oxygen demand is a crucial parameter used to assess the quality of wastewater. The required amount of oxygen serves as an indicator of the level of organic pollution in the wastewater, as analyzed by UV spectrophotometer (DR 6000 model).

In order to study the vanadium metal ion, a range of 50-150 mg/L was chosen as the concentration, based on the wastewater obtained from the thorium precipitation process mentioned in reference [13]. The

retention time of solid particles, flux through the membrane, type of membrane, and the maximum pressure at both ends of the membrane were set at 15 days, 283 liters per hour per square meter, PVDF flat plate membrane, and 250 mbar, respectively.

Results and Discussion

Fig.2 displays the impact of hydraulic retention time on the elimination of vanadium at a concentration of 150 mg/L. When the retention time is short, the small size of the clusters consisting of metals and microorganisms causes a lower percentage of removal through membrane filtration compared to retention times longer than 24 hours. Moreover, microorganism's resistant to vanadium metal, which are responsible for the biological removal process, have limited time to carry out their biological activities. The graph also demonstrates the effect of residence time on the removal of COD, indicating an increasing trend with the advancement of the process. Apart from the elimination of vanadium, it is also feasible to remove carbon compounds.

Fig.3 presents the findings regarding the elimination of vanadium ions. The data acquired indicated that the maximum removal rate reaches 99.6% when the initial concentration is 150 mg/L. Table 1 displays additional factors and procedural elements involved in the vanadium removal process using a membrane bioreactor.

Fig.4 demonstrates that there is no apparent change in the removal of COD as the concentration of vanadium ions is altered. The organic loading of wastewater decreases from 1230 mg/L to 75 mg/L.

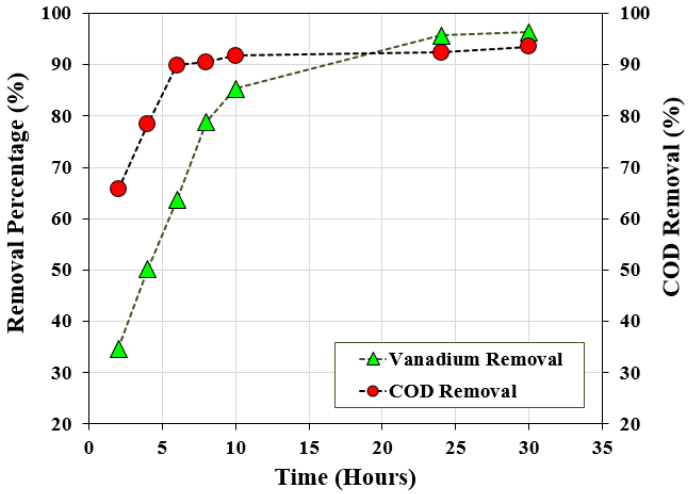

Fig.2. Removal percentage of vanadium and COD removal in the membrane bioreactor influenced by the hydraulic retention time

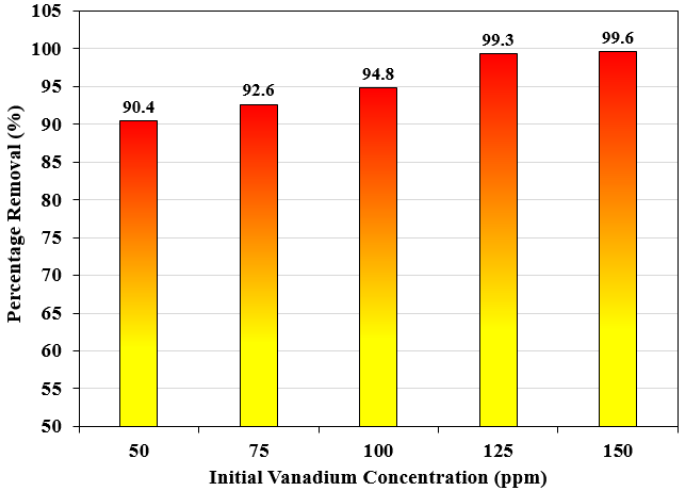

Fig.3. Removal percentage of the membrane bioreactor influenced by the concentration of vanadium ions

Table 1. Results for the removal of vanadium ions in the membrane bioreactor

Vanadium concentration (mg/L)	MLSS (mg/lit)	MLVSS (mg/lit)	pH	DO	HRT (h)	TMP (mbar)	Temperature (ºC)
50	5380	3870	8.06	9.8	24	250	25
75	4320	3320	8.12	10.2	24	250	25
100	4120	3156	8.08	11.0	24	250	25
125	3890	2950	8.09	10.4	24	250	25
150	3860	2780	8.14	11.3	24	250	25

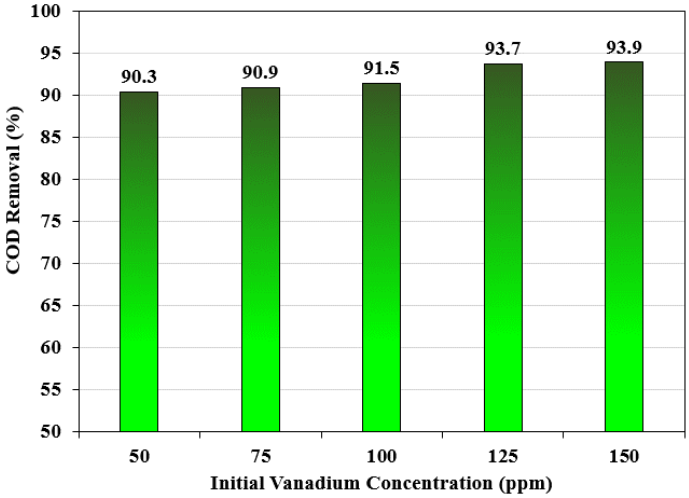

Fig.4. COD Removal of the membrane bioreactor influenced by the concentration of vanadium ions

To examine the impact of pH on the membrane bioreactor, soda compounds and hydrochloric acid were utilized to regulate the pH levels. The experiment involved four pH values: 2, 4, 6, and 8. The bioreactor's outlet flow rate was used to quantify the amount of organic loading. In order to compare sewage pollution

levels, the initial organic loading was set at 1230 mg/L. According to Fig.5, the removal of organic loading diminishes under acidic conditions, resulting in the lowest output of 790 mg/L. Additionally, the removal of vanadium ions is less effective in acidic environments but achieves maximum removal in alkaline conditions.

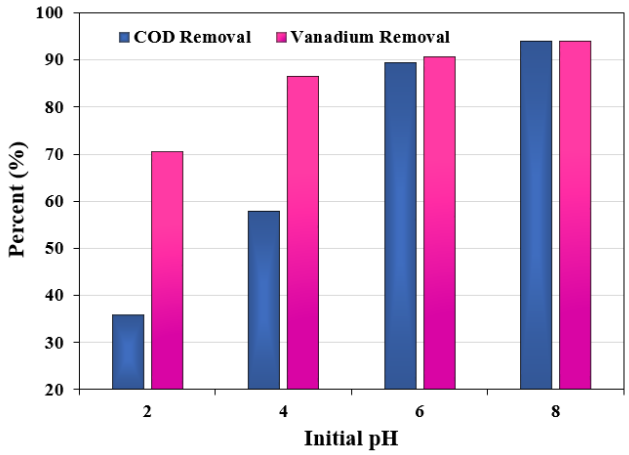

Fig.5. Effect of pH on COD removal and the vanadium removal percentage

Conclusions

The findings indicated that the maximum elimination rate achieved was 99.6% for vanadium ions when the initial concentration was 150 mg/L. As the concentration of vanadium ions in the input increased, the removal rate of vanadium metal also increased. The enlargement of purifying sludge flakes due to higher concentrations of vanadium metal hindered the passage of metal ions through the membrane. When the concentration of vanadium metal was low, the removal of organic load by the membrane bioreactor remained unaffected. The environmental pH was identified as a significant factor affecting the reduction of the removal rate of chemical pollution. The biological process played a role in the removal process within the bioreactor environment. The acidic pH levels led to the destruction of microorganisms in this environment. Hence, an alkaline medium in the membrane bioreactor was found to be effective in achieving the desired removal rate.

References

[1] Yuan, R., Li, Sh., Che, Y., He, J., Song, J., and Yang, Bi. (2021) A critical review on extraction and refining of vanadium metal, International Journal of Refractory Metals and Hard Materials, 101:105696.

[2] Zhang, B., Zhang, H., He, J., Zhou, Sh., Dong, H., Rinklebe, J., and Sik Ok, Y. (2023) Vanadium in the Environment: Biogeochemistry and Bioremediation, Environmental Science & Technology, 57(39): 14770–14786.

[3] Liu, J., Huang, Y., Li, H., and Duan, H. (2022) Recent advances in removal techniques of vanadium from water: A comprehensive review, Chemosphere, 287: 132021.

[4] Patel, A.K., Tambat, V.S., Singhania, R.R., Chen, Ch., Pandey, A., Chang, J., Dong, Ch. (2023) Advanced strategies for effective treatment of vanadium (III) polluted water by potential microalgae, Journal of the Taiwan Institute of Chemical Engineers, Article in press: 105166.

[5] Komesli, O.T. (2014) Removal of heavy metals in wastewater by membrane bioreactor: Effects of flux and suction period, Journal of the chemical society of Pakistan, 36(4): 654-661.

[6] Bosu, S., Rajamohan, N., Rajasimman, M., Raut, N., Vasseghian, Y. (2023) Hydrogen based membrane bioreactor for environmental remediation of pollutants- Review on applications and mechanism, International Journal of Hydrogen Energy, 48 (17): 6546-6559.

[7] Sengupta, A., Jebur, M., Kamaz, M., and Wickramasinghe, R.S. (2022) Removal of Emerging Contaminants from Wastewater Streams Using Membrane Bioreactors: A Review, Membranes, 12: 60-85.

[8] Giwa, A., Dindi, A., and Kujawa, H. (2019) Membrane bioreactors and electrochemical processes for treatment of wastewaters containing heavy metal ions, organics, micropollutants and dyes: Recent developments, Journal of Hazardous Materials, 370: 172-195.

[9] Zhang, B., Qiu, R., Lu, L., Chen, X., He, C., Lu, J., and Ren, Zh. (2018) Autotrophic Vanadium(V) Bioreduction in Groundwater by Elemental Sulfur and Zerovalent Iron, Environmental Science & Technology, 52(13):7434–7442.

[10] Wang, G., Zhang, B., Li, Sh., Yang, M., and Yin, Ch. (2017) Simultaneous microbial reduction of vanadium (V) and chromium (VI) by Shewanella loihica PV-4, Bioresource Technology, 227: 353-358.

[11] N.K. Lazaridis, M. Jekel, A.I. Zouboulis (2003) Removal of Cr(VI), Mo(VI), and V(V) Ions from Single Metal Aqueous Solutions by Sorption or Nanofiltration, Separation Science and Technology, 38(10): 2201-2219.

[12] Shang, G., Zhang, G., Gao, C., Fu, W., and Zeng, L. (2014) A novel nanofiltration process for the recovery of vanadium from acid leach solution, Hydrometallurgy, 142: 94-97.

[13] Amiri, M., Keshtkar, A.R., Moosavian, M.A. (2023) Th(IV), V(V), and Fe(III) biosorption from real wastewater of thorium chemical precipitation process by Ca-pretreated Cystoseria indica alga: breakthrough curves modeling in a fixed bed column and biosorption mechanism study, 45 (3): 125-136.

ICNST 2024 International Conference on Nuclear Science and Technology
6- 8 MAY 2024 | Isfahan, Iran

Elimination of Molybdenum Ions from Wastewater using Submerged Membrane Bioreactor in Conjunction with NaA Zeolite (Paper ID : 1127)

Mehdi Asadollahzadeh, Rezvan Torkaman*
Nuclear Fuel Cycle Research School, Nuclear Science and Technology Research Institute, P.O. Box: 11365-8486, Tehran, Iran

Abstract

The presence of toxic heavy metals in the discharged waste of nuclear industry is recognized as a significant threat to living organisms. When these metals reach high concentrations in the water sources that enter the body of living organisms, they disrupt the proper functioning of body's tissues. The membrane bioreactor is a suitable method that combines biological and membrane stages to effectively control the concentration of heavy metals, including molybdenum ions, in wastewater. This research demonstrated that a flat sheet membrane bioreactor achieved a remarkable 99.2% removal of molybdenum from wastewater within a hydraulic retention time of 24 hours. Under optimal conditions, the retention time of solid particles, the maximum trans-membrane pressure and temperature were 15 days, 250 mbar, and 25 °C, respectively. The presence of NaA zeolite does not impact the removal of molybdenum ions, but it does lead to a notable increase in the amount of purified water produced and helps in the reduction of membrane fouling.

Keywords: Membrane Bioreactor, Molybdenum Ions, Fouling, Adsorption, Nuclear Wastewater Treatment

Introduction

Molybdenum has a crucial function in various chemical applications, such as catalysts, lubricants, and pigments. Furthermore, it is mainly employed as a constituent in steels, cast iron, and reactor vessels, improving characteristics like hardenability, strength, and resistance to corrosion [1]. The concentration of molybdenum, which is one of the fission products, is significant in the high-level waste produced by the PUREX reprocessing process. Several countries are producing high-level waste streams from nuclear reactors that include molybdenum oxides as a crucial element [2]. The World Health Organization (WHO) recommends a maximum allowable level of 0.07 mg/L of molybdenum in drinking water. In Flanders, the European Water Framework Directive (2000/60/EC) set the standard quality for surface water at a permissible limit of 0.34 mg/L starting in January 2011 [3]. Therefore, the concentration of molybdenum in wastewater should not exceed this value. Molybdenum is typically found in wastewater as an oxyanion, with the most common form being the molybdate anion, MoO_4^{2-}[4]. Due to the complex chemical composition of molybdenum, it has the potential to form both soluble and insoluble complexes. This can lead to various problems related to the concentration, storage, and solidification of high-level waste. Consequently, it is necessary to regulate the concentration of molybdenum and eliminate or adsorb any

excess of it [5]. A variety of methods can be employed to distinguish molybdenum ions, such as electrolysis, removal through membrane bioreactor, ion exchange, liquid-liquid extraction, adsorption process, and chemical precipitation [6].

One effective approach is the membrane bioreactor, which incorporates both biological and physical cleansing techniques. MBR plants are formed by combining the biological process and membrane filtration, which offers several advantages compared to traditional methods like activated sludge. MBR is extensively utilized for treating municipal and industrial wastewater [7]. Typically, the characteristics of microorganisms such as size, filamentous microorganism content, and growth rate are strongly influenced by the operating conditions of the bioreactor. Conversely, the activity of microorganisms can impact the performance of the MBR in two distinct ways: the quality of the effluent and the capacity of the MBR to treat the wastewater pollutant, as well as the fouling properties of the membranes [8]. Therefore, it is essential to thoroughly examine the principles of biological wastewater treatment, including microbiology, microorganism metabolism, microbial stoichiometry, and bioreactor kinetics. This is necessary in order to determine the optimal operating conditions for the bioreactor and design characteristics of MBR plants [9].

Kumar and colleagues conducted an experimental study on the recovery and recycling of the valuable metal molybdenum during the treatment of industrial wastewater. They utilized a unique technology combining membranes to achieve this objective. By employing hollow-fiber crossflow modules that incorporated ultrafiltration and nanofiltration membranes in a recirculation mode, they were able to effectively separate 96.5% of the molybdenum from the industrial wastewater [10]. Wu and co-workers devised a technique for creating uniformly distributed mixed matrix membranes (MMMs) by employing a method involving wet fillers. The fillers in this study consisted of a highly stable UiO-66-NH_2 metal organic framework. By incorporating wet UiO-66-NH_2 into a poly(vinylidene fluoride) (PVDF) matrix, the researchers successfully developed MMMs capable of efficiently removing Rhodamine B (RhB), Congo red (CR), and molybdenum (VI) ions from aqueous solutions. These MMMs not only exhibited effective dye and molybdenum (VI) removal due to the well-dispersed filler, but also offered valuable insights for the advancement of industrial membranes [11]. Tambat and co-workers introduced a method with the objective of enhancing the effectiveness of bioremediation for molybdenum and other inorganic pollutants on an industrial level through the use of microalgal treatment. Two strains of fast-growing microalgae, Chlorella sorokiniana TU5 and Picochlorum oklahomensis, were utilized for the purpose of molybdenum treatment. The highest capacity for removing molybdenum was recorded at 115.65 mg/L, while the biomass and lipid

yield reached 2.35 g/L and 579.3 mg/L, respectively, after a growth period of 14 days followed by exposure to the molybdenum pollutant [12].

Fouling is a major topic of concern in membrane bioreactors. The main reason for fouling in submerged bioreactors is the accumulation of sediment on the membrane. The aim of this study is to analyze how effective NaA zeolite is in removing molybdenum ions from the membrane bioreactor. The research is concentrated on understanding the main factors that impact the removal of molybdenum ions from synthetic nuclear wastewater using a membrane bioreactor.

Experimental

Characteristics of Feed and Membrane Bioreactor

The research focused on evaluating the efficiency of a membrane bioreactor in treating wastewater including molybdenum ions. Additionally, the impact of NaA zeolite powder in the system was examined. Fig.1 illustrates the layout of the submerged membrane bioreactor.

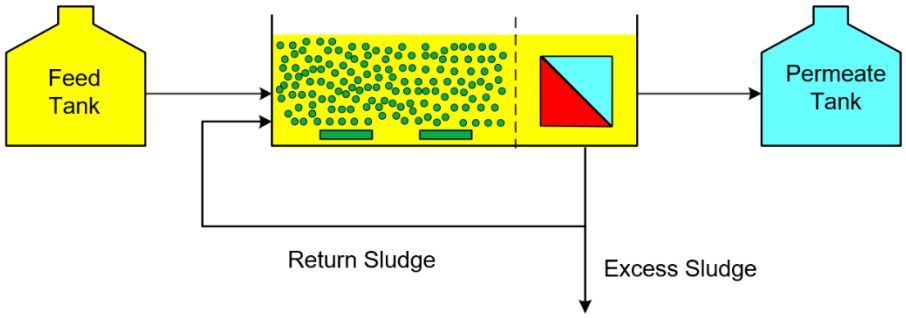

Fig.1. Schematic of the submerged membrane bioreactor

The effluent produced had a C/N/P ratio of 100/5/1. Glucose, potassium dihydrogen phosphate, and ammonium chloride were utilized as the main sources of carbonate, phosphate, and nitrate. Table 1 provides details on the flat sheet membrane employed in the study.

Table 1. Membrane Characteristics

Flat sheet membrane	
Pore size (micrometer)	0.1-0.4
MLSS (mg/L)	2000-15000
Effluent turbidity (NTU)	<1.0
Membrane Substance	PVDF (Polyvinylidene fluoride)
Membrane Area	34×46 cm 2 sides 0.25 m^2

Procedure

Removing heavy metals from wastewater is crucial for public health as these substances can be harmful. Activated sludge, which contains living microorganisms, plays a significant role in this process by utilizing bioaccumulation and bioremediation. Maintaining an alkaline pH level, typically between 7.5-8, is essential for the proper functioning of these microorganisms. By adjusting the pH level and utilizing an MBR system, heavy metals can be effectively removed from wastewater. Prior to conducting experiments, a 120-liter reactor containing 40 liters of activated sludge was allowed to stabilize for 15 days. Samples were collected before and after the membrane filtration process to study the impact of the membrane and activated sludge process on heavy metal removal. Different concentrations of molybdenum ions (5, 10, 15, 20, and 25 ppm) were introduced into the feed tank from the molybdenum solution made with $Na_2MoO_4.2H_2O$. Analysis of samples from the bioreactor and effluent tank was performed using a UV spectrophotometer. Chemical oxygen demand is a crucial parameter used to assess the quality of wastewater. The required amount of oxygen serves as an indicator of the level of organic pollution in the wastewater, as analyzed by UV spectrophotometer (DR 6000 model).

Results and Discussion

Fig.2 illustrates how the removal of molybdenum ions from synthetic feed with a concentration of 5 mg/L is affected by hydraulic retention time. When the retention period is short, the size of the flakes formed by metals and microorganisms is small, resulting in a lower percentage of membrane removal compared to retention periods exceeding 24 hours. Additionally, microorganisms that are resistant to molybdenum metal and responsible for biological removal have limited time to carry out their activities. Thus, a hydraulic retention time of 24 hours is required for effective removal of molybdenum metal.

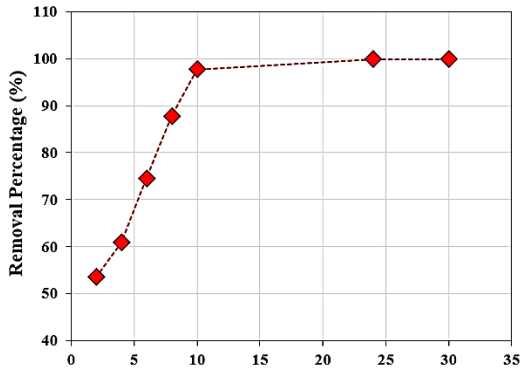

Fig.2. Effect of the hydraulic retention time on the molybdenum removal percentage (%) (TMP=250 mbar, T=25ºC)

The outcomes of the experiments carried out to analyze the impact of transmembrane pressure (TMP) on the elimination of molybdenum and COD in the membrane bioreactor system can be found in Table 2. The maximum pressure applied on either side of the membrane is a factor that arises from the suction of water and sludge from the membrane layers inside the reactor, and increasing it to higher values indicates that more active sites on the membrane are covered. In the case of industrial membranes made of flat plate fibers, applying pressure leads to higher flow loss due to the extensive contact surface. The research suggests that increasing the transmembrane pressure does not significantly affect the rate of molybdenum removal, with the most efficient removal of molybdenum occurring in the membrane bioreactor system. The findings indicate that a greater efficiency in COD removal was attained by increasing the maximum pressure at each end of the membrane.

Table 2. Effect of the transmembrane pressure in the membrane bioreactor system for molybdenum removal percentage (%) and COD removal

TMP (mbar)	HRT (h)	T(ºC)	Mo(VI) Concentration (ppm)	COD	Removal percentage (%)
150	24	25	25	589	99.1
200	24	25	25	165	98.8
250	24	25	25	127	99.2

Table 3 presents the impact of temperature fluctuations on the performance of membrane bioreactors. Elevated temperatures promote greater activity among thermophilic microorganisms compared to other microorganisms. However, exceeding this threshold can lead to the destruction of mechanisms in other microorganisms, making higher temperatures unsuitable for achieving maximum removal efficiency.

Table 3. Effect of the temperature in the membrane bioreactor system for molybdenum removal percentage (%)

T(ºC)	TMP (mbar)	HRT (h)	Mo(VI) Concentration (ppm)	COD	Removal percentage (%)
25	250	24	25	127	99.2
30	250	24	25	152	84.5
35	250	24	25	178	77.5

Fig.3 illustrates that around 60% of removal takes place through bioremediation. This is indicated by the metal concentration in the bioreactor. The remaining metal in the aqueous environment of the reactor forms sludge flakes on the membrane surface, rather than passing through the membrane holes, which have a value of 0.21 at the highest molybdenum metal concentration of 25 ppm. As the concentration of molybdenum ion in the synthetic effluent increases, the bioreactor's removal decreases. For initial

concentrations of 5, 10, 15, 20, and 25, the removal percentages were 99.9%, 99.8%, 99.7%, 99.4%, and 99.2%, respectively.

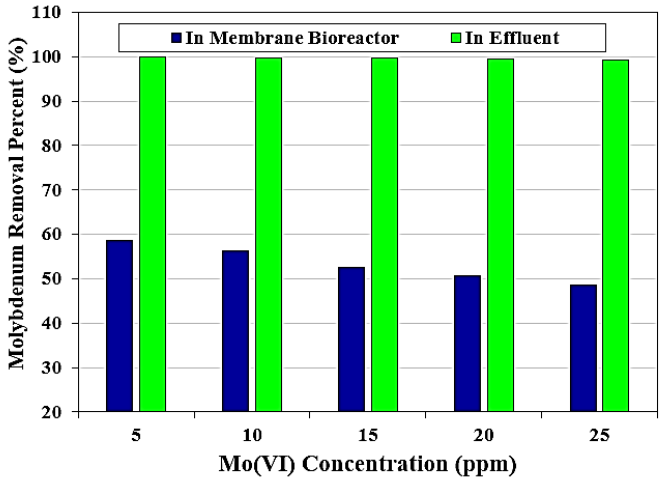

Fig.3. Effect of molybdenum concentration on the removal percentage in bioreactor and effluent

Various processes were combined to improve the performance of the membrane bioreactor. In the field of wastewater treatment, the combination of membrane bioreactor process with either chemical coagulation or an adsorbent is a common practice. The choice of adsorbent relies on factors such as cost and the ability to adsorb the pollutants. The NaA zeolite is considered a superior adsorbent due to its high surface area, volume ratio, and large pores. In the subsequent trials, powdered NaA zeolite was utilized as an adsorbent. Different amounts of 5, 10, 15, and 20 grams of adsorbent were tested in the experiments. The impact of NaA zeolite on molybdenum removal was found to be insignificant, as illustrated in Table 4.

Table 4. Effect of NaA zeolite in MBR reactor for Mo(VI) removal percentage (%)

NaA zeolite (g)	TMP (mbar)	HRT (h)	T(ºC)	Mo(VI) Concentration (ppm)	COD	Removal percentage (%)
5	250	24	25	25	127	99.2
10	250	24	25	25	134	89.8
15	250	24	25	25	123	99.3
20	250	24	25	25	131	89.6

In order to study the impact of zeolite on membrane fouling, the water flow rate from the clean membrane was examined, with the findings presented in Table 5. The amount of water leaving the used membrane decreases at various operating pressures compared to the clean membrane at the same pressures. The number of blocked holes in the fouled membrane is higher compared to the clean membrane, leading to increased particle penetration into the holes. This results in suspended particles settling on the membrane

surface and microorganisms being adsorbed, gradually thickening the cake layer on the membrane. As a result, the flux passing through the membrane decreases and the membrane surface resistance increases. These changes impact the volume of purified water, causing a decrease in output water. The use of zeolites for membrane cleaning helps the reduction in fouling and the cake layer on the surface, ultimately increasing water output. Zeolites improve the membrane surface hydrophilicity and reduce membrane fouling.

Table 5. Fouling membrane in the MBR

Type	TMP (mbar)	Time (s)	NaA zeolite (g)	V(L) in permeate tank
Clean Membrane	250	30	0	150
Used Membrane	250	30	0	55
Clean Membrane	250	30	5	275
Used Membrane	250	30	5	130
Clean Membrane	250	30	10	315
Used Membrane	250	30	10	178
Clean Membrane	250	30	15	325
Used Membrane	250	30	15	185
Clean Membrane	250	30	20	355
Used Membrane	250	30	20	190

Conclusion

This study utilized a 120-liter reactor and a flat plate membrane in a membrane bioreactor system to examine the removal of molybdenum metal from synthetic wastewater with a C/N/P ratio of 100:5:1. The research also looked into the effectiveness of NaA zeolite in reducing membrane fouling. The findings demonstrate that the combination of a 24 hour duration and a maximum pressure of 250 mbar at both ends of the membrane leads to the most effective removal of Mo(VI) ions. The impact of temperature on metal removal indicates that the highest rate of removal was seen at room temperature, with higher temperatures leading to a decrease in the removal efficiency. Adding more zeolite does not impact the elimination of Mo(VI) ions, however, it does have a notable beneficial impact on the amount of liquid permeate coming from the bioreactor and is linked to a decrease in membrane fouling.

References

[1] Pathak, S.K., Singh, S.K., Mahtele, A., and Tripathi, S.C. (2010) Studies on extraction behaviour of molybdenum (VI) from acidic radioactive waste using 2(ethylhexyl) phosphonic acids, mono 2(ethylhexyl) ester (PC-88A)/n-dodecane, Journal of Radioanalytical and Nuclear Chemistry, 284(3): 597-603.

[2] Brehault, A., Patil, D., Kamat, H., Youngman, R.E., Thirion, L.M., Mauro, J. C., Corkhill, C., McCloy, J., S., and Goel, A. (2018) Compositional Dependence of Solubility/retention of Molybdenum Oxides in Aluminoborosilicate Based Model Nuclear Waste Glasses, Journal of Physics and Chemistry B, 122(5):1714-1729.

[3] Verbinnen B., Block C., Lievens P., Brecht A.V., and Vandecasteele C. (2013) Simultaneous Removal of Molybdenum, Antimony and Selenium Oxynions from Waste water by Adsorption on Supported Magnetite, Waste Biomass Valorization, 4: 635-645.

[4] Joseph, M., Venkatachalam, M.S., and Kumar, P.A. (2022) Adsorption of Molybdenum from Wastewater by Surface Altered Agricultural Solid Waste, Iranian Journal of Chemistry and Chemical Engineering 41 (6):1883-1895.

[5] Atia, A.A., Donia A.M., and Awed H.A. (2008) Synthesis of magnetic chelating resins functionalized with tetraethylenepentamine for adsorption of molybdate anions from aqueous solutions. Journal of Hazardrous Materials, 155(1): 100-108.

[6] Namasivayam, C., and Sangeetha, D. (2006) Removal of molybdate from water by adsorption onto ZnCl2 activated coir pith carbon. Bioresource Technology, 97(10):1194-1200.

[7] Rahman, T.U., Roy, H., Islam, R., Tahmid, M., Fariha, A., Mazumder, A., Tasnim, N., Pervez, N., Cai, Y., Naddeo, V., and Islam, Sh. (2023) The Advancement in Membrane Bioreactor (MBR) Technology toward Sustainable Industrial Wastewater Management, Membranes, 13(2), 181-209.

[8] Deng, L., Guo, W., Ngo, H.H., Zhang, X., Chen, Zh., Ni., Sh., and Wang., Q. (2022) Recent advances in attached growth membrane bioreactor systems for wastewater treatment, Science of The Total Environment, 808: 152123.

[9] Al-Asheh, S., Bagheri, M., and Aidan, A., (2021) Membrane bioreactor for wastewater treatment: A review, Case Studies in Chemical and Environmental Engineering, 4: 100109.

[10] Kumar, R., Liu, Ch., Ha, G., Ho Kim, K., Chakrabortty, S., Tripathy, S.K., Park, Y., Khan, A., Yadav, K.K. Pinto, M.M., and Jeon, B. (2023) A novel membrane-integrated sustainable technology for downstream recovery of molybdenum from industrial wastewater, Resources Conservation and Recycling, 196: 107035.

[11] Wu, Zh., Zeng, J., Huang, X., Zhang, R., Liu, P. (2023) Mixed matrix membranes with highly dispersed UiO-66-NH2 filler for removal of dyes and molybdenum(VI) ions from aqueous solutions, Colloids and Surfaces A: Physicochemical and Engineering Aspects, 674: 2023-06-28.

[12] Tambat, V.S., Tseng, Y.S., Kumar, P., Chiu-Wen Chen, Singhania, R.R. Chang, J., Dong, C., Patel, A. (2023) Effective and sustainable bioremediation of molybdenum pollutants from wastewaters by potential microalgae, Environmental Technology & Innovation, 30(1):103091.

ICNST 2024 International Conference on Nuclear Science and Technology
6- 8 MAY 2024 | Isfahan, Iran

Control of Excessive Reactivity of the VVER-type Reactor Using Zirconium rod as a water displacer in the Uranium Fuel Cycle (Paper ID : 1131)

Anisur SK Rahman

Bangladesh Atomic Energy Regulatory Authority (BAERA), Authority Bhabon, E-12/A, Agargaon, Dhaka-1207, Bangladesh
*E-mail: ranisur01@gmail.com

Abstract

The compensation for the excess reactivity in the pressurized water reactors VVER is realized with high neutron absorber materials. The traditional excess reactivity regulation methods lead to unfeasible neutron utilization and reduce the multiplying coefficient. The article analyzes current problems and successful practices of implementing the change of moderator-to-fuel ratio as one of the methods for excess reactivity control. To investigate the trends in the formation of Cylindrical Zirconium rods (Zr rods) are used to fulfill the moderator-to-fuel ratio change. The Zr rods are placed between fuel rods in VVER fuel assembly as water displacer. The current work calculations are performed for the Uranium fuel cycle (U^{235}). The main problems of implementation the multiplying coefficient depends on the fuel burnup time in the presence of Zr rods between the fuel assembly (FA). The purpose of the research is to evaluate the dependence of the range regulation of the moderator to fuel ratio from the radius of the zirconium displacer. The change of the Zr rods diameter leads to the variation in moderator to fuel ratio. A comparison between the Zr rods as a reactivity regulator in VVER fuel assembly for the fuel cycle UO_2. The concentration of the fertile and fissile fuel components for the fuel cycle has been analyzed.

Keywords: excess reactivity, VVER, neutron absorber, multiplying coefficient, burnup, moderator-to fuel ratio, water displacers, reactivity, fuel assembly, fuel cycle.

Introduction

In order to reduce the cost of electricity produced at nuclear power plants, VVER-type reactors are currently using extended campaigns and reducing the use of neutrons in burnable absorber of the excess reactivity compensation system. As is known, the largest reactivity margin of the reactor is realized at the beginning of the campaign when loading fresh fuel. To compensate for it, a boron absorber dissolved in the coolant (liquid system) and burnable absorbers (Gd) are used in the fuel rods [1,2]. At high concentrations of boron absorber in the coolant, the density reactivity coefficient can change sign and become negative. In addition, liquid control generates a large amount of low-level liquid radioactive waste. Integrated burnable absorbers

(IBA) based on gadolinium (Gd) reduce the thermal conductivity of fuel rods and lead to an increase in the coefficient of uneven energy release inside the fuel assembly (FA). Consequently, the rejection of traditional methods of compensating for excess reactivity and the use of excess neutrons to increase the breeding of nuclear fuel are considered economically feasible from the point of view of the financial costs of operating the reactor. In this work, studied the possibility control of the reactivity margin based on changing the moderator-fuel ratio by introducing hollow zirconium rods into the inter-fuel space of fuel assembly's reactor type of VVER. In here zirconium displacers were placed in some guide channels, which made it possible to increase the duration of the campaign. By using Zr rods for the upgraded VVER core with uranium fuel is studied [2,3]. The use of Zr rods as water displacers changes the moderator-fuel mechanical ratio. The VVER- reactor's fuel assemblies 126 fuel assemblies with Zr rod as water displacers and 61 fuel assemblies with control rods. A large number of fuel assemblies and a decrease in the specific energy intensity of the core make it possible to abandon compensation of the reactivity margin for burnup by boric acid and make it possible to extend the fuel cycle up to six years with an average burnup of 50 MWday/kg[4,5].

Test problem and calculation code

The dimensions of the fuel assemblies and fuel elements are the same as the fuel assemblies of the VVER reactor. The calculations were carried out in the GETERA program is designed for neutron-physical calculation of cells and poly-cells of nuclear reactors, both fast and thermal, in spherical, cylindrical and planar geometry [6]. The program can be used to solve a wide range of problems: preparation of small-molecule cross sections for subsequent large-scale calculations, investigation of various characteristics of reactors in cell and poly-cellular models, solving problems related to burnup of fuels, modeling of various reactor regimes. The neutron-physical distribution of neutrons is calculated in the probability method of the first collisions. The GETERA program can be used to solve a wide range of tasks, both research and applied. With its help, it is possible to study the neutron-physical characteristics of the reactors at the cell and poly cell level. The algorithm for the multiplication of the cell makes it possible to simulate sufficiently large fragments of the reactor on a small number of cells. In addition to calculations of the fragments of the reactor, the built-in algorithms allow modeling the burnup processes in the reactor and calculating the characteristics of fuel cycles: for example, the coarse fuel burnup in reactors with cyclic and in reactors with continuous fuel overload. By using the program GETERA for a computational analysis of the effect

of a gadolinium absorber integrated into fuel rods to the fraction of the reactivity margin compensated by the liquid system regulation, the following model was considered [7,8].

Short description about Zirconium (Zr) and Boron (B)

Zirconium is a chemical element with the symbol Zr and atomic number 40. It has a very low thermal neutron absorption cross section, high hardness, ductility and corrosion resistance. One of the main uses of zirconium is in nuclear technology, especially in water reactors. The typical composition of nuclear grade zirconium alloys is more than 95 weight percent zirconium and less than 2% tin, niobium, iron, chromium, nickel and other metals, which are added to improve mechanical properties and corrosion resistance. There are several reasons. Why zirconium is the optimal material to surround uranium pellets: this metal is extremely resistant to corrosion and high temperatures and absorbs very few neutrons produced by nuclear fission reactions [9,10].

A major requirement associated with the development and operation of nuclear reactors is the control and containment of the neutrons that are maintained as well as produced during the fission reaction. Boron is one of the few elements that have nuclear energy regulation in a VVER reactor, which proves its feasibility as a neutron absorber material. Boron and its compounds, boric acid, boron carbide, etc. Boron has two main isotopes: B^{10} and B^{11}. The effectiveness of boron as a neutron absorber is due to its high absorption cross sections. The thermal neutron absorption cross section for B^{10} and B^{11} is 3837 barn and 0.005 barn, respectively. The neutron absorption of natural boron 20% 10B is quite high ~ (4000 barn) in the low neutron energy range, making it an excellent candidate for use in VVER reactors [11]. In addition to its high absorption cross section, boron has another advantage over other materials that are potential neutron absorbers. $_5B^{10}+_0n^1 \longrightarrow _2He^4+_3Li^7+2.4Mev$

Formulation of the problem

A full-scale fuel assembly (FA) consists of 331 rods. Among them 285 fuel rods, 27 fuel with absorber rods, 18 guide channels and 1 central rod Fig-1. In the computational studies Zr rods were placed in the inter-fuel space of VVER fuel assemblies operating on UO_2 (4.95%) fuel.

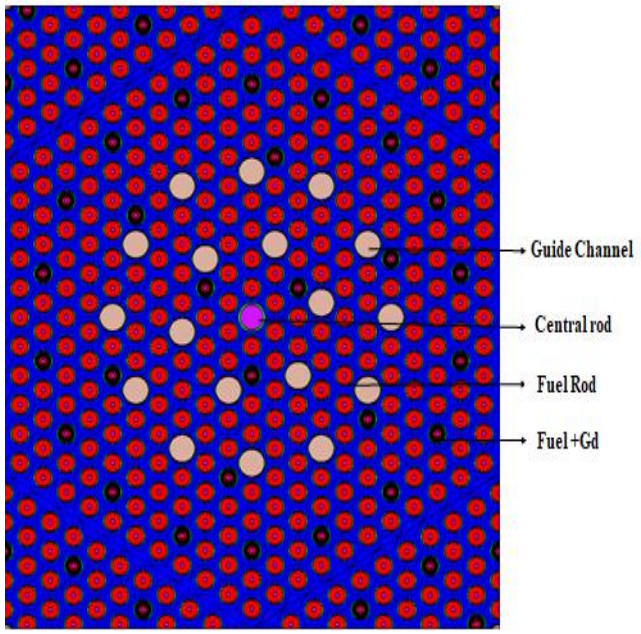

Fig.1. Fuel assembly

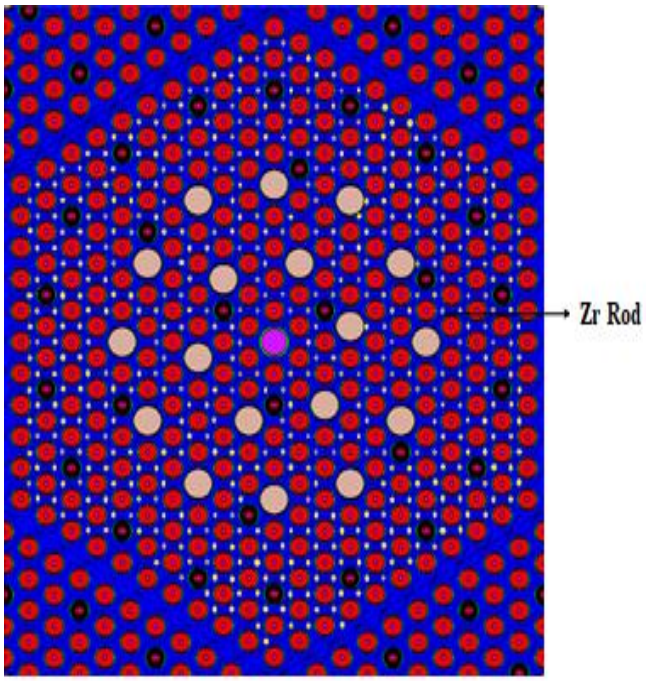

Fig.2. Fuel assembly with Zr rod

This paper compares the use of Zr rods as water displacers in fuel cycles based on low enriched Uranium and the Uranium cycle in VVER fuel assemblies. Enrichment in fissile material in both fuel structures is 4.95%. The Zr rods are located in the space between the fuel rods, and the diameter of the Zr rods varied shown in Fig-2.Moderator-fuel ratio calculation by the equation $\frac{V_{Moderator}}{V_{Fuel}} = \frac{(d^2-\pi R^2)h}{\pi R^2 h}$, here V=volume, d=pin pitch, R= outer radius of fuel, h=length of the pin. This equation shows that, when Zr rod inserted between fuel rod then pin pitch distance will be reduce. It means amount of water between fuel rod will be reduce shown in Fig-3.

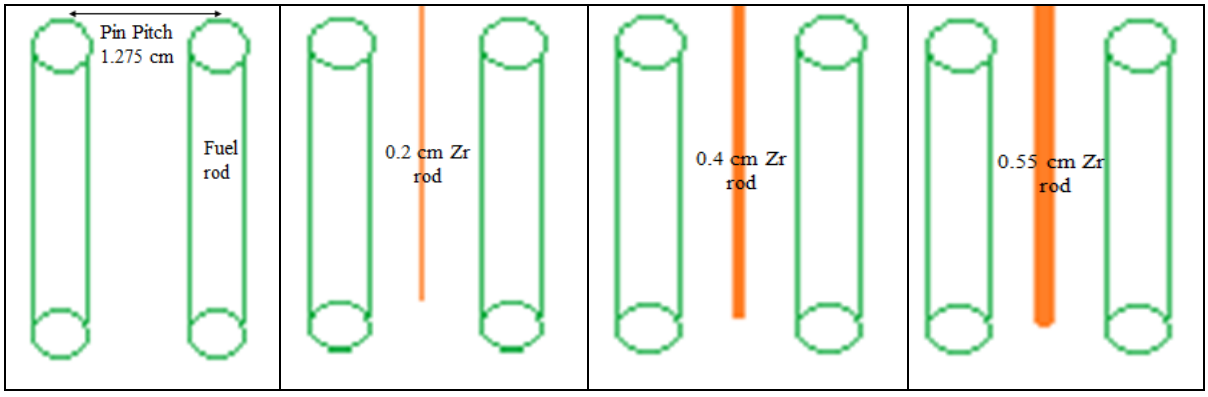

Fig.3. Different radius of Zr rod inserted between fuel rod as a water displacer

Results and discussions

The use of Zr rods as a water displacer for control neutron spectrum and excess reactivity inside a nuclear reactor is given considerable attention in new VVER projects. The basic operating principle of Zr-rods is that at the beginning of the reactor cycle, these rods are completely immersed in the core, which significantly reduces its reactivity margin. Next, by as fuel burnup and reactivity decreases, gradual extraction of these rods, which leads to an increase in the amount of moderator in core and keeps the reactor in critical condition. Previously considered the use of water displacers (Zr-rods) for regulating neutron spectrum and control of excess reactivity in a reactor with water under pressure VVER with conventional fuel composition (UO_2) from the neutronic point of view. The effect of displacers on safe operation of the reactor.

In the Fig-4 fuel assembly (FA) of VVER is shown with Zr-rods of different diameters, where Zr-rods are inserted between the fuel rods. Computational studies of the influence of Zr-rods on the multiplying properties of the fuel assemblies VVER-type reactors were carried out without the presence of a boron (B) absorber in the coolant and burnable absorbers (BA) in fuel rods. In principle, in reactors of this type, the main share initial fuel reactivity margin for burnup is compensated by using partial refueling. The higher multiplication coefficient of partial overloads, the less residual stock is compensated by absorbers, including boron regulation. The diameter of the Zr rods varies from 0 (absence) mm to 5.5 mm (maximum the diameter of the Zr rods that can be inserted between the fuel rods). The maximum diameter of the Zr rods depends on the distance between the fuel rods. It is assumed that Zr-rods will be continuously removed from the core regardless of the regulators. When changing the diameter Zr of the rod there is a change in the moderator-fuel ratio. Table-1 shows the initial values of the multiplication coefficient of VVER fuel assemblies for different diameters Zr of the rods and the corresponding value of the water-fuel ratio.

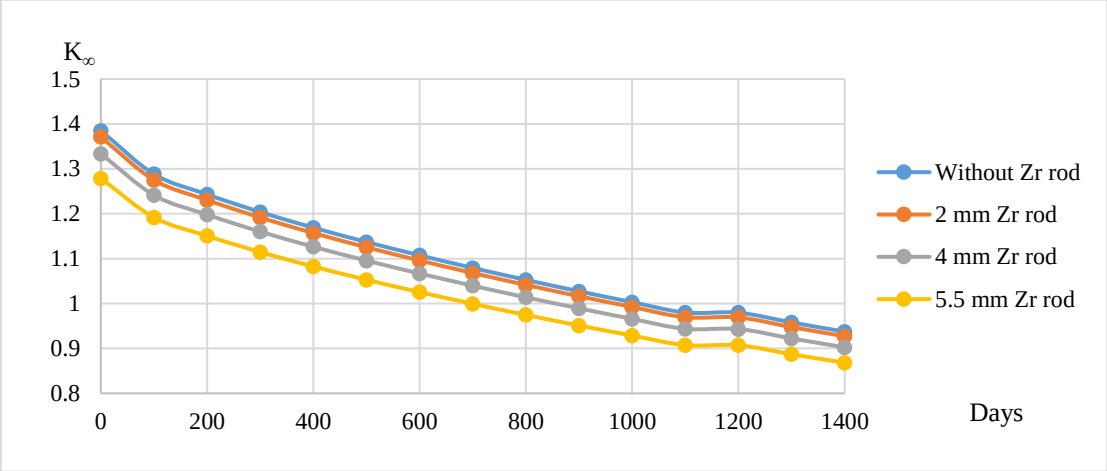

Fig.4. Multiplying Coefficient vs Days for the VVER-1200 fuel assembly with Zr-rods of different diameters located between the fuel rod

Table.1 The multiplication factor (K_∞) for the VVER-1200 fuel assemblies at different values of the water-fuel ratio for the fuel cycle (UO_2 -4.95%)

Z-rod diameter (mm)	Water-fuel attitude	K_∞ (UO_2)
Without Zr rod	1.67	1.39
2	1.46	1.37
4	1.25	1.33
5.5	1.09	1.28

Figures 5 and 6 shown the concentration change of U^{238} and Pu^{239} with burnup time at different values of the moderator-fuel ratio for both fuel structures of UO_2. Introduction of Zr rods to fuel assembly reduces the amount of moderator, which leads to an increase in the resonant absorption of neutrons on U^{238} and a decrease in the probability avoid resonant absorption. As a result, the concentration of U^{238} decrease from an increase in the diameter of the Zr rod.

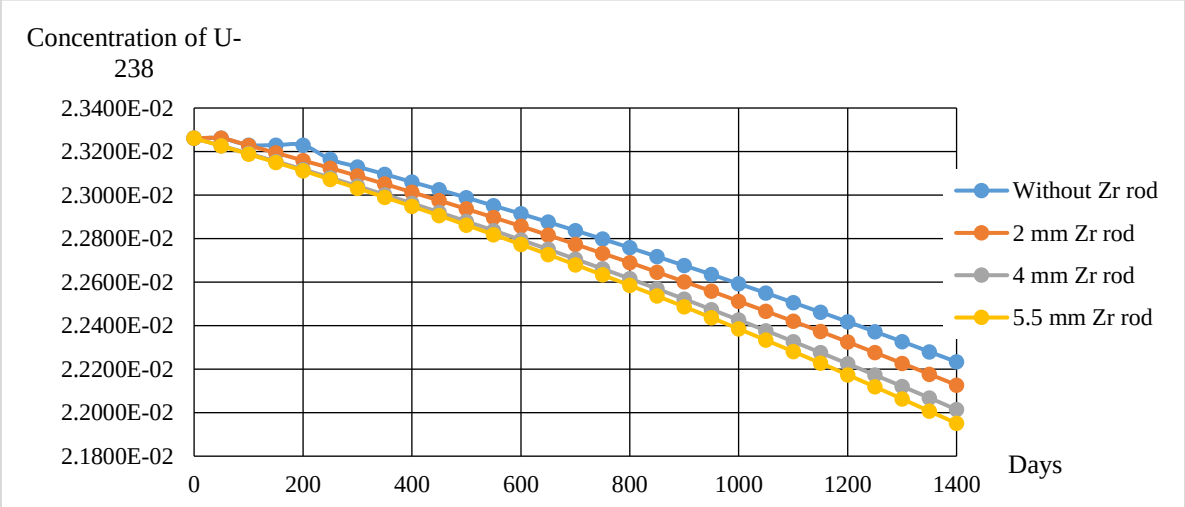

Fig. 5. Concentration of U^{238} decreasing with increasing the diameter of Zr rod vs Time

The consumption of U^{238} decreased from the presence of Zr rods inside the fuel assemblies, and the concentration of Pu^{239} isotopes increased by absorbing neutron, which leads to an increase in the production of fissile isotopes (Fig-6). At the beginning of the cycle with the lowest water-fuel ratio in the core, excess neutrons are absorbed by fertile isotopes, which play a role neutron poisons, resulting in a longer fuel cycle and a minimal amount of neutron poisons used to control the excess reactivity of reactor (burnable poisons and diluted boron in the moderator).

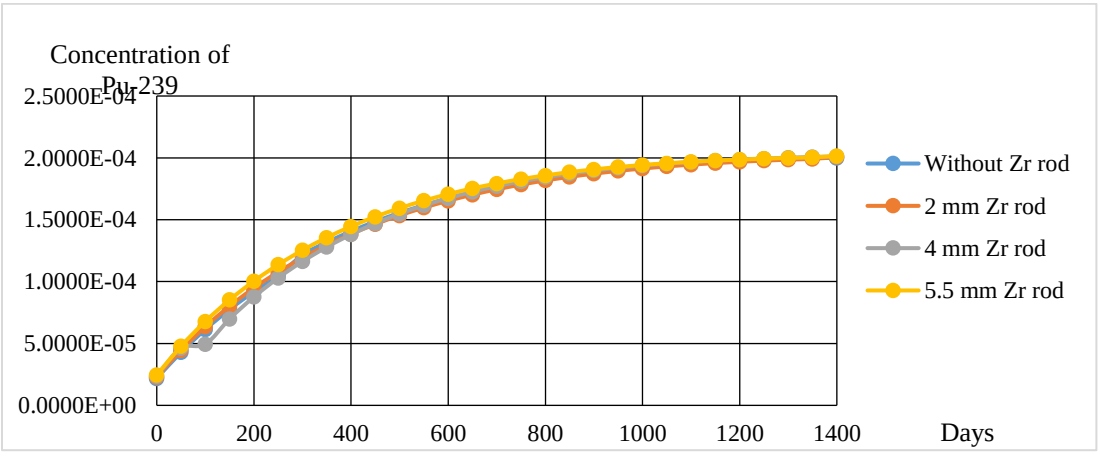

Fig.6. Concentration of Pu-239 increasing with Time

Conclusion

The results of the studies performed showed that the use of Zr rods makes it possible to compensate for excess reactivity. The maximum value is determined by the maximum displacer (Zr) diameter. In this case, the coolant flow through the fuel assembly will be minimal, which can lead to exceeding the

thermomechanical limits for the linear load. This may require a reduction in the average energy intensity of the core, i.e., reduction in the nominal power of nuclear power plants. Simultaneous use of boron and spectral control of the reactivity margin would be economically unjustified. Therefore, to abandon boron regulation, it is necessary to choose such a factor of partial fuel refueling that the reactivity margin at the beginning of the campaign can be compensated by zirconium rods.

References

[1] Anisur, R S K, Uvakin M A, Uncertainty analysis in the physical calculation of VVER cells in the daily maneuvering schedule. (2018) Journal of Physics: Conference Series, 1133(1) № 012048.

[2] Rahman Anisur S K, Uvakin M A, Compare the Result of Uncertainty Analysis in the Physical Calculations of WWER Cells in the Daily Maneuvering Schedule by GETERA and WIMS Programs. №1 (30)-2019 Global Nuclear Safety, Page 90-100.

[3] Rahman S.K. Anisur, M.A. Uvakin, Investigation of absorber concentration changes during maneuvering operation in VVER 1000 reactor. Global Nuclear Safety, 2020 № 2(35), page.83-91.

[4] Nikolaev A.L., Uvakin M.A. Investigation of VVER reactivity in a mode with uncontrolled extraction of a CPS OR group at the lowest possible initial neutron flux. Problems of Atomic Science and Technology. Series: Nuclear Reactor Constants. 2019. No. 2. P. 170–179.

[5] Uvakin M.A., Demekhin A.P. Analysis of Reactivity Coefficients of a VVER Reactor in Normal Operation Modes with a Change in External Load. AtomnayaEnergiya, 2017, vol. 123, no. 4. pp. 193-196.

[6] Bryukhin V.V., Kurakin K.Y., Uvakin M.A. Analysis of the uncertainties in the physical calculations of water-moderated power reactors of the VVER type by the parameters of models of preparing few-group constants. Physics of atomic nuclei, 79, 2016 (8), p. 1305-1314.

[7] Uvakin M.A., Alekhin G.V., Bykov M.A., Zaitsev S.I. Verification of three-dimensional neutron kinetics model of TRAP-KS code regarding reactivity variations. KERNTECHNIK, 81, 2016 (4).

[8] A.I. Sinegribova, M.A. Uvakin, M.A. Bykov Assessment of the fuel assembly pin-by-pin model in the KORSAR/GP code. KERNTECHNIK,84/4, 2019.

[9] M.V. Suslov, I.G. Petkevich, M.A. Uvakin. Leningrad NPP-2 start-up loss of power test and its Simulation with use of KORSAR/GP code. KERNTECHNIK, 84/4, 2019.

[10] A.I. Sinegribova, M.A. Uvakin, M.A. Bykov Development of the fuel assembly pin-by-pin model in the KORSAR/GP code. Nuclear Engineering and Design 354 (2019) 110203.

[11] Melikhov V I, Melikhov O I,Yakush S E and others. A study of boron dilution in VVER-1000 reactor. Thermal Engineering, 2002. Volume 49. No 5, page372-376.

ICNST 2024 International Conference on Nuclear Science and Technology
6- 8 MAY 2024 | Isfahan, Iran

Novel Adsorbent for Efficiently Capturing Lanthanum Ions using NWPP Fiber Functionalized with Diethylenetriamine-Phosphonic Acid through Gamma Irradiation (Paper ID : 1135)

Mehdi Asadollahzadeh*, Rezvan Torkaman
Nuclear Fuel Cycle Research School, Nuclear Science and Technology Research Institute, P.O. Box: 11365-8486, Tehran, Iran

Abstract

The efficient elimination of La(III) was achieved by developing a new adsorbent through a combination of gamma irradiation grafting and chemical modification. The process involved grafting glycidyl methacrylate to non-woven polypropylene fiber (NWPP) under simultaneous irradiation. Subsequently, the fiber was aminated with diethylenetriamine through nucleophilic substitution between amino and epoxy group and phosphorylated with phosphorous acid. The adsorbent that was obtained underwent characterization using Fourier-transform infrared and scanning electron microscopy techniques, revealing the successful preparation of amino-phosphonic acid chelating agents with distinct morphology. The research findings demonstrate that at a temperature of 298.15 K and pH value of 6, the highest level of adsorption capacity was 127.59 mg/g. The sorption kinetics for La(III) were best described by the pseudo-second-order model. The results indicate that the adsorption of La(III) with the Freundlich equation, suggesting a multilayer adsorption mechanism. This study presented a novel technique for rare earth ion adsorption through irradiation grafting.

Keywords: Adsorption, Lanthanum Ions, Radiation-Induced Grafting Method, Amination, non-Woven Polypropylene Fiber

Introduction

Rare-earth elements with distinctive physical and chemical properties are used in important technologies [1]. The demand for pure rare-earth metals and their compounds in the market is rising significantly due to increased interest from various industries [2]. Therefore, the industrial process heavily depends on the crucial separation and purification of these elements for their applications [3]. Lanthanum, a scarce element, is frequently employed in the production of lenses for electronic gadgets, as a catalyst in oil refining, and in the anode of nickel-metal hydride batteries [4]. The challenges lie in the extraction and separation of lanthanum from cerium, which is another rare earth element, as they share similar chemical characteristics when they interact with acid or base extractants [5].

Rare earth (RE) elements can be separated based on changes in their essential properties while preserving their oxidation state using various methods such as fractionation-precipitation, adsorption, ion exchange, solvent extraction, and membrane separation. High selective separation can be achieved through adsorption process [6]. Functional groups on the surface of the adsorbent are used to selectively adsorb RE ions for the extraction and separation [7]. Adsorption can also eliminate metals from solutions with low concentrations, making it suitable for treating industrial wastewater before they are discharged into groundwater. Consequently, adsorption allows for the efficient extraction of RE metals from wastewater and helps reduce environmental pollution [8].

Currently, various new materials such as carbon nanotubes, graphene, biomaterials, and new nano materials have been utilized as adsorbents for the recovery of RE with outstanding adsorption capabilities. However, their high cost hinders large-scale usage [9, 10]. In comparison to these expensive materials, polymeric adsorbents are recognized as crucial materials for eliminating pollution. This is because of their significant adsorption capacity, strong selectivity, adjustable surface chemistry, and effective regeneration capability [11]. Radiation-induced graft polymerization is a successful technique used to create new adsorbents with a high capacity for adsorption through the development of grafted branches that are then functionalized. The resulting adsorbents exhibit a desirable adsorption capacity and are crafted from cost-effective raw materials, making them highly effective for treating wastewater [12]. One major advantage of radiation-induced graft polymerization is the high purity of the final product, as well as the ability to polymerize any monomer and regulate optimization parameters. Furthermore, this technique enables the blending of incompatible substances and the utilization of any type of adsorbent [13].

Khedr created PP-g-p-(An-AAc) films using the irradiation method. The films were produced by using a solvent mixture of 30% methanol and 70% water in a nitrogen atmosphere. The highest graft yield obtained was 115% with a radiation dose of 20 kGy, a monomer ratio of 40/60, and an 80% comonomer concentration. An adsorption capacity of up to 100 mg/g for Cd(II) adsorption was reached after 48 hours of contact time at pH~ 9 and an initial metal ion concentration of 2 ppm [14]. Ting and colleagues carried out a research study on the removal of boron from real industrial wastewater. The adsorbent was created by bonding glycidyl methacrylate (GMA) to nylon-6 fibers through radiation-induced emulsion grafting and then treating it with N-methyl-D-glucamine (NMDG). The efficiency of the adsorbent in removing boron from industrial wastewater was tested in a fixed bed-column. The boron adsorbed was recovered

using a 1 M HCl solution and the stability of the adsorbent was evaluated through 5 cycles of adsorption and desorption [15].

Hayashi and co-workers proposed the use of radiation-induced graft polymerization as a simple and secure approach to convert toxic chromium(VI) into less harmful chromium(III). They developed a fibrous adsorbent with amidoxime functional groups that exhibit a strong attraction towards chromium, and monitored the variations in chromium valence states on the amidoxime-grafted adsorbent over time. Although it took more than a day for the chromium(III) structure to fully stabilize, this method provides a secure approach for chromium(VI) removal [16]. The Zeolite-g-polyacrylamide is produced using a technique involving radiation-induced grafting. Natural zeolite Clinoptilotite is used as the matrix for this process. To enhance the grafting of polyacrylamide into the zeolite, the surface is first modified with a silane compound and a method using a mixture of toluene and H_2O is used during the grafting process. The irradiation doses vary from 10 to 50 kGy, with the optimal conditions being 40% w/w acrylamide, a temperature of 60 °C, and a grafting period of 3 hours. At an irradiation dose of 25 kGy, the maximum degree of grafting achieved is 93%. The zeolite-g-polyacrylamide shows maximum adsorption capacities of 544 mg/g for Cr(III), 345 mg/g for Pb(II), and 1046 mg/g for Zn(II) [17].

The objective of this research was to examine the adsorption of lanthanum ions from a water-based solution using novel adsorbents synthesized through radiation-induced graft polymerization. The technique involved binding glycidyl methacrylate to non-woven polypropylene fiber (NWPP) while exposing it to radiation at the same time. Then, the fiber underwent a treatment with diethylenetriamine to add an amino group through a nucleophilic substitution reaction with the epoxy group, and subsequently underwent phosphorylation with phosphorous acid. Various techniques were used to characterize the adsorbents before they were employed to adsorb lanthanum ions.

Experimental

Materials

Lanthanum nitrate hexahydrate was utilized as the rare earth ion source in the aqueous solution. The monomer used in this study was Glycidyl methacrylate (GMA), while Diethylenetriamine (DETA) for amination stage and phosphorous acid for the phosphorylation stage were provided by the Merck company. A non-woven polypropylene fiber (NWPP) from the Iranian Baftineh company was chosen as the substrate for the adsorption preparation in this research.

Preparation of Adsorbent

Initially, NWPPs were immersed in a solution containing 20% GMA monomer in methanol. To avoid the formation of homopolymers, 1 wt% of iron ammonium sulfate salt was added to the monomeric solution. The container was fitted with a substrate and a monomeric solution that had been purged with nitrogen gas to eliminate oxygen, and then sealed. The polymerization process was triggered using a ^{60}Co gamma source. Following that, the grafted NWPPs were dried in an electric oven at 60 ºC. The grafting yield (GY) was calculated using the formula described in Eq.(1).

$$\%Grafting \quad Percentage = \frac{W_g - W_o}{W_o} \times 100 \qquad (1)$$

In the equation provided, W_o and W_g stand for the original weight and the weight after grafting of the fabric, respectively. To enhance the availability of specific binding sites for the desired metal, the polymeric fibers that had undergone grafting were modified using diethylenetriamine. Introduction of amine groups was achieved by immersing the grafted samples in a solution containing 30% amine and exposing them to a steam bath at 65°C for 5 hours. The resulting modified adsorbent with amine groups was then rinsed, and dried in an oven at 65°C. Phosphorous acid (4 g) was dissolved in 80 mL of diluted HCl (1:1 ratio). The adsorbents were then placed in a 250 mL three-neck flask, heated to 95°C, and refluxed. The slow addition of 16 mL of formaldehyde solution drop by drop over the course of 1 hour was followed by the 8-hour reflux reaction. The functionalized adsorbents were finally rinsed with ethanol and water, and dried in an oven for 24 hours to obtain the ultimate product.

Characterization

The fabric adsorbents' structural features were observed through the use of a scanning electron microscope (Hitachi Su3500 model) after creating the adsorbent via radiation-induced graft polymerization. Fourier-transform infrared spectroscopy (FTIR) analysis of the composite was carried out with a Bruker victor22 model in transmittance mode using potassium bromide (KBr) pellets.

Adsorption Experiments

Adsorption experiments were conducted to assess the adsorption efficiency of the specified adsorbent under varying conditions including temperature, pH, concentration of La(III) ions, concentrations of adsorbent monomers, and dose rate. The volume of the adsorption solutions used in the tests was 40 mL, with a lanthanum ion concentration of 50 ppm. The percentage of adsorption was calculated based on the initial

(C_0) and equilibrium (C) concentrations of lanthanum ions in the aqueous solution (mg/L), which were determined using a UV spectrometer.

$$\%Adsorption = \frac{C_0 - C}{C_0} \times 100 \qquad (2)$$

Results and Discussion

Fig.1 shows the structure of the polymer adsorbents that were created for NWPP fabric and the synthetic adsorbent (NWPP-g-GMA-DETA-PA). By comparing these images, it is evident that there is a noticeable contrast in the level of grafting between the irradiated sample and the polymer base. The increased fiber diameter in the adsorbent structure implies a significant level of grafting due to irradiation and the existence of both monomers and functional groups in combination.

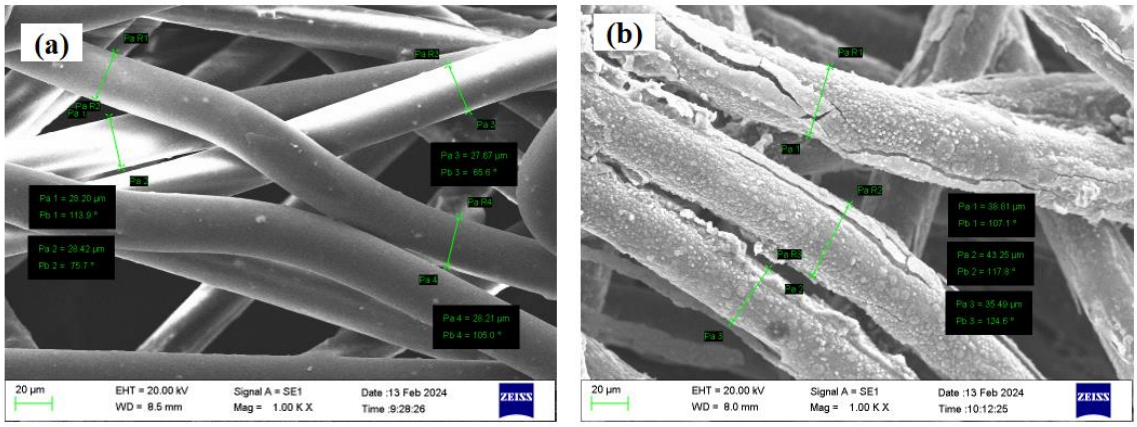

Fig.1. SEM images of (a) NWPP fabric; (b) NWPP-g-GMA-DETA-PA adsorbent

FT-IR was used to confirm that GMA, DETA, and phosphorous acid were effectively attached to the NWPP fabric. The results of the FTIR analysis can be seen in Fig.2.

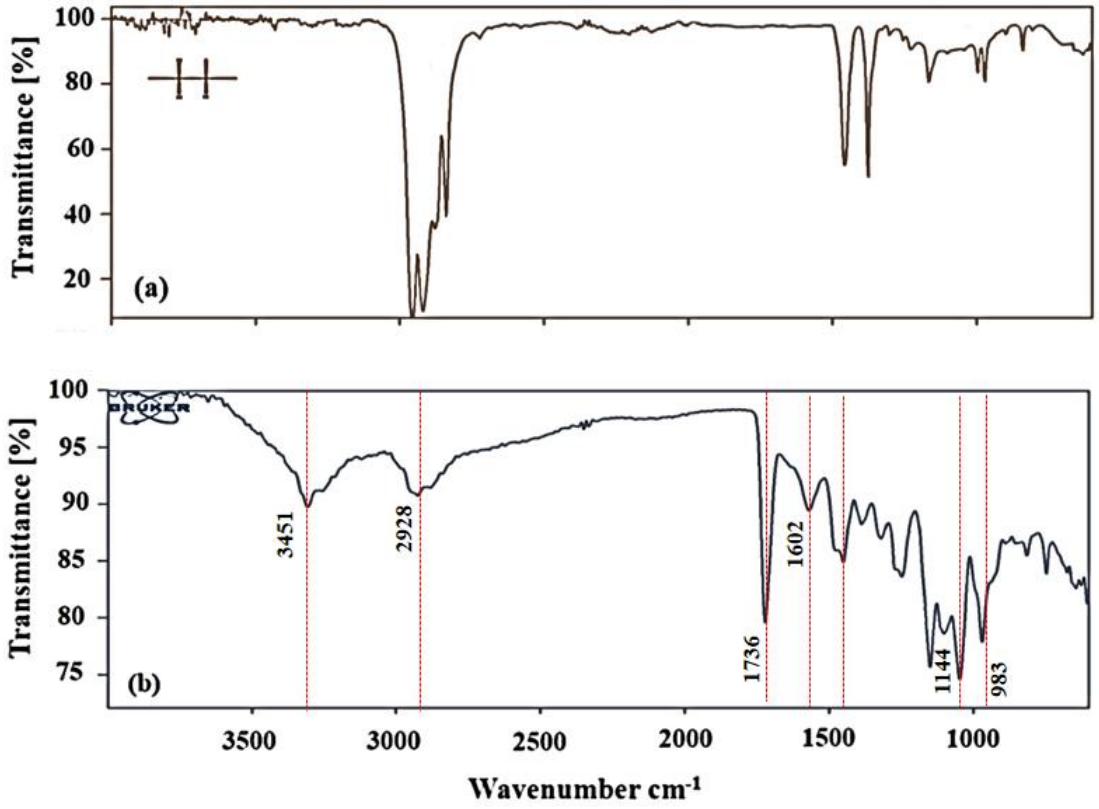

Fig.2. Infrared spectra analysis of (a) NWPP fabric; (b) NWPP-g-GMA-DETA-PA adsorbent

Following radiation grafting, the stretching peaks representing C=O and C-O in the adsorbent were identified at 1736 cm^{-1} and 1136 cm^{-1}, respectively. The peaks indicating the symmetric and asymmetric vibrations of the epoxy ring in the GMA group were also seen at 1217 cm^{-1} and 934 cm^{-1}. Despite modification with DETA, the significant presence of the 1736 cm^{-1} peak suggested minimal impact on the carbonyl groups due to the chemical alteration. The appearance of new peaks at 1613 cm^{-1} and 3441 cm^{-1} was associated with the presence of N-H groups. The disappearance of the distinct peak of the epoxy ring at 934 cm^{-1} confirmed the presence of the grafted amine compound on the NWPP-g-GMA-DETA-PA adsorbent. Additionally, a new peak related to P-based characteristic groups was observed after the phosphoric acid modification. The band related to the P-O- bond was detected at 983 cm^{-1}, confirming the successful grafting of the phosphorus groups.

Table 1 illustrates the impact of GMA monomer concentration on adsorption capacity and grafting percentage. The percentage of grafting increased with higher concentrations of GMA, ranging from 10 to 40 wt%, which facilitated improved access of free radicals to the monomer molecules. However, when the GMA concentration was raised from 30 to 40% by weight, a cross-linking effect occurred, causing a

reduction in adsorption percentage as a result of potential homopolymers formation and reactive chains disruption. Table 1 demonstrates that as the radiation dose increases from 10 kGy to 50 kGy, the percentage of GY also increases. The rise in radiation dose from 10 kGy to 20 kGy leads to an increase in adsorption capacity, possibly due to the increased release of radicals and the formation of more active sites for grafting, resulting in enhanced adsorption capacity. However, at higher radiation doses, the formation of homopolymers decreases the number of active sites available for amination with the reduction in the adsorption percentage (%).

Table 1. Effect of GMA concentration and radiation dose on grafting and adsorption percentages

GMA concentration (%V)	Dose rate (kGy)	Grafting Percentage (%)	Adsorption Percentage (%)
5	20	10.5	20.9
10	20	40.6	40.5
15	20	70.7	60.3
20	20	85.8	80.4
25	20	95.5	90.6
30	20	107.3	99.7
35	20	109.5	98.7
40	20	110.3	96.5
30	10	79.6	80.3
30	30	112.4	98.6
30	40	120.5	96.5
30	50	132.1	93.2

The acidity or alkalinity of the solution is an important factor in determining the chemical properties of the solution and how well the surface of the adsorbent works. It was observed that the adsorption of lanthanum ions increased as the pH level of the solution increased up to 6, as illustrated in Fig.3. This increase is because at lower pH levels, the adsorbent surface's high positive charge density leads to repulsion between the surface and the lanthanum ions. However, once the pH level goes beyond 6, the amount of La(III) adsorbed begins to decrease gradually, potentially due to the creation of La(III) hydroxo colloids. Based on these findings, a pH level of 6.0 was identified as the best condition for adsorption.

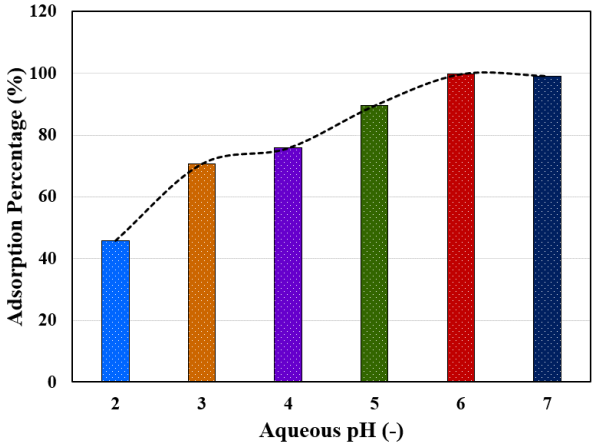

Fig.3. Effect of the pH values on the La(III) adsorption by NWPP-g-GMA-DETA-PA adsorbent (Dose rate = 20 kGy, GMA= 30 % V/V, contact time = 24 h).

The kinetic data of adsorption is shown in Fig.4. The R^2 value for the quasi-second order model was 0.99, so this model was chosen as the best kinetic model for this study with the optimized adsorbent.

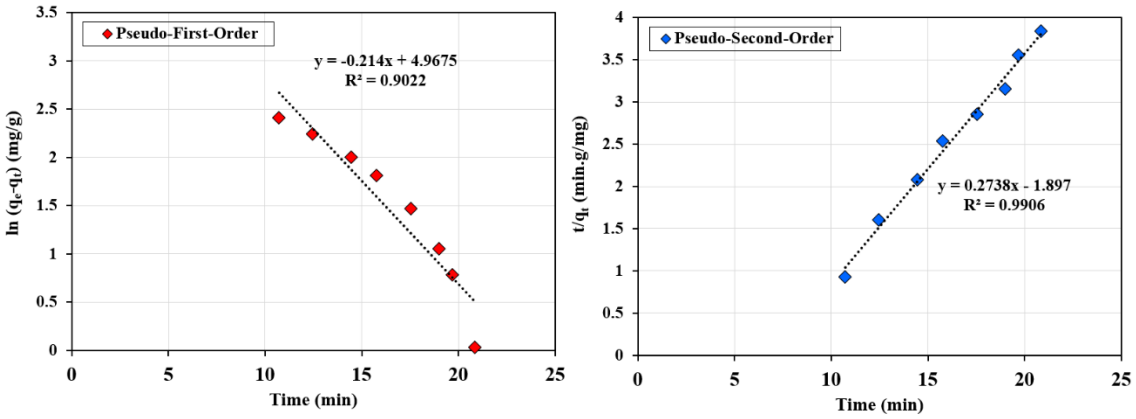

Fig.4. Fitting of pseudo-first-order and pseudo-second-order kinetic models

The data from the simulation of the fitting process for isotherm analysis is shown in Fig.5. It is clear that the Freundlich model was able to accurately fit the data, as shown by the highest R^2 values. This suggests that the adsorption of La(III) onto NWPP-g-GMA-DETA-PA adsorbent occurred through a multilayer process. As a result, the NWPP-g-GMA-DETA-PA adsorbent had a high uptake capacity of 127.59 at 298.15 K.

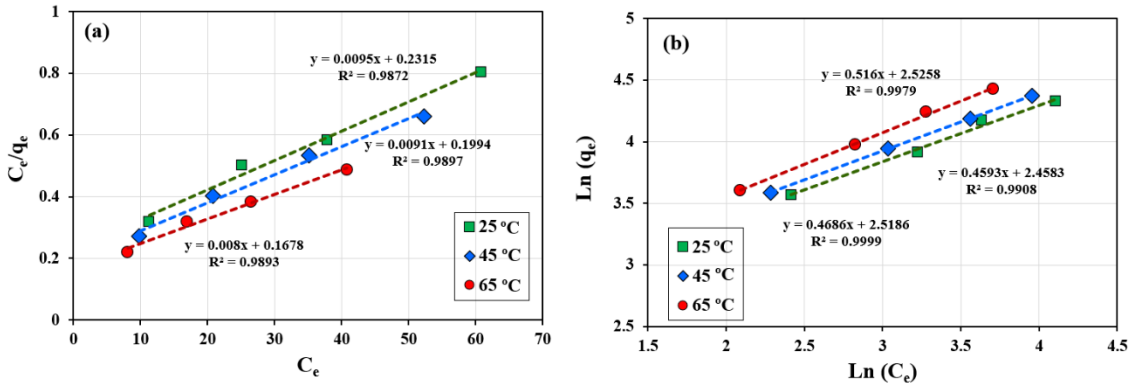

Fig.5. Adsorption isotherm of La(III) adsorption fitted by linear (a) Langmuir and (b) Freundlich models

Conclusion

In summary, a novel NWPP-g-GMA-DETA-PA adsorbent was successfully fabricated through gamma irradiation and subsequent chemical modification to effectively remove rare earth ions from water. The successful formation of the adsorbent was confirmed through FTIR and SEM analysis. The optimum pH for adsorption, the concentration of GMA and the radiation dose were found to be 6.0, 30%(V/V) and 20 kGy based on batch adsorption experiments. Experimental results demonstrated that the adsorption of La(III) followed the pseudo-second-order rate equation and the Freundlich equation, indicating a multi-layer chemical adsorption mechanism. The NWPP-g-GMA-DETA-PA adsorbent developed is highly capable of capturing and separating La(III), offering a viable solution for the recovery and utilization of rare earth elements from intricate solutions.

References

[1] Xu, T., Zheng, X., Biao, J., Xu, Z., Bao, S., Zhang, X., Guomeng Li, G., Jinfeng Mei, J., and Li, Z. (2024) Green recovery of rare earth elements under sustainability and low carbon: A review of current challenges and opportunities, Separation and Purification Technology, 330: 125501.

[2] Filho, W.L., Kotter, R., Özuyar, P.G., Abubakar, I.R., Eustachio, J., and Matandirotya, N.R. (2023) Understanding Rare Earth Elements as Critical Raw Materials, Sustainability 15(3):1919-1937.

[3] Opare, O., Struhs, E., and Mirkouei A. (2021) A comparative state-of-technology review and future directions for rare earth element separation, Renewable and Sustainable Energy Reviews, 143: 110917.

[4] Traore, M., Gong, A., Wang, Y., Qiu, L., Bai, Y., Zhao, W., Liu, Y., Chen, Y., Liu, Y., Wu, H., Li, S., and You, Y. (2023) Research progress of rare earth separation methods and technologies, Journal of Rare Earths, 41(2): 182-189.

[5] Iftekhar, S., Ramasamy, D.L., Srivastava, V., Asif, M.B., and Sillanpää, M. (2018) Understanding the factors affecting the adsorption of Lanthanum using different adsorbents: A critical review, Chemosphere.
[6] Anastopoulos, I., Bhatnagar, A., and Lima, E.C. (2016) Adsorption of rare earth metals: A review of recent literature, Journal of Molecular Liquids, 221: 954-962.
[7] Kegl, T., Košak, A., Lobnik, A., Novak, Z., Kovač Kralj, A., and Ban, I. (2020) Adsorption of rare earth metals from wastewater by nanomaterials: A review, Journal of Hazardous Materials, 386: 121632.
[8] Asadollahzadeh, M., Torkaman, R., and Torab-Mostaedi, M. (2021) Extraction and Separation of Rare Earth Elements by Adsorption Approaches: Current Status and Future Trends, Separation & Purification Reviews, 50(4): 417-444.
[9] Artiushenko, O., Silva, R., and Zaitsev, V.N. (2023) Recent advances in functional materials for rare earth recovery: A review, Sustainable Materials and Technologies, 37: e00681.
[10] Zhang, H., and Gao, Y. (2023) Polymeric Materials for Rare Earth Elements Recovery, Gels, 9(10).
[11] Gabriel Salfate, G., and Sánchez, J. (2022) Rare Earth Elements Uptake by Synthetic Polymeric and Cellulose-Based Materials: A, Polymers, 14(21): 4786-4806.
[12] Torkaman, R., Maleki, F., Gholami, M., Torab-Mostaedi, M., and Asadollahzadeh, M. (2021) Assessing the radiation-induced graft polymeric adsorbents with emphasis on heavy metals removing: A systematic literature review, Journal of Water Process Engineering, 44: 102371.
[13] Dong, Z., Yue Wang, Y., Wen, D., Peng, J., Zhao, L., and Maolin, Z. (2022) Recent progress in environmental applications of functional adsorbent prepared by radiation techniques: A review, Journal of Hazardous Materials, 424: 126887.
[14] Khedr, R.F. (2023) Radiation-Grafting on Polypropylene Copolymer Membranes for Using in Cadmium Adsorption, Polymers 2023, 15(3): 686-691.
[15] Ting, T.M., Nasef, M.M., Aravindan, D., Rosslan, N., and Ruslan N. (2021) Selective removal of boron from industrial wastewater containing high concentration of ammonia by radiation grafted fibrous adsorbent in fixed bed column, Journal of Environmental Chemical Engineering, 9(1): 104993.
[16] Hayashi, N., Matsumura, D., Hoshina, H., Ueki, Y., Tsuji, T., Chen, J., and Seko, N. (2021) Chromium(VI) adsorption–reduction using a fibrous amidoxime-grafted adsorbent, Separation and Purification Technology, 277:119536.
[17] Nuryanthi, N., Syahputra, A.R., Oktaviani, Puspitasari, T., Pangerteni, D.S., Rendi Kurniawan, R.K., Astuti, D., and Darwis, D. (2020) Preparation of Zeolite-g-Polyacrylamide using Radiation Induced Grafting and Its Adsorption Isotherms Study on Several Heavy Metal Ions, Macromolecular Symposia.

ICNST 2024 International Conference on Nuclear Science and Technology
6- 8 MAY 2024 | Isfahan, Iran

Effective Adsorption of Sm(III) Using a Vinyl Acetate-Polypropylene Fibrous through Induced-Grafted Polymerization Procedure (Paper ID : 1136)

Rezvan Torkaman, Mehdi Asadollahzadeh*
Nuclear Fuel Cycle Research School, Nuclear Science and Technology Research Institute, P.O. Box: 11365-8486, Tehran, Iran

Abstract

In this research, polypropylene polymer fibers were exposed to gamma-ray irradiation at a dosage of 20 kGy in order to graft vinyl acetate monomers onto the fibers. The grafted polymer was then saponified using a NaOH solution of concentration 0.5 M. To immobilize the ligand, the fibers were immersed in a solution containing diglycolic anhydride and 1,4-dioxane at a temperature of 80 °C for a duration of 24 hours. As a result, a modified polymer adsorbent with exceptional efficiency for adsorbing samarium ions was successfully synthesized and tested. The study examined various parameters for samarium adsorption, including contact time, pH, and samarium ion concentration. The structure of the adsorbent was analyzed using FTIR and SEM techniques, revealing a high grafting percentage and adsorption capacity. The kinetics and equilibrium isotherms were investigated, and the experimental data aligned with the pseudo-second-order and Langmuir models, respectively. This adsorbent could be suggested as a possible choice for use in industry.

Keywords: Grafting Type Adsorption, Samarium Ions, Radiation Method, Amination, Imobilization, Saponification, Polypropylene Fiber

Introduction

Rare earth elements (REEs) and their alloys have seen a notable surge in usage over the last thirty years in a variety of technological gadgets [1]. The utilization of these metals has grown rapidly across a multitude of applications. Because of their essential role in cutting-edge technology devices, these elements have been labeled as "The Vitamins of Modern Industry" [2]. Samarium, a rare earth metal, has similarities to zinc in terms of hardness and thickness. Compared to other lanthanides, it has the third highest boiling point at 1794 °C, behind ytterbium and europium [3]. This high boiling point facilitates the extraction of samarium from mineral ores. The magnetic properties of samarium have been valuable in a variety of uses like small motors, headphones, and musical instruments [4]. Samarium is commonly used as a catalyst in chemical procedures for purifying industrial chemicals. It is also utilized as a catalyst in chemical reactions that degrade plastic and remove contaminants [5]. Recently, there has been a noticeable emphasis on utilizing industrial waste, like urban mining, for the extraction of rare earth metals. This has led to a necessity to retrieve and reuse rare earth metals from urban mining waste. In the future, there will be a

growing significance in retrieving samarium and cobalt from recycled materials and repurposing waste SmCo magnets. This is due to the high cost of manufacturing SmCo magnets and the depletion of raw materials through the production process [6].

It has been recommended that the use of eco-friendly technology for recycling rare earth elements could enhance the ore treatment process. Electronic devices at the end of their life (e-waste) show promise as a valuable source for reclaiming REEs. Conventional ore treatment methods are ineffective in extracting REEs from e-waste because of their unique chemical makeup [7]. Instead of traditional approaches, extraction and adsorption techniques could be more appropriate. Solvent extraction is currently recognized as the most cutting-edge method for extracting REEs from complicated matrix [8]. Adsorption of REEs on ion exchange resins and selective adsorbents is considered as a suitable method. Compared to solvent extraction, the adsorption process offers several advantages such as reduced waste generation, less reliance on organic solvents, a high level of enrichment, and rapid phase separation [9].

Polymeric adsorbents are made up of organic polymers with unique crosslinkers. These adsorbents exhibit both hydrophilic and lipophilic properties. It is common practice to improve the capacity and selectivity of these adsorbents for specific compounds by introducing different functional groups like ion-exchange or chelating groups. Factors like porous structure, polymer composition, and morphology affect the adsorption properties of these materials [10].

Ionizing radiations like gamma and electron beams are crucial in altering different types of industrial polymers [11]. Exposure to gamma radiation results in the ionization of the polymer chain, leading to the formation of crosslinks and chain breaks due to the presence of free radicals. Several factors such as the structure of the polymer, phase morphology, controlled level and duration of gamma radiation exposure, and the source of gamma radiation can influence the extent of crosslinking [12].

Vijayasri and Tiwari found that Chitosan-based adsorbents are commonly used in water treatment because they are cost-effective and readily available for removing arsenic. The grafted Chitosan had a maximum adsorption capacity of 16.8 mg/g, while un-grafted Chitosan had a capacity of 1.78 mg/g, both achieved with 0.1 g of adsorbent dose at pH 3-4 within 35 minutes, starting with an initial As(V) concentration of 60 mg/L [13]. Limsuwan et al. conducted a study with the goal of developing adsorbents through simultaneous grafting induced by radiation in order to eliminate copper ions. They utilized PE/PP NWF fabric and treated it with bis [2-(methacryloyloxy) ethyl] phosphate (BMEP) using radiation-induced graft polymerization. The ideal conditions for producing adsorbent were found to be 2.5% BMEP concentration and 1 kGy

gamma radiation through simultaneous grafting. The highest adsorption capacity of the adsorbent was attained at 35.96 mg/g with an initial Cu(II) concentration of 90 mg/L at pH 5 [14]. Shaheen and colleagues demonstrated the preparation of a biosorbent (bamboo fibers) using the radiation-induced graft polymerization (RIGP) method with a glycidyl methacrylate (GMA) monomer. Bamboo materials were functionalized for the grafting process. The Langmuir isotherm revealed a maximum copper adsorption capacity of 198 mg/g. The copper adsorption process followed pseudo-second-order kinetics with an R^2 value of 0.999. This cost-effective and environmentally friendly biosorbent successfully removed 96% of copper ions from the solution [15]. In the research of Zheng and co-workers, polyethersulfone nanofibrous membranes were modified with ionic liquid through radiation-induced grafting and electrospinning techniques. The synthesis membranes exhibited impressive adsorption efficiency for heavy metals and dyes, along with good reusability. The capacity for adsorption was found to be 120.3 mg/g for the anionic dye Congo Red and 187.3 mg/g for heavy metal ions like Cd(II) [16]. Khedr carried out research in which Low density Polyethylene underwent radiation grafting with Acrylonitrile and acrylic acid to improve its ability to adsorb Pb (II). The maximum graft yield obtained was 320% after being treated with a radiation dose of 25 kGy using a monomer ratio of 80/20 and a comonomer concentration of 60%. The adsorption capacity was found to be 150 mg/g [17].

The study utilized simultaneous gamma radiation to generate active sites on polypropylene polymer fibers, allowing for the addition of monomers and radicals to form grafts. Additionally, the research investigated the potential of using the synthetic adsorbent for the adsorption of Sm(II) from aqueous solution. Various factors affecting metal removal were examined, including metal ion concentration, temperature, contact time, and pH levels.

Experimental

Materials

The Iranian Baftineh company supplied polypropylene non-woven fabric, which served as the primary polymer material. Merck company provided vinyl acetate (VAc), acetone, methanol, and sodium hydroxide (NaOH) for use in the study. Diglycolic anhydride (DGA) was obtained from Aldrich company. Samarium nitrate hexahydrate was used as the source of rare earth ions in the aqueous solution.

Preparation of Adsorbent

The non-woven PP fabric were first placed in a solution with 20% vinyl acetate monomer in methanol. To prevent the formation of homopolymers, 1 wt% iron ammonium sulfate salt was included in the solution. The container holding the substrate and monomeric solution was purged with nitrogen gas to remove oxygen before being sealed. Polymerization was initiated using a ^{60}Co gamma source (20 kGy). The grafted non-woven PP-VAc were then dried in an electric oven at 60 ºC. The grafting yield (GY (%)) was determined using the formula outlined in Eq.(1).

$$Grafting \quad Yeild(\%) = \frac{W_g - W_o}{W_o} \times 100 \qquad (1)$$

In the equation, W_o represents the original fabric weight and W_g stands for the weight after grafting. The grafted fibers were placed in a solution of 0.5-1 M NaOH in methanol at 50 °C for 2 hours to saponify the ester. Subsequently, the non-woven fabric was removed, washed with methanol several times, and soaked in water at 50 °C for 2 hours. To attach the ligand, the adsorbent was immersed in a 2 M solution of Diglycolic anhydride/1,4-dioxane at 80 °C for 24 hours. The resulting PP-VAc-DGA was rinsed with 1,4-dioxane, water, and acetone sequentially and then dried in a vacuum oven at 60 °C for 5 hours.

Characterization

Characterization of the fabric adsorbents' physical properties was carried out with a scanning electron microscope (Hitachi Su3500 model) after the adsorbent was created through radiation-induced graft polymerization. Analysis of the composite was done using Fourier-transform infrared spectroscopy (FTIR) with a Bruker victor22 model in transmittance mode using potassium bromide (KBr) pellets.

Adsorption Tests

Adsorption tests were performed to evaluate the effectiveness of the designated adsorbent in different situations such as temperature, pH, levels of Sm(III) ion concentrations, and duration. The research included utilizing 40 mL of adsorption solutions with 50 ppm of samarium ions. The adsorption efficiency was calculated by comparing the initial (C_0) and final (C) concentrations of Sm(III) ions in the aqueous solution (mg/L), which were gauged using a UV spectrophotometer.

$$\%Adsorption = \frac{C_0 - C}{C_0} \times 100 \quad (2)$$

Results and Discussion

Fig.1 depicts the design of the polymer adsorbents made for non-woven PP fabric and the grafted fabric PP-g-VAc. A comparison of these visuals clearly shows a distinct difference in the level of grafting between the fabric treated with irradiation and the original polymer. The larger diameter of the fibers in the adsorbent structure suggests a high level of grafting as a result of irradiation and the presence of monomer (GY (%) at 116.8%).

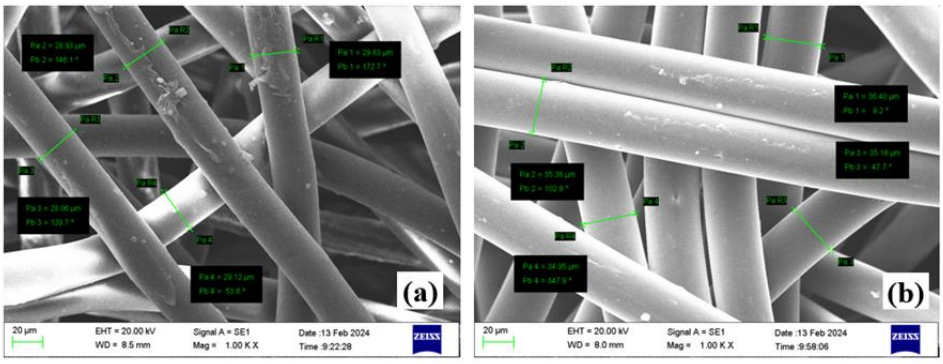

Fig.1. SEM images of (a) non-woven PP fabric; (b) PP-g-VAc grafted fabric

FTIR analysis was conducted to verify the successful removal of acetyl groups from the non-woven PP fabric and PP-g-VAc-DGA. The findings of the FTIR analysis are displayed in Fig.2. The spectrum shows intense adsorption peaks at 2896 cm^{-1}, representing CH stretching vibrations. Also, a peak indicative of the carbonyl group is observed at 1739 cm^{-1}. After saponification, a peak related to the hydroxy group appears around 3300 cm^{-1}. The bands seen in the 1455 cm^{-1} region are due to CH_2 group scissoring vibrations, while the peak at 1505 cm^{-1} indicates C-H deformation. The band at 1170 cm^{-1} is linked to C–O–C vibration, in line with previous DGA studies. The band at 1101 cm^{-1} is linked to the methylene group. The vibrational frequency around 873 cm^{-1} is identified as the out-of-plane C–O bending mode.

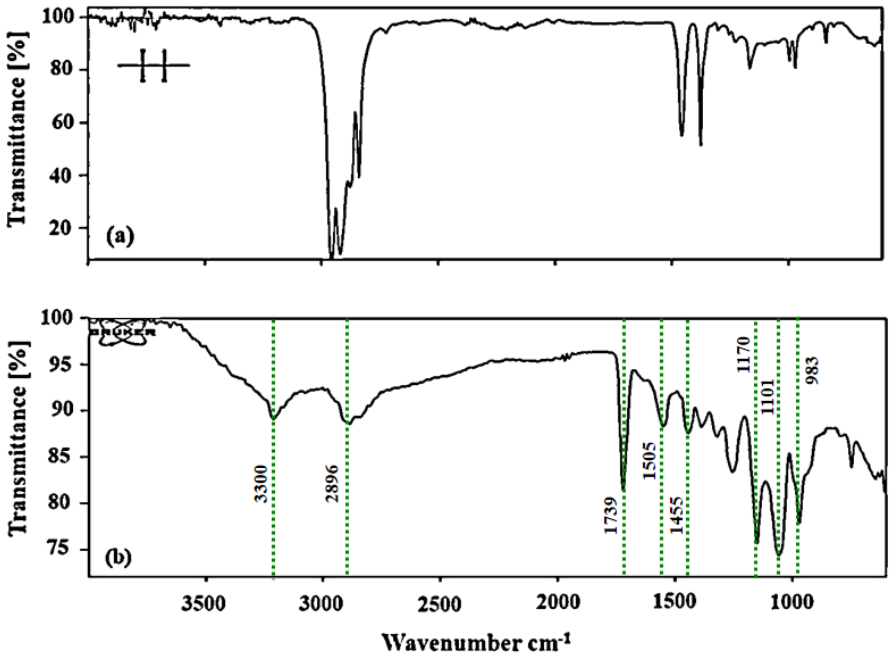

Fig.2. Infrared spectra analysis of (a) non-woven PP fabric; (b) PP-g-VAc-DGA adsorbent

Contact time plays a crucial role in the industry from an economic perspective. The contact duration ranged from 0.1 to 24 hours. Experiments involved the use of 0.1 g of adsorbent to adsorb the Sm(III) solution with a volume of 40 mL, pH=6.5 and the concentration of 50 ppm at 25°C. The outcomes of these tests are illustrated in Fig.3. According to the graph, the adsorption of samarium ions starts off strong but eventually stabilizes after four hours. Initially, the adsorption process is rapid due to a higher number of available sites. When adsorption occurs on the surface, the initial adsorption is swift. However, as time progresses, the number of available sites diminishes, resulting in a slower adsorption rate.

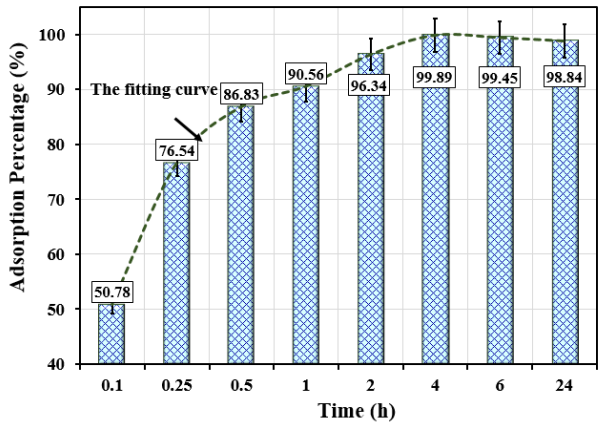

Fig.3. Effect of time on the adsorption of Sm(III) ions with PP-g-VAc-DGA adsorbent

The pH level of the solution is a crucial factor in the adsorption process. Alterations to this level have a significant impact on adsorption. This research focused on investigating aqueous pH levels ranging from 0.5 to 6.5. According to Fig.4, the amount of adsorption varies depending on the solution's pH. It is evident that at a pH of 0.5, the adsorption rate is minimal. Between pH 0.5 and 2.5, there is a notable increase in the adsorption rate, but from pH 4.5 to 6.5, the increase is not substantial. These results indicate that the initially low pH creates a strong positive charge density on the substrate surface, leading to electrostatic repulsion between the metal ion and the surface, which inhibits adsorption. Conversely, at higher pH levels, the positive charge density on the substrate surface decreases, attracting metal ions to the surface and significantly enhancing the adsorption rate.

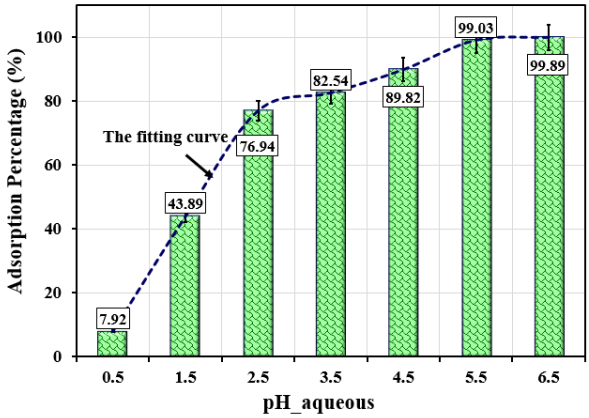

Fig.4. Effect of aqueous pH on the adsorption of Sm(III) ions with PP-g-VAc-DGA adsorbent (Conditions: 0.1 g of adsorbent, concentration of 50 ppm, 25°C, time=4 h)

According to the findings depicted in Fig.5, an increase in the initial quantity of metal ions leads to a decrease in the adsorption percentage. With low initial concentrations, the proportion of initial moles of the metal ion to the surface area of the adsorbent is also low, causing all ions to be adsorbed and making the adsorption unaffected by the initial concentration. However, with higher concentrations, the available adsorption sites are limited compared to the amount of moles in the solution, resulting in the removal of metal ions being heavily dependent on the initial concentration. Additionally, as the active sites become saturated, more ions remain unadsorbed in the solution, reducing the effectiveness of removal.

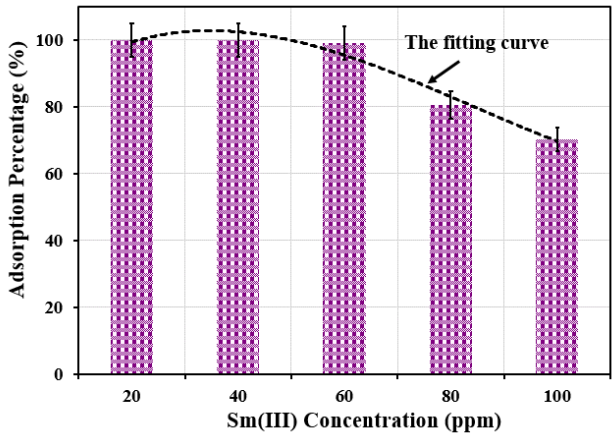

Fig.5. Effect of Sm(III) concentration on the adsorption of Sm(III) ions with PP-g-VAc-DGA adsorbent (Conditions: 0.1 g of adsorbent, pH=6.5, 25°C, time=4 h)

Two models of kinetics, specifically the pseudo-first-order (Eq.3) and pseudo-second-order (Eq.4), were utilized to analyze the kinetics data obtained from batch experiments.

$$q_t = q_{e,cal}\left(1-e^{-k_1 t}\right) \quad (3)$$

$$q_t = \frac{k_2 q_{e,cal}^2 t}{1+k_2 q_{e,cal} t} \quad (4)$$

In the above equations, q_e , $q_{e,cal}$, and q_t are the experimental adsorption capacity (mg/g), calculated adsorption capacity (mg/g) and adsorption capacity (mg/g) at time t (min), respectively. The rate constant k_1 (min^{-1}) is for the pseudo-first-order reaction, while k_2 ($g.mg^{-1}$).min^{-1}) is the rate constant for the pseudo-second-order reaction. Fig.6 illustrates the kinetic modeling of Sm(III) adsorption on PP-g-VAc-DGA adsorbent. The results suggest that the pseudo-second-order kinetics model is a better representation of the adsorption process than the pseudo-first-order model. This finding suggests that the adsorption of Sm(III) on PP-g-VAc-DGA is a chemical coordination process.

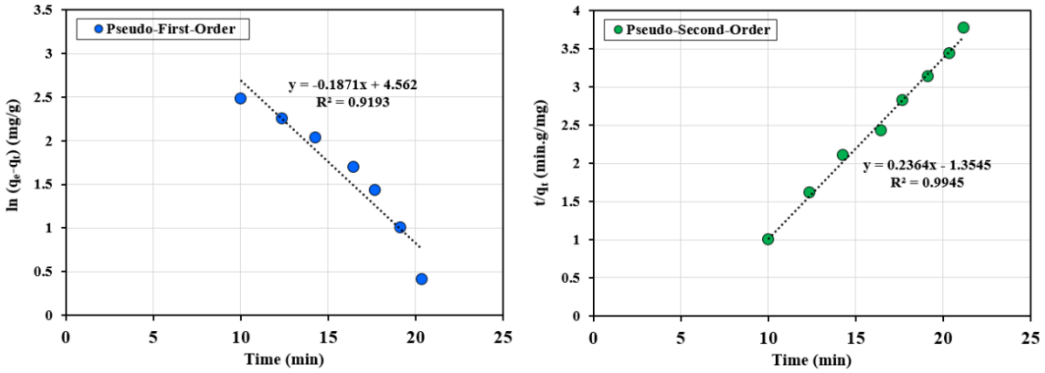

Fig.6. Investigation of adsorption kinetics with PP-g-VAc-DGA adsorbent

The results on the adsorption isotherm equilibrium at various temperatures are depicted in Fig.7. The Langmuir model focuses on adsorption occurring on a single layer on the adsorbent's surface, whereas the Freundlich model is associated with adsorption happening on multiple layers. Unlike the Langmuir model, the Freundlich model is capable of accommodating non-uniform surfaces and varying adsorption potentials. To elucidate the isotherms, one possible approach is as follows:

$$\frac{C_e}{q_e} = \frac{1}{q_m K_L} + \frac{C_e}{q_m} \quad (5)$$

$$\ln q_e = \ln K_F + \frac{1}{n} \ln C_e \quad (6)$$

where q_e (mg/g) is the adsorption capacity at equilibrium, q_m (mg/g) is the maximum adsorption capacity (theoretical isotherm saturation capacity), and C_e is the concentration after adsorption.

The correlation coefficient of the Langmuir isotherm model at 298 K was found to be 0.996 according to Fig.7 with q_m equal to 119.05 mg/g. This suggests that the adsorption behavior follows the Langmuir model, indicating a monolayer adsorption process.

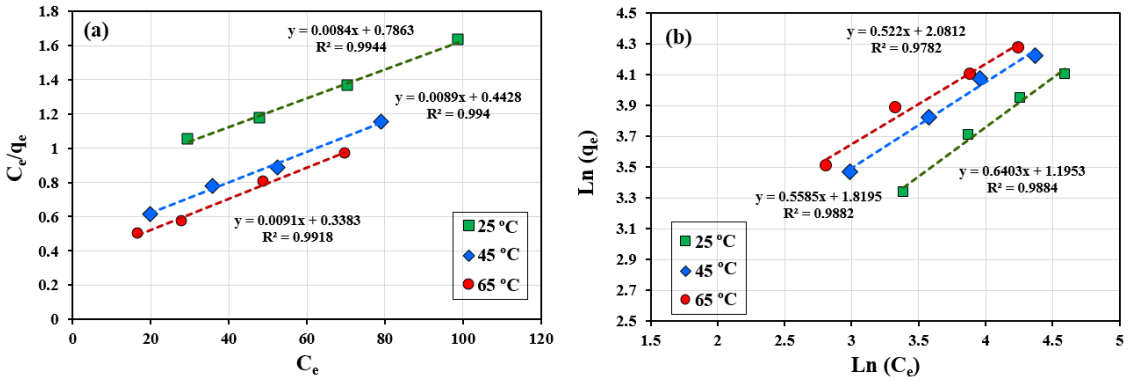

Fig.7. Investigation of adsorption isotherm for (a) Langmuir model, (b) Freundlich model

Conclusion

The adsorbent used in this study was created through gamma-irradiation by copolymerizing vinyl acetate onto the non-woven PP fabric surface. It was then chemically modified with diglycolic anhydride to enhance samarium adsorption from water-based solutions. Factors such as initial ion concentration, pH, temperature, and contact time were found to influence the adsorption capacity of Sm(III). The findings

indicated that the PP-g-VAc-DGA adsorbent produced in the study had a high adsorption capacity of 119.05 mg/g, making it an effective adsorbent for selectively capturing samarium from aqueous solutions.

References

[1] Dutta, D., Rautela, R., Srinivas, G.L., Kundu, D., and Sharma, P. (2023) A review on recovery processes of metals from E-waste: A green perspective, Science of The Total Environment, 859 (2): 160391.

[2] Jha, M.K., Kumari, A., Panda, R., Kumar, J.R., Yoo, K., and Lee, J.Y. (2016) Review on hydrometallurgical recovery of rare earth metals, Hydrometallurgy, 165: 2-26.

[3] Xu, T., Zheng, X., Ji, B., Xu, Z., Bao, S., Zhang, X., Li, G., Mei, J., and Li, Z. (2024) Green recovery of rare earth elements under sustainability and low carbon: A review of current challenges and opportunities, Separation and Purification Technology, 330: 125501.

[4] Aman, S., Ahmad, N., Tahir, M., Gouadria, S., Alburaih, H., Zeshan, M., and Farid, T. (2023) Enhanced electrical and magnetic properties of samarium substituted spinel ferrites, Journal of Electroceramics 50: 50–56.

[5] Safaripour, M., Saidi, M., and Jahangiri, A. (2023) Application of samarium doped lanthanum nickel oxide perovskite nanocatalyst for biodiesel production, Energy Conversion and Management

296: 117667.

[6] Gaustad, G., Williams, E., and Leader, A. (2021) Rare earth metals from secondary sources: Review of potential supply from waste and byproducts, Resources, Conservation and Recycling, 167: 105213.

[7] Opare, E., Struhs, E., Mirkouei, A. (2021) A comparative state-of-technology review and future directions for rare earth element separation, Renewable and Sustainable Energy Reviews, 143: 110917.

[8] Traore, M., Gong, A., Wang, Y., Qiu, L., Bai, Y., Zhao, W., Liu, Y., Chen, Y., Liu, Y., Wu, H., Li, S., You, Y. (2023) Research progress of rare earth separation methods and technologies, Journal of Rare Earths, 41(2): 182-189.

[9] Artiushenko, O., Silva, R., and Zaitsev, V. (2023) Recent advances in functional materials for rare earth recovery: A review, Sustainable Materials and Technologies, 37: e00681.

[10] Anastopoulos, I., Bhatnagar, A., and Lima, E.C. (2016) Adsorption of rare earth metals: A review of recent literature, Journal of Molecular Liquids, 221: 954-962.

[11] Torkaman, R., Maleki, F., Gholami, M., Torab-Mostaedi, M., and Asadollahzadeh, M. (2021) Assessing the radiation-induced graft polymeric adsorbents with emphasis on heavy metals removing: A systematic literature review, Journal of Water Process Engineering, 44: 102371.

[12] Clough, R.L. (2001) High-energy radiation and polymers: A review of commercial processes and emerging applications, Nuclear Instruments and Methods in Physics Research Section B: Beam Interactions with Materials and Atoms, 185: 8-33.

[13] Vijayasri, K., and Tiwari, A.(2021)Detoxification of arsenic from contaminated water using chitosan and radiation-induced grafted chitosan: a comparative study, Chemistry and Ecology, 37: 323-341.

[14] Limsuwan, Y., Rattanawongwiboon, Th., Lertsarawut, P., Hemvichian, K., and Pongprayoon, Th. (2021) Adsorption of Cu(II) ions from aqueous solution using PE/PP non-woven fabric grafted with poly(bis[2-(methacryloyloxy) ethyl] phosphate), Journal of Environmental Chemical Engineering, 9(6): 106440.

[15] Shaheen, R., Yasin, T., Ali, Z., Khan, A.S., Adalat, B., Tahir, M., and Khan, S.B. (2023) Synthesis, Characterization, and Adsorptive Characteristics of Radiation-Grafted Glycidyl Methacrylate Bamboo Fiber Composites, ACS Omega, 8(42): 38849–38859.

[16] Zheng, X., Ni, Ch., Xiao, W., Liang, Y., Li, Y.(2022) Ionic Liquid Grafted Polyethersulfone Nanofibrous Membrane as Recyclable Adsorbent with Simultaneous Dye, Heavy Metal Removal and Antibacterial Property, Chemical Engineering Journal, 428: 132111.

[17] Khedr, R. F. (2022) Synthesis of Amidoxime Adsorbent by Radiation-Induced Grafting of Acrylonitrile/Acrylic Acid on Polyethylene Film and Its Application in Pb Removal, Polymers, 14(15): 3136.

ICNST 2024 International Conference on Nuclear Science and Technology
6- 8 MAY 2024 | Isfahan, Iran

Synthesis of sodalite and nanosodalite zeolite membranes by hydrothermal method with thermal layering on tubular alumina support (Paper ID : 1140)

Honarjoo. P[1], Alahyarizadeh. Gh[1*], Charkhi A[2], Kargaran. H[3]
[1]Faculty of Engineering, Shahid Beheshti University, Tehran, Iran
[2]Atomic Energy Organization Fuel Cycle Research Institute, Tehran, Iran
[3]Faculty of Engineering, Shahed University, Tehran, Iran

Abstract

This research focused on the synthesis and characterization of hydroxy-sodalite zeolite membranes using hydrothermal and temperature-controlled seeding methods on an alumina tubular support. The study aims to evaluate the synthesis characteristics and mechanical strength of the hydroxy-sodalite zeolite membrane through X-ray diffraction (XRD) and scanning electron microscopy (SEM) analyses. The XRD analysis of the synthesized hydroxy-sodalite zeolite membrane demonstrates a close resemblance to the standard card (reference number: 01-085-2066). The results indicate the presence of both zeolite and sodalite phases, with sodalite being the predominant phase. Furthermore, SEM examination reveals zeolite crystals covering the pores of the alumina support. The SEM results show that the synthesized crystal range in size from 1.5 to 2.5 um, and appearing as semi-spherical particles. Based on the analysis conducted and the consistent layer formation of zeolites on the alumina support, it can be inferred that the hydroxy-sodalite zeolite membrane exhibits significant potential for the intended application. The study provides valuable insights into the synthesis process, structural composition, and morphology of the hydroxy-sodalite zeolite membrane, highlighting its suitability for specific applications within the field of membrane technology.

Keywords: Zeolites, Hydrothermal method, Alumina tubular support, Sodalite

Introduction

Natural zeolites were initially discovered in 1756. During the 19th century, the unique microporous properties of natural zeolites and their applications in adsorption and ion exchange gained increasing recognition. Zeolites [1] possess distinct features like well-defined and uniform pore structure, providing high mechanical strength, thermal properties similar to ceramic supports, high resistance to chemical corrosion, and biocompatibility. As a result, zeolite membranes have potential applications in gas membrane separators, membrane reactors, chemical sensors and microdevices. The study of zeolite membranes has become a significant focus in membrane research [2]. Zeolites can operate effectively under high-temperature and high-pressure conditions, offering exceptional permeance and separation capabilities due to their uniform distribution of molecular sieving pore size and excellent adsorption properties [3].

Various methods are available for zeolite synthesis, including in situ hydrothermal synthesis, vapor phase transport, secondary growth or embedding microcrystals of zeolite [4]. Zeolites exhibit regular and uniform porous structures. Several parameters are utilized to characterize these structures, such as pore size and shape, channel dimensionality and orientation, composition and features of channel walls, etc. Among these parameters, pore size and pore shape are the most important [1]. Zeolites are defined as microporous solids with a relatively open, three-dimensional (3D) crystal structure. Figure 1 illustrate zeolite membranes prepared by growing a thin selective zeolite layer known as a "thin-film" on top of a support using the direct hydrothermal synthesis method and the secondary-seeded growth method [5].

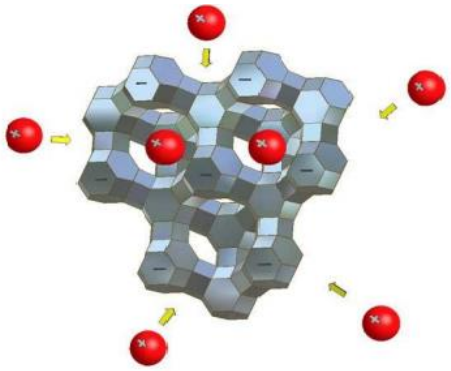

Fig. 1. typical schematic of a zeolite [1]

Hydroxy sodalite (HS) zeolite, a member of the sodalite family, forms by linking sodalite cages through shared 4- and 6-ring [5]. Khajavi and satrapy have shown that HS crystals can be successfully synthesized at various temperatures (90–140 °C) and durations (3.5–24 h) through direct hydrothermal synthesis [6]. Nabavi and Mohammadi developed a new method to synthesize sodalite zeolite membrane by considering different H_2O/Al_2O_3 molar compositions, investigating the impact of water on particle morphology. They concluded that the water molar ratio influences zeolite crystal size [7]. Liang Yu et al conducted an assessment of thin MFI membranes at temperatures ranging from 120 to 293 K for separating $He/N_2/CH_4$. Their findings revealed that the synthesized membrane exhibited high selectivity towards CH_4 and N_2 at lower temperatures. They reported a maximum $(CH_4+N_2)/He$ separation factor of 152 at 153 K, with individual factors of 265 for CH_4/He and 38 for N_2/He at the same temperature [8]. Shurraya Denning et al. showcased the effectiveness of chabazite zeolite SAPO-34 membranes in separating equimolar helium/methane mixtures. These SAPO-34 membranes demonstrated helium permeance as high as 2.28×10^{-7} mol/(m^2sPa) and separation selectivity reaching 13.8 for He/CH_4 mixtures. The separation of this binary mixture was facilitated by molecular sieving and diffusivity variances. The top-performing SAPO-34 membrane exceeded the upper bound of the Robeson limit, positioning these membranes as

attractive options for helium recovery from natural gas [9]. Hydrothermal synthesis of zeolite membranes offers a cost-effective and standardized synthesis method compared to others. This along with well-defined intra-crystalline pores and superior properties of zeolite membrane, has garnered significant attentions for gas separation processes [10]. This particular membrane type provides an appealing and potentially cost-effective technique for recovering helium from natural gas, which consists mainly of methane. Helium is utilized in various applications in the nuclear industry, such as heat transfer in both fission-based nuclear power plants and experimental fusion devices, as well as in several related analytical instruments like NMR, BET, and others [9]. This study aims to synthesize an inorganic HS membrane on the outer surface of microporous tubular alumina support using the hydrothermal method. The membrane's morphology and crystallinity were assessed through SEM and XRD analyses, respectively.

Experimental

Basic preparation

A homemade tubular α-alumina support was prepared with dimensions of 9 mm inner diameter, 13 mm outer diameter, and 4 mm thickness, exhibiting a porosity ranging from 44% to 47%. The pore sizes range from 180 and 270 nanometers on average. SEM images of the support were taken to verify the presence of porosity and absence of cracks in the initial support (Figure 2). They confirm the high-level image and show the porosity of the foundations. Initially, the support is washed with 3 liters of distilled water, followed by immersion in boiling water for 45 minutes to ensure complete removal of particles from the pores. Subsequently, the support is dried at 80℃ for 4 hours.

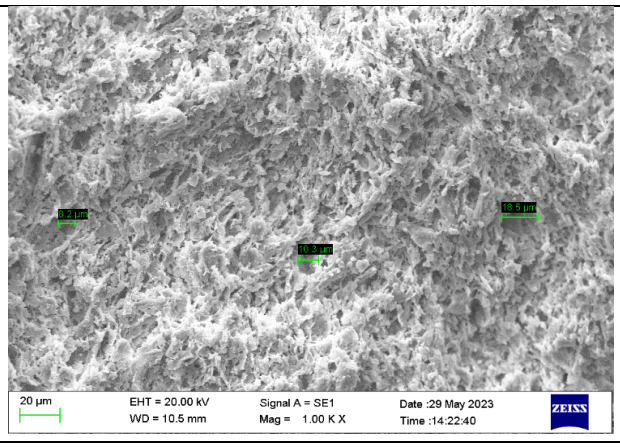

(a)

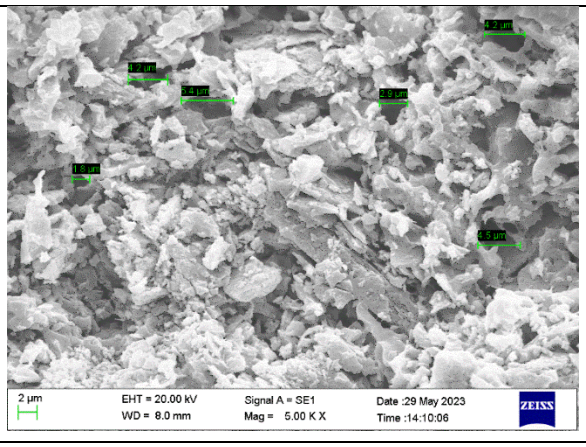

(b)

Fig. 2. SEM images of the homemade tubular α-alumina support (a) side view and (b) top view

1.2 HS zeolite crystals synthesis

The HS Solution was prepared by combining aluminate and silicate solutions in a polypropylene bottle. Initially, the aluminate solution was prepared by dissolving sodium hydroxide and sodium aluminate in deionized water. This mixture was then stirred for 3 hours at room temperature using a magnetic stirrer. The silicate solution was made by mixing tetraethyl orthosilicate and deionized water. Clear solutions were quickly obtained, followed by providing the specifications and chemicals used, as detailed in Table 1.

Table 1. Synthesized Solution

Name of the chemical	Chemical formula	Manufacturer	Application
1-Aluminium isopropoxide	$[(CH_3)_2CHO]_3Al$ 98%	Merck	Source Al
2-Sodium hydroxide	NaOH	Merck	Source Si
3-Tetraethyl orthosilicate	$[CH_2\text{- }CH_3\text{-O}]_4Si$ TEOS 98%	Aldrich	Alkaline mineral form
4-deionized water	H_2O	--------	Solvent

1.3 Membrane synthesis

The crystalline solation was prepared for synthesizing the hydroxy sodalist zeolite membrane. It is important to note that the preparation process for the liquid solution used for both the zeolite powders and the zeolite membranes was identical, without any distinction between the two. The molar ratio of the solution was $5SiO_2$: Al_2O_3: $50Na_2O$:$1000H_2O$. Subsequently, the liquid solution was poured into the autoclave, and the synthesis was conducted at 120℃ for 9 hours. Afterward, the prepared membrane underwent a washing process with 3 liters of deionized water to adjust its pH, following which the membranes were dried at 90℃ for 3 hours.

Results and Discussion

The synthesized membrane was characterized through XRD, SEM and EDX analyses. The high intensity of sodalite peaks in the XRD analysis indicates the prevalence of sodalite in the structure. SEM images depicted in Figure 3 illustrate a 25 μm thick layer of sodalite on the alumina support. Two methods were employed for layering: in the first method, nanosodalite powder was mixed with the sodalite solution and applied using a droplet method. An SEM image in Figure 4 revealed a crack on the membrane. Additionally, SEM images exhibited the presence of a fragile and cracked layer, likely attributed to low temperature effects. Figure 3 illustrates the impact of temperature on the uniformity of zeolite layer formation.

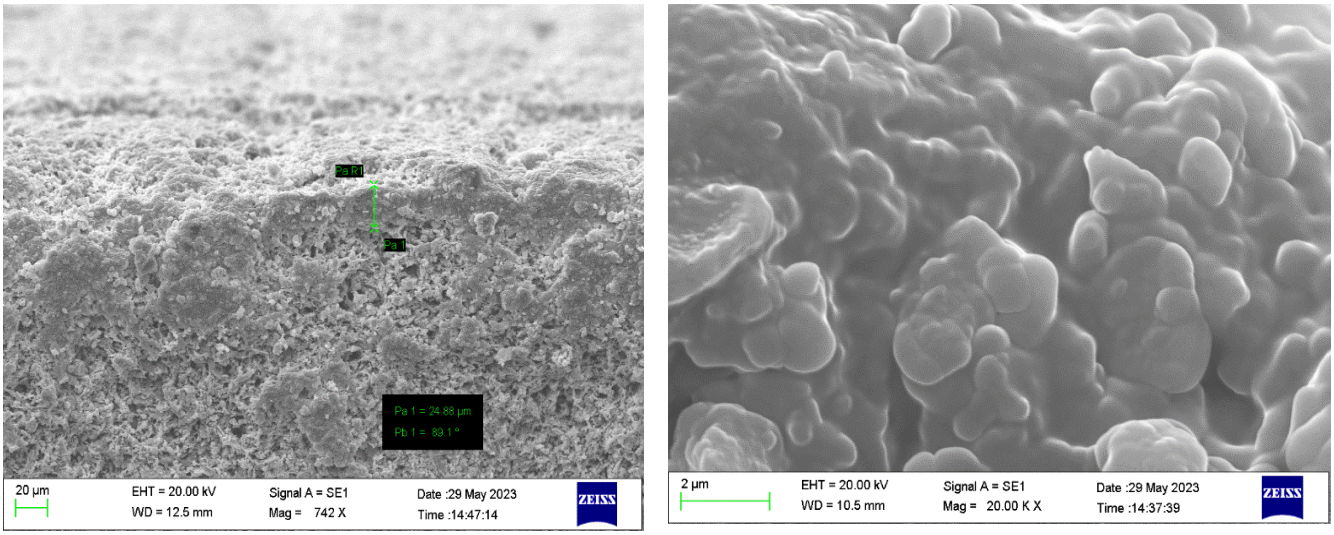

Fig. 3. SEM image of sodalite layer support on alumina

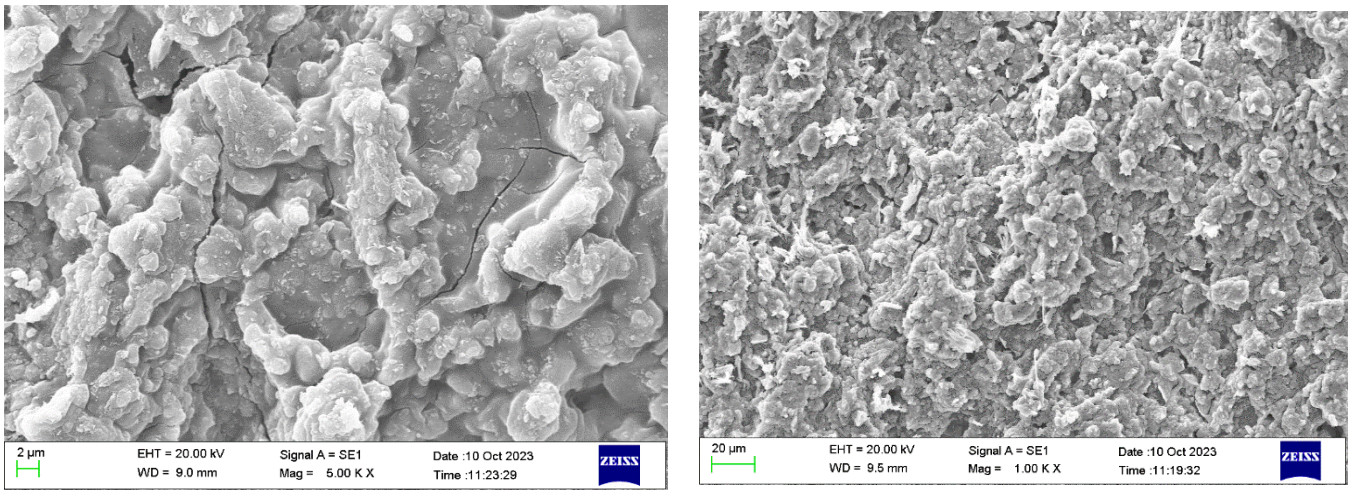

Fig. 4. SEM image Cracking the membrane on its surface

The sodalite powder and nano sodalite, synthesized at 120 degrees and 9 hours and separated at 5000 rpm and 15 minutes, were also analyzed using EDX and SEM. The analysis revealed that the sodalite powder was uniformly formed with a high sodalite content, as shown in Figures 5, 6, 7, and 8. Therefore, it is crucial to determine the optimal conditions for synthesizing HS zeolite seeds. In order to achieve a uniform and defect-free hydroxysodalite membrane, the zeolite grains should be finely and uniformly grained. As a result, a maximum synthesis time of 12 hours was chosen for the synthesis and growth of HS crystals.

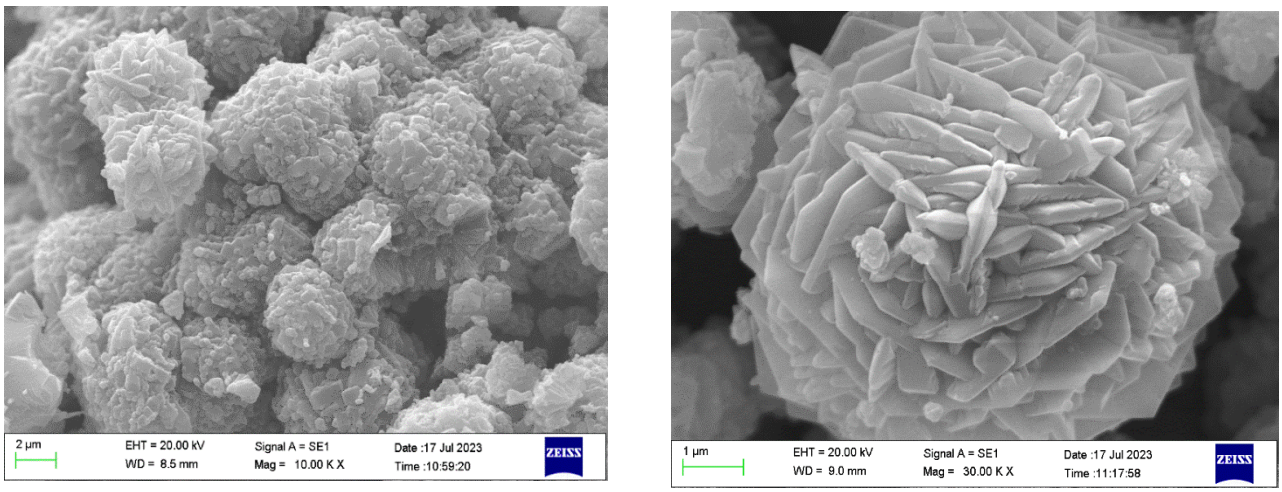

Fig. 5. SEM image Sodalite zeolite powder

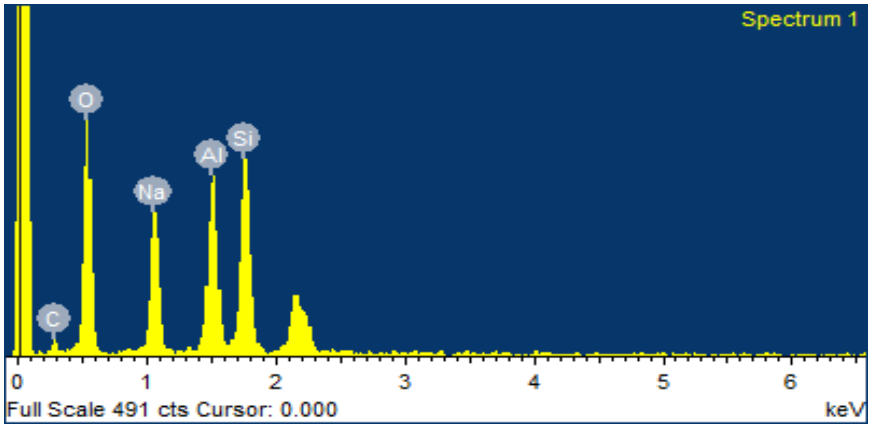

Fig. 6. EDX image Sodalite zeolite powder

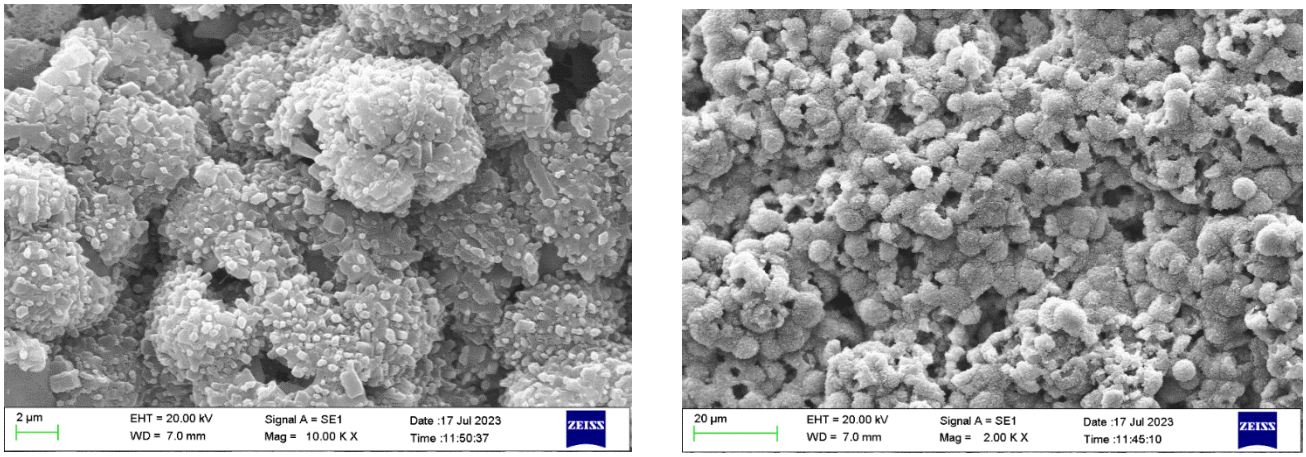

Fig. 7. SEM image nano Sodalite zeolite powder

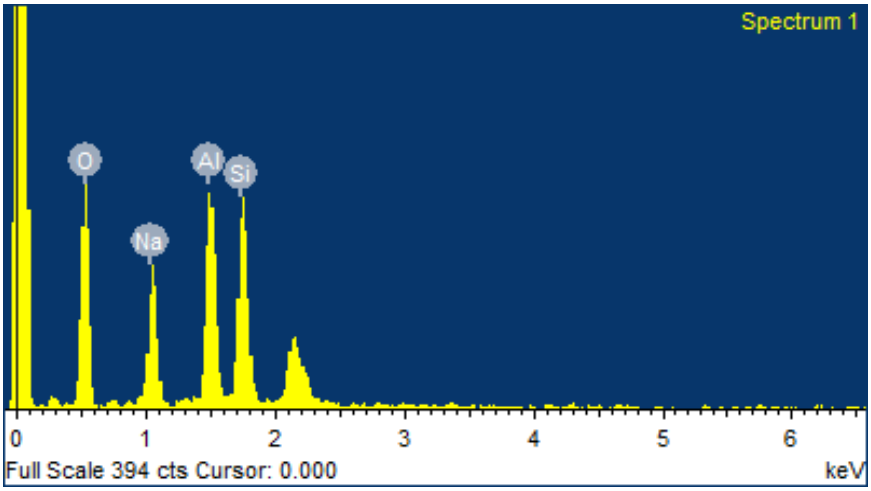

Fig. 8. EDX image nano Sodalite zeolite powder

In the second method, influenced by temperature and duration, the XRD analysis revealed that sodalite displayed a significant overlap on the alumina substrate. The XRD patterns in Figure 9 clearly demonstrate that all samples exhibit distinct and strong characteristic peaks indicative of a sodalite structure, although with varying relative peak intensities. Subsequently, all peaks were compared and cross-referenced with PDF cards. The diffraction sodium aluminum silicate confirmed the formation of the sodalite phase, while the diffraction sodium aluminum phosphate indicated the formation of the zeolite phase.

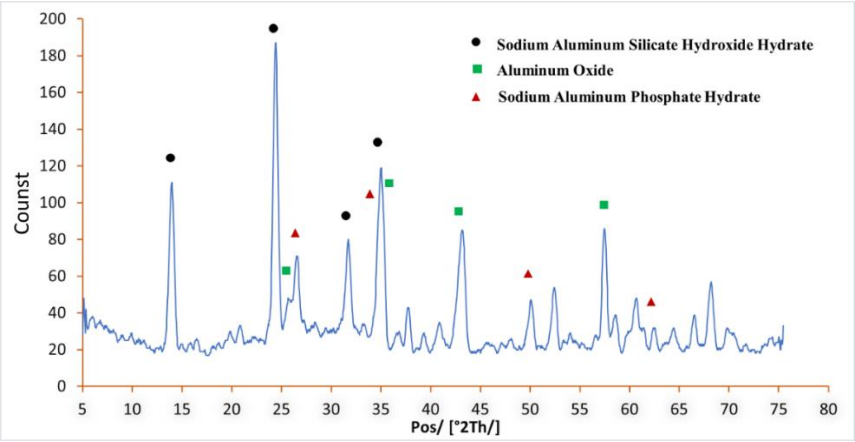

Fig. 9. The XRD of membrane of sample 2

A comparative analysis that can be conducted using XRD patterns involves determining the average crystallite size of the synthesized samples. The average crystallite size ($D_{h\,k\,l}$) of nanoparticles is estimated using the Scherrer equation as shown below [11]:

$$D_{hkl} = 0.89\lambda/\beta\cos(\theta) \quad (1)$$

Here, β represents the full-width at half-maximum (FWHM) of XRD diffraction lines, with the wavelength denoted as ƛ = 0.1540598 nm. The average crystallite sizes of the synthesize nanoparticles for the (1) diffraction peak range from 0.21 to 0.78 µm for nano sodalites, while the crystallite size for the other peaks have been computed and summarized in Table 2.

Table 2. Crystallite size values of nanosodalite synthesized
D_{hkl}= Calculated crystallize size [um]

hkl	2θ	FWHM	D_{hkl}
1	13.3680	0.5904	0.0785
2	20.8477	0.5510	0.0647
3	24.4172	0.5510	0.0687
4	26.5712	0.4330	0.0530
5	31.7168	0.3542	0.0413
6	35.0085	0.3149	0.0353
7	37.7438	0.4723	0.0512
8	40.8772	0.6298	0.0652
9	43.1693	0.3936	0.0393
10	50.1088	0.4723	0.0415
11	52.4391	0.3542	0.0296
12	57.4840	0.5117	0.0377
13	58.5612	0.4723	0.0377
14	60.6642	0.4723	0.0481
15	62.4567	0.4723	0.0299
16	64.2923	0.9446	0.0561
17	66.5064	0.3936	0.0215
18	68.1940	0.6720	0.0342

Conclusions

This study aims to synthesize and evaluate hydroxy-sodalite zeolite membranes using hydrothermal and temperature-controlled seeding methods on an alumina tubular support. The tubular alumina support undergoes steam treatment at 100℃ for 1 hour to remove particles, followed by a 15-minute ultrasonic cleaning to clear its pores and subsequent drying at 50℃ for 3 hours. The synthesis of sodalite zeolite involves a molar ratio of $5SiO_2$: Al_2O_3: $50Na_2O$: $1000H_2O$ in a Teflon-lined autoclave at 120℃ for 12 hours. The resulting zeolite membrane is rinsed with deionized water for 5 minutes and dried at 40℃ for 10 hours. Characterization of the hydroxy-sodalite zeolite membrane includes assessment of synthesis characteristics and mechanical strength using XRD and SEM. The XRD pattern of the synthesized hydroxy-sodalite zeolite closely matches the standard reference card (reference number: 01-085-2066), indicating the presence of both zeolite and sodalite phases, with sodalite predominating. SEM analysis reveals zeolite crystals coating the pores of the alumina support, with crystal sizes ranging from 1.5 to 2.5 µm in semi-spherical particles. Based on the analysis, characterization, and consistent layer formation of zeolites on the

alumina support, it is evident that the hydroxy-sodalite zeolite membrane holds significant promise for its intended application. Our finding also indicated that high temperatures can lead to membrane cracking, while low temperatures may result in inadequate layering on the support surface. Various methods can be employed in sodalite synthesis, and to enhance efficiency and save time, it is advisable to investigate the impact of time reduction and temperature elevation.

References

[1] Moises A. Carreon, ” Molecular sieve membranes for N2/CH4 separation”, Journal of Materials Research 33, 32–43 (2018). https://doi.org/10.1557/jmr.2017.297.

[2] ZHANG Xiongfu, ” Factors affecting the formation of zeolite seed layers and the effects of seed layers on the growth of zeolite silicalite-1 membranes”, Frontiers of Chemical Science and Engineering, Volume 1, Issue 2, 2007.

[3] Jiang, H et al, ” Synthesis of zeolite Membranes ”, Chin.Sci.Bull. 49, 2547–2554 (2004). https://doi.org/10.1360/03wb0146.

[4] Xiaochun Xu et al, ” Microwave-assisted hydrothermal synthesis of hydroxy-sodalite zeolite membrane”, Microporous and Mesoporous Materials, Volume 75, Issue 3, 2 November 2004, Page 173.

[5] Eterigho-Ikelegbe O, et al, ” Preparation and Evaluation of Nanocomposite Sodalite/α-Al2O3 Tubular Membranes for H2/CO2 Separation”, Membranes (Basel). 2020 Oct 29;10(11):312. doi: 10.3390/membranes10110312. PMID: 33137909; PMCID: PMC7692824.

[6] Sheida Khajavi et al., ” Thermostability of hydroxy sodalite in view of membrane applications”, Microporous and Mesoporous Materials, Volume 132, Issue 3, August 2010, Pages 510-517 .

[7] Mohammad Sadegh Nabavi, et al, ”Hydrothermal synthesis of hydroxy sodalite zeolite membrane: Separation of H2/CH4”, Ceramics International, Volume 40, Issue 4, May 2014, Pages 5889-5896.

[8] Liang Yu, et al,” Recovery of helium from natural gas using MFI membranes Journal of Membrane Science, Volume 644, 15 February 2022, 120113.

[9] Shurraya Denning, et al., ” Chabazite Zeolite SAPO-34 Membranes for He/CH4 Separation ” ACS Materials Lett. 2019, 1, 6, 655–659.

[10] Sadao Araki1 et al, ” Preparation and gas permeation properties of all-silica CHA zeolite hollow fiber membranes prepared on amorphous-silica hollow fibers”, Journal of Membrane Science, Volume 634, 15 September 2021.

[11] M. JAMSHIDIYAN et al, ” Solvothermal synthesis and characterization of magnetic Fe3O4 nanoparticle by different sodium salt sources”, Materials Science Poland, Vol. 35, No. 1, 2017.

ICNST 2024 International Conference on Nuclear Science and Technology
6- 8 MAY 2024 | Isfahan, Iran

Efficient Optimization of Q-Cascade for Stable Cadmium Isotopes using Newton-Raphson Algorithm and Direct Substitution Method (Paper ID : 1153)

Mohamad Mahdi Shadman*, Fatmeh Mansourzadeh, Valiyollah Ghazanfary, Younes Amini
Nuclear Fuel Cycle Research School, Nuclear Science and Technology Research Institute, P.O.BOX: 11365-8486, Tehran, Iran

Abstract

The Q-cascade model has been proposed to rapidly evaluate and optimize cascade parameters in isotope separation. The calculation and design of such separation cascades involve determining the total number of stages, both in the enrichment and stripping sections, the flow distribution within the cascade stages, and the specification of values for the product and waste streams. In the context of isotope separation using the Q-cascade algorithm, the parameter M* is defined as the hypothetical mass number of a component, and separations are assessed based on this parameter. In this study, the objective is to separate cadmium isotopes using the Q-cascade model. To determine the optimal value of the parameter M*, the function $\frac{\sum L\varepsilon_0^2}{2P}$ is calculated within the Q-cascade for specific values of the target isotope in the product and waste streams. To overcome computational challenges, the Newton-Raphson solver and direct substitution algorithm are proposed to solve the system of two nonlinear equations. Given the nature of these nonlinear equations in the cascade design, it is necessary for the user to provide an appropriate initial guess for problem-solving. Therefore, using the direct substitution method before employing the Newton-Raphson method can be beneficial as it allows for the examination of possible solution sets and provides a suitable initial guess for the Newton-Raphson method. To validate the developed algorithms, stable cadmium isotope modeling was compared using an enrichment coefficient of 0.0875. The validation results demonstrated that as the molar percentage of the target isotope in the waste stream increased from 40% to 70%, the validation error also increased from 0.27% to 2.72%. These results indicate that the value of M* undergoes slight changes with variations in the percentage of the target isotope in the product and waste streams. For the enrichment of ^{106}Cd in the product, M* is approximately equal to 108.5, which corresponds to the average molar mass of ^{106}Cd and ^{111}Cd, suggesting the non-mixing condition for these two isotopes. Furthermore, with an increase in the target isotope concentration in the product, the number of enrichment stages increases more steeply compared to the number of stripping stages, with respective increases of 90% and 13%. Similarly, with an increase in the enrichment of ^{116}Cd in the waste stream from 20% to 60%, the number of enrichment stages increases by 34%, while the number of stripping stages increases by 218%.

Keywords: Isotope separation, Newton-Raphson solver, Q-cascade model

Introduction

Cascade separation of stable isotopes is academically important for extracting and purifying specific isotopes in various scientific disciplines. It enables precise investigation of isotopic properties and behavior, advancing knowledge in fields like chemistry, physics, materials science, and environmental studies. Additionally, it has valuable applications in medical research, providing isotopically enriched compounds for radiopharmaceuticals and diagnostics. Cascade separation plays a crucial role in academic research by controlling isotopic compositions effectively. The study of continuous flow cascade models is useful for the rapid evaluation of cascade separation parameters and their optimization for isotope separation. Cascade separations of multicomponent mixtures, consisting of separation stages with overall enrichment factors ε_{ij} significantly less than one plays a crucial role in the separation of multicomponent systems. The design calculation of such separation cascades for specific concentration values of a target component in the product and waste streams involves determining the total number of separation stages in a cascade *N*, the number of stages in the enrichment sections S_p and in the stripping sections S_w, the distribution of flow rates in the cascade stages L(s), and the determination of the product or waste stream values [1]. However, the set of obtained parameters should be consistent with the optimal values. In the theory of mixture separation, this issue is addressed through the concept of the Model Cascade of Continuous Profile (MCCP). Cascade parameters are obtained analytically using this tool. These calculations provide a basis for further calculations and optimization of square cascades [2-4]. Various models have been proposed for cascade design in multicomponent isotope separation [1, 4-7]. The Q-cascade model has been proposed for rapid evaluation of cascade parameters and their optimization in isotope separation. While the Q-cascade model is valid for cascades with low separation factors, it is also applicable to cascades with high separation factors [7, 8]. Borisevich et al. investigated the separation of cadmium isotopes ^{114}Cd and ^{116}Cd using the Q-cascade and determined the necessary number of stages to minimize interstage flows [2].

In this study, the equations and solution methods of the MCCP model for stable cadmium isotopes are presented using the Newton-Raphson and direct substitution methods. Stable cadmium isotopes, particularly ^{111}Cd and ^{110}Cd, have various applications in industries and research. For example, ^{111}Cd is used as a radioactive source in hydroponic and liquid culture techniques. Additionally, ^{110}Cd is used as a radioactive source in medical diagnosis [9].

2. Modeling

2.1 .Governing Equations

The main computational idea in the Model Cascade of Continuous Profile (MCCP) is to replace the component concentration, $C_i(s)$, in the separating mixture with certain characteristic functions $\varphi_i(s)$, which leads to the mass transfer equation in a cascade in the following form:

$$\varphi_i(s) + \sum_{j=1}^{m} \frac{2PC_{j,P}}{L(s)} \int_0^{S_P} \varphi_i(t) exp\big(\varepsilon_{ij}(S-t)\big)dt = \sum_{j=1}^{m} \frac{C_{i,F}L_F}{L(s)}\, exp\big(\varepsilon_{ij}S\big) \quad i = 1, \dots, m \tag{1}$$

Where P is the product stream flow of the cascade, $C_{j,P}$ is the concentration of component j in the product stream, $L(s)$ is the flow rate in stage s, $C_{i,F}$ is the concentration of component i in the feed stream, F is the feed stream flow of the cascade, and L_F is the input feed flow rate to the feed stage [5, 6].

One of the mathematical functions that can be assigned to the characteristic function $\varphi_i(s)$ is given by [2]:

$$\varphi_i(l) = \exp\,(Q_i \mathrm{l}) \tag{2}$$

Where, Q_i and Q_j parameters are related as:

$$Q_i - Q_j = \varepsilon_{ij} \tag{3}$$

The general separation parameter ε_{ij} (equivalent to the logarithmic factor α_{ij}, which is the separation factor) is defined as:

$$\varepsilon_{ij} = \varepsilon_0(M_j - M_i) \tag{4}$$

where M_i and M_j are the molar mass of components i and j, respectively. ε_0 is the separation factor of unit mass difference. The parameter Q_i for isotope i can be calculated from [2]:

$$Q_i = \varepsilon_0(M^* - M_i) \tag{5}$$

Where M* is a hypothetical mass number, and separations are measured based on it. Components with molar mass values less than M* ($M_i < M^*$) are in the light stream, while components with mass numbers greater than M* ($M_i > M^*$) are in the heavy stream. By establishing the overall mass balance, partial mass balance, and the condition $\sum_{j=1}^{m} C_j = 1$, the distribution of component concentrations in the product and waste streams can be obtained as [2]:

$$C_{\mathrm{i,P}} = \frac{1 - \exp\,(Q_i S_W)}{\exp\big(-Q_j S_P\big) - \exp\,(Q_j S_W)} C_{i,F} \Big/ \sum_{j=1}^{N_c} \Big(\frac{1 - \exp\,(Q_j S_W)}{\exp\big(-Q_j S_P\big) - \exp\,(Q_j S_W)} C_{j,F}\Big) \tag{6}$$

$$C_{i,W} = \frac{\exp(-Q_i S_P) - 1}{\exp(-Q_j S_P) - \exp(Q_j S_W)} C_{i,F} / \sum_{j=1}^{N_c} \left(\frac{\exp(-Q_i S_P) - 1}{\exp(-Q_j S_P) - \exp(Q_j S_W)} C_{j,F} \right) \quad (7)$$

The ratio of product flow to feed flow and the ratio of waste flow to feed flow is obtained as:

$$\frac{P}{F} = \sum_{j=1}^{m} \left(\frac{\exp(Q_j S_W) - 1}{\exp(Q_j S_W) - \exp(-Q_j S_P)} C_{j,F} \right) \quad (8)$$

$$\frac{W}{F} = \sum_{j=1}^{N_c} \left(\frac{1 - \exp(-Q_j S_P)}{\exp(Q_j S_W) - \exp(-Q_j S_P)} C_{j,F} \right) \quad (9)$$

The total interstage flow rate is also determined using:

$$\sum L = 2 \sum_{i=1}^{m} \left\{ \frac{P C_{i,P} [exp(-Q_i S_P) - 1] + W C_{i,W} [exp(Q_i S_W) - 1]}{Q_i^2} + \frac{P C_{i,p} S_P - W C_{i,W} S_W}{Q_i} \right\} \quad (10)$$

2.2 Solution Algorithm

In this study, the goal is to design an optimal cascade using the Q model. To find the optimal value of the parameter M*, the function $\frac{\sum L \varepsilon_0^2}{2P}$ is calculated for a specified range of the target isotope in the product and waste streams of the Q-cascade. It is more important, in terms of cascade separation objectives, to have lower interstage flows and a higher production yield. Therefore, the mentioned objective function represents a relative interstage flow that needs to be minimized. The solution algorithm consists of the following steps:

a) The target isotope (n) is selected, and design values are assigned to $C_{n,P}$ and $C_{n,W}$.

b) A value for the unit mass difference separation factor, ε_0 , is chosen.

c) If the total number of isotopes is m, the parameter M* is selected within the bounds of M_1 to M_m.

d) Considering the known values of $C_{n,P}$ and $C_{n,W}$, Eq. 6 and Eq. 7 are formulated for the target isotope n, and the values of S_P and S_W are solved. The nature of Eq. 6 and Eq. 7 is nonlinear, and there is no analytical solution for them. It should also be noted that if M* is exactly equal to one of the components M_1 to M_m, the solutions of the problem become divergent. To overcome these computational difficulties, two methods are proposed to find the values of S_P and S_W.

2.2.1 First Algorithm

In the first algorithm, the Newton-Raphson method is proposed to solve the system of two nonlinear equations. This method relies on developing an equation based on an approximation of the root of the original equation and converges to the root using successive approximations. The system of two nonlinear equations and successive solution is as follows:

$$F_1(S_P, S_W) = C_{\mathrm{n,P}} - \frac{1-\exp(Q_n S_W)}{\exp(-Q_n S_P) - \exp(Q_n S_W)} C_{n,F} / \sum_{j=1}^{N_c} \left(\frac{1-\exp(Q_j S_W)}{\exp(-Q_j S_P) - \exp(Q_j S_W)} C_{j,F} \right) \quad (11)$$

$$F_2(S_P, S_W) = C_{\mathrm{n,W}} - \frac{\exp(-Q_n S_P) - 1}{\exp(-Q_n S_P) - \exp(Q_n S_W)} C_{n,F} / \sum_{j=1}^{N_c} \left(\frac{\exp(-Q_i S_P) - 1}{\exp(-Q_j S_P) - \exp(Q_j S_W)} C_{j,F} \right) \quad (12)$$

$$\begin{bmatrix} S_P \\ S_W \end{bmatrix}^{(k+1)} = \begin{bmatrix} S_P \\ S_W \end{bmatrix}^{(k)} - \begin{bmatrix} \frac{\partial F_1}{\partial S_P} & \frac{\partial F_1}{\partial S_W} \\ \frac{\partial F_2}{\partial S_P} & \frac{\partial F_2}{\partial S_W} \end{bmatrix}^{-1} \times \begin{bmatrix} F_1(S_P, S_W) \\ F_2(S_P, S_W) \end{bmatrix}^{(k)} \quad (13)$$

Where k represents the number of computational iterations. It should be noted that if the solution diverges for a specific value of M*, the range of M* needs to be adjusted. Various solvers for Eq. 11 and Eq. 12 were examined, including the Solve function in MATLAB, which resulted in divergent solutions. The Newton-Raphson method has high convergence, meaning that the number of iterations required to reach the root of the equation significantly decreases. Generally, the Newton-Raphson method is based on the Taylor approximation of the target function and provides an estimation of the root by assuming that the function behaves like a linear function in the vicinity of the initial guess. By applying this method to different isotopes, it can be observed that it has limited dependence on the initial guess for some isotopes [10]. Generally, it is necessary for the user to provide an appropriate initial guess to solve the problem, considering the non-linearity of Eq. 11 and Eq. 12. If the desired method diverges, this issue can be examined from two perspectives. First, the problem may not have a solution for certain design values of $C_{n,P}$, $C_{n,W}$and M*. Second, the initial starting point entered as the initial guess for the Newton-Raphson method may have caused the divergence. Therefore, before using the Newton-Raphson method, it would be beneficial to utilize a direct substitution method.

2.2.2 Second Algorithm

In the direct substitution method, a range is initially considered for searching the solution for the values of S_P and S_W. All values within this range are substituted into Eq. 11 and Eq. 12. If the following condition is satisfied:

$$|F_1(S_P, S_W)| < \varepsilon \quad (14)$$
$$|F_2(S_P, S_W)| < \varepsilon$$

Where ε is a small tolerance value, the solutions for S_P and S_W are recorded, and the search continues. This process is performed with different values of ε, such as 0.1, 0.01, and 0.001, covering all the examined regions. If all the examined regions do not yield any solutions, it means that the cascade design problem does not have a solution for the given input values of $C_{n,P}$, $C_{n,W}$, and M*, and using the Newton-Raphson method and other methods would be pointless.

e. With the values of S_P and S_W determined, the values of $C_{i,P}$ and $C_{i,W}$ are calculated using Eq. 6 and Eq. 7.

f. The value of $\frac{\sum L\varepsilon_0^2}{2P}$ is calculated using Eq.8, Eq. 9, and Eq. 10.

2.3. Model Parameters

Table 1 presents the natural abundance of stable isotopes of cadmium.

Table 1. The natural abundance ratio of stable isotopes of cadmium [2]

Isotopes	^{106}Cd	^{108}Cd	^{110}Cd	^{111}Cd	^{112}Cd	^{113}Cd	^{114}Cd	^{116}Cd
Molar Percent	1.25	0.89	12.49	12.80	24.13	12.22	28.73	7.49

3. Results and discussion

3.1 Validation

To validate the developed code, the reference [2] was used. The molar concentration of the target component, ^{116}Cd, in the waste stream was set to 40%, 60%, and 70%, while in the product stream it was set to 5%. The factor ε_0 (unit mass difference separation factor) is considered to be 0.0875.

According to Table 2, the predicted values using the Newton-Raphson method have an error of less than 3% compared to the reference [2]. However, as the molar percentage of the target isotope in the waste stream increases from 40% to 70%, the error in the trend with respect to S_P and S_W increases from 0.27% to 2.72%.

Table 2. Optimal design values for the target isotope ^{116}Cd.

$C_{n,W}(\%)$	$\frac{\sum L\varepsilon_0^2}{2P}$		M^*		S_P			S_W		
	reference [2]	First Algorithm	reference [2]	First Algorithm	reference [2]	First Algorithm	Validation Error	reference [2]	First Algorithm	Validation Error
40	*1.20248*	1.20248	112.593	112.6001	18.7481	18.7986	0.27	6.26228	6.2395	0.36
60	2.43388	2.43393	113.057	113.0501	25.9765	25.8489	0.49	21.3022	21.4228	0.57
70	4.04923	4.05117	113.320	113.3001	35.2939	34.4929	2.27	37.0640	38.0725	2.72

3.2 Optimization of ^{106}Cdmium

The results of designing a cascade for the target isotope ^{106}Cd are presented below. In the current modeling, the concentration of the target component, ^{106}Cd, in the waste stream was set to 0.5%, and the concentration of the target component, ^{106}Cd, in the product stream was set to 20%, 40%, and 60%. The graph of the parameter $\frac{\sum L\varepsilon_0^2}{2P}$ versus the parameter M^* for different values of the concentration of ^{106}Cd in the product stream is shown in Fig. 1. This figure demonstrates the optimization process using the Newton-Raphson algorithm, as explained above. It can be observed that the Newton-Raphson algorithm has acceptable convergence. Figure 1c shows the graph divided into two different regions. the initial estimation for both S_P and S_W in the black region ($M^* < 109.2$) was set to 10. The continuation of solving for M^* greater than 109.2 will not converge with this initial estimation. For the blue region, ($M^* > 109.2$), the direct substitution method was used, and according to Table 2, the initial estimation for S_P and S_W was chosen as 41 and 6, respectively.

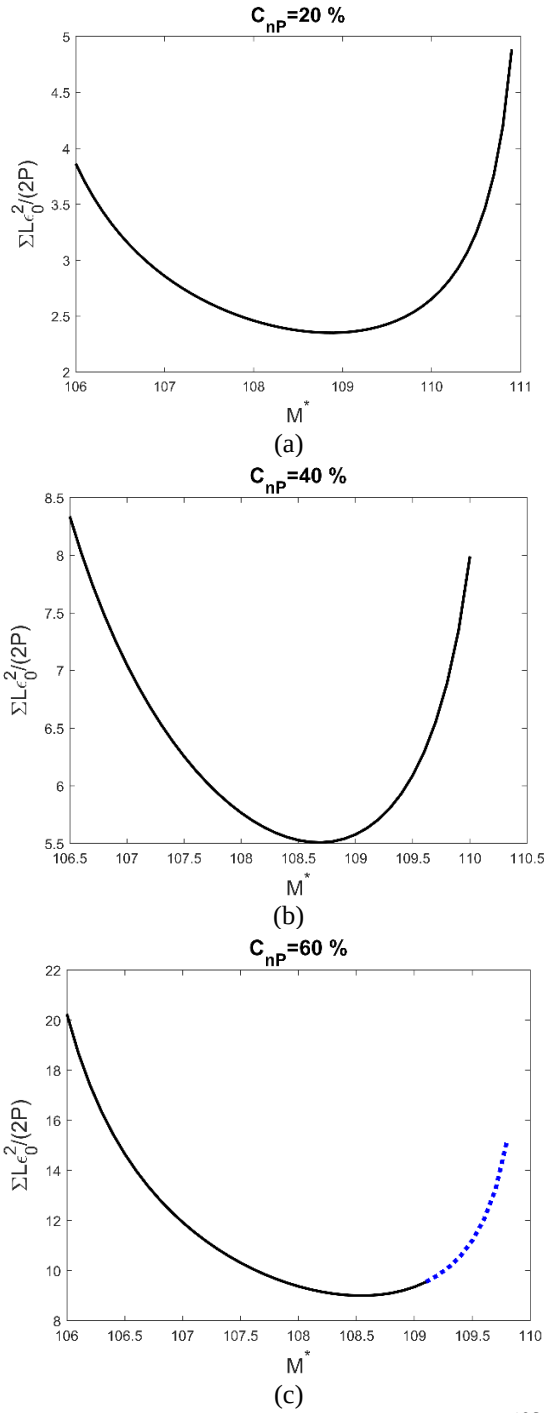

Figure 1. Optimization of M* for different concentrations of the ^{106}Cd in the product stream

Table 2. The optimal variable values ^{106}Cd from the second algorithm for $M^* = 109.2$ and $C_{n,P} = 60$ %

S_P	34	41	34	39
S_W	2	6	2	5
$C_{n,P}(\%)$	0.60125	0.59776	0.60125	0.59708
$C_{n,W}(\%)$	0.00720	0.00237	0.00720	0.00313
Error based on $C_{n,P}(\%)$	0.20844	0.37338	0.20844	0.48713
Error based on $C_{n,W}(\%)$	44.08226	52.60044	44.08226	37.36365

In Table 3, the optimal variable values for the target isotope 106Cd from the first algorithm are demonstrated. It can be seen that M^* depends significantly on the target isotope. The value of M^* changes slightly with variations in the percentage of the target isotope in the product stream and is approximately 108.5, which is the average molar mass of 106Cd and 111Cd, indicating the condition of no mixing for these two isotopes. As the concentration of the target isotope in the product stream increases, the number of enrichment stages increases compared to the number of stripping stages with a sharper slope.

Table 3. Optimal values for the 106Cd from the first algorithm

$C_{n,P}(\%)$	$\frac{\sum L\varepsilon_0^2}{2P}$	M^*	S_P	S_W
20	2.352	108.901	12.541	3.663
40	5.508	108.701	18.3128	3.9255
60	9.003	108.501	23.9007	4.2302

Table 4 presents the optimal values of the S_P and S_W from the direct substitution algorithm. If the value of ε in Eq.14 is changed, the number of solutions will vary. Using this table, initial estimation values and the possible solution region can be obtained. For example, according to Figure 1a and the direct substitution algorithm, designing a cascade for M^* equal to 111 will not be feasible.

Table 4. The optimal variable values ^{106}Cd from the second algorithm for $M^* = 106.1$ and $C_{n,P} = 20$ %

S_P	7	7	8	7
S_W	10	11	3	10
$C_{n,P}(\%)$	0.19907	0.20411	0.19661	0.19907
$C_{n,W}(\%)$	0.00512	0.00481	0.00913	0.00512
Error based on $C_{n,P}(\%)$	0.46413	2.05393	1.69740	0.46413
Error based on $C_{n,W}(\%)$	2.35502	3.71378	82.69433	2.35502

3.3 Optimization of ^{116}Cd

The results of modeling for the target isotope ^{116}Cd in the waste stream are presented below. In the current modeling, the concentration of the target component ^{116}Cd in the product stream was set to 1%, and the concentration of the target component ^{116}Cd in the waste stream was set to 20%, 40%, and 60%. The graph

of the parameter value $\frac{\sum L\varepsilon_0^2}{2P}$ versus the parameter M^* for different values of the concentration of the ^{116}Cd target component in the waste stream are shown in Figure 2.

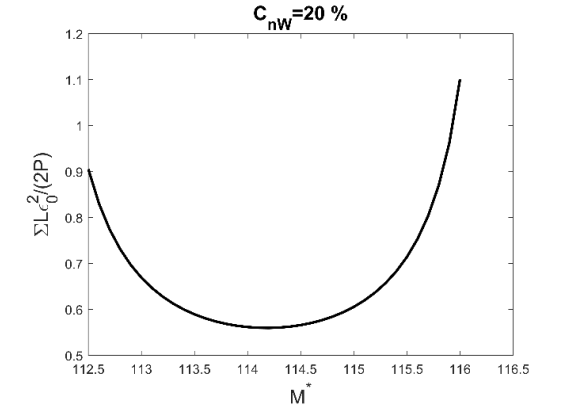

(a)

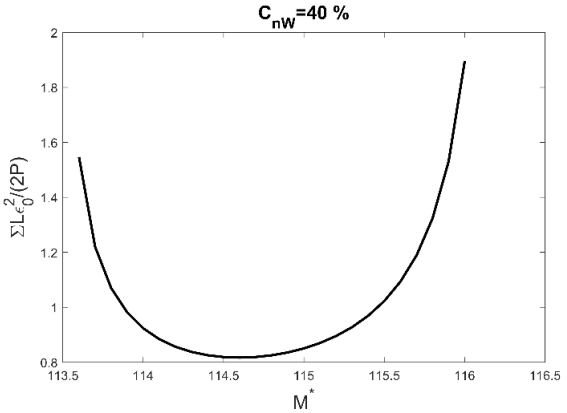

(b)

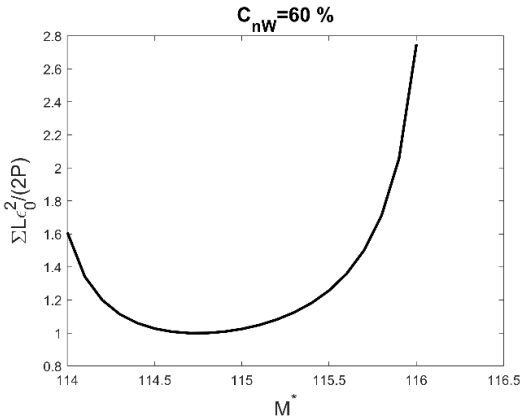

(c)

Figure 2. Optimization of M* for different concentrations of the ^{116}Cd in the waste stream

Table 5 presents the optimal variable values for the target isotope ^{116}Cd from the first algorithm.

Table 5. Optimal values for the ^{116}Cd from the first algorithm

$C_{n,W}(\%)$	$\frac{\sum L\varepsilon_0^2}{2P}$	M^*	S_P	S_W
20	*0.559*	1114.201	13.6397	8.2848
40	0.817	114.601	16.9676	16.9367
60	0.999	114.701	18.3434	26.3388

4. Conclusions

The Q-cascade model has been proposed for the rapid evaluation of cascade parameters and their optimization in isotope separation. The design calculation of such separation cascades for specific concentration values of a target component in the product and waste streams involves determining the total number of separation stages in a cascade (N), the number of stages in the enrichment sections (S_p), the number of stages in the strip sections (S_w), the flow distribution in cascade stages, as well as determining the product or waste stream values. In the context of isotope separation using the Q-cascade algorithm, the parameter M* is defined as a hypothetical mass number, and separations are quantified based on it. Isotopes with a molecular weight less than M* ($M_i < M^*$) are separated in the light stream, while isotopes with a molecular weight greater than M* ($M_i > M^*$) are separated in the heavy stream of the cascade. In this study, the objective is the separation of cadmium isotopes using the Q-cascade. To find the optimal value of the parameter M*, the function $\frac{\sum L\varepsilon_0^2}{2P}$ is calculated for specific values of a target isotope in the product and waste streams. To overcome computational difficulties, the Newton-Raphson algorithm and the direct substitution algorithm have been proposed for solving the system of two nonlinear equations. Using this approach, different possible solution sets are examined for values of $C_{n,P}$, $C_{n,W}$, and M*, and a suitable initial guess is obtained for the Newton-Raphson method. To validate the developed algorithms, stable cadmium isotope modeling is compared with a parameter value of ε_0 equal to 0.0875. The validation results show an error of less than 3%. As the molar percentage of the target isotope in the waste stream increases from 40% to 70%, the validation error increases from 0.27% to 2.72% for S_P and S_W. The results indicate that the value of M* changes slightly with variations in the percentage of the target isotope in the product and waste streams. For the enrichment of 106Cd in the product, the value of M* is approximately 108.5, which is the average molar mass of 106Cd and 111Cd, indicating the condition of no mixing for these two isotopes. As the target isotope concentration in the product increases, the number of enrichment stages increases with a higher slope compared to the number of stripping stages, with respective increases of 90% and 13%.

Furthermore, as the enrichment of ^{116}Cd isotope in the waste stream increases from 20% to 60%, the number of enrichment stages increases by 34%, and the number of stripping stages increases by 218%.

References

[1] Zeng, S., et al., Maximizing separation performance of q-cascades for multicomponent isotope separation. Separation Science and Technology, 2018. 53(1): p. 97-109.

[2] Borisevich, V., G. Sulaberidze, and S. Zeng, New approach to optimize Q-cascades. Chemical engineering science, 2011. 66(3): p. 393-396.

[3] Song, T., et al., Comparative study of the model and optimum cascades for multicomponent isotope separation. Separation Science and Technology, 2010. 45(14): p. 2113-2118.

[4] Zeng, S., et al., The Q-cascade explanation. Separation Science and Technology, 2012. 47(11): p. 1591-1595.

[5] Zeng, S., et al., Use of the Q-cascade in calculation and optimization of multi-isotope separation. Chemical engineering science, 2011. 66(13): p. 2997-3002.

[6] Zeng, S., et al. Enhancing the performance of Q-cascade for separating intermediate components. in Journal of Physics: Conference Series. 2016. IOP Publishing.

[7] Zhang, Y., et al., Further optimization of Q-cascades. Chemical Engineering Research and Design, 2015. 100: p. 509-517.

[8] Sulaberidze, G.A. and V.D. Borisevich, Cascades for separation of multicomponent isotope mixtures. Separation science and technology, 2001. 36(8-9): p. 1769-1817.

[9] Zhong, Q., et al., Cadmium isotopes as tracers in environmental studies: A review. Science of the Total Environment, 2020. 736: p. 139585.

[10] Mohamad Mahdi Shadman, V.G., Fatmeh Mansourzadeh, Q cascade optimization for tungsten stable isotopes with Newton-Raphson algorithm, in The 29th National Conference on Nuclear Science and Technology. 2023: Tehran

ICNST 2024 International Conference on Nuclear Science and Technology
6- 8 MAY 2024 | Isfahan, Iran

Investigating the multicomponent isotopes separation cascade considering corrosion rate in gas centrifuges (Paper ID : 1157)

Mansourzadeh F.[1*], Ghazanfari V.[1], Sadman M. [1], Norouzi A.[2]

[1] *Nuclear Fuel Cycle Research School, Nuclear Science and Technology Research Institute, Tehran, Iran.*

[2]*Advanced Technologies Company, AEOI, Tehran, Iran.*

Abstract

Due to process gas contact with centrifuge rotor walls, corrosion is inevitable. Because the composition of the process gas is often corrosive or in the form of a volatile compound, this problem affects the separation of multicomponent isotopes and should be investigated in the modeling of enrichment cascades to evaluate its effect on isotope separation. In this regard, a calculation code has been prepared for modeling the square cascade, which examines the effect of the corrosion rate of the separation unit on the amount of the product and its concentration. In this situation, to model a cascade, the corrosion rate in the separation unit is considered by introducing additional terms in the mass transfer equations, which makes solving the mass equations much more difficult due to their non-linearity. In this research, by applying the corrosion parameter in the equations governing flow and mass separation, the square cascade algorithm is developed and the investigations are applied to $^{180}WF_6$ as an example. Modeling is done for two cascades with 25 and 50 stages and the results are compared for the cascades with the same cut and feed rate. According to the studies done, with the increase in the corrosion rate, the amount of target isotope enrichment in the product and waste stream decreases and the product flow rate decreases. Also, if the product flow rate is considered constant in the square cascade, in the cascade with more stages, the amount of product will be less because the number of stages is more and the amount of leakage of process material from the cascade will be more. Moreover, the percentage of changes in the target isotope concentration in the product flow compared to the non-corrosion condition is higher for the long cascade.

Keywords: Corrosion, gas centrifuge, multicomponent isotopes, separation cascade

Introduction

Due to the effect of all components on the transfer of the target isotope, the separation of multicomponent isotopes is very complicated and compared to the separation of two-component mixtures, it has wider dimensions [1,2]. Unlike the first and end components which show a uniform behavior along the cascade and increase towards the two ends of the cascade, the enrichment of the intermediate components strongly depends on the isotope composition in the feed and the mass number of the isotopes. In the separation of stable isotopes, it is necessary to determine the characteristics of the cascade, including the flow rates in

the stages, the number of separation units (gas centrifuges) in each stage, and the concentration of isotopes in the input and output of all stages. In this regard, many researches have been conducted, in which numerical methods play an important role [3-8]. Utilizing the numerical methods, the structure of the cascade can be modeled and the influence of practical and effective parameters on the isotope separation can be evaluated. Among the important issues that should be investigated in the modeling of enrichment cascades and their effect on the amount of separation and the amount of enriched product, is the corrosion in the gas centrifuge due to the chemical composition of the process material used in the cascade.

Corrosion in the gas centrifuges is largely unavoidable. Since the multicomponent mixture that needs to be separated (i.e., process gas) is often corrosive, the feed material is removed from the process. It means process material is precipitated or removed in the form of another compound from the separation process. An example that is often seen in enrichment cascades is related to fluoride-type process gas compounds, which usually react with the humidity of the environment and cause corrosion in the wall of the gas centrifuge [9, 10].

Without taking into account the corrosion rate in the separation of multicomponent isotopes, it is very difficult and complicated to investigate the cascade, and considering this parameter, the analysis of the cascade performance becomes much more complicated. The only existing reference related to square cascade is reference [10], which does not fully specify the solution method. References [9, 11] have also addressed the modeling of the ideal taper cascade in which the structure of the equations and their solution is different from the square cascade. Therefore, there is a need to develop a numerical method to investigate the effect of corrosion rate on cascade performance. Considering the importance of this topic and on the other hand, limited research has been done on it, the numerical code has been developed to determine the state of isotope separation in a square cascade and concentration distribution by applying the corrosion rate in a gas centrifuge. The results of the code in this research are presented as an example of the isotope separation of W-180 with the WF_6 process mixture. As can be seen, in the reaction of WF_6 with the humidity of the environment, HF gas is produced, which leads to corrosion;

$$WF_6 + 3H_2O \rightarrow WO_3 + 6HF$$

The value of the corrosion rate in the centrifuge machine is calculated from the experimental test of the centrifuge machine with the desired process gas, and hypothetical values are used in this research.

Research Theories

Figure (1) shows a view of a square cascade with countercurrent flow. In this figure, the parameters M_s, N_s, and Z_s refer to the up, down, and input flow rates of stage s, respectively. The l_s is the corrosion rate in each stage, which appears in the form of leakage in the equations.

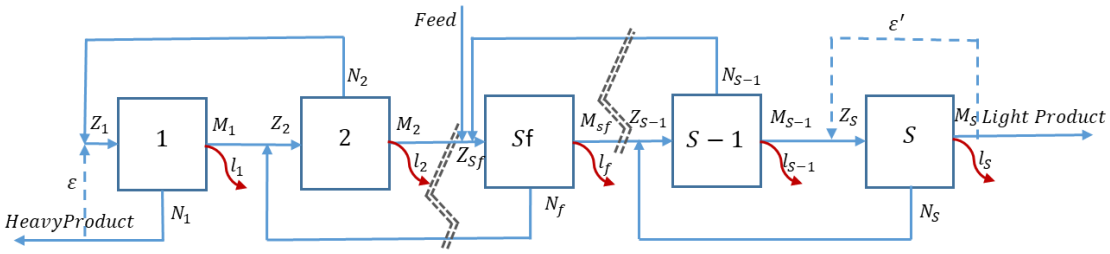

Fig. 1. A view of the square cascade with countercurrent flow

In the square cascade, the input feed flow rate to all stages, Z_s, is the same. In the following, the equations used for cascade modeling are introduced:

$$Z = M_{s-1} + N_{s+1} \quad s \neq s_f \tag{1}$$

$$Z = M_{s-1} + N_{s+1} + F \quad s = s_f \tag{2}$$

$$Z = \varepsilon + N_2 \quad s = 1 \tag{3}$$

$$Z = \varepsilon' + M_{S-1} \quad s = S \tag{4}$$

$$\theta_s = \frac{M_s}{N_s + M_s} \tag{5}$$

$$Z = M_s + N_s + l_s \quad s \neq s_f \tag{6}$$

$$W = N_1 - \varepsilon \tag{7}$$

Equations (1) to (4) are related to the material balance in all the intersection points. Also, using the cut definition for stage s, relation (5) is established. The parameter θs in equation (5) refers to the cut of stage s. Equation (6) is also related to the material balance in all stages and equation (7) is related to the flow balance in the waste separation node from stage 1. The parameters ε and ε' are related to reflux flows in stages 1 and S respectively.

Equation (8) is related to the mass conservation for the ith component in the sth stage. Equations (9) and (10) show the mass conservation at the mixing points of the flows. The relation of the separation factor for use in the separation cascade is as equation (11) and with the help of equation (12), the condition of limiting the concentration of isotopes is applied in all stages.

$$Zz_{i\,s} = M_s y_{i\,s} + N_s x_{i\,s} + l_s z_{i,s} \tag{8}$$

$$Zz_{i\,s} = M_{s-1} y_{i\,s-1} + N_{s+1} x_{i\,s+1} + F z_{i,F} \quad s = s_f \tag{9}$$

$$Zz_{i\,s} = M_{s-1} y_{i\,s-1} + N_{s+1} x_{i\,s+1} \quad s \neq s_f \tag{10}$$

$$\alpha_{ij\,s} = \frac{(y_{i\,s}/y_{j\,s})}{(x_{i\,s}/x_{j\,s})} = \alpha_{0\,s}^{(M_j - M_i)} \quad (i = j-1 \qquad j = 2 \ \dots \ N_c) \tag{11}$$

$$\sum_{i=1}^{N_c} z_{i\,s} = \sum_{i=1}^{N_c} y_{i\,s} = \sum_{i=1}^{N_c} x_{i\,s} = 1 \tag{12}$$

In these relations, $\boldsymbol{y_{i,s}}$, $\boldsymbol{x_{i,s}}$, and $\boldsymbol{z_{i,s}}$ refer to the concentration of isotope i^{th} in the stage s for the up, dow, and input flows, respectively. Also, Nc represents the number of isotopes in the feed stream, and M_i and M_j in relation (11) represent the molecular mass for isotopes i and j.

Methodology

In this research, a code was prepared using MATLAB software, which models the square cascade considering the corrosion rate in the gas centrifuge. This code consists of two main parts: calculating the flow rates in the cascade and calculating the concentration of isotopes. The input of the calculation code is the following information:

The number of stages in the cascade

feed flow rate of the cascade and its location

Amount of input feed rate to the gas centrifuge

Separation factor of the gas centrifuge

Corrosion rate in the gas centrifuge

Since the above parameters are known, the number of unknown flow parameters are Ms, Ns, ε, ε', P, and W, which is equal to 2S+4. Therefore, by using 2S+4 independent equations in the cascade, all unknowns can be calculated. But since there are only 2S+2 independent equations (equations 1 to 7), so, considering 2 parameters with a certain value, the number of equations and unknowns becomes the same. So, the system of equations can be solved.

As the cut of stages and the cascade cut are important tools in controlling the separation process, in this research, these two parameters are used as known. In this way, the flow rates at all stages are calculated.

Unlike the flow equations, the concentration equations are non-linear, and linearization methods must be used. In this research, using the definition of the q parameter, the method of solving and determining the concentration of isotopes is introduced.

By extracting $z_{i,s}$ from equation (8) and putting it in equation (9) as well as expanding it, the following equations are established for all stages:

$$\frac{\varepsilon}{Z_1}x_{i,1}+\frac{N_2}{Z_1}x_{i,2}-\frac{M_1}{Z_1-l_1}y_{i,1}-\frac{N_1}{Z_1-l_1}x_{i,1}+\frac{Feed}{Z_1}x_{i,feed}=0 \qquad s=1 \qquad (13)$$

$$\frac{M_{s-1}}{Z_s}y_{i,s-1}+\frac{N_{s+1}}{Z_s}x_{i,s+1}-\frac{M_s}{Z_s-l_s}y_{i,s}-\frac{N_s}{Z_s-l_s}x_{i,s}+\frac{Feed}{Z_s}x_{i,feed}=0 \qquad s=2\dots S-1 \qquad (14)$$

$$\frac{M_{S-1}}{Z_S}x_{i,S-1}+\frac{\varepsilon'}{Z_S}x_{i,S}-\frac{M_S}{Z_S-l_S}y_{i,S}-\frac{N_S}{Z_S-l_S}x_{i,S}+\frac{Feed}{Z_S}x_{i,feed}=0 \qquad s=S \qquad (15)$$

By defining $q_{i,s}=\frac{y_{i,s}}{x_{i,s}}$, we will have relations (16) to (18) in terms of $x_{i,s}$:

$$(\frac{\varepsilon}{Z_1}-\frac{M_1q_1}{Z_1-l_1}-\frac{N_1}{Z_1-l_1})x_{i,1}+\frac{N_2}{Z_1}x_{i,2}=\frac{Feed}{Z_1}x_{i,feed} \qquad s=1 \qquad (16)$$

$$\frac{M_{s-1}q_{s-1}}{Z_s}x_{i,s-1}-\frac{M_sq_s+N_s}{Z_s-l_s}x_{i,s}+\frac{N_{s+1}}{Z_s}x_{wn+1}=\frac{Feed}{Z_s}x_{i,feed} \qquad s=2\dots S-1 \qquad (17)$$

$$\frac{M_{S-1}q_{S-1}}{Z_S}x_{i,S-1}+(\frac{N_{S+1}q_S}{Z_S}-\frac{M_Sq_S}{Z_S-l_S})x_{i,S}-\frac{N_S}{Z_S-l_S}x_{i,S}=\frac{Feed}{Z_s}x_{i,feed} \qquad s=S \qquad (18)$$

The above set of linearized equations are in terms of $x_{i,s}$, which can be calculated for all isotopes in all phases. After calculating $x_{i,s}$ it is possible to calculate the value of $y_{i,s}$ using the definition of $q_{i,s}$ and $z_{i,s}$ can be calculated from the balance equation of concentration in the stages. After that, by checking the convergence condition according to equation (12), the value of $q_{i,s}$is modified and the solution steps are repeated again until the convergence is established. It should be noted that in this research, the corrosion rate and separation factor and other required information are used hypothetically.

Results and Discussion

In this section, the results of the calculations for the square cascade with 25 and 50 stages for the first isotope of tungsten are given. Changes in the concentration of W-180 and the amount of product with changes in the corrosion rate from 10-7 to 10-3 (mg/s) have been investigated. These hypothetical numbers are based on the values available in the references for tungsten.The main parameters of the cascade as well as the abundance of tungsten isotopes in the feed stream are given in tables (1) and (2), respectively.

Table 1. Input parameters in the cascade

Feed(mg/s)	**Cut**	$\boldsymbol{\theta_1}$	**Z**	$\boldsymbol{\alpha_0}$
12.02	0.0015	0.3345	36.187	**1.163**

Table 2. The concentration of tungsten isotopes in the feed stream

Isotope	**W-180**	**W-182**	**W-183**	**W-184**	**W-185**
Concentration	0.0012	0.2650	0.1431	0.3046	**0.2843**

According to Figure (2), with the increase of the corrosion rate in the gas centrifuge, the concentration of the target isotope in the product stream decreases. Since the amount of the process substance decreases with the increase in the corrosion rate, the decrease in the concentration of the target isotope can also be predicted .Also, as can be seen from Figures (2) and (3), the slope of lines for the cascade with 50 stages is higher than the 25 stages cascade. Therefore, in the longer cascade, the product concentration is more affected by corrosion. It is also observed that in corrosion values less than 10^{-5}, isotope concentration changes in the product flow is ignorable.

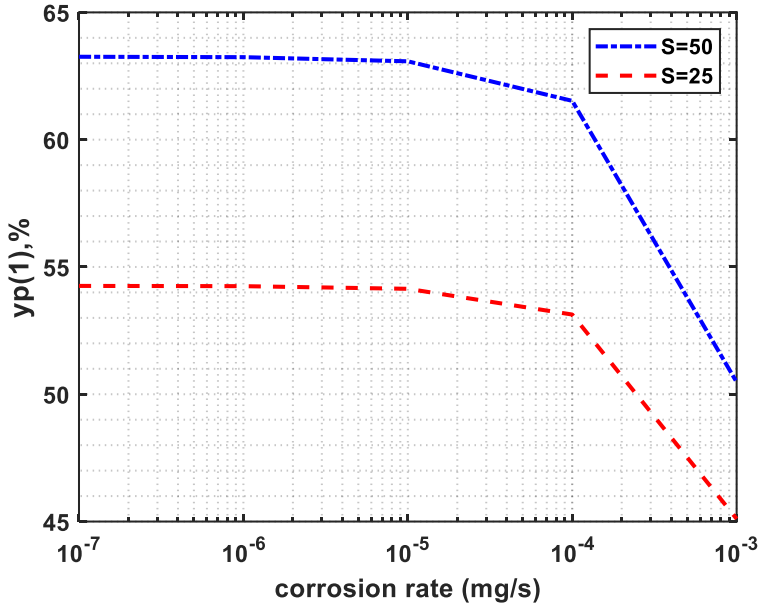

Fig. 2. isotope concentration changes in the product stream for two cascades with 25 and 50 stages

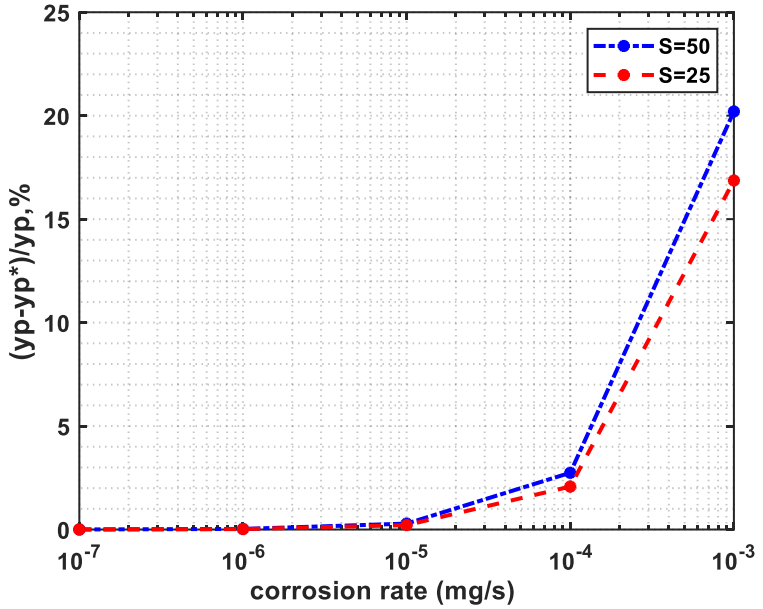

Fig. 3. The relative deviation of the target isotope concentration in the product stream for two cascades with 25 and 50 stages

According to Figure (4), the concentration of the target isotope in the waste stream also decreases with the increase in the corrosion rate. In contrast to the previous figures, the slope of the lines in Figure (5) for the 25-stage cascade is greater than the 50-stage cascade.

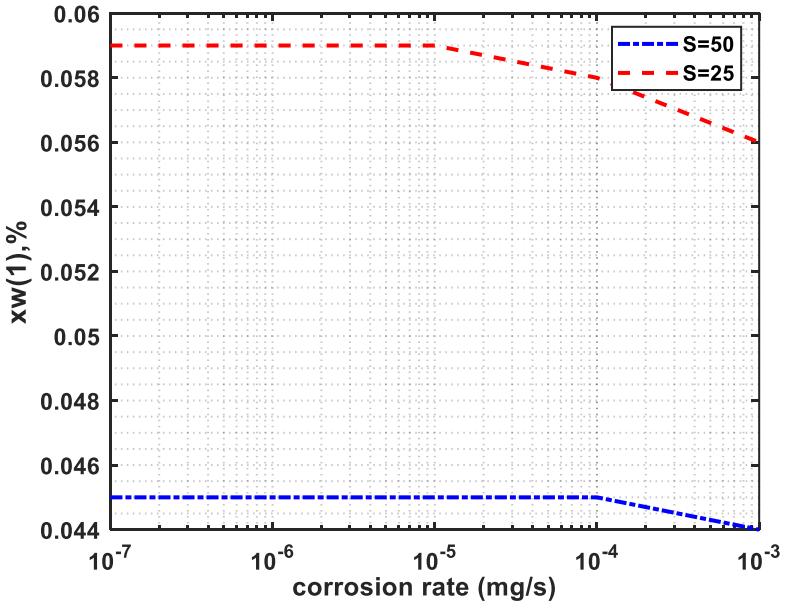

Fig. 4. Isotope concentration changes in the waste stream for two cascades with 25 and 50 stages

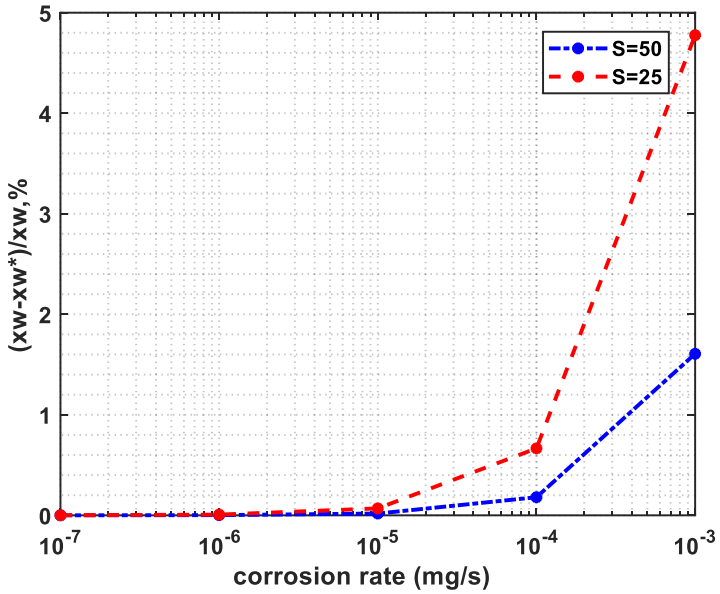

Fig. 5. The relative deviation of the target isotope concentration in the waste stream for two cascades with 25 and 50 stages

Based on Figure (6), since the cascade cut value is the same in all tests, the value of the product flow rate is independent of the number of stages and remains constant in . However according to Figure (7), the waste flow rate decreases with the increase of the corrosion rate, and its changes are greater for the cascade with 50 stages than the cascade with 25 stages. In the longer cascade, more gas centrifuges are used. Therefore, the amount of leakage from the cascade increases, and according to the flow conservation, since the flow rate of product and feed is constant, the amount of waste flow rate decreases.

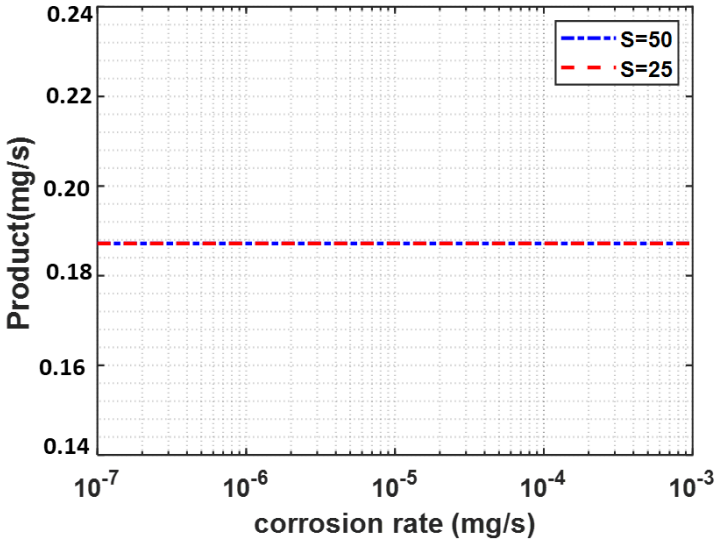

Fig. 6. Product flow rate changes for two cascades with 25 and 50 stages

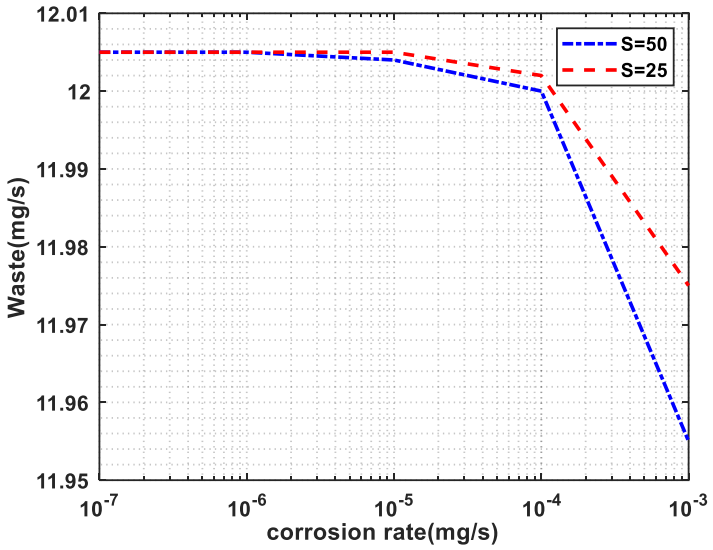

Fig. 7. Waste flow rate changes for two cascades with 25 and 50 stages

If the number of gas centrifuges is the same for 50 and 25 stages cascades, this result is not valid. According to Figure 8, for two cascades with 100 gas centrifuges, the waste flow changes are the same. Because the number of centrifuges is the same and so the amount of leakage from the cascade is the same for both cases.

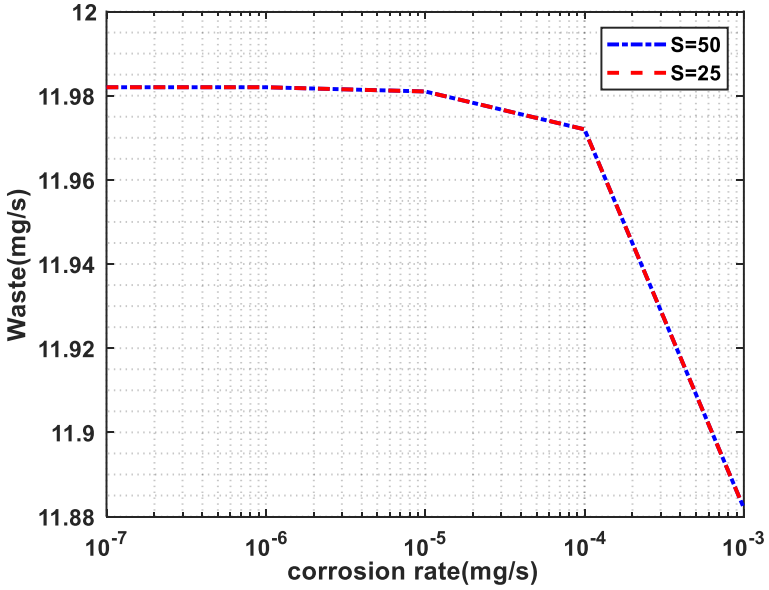

Fig. 8. Waste flow rate changes for two cascades with 100 gas centrifuges

Based on Figures 7 and 8 the waste flow rate also suddenly shifts when transitioning from a corrosion rate of 10^{-4} to 10^{-3}. This affects the cascade that straightly resulted in the isotope concentration variation. Therefore the concentration value suddenly shifts in Figures 2 and 3 when transitioning from a corrosion rate of 10^{-4} to 10^{-3}.

Conclusion

Due to the type of feed chemical composition in the isotope separation cascades, including fluoride compounds, the corrosion in the gas centrifuge is inevitable. The amount of corrosion in the gas centrifuge is very small, but due to the large number of centrifuges in the cascade, determining its value needs to be evaluated in the whole cascade. Therefore, this leads to a reduction in the amount of feed in the separation process. Since some materials used in the separation of stable isotopes are very expensive, this issue is of great importance. On the other hand, the amount of separation depends on the feed flow rate in the gas centrifuge, so it seems necessary to investigate this issue. In this research, a calculation code has been prepared to apply the corrosion rate of the gas centrifuge and investigate its effect on the cascade performance. The results show that for the cascade with more stages in the same amount of feed, this parameter has a greater impact on the performance of the cascade, and with the increase in the corrosion rate, the concentration of the target isotope in the product stream decreases. Also, the results for the separation of the W-180 show that the effect of corrosion rates less than 10^{-5} (mg/s) is negligible and the change in its concentration is more significant for higher corrosion rates.

Rferences

[1]. Zeng S., (2000). A Method of Separating a Middle Component in Multicomponent Isotope Mixtures by Gas Centrifuge Cascades, Separ. Sci. Technol. 35(14).

[2]. Mansourzadeh, F., Safdari, J., Khamseh, A.G.H., Norouzi, A., Khajenouri, M. (2018). Comparison of optimum tapered cascade and optimal square cascade for separation of xenon isotopes using enhanced TLBO algorithm, Separ. Sci. Technol. 53: 2074–2087.

[3]. Khooshechin, S., Mansourzadeh, F., Imani, M., Safdari, J., Mallah, M.H. (2021). Optimization of flexible square cascade for high separation of stable isotopes using enhanced PSO algorithm, Prog. Nucl. Energy. 140: 103922.

[4]. Mansourzadeh, F., Safdari, J., Khamseh, A., Norouzi, A. (2019). Utilization of harmony search algorithm to optimize a cascade for separating multicomponent mixtures, Prog. Nucl. Energy. 111: 165.

[5]. Zeng, S., Cheng, Y. (2013). A numerical method of cascade analysis and design for multicomponent isotope separation, Chem. Eng. Res. Des. 92: 2649.

[6]. Kholpanov, L. P. (1998). On the calculation of a squared-off cascade for multicomponent isotope separation, Chem. Eng. Pro. 37.

[7]. Migliorini. (2013). Modeling and Simulation of Gas Centrifuge Cascades for Enhancing the Efficiency of IAEA Safeguards, University of Virginia.

[8]. Raichura. (1991). The effect of the ‘key’ molar mass on the design of a cascade handling a multi-isotopic mixture, Ann. Nucl. Energy, 18.

[9].Wang, L. M., Zeng, S., Jiang, D. J., Song, T. M. (2008). A Calculation Procedure for Designing Ideal Centrifugal Separation Cascades, Separ. Sci. Technol. 43: 3393.

[10]. Kholpanov. L. P., Tsyuan’sin. Se., Sulaberidze, G. A., Borisevich. V. D. (2008). Calculation of a Square Cascade with Losses of the Working Material in the Steps and Pipelines during Separation of Multicomponent Isotopic Mixtures, Atomic Energy. 104 (1).

[11]. Kholpanov, L.P., Sulaberidze, G.A., Potapov, D.V., Chuzhinov, V.A. (1997). Multicomponent Isotope Separating Cascade with Losses, Chem. Eng. Pro. 36: 189.

ICNST 2024 International Conference on Nuclear Science and Technology
6- 8 MAY 2024 | Isfahan, Iran

Study on the immobilization of spent ion exchange resins of Tehran research reactor in borosilicate glass matrix (Paper ID : 1172)

Pourya Rastgoo[1], Ali Yadollahi[2]*, Hamid Sepehrian[2], Mohammad Samadfam[1]

[1] *Department of Energy Engineering, Sharif University of Technology, Tehran, Iran*

[2] *Nuclear Fuel Cycle Research School, Nuclear Science and Technology Research Institute, AEOI, Tehran, Iran*

Abstract

In this study, the immobilization of Tehran Research Reactor's spent ion exchange resin (IER) in a borosilicate glass matrix was investigated on a laboratory scale. For this purpose, the simulated spent IER waste prepared by doping non-radioactive cesium and cobalt elements on a mixture of cationic C-100 and anionic A-300 purolite IER. In order to conduct the experiments, the thermal pretreatment of the IER was done at 150 °C. Then, glass wasteforms were prepared by mixing borosilicate glass ferrite and spent IER (by 20-40 wt.% loading) and melted at 1200 ^{0}C. The volume reduction ratio (VRR) and chemical stability of the prepared glass wasteforms were investigated. According to the obtained results, with the increase in the spent IER loading, the volume reduction ratio of the final wasteform increases. However, in the samples with spent IER loading higher than 30 wt.%, phase separation (white color containing insoluble sulfate) was observed on the surface of the glass. Investigations showed that glass wasteform containing 30 wt.% spent IER provides the best conditions for waste immobilization. The relative volume reduction ratio of this sample was measured as 86.61%. The normalized leaching rate of cesium and cobalt from this glass wasteform was calculated as 7.43×10^{-5} and 6.93×10^{-5} g/m^2.day, respectively, using the PCT method.

Keywords: Ion Exchange Resin, Borosilicate Glass, Immobilization, wasteform, Cesium, Cobalt.

Introduction

With the rapid development of the nuclear industry in IRAN, a significant amount of radioactive waste has been generated. The spent ion exchange resins (IER), in term of volume, constitute a major portion of solid radioactive waste produced in the nuclear industry. These IERs are produced during the purification process of wastewater streams containing water-soluble radionuclides such as strontium-90, cobalt-60, cesium-137, etc. These IER can be used for the treatment of large volumes of radioactive effluents, and their only limitation is the capacity of the resin to absorb different radioactive materials. In such cases, the spent IER need to be regenerated or replaced with fresh IER. However, IER are not usually regenerated but are stored for disposal after use, as the regeneration process is not cost-effective compared to the IER replacement. Even though the organic IER used for this process are highly effective in removing radionuclides from

wastewater, they are themselves problematic to immobilize or safely store. As a result, a large and growing inventory of this type of waste now exists that requires a route for disposal [1].

Spent IER produced in the Tehran research reactor are known as one of the most important radioactive waste streams that need to be managed properly. These spent IER are classified as low and intermediate level radioactive waste.

Various methods for the management of spent IERs have been investigated. However, among the investigated methods, the immobilization of these wastes in a glass matrix, in a way that incorporates the radionuclides into the macro and micro-structure of the final wasteform, has several advantages over other immobilization methods. The foremost of these advantages is that vitrification method reduces the volume of the IERs by a significant factor, through organic destruction, moisture evaporation, and reduction in porosity. This sets it apart from other methods available that increase the volume of material requiring disposal, such as cementation [2]. Alongside this benefit, the high chemical resistance of glass matrix allows the final wasteform to remain stable in corrosive environments for thousands or even millions of years, and it is also less susceptible to damage from radiation, chemical damage, and mechanical damage than other available wasteforms [3]. Consequently, the disposal of vitrified wasteform can be achieved without additional engineering barriers in near-surface disposal and diverse geological environments, enabling the transportation and long-term storage of glass wasteform due to its strength and long-term safety in waste repositories.

In the United States, South Korea, Switzerland, Russia, England, and Ukraine, vitrification has been considered as an alternative method to cementation for more than 40 years, even for low-level wastes (LLW). Generally, borosilicate glasses are the primary choice globally for immobilizing both high-level and intermediate to low-level radioactive waste [3].

The plasma discharge vitrification technique, as proposed by the Mexican Institute of Nuclear Research, demonstrates the feasibility of incorporating SIER into a glass matrix, with morphological structure characterization performed using SEM, XRD, and TGA techniques [4].

In England, a study was conducted by Hamodi et al. to determine the appropriate glass formulation for the immobilization of spent IERs from a PWR reactor, focusing on the leaching of cobalt-60 and cesium-137 radionuclides. This study provided comprehensive experimental and analytical results, demonstrating that

the waste volume of spent IERs can be minimized through vitrification while maintaining the required wasteform safety levels [5].

In 2013, Owen J. McGann et al. in the Department of Materials Science and Engineering at the University of Sheffield worked on the development of glass compositions for the vitrification of ion exchange resin wastes from the nuclear industry [6]. They reported that ZnO-containing alkali alkaline-earth silicate glass compositions are suitable candidate for immobilization of the spent IERs, with the ability to achieve high Cesium retention.

Experimental

Materials and Equipments

All chemicals employed in this study were prepared and utilized in laboratory-grade purity. The IER was provided by the Tehran Research Reactor. The cationic resin was Purolite C-100, which is a sulfonic acid-based resin in sodium form and the anionic resin was Purolite A-400, which is an ammonium-based resin in chloride form. A magnetic stirrer model MSH-20A from Switzerland was used for the IER impregnation process. A laboratory scale with a measurement accuracy of one ten-thousandth, model AS 220 R2 PLUS from RADWAG Company was employed for weighing the samples. Also, a density kit, model KIT 85, was used for density measurements. A furnace model F11L-1250 made by AzarFurnace company (Iran) was used for the glass samples preparation. An oven model ACE400L made by ATRA company (Iran) was used for the PCT leaching test [7]. The Cesium and Cobalt concentration in the leachate samples was determined using an atomic absorption spectrometer (AAS) model SPECTRA AA200 from Germany. Scanning electron microscope (SEM) model EVO 18 made in Germany was employed for imaging of the prepared wasteforms and EDX and EBSD analysis.

SAMPLE PREPARATION (simulated non-radioactive spent IER)

Initially, the IER impregnation process was carried out with non-radioactive cesium and cobalt. For this purpose, a solution containing specific amounts of cesium nitrate ($CsNo_3$) and cobalt nitrate ($Co(No_3)_2$) was prepared. The solution was then placed in contact with 300 grams of ion exchane resin (150 grams of cationic resin and 150 grams of anionic resin) for 48 hours at room temperature and stirred at a speed of 180 rpm using the MSH-20A magnetic stirrer. This allowed the cesium and cobalt to be loaded onto the ion exchane resin completely. The results of the cesium and cobalt doping process on the IER are shown in Table 1. In the next step, the loaded IER was placed in a furnace and subjected to a temperature of 150°C

for thermal treatment. This thermal treatment caused the IER to lose 50% of its weight, primarily in the form of moisture. Additionally, the thermal treatment allowed the IER to become compatible and homogenized with the borosilicate glass composition during the melting process.

Table 1. The results of doping cesium and Cobalt on the clean IER

Element	Loading wt.%	Initial Concentration (ppm)	Final Concentration (ppm)	Absorption Capacity (mg/g $_{IER}$)
Cesium	4.13	6900	4620	43
Cobalt	1.57	1258	409	16

Simulated Spent Ier Immobilization Process

Table 2 shows the composition of the borosilicate glass used in this study. To create the glassy wasteform, a mixture consisting of 20 grams of borosilicate glass and the waste resin was considered. The characteristics of the waste (resin and glass frit) are reported in Table 3. Subsequently, the glass frrite-simulated resin waste mixture was poured into an alumina crucible and placed inside the furnace. The rate of temperature increase was also 5 degrees per minute. The glass mixture eventually reached a temperature of 1200 °C and was held at this temperature for 3 hours. After the melting process was complete, the alumina crucible was removed from the furnace and placed in a preheated annealing furnace at a temperature of 500 °C to allow the annealing process of the wasteform to proceed slowly.

Table 2. The composition of borosilicate glass ferrite

SiO_2	B_2O_3	Al_2O_3	Fe_2O_3	BaO	CaO	Na_2O	Li_2O	ZnO
51.72	0.38	2.23	2.92	23.22	2.08	5.64	7.81	5.00

Table 3. Weight percentage of borosilicate glass frrite and simulated waste resin

Temperature (^{0}C)	1200	1200	1200	1200	1200
Glass frrite (wt.%)	80% (16 g)	75% (15 g)	70% (14 g)	65% (13 g)	60% (12 g)
Resin (wt.%)	20% (4 g)	25% (5 g)	30% (6 g)	35% (7 g)	40% (8 g)

In order to determine the volume reduction ratio in the spent IER vitrification process, the density of the vitrified wasteform was measured according to the Archimedes method using a density measurement device connected to an analytical scale. The initial volume of the spent IERs were also measured using a graduated cylinder. By knowing the waste volume before and after immobilization process, the volume reduction ratio (VRR) was calculated according to Equation 1.

$$VRR = \frac{(V_i - V_f)}{V_i} \times 100 \quad (1)$$

In this equation, V_i is the initial volume of waste and V_f is the final volume of the glass wasteform. For determining the normalized leaching rate of cesium and cobalt from final wasteforms, leaching tests were performed according to the PCT[2] standard test method [7]. For this purpose, the produced glass wasteforms were powdered in the range of 75-150 μm and placed in contact with the leaching solution of distilled water in a closed PTFE container and placed in the oven for 7 days at 90 ^{0}C. 10 ml of leaching solution and 1 g of sample material was used in each individual test. Then, the samples were filtered by filter paper and the cesium and cobalt concentration in the solution was measured. The normalized leaching rate was calculated using Equation 2.

$$NLR = \frac{C}{(f)(SA/v)(t)} \quad (2)$$

In this equation, C is the concentration of cesium and cobalt in the leachate solution (g/L), f is the weight fraction of cesium and cobalt in the initial matrix, SA/V is the surface area ratio of the glass samples to the volume of the leachate solution in terms of cm^2/L, and t is the leaching time in days [4].

Result & Discussion

Normalized leaching rate of cesium and cobalt as a function of spent IER waste loading at 1200 °C are shown in Figures 1 and 2, respectively. As observed, with an increase in the waste loading from 20 to 40 wt.%, the normalized leaching values are increases from 6.43E-05 to 1.26E-04 for cobalt and from 1.11E-04 to 4.99E-04 for cesium, respectively. Therefor the immobilization of cesium and cobalt within the glassy wasteform decreases by increasing the waste loading. Additionally, the values corresponding to the volume reduction ratio (VRR) of different wasteforms are pictured in Figure 3, indicating the effect of the waste loading on the volume reduction ratio at 1200 °C melting temperature. As we can see in Figure 3, the VRR increases with increasing waste loading.

[2] Product Consistency Test

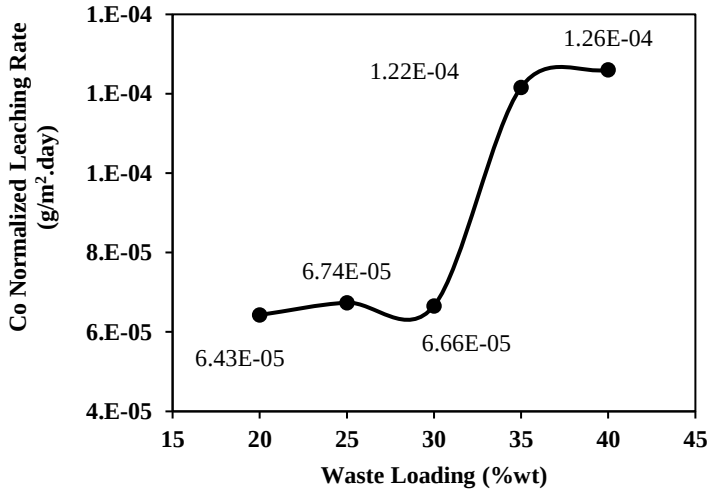

Fig. 1. Normalized leaching Rate of Cobalt as a Function of waste Loading at 1200°C

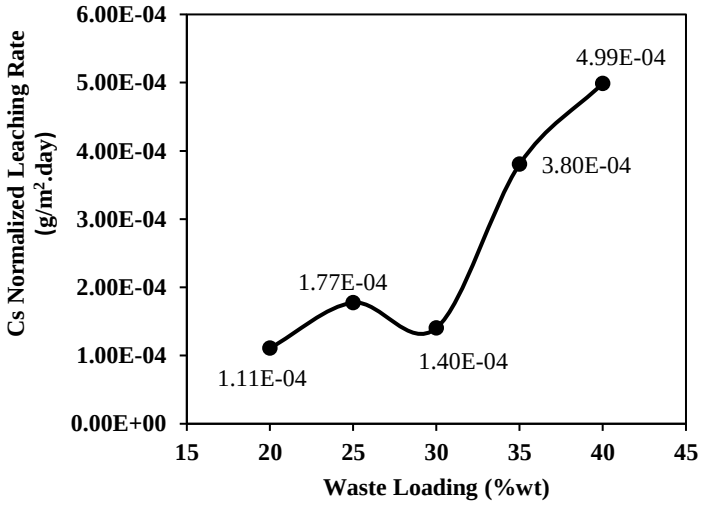

Fig. 2. Normalized leaching Rate of Cesium as a Function of waste Loading at 1200°C.

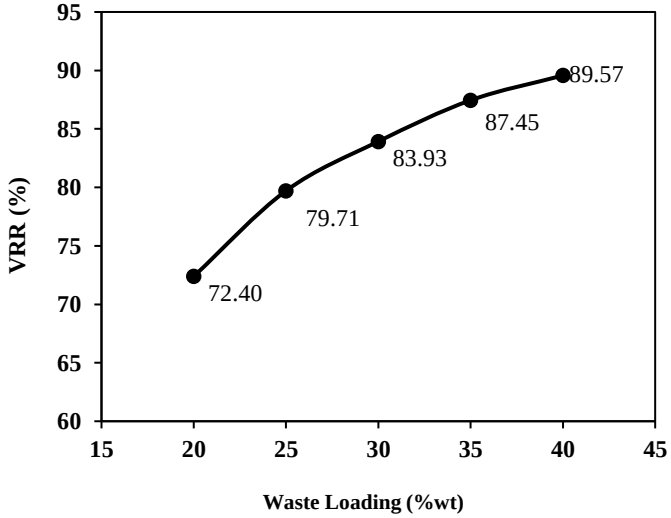

Fig. 3. The VRR as a function of waste loading at 1200°C.

In order to determine the optimal conditions of spent IER immobilization, the appearance of wasteforms prepared at different waste loadings was investigated. The appearance of wasteforms containing 30 and 35 wt.%, spent IER are shown in Figures 4 and 5, respectively. As can be observed from Figure 5, the phase separation occurs on the surface of samples with waste loading of 35 wt.%. Moreover, in order to characterize the produced wasteforms and investigate secondary phase generated, the SEM-EDX analysis of the samples were obtained and showed that this phase contains high amounts of sulfur, iron, and cesium.

Based on the obtained results, the immobilization of spent IER in the borosilicate glass matrix with 30 wt.% loading, leads to the production of a completely homogeneous glass wasteform sample (Figures 4).

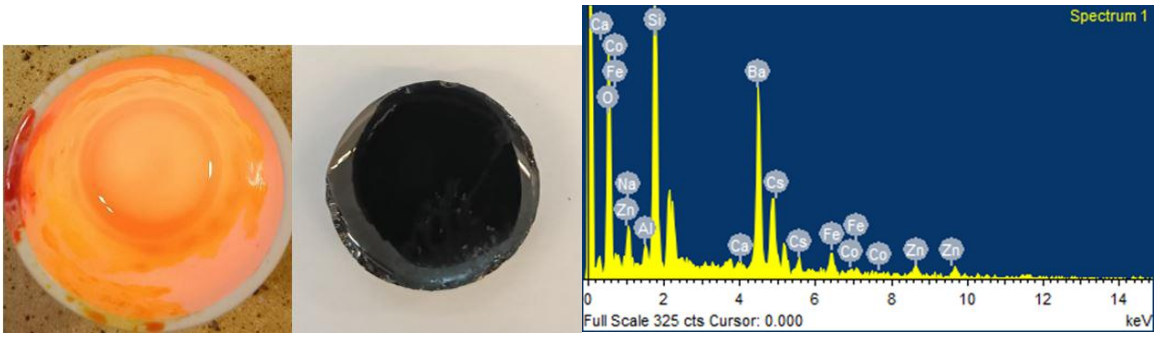

Fig. 4. The appearance and SEM-EDX analysis of wasteform containing 30 wt.% spent IER.

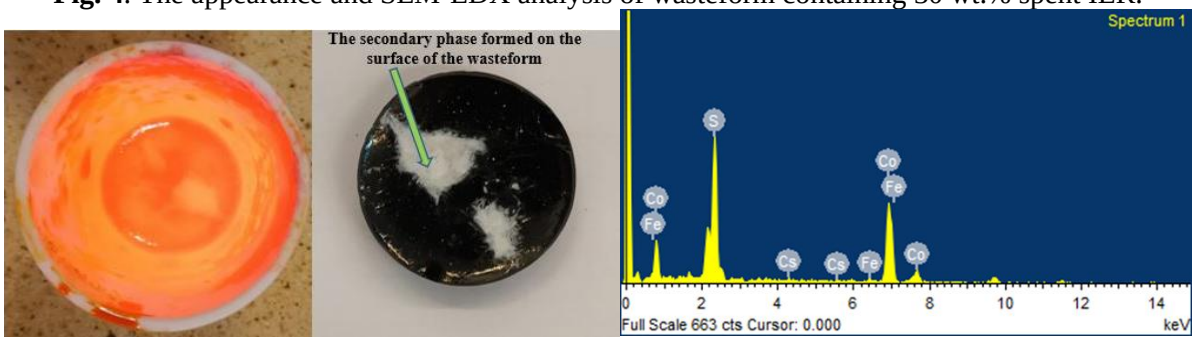

Fig. 5. The appearance and SEM-EDX analysis of wasteform containing 35 wt.% spent IER.

Cnoclusions

The results of this study show that the borosilicate glass wasteform is suitable for immobilizing the spent IER of the Tehran Research Reactor up to 30 wt.% at a temperature of 1200 °C. Under these conditions the relative volume reduction ratio of this final wasteform sample was measured as 86.61%. The normalized leaching rate of cesium and cobalt from this wasteform was calculated as 7.43×10^{-5} and 6.93×10^{-5} g/m^2.day, respectively, which is considered an acceptable value based on the available literature. Owen J. McGann et al reported a value of 1.43×10^{-2} g/m^2.day for the normalized leaching rate of cesium from ZnO-containing alkali alkaline-earth silicate glass wasteform containing 30 wt% spent IERs [6].

Additionally, at higher waste loadings, a secondary phase containing significant amounts of sulfur, cesium, and iron was formed on the surface of the borosilicate glass wasteform. The results of the glass waste leaching test revealed that this phase has a high dissolution capability when in contact with water, resulting in a significant increase in cesium and cobalt leaching results.

References

Wang, Jianlong, and Zhong Wan. "Treatment and disposal of spent radioactive ion-exchange resins produced in the nuclear industry." Progress in Nuclear Energy 78 (2015): 47-55.

Cicero-Herman, Connie A. Commercial ion exchange resin vitrification studies. No. WSRC-TR-97-00282, Rev. 1. Savannah River Site (SRS), Aiken, SC (United States), 2002.

M. I. Ojovan, W. E. J. M. Lee, and M. T. A, "Glassy wasteforms for nuclear waste immobilization," vol. 42, no. 4, pp. 837-851, 2011.

Díaz A, Laura V., et al. "Ion Exchange Resin and Clay Vitrification by Plasma Discharges." AIP Conference Proceedings. Vol. 875. No. 1. American Institute of Physics, 2006.

N. H. Hamodi and Y. J. J. o. P. M. S. Iqbal, "Immobilization of Spent Ion Exchange Resin Arising from Nuclear Power Plants: An Introduction," vol. 3, no. 1, pp. 7-18, 2009.

O. J. McGann, "The Development of Glass Compositions for the Vitrification of Ion Exchange Resin Wastes from the Nuclear Industry," University of Sheffield, 2014.

P. A. E. Spectrometry, "Standard Test Methods for Determining Chemical Durability of Nuclear, Hazardous, and Mixed Waste Glasses and Multiphase Glass Ceramics: The Product Consistency Test (PCT) 1," 2002.

ICNST 2024 International Conference on Nuclear Science and Technology
6- 8 MAY 2024 | Isfahan, Iran

Application of combined design of experiment method for immobilization of radioactive spent zeolites in Glass-Ceramic Matrix (Paper ID : 1185)

Mohammad Reza Vaseghi[1], Ali Yadollahi[2]*, Hamid Sepehrian[2], Amir Saeed Shirani[1]
[1] Department of Fuel Cycle, Faculty of Nuclear Engineering, Shahid Beheshti University, Tehran, Iran
[2] Nuclear Fuel Cycle Research School, Nuclear Science and Technology Research Institute, AEOI, Tehran, Iran

Abstract

The present study investigated the immobilization of spent zeolites, produced in the Cesium-137 containing liquid radioactive waste treatment process, in a Glass-Ceramics matrix. The combined design of experiment method was employed to evaluate the effect of spent zeolite loading (40-80 %wt) and heat treatment process temperature (650-850°C) on the characteristics of Glass-Ceramics wasteforms. Experimental data were analyzed using Design Expert 12.0 software and correlations were proposed for the Cs leaching rate and volume reduction ratio of the final wasteform based on polynomial models. The adequacy of the models was verified using model analysis, coefficient of determination (R^2), and the lack-of-fit test. According to the obtained results, the volume reduction ratio increases with increasing temperature and decreases with increasing waste loading. Investigations show that Glass-Ceramics matrix containing 70% spent zeolite prepared at 750°C provides the best conditions for waste immobilization, which results in the lowest Cs leaching rate (1.94×10^{-6} g/m^2.day) and the highest volume reduction ratio (62.69%). These optimal conditions were applied to the real radioactive waste and no cesium leakage was detected by gamma analysis (measurement accuracy of the device 1Bq/250mL (4Bq/L)). According to the obtained results, the final wasteform was in favorable conditions, which confirmed the successful immobilization of radioactive spent zeolites in Glass-Ceramics matrix.

Keywords: Zeolite, Cesium-137, Immobilization, Glass-Ceramics matrix, leaching rate, volume reduction ratio.

Introduction

One of the major challenges of the nuclear industry is the high volume of radioactive waste generated by various nuclear activities and the subsequent separation, removal and immobilization of hazardous radionuclides with long half-lives. Cesium-137 is a gamma-emitting radionuclide found in radioactive wastes, which is considered one of the environmental hazards due to its radiological property and long half-life [1]. Zeolite is a naturally occurring crystalline mineral recognized as a promising adsorbent to remove Cesium-137 radionuclide from radioactive wastewater [2]. Smiclas et al. [3] investigated the removal of

Cs^{+}, Sr^{2+} and Co^{2+} from aqueous solutions by using a local natural clinoptilolite from Serbia. According to their study, Cs^{+} is preferably adsorbed by the natural clinoptilolite, followed by Sr^{2+} and Co^{2+}. Osman Liyugo [4] employed natural diatomaceous earth (diatomite) as an alternative material for removal of radioactivity from liquid waste. The aim of his study was to remove Cs-137, Cs-134 and Co-60 using natural Turkish diatomite and the results showed that the final radioactivity concentration decreased from 2.60 to 0.4 Bq/mL by processing with this natural adsorbent.

Ali Abbasi et al. [5] developed nanoporous aluminum borosilicate as a new matrix for the stable adsorption and immobilization of cesium ions. They employed nanoporous aluminum borosilicate (Al-B-MCM-41) to remove cesium (Cs) from liquid wastes with a maximum adsorption capacity of 119.05 mg/g. The heat treatment process of adsorbent at around 1100 ºC resulted in the effective immobilization of Cs in the Al-B-MCM-41 matrix, as only 1.9% of the initial adsorbed Cs was leached.

The spent zeolites produced in the radioactive waste treatment process is a secondary radioactive waste that must be immobilized in a solid wasteform to prevent the escape of Cesium-137 radionuclides to the surrounding environment [1]. Several immobilization methods including cementation, bituminization, polymer encapsulation, and vitrification can be employed for the solidification of this radioactive waste. Recently, the glass composite material (GCM) as a material consisting of both glass and crystalline phases has been introduced as a suitable matrix for the immobilization of radioactive waste [6]. Glass composite materials (GCM) are versatile wasteforms for immobilizing various types of radioactive wastes. GCMs including glass-ceramics matrix can employed for the immobilization of spent zeolites produced in radioactive waste treatment process by a low-pressure, low-temperature sintering route. Ojovan et al. [7] investigated the microstructure and leaching durability of glass composite wasteforms for Simulated spent Cs-clinoptilolite waste immobilization. They observed significant changes in microstructure, and durability of the wasteform at different waste loading ratios (37 to 88 wt%). They reported that at waste loading up to 73 wt%, the normalized leaching rate of Cs from GCM wasteform is below 6.35×10^{-6} g/cm^2. By increasing the waste loading, the crystalline phases present in the GCM were not completely enclosed by the glass matrix, which resulted in an increase in the Cs leaching rate. According to the reported results, microstructural characterization shows good encapsulation of simulant waste sorbent in a GCM at waste loading up to 73 wt%.

The purpose of the present study is to investigate the immobilization of spent zeolites produced in the Cesium-137-containing liquid radioactive waste treatment process in a Glass-Ceramics matrix. For this

purpose, mathematical models based on the combined design of experiment method were developed to evaluate the effect of spent zeolite loading (40-80 %wt) and heat treatment process temperature (650-850°C) on the characteristics (i.e. the Cs leaching rate and volume reduction ratio) of the Glass-Ceramics wasteform.

Experimental

Materials

Natural zeolite with Specific Gravity of 2.3 g/cm³ obtained from the Semnan, Iran via Afrazand Mineral Co. was employed in the experiments. The major part of the natural zeolite was in the form of Clinoptilolite with chemical formula of $K\,Na_2\,Ca_2\,(Si_{29}\,Al_7)\,O_{72}\,.24\,H_2O$ and its main exchangeable cation was potassium (K). To prepare the spent zeolite waste, zeolite was milled and meshed in the range of 44 to 74 μm and then exposed to ion exchange reaction with a cesium nitrate solution. After 24 hours, the cesium-impregnated zeolite was removed from the solution and dried for 24 hours at 70 ℃. Then the cesium-impregnated zeolite containing 14.58 wt.% cesium were employed for further experiments.

The borosilicate glass with the composition (wt.%) of SiO_2 (50.05), Na_2O (16.72), CaO (16.61), Al_2O_3 (2.60), TiO_2 (1.56), B_2O_3 (9.34), Li_2O (3.12) was produced from a glass batch melted at 1200℃ for 2 hours and then annealed at 500℃ for 24 hours. The Density of borosilicate glass was 2.60 g/cm^3. The prepared glass sample was milled and its particles was meshed in the range of 44 to 74 μm for Glass-Ceramics wasteform farication.

Experimental design

To investigate the immobilization of spent zeolite wastes in glass-ceramic matrix, a combined design of experiment method considering 2 mixture component (spent zeolite and borosilicate glass loading) and 1 numeric factor (heat treatment process temperature) was adopted.

The effect of spent zeolite loading (40-80 wt.%), borosilicate glass loading (20-60 wt.%), and heat treatment process temperature (650-850°C) on the Cs leaching rate and volume reduction ratio of the Glass-Ceramics wasteform was evaluated by conducting the 17 experimental runs developed according to the combined design of experiment method as shown in Table 1.

After performing the experiments, obtained data were Analyzed using the Design Expert 12.0 statistical software to evaluate experimental models. The experimental data were applied to the polynomial model to

correlate the investigated responses with the variable parameters. The validity of the model was expressed by the coefficients of determination (R^2) and the adequacy of the model was further evaluated by analysis of variance (ANOVA) and lack of fit test.

Glass-Ceramics wasteform Fabrication and Characterization

For Glass-Ceramics wasteform fabrication, a homogeneous mixture of borosilicate glass and cesium-impregnated zeolite was prepared using a Tubula Mixer (NARYA-LTM 2000) at 100 rpm for 20 min. The mixture then compressed at room temperature in a stainless steel mold with a diameter of 13 mm using uniaxial pressure of 30 MPa. Then each compacted disc was sintered at the desired temperature with a heating and cooling rate of 2 °C per minute according to the experimental design tables (Table 1 and Table 2).

The density of the Glass-Ceramics wasteform samples was determined by the Archimedes method using a density kit, model KIT 85, connected to a laboratory scale (AS 220 R_2 PLUS from RADWAG co.). The volume reduction ratio (VRR) of the preapered wasteforms were determined according to Equation 1.

$$VRR = \frac{(V_i - V_f)}{V_i} \times 100 \quad (1)$$

where, V_i is the initial volume of waste and V_f is the final volume of the Glass-Ceramics wasteform.

Finally, in order to evaluate the normalized leaching rate of cesium from Glass-Ceramics wasteform samples, leaching tests were performed according to ASTM C1285−14 standard test method [8]. For this purpose, the produced Glass-Ceramics wasteforms were powdered in the range of 75-150 μm and placed in contact with the leaching solution of distilled water in a closed PTFE container and placed in the oven for 7 days at 90 °C. 10 ml of leaching solution and 1 g of sample material was used in each individual test. Then, the samples were filtered by filter paper and the amount of cesium leached in the solution was measured. The cesium normalized leaching rate (NLR_{Cs} (g(Bq)/cm^2.day)) was calculated using Equation 2.

$$NLR_{Cs} = \frac{C}{(f)(SA/v)(t)} \quad (2)$$

where, C is the concentration of cesium in the leachate solution (g/L or Bq/L), f is the fraction of cesium in the initial matrix, SA/V is the surface area ratio of the material samples to the volume of the leachate solution in terms of cm^2/L, and t is the leaching time in days.

Experiment with real radioactive waste

After confirming the successful immobilization of simulated spent zeolite waste in glass-ceramic matrix, the optimal conditions for waste immobilization were applied to the real radioactive waste sample containing cesium-137 radionuclide. For this purpose, 250 ml of radioactive wastewater from Tehran research reactor (TRR) effluent was prepared. Then, gamma analysis was performed to measure the amount of cesium-137 in the wastewater and the sample was placed in contact with 15 gr of zeolite for 24 hours. Then, the solution was filtered with filter paper and the zeolite impregnated with cesium-137 was employed for further experiments.

Results and Discussion

Statistical Analysis

The immobilization of spent zeolites in Glass-Ceramics matrix was optimized using the combined design of experiment method. Accordingly, 17 experiments were performed based on the experimental design. The borosilicate glass loading (A), spent zeolite loading (B) and heat treatment process temperature (C) were selected as three variables that could potentially affect the NLR_{Cs} and VRR of the preapered Glass-Ceramics wasteforms. According to the experimental results presented in Table 1, the the NLR_{Cs} and VRR of the preapered Glass-Ceramics wasteforms were varied observably depending on the immobilization conditions. The obtained results were evaluated by analysis of variance (ANOVA) as presented in Table 2. According to the ANOVA results, the Linear Mixture-Cubic process polynomial model and Linear Mixture-Linear process polynomial model was best fitted for NLR_{Cs} and VRR responces, respctively. Also, the logarithmic transformation function was recommended for evaluating the NLR_{Cs} response. The ANOVA results (Table 2) demonstrates that the models are highly significant as evident from the calculated F-values and very low p-values [9].

Table 1. Experimental Run and corresponding response values

Run	Variables			f_{Cs}	NLR_{Cs} (g/cm^2 day)		VVR	
	Glass (wt%)	Zeolite (wt%)	Temperature (^0C)		Experimental	predicted	Experimental	predicted
1	***20***	***80***	***650***	***0.117***	***5.69×10^{-6}***	***5.88×10^{-6}***	***59.22***	***59.09***
2	***30***	***70***	***650***	***0.102***	***5.18×10^{-6}***	***5.14×10^{-6}***	***59.27***	***59.81***
3	***40***	***60***	***650***	***0.087***	***3.32×10^{-6}***	***3.43×10^{-6}***	***62.20***	***61.98***
4	***60***	***40***	***650***	***0.058***	***4.88×10^{-6}***	***4.49×10^{-6}***	***60.84***	***60.54***

5	*30*	*70*	*700*	*0.102*	5.17×10^{-6}	6.11×10^{-6}	*61.56*	*61.09*
6	*50*	*50*	*700*	*0.073*	2.58×10^{-6}	2.85×10^{-6}	*62.15*	*62.31*
7	*20*	*80*	*750*	*0.117*	3.96×10^{-6}	3.23×10^{-6}	*61.95*	*61.86*
8	*20*	*80*	*750*	*0.117*	3.29×10^{-6}	3.23×10^{-6}	*61.39*	*61.86*
9	*40*	*60*	*750*	*0.087*	8.38×10^{-7}	8.49×10^{-7}	*62.86*	*62.86*
10	*40*	*60*	*750*	*0.087*	7.956×10^{-7}	8.49×10^{-7}	*62.66*	*62.86*
11	*60*	*40*	*750*	*0.058*	2.679×10^{-7}	2.24×10^{-7}	*63.27*	*63.87*
12	*30*	*70*	*800*	*0.102*	2.46×10^{-7}	2.90×10^{-7}	*64.16*	*63.63*
13	*50*	*50*	*800*	*0.073*	6.00×10^{-8}	6.62×10^{-8}	*64.86*	*64.42*
14	*20*	*80*	*850*	*0.117*	1.35×10^{-7}	1.33×10^{-7}	*64.52*	*64.62*
15	*40*	*60*	*850*	*0.087*	6.63×10^{-8}	6.64×10^{-8}	*64.99*	*65.19*
16	*40*	*60*	*850*	*0.087*	6.64×10^{-8}	6.64×10^{-8}	*65.13*	*65.19*
17	*60*	*40*	*850*	*0.058*	3.36×10^{-8}	3.33×10^{-8}	*65.88*	*65.75*

Lack of fit, as a specific diagnostic test for the reliability of a model, formally tests the fit of the model to the data. As a statistical parameter, the F-value is used to determine the significance or insignificance of the lack of fit at the significant level. For NLR_{Cs}, the lack of fit F-value is 3.93 and P-value is 0.1445 and VRR the lack of fit F-value is 2.66 and P-value is 0.2276, which means the lack of fit is not significant (Table 2). Also, considering that the lack of fit p-value in the ANOVA table is greater than or equal to 0.10, the model seems appropriate. If the model does not fit well with the data, it will be noticeable. A small F value is desirable for the lack of fit, indicating that it is not significant. The regression coefficients and their significance in the second-degree regression models for NLR_{Cs} and VRR are given in Table (2). The goodness of fit of the statistical model was also estimated by the coefficient of determination (R^2). The R^2 value for NLR_{Cs} (0.9971) and VRR (0.9704) are close to 1, which is desirable. The plot of the experimental (actual) and predicted values of NLR_{Cs} and VRR are shown in Figure (1). A good correlation between the input and output variables were also shown by the model.

Table 2. Analysis of variance (ANOVA) for the polynomial models

	Source	*Sum of Squares*	*df*	*Mean Square*	*F-value*	*p-value*
NLR_{Cs}						
	Model	***10.68***	***7***	***1.53***	***447.97***	***< 0.0001***
	Linear Mixture	***1.55***	***1***	***1.55***	***454.88***	***< 0.0001***
	AC	***0.4707***	***1***	***0.4707***	***138.17***	***< 0.0001***
	BC	***0.1843***	***1***	***0.1843***	***54.10***	***< 0.0001***
	AC^2	***0.0329***	***1***	***0.0329***	***9.65***	***0.0126***
	BC^2	***0.4355***	***1***	***0.4355***	***127.84***	***< 0.0001***
	AC^3	***0.1136***	***1***	***0.1136***	***33.34***	***0.0003***
	BC^3	***0.0222***	***1***	***0.0222***	***6.53***	***0.0309***
	Residual	***0.0307***	***9***	***0.0034***		
	Lack of Fit	***0.0272***	***6***	***0.0045***	***3.93***	***0.1445***
	Pure Error	***0.0035***	***3***	***0.0012***		
	Cor Total	***10.71***	***16***			
	R^2	***0.9971***				
	Adjusted R^2	***0.9949***				
VVR						
	Model	***61.29***	***3***	***20.43***	***141.82***	***< 0.0001***
	Linear Mixture	***10.93***	***1***	***10.93***	***75.84***	***< 0.0001***
	AC	***9.83***	***1***	***9.83***	***68.27***	***< 0.0001***
	BC	***24.50***	***1***	***24.50***	***170.07***	***< 0.0001***
	Residual	***1.87***	***13***	***0.1441***		
	Lack of Fit	***1.68***	***10***	***0.1683***	***2.66***	***0.2276***
	Pure Error	***0.1898***	***3***	***0.0633***		
	Cor Total	***63.16***	***16***			
	R^2	***0.9704***				
	Adjusted R^2	***0.9635***				

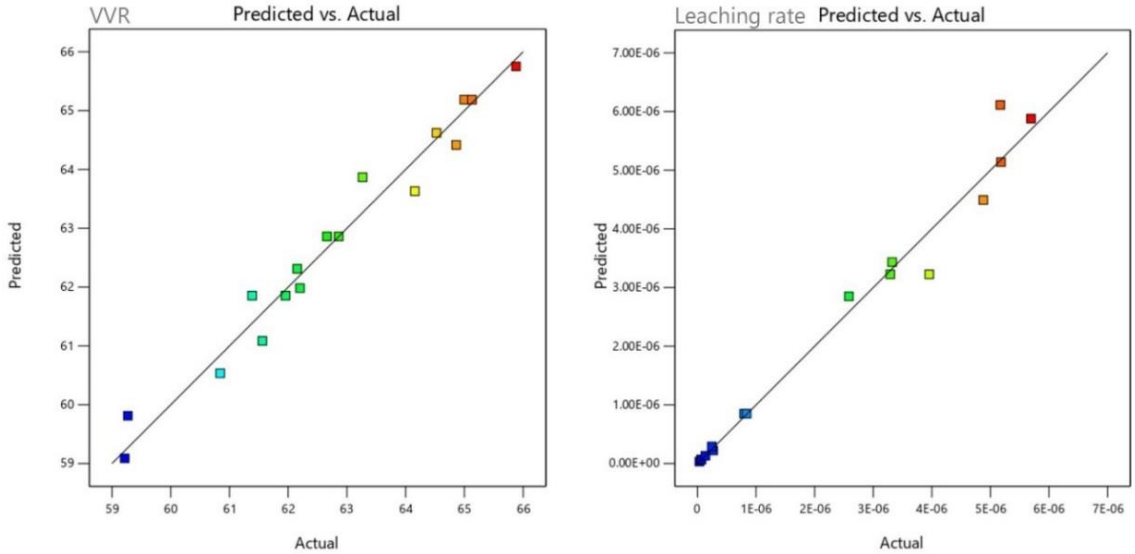

Fig. 1. Diagram of empirical (real) and predicted values of NLR_{Cs} (right) and VRR (left)

Effect of immobilization operating conditions on NLR_{Cs} and VRR

Using the statistical method, the polynomial models describing the correlation between responses (NLR_{Cs} and VRR) and the three variables (borosilicate glass loading (A), spent zeolite loading (B) and heat treatment process temperature (C)) were evaluated as follows:

$$(NLR_{Cs}) = -6.65*A -5.50*B -2.05*AC -1.28*BC +0.1792*AC^2 -0.5626*BC^2 +1.04*AC^3 +0.4594*BC^3$$

$$(VRR) = 63.87*A +61.86*B +1.88*AC +2.77*BC$$

The terms with a plus sign in front indicates synergistic effect, while minus sign in front designates antagonistic effect. In the NLR_{Cs} model, A, B, AC, BC, AC^3 terms are more significant than AC^2, BC^2 and BC^3 terms. For VRR model, A and B terms have a much greater effect than AC and BC.

To visualize the relationship between the investigated responses and the immobilization operating conditions, three-dimensional surface diagrams were pictured in Figures 2 and 3. Figure 2 presents the combined effect of heat treatment process temperature (C) and spent zeolite loading (B) on NLR_{Cs}. As can be seen from this diagram, both independent variables have a significant effect on the NLR_{Cs}. NLR_{Cs} increases by increasing temperature from 650 to 750 °C with a steep slope. The reason for this is that at low temperatures, germination and crystal formation in Glass-Ceramics matrix do not occur well. However, at temperatures higher than 750 °C, NLR_{Cs} decreases, which is due to the desirable germination of crystals and trapping of cesium-impregnated spent zeolite in Glass-Ceramics matrix. According to the obtained results, the optimum temperature for Glass-Ceramics wasteform sintering is 750 °C. Spent zeolite loading is another important factor for NLR_{Cs}. As we can see in Figure 2, the cesium leaching increases with increasing spent zeolite loading, especially at low temperatures. However, this factor is less important than the operating temperature for NLR_{Cs}. Figure 3 shows the combined effect of heat treatment process temperature (C) and spent zeolite loading (B) on VRR. As can be seen from this diagram, both variables have a significant effect on the VRR and the VRR increases with increasing temperature and decreases with increasing waste loading.

Experimental validation of the optimal conditions

The optimization of the immobilization process condition was performed by setting the target criteria as maximum values for VRR and minimum values for NLR_{Cs} while the spent zeolite loading was maximized and heat treatment process temperature was minimized.

The overly plot of the investigated responses in the desired criteria, i.e. NLR_{Cs} $<3\times10^{-6}$ g/m^2.day and VRR>62 is presented in the Figure 4. As observed in the Figure 4, for obtaining the desired value for NLR_{Cs} and VRR, the heat treatment process temperature must be equal or higher than 750°C. To achive the maxium spent zeolite waste loading in final Glass-Ceramics wasteform, the 70 wt.% spent zeolite loading and heat treatment at 750°C was nominated as the optimum condition. The predicted and experimental results of NLR_{Cs} and VRR at the optimum condition are presented in Table 3. As can be seen, the obtained experimental values were in good agreement with the predicted values from the models.

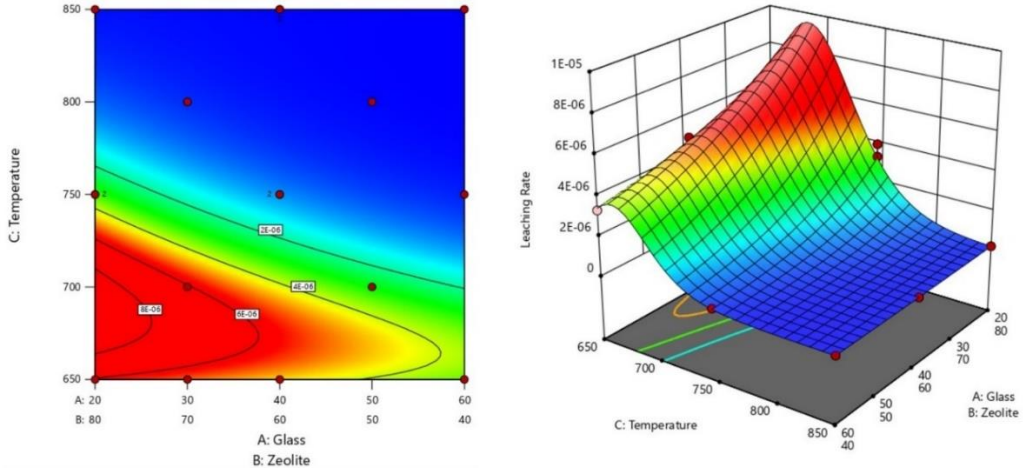

Fig. 2. Three-dimensional surface diagram of the combined effect of heat treatment process temperature and spent zeolite loading on NLR_{Cs}

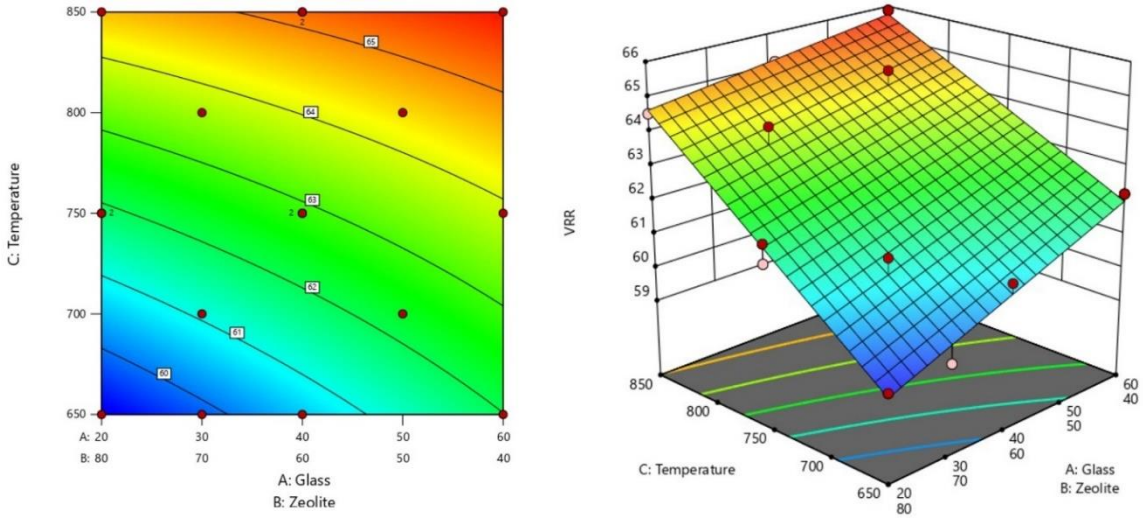

Fig. 3. Three-dimensional surface diagram of the combined effect of heat treatment process temperature and spent zeolite loading on VRR

Table 3. Optimum condition derived from DOE for NLR_{Cs} and VRR

Variables				*NLR_{Cs} (g/cm^2 day)*		*VVR*	
Glass (wt%)	*Zeolite (wt%)*	*Temperature (°C)*	*f_{Cs}*	*Experimental*	*predicted*	*Experimental*	*predicted*
30	***70***	***750***	***0.102***	***1.94×10^{-6}***	***1.65×10^{-6}***	***62.69***	***62.36***

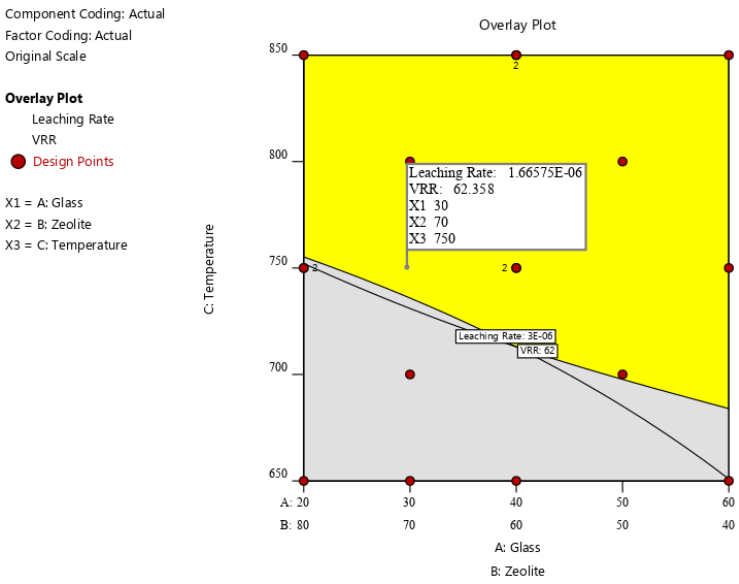

Fig. 4. The overly plot of the NLRCs and VRR responses

Results of real radioactive waste immobilization

The analysis of radioactive wastewater from the Tehran research reactor (TRR) was performed by the High Purity Germanium (HPGe) detector and the cesium-137 concentration was measured as 3328.5 (Bq/L). The cesium-137 concentration in the solution after the zeolite impregnation process was measured as 21.5 (Bq/L). Therefore the spent zeolite impregnated with cesium-137 has an activity concentration of 220.47 Bq/g. For Glass-Ceramics wasteform preparation 70 wt.% of this radioactive spent zeolite waste was homogeneously mixed with 30 wt.% borosilicate glass powder and compressed to a compacted disc. The produced sample was placed in the furnace for sintering operations at 750 ^{0}C. The gamma dose rate of the prepared compacted disc samples was measured before and after the sintering process and the results showed that cesium was not lost during the sintering process.

Finally, the radioactive Glass-Ceramics wasteform was subjected to leaching tests according to ASTM C1285−14 standard test method. The cesium-137 concentration in the leachate solution was reported to be zero, it should be noted that the accuracy of the HPGe detector is 1 Bq/250mL (4 Bq/L). The obtained result indicates the successful immobilization of spent zeolite impregnated with cesium-137 in the Glass-Ceramics matrix.

Conclusions

The combined design of experiment method was utilized for analysis and optimization of the spent zeolite waste immobilization process. The results demonstrated that the developed mathematical models are reliable and feasible for NLR_{Cs} and VRR evaluation. Investigations show that Glass-Ceramics wasteform prepared at 750°C containing 70 wt.% spent zeolite provides the best conditions for waste immobilization, which results in the lowest Cs leaching rate (1.94×10^{-6} g/m^2.day) and the highest volume reduction ratio (62.69%). The normalized leaching rate of Cs from spent zeolite heat treated matrix was measured as 1.11×10^{-4} g/m^2.day which is much higher than the value reported for Glass-Ceramics wasteform. Validation experiments were also performed to verify the reliability and accuracy of the models, and the result indicated that the predicted data was in good agreement with the experimental data. Finally, the Glass-Ceramics wasteform was successfully employed for the safe immobilization of cesium-137-impregnated spent zeolites.

References

[1] Ojovan, M. I., Lee, W. E., & Kalmykov, S. N. (2019). *An introduction to nuclear waste immobilisation*. Elsevier.

[2] Abtahi, M., Fakhri, Y., Sarafraz, M., Keramati, H., OliveriConti, G., Ferrante, M., ... & Baninameh, Z. (2018). Removal of cesium through adsorption from aqueous solutions: A systematic review. *Journal of Advances in Environmental Health Research*, *6*(2), 96-106.

[3] Smičiklas, I., Dimović, S., & Plećaš, I. (2007). Removal of Cs1+, Sr2+ and Co2+ from aqueous solutions by adsorption on natural clinoptilolite. *Applied Clay Science*, *35*(1-2), 139-144.

[4] Osmanlioglu, A. E. (2007). Natural diatomite process for removal of radioactivity from liquid waste. *Applied Radiation and Isotopes*, *65*(1), 17-20.

[5] Abbasi, A., Davarkhah, R., Avanes, A., Yadollahi, A., Ghannadi-Maragheh, M., & Sepehrian, H. (2020). Development of nanoporous alumino-borosilicate as a novel matrix for the sorption and stable immobilization of cesium ions. *Journal of Inorganic and Organometallic Polymers and Materials*.

[6] Ojovan, M. I., Juoi, J. M., Boccaccini, A. R., & Lee, W. E. (2008). Glass composite materials for nuclear and hazardous waste immobilisation. *MRS Online Proceedings Library (OPL)*, *1107*, 245.

[7] Juoi, J. M., Ojovan, M. I., & Lee, W. E. (2008). Microstructure and leaching durability of glass composite wasteforms for spent clinoptilolite immobilisation. *Journal of nuclear materials*, *372*.

[8] Jantzen, C. M., & Bibler, N. E. (2012, April). The product consistency test (ASTM C1285) for waste form durability testing. In *Environmental issues and waste management technologies in the ceramic and nuclear industries XI: proceedings of the 107th annual meeting of the American ceramic society, Baltimore, Maryland, USA*.

[9] Mahmoudiani, F., Milani, S. A., Hormozi, F., & Yadollahi, A. (2022). Application of response surface methodology for modeling and optimization of the extraction and separation of Se (IV) and Te (IV) from nitric acid solution by Cyanex 301 extractant. *Progress in Nuclear Energy, 143*,

ICNST 2024
International Conference on Nuclear Science and Technology
6- 8 MAY 2024 | Isfahan, Iran

Simulation of isotope effects in electrolysis of LiOH on mercury and graphite cathodes: comparison of the separation factors (Paper ID : 1191)

Ahmadi J. [1,2], Sharifi M.[1], Aghaie M.[1*], Yousefi Nasab S. [2], Arzhangmehr A.[2]

[1]Nuclear Engineering Department, Shahid Beheshti University, Tehran, Iran

[2]Iran Advanced Technologies Company, Atomic Energy Organization of Iran (AEOI), Tehran, Iran

Abstract

One of the main ways of extracting clean energy in the future world is through the use of fusion reactors, especially tokamaks. The fuel needed for these reactors is deuterium-tritium. Tritium, not naturally available, is produced through the collision of neutrons with lithium-6 within the environment of these reactors. Various compounds, including lithium hydroxide solution (LiOH), one of the most accessible lithium compounds, can be employed to extract lithium-6. It is worth noting that this isotope naturally occurs with an abundance of 7.5%, which is insufficient for tritium production and requires further enrichment. Various methods, including electrolysis, can be employed to increase the enrichment of lithium-6. In this theoretical study, the electrolysis method, which is a well-known and relatively simple technique for the separation of low-atomic-weight isotopes, has been used to extract lithium-6 from LiOH with a favorable separation factor. In this simulation, the Nernst-Planck and Navier-Stokes equations are employed to study mass transfer and fluid motion, respectively. These equations are solved using the Finite Element Numerical Method (FEM) through the Electrodeposition Module, which is suitable for performing the electrolysis process. The type of cathode is an important factor in increasing the efficiency of electrolysis. For this reason, two types of graphite and mercury cathodes were used, and finally, their results were compared. According to this theoretical study, the mercury cathode achieved a separation factor of 1.05, whereas under the same conditions, the graphite cathode exhibited a much smaller separation factor of about 1.013. Additionally, lithium-6 inherently tends to adsorb to mercury, leading to the production of a solution containing Li-6, known as amalgam (LiHg). Based on the results obtained, it is recommended to use a mercury cathode in LiOH electrolysis.

Keywords: fusion reactors, Lithium-6, electrolysis, mercury, graphite, Separation factor

Introduction

In fusion reactors, deuterium and tritium, two isotopes of hydrogen, are used as fuel. Deuterium isotopes are commercially available in sufficient quantities, but tritium must be produced inside the fusion reactor in structures called breeding blankets. These structures are lithium-containing boxes that generate tritium upon exposure to neutrons [1]. Lithium consists of two isotopes, lithium-6 and lithium-7. According to the following reactions, lithium-6 is very suitable for the production of tritium, but its natural abundance is about 7.5%, and a minimum abundance of 10% is needed for the production of tritium [2].

$$^{6}_{3}Li + ^{1}_{0}n \rightarrow ^{3}_{1}T + ^{4}_{2}He + 4.8Mev \ \ (940barn) \qquad (1)$$

$$^{7}_{3}Li + ^{1}_{0}n \rightarrow ^{3}_{1}T + ^{4}_{2}He + ^{1}_{0}n' - 2.5Mev \ \ (34mbarn) \qquad (2)$$

There are several methods for the enrichment of lithium-6 to achieve higher abundances. Examples of these methods include electrolysis, chemical exchange, laser techniques, electromagnetic separation, distillation, etc. Various research projects and works in the field of lithium separation and enrichment have been conducted through both experimental methods and simulations. Some of them are mentioned below.

Giegerich et al. conducted research to establish a viable method for supplying lithium-6 to both experimental and future fusion power plants in the field of chemical exchange. They increased the enrichment of lithium-6 by utilizing a column exchange process and facilitating contact between a lithium hydroxide solution and mercury [1]. Kosri et al. employed electrolysis in the realm of lithium isotopes applications and their separation methods, utilizing a special approach. In this method, they employed a mercury cathode and a titanium anode [3]. Brooks et al. investigated the history and causes of mercury use and the associated environmental pollution in lithium separation centers in the United States, specifically focusing on the Oak Ridge Y-12 Plant [4]. Sun et al. have been exploring the separation of lithium isotopes through the utilization of a solvent extraction system involving crown ether-ionic liquid [5]. Davoudi et al. have experimentally enriched the lithium-6 isotope using dispersed liquid-liquid microextraction, employing the highly efficient technique with benzo-15-crown-5 [6].

In this study, given the significance of fusion reactors and tritium production, the extraction and enrichment of lithium-6 were simulated using the electrolysis method. Initially, a container containing lithium hydroxide solution was considered. By applying a current between the anode and cathode, the components of this solution were separated and moved towards the electrodes.[7]. The electrolysis setup comprised two basic graphite electrodes, with a paper filter positioned in the center of the box (Fig.e1). This filter serves to limit the passage of lithium-7, promoting the accumulation of lithium-6 in the final product [8]. In the second stage, the geometry of the electrolysis box was changed (Because mercury is liquid); in this case, a sloping surface was considered in which mercury continuously flowed as a cathode (Fig.1). By applying a current between the anode (usually made of titanium or platinum) and the mercury cathode, Li^{+} migrates towards the cathode, and OH^{-} towards the anode. In this case, due to the inherent affinity of lithium-6 to mercury and its higher mobility compared to lithium-7, a greater accumulation of lithium-6 occurs in the final product (LiHg) [3]. It is clear that the desired enrichment can be achieved by performing this process in several stages. Finally, the separation factor of LiOH in the above two cases has been compared. It is worth noting that the simulation and theoretical study of ion mass transfer and fluid motion in the electrolysis box involves solving the Nernst-Planck and Navier-Stokes equations using the finite element numerical method through the Electrodeposition Module, which is suitable for simulating the electrolysis process.

Research Theories

To implement the electrolysis process based on the concepts outlined in the preceding section, a cubic geometry with specific dimensions (refer to Table 1) was initially simulated. Electrodes were positioned on both sides, with a paper filter in the middle (see Fig. 1-a). In this system, the application of an electric current between two graphite electrodes initiates the electrolysis and lithium-6 separation processes. In the second stage, the electrode materials were modified, with a platinum anode and mercury cathode employed. To facilitate the movement of mercury, corresponding changes were made to the geometry, as illustrated in Fig. 1-b.

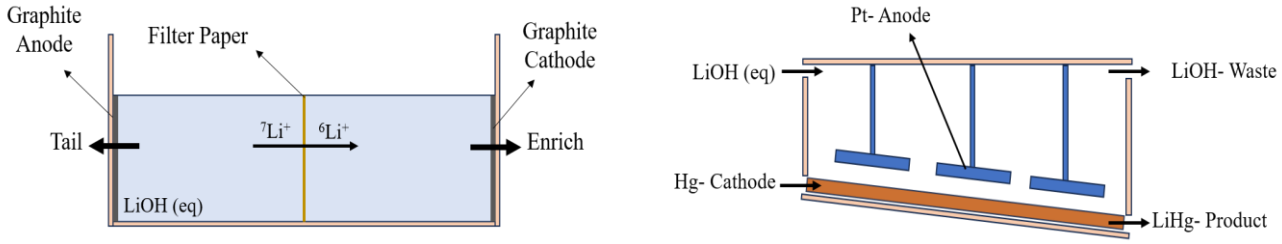

(a) (b)

Fig. 1. General geometry and placement of electrodes in the electrolysis system

Table 1 presents the dimensions and some of the most important parameters necessary to simulate the electrolysis process in the two aforementioned geometries. It should be noted that each of the parameters in Table 1, such as temperature and voltage, is very effective in the electrolysis process. However, in this theoretical study, these values are reported as the most optimal based on various experimental and theoretical references. In this research, the effect of the type of electrodes (cathode) has been investigated while utilizing other optimal parameters.

Table 1. Some parameters used in LiOH electrolysis[3, 7, 9, 10]

parameter	value
Temperature (K)	293.15
Voltage (V)	10
System size (approx.) (m^3)	1
LiOH input concentration (mol/m^3)	2300
LiOH density (kg/m^3)	1056.6
Hg density (kg/m^3)	13110
LiOH viscosity (Pa. s)	1.6909E-3
Hg viscosity (Pa. s)	1.5260E-3
Pt Electrical conduction (S/m^3)	9.5E6
Graphite Electrical conduction (S/m)	2.5E6
Mercury Electrical conduction (S/m)	1.02E6

[3] S/m = Siemens per meter

The Nernst-Planck equations and Navier-Stokes equations (Equation related to momentum conservation) have been employed to simulate the process of lithium hydroxide electrolysis and lithium-6 separation. This set of equations describes the movement of ions and their mass transfer under the influence of electrical gradients and concentration, taking into account the effects of viscosity and momentum transfer. The set of equations is as follows:

Nernst-Planck equations[11]:

$$J_i = -D_i \nabla c_i - z_i u_{m,i} F c_i \nabla \emptyset_l \quad (3)$$

Equation 3 is the Nernst-Planck equation that describes the ion flux (i) in an electrolyte. According to this equation, J is the ion flow (mol/m². s), D is the diffusion coefficient (m²/s), C is the concentration (mol/m³), Z is the number of charges, u_m is the ion mobility under the influence of the electric field (mol. s/kg), F is Faraday's constant (C/mol), and ∅ is the electric potential of the ion in the electrolyte (V).

Navier-Stokes equations (momentum conservation) [12]:

$$\boldsymbol{\rho \frac{\partial u}{\partial t} + \rho(u.\nabla u) = \nabla.[-pI + K] + F} \quad (4)$$

Equation 4 is type of the Navier-Stokes equations that describe the conservation of momentum in fluid dynamics. According to this equation, ρ is the density (kg/m³), u is the fluid velocity vector (m/s), p is the pressure (Pa), I is the identity matrix (dimensionless), K represents the stress tensor that includes viscous stresses (Pa), and F is the force vector on the fluid volume (N/m³). Utilizing the aforementioned equations (3 and 4), the fluid velocity is initially calculated. Subsequently, the concentration of ions can be determined at various locations within the electrolysis geometry. The separation factor ($\boldsymbol{\alpha}$) can be calculated by determining the concentrations of ions (C_{Li6} and C_{Li7}) at both the product site (enrich) and the waste (tail) using Equation 5 (See Fig.1).

$$\boldsymbol{\alpha = \frac{(\frac{C_{^6_3Li}}{C_{^7_3Li}})_{enrich}}{(\frac{C_{^6_3Li}}{C_{^7_3Li}})_{tail}}} \quad (5)$$

Equation 6 calculates the lithium-6 enrichment at the product site (or enrich, fig.1) in percent. This equation is as follows:

$$\boldsymbol{\%\, Enrichment = \frac{C_{Li6}}{C_{Li6}+C_{Li7}} \times 100} \quad (6)$$

Results and discussion

Considering the equations and assumptions outlined in the preceding sections, the separation factor of lithium hydroxide solution is as follows:

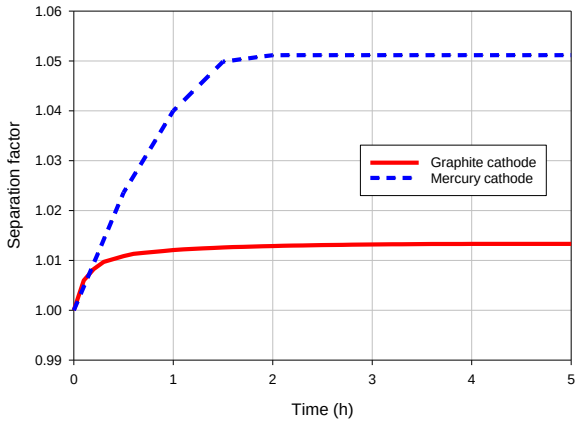

Fig. 2. Effect of different cathodes on the separation factor (α)

Figure 2 illustrates the impact of changing the cathode on the separation factor value. According to the diagram, when the cathode is made of mercury, the separation factor value shifts from 1.013 (with a graphite cathode) to approximately 1.05.

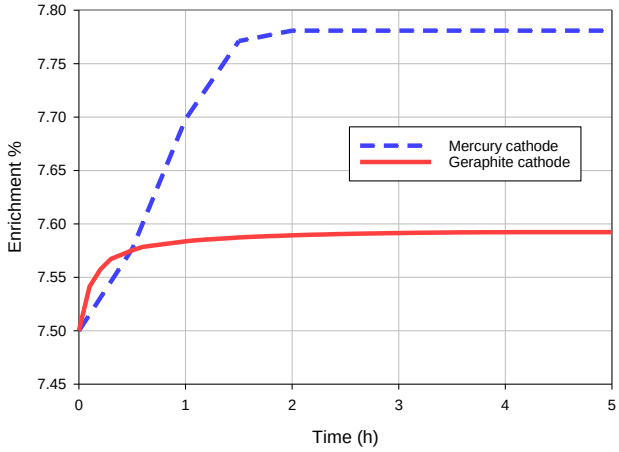

Fig. 3. The enrichment of the final product (lithium 6) based on the use of different cathodes

It is evident that a higher separation factor corresponds to a greater enrichment in the final product. Figure 3 clearly demonstrates that, with the assistance of a mercury cathode, the electrolysis process achieved a 7.78% enrichment of lithium-6 after 5 hours. In comparison, under similar conditions (Table 1), the use of a graphite cathode resulted in a slightly lower enrichment of 7.59%.

Figure 4 illustrates the distribution of lithium-6 concentration at the beginning and end (t=0 and 5 hours) of electrolysis for two geometries and different cathodes. Figures "a" and "b" correspond to cubic geometry with graphite electrodes, while Figures "c" and "d" correspond to inclined geometry with a mercury cathode and platinum anode. Figures "a" and "b" indicate that the concentration of lithium-6 in the cubic geometry has decreased on the left side (tail) and increased on the right side (enrich) over the course of 5 hours (refer to Fig. 1-a). Figures "c" and "d" depict the same trend. In essence, during the electrolysis process, lithium-6 migrates towards mercury, and it is evident that after 5 hours, the concentration of lithium-6 in the "product" area (Fig. 1-b) is higher than in other regions. From the concentration comparison depicted in these figures, it is evident that the mercury cathode outperformed the graphite cathode significantly. Figure 4 clearly illustrates that the rise in the concentration of lithium-6 in the system with a graphite cathode is significantly lower than the increase observed when a mercury cathode was employed.

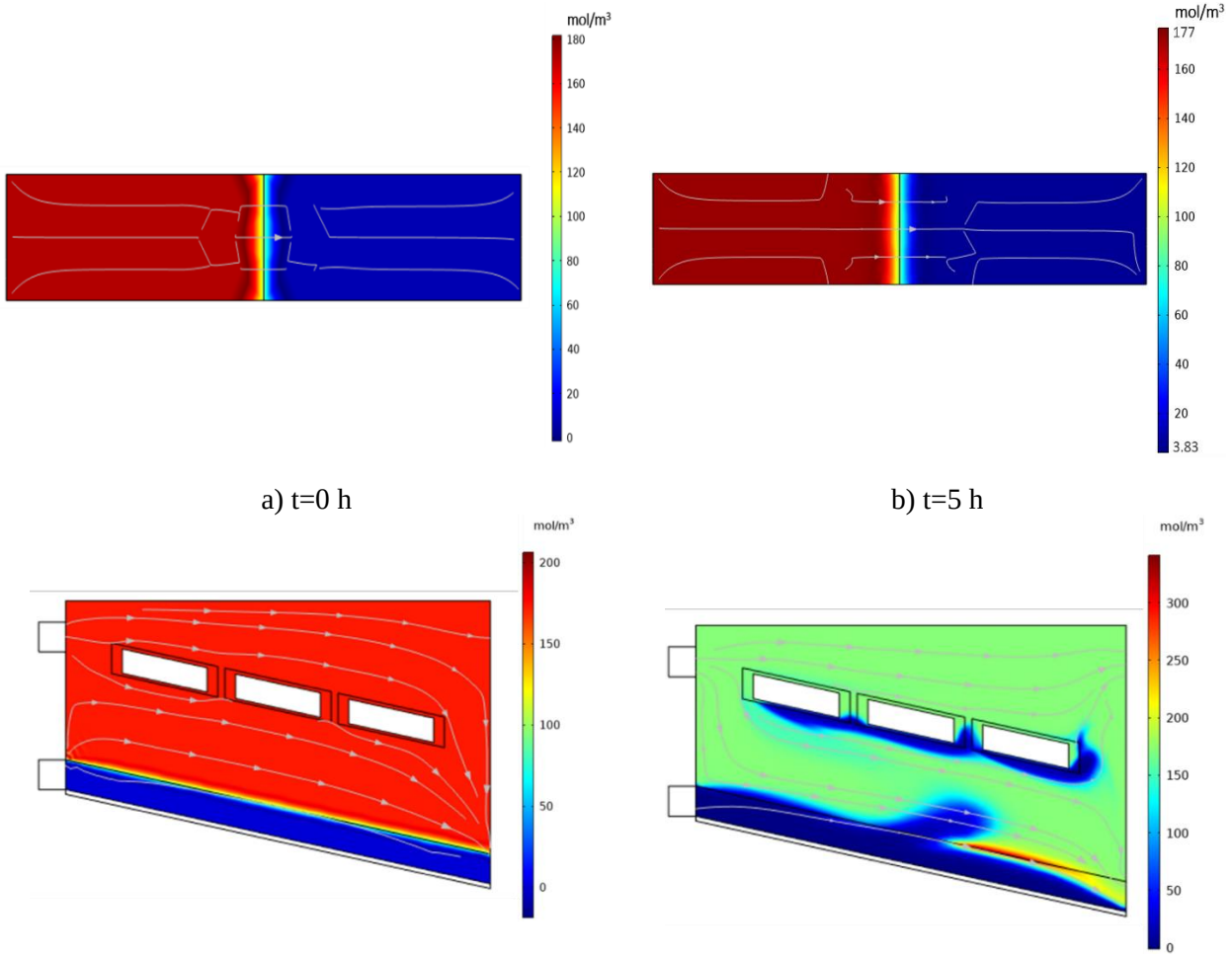

a) t=0 h

b) t=5 h

c) t=0 h

d) t=5 h

Fig. 4. Distribution of lithium 6 concentration at the first moment and after 5 hours of electrolysis

Based on the obtained values for the separation factor and the concentration of lithium-6 in the final product harvesting location, it is evident that the mercury cathode outperformed the graphite cathode under identical conditions. Consequently, it can be concluded that the mercury cathode is a suitable agent and can be utilized to enhance the efficiency of electrolysis and the separation factor of lithium hydroxide solution.

Conclusions

In this article, due to the importance of paying attention to fusion reactors and the production of tritium fuel through lithium-6, a review and comparison of the electrolysis of lithium hydroxide solution for the separation and enrichment of lithium-6 have been conducted. One of the most effective parameters in increasing the efficiency of electrolysis has been the type of cathode that has been used; for this reason, in this study, electrolysis with graphite and mercury cathodes has been compared. It should be noted that, because mercury is in a liquid state, the electrolysis geometry undergoes changes, as depicted in Figure 1-b. The simulation of the electrolysis process has employed the Nernst-Planck and Navier-Stokes equations, which were analyzed using the finite element numerical method (FEM). The Navier-Stokes equations determine the solution's speed at different points in the electrolysis system. By substituting these values into the Nernst-Planck equation, concentrations of the desired solution and lithium-6 at different points are obtained. The calculation of concentrations and the separation coefficient (Equation 5) indicate that the use of a mercury cathode has better results compared to a graphite cathode. Specifically, the mercury cathode resulted in a separation factor of 1.05, whereas the graphite cathode resulted in a separation factor of 1.013. Additionally, due to the higher affinity of lithium-6 for mercury over lithium-7 (Because of Li-6 mobility), the use of a mercury cathode increases the abundance of lithium-6. Based on these results, the use of a mercury cathode is recommended to achieve a higher separation factor.

Acknowledgements

The authors of this article extend their sincere appreciation for the generous support received from the 'Iran Advanced Technologies Company' and express their gratitude to the esteemed CEO of the company, Dr. Ali Norouzi.

References

[1] Giegerich, T., et al., (2019). Development of a viable route for lithium-6 supply of DEMO and future fusion power plants. Fusion Engineering and Design. 149: p. 111339.

[2] Bradshaw, A.M., Hamacher, T., and Fischer, U., (2011). Is nuclear fusion a sustainable energy form? Fusion Engineering and Design. 86(9-11): p. 2770-2773.

[3] Kosari M., Otokesh .M., Ahmadi S.J., Rafiei J., Aminian A., (2013). Applications of Lithium Isotopes and Their Separation Methods.; (https://www.sid.ir/paper/851783/fa#downloadbottom).

[4] Brooks, S.C. and Southworth, G.R., (2011). History of mercury use and environmental contamination at the Oak Ridge Y-12 Plant. Environmental pollution,. 159(1): p. 219-228.

[5] Sun, H., et al., (2019). Separation of lithium isotopes by using solvent extraction system of crown ether-ionic liquid. Fusion Engineering and Design,. 149: p. 111338.

[6] Davoudi, M. and Mallah, M.H., (2013). Enrichment of 6Li using dispersive liquid–liquid microextraction as a highly efficient technique. Annals of Nuclear Energy,. 62: p. 499-503.

[7] https://en.wikipedia.org/wiki/Electrolysis.

[8] Zhang, Z., et al., (2019). Investigation on lithium isotope fractionation with diffusion, electrochemical migration, and electrochemical isotope effect in PEO-PC based gel electrolyte. Journal of The Electrochemical Society,. 166(6): p. E145.

[9] Fujie, M., et al., (1986). Isotope effects in electrolytic formation of lithium amalgam. Journal of Nuclear Science and Technology,. 23(4): p. 330-337.

[10] Lide, D.R., (1995). CRC Handbook of Chemistry and Physics: A Ready-reference Book of Chemical and Physical Data.: CRC-Press.

[11] Maexa, R., (2022). Nernst-Planck Equation. Encyclopedia of Computational Neuroscience,: p. 2182-2187.

[12] Foias, C., et al., (2001). Navier-Stokes equations and turbulence. Vol. 83: Cambridge University Press.

ICNST 2024
International Conference on Nuclear Science and Technology
6- 8 MAY 2024 | Isfahan, Iran

Adsorption of strontium by Dowex 50W-X8 resin loaded with TOPO extractant (Paper ID : 1193)

Ghorbanpour Khamseh A.A. *, **Khani M.H., Aghayan H.**
Nuclear Fuel Cycle Research School, Nuclear Science and Technology Research Institute, Tehran, Iran,
E-mail: akhamseh@aeoi.org.ir

Abstract

In this research work, the adsorption of strontium ions from aqueous solutions was studied using Dowex 50W-X8 resin loaded with TOPO extractant. The influence of effective operational parameters such as initial pH of the solution, adsorbent dosage, initial strontium concentration in the solution, and contact time was evaluated. In order to investigate the kinetics of the adsorption process, pseudo-first-order and pseudo-second-order models were used. The results indicated a very good agreement between the experimental data and the pseudo-second-order kinetic model. Langmuir and Freundlich models were used to model the equilibrium of the adsorption. Langmuir isotherm model showed good agreement with the experimental data. The maximum adsorption capacity of Dowex 50W-X8 resin loaded with TOPO for strontium sorption was obtained 129.87 mg/g of adsorbent calculated by the Langmuir model. The result of the present study showed that Dowex 50W-X8 resin loaded with TOPO extractant can be an effective adsorbent for the sorption of strontium from aqueous solutions and industrial wastewater.

Keywords: Adsorption, Strontium, Dowex 50W-X8 resin, TOPO extractant

Introduction

The management of the entry of radioactive materials into the environment is one of the critical issues in various industries, especially in the nuclear industry [1,2]. One of the most important radionuclides that can pollute the environment is strontium Sr (90). This radionuclide with a half-life of 28.9 years is a beta emitter that is produced during nuclear fission reactions [3].

One of the effective methods in the process of separation and purification of wastewater is adsorption [4].

Ion exchange resins are among the adsorbents that have been widely studied for the removal of heavy metals [5]. Studies have shown that the use of extractants as modifiers can improve the adsorption properties of resins [6]. Solvent-impregnated resins (SIRs) have several advantages over conventional extraction systems including the selectivity of extractants, ease of phase separation, easy recovery of the loaded materials in the desorption step, and the wide variety of extractants [7]. Trioctyl phosphine oxide

(TOPO) is one of the most popular extractants for the extraction of heavy metals, which plays a role according to the following mechanism [8-11]:

$$M^{n+} + mTOPO \leftrightarrows M(TOPO)_m{}^{n+} \quad (1)$$

The purpose of this research work is to investigate the adsorption potential of Dowex 50W-X8 resin loaded with TOPO extractant as a new SIR adsorbent for strontium removal from aqueous solutions. In this regard, the effect of the main effective parameters on adsorption process such as initial pH of the solution, adsorbent dosage, initial strontium concentration in the solution, and contact time have been investigated. Also, the kinetics and the equilibrium of the adsorption process have been studied.

Research Theories

First and second-order reaction rate kinetic models commonly used to describe the rate of the adsorption processes. The linear forms of pseudo - first and -second-order kinetic models are as follows respectively [12]:

$$\log(q_{eq} - q_t) = \log q_{eq} - \frac{k_1 t}{2{,}303} \quad (2)$$

$$\frac{t}{q_t} = \frac{1}{k_2 q_{eq}^2} + \frac{1}{q_{eq}} t \quad (3)$$

where q_{eq} and q_t (mg/g) are the amount of strontium adsorbed at equilibrium and at time t (min), respectively, k_1 (1/min) and k_2 (g/mg.min) show the equilibrium rate constant of pseudo - first and - second-order adsorption, respectively.

The Langmuir and Freundlich isotherms can be used to determine the relationship between adsorbed strontium ions on the SIR adsorbent (q_{eq}) and unadsorbed strontium ions in solution (C_{eq}). The linear form of these Langmuir and Freundlich isotherms are given by the following equations, respectively [13]:

$$\frac{1}{q_{eq}} = \frac{1}{b q_m C_{eq}} + \frac{1}{q_m} \quad (4)$$

$$\log q_{eq} = \log k_f + \frac{1}{n} \log C_{eq} \quad (5)$$

where q_{eq} (mg/g) is the amount adsorbed at the equilibrium, C_{eq} (mg/L) is the equilibrium concentration, q_m (mg/g) is the Langmuir constant representing the maximum monolayer adsorption capacity and b (L/mg) is the Langmuir constant related to the energy of adsorption and the affinity of the binding sites, k_f (L/g) is

the Freundlich constant which is related to the adsorption capacity, and n is the dimensionless Freundlich constant.

Experimental

Impregnation

To impregnate Dowex 50W-X8 resin with TOPO extractant, first, 30 grams of resin were washed three times with deionized water to remove impurities and prepare the internal pores of the resin for the impregnation process. Then the washed resin was filtered and completely dried at room temperature for 24 hours. Then, 20 grams of dry resin was contacted with 40 ml of TOPO in a 0.5 M toluene solution at room temperature using a constant speed stirrer for two hours. Then the resin beads were separated from the organic phase and washed several times with 2 M nitric acid. Finally, the impregnated resin beads were washed with deionized water and completely dried for 24 hours at room temperature.

Adsorption experiments

To carry out the strontium adsorption process by TOPO-impregnated resin, a certain amount of adsorbent was added to a set of 250 ml Erlenmeyer flasks containing 100 ml of strontium nitrate solution with predetermined concentrations. The flasks were shaken for a certain period in the incubator shaker at a speed of 150 rpm and a temperature of 25 °C. After the adsorption process was completed, Whatman filter paper was used to filter the strontium solution. Sampling was done at specified time intervals and the remaining strontium concentration was measured by ICP-AES device. The amount of adsorbed metal ions per unit mass of resin (mg/g) was calculated using the following Eq. (6).

$$q = (C_i - C_e) \times \frac{V}{M} \quad (6)$$

where C_i and C_e (mg/L) is the initial and the equilibrium concentrations, respectively. V (L) is the volume of test solution and M (g) is the amount of the adsorbent in the solution. The percentage of metal ion adsorption was calculated by Eq. (7).

$$\%\ \text{Adsorption} = \frac{C_i - C_e}{C_i} \times 100 \quad (7)$$

Results and discussion

Effect of pH

The effect of pH on the adsorption of strontium from aqueous solutions was investigated using Dowex 50W-X8 resin loaded with TOPO in the range of 2 to 7. Fig. 1 shows that the optimum pH value at which maximum adsorption occurs is 6. At lower pH, the competition of H^+ cations with Sr^{2+} cations for the exchange sites in the adsorbent causes a noticeable reduction in the amount of strontium adsorption. With the increase of pH, the adsorption rate increases, and with the increase of pH higher than about 6, the adsorption rate starts to decrease. At alkaline pHs, adsorption was not investigated due to the possibility of strontium precipitation [14].

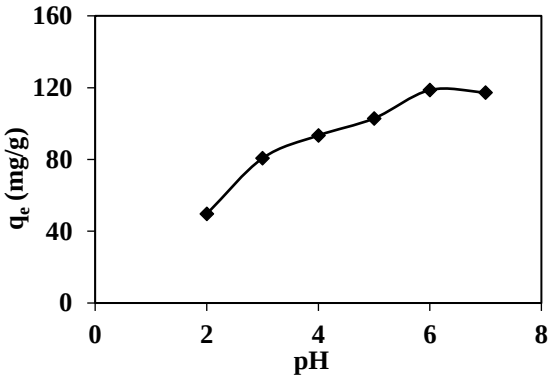

Fig. 1. Effect of pH on strontium adsorption
(C_o: 90 mg/L, Adsorbent dosage: 0.5 g/L, contact time: 24 h)

Effect of contact time on strontium adsorption, and kinetic modeling

The kinetic study of the adsorption process of strontium ions by impregnated resin shows that this adsorption process is relatively fast at the beginning, so that approximately 70% of the adsorption occurs in the first 50 minutes. Subsequently, the adsorption rate decreased and reached equilibrium in approximately 120 minutes, after which very little adsorption occurred (Figure 2). The results of kinetic modeling of this process using pseudo first and second order models are presented in Table 1. As can be seen, the experimental results are in better agreement with the pseudo-quadratic kinetic model.

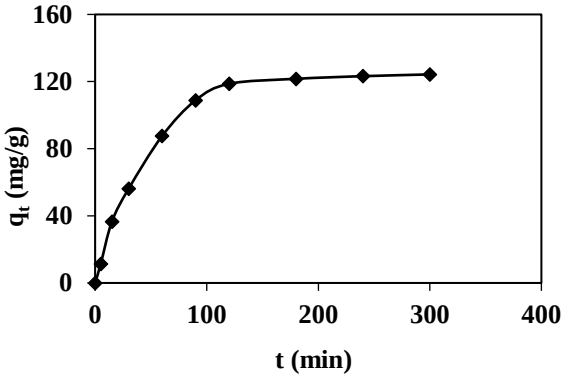

Fig. 2. Effect of contact time on strontium adsorption
(pH: 6, Co: 90 mg/L, Adsorbent dosage: 0.5 g/L)

Table 1. Kinetic modeling parameters

Psudo-first-order			Psudo-second-order		
k_1 (1/min)	q_{eq} (mg/g)	R^2	k_2 (g/mg.min)	q_{eq} (mg/g)	R^2
0.0223	125.69	0.9829	0.0002	147.06	0.9905

Effect of adsorbent dosage

The effect of the adsorbent dosage in the range of 0.1 to 1.2 g/L on the amount of adsorption and the removal percentage of strontium ions was investigated and the results are shown in Fig. 3. According to the results, increasing the amount of adsorbent causes an increase in the percentage of adsorption because more sites for adsorption are available for metal ions. On the other hand, with increasing adsorbent dosage, the amount of adsorption decreases because the amount of adsorption is defined based on the amount of unit weight of the adsorbent. Based on this, next series of adsorption experiments have been performed using an adsorbent dosage of 0.5 g/L.

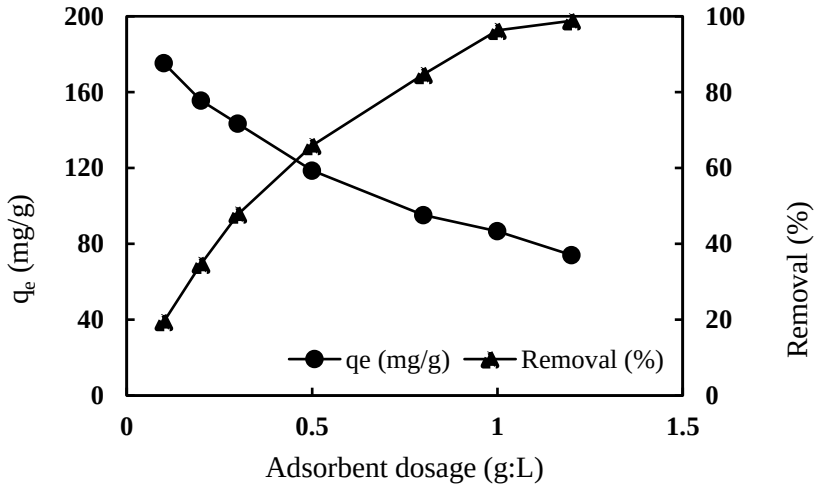

Fig. 3. Effect of adsorbent dosage on equilibrium sorption of strontium
(pH: 6, Co: 90 mg/L)

Effect of initial solution concentration

Fig. 4 shows the results of investigating the effect of the initial concentration of strontium on its adsorption amount. According to the figure, as the initial concentration of strontium increases, the amount of adsorption increases. The increase in the amount of adsorption with the increase in initial concentration is due to the availability of more adsorbent sites for the adsorption of strontium ions, which gradually approaches a constant value. At higher initial solution concentrations, due to the saturation of the adsorbent active sites, the amount of adsorption remains constant.

Experimental equilibrium data were modeled using Langmuir and Freundlich isotherms. The results are presented in Table 2, which shows that the Langmuir isotherm model has better compatibility with the experimental data, which means that the adsorption mechanism can be considered as a monolayer and the adsorbent surface is homogeneous in terms of adsorption energy. The Langmuir model predicts the maximum adsorption capacity of 129.87 mg/g adsorbent.

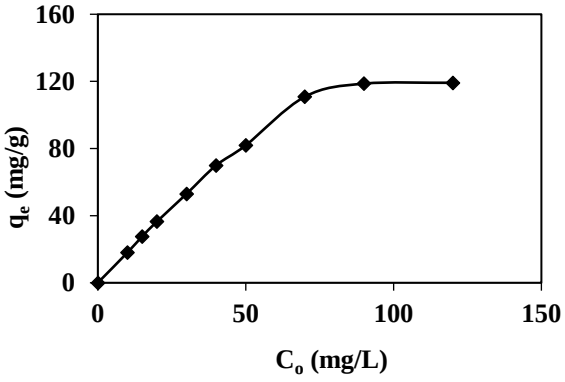

Fig. 4. Effect of initial concentration on equilibrium sorption of strontium
(pH: 6, Adsorbent dosage: 0.5 g/L)

Table 2. Adsorption isotherm parameters

Langmuir constants			**Freundlich constants**		
q_m (mg/g)	b (L/mg)	R^2	k_f (L/g)	n	R^2
129.87	0.2175	0.9963	26.55	2.23	0.8875

Conclusions

Adsorption of strontium ions from aqueous solutions was investigated using Dowex 50W-X8 resin impregnated with TOPO. The effect of parameters including pH, adsorbent dose, initial concentration of solution and contact time on the adsorption was evaluated and their optimal values were determined. Also, the kinetics of the adsorption process followed the pseudo-second order model and the Langmuir isotherm

model showed a good agreement with the equilibrium experimental data. The results of the present study showed that Dowex 50W-X8 resin loaded with TOPO extractant can be an effective adsorbent for the sorption and removal of strontium from industrial wastewater.

References

[1] Apted, M.J. and Ahn, J. (2017). Repository 101: Multiple-barrier geological repository design and isolation strategies for safe disposal of radioactive materials. In:Geological Repository Systems for Safe Disposal of Spent Nuclear Fuels and Radioactive Waste. Elsevier, pp 3-26.

[2] Liang, L. and Guixiang, Y. (2021). Study on Aging Management of Operating Nuclear Power Plants in China. In: International Conference on Nuclear Engineering, 2021. American Society of Mechanical Engineers, p V002T006A003.

[3] Pathak, P. and Gupta, D.K. (2020) Strontium contamination in the environment. Springer.

[4] Singh, N., Nagpal, G., Agrawal, S. (2018) Water purification by using adsorbents: a review. Environmental technology & innovation 11:187-240.

[5] Inan, S. (2022). Inorganic ion exchangers for strontium removal from radioactive waste: a review. Journal of Radioanalytical and Nuclear Chemistry, 331(3): 137-1154.

[6] Mousavi, S.E., Kalal, H.S., Ghorbanian, S.A., Khamseh, A.A.G. and Khanchi, A.R. (2023). A comparison of various XAD-Amberlite resins impregnated with dicyclohexyl-18-crown-6 for strontium removal. Progress in Nuclear Energy, 166: 104965.

[7] Navarro, R., Saucedo, I., Nunez, A., Ávila, M. and Guibal, E. (2008). Cadmium extraction from hydrochloric acid solutions using Amberlite XAD-7 impregnated with Cyanex 921 (tri-octyl phosphine oxide). Reactive and Functional Polymers, 68(2): 557-571.

[8] Iwasaki, S., Umetani, S., Sasayama, K., Matsui, M. (1982). Solvent Extraction of Alkaline Earths with 1-Phenyl-3-Methyl 4 Stearoylpyrazol-5-One and Topo. Analytical Letters, 5(14): 1159-67.

[9] Sasaki, T., Umetani, S., Matsui, M., Tsurubou, S. Quantitative Extraction-Separation of Calcium and Strontium Using Cryptand (2.2. 2) as a Masking Reagent, Chemistry letters, 7: 1195-8.

[10] Onizaki, M., Morita, K., Hirayama, N. Synergistic ion-pair extraction of strontium ion with tri-n-octylphosphine oxide and dicyclohexano-18-crown-6. Analytical Sciences, 32(12): 1367-70.

[11] Batchu, N.K., Li, Z., Verbelen, B., Binnemans, K. Structural effects of neutral organophosphorus extractants on solvent extraction of rare-earth elements from aqueous and non-aqueous nitrate solutions. Separation and Purification Technology, 15(255): 117711.

[12] Mahmoud, A.E.D., Fawzy, M., Hosny, G. and Obaid, A. (2021). Equilibrium, kinetic, and diffusion models of chromium (VI) removal using Phragmites australis and Ziziphus spina-christi biomass. International Journal of Environmental Science and Technology, 18: 2125-2136.

[13] Bhatnagar, A., Minocha, A.K. and Sillanpaa, M. (2010). Adsorptive removal of cobalt from aqueous solution by utilizing lemon peel as biosorbent. Biochemical Engineering Journal, 48(2): 181-186.

[14] Thorpe, C.L., Lloyd, J.R., Law, G.T., Burke, I.T., Shaw, S., Bryan, N.D. and Morris, K. (2012). Strontium sorption and precipitation behaviour during bioreduction in nitrate impacted sediments. Chemical Geology, 306:114-122.

ICNST 2024 International Conference on Nuclear Science and Technology
6- 8 MAY 2024 | Isfahan, Iran

Strontium removal from aqueous solutions using Amberlite XAD-7 resin impregnated with TOPO extractant (Paper ID : 1194)

Khani M.H.*, Ghorbanpour Khamseh A.A., Aghayan H.
Nuclear Fuel Cycle Research School, Nuclear Science and Technology Research Institute, Tehran, Iran,
E-mail: mhkhani@aeoi.org.ir

Abstract

Strontium 90 is a radioactive and dangerous isotope that is produced in the processes of uranium fission, and its penetration into the environment through surface water causes serious problems for human health and the environment. In this study, the performance of Amberlite XAD-7 resin impregnated with TOPO extractant was evaluated to remove strontium ions from aqueous media in a batch system. The effect of effective operating parameters such as initial pH of the solution, adsorbent dosage, initial adsorbate concentration, and contact time was assessed. The results of the kinetic investigations of the strontium removal process showed that the obtained experimental data is in good agreement with the pseudo-second order kinetic model. Also, the adsorption equilibrium modeling showed that the Langmuir isotherm model can well describe the equilibrium behavior of the strontium-TOPO impregnated amberlite adsorption system. The maximum amount of adsorption obtained from the Langmuir model was 37.45 mg/g of adsorbent.

Keywords: Strontium, Amberlite XAD-7 resin, TOPO, Impregnation

Introduction

Strontium is one of the main generators of heat in high-level nuclear waste, and Sr-90 is a radioactive and dangerous isotope produced in uranium fission processes [1]. This radionuclide has a long physical (29 years) and biological (49 years) half-life. In addition, if an accident occurs in a nuclear facility, strontium can easily dissolve in water and cause serious problems for human health [2]. Therefore, it is highly desirable to manage this fission product to prevent any human exposure and any disposal in the environment [3]. Chemical methods such as precipitation, electrochemical treatment, filtration, ion exchange, adsorption, reverse osmosis, solvent extraction and membrane technologies have been used to remove strontium from industrial wastewater [4]. Solvent extraction is widely used in the industry due to the ease of the process and the possibility of selectivity in the separation of heavy metals [5].

Extractants such as tributyl phosphate (TBP), trioctyl phosphine oxide (TOPO), and other members of the Cyanex family of extractants are very powerful solvent extraction agents for a number of metals from water [6]. The use of TOPO to extract strontium from wastewaters can be examined. Due to the liquid nature of

this extractant, by loading it on a resin such as Amberlite XAD7, a solid adsorbent can be prepared, which enables the use of the adsorption method to remove strontium from aqueous solutions. The advantage of this method is the simultaneous use of extractant and resin capabilities to adsorb heavy metals. In this research, the adsorption ability of Amberlite XAD-7 resin impregnated with TOPO extractant to remove Sr (II) ions from aqueous solutions was investigated. Important factors affecting the removal efficiency, including initial solution pH, contact time, adsorbent dosage, initial concentration of Sr (II) was investigated in detail.

Experimental

Reagents

Amberlite namely XAD-7 resins (20-50 mesh), analytical grade, purchased from Fluka. Trioctyl phosphine oxide (TOPO) with a purity of more than 98%, Strontium nitrate, and all other chemical reagents (analytical grade) were provided from Merck (Darmstadt, Germany).

Procedure

First, Amberlite XAD-7 was impregnated with TOPO extractant before performing experiments. The amount of 30 grams of resin was washed three times with deionized water to remove impurities, and then it was filtered and dried for 24 hours at room temperature. Then 20 grams of this resin was contacted at room temperature with 40 mL of TOPO in 0.5 M toluene solution for two hours. The impregnated resin beads were separated from the organic phase and washed several times with 2 M nitric acid. Finally, the prepared resin beads were washed with deionized water and dried for 24 hours at room temperature and stored for further use.

A certain amount of adsorbent was added to a set of 250 ml Erlenmeyer flasks containing 100 ml of strontium nitrate solution with predetermined concentrations. The flasks were shaken for a certain period in the incubator shaker at a speed of 150 rpm and a temperature of 25 °C. The concentrations of metal ions in the samples were determined by inductively coupled plasma atomic emission spectroscopy (ICP-AES, PerkinElmer, Optima 7300 DV. USA). In order to calculate the amount of metal adsorbed per unit mass of adsorbent (mg/g) and its removal percentage Eqs. (1) and (2) are used, respectively.

$$q = (c_i - c_e) \times \frac{V}{M} \quad (1)$$

$$\% \text{ Adsorption} = \frac{c_i - c_e}{c_i} \times 100 \quad (2)$$

Results and discussion

Effect of pH

The effect of pH on the adsorption of strontium ions is shown in Fig. 1. As shown in this figure, at lower pHs the adsorption value is low. With increasing the pH, the amount of adsorption increases and reaches its maximum value at pH 6. With a further increase in pH, the amount of adsorption decreases again. This phenomenon is due to the competition of H+ cations with Sr2+ cations to occupy the available exchange sites, which at low pH has a high concentration of H+ cations and therefore the amount of the adsorption is low. At alkaline pHs, adsorption was not investigated due to the possibility of strontium precipitation [7].

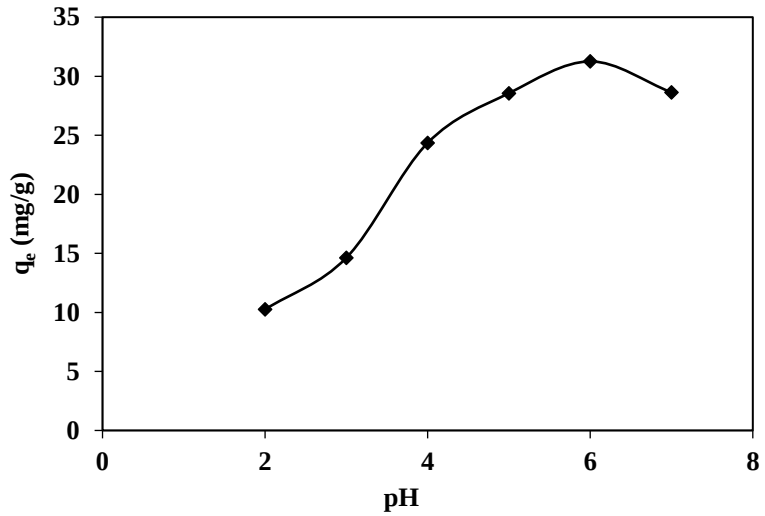

Fig. 1. Effect of pH on strontium adsorption
(Co: 50 mg/L, Adsorbent dosage: 1 g/L, contact time: 24 h)

Effect of contact time

The results of dynamic experimental of strontium adsorption by impregnated resin shows that this process is fast at the beginning, so that approximately 70% of the adsorption occurs in the first 30 minutes.

Subsequently, the adsorption rate decreased and reached equilibrium in approximately 240 minutes (Figure 2).

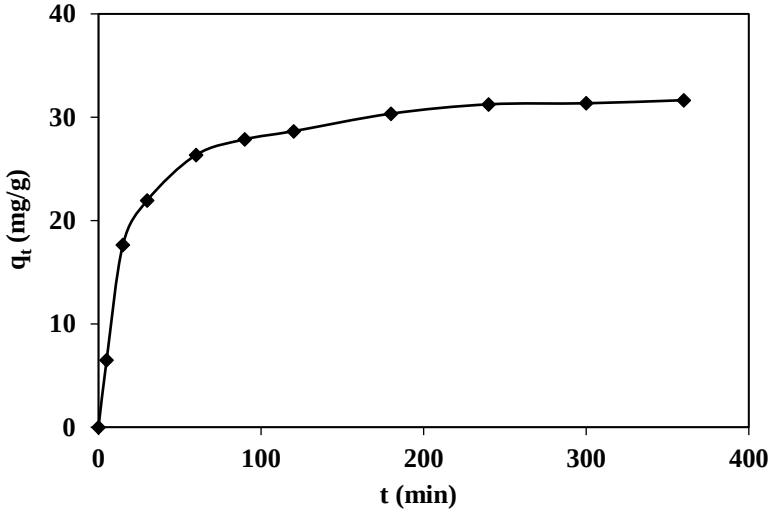

Fig. 2. The Effect of contact time on strontium adsorption
(pH: 6, Co: 50 mg/L, Adsorbent dosage: 1 g/L)

Effect of adsorbent dosage

The effect of adsorbent dosage on the adsorption of strontium by the impregnated resin was studied in the range of 0.25 to 2 g/L, as shown in Fig. 3. It is clear that removal percentage increased by increasing the dosage of the adsorbent, due to the availability of more sites for adsorption of metal ions. With increasing adsorbent dosage, the amount of adsorption decreases because the amount of adsorption is defined based on the amount of unit weight of the adsorbent. Therefore, 1 g of TOPO impregnated XAD-7 /1 litter of solution, was considered as an optimum dosage for all the adsorption experiments.

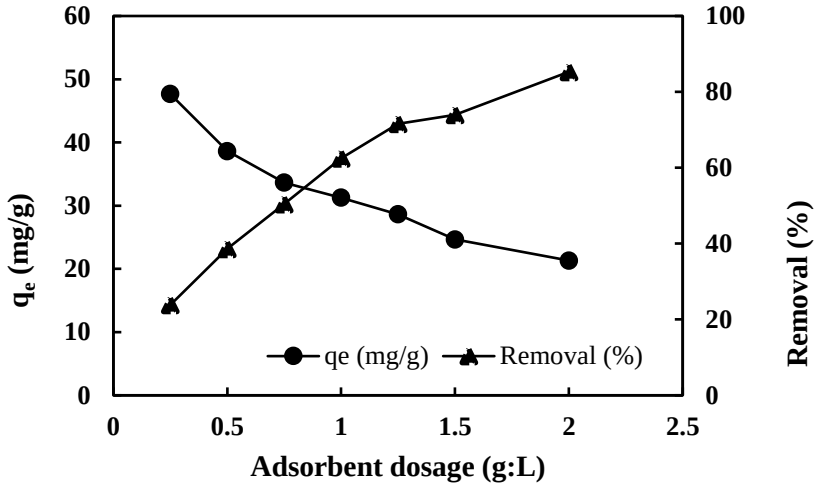

Fig. 3. Effect of adsorbent dosage on adsorption of strontium
(pH: 6, Co: 50 mg/L)

Effect of initial solution concentration

The effect of the initial concentration of the solution (in the range of 10 to 100 mg/liter) on the adsorption is shown in Fig. 4.

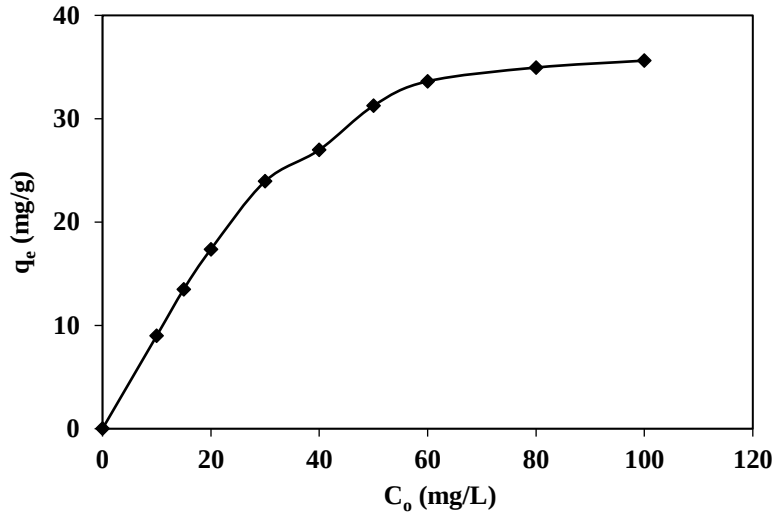

Fig. 4. Effect of initial concentration on strontium adsorption
(pH: 6, Adsorbent dosage: 1 g/L)

According to the figure, the amount of strontium adsorption increases with the increase of the initial concentration with a relatively high slope until it reaches to a plateau state. The reason for this is that the initial concentration acts as the driving force of adsorption and increases the amount of adsorption. But at

higher concentrations, due to the saturation of the adsorption sites, there is no improvement in the adsorption amount.

Kinetic study

Pseudo first and second order kinetic models commonly used to describe the rate of the adsorption processes. The linear forms of pseudo - first and -second-order kinetic models are as follows respectively [8]:

$$\log(q_{eq} - q_t) = \log q_{eq} - \frac{k_1 t}{2.303} \quad (3)$$

$$\frac{t}{q_t} = \frac{1}{k_2 q_{eq}^2} + \frac{1}{q_{eq}} t \quad (4)$$

where qeq and qt (mg/g) are the amount of strontium adsorbed at equilibrium and at time t (min), respectively, k1 (1/min) and k2 (g/mg.min) show the equilibrium rate constant of pseudo - first and - second-order adsorption, respectively. The results of kinetic modeling of this process using pseudo first and second order models are presented in Figs. 5 & 6.

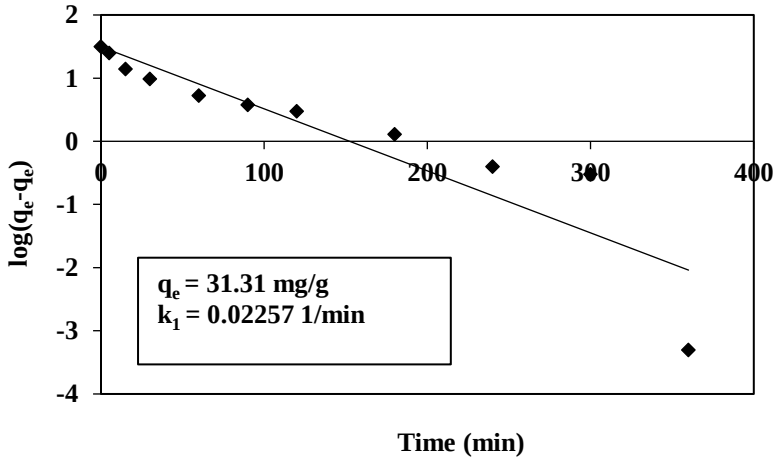

Fig. 5. Pseudo-first-order kinetic model

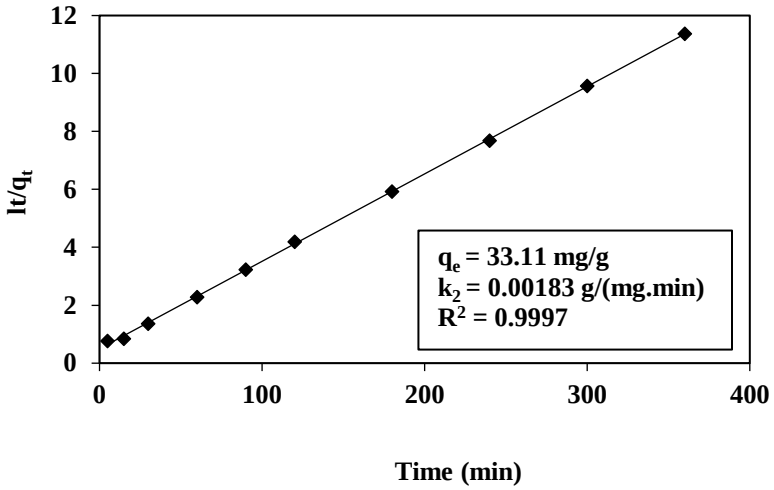

Fig. 6. Pseudo-second-order kinetic model

By comparing the fitting results of the models, it is clear that the experimental results are in better agreement with the pseudo-second-order kinetic model.

Adsorption isotherms

In order to design an adsorption system for the separation of metal ions, it is necessary to find a suitable relationship (isotherm) to describe the results of equilibrium experiments. In this research, Langmuir and Freundlich equilibrium isotherms have been studied to fit the equilibrium data. The linearized form of Langmuir isotherm model is expressed by Eq. (5).

$$\frac{1}{q_e} = \frac{1}{bq_m C_e} + \frac{1}{q_m} \quad (5)$$

where q_e is the amount of adsorbed metal per specific amount of adsorbent in mg/g, C_e is the equilibrium concentration of the solution in mg/L, b is the Langmuir constant in L/mg and q_m is the maximum amount of adsorbent capacity in mg/g is. The linearized form of Freundlich isotherm model is expressed by Eq. (6).

$$\log q_e = \log k_f + \frac{1}{n} \log C_e \quad (6)$$

where k_f (L/g) is the Freundlich constant which is related to the adsorption capacity, and n is the dimensionless Freundlich constant which is related to the bond strength. The results of the isotherms modeling are presented in Figs. 7 & 8. According to this figure, it is clear that the Langmuir model has better compatibility with the experimental data. From this point, it can be concluded that the adsorption mechanism can be considered a single-layer and the adsorbent surface is homogeneous in terms of adsorption energy. The Langmuir model predicts the maximum adsorption rate of 37.45 mg/g adsorbent.

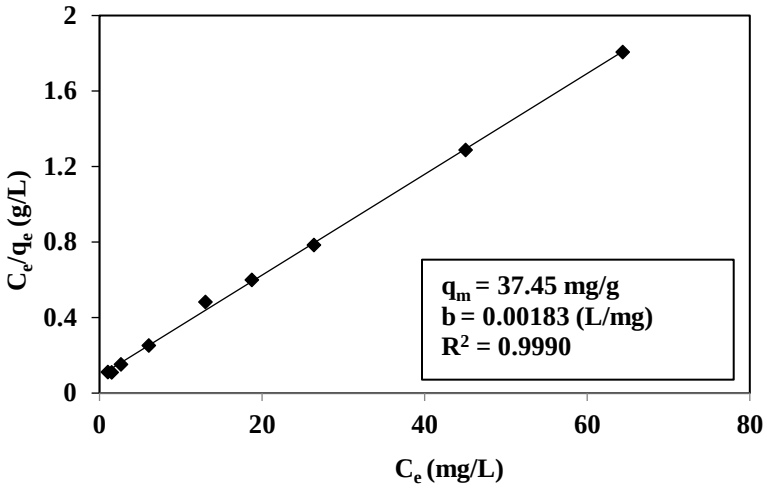

Fig. 7. Langmuir adsorption isotherm model

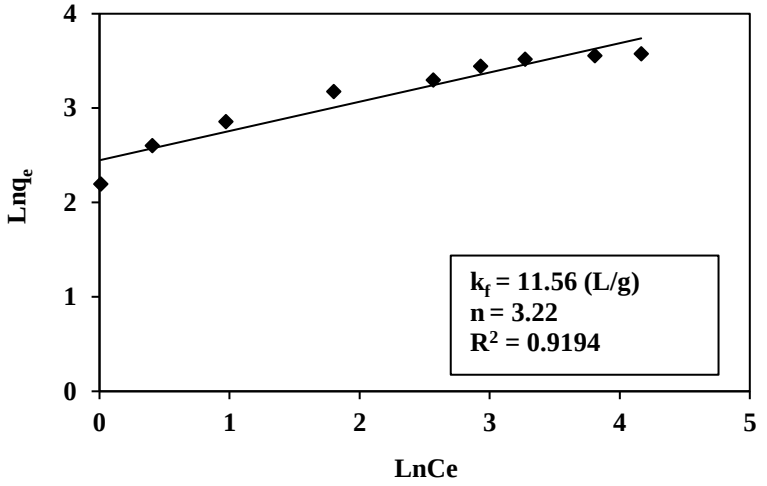

Fig. 8. Freundlich adsorption isotherm model

Conclusions

In the present research, the absorption of strontium on Amberlite XAD-7 impregnated with TOPO was investigated. The effects of independent process variables including pH, contact time, adsorbent dosage, and initial strontium concentration on the absorption amount were investigated. Moreover, the adsorption kinetics of strontium on this adsorbent follows the pseudo-second-order model. The adsorption process reached equilibrium after about 240 minutes of contact. The Langmuir equation provides a good fit to the experimental data. From the results of the Langmuir model, the maximum adsorption amount of strontium on Amberlite XAD-7 impregnated with TOPO was 37.45 mg/g.

References

[1] Piraner, O., Jones, R.L. (2021). Urine strontium-90 (Sr-90) manual and automated pre-analytical separation followed by liquid scintillation counting. Journal of radioanalytical and nuclear chemistry 329(1): 383-390.

[2] Lee, Choi, B., J.H., Lee, K.R., Kang, H.W., Eom, H.J., Shin, K., Park, H.S. (2022). Separation and purification of Sr-90 nuclide from a waste mixture. Journal of Radioanalytical and Nuclear Chemistry 331:275-281.

[3] Tuzen, M., Saleh, T.A., Sarı, A. (2020). Interfacial polymerization of trimesoyl chloride with melamine and palygorskite for efficient uranium ions ultra-removal. Chemical Engineering Research and Design 159: 353-361.

[4] Bashir, M., Batool, M., Arif, N., Tayyab, M., Zeng, Y.J. and Zafar, M.N. (2023). Strontium-based nanomaterials for the removal of organic/inorganic contaminants from water: A review. Coordination Chemistry Reviews, 492:215286.

[5] Peng, H., Guo, J., Li, B., Huang, H., Shi, W., Liu, Z. (2022). Removal and recovery of vanadium from waste by chemical precipitation, adsorption, solvent extraction, remediation, photo-catalyst reduction and membrane filtration. A review. Environmental Chemistry Letters 20(3): 1763-1776.

[6] Baker, R.J., Fuchs, J., Richards, A.J. and Ogilvie, H.V. (2011). Perfluorinated phosphine oxide and sulfides as extractants for heavy metals and radionuclides. Journal of environmental management, 92(10): 2781-2785.

[7] Thorpe, C.L., Lloyd, J.R., Law, G.T., Burke, I.T., Shaw, S., Bryan, N.D. and Morris, K. (2012). Strontium sorption and precipitation behaviour during bioreduction in nitrate impacted sediments. Chemical Geology, 306:114-122.

[8] Mahmoud, A.E.D., Fawzy, M., Hosny, G. and Obaid, A. (2021). Equilibrium, kinetic, and diffusion models of chromium (VI) removal using Phragmites australis and Ziziphus spina-christi biomass. International Journal of Environmental Science and Technology, 18: 2125-2136.

[9] Bhatnagar, A., Minocha, A.K. and Sillanpaa, M. (2010). Adsorptive removal of cobalt from aqueous solution by utilizing lemon peel as biosorbent. Biochemical Engineering Journal, 48(2): 181-186.

ICNST 2024 International Conference on Nuclear Science and Technology
6- 8 MAY 2024 | Isfahan, Iran

Uranium removal from aqoueos solution using new composite adsorbent based on heteropoly metalate-palatelat SBA-15 (Paper ID : 1217)

Aghayan. H*, Gorbanpour. A.A, Khani. M.H
Nuclear Fuel Cycle Research Institute - Research Institute of Nuclear Sciences and Technologies - PO Box 14395-836, Tehran - Iran

Abstract

In this research, a novel inorganic composite adsorbent based on heteropoly acid/mesoporous silica SBA-15 with platelet morophology were synthesized and applied for uranium ions from aqueous solution. Inductively coupled plasma (ICP), XRD and scanning electron microscopy (SEM) were used to characterize of the sample. Then, the ability of the composite was examined for the removal of uranium ions from aqueous solution under various initial concentrations of metal ions. The equilibrium data were fitted to commonly used isotherms models such as Langmuir, Freundlich and Dubinin-Radushkevich. The values of the calculated correlation coefficients of the linear regressions (R2) indicate that, the adsorption data was fitted by the Langmuir isotherm model very well. The obtained amount of RL (0.1) showed that the adsorption process is favorable. The amount of E obtained by the Dubinin-Radushkevich model, suggested that the predominant mechanism is physisorption process. The experiment results showed that the adsorbent exhibited high sorption toward uranium ion. Consequently, this material can be potential candidate for the removal of even trace amount of uranium ions from nuclear and other industrial wastewater. Finally, the obtained maximum adsorption capacity of uranium (117.6mg.g-1) on composite indicates that the prepared material is a perfect candidate for the adsorption and removal of the uranium from wastewater.

Keywords: Uranium, Removal, SBA-15, Heteropoly, Composite

Introduction

Uranium “due to its high chemical toxicity and radioactivity” is considered as serious threat to living organisms and the environment. This issue becomes much more complicated by increasing activities of the nuclear and other industries that use this element. In various stages of nuclear industry, the volumes of nuclear waste containing different concentrations and radiation levels of uranium are produced. Uranium and its fission by-products usually emit alpha particles that have low penetrating power. In spite of that, when they enter the human body and other living organisms through swallowing food, drinks or inhalation of aerosols and dust particles, they are concentrated in some internal organs and cause some diseases such as bronchial, lung, stomach, liver, intestine, bladder, kidney and skin cancers, blood diseases, psychological

disorders and birth defects [1]. Therefore, the effective removal and recovery of small amounts of uranium from wastewater has always been of interest. In the past, various methods such as chemical deposition [2], solvent extraction [3], ion exchange, surface adsorption [4], biosorption and membrane processes were used to remove uranium from Effluent has been developed. Among these methods, adsorption due to high selectivity, fast rate, low cost, Simplicity in use, possibility of adsorbent recovery and their availability have recently attracted the attention of researchers in this field [5]. During the past years, mesoporous silica MCM-41, MCM-48, FSM-16 and MSU-1 have been used to remove and separate some metal ions [6]. Among these materials, SBA-15 as a structuring agent has special characteristics such as high surface area (>700 m2g-1) with large pore diameter, regular channels, high thickness of the pore wall and thermal stability [7]. With these capabilities, SBA-15, like other members of its family, has proven to be a promising candidate for use in a wide range of applications such as adsorbents, adsorbent carriers, catalysts, templates for the architecture and design of nanoparticles, and molecular sieves for large molecules [8-9]. In this context, different structures of SBA-15 such as fine powders, fibrous, platelate and spherical morpholgy have been synthesized and characterized [10-11], However, compared to other morphologies, the platelate structure has advantages in terms of maximum absorption and adsorption kinetics due to having shorter channels and, as a result, more access of host species to pores or active sites.Despite this, the lack of suitable surface properties due to the lack of functional groups creates problems in using them for many applications. One of the effective ways to modify the surface properties and increase the adsorption capacity of SBA-15 spherical particles is to prepare composite materials with inorganic ion exchangers. Heteropoly acid salts having nano- sized structure, physical and chemical stability in aqueous solution and high strong exchangeable acidic protons in their structures have such capability. [12–14]. In fact the protons in the structure of heteropoly acidc an exchange with metal ions in solution thus they can act as inorganic cation exchanger.Therefore, the preparation of coposite materials including polyoxometalate (based on phosphate and molybdate, which show the highest absorption for uranyl ion) and platelate SBA-15 as adsorbent and carrier, respectively, is valuable for improving the uranium adsorption process.

Experimental

Chemicals and Instruments

All materials were of analytical reagent grade. P123 (poly (ethylene oxide)-poly (propylene oxide)-poly (ethylene oxide) (EO20-PO70-EO20), tetraethyl orthosilicate (TEOS 98%), absolute ethanol (99.98٪), fuming hydrochloric acid (HCl 37%), Tin chloride (SnCl4.5H2O), zirconium oxychloride (ZrOCl2.8H2O),

Disodium phosphate (Na2HPO4), Sodium molybdate (Na2MoO4· 2H2O), sodium tungstate (Na2WO4. 2H2O), diethyl ether, nitric acid (HNO3) and sulfuric acid (H2SO4) were purchased from Merck company. Characterization of the samples was performed by different conventional techniques. X- ray powder diffraction (XRD) data was acquired on Philips X-pert diffractometer using Cu Kα radiation. SEM images was recorded by Philips XL-300 instrument. Inductively coupled plasma (ICP) data was provided by Varian vista-PRO.

Preparation of samples

Mesoporous silica SBA-15 with platelet morphology (denoted as P-SBA-15) was prepared according to the literature [15]. In a typical synthesis, 2.0 g of P123 and a 0.5 g of Zr(IV) ions was dissolved in 60 ml of 2 M aqueous HCl and 15 ml of distilled water was added under stirring until the polymer was dissolved completely. Then 4.4 g of tetraethyl orthosilicate was added drop wise to the solution at 40 °C and was stirred for another 24 h. After that the mixture was transferred to an autoclave for hydrothermal treatment at 100 °C for 24 h. Finally the resulting precipitate was filtered, washed carefully with distilled water, air dried. Surfactants were removed by calcination at 550 °C for 6 h in air. H3[PMo6W6O40]. nH2O was prepared according to the procedure of Huixiong et al denoted as HMWP [16] . Then stannic salt of HMWP was supported on mesoporous silica SBA-15 as the follow procedure: at first, 0.3 gr of SnCl4·5H2O was dissolved in aqueous containing 0.3 M HCl and 1 g of parent SBA-15 was added to it, stirred at 100 ˚C until the solvent was completely volatilized. Subsequently, the precipitate collected was dispersed in 10 ml of saturated aqueous solution of heteropolyacid to obtain maximum loading of heteroploy acid. The sample was filtered and washed with deionized water and ethanol and dried at 40°C overnight. Finally, the obtained product was immersed in acid (HNO3, 0.1M) to be converted to the H+ form.

Adsorption Experiments

The adsorption study was conducted by suspending of 0.05 g of solid samples into a 20ml of the metal ion solution at desired concentration and contact times. Then the solution was transferred to a polyethylene container, and it was stirred in a shaker at a speed of 150 rpm and at temperature of 25 °C for 24 h. The pH of the above solution was also adjusted using a solution of nitric acid and sodium hydroxide 0.1 M. At the end of each experiment, the samples were smooth and the amount of uranyl ions in the solution, before and after each experiment, was measured by the Inductively Coupled Plasma Optical Emission Spectrometer (ICP-OES) and the percentage of uranium absorption and absorption capacity of the adsorbent was calculated as follows.

$$\textbf{Adsorption Percentage}: p = \frac{(c_0 - c_e)}{c_e} \times 100\% \quad (1)$$

$$\textbf{Adsorption Capcity}: q_e = \frac{(c_0 - c_e)\vartheta}{M} \quad (2)$$

Where C0 and Ce are the initial and final concentration of the metal ions, ϑ is the volume of the initial solution (ml) and M is the mass of the sample in gram.

Results and discussion

Characterization of samples

X-ray diffraction spectra at small angles for pristine SBA-15 and SBA-15-MWP are shown in Figure 1. As seen in the X-ray diffraction pattern at small 2θ angles of SBA-15, the formation of mesoporous structure of SBA-15 is confirmed with peaks in the range of 0.85-2 2Θangles which can be indexed to the (100), (110) and (200) diffraction peaks of a two-dimensional hexagonal symmetry (p6mm) pattern. However, by immobilization of MWP on the support, the intensity of diffraction peaks becomes weaker with shifting to higher degree which was indicative of the reduction in X-ray contrast as the heteropoly compounds filled the empty pores. This phenomenon indicates a decrease in the d distance as a result of occupying mesoporous silica channels by MWP species.

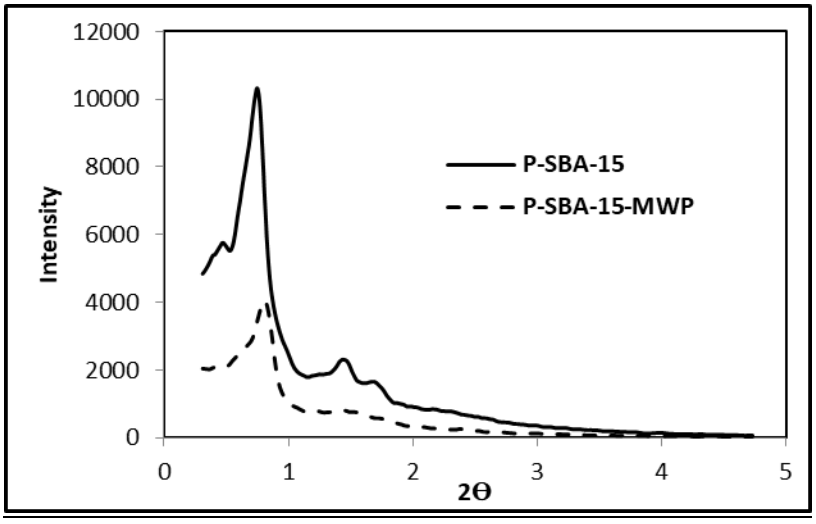

Figure.1. Low angle XRD pattern of pure mesoporous silica P-SBA-15and P-SBA-15- MWP

Figure 2 shows the SEM images of the samples. It is observed that the prepared samples present platelet morphologies and is combination of uniform tablets that more of them have regular hexagonal tablets

consisting of 8 crystal faces, 2 hexagonal and 6 rectangular symmetries. The diameter and thickness of tablets are approximately 1 µm and 200-250 nm, respectively.

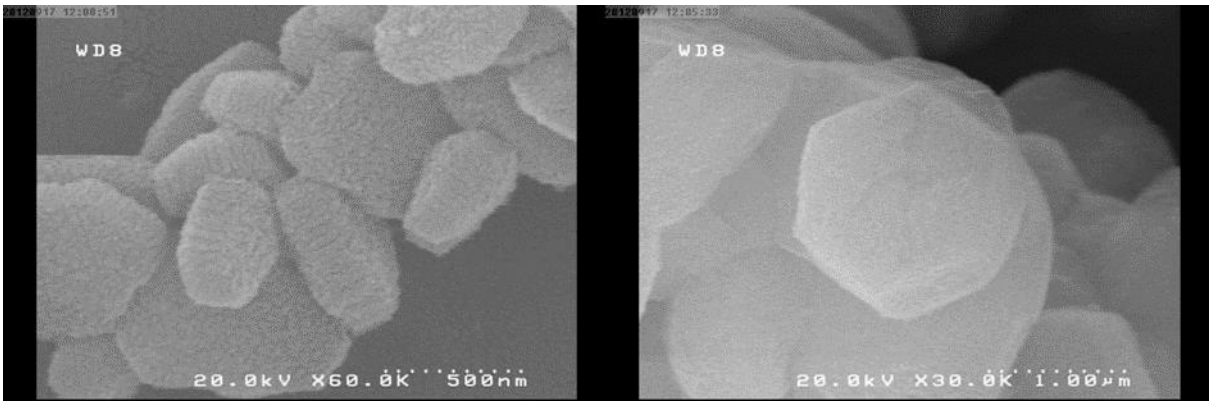

Figure.2. the SEM image of mesoporous silica SBA-15 with platelet morphology

Adsorption isoterms

Figure 3 shows the adsorption isotherms of uranyl ions on SBA-15-MWP in the concentration range of 20 to 1000 mgL^{-1}. By using this isotherm, the maximum adsorption capacity of the adsorbent for uranyl ions can be obtained. As can be seen, the amount of uranium adsorbed on the adsorbent increases with the increase of the initial concentration of uranyl ions and reaches the maximum value of 117 mgL^{-1} at the equilibrium concentration. The adsorption equilibrium data obtained from these experiments can be fitted with different types of isothermal statistical models. These models are usually used to describe the distribution of the dissolved substance between the aqueous and solid phase in different equilibrium concentrations. In other words, by fitting the experimental data with these models and using the extracted constants, useful information about the efficiency of the adsorber is obtained. Among different types of mathematical models, two-parameter models such as Langmuir, Freundlich and Dubinin-Radeshkovich equations are mainly used for this purpose. These models are generally characterized for certain constants that describe the properties of the adsorbent surface and its tendencies for cations and anions. Therefore, they can be used to evaluate the adsorption capacity of sorbents. According to the Langmuir isothermal model, the adsorbent surface is homogeneous, the adsorption of ions occurs only in a limited number of the same sites, and each active site can trap only one ion. The dimensionless coefficient, which is called the separation coefficient (R_L) is applied to prove the agreement of the data with this isotherm [17]. The linear terms of Langmuir model and separation coefficient are shown as follows

$$\frac{C_e}{q_e} = \frac{1}{ba} + \frac{C_e}{a} \qquad (3)$$

$$R_l = \frac{1}{1+bC_e} \quad (4)$$

In the above equations, qe is the equilibrium capacity of the adsorbent per unit mass of the adsorbent mgg^{-1}, Ce and C_0 are respectively the equilibrium and initial concentration of uranyl ions in the solution, a is the maximum amount of adsorption and b is the Langmuir adsorption constant ($dm^3\ mg^{-1}$) which is related to energy of adsorption.

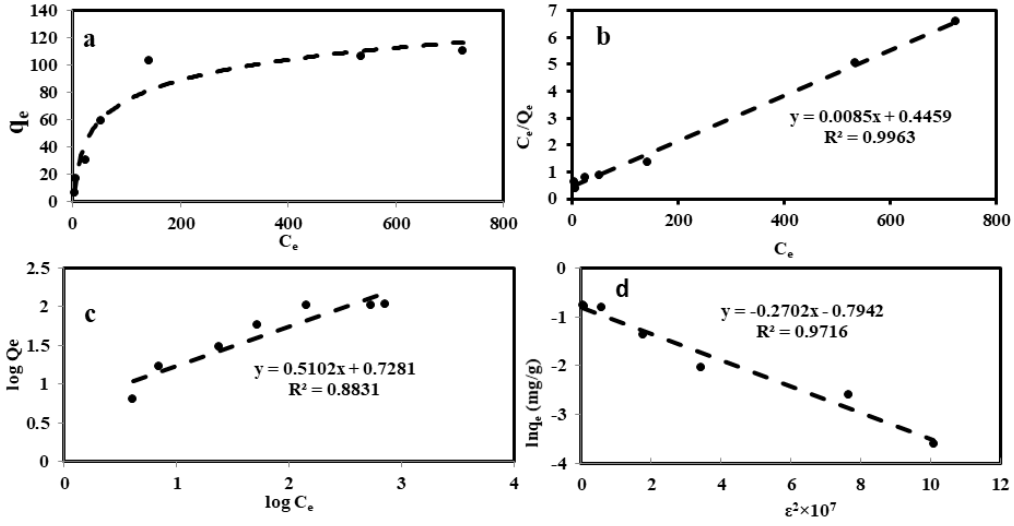

Figure.3. Adsorption isotherm of thorium on SBA-15-MWP (a), linear diagram of Langmuir (b), Freundlich (c) and Dubinin-Radeshkovich (d) models

The Freundlich model is an empirical equation that describes the absorption of a solute from a solution on a heterogeneous absorbent surface and assumes that different sites are involved with several adsorption energies. This model shows that the absorption sites are exponentially distributed with respect to the heat of absorption. This model can correctly describe multilayer absorptions. The linear expression of the Freundlich model can be expressed as follows

$$logq_e = logk_f + \frac{1}{n} logC_e \quad (5)$$

where, K_f and n represent the capacity (dm^3mg^{-1}) and intensity of adsorption respectively. Dubinin-Radeshkovich model as another experimental model is generally used to express the adsorption mechanism with Gaussian distribution of energy on two homogeneous and heterogeneous surfaces [18] The linear form of this equation is;

$$Lnq_e = Lnq_{DR} - B_{DR}\varepsilon^2 \quad (6)$$

where q_{DR} ($mmolg^{-1}$) and B_{DR} (mol^2J^{-1}) are the constants indicating the theoretical saturation capacity and free energy of adsorption per mole of adsorbed, respectively. Also, the free energy, ε, in terms of kJ mol^{-1} is expressed as follows;

$$\varepsilon = RT\ Ln\ (1 + \frac{1}{C_e}) \quad (7)$$

where R is the gas constant (8.314 $Jmol^{-1}K^{-1}$) and T is the absolute temperature of adsorption in Kelvin. By drawing the linear graph of Lnq_e in terms of ε^2 and obtaining the B_{DR} constant from its slope, one of the most important parameters of Dubinin-Radeshkovich equation (E) which estimates the type of absorption process is calculated as follows

$$E = \frac{1}{\sqrt{2B_{DR}}} \quad (8)$$

If 1< E <8 and 8< E <12 the dominant mechanism in the absorption process is physical and chemical respectively [19]. To obtain the constants of the mathematical models, the linear diagram of the equations in Figure 3 (b: Langmuir) (c: Freundlich) and (d: Dubinin-Radeshkovich) was shown. the constants was calculated from the slope and width from their origin and listed in Table 1. As can be seen, the correlation coefficient (R^2) for the Langmuir model has the highest value (0.996), which indicates that this model is in good agreement with the experimental data. This correspondence is due to the uniform distribution of active adsorption sites on the surface of P-SBA-15-MWP. Also, based on the values for R_L, it can be concluded that the matching of the absorption data with the Langmuir model is favorable. On the other hand, the R^2 value for the Dubinin-Radeshkovich isotherm shows that this isotherm gives a good description of the adsorption process. Also 1< E <8, which indicates the dominance of the physical process (surface adsorption) in the adsorption mechanism. At the same time, the positive value of E indicates the exothermic nature of the absorption process.

Table 3. Constants of Langmuir, Freundlich and Dubinin-Radeshkovich isotherms for adsorption of uranyl ions on P-SBA-15-MWP at 25˚C

Langmuir model				Freundlich model			Dubinin-Radeshkovich model			
a (mgg^{-1})	b (Lmg^{-1})	R_L	R^2	K_F (mgg^{-1})	n	R^2	q_{DR} ($mmolg^{-1}$)	B_{DR} (mol^2J^{-1})	E ($kJmol^{-1}$)	R^2
117	0.019	0.1	0.996	5.34	1.96	0.883	0.723	$2.16*10^{-8}$	6.8	0.971

Conclusions

Since the high concentration of uranium in the environment is considered a serious problem for living organisms, it is necessary and necessary to remove this element by an effective method from waste water, which is the main polluting source of the environment. The present research work was done by using the ability of the platelate structure of SBA-15 as a carrier and stannic tungstomolybdophosphate as an adsorbent in a single composit material SBA-15-WMP to remove uranium from water environments. The fixation of MWP on SBA-15 was confirmed by XRD analytical techniques. The adsorption behavior of uranium on the adsorbent showed that the maximum adsorption of uranium at the equilibrium concentration is 117mg L-1. Homogene- ous distribution of adsorption active sites on the surface of SBA-15-MWP showed that the Langmuir isothermal model has good agreement with the adsorption data. The E value obtained using the Dubinin-Radeshkovich model indicates that the dominant mechanism is physical absorption and the absorption process is exothermic in nature.

Acknowledgements

Support of this investigation Nuclear Fuel Cycle Research Institute - Nuclear Sciences and Technologies Research Institute (NSTRI) is gratefully acknowledged.

References:

[1] Z. Yi, J.S. Xu, M.S. Chen, W. Li, J. Yao, H.L. Chen, F. Wang .(2013). Removal of Uranium (VI) from aqueous solution using sponge iron. J. Radioanal. Nucl. Chem. 298, 955–961.

[2] A. Mellah, S. Chegrouche, M. Barkat. (2007). the precipitation of ammonium uranyl carbonate (AUC): thermodynamic and kinetic investigations. Hydrometallurgy, 85, 163–171.

[3] K. Kiegiel, A. Abramowska, P. Biełuszka, G. Zakrzewska-Kołtuniewicz, S. Wołkowicz. (2017). Solvent extraction of uranium from leach solutions obtained in processing of Polish low-grade ores. J. Radioanal. Nucl. Chem., 311, 589–598.

[4] S. Chen, J. Hong, H. Yang, J. Yang, (2013). Adsorption of uranium (VI) from aqueous solution using a novel graphene oxide-activated carbon felt composite. J. Environ. Radioact.126, 253-258.

[5] N. Asadollahi, R. Yavari, H. Ghanadzadeh. (2015). J. Radioanal. Nucl. Chem., 303, 2445–2455.

[6] D.M. Singer, H. Guo, J.A. Davis. (2014). U (VI) and Sr (II) batch sorption and diffusion kinetics into mesoporous silica (MCM-41). Chem. Geol., 390, 152-163.

[7] W. Zhu, X. Li, D. Wu, J. Yu, Y. Zhou, Y. Luo, K. Wei, W. Ma. (2016). Synthesis of spherical mesoporous silica materials by pseudomorphic transformation of silica fume and its Pb2+ removal properties. Micropor. Mesopor. Mat., 222, 192- 201.

[8] M. Ahmadi, R. Yavari, A.Y. Faal, H. Aghayan. (2016). Preparation and characterization of titanium tungstophosphate immobilized on mesoporous silica SBA-15 as a new inorganic composite ion exchanger for the removal of lanthanum from aqueous solution. J. Radioanal. Nucl. Chem., 310, 177–190.

[9] N. Azizi, M. Edrisi. (2017). Deep eutectic solvent immobilized on SBA-15 as a novel separable catalyst for one-pot three-component Mannich reaction. Micropor. Mesopor. Mat., 240, 130–136.

[10] A. Katiyar, S. Yadav, P.G. Smirniotis, N.G. Pinto. (2006). Synthesis of ordered large pore SBA-15 spherical particles for adsorption of biomolecules. J. Chromatogr. A., 1122, 13-21.

[11] K. Kosuge, N. Kikukawa, M. Takemori. (2004). One-step preparation of porous silica spheres from sodium silicate using triblock copolymer templating. Chem. Mater., 16, 4181–4186.

[12] R. Yavari, S.J. Ahmadi, Y.D. Huang, A.R. Khanchi, G. Bagheri, J.M. He. (2009). Synthesis, characterization and analytical application of a new inorganic cation exchanger—Titanium (IV) molybdophosphate Talanta., 77, 1179- 1184.

[13] M.G. Marageh, S.W. Husain, A.R. Khanchi. (1999). Selective sorption of radioactive cesium and strontium on stannic molybdophosphate ion exchanger.Applied. Radiation. Isotopes., 50, 459-465.

[14] M.G. Marageh, S.W. Husain, A.R. Khanchi. (1999). Sorption of radionuclides on cerium (IV) molybdophosphate ion exchanger. J. Radioanal. Nucl. Chem., 241, 139-143.

[15] L. Y-Chen, L. D-Jong, C. C-Chia. (2018). Zirconium involved platelet SBA-15: Synthesis and application to tannic acid adsorption, J. Taiwan Inst. Chem., 124-130.

[16] W. Huixiong, Z. Mei, Q. Yixin, L. Haixia, Y. Hengbo. (2009). Preparation and characterization of tungsten-substituted molybdophosphoric acids and catalytic cyclodehydration of 1, 4-butanediol to tetrahydrofuran. Chin. J. Chem. Eng. 17, 200-206.

[17] S. Svilovi, D. Ruš, R. Aneti. (2008). Thermodynamics and adsorption isotherms of copper ions removal from solutions using synthetic zeolite X. Chem. Biochem. Eng. 22, 299–305.

[18] X. Chen. (2015). Modeling of experimental adsorption isotherm data. Information. 6, 14-22.

[19] A.O. Dada, A.P. Olalekan, A.M. Olatunya, O. Dada. (2012). Langmuir, Freundlich, Temkin and Dubinin–Radushkevich isotherms studies of equilibrium sorption of Zn2+ unto phosphoric acid modified rice husk. J. Appl. Chem, 3, 38-45.

ICNST 2024 International Conference on Nuclear Science and Technology
6- 8 MAY 2024 | Isfahan, Iran

The study of HF adsorption to the pristine and modified SnS-Monolayer: A theoretical study (Paper ID : 1277)

Masoud Arabieh[1*] and Mohammad-Reza Basaadat[1]
[1]Nuclear Science and Technology Research Institute (NSTRI), Tehran, Iran

Abstract

Hydrogen fluoride (HF) is an important and toxic gas which is widely used in several industries such nuclear plants, air and space and chemical production factories. From the other hand tin sulfide (SnS), a chemical compound with high adsorption coefficient, is an appropriate candidate for gas capturing. Adsorption of molecular gases over the 2D surface of such materials is an enthusiastic open question for the application of gas sensing or capturing. In this study the probable potential of monolayer SnS toward the adsorption of toxic HF molecular gas have been examined based on density functional theory approach. The results showed that HF is physiosorbed on SnS surface with adsorption energy value of -0.63 eV. The calculated of density of states (DOS) and differential charge transfer (DCT) confirmed the existence of weak interaction between HF and SnS surface. Imposing mono vacancy defect via removing single Sn atom from SnS monolayer caused to increase the adsorption energy to the value of -1.62 eV which is an indicator of chemisorption. Comparison of DOS, DCT and electron localization function (ELF) results for this system suggest that defected SnS can be introduced for HF capturing devices in related industries.

Keywords: HF, Adsorption, SnS, theoretical study

Introduction

Hydrogen fluoride (HF) which widely utilizes in nuclear fuel processing and manufacturing is a colorless, toxic and highly corrosive material. This gas is categorized as hazardous material due to causing intense onset of eyes, nose and throat irritation. With strong irritating odor and being lighter than air, HF is detectable at low concentration(0.04ppm). There are two main origins of HF releasing in the atmosphere including anthropogenic and natural sources. The first one is mainly due to industrial manufacturing plants such as glass, brick, tile, plastics and even some of transition metals production. Volcanic eruptions and marine aerosols are the most important elements of natural sources of HF. Several theoretical and experimental scientific research groups have introduced potent materials for the aim of capturing or sensing HF toxic gas. Particularly, theoretical studies based on molecular modeling approaches have been extensively conducted in this area, which led to the proposal of new materials applicable in detection or adsorption of HF gas. A brief survey in the literature reveals that various bulk materials including TiO_2,

Al_2O_3, AlF_3, YF_3. HoF_3, MgF_2, $Mg_{12}O_{11}$-X (X = S, P, N, B), $LiMn_2O_4$ and so on have been theoretically evaluated for HF capturing or detection applications. Moreover, due to the increased ratio of surface to volume in 2D materials, selected structures such as $PdAs_2$, boraphene, ZnS monolayer, Pt-decorated graphene, CNT, AlN nanotube and etc. have been studied for the aim of HF adsorption. Recently, tin(II) sulfide monolayer (SnS) has been the subject of several theoretical and experimental studies in the field of gases adsorption. This 2D material not only has been experimentally sensitized but also has been shown to have superior properties such as high electron mobility, high adsorption coefficient. The main goal of current study is to examine the adsorption potential of pristine and modified SnS monalayer toward toxic HF gas. To achieve this goal, the adsorption of molecular HF on pristine, functionalized and defected SnS has been systematically investigated based on density function theory calculations. It is expected that the results of current study shed on light on new features in designing HF capturing/sensing devices.

Research Theories

All of the electronic structure calculations including systems relaxation and post processing features were carried out based on density functional theory (DFT) method as implemented in the SIESTA package [84]. Atomistic Simulation Environment (ASE) in connection with SIESTA was utilized to find reaction paths based on Nudged Elastic Band (NEB) method [85]. The generalized gradient approximation (GGA) in the form of Perdew, Burke and Ernzerhof (PBE) in conjugate with double zeta polarization (DZP) basis set were applied for electronic structure calculations[86]. A supercell of 4×4×1 including 64 atoms (Sn and S) was constructed and fully relaxed for further calculations. Sampling the Brilloun zone was conducted by k-grid of (4×4×1) based on Monkhorst-Pack algorithm. The cut-off energy value was set to 300 Rydberg. For the force calculations, the convergence criteria was fixed to 0.04 eV/Å and the convergence tolerance of energy was set to 10^{-5} eV. To avoid the probable interaction between periodic images along z direction, a vacuum of 15 Å was considered. The adsorption energy (E_{ad}) of the gas molecule on pristine SnS mono-layer was calculated based on the following well-known equation:

$$E_{ad}=E_{(gas/SnS)}-E_{SnS}-E_{gas} \quad \text{(Eq.1)}$$

wherein $E_{(gas/SnS)}$, E_{SnS} and E_{gas} are the total energy of gas+SnS system, total energy of pristine SnS monolayer and total energy of free gas molecule.

Results and discussion

Fig.1 shows the relaxed structure of pristine SnS monolayer. SnS has constructed of two atoms of S and Sn. In the unit cell of this system the metal(Sn) and non-metal(S) atoms are arranged in a such away that they adopt an orthorhombic puckered structure which is analogous to the structure of black phosphorous(BP) monolayer. To evaluate the interaction nature of HF molecule on the pristine SnS, several initial configurations for the adsorption of the gas molecule on different sites of the SnS layer (at top, bridge and hollow) were considered. The gas molecule was located at 5.0Aº far from the SnS layer and then the system was fully relaxed with no constrain. The results of the most stable configuration of HF@SnS system are collected in Fig.2. HF is adsorbed on the hallow site of SnS at 2.45 Aº far from the surface. The hydrogen atom of HF molecule is oriented toward to sulphur atom of SnS surface. The bond length of HF before and after adsorbption on SnS surface fond to be 0.93 A and 0.96A which suggests weak interaction between the gas molecule and the SnS. The adsorption energy value of -0.63 eV confirms that HF molecule is physisorbed on pristine SnS.

(a) (b) (c)

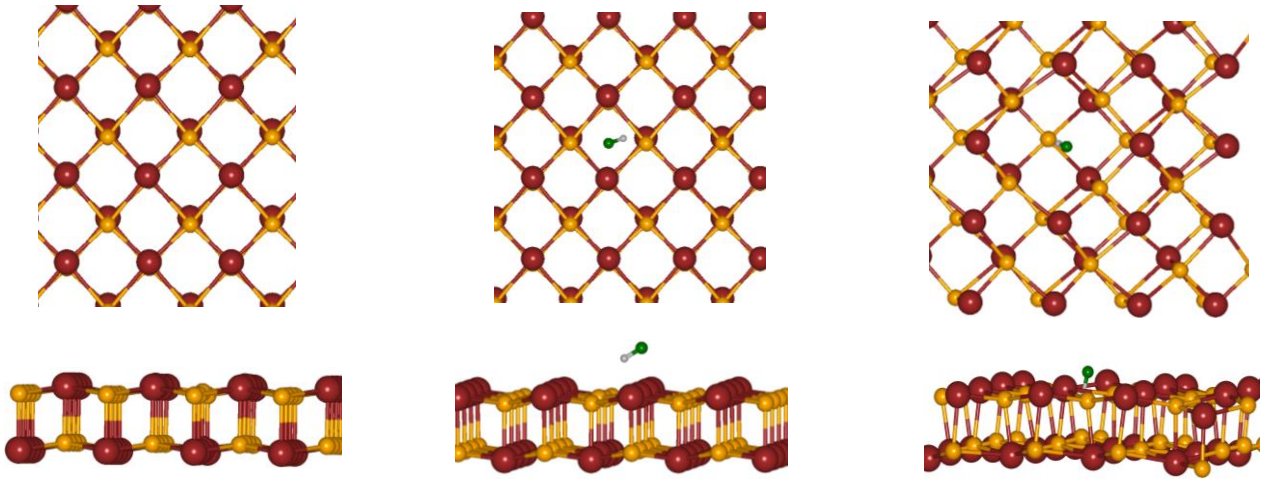

Fig.1-Up and side view for optimized geometry of SnS (a), HF@SnS(b) and HF@VSn-SnS©

Fig.2 Shows the DOS and PDOS of SnS before and after the adsorption of HF molecule. It is clear that the DOS of the system has not changed significantly as a result of gas adsorption. In the other words HF adsorption dose not affect the electronic structure of sorbent because the contribution of DOS of HF molecule is not localized in gap region.

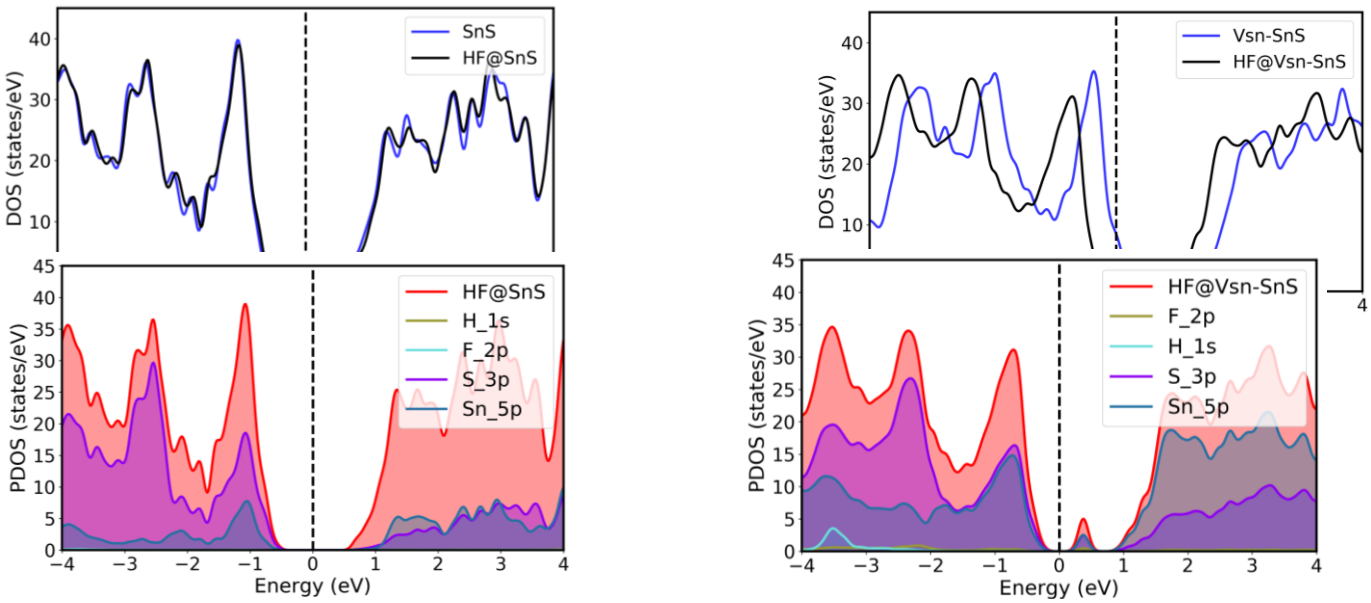

Fig.2 -DOS and PDOS for HF@SnS and HF@V_{Sn}-SnS systems

Electron localization function (ELF) is an useful tool to evaluate the extent of spatial localization of the reference electron which helps to map of electron pair probability in a molecular system. The ELF plot (see Fig.3) shows there is no electron sharing between HF molecule and SnS which is due to the weak interaction between gas and adsorbent. Fig.4 shows the graphical representation of differential charge density (DCT) for HF@SnS system. In this figure the green and blue parts demonstrate charge depletion and accumulation, respectively. As seen, for this system the charge is mainly accumulated on the gas molecule while the charge depletion is located on the SnS surface. Accordingly, SnS surface can be considered as charge donor to HF molecule. Accordingly, due to above discussion, it is concluded that HF molecule is physisorbed on SnS.

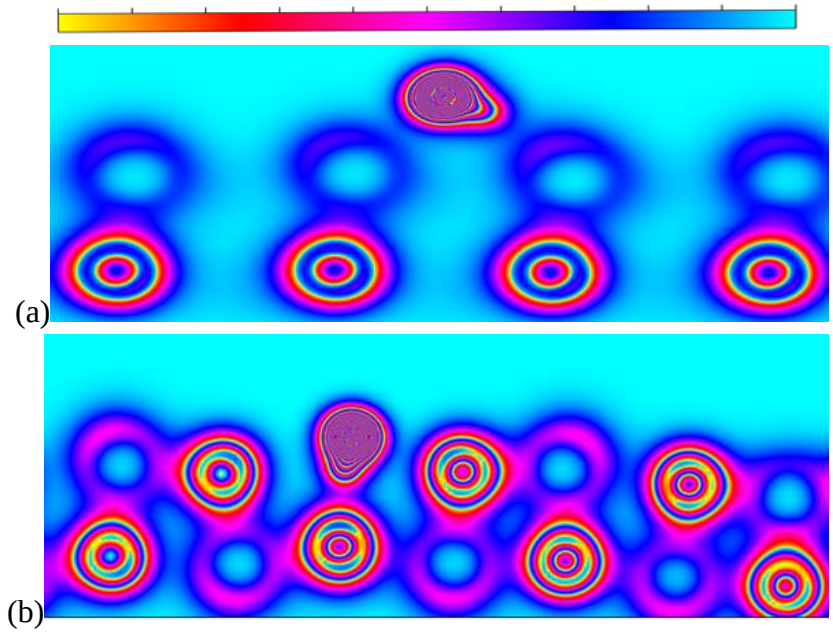

Fig.3- Representation of ELF for HF@SnS(a) and HF@V_{Sn}-SnS(b)

We also checked the effect of Sn vacancy on the adsorption of HF molecule on SnS surface. Fig.1 illustrates that removing single Sn atom leads to diffuse HF molecule in SnS second layer. In this configuration the hydrogen atom of HF is oriented toward to tin atom of SnS surface at distance of 2.11 A. A glannce to DOS curves after gas adsorption confirms the strong interaction between HF and V_{Sn}-SnS (see Fig.2). Appearing a new state in 1.6 eV above the fermi level and changing the overall shape of DOS are in line with chemisorption of HF on the sorbent. Examining the ELF plot in this system proves nearly electron sharing between gas molecule and SnS (see Fig.3) . The analysis of DCT of HF@V_{Sn}-SnS system shows electron depletion on gas molecule which is in line with ELF conclusion. In this system sulfur atom in second layer withdraw electron density toward itself as a result of higher electronegativy (see Fig.4). It is well-known that adsorption energy values higher than 1.0 ev are categorized as chemisorption while the smaller values are treated as pysisorption.Due to calculated adsorption energy value of -1.26 eV and aforesaid results of ELF and DCT, we suggest that HF is adsorbed on Vsn-SnS via chemisorption process.

(a) (b)

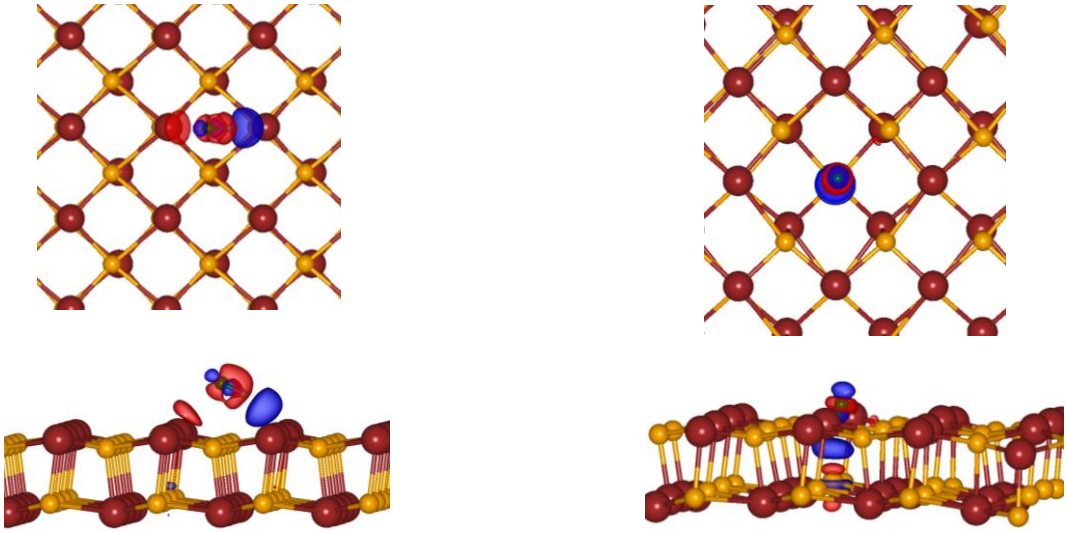

Fig.4- Representation of DCT for HF@SnS(a) and HF@V_{Sn}-SnS (b)

Conclusions

In this theoretical research adsorption of HF molecule on the pristine and modified SnS-Monolayer had been modeled based on density functional theory method. It was found that HF can be physiosorbed on pristine SnS surface with adsorption energy value of -0.63 eV. This conclusion was confirmed via analyzing DOS, ELF and DCT results. Modifying the sorbent by considering mono vacancy defect via removing single Sn atom from SnS monolayer caused to increase the adsorption energy to the value of -1.62 eV which is an indicator of chemisorption. Comparison of DOS, DCT and ELF results for this system suggest that defected SnS can be utilized for HF removing while pristine SnS can be suggested for HF sensing devices.

References

[1] J.M. Soler, E. Artacho, J.D. Gale, A. García, J. Junquera, P. Ordejón, D. Sánchez-

Portal, (2002). The SIESTA method for ab initio order-N materials simulation, J. Phys.: Condens. Matter, 14 (11) : 2745–2779.

[2]Ask Hjorth Larsen, et al, (2017). The Atomic Simulation Environment—A Python library for working with atoms J. Phys.: Condens. Matter (29):273002.

[3]J.P. Perdew, K. Burke, M. Ernzerhof, (1996). Generalized gradient approximation made simple, Phys. Rev. Lett. (77): 3865–3868.

[4] Georgios A. Tritsaris, Brad D. Malone, and Efthimios Kaxiras, Optoelectronic properties of single-layer, double-layer, and bulk tin sulfide: A theoretical study, (2013).J. Appl. Phys. (113): 233507.

[5]Aarti Shukla , N.K. Gaur, Adsorption of O3 , SO3 and CH2O on two dimensional SnS monolayer: A first principles study, (2019). Physica B: Condensed Matter (572):12–17.

[6]Jincong Wang, Xiaoxing Zhang, Li Liu, and Zengting Wang, Adsorption of SF6 Decomposition Products by the S Vacancy Structure and Edge Structure of SnS 2 : A Density Functional Theory, (2021). StudyACS Omega, (6): 28131−28139.

[7]Yuxiang Qin , Zeji Wei , Yinan Bai, Effect of vacancy defects of SnS on gas adsorption and its potential for selective gas detection, (2021). Vacuum, (183):109792,

[8]Tian-Yi Sang, Hao Sun , Tao Li , Yihao Yang , Ziyi Wang , Zhixian Zhang , Ruyue Zhang , Ruyue Zhang , Pd, Ni, Cu and Ag modified SnS: A potential candidate for NH3 and NO2 detection and scavenging, (2023). Applied Surface Science (609): 155404.

ICNST 2024 International Conference on Nuclear Science and Technology
6- 8 MAY 2024 | Isfahan, Iran

Simultaneous separation and purification of heavy Lanthanides from leaching solution Saghand ore using the bis (2-etylhexyl) phosphoric acid (HDEHP) (Paper ID : 1308)

Mehran Heydari[1]*, Akram Pourmatin[2], Neda Akbari[3]
1.2.3- [1]Nuclear Fuel Cycle Research School, Nuclear Science and Technology Research Institute, Tehran, Iran
mrheydari@aeoi.org.ir

Abstract

Solvent extraction (SE) has come to be one of the most significant separation processes in hydrometallurgy. The solvent extraction of trivalent lanthanides (La, Nd, Eu, Sm, Gd, Dy, Er and Lu) in the presence of interfering ions such as Fe, Al, and Ca in nitrate media by bis(2-etylhexyl) phosphoric acid (HDEHP) solution in kerosene has been studied.

Batch tests were carried out to investigate the conditions which most affect extraction, such as concentration of extractant, phase ratio (O/A), pH in the aqueous phase, and contact time.

The optimum efficiency was reached in the phase ratio, Qorg/Qaquese, equal to 1:1 in pH 1.7 for 30s. In this condition, distribution coefficients of heavy rare earths are higher than light lanthanides and interfering ions, when the solvent is 0.15 M of HDEHP in kerosene. Therefore, heavy lanthanides were easily stripped from the organic phase with dilute nitric acid, while iron and light lanthanides remained in the aqueous phase.

Keywords: Solvent extraction, trivalent lanthanides, separation, purification

Introduction

Recently, there is an increasing demand for rare earths utilization in various industries so their separation and purification have high importance [1]. The lanthanides series is the subset of rare earths and contains elements with 57 to 71 atomic numbers; the first seven lanthanides including Lanthanum to Europium are the subgroup of cerium and known as lightweight rare earths. The remaining eight elements including Gadolinium to Lutetium together with Yttrium are the yttrium subgroup and are known as heavy-weight rare earths. Samarium to Dysprosium elements is known as middle-weight rare earths [2].

Chemical properties of Lanthanides are very similar to each other so their separation is among the most difficult processes and requires efficient techniques [3]. Ion exchange [4], Precipitation [5], and Extraction [6] are important methods for preconcentration of rare earths. Solvent extraction is an efficient technique

for the separation of rare earths from acidic solutions [7-9] and in recent decades is frequently used [1] in industry for the separation of rare earths.

Regardless of the primary mineralogy of rare earths, leaching solutions often contain Fe (III) impurities [10]. Generally, Fe (III) is an interference in the separation and purification of rare earths [11,12] due to its similar chemical behavior (hard Lewis's acid aspect) to lanthanides.

Most existing methods for the separation of Fe (III) from other metal ions by various reagents have defects such as difficult phase separation, multiple extractions, co-extraction of mineral acids, long equilibrium time, and mutual solubility of two phases [13].

To prevent solid precipitate formation and reduce the efficiency of extraction compared with the precipitation method [14], Iron (III) absorption from other metal ions by (SE) with Organophosphoric and carboxylic acid extractants has been studied by researchers [15-19]. These extractants have high selectivity toward iron (III) [20]. Organophosphoric extractants and their derivatives that have been used for the separation of Fe (III) and other metal ions are including Di-(2-ethylhexyl) phosphoric acid (D2EHPA), Di-(2-ethylhexyl) phosphonic acid (PC 88A) [16,17], tribultyl phosphate (TBP), methyl isobutyl ketone (MIBK) [19], trioctylphosphin oxide (TOPO) and phosphine oxide (Cyanex® 923) [15,18]. Quantitative extraction of Fe (III) ions by TBP and TOPO is less effective in the presence of nitrate ions than hydrochloric medium [21].

Sato et al. have studied the extraction of Fe (III) ions by D2EHPA in aqueous solutions of Sulphuric acid, Hydrochloric acid, and Nitric acid [22], and found that rate of extraction in sulfuric acid is relatively lower than in two other acids. Fe (III) ions in hydrochloric acid solution have a strong tendency to form a complex with chloride ions (Cl-) in the aqueous phase that is non-extractable to the organic phase and thus the efficiency of extraction and stripping would decrease [23]. To study the effect of iron as interference on rare earths separation, L. Jian-Min et al. [24] have studied the separation of Sc (III) from La (III), Y (III), Fe (III, II) and Sn (IV, II) by 1,10-bis (1-phenyl-3-methyl-5-oxopyrozol-4-yl) Decan-1,10-dion (BPMOPD) in hydrochloric acid solution and could separate Sc (III) and Fe (III) from other mentioned lanthanides. Khujaev and Nushtaeva [25] have studied the effect of macro-quantities of Fe (III) on rare earths separation by chromatographic extraction system, while D2EHPA-Fe (III) was used as stationary phase.

Various investigations based on the use of D2EHPA as an organic extractant in hydrochloric and nitric and sulphuric acid solutions containing rare earths and their extractability mechanism have been done [26-28].

D2EHPA compared to other extractants is easily usable in most acidic mediums. This extractant can form a stable complex with high selectivity towards cations, while TBP usage is limited to nitric and chloride acid solutions and is affected by complex formation by F-, SO42-, PO43-, and CO32- anions. TOPO as an extractant has low selectivity [29].

Up to now, competitive behaviors of Iron and lanthanides in complex formation with D2EHPA have not been accurately examined. In this research work, the separation and extraction of light lanthanides from heavy lanthanides and the separation and removal of iron (III) from rare earths samples in nitric acid solution by D2EHPA as an extractant diluted in kerosene is studied.

Experimental

Di-(2-ethylhexyl) phosphoric acid, HDEHP, 95% (Sigma) was used as the extractant. Kerosene (Jet A-1, Shell) was applied as the organic diluent. All other reagents were of analytical grade and their solutions were prepared with distilled water. A water bath incubator shaker was spent for all equilibrium tests. Varian liberty 150 XL inductively coupled plasma (ICP) was applied for the analysis of (MIs) and for individual analysis. Adjusting of pH was measured by a Schott pH-meter. A solution comprising rare earths was supplied by acid leaching from Saghand's mine in Iran. The sample was prepared from Saghand ore crushed and powdered to less than 7 microns using a Zm205 abrasive mill, then 100 g of Saghand anomaly 5 ore sample was blended with sulfuric acid 10 M, and nitric acid 5 M was leached for 2 hours at 200 °C. After filtering with distilled water, a certain volume was added to the resulting solution of 1:1 ammonia (25%) to reach pH=3.8 until the iron element inside the container precipitates. After the removal of iron, the resulting solution was filtered and pH was calculated.

The chemical composition of leach liquor after precipitation is shown in Table 1. A maximum of interfering ions was precipitated from the leach liquor but extraction of iron (III) from aqueous solutions is very complicated.

Table1. The chemical composition of leach liquor of Saghand's mine in Iran

Element	Fe	Al	Ca	La	Nd	Sm	Eu	Gd	Tb	Dy	Er	Lu
Concentration (mg/L)	114.4	73.44	47.87	112.90	2.83	2.24	0.20	6.74	1.24	10.76	180.50	2.73

A fast technique was established for the (SE) separation of heavy lanthanides from other lanthanides and Fe, Al, and Ca. Aliquots of a solution containing trivalent lanthanoids (La, Nd, Eu, Sm, Gd, Dy, Er, and Lu) in the presence of interfering ions such as Fe, Al, and Ca were taken and the pH was adjusted with

nitric acid and ammonia solution. The aqueous phase must be kept at a constant ionic strength; therefore, sodium nitrate is added to the solution. The total volume was prepared up to 20 ml. The solution was then moved to a separating funnel, 5ml of HDEHP solution in Kerosene of suitable concentrations was introduced and the solution was shaken. The two phases were allowed to settle and separate. The metals were stripped from the organic phase with nitric acid. The metals in the aqueous phase were determined with ICP-AES.

Results and discussion

Leach liquor containing rare earth was subjected to extraction experiments. In extraction runs, the impact of the aqueous to organic phase ratios, pH of the aqueous phase, extraction time, and concentration of extractant and nitrate ion was studied. The extraction of trivalent lanthanide ions with HDEHP is defined by Eq. 1:

$$M^{3+} + n(HA)_{2org}[M(HA_2)_n]^{3-n}{}_{org} + nH^+ \quad (1)$$

The distribution ratio and separation factor were computed using Eq. 2, 3.

$$D_M = \frac{[M^{3+}]_{Org}}{[M^{3+}]_{Aq}} \quad (2)$$

$$SF = \frac{D_{M1}}{D_{M2}} \quad (3)$$

Where M is lanthanide concentration and HA and H represent HDEHP and deprotonated HDEHP (DEHP), respectively [30, 31], which forms a dimer in the organic solvent [32]. The distribution radio D of M3+ between the aqueous and organic phases is defined as:

Since the kinetic of the Fe (III) absorption was slower than lanthanides, the effect of pH on the extraction of Fe (III) was studied in the range 0.1- 2 for 10 min.

Effect of concentration of extractant

The effects of the concentration of the bis (2- ethylhexyl) phosphoric acid on the extraction of Ln and ions such as Fe, Al, and Ca were studied at constant temperatures. The organic phase used was 0.005–0.15M HDEHP in kerosene.

Determining an appropriate concentration of extractant is a crucial step in solvent extraction to obtain the best condition of separation, so different concentrations of HDEHP were applied to the aqueous phase in a

phase proportion of 1:1. As shown in Figure 1, the separation of heavy lanthanides from light ones and interfering ions increased as the concentration of HDEHP increases and it has resulted to better extraction percent, and when the concentration of HDEHP becomes 0.15M, extraction percent reaches to its maximum value. When the concentration of HDEHP is low (i.e., 0.005 M), the yield of extraction and separation factor will be decreased. The investigation revealed that the selectivity factor depended on the extractant concentration in the organic phase.

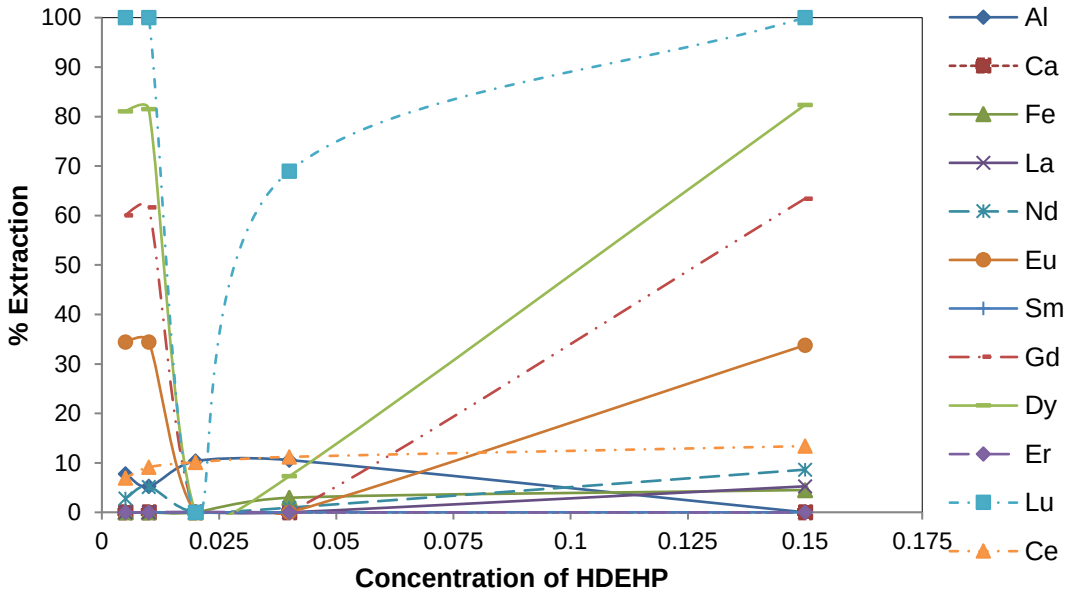

Figure 1. Effect of extractant concentrations on Extraction of heavy lanthanides from light ones and interfering ions

Effect of phase ratio

According to the obtained results, HDEHP extractant with 0.15 M is used for the organic phase and Kerosene is used as a diluent. 1. Decanol with a concentration of 2% v/v was added to the organic phase solution to prevent the formation of the third phase. The organic and aqueous phases were stirred in a decanter at different times with the same intensity.

In order to survey the effect of aqueous (A) to organic phase (O) ratios, some experiments were carried out in 30s with (A)/(O) equal to 1:1, 1:2, 1:3, and 1:4 ratios. The concentration of HDEHP was 0.15M and pH was adjusted to 1.7 in each experiment. As can be seen from Figure 2 when the aqueous to organic phase proportion is 1:1, maximum separation is obtained so in further experiments this proportion was used to achieve a better separation and extraction percent.

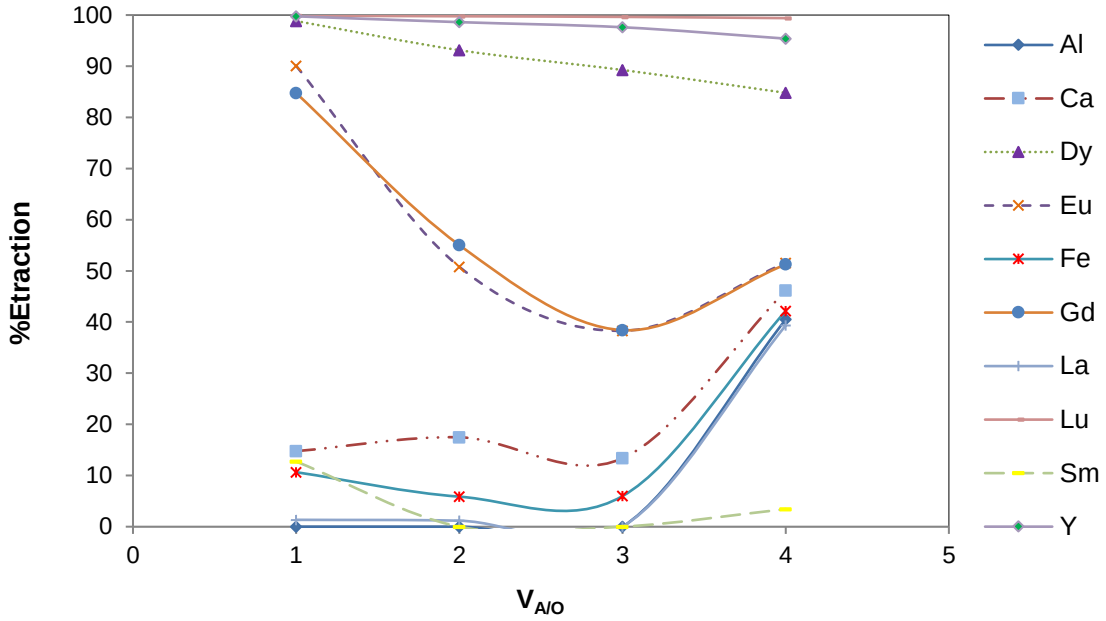

Figure 2. Effect of the aqueous to organic phase ratio on Extraction of heavy lanthanides from light ones and interfering ions

Effect of phase contact time

To determine the time to achieve equilibrium, the percentage extraction of lanthanides and interfering ions by HDEHP in Kerosene were defined concerning the time at contact pH equal to 1.7. As seen in Fig 3 distribution coefficients increase with increasing atomic number. The distribution factors of heavy rare earths are higher when the time is minimum. Heavy lanthanides are more rapidly absorbed than Fe, Al, Ca, and light lanthanides, therefore, in 30s, heavy lanthanides transfer to the organic phase, and Fe, Al, Ca, and light lanthanides remained in the aqueous phase and it can be concluded that kinetic of the heavy lanthanide's absorption was rapid. It was found that Extraction increases with increasing phase contact time. It is concluded that the equilibration time with a high separation factor for heavy lanthanides is about 30 seconds.

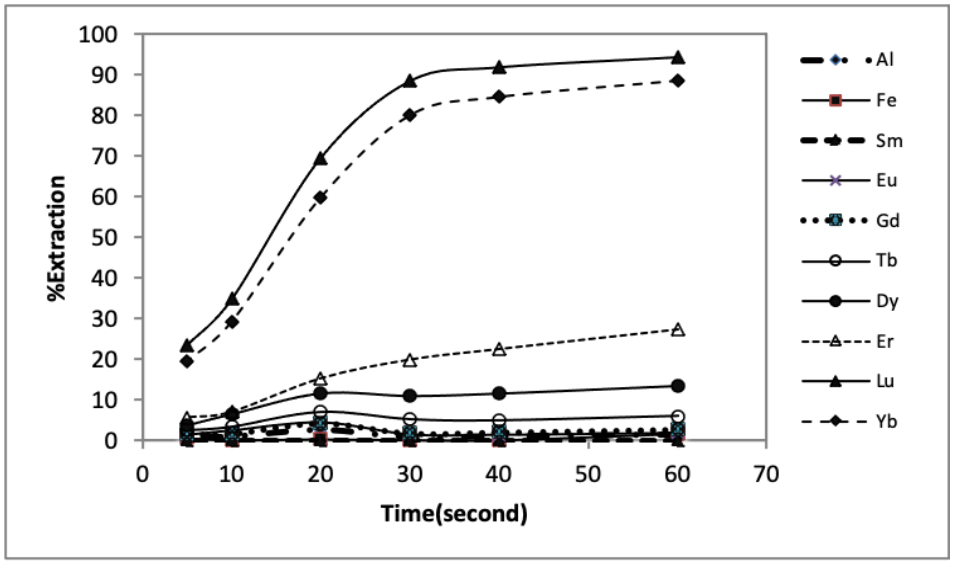

Figure 3. Effect of phase contact time on Extraction of heavy lanthanides from light ones and interfering ions

Effect of pH

The impact of pH on the extraction of lanthanides and interfering ions by HDEHP in Kerosene was studied in the range 0.1- 2 for 30 seconds. It was detected that the distribution ratio of these metal ions diminishes with an increase in the concentration of nitric acid. As shown in Fig 4, the extraction of lanthanides and interfering ions increases with increasing pH.

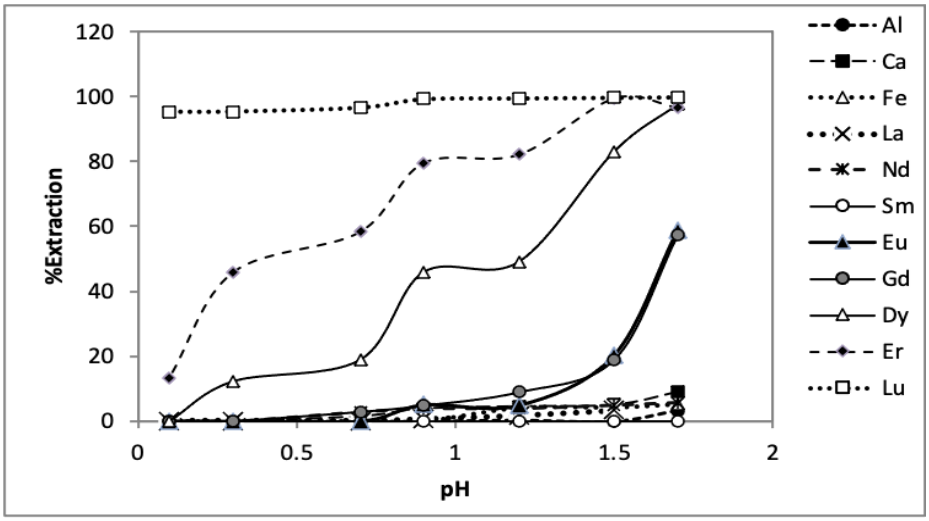

Figure 4. Effect of pH on Extraction of heavy lanthanides from light ones and interfering ions

Removal of Fe (III)

To remove interfering ions by solvent extraction technique with 0.15 M HDEHP, with the progress of pH, the percentage of Lanthanides absorption was reported to be higher than that of interfering ions. Therefore,

Lanthanides can be easily transferred from the aqueous phase into the organic phase in minimum time in this condition whereas the interfering ions remained in the aqueous phase with minimal absorption.

Consequently, at a pH of 1.7, it is possible to separate lanthanides from interfering elements. In this situation, more than 70 percent of iron ions and about 90 percent of aluminum and calcium impurities are eliminated. Similarly, at a pH equal to 1.7, heavy lanthanides are absorbed in the organic phase, if other lanthanides remain in the aqueous phase, and it is possible to distinguish heavy lanthanides in this condition.

According to the results obtained in the solvent extraction experiments, to separate heavy lanthanides from other lanthanides and iron and aluminum ions, the pH of the current solution was adjusted to 1.7 using 25% ammonia. Then the aqueous phase was contacted with the organic phase comprising 0.15 M HDEHP diluted in Kerosen and 2% Decanol for 30 seconds. In this condition, heavy lanthanides were absorbed into the organic phase, while other lanthanides remained along with interfering ions in the aqueous phase. To separation the heavy lanthanides that were absorbed in the organic phase, 1 M nitric acid was applied for stripping. The results are described in Figure 5.

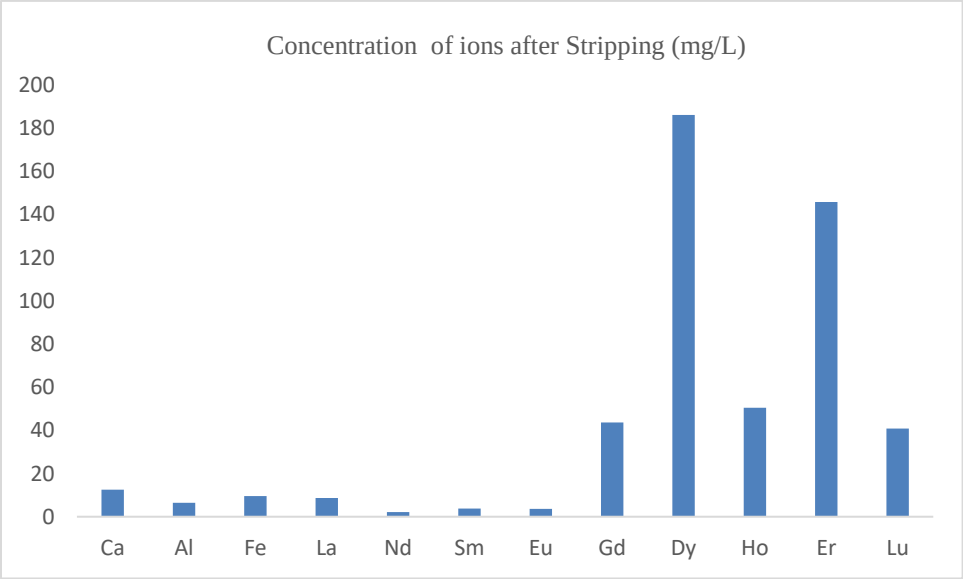

Figure 5. The chemical composition of the stripped solution.

Conclusions

The results show that it is possible to remove interfering ions by the solvent extraction method with HDEHP extractant with a concentration of 0.15 M, at a pH of 1.7. Therefore, Lanthanides can be easily transferred from the aqueous phase into the organic phase in minimum time in this condition whereas the interfering ions remained in the aqueous phase with minimal absorption.

In this situation, more than 70 percent of iron ions and about 90 percent of aluminum and calcium impurities are eliminated. Similarly, at a pH equal to 1.7, heavy lanthanides are absorbed in the organic phase whereas other lanthanides remain in the aqueous phase, and it is possible to distinguish heavy lanthanides in this condition.

References

1. N.V.Thakur, Separation of Rare Earths by Solvent Extraction. Min. Pro. Exr. Met. Rev. 21(1-5): 277-306 (2000.).

2. J. Kraikaew, W. Srinuttrakul and C. Chayavadhanakur, Solvent Extraction Study of Rare Earths from Nitrate Medium by the Mixtures of TBP and D2EHPA in Kerosene. J. Met. Mat. Min. 15(2): 89-95 (2005).

3. F.A. Cotton and G.W. Wilkinson, The Lanthanides – Principles and Energetics, Advanced Inorganic Chemistry. (Interscience Publishers, New York. 9-22 ,(1985).

4. C.S.K. Raju and M.S. Subramanian, Sequential separation of lanthanides, thorium, and uranium using novel solid phase extraction method from highly acidic nuclear wastes. J. Hazard. Mater. 145(1-2): 315-22 (2007).

5. X.-P. Yan, R. Kerrich and M.J. Hendry, Flow injection online group preconcentration and separation of (ultra)trace rare earth elements in environmental and geological samples by precipitation using a knotted reactor as a filterless collector for inductively coupled plasma mass spectrometric determination. J. Anal. At. Spectrom. 14(2): 215-221(1999).

6. K.A. Rabie, A group separation and purification of Sm, Eu, and Gd from Egyptian beach monazite mineral using solvent extraction. Hydrometallurgy. 85(2-4): 81-86 (2007).

7. R.D. Abreu and C.A. Morais, Purification of rare earth elements from monazite sulphuric acid leach liquor and the production of high-purity ceric oxide. Miner. Eng. 23(6): 536-540 (2010).

8. S. Radhika, B.N. Kumar, M.L. Kantam and B.R. Reddy, Liquid–liquid extraction and separation possibilities of heavy and light rare earths from phosphoric acid solutions with acidic organophosphorus reagents. Sep. Purif. Technol. 75(3): 295-302 (2010).

9. S. Radhika, B.N. Kumar, M.L. Kantam and B.R. Reddy, Solvent extraction and separation of rare-earths from phosphoric acid solutions with TOPS 99. Hydrometallurgy. 110(1-4): 50-55 (2011).

10. F. Xie, T.A. Zhang, D. Dreisinger and F. Doyle, A critical review on solvent extraction of rare earths from aqueous solutions. Miner. Eng., 56, 10-28 (2014).

11. A. Ali and M. Ahmed, Extraction of Sm(III), Gd(III) and Ho(III) ions with picrolonic acid in methylisobutylketone. J. Radioanal. Nucl. Chem. 266(3): 481-484 (2005).

12. Y. Miyamoto, K. Yasuda, M. Magara, T. Kimura and S. Usuda, Sequential Separation of U, Th, Pb, and Lanthanides with a Single Anion-Exchange Column. J. Nucl. Radiochem. Sci. 10(2): 7-12 (2009).

13. G.H. Morrison and H. Freiser, Solvent extraction in analytical chemistry. (John Wiley, New York. 212,1957).

14. Y. Liu, S. H. Nam and M. Lee, Stripping of Fe(III) from the Loaded Mixture of D2EHPA and TBP with Sulfuric Acid Containing Reducing Agents. Bull. Korean Chem. Soc. 35(7): 2109-2113 (2014).

15 B. Gupta, A. Deep, V. Singh and S.N. Tandon, Recovery of cobalt, nickel, and copper from sea nodules by their extraction with alkylphosphines. Hydrometallurgy. 70(1-3): 121-129 (2003).

16. J. Jayachandran and P.M. Dhadke, Liquid-liquid extraction separation of iron (III) with 2-ethyl hexyl phosphonic acid mono 2-ethyl hexyl ester. Talanta. 44(7): 1285-1290 (1997).

17. C. Lup, and D. Pilone, Reductive stripping in vacuum of Fe(III) from D2EHPA. Hydrometallurgy. 57(3): 201-207 (2000).

18. J. Saji, T.P. Rao, C.S.P. Iyer and M.L.P. Reddy, Extraction of iron (III) from acidic chloride solutions by Cyanex 923. Hydrometallurgy. 49(3): 289-296 (1998).

19. J. Saji, and M.L.P. Reddy, Liquid–liquid extraction separation of iron (III) from titania wastes using TBP–MIBK mixed solvent system. Hydrometallurgy. 61(2): 81-87(2001).

20. A.J.V.d. Zeeuw, Purification of zinc calcine leach solutions by exchange extraction with the zinc salt of "verastic" acid. Hydrometallurgy. 2(3): 275-284 (1977).

21. J.O. Hibbits, W.F. Davis and M.R. Menke, Effect of nitric acid on the extraction of iron with tri-n-octylphosphine oxide. Talanta. 8(2-3): 164-165 (1961).

22. T. Sato, T. Nakamura and M. Ikeno, The extraction of Iron(III) from aqeous acid solutions by di(2-ethylhexyl)phosphoric acid. Hydrometallurgy. 15(2): 209-217 (1985).

23. R.K. Biswas and D.A. Begum, Solvent extraction of Fe3+ from chloride solution by D2EHPA in kerosene. Hydrometallurgy. 50(2): 153-168 (1998).

24. L. Jian-min, Y. Ru-dong and M. Yong-xiang, Extractive Separation of Scandium, Yttrium, Lanthanum, Iron, and Tin in Hydrochloric Acid System with 1,10-Bis(1-phenyl-3-methyl-5-oxopyrazol-4-yl)decane-1,10- dione. Chem. Papers. 46(5): 290-292 (1992).

25. S. Khujaev and L.B. Nushtaeva, Influence of Fe (III) macroquantities on rare earth elements separation by di(2-ethylhexyl)orthophosphoric acid. Abstracts of the second conference on radioisotopes and their applications: 20-21(2000).

26. G.M. Ritcey and A.W. Ashbrook, Solvent Extraction; Principles and Applications to Process Metallurgy. Process Metallurgy. Elsevier Scientific Pub. Comp., New York, USA (1979).

27. T. Sato, The extraction of Indium(Ill), Lanthanum(Ill) and Bismuth(Ill) from sulphuric acid solutions by di-(2-ethylhexyl)-phosphoric acid. J. Inorg. Nucl. Chem. 37(6): 1485-1488 (1975).

28. E. Sminčáková, L. Komorová and M. Gálová, Extraction of Rare Earth Metals by Bis(2-Ethylhexyl) phosphoric Acid. Chem. Papers, 48(4): 242-245 (1994).

29. B. Gupta, P. Malik and A. Deep, Extraction of uranium, thorium and lanthanides using Cyanex-923: Their separations and recovery from monazite. J. Radioanal. Nucl. Chem. 271(3): 451-456 (2002).

30. V. N. Kosyakov, E. A. Yerin, Separation of transplutonium andrare-earth elements by extraction with HDEHP from DTPA solutions.J. Radioanal. Chem. 43, 37 (1978).

31. M. Aguilar, D. H. Liem, Studies on the solvent extraction ofeuropium(III) by di-(2-ethylhexyl) phosphoric acid (HDEHP) intoluene. Acta. Chem. Scand. A30, 313 (1976).

32. D. H. Liem, Studies of the complex formation between di-2-ethylhexyl-phosphate (HDEHP) and tributylphosphate (TBP) ortrioctylamine (TOA) in toluene. Acta. Chem. Scand. 26, 191(1972).

ICNST 2024 International Conference on Nuclear Science and Technology
6- 8 MAY 2024 | Isfahan, Iran

Reliability evaluation of rotating machine using fuzzy fault tree and Bayesian networks (Paper ID : 1342)

Amini E., Fatemi Ghomi S.M.T. Correspondent *,
Department of Industrial Engineering Amirkabir University of Technology, Tehran, ***Iran***

Abstract

Rotating machinery is key component in the most industries and its reliable operation plays a basic role in the mitigating the risks associated with safety-critical industry including the nuclear, defense, avionics, automotive and railroad domains. Specially some rotating machines are irreparable during their mission period. Therefore, it is necessary to evaluate their reliability and improve it by corrective or preventive actions in structure or operation of machines. The present study firstly used failure mode and effect analysis and fault tree analysis to determine the root causes involved in the failure of rotating machine and fuzzy set theory to determine prior probabilities of root nodes. Then it used Bayesian networks to determine posterior probabilities of root nodes and evaluate the reliability of rotating machine. Finally, the reliability of one rotating machine with 50 parts and numerous identified basic events is estimated and the most important factors in the failure of this rotating machine is found.

Keywords: Reliability evaluation, Rotating machine, Fault tree, Failure modes, Bayesian networks, Fuzzy set theory

Introduction

Rotating machinery represents a broad category of equipment, which includes pumps, compressors, fans, gas turbines, electric motors, internal combustion engines, some types of separators, etc., that are critical to the efficient operation of process facilities around the world. This equipment should be designed to move gases and liquids safely, reliably, and in an environmentally friendly manner. Reliability is defined as the probability that a product, system, or service will perform its intended function adequately for a specified period of time, or will operate in a defined environment without failure. System reliability is determined by the technical decisions made during the design, development, and production phases of the product life cycle. Reliability analysis deals with all levels of a complex

system, from component level to system level.

A number of researchers have addressed the issue of reliability prediction, assessment, evaluation, allocation and improvement during period of design and construction of systems. Reliability analysis can be

divided into two broad categories: qualitative and quantitative. Some methods are simulation based and some methods are analytical. In analytical category, the two main methods in the qualitative analysis are failure mode and effect analysis (FMEA) and fault tree analysis (FTA) and the two main methods in the quantitative analysis are bayesian networks (BNs) and petri nets (PNs). These methods have been used in two different ways: standalone approaches and model-to-model transformation approaches.

Kabir and Papadopoulos have presented a review of the applications of BNs and PNs in system safety, reliability and risk assessments [7]. Bobbio et al. have mapped FTA into BNs to improve the analysis of dependable systems [3]. Chengshan and Yinghua have translated FMEA to BNs [5]. Yang et al. have used BNs with FMEA and fuzzy set theory for risk prioritization in FMEA [16].Yan et al. have used PNs with FTA and FMEA for mission modelling of automated guided vehicles [15]. Martins and Maturana have integrated FTA with BNs for human reliability analysis in oil tanker operations [10]. Some other applications include the reliability evaluation of: steel construction, train control systems and power systems using BNs [7].

Data generated from testing constitutes the basis for reliability assessment. All types of testing are time-consuming and require resources. Sometimes testing is dangerous and harmful too. In some application in the absence of data, the fuzzy set theory and expert elicitation were used to determine the probability of basic events [6]. Xue et al. have used fuzzy-logic-based method for FMEA for reliability improvement in engine systems [14]. Liu et al. have used FMEA combining fuzzy weighted average with fuzzy decision-making trial and evaluation laboratory [8]. Jafari et al. have estimated reliability of fire alarm systems using dynamic BNs and fuzzy FTA [6]. Chen et al. have evaluated dynamic reliability for a pantograph system based on a multistate FTA and dynamic BNs [4].

The current study aimed to advise an approach to evaluate the reliability of irreparable rotating machineries in uncertainty conditions. In the following, first the summary of the theoretical basis and current methodology is given and then results of its implement on a rotating machine is discussed.

Research Theories

Reliability

Reliability can be seen as probability of success, durability, dependability, quality over time and availability to perform a function. Reliability is a process, not action or conclusion. It is of great interest to both customers and manufacturers. There are several different notions of product reliability as indicated in

Figure 1. Several techniques are applied to improve the reliability: redundancy, preventive maintenance, increasing quality, diversity, oversizing, etc. Reliability improvement is categorized into aspects: operational and structural. Safety is another important attribute of many products. To protect people and the environment, a number of laws, regulations, and standards give requirements to product safety. Some of these requirements are overlapping with reliability requirements. A main difference between safety requirements and the reliability requirements is that safety requirements are often mandatory and cannot be traded based on cost-benefit arguments.

Several methods are introduced by researchers or engineers for reliability analysis that can be chosen based on: degree of system complexity, phase of life cycle, type and size of gathered data, multiple failure mode/states for components/systems, uncertainty in system behavior and failure data, etc. Figure 2 categorizes quantitative methods for reliability analysis.

Failure modes and effect analysis

FMEA is a structured process for complex engineering analysis used to identify potential failure modes for a product or process, assess the risks associated with these failure modes, rank the issues in term of importance and identify and carry out corrective actions to address the most serious concerns. Application of FMEA can be divided into two broad categories: FMEA of a design and FMEA of a process. This study concerns the former category. Failure is a continouse interruption of the system's ability to perform required functional under specified operating function but malfunction is an intermittent irregularity in the fulfillment of a system's desired function. Fault is an unpermitted deviation of at least one characteristic property (feature)of the system from the acceptable, usual or standard condition that may lead to a failure or a malfunction.

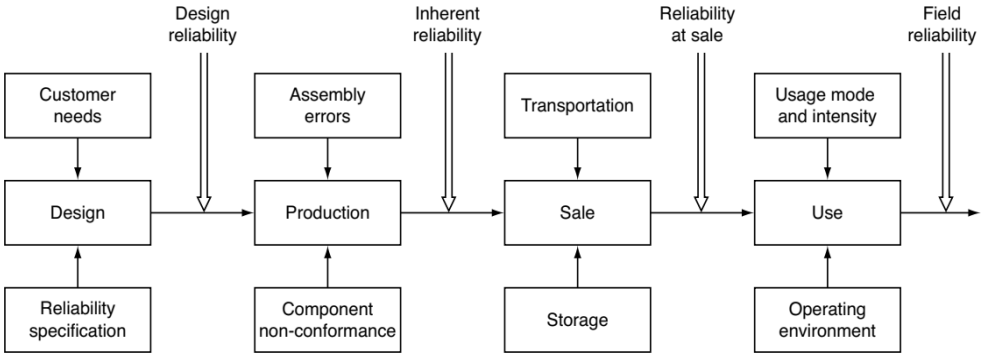

Fig. 1. Different notions of product reliability [1]

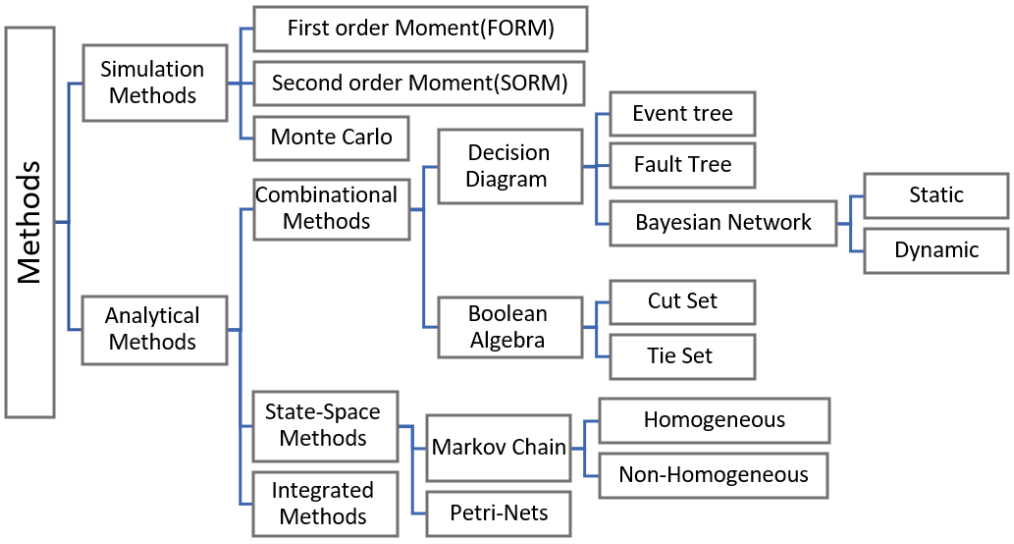

Fig. 2. Quantitative methods for reliability evaluation

FMEA terms are:

Items are defined as subsystems, interfaces, or parts.

Failure modes are defined as the manner in which a component, subsystem, or system could potentially fail to meet or deliver the intended function described in the item column.

Failure effects are defined as the effects of the failure mode on the function, as perceived by the customer(s).

Failure causes are defects in design, process, quality, or part application, which are the underlying cause of a failure or which initiate a process which leads to failure.

Severity is the value associated with the most serious effect for a given failure mode.

Occurrence is the likelihood that a specific cause/mechanism will occur resulting in the failure mode within the design life.

In this paper, severity and occurrence numbers for every cause of failures(CF) are ranked from (1- 10) to (1-5), as Table 1. Then for every CF, risk numbers are calculated as product of ranked severity and occurrence numbers. Finally risk number are ranked and converted from numbers to linguistic terms using Table 2. Terms: very low, low, fairly low, medium, high, fairly high and very high are defined as: VL, L, FL, M, H, FH and VH respectively.

Fault tree analysis

FTA is a systematic approach that identifies the primary causes of operational and maintenance issues. It is a deductive analysis tool that begins with a general conclusion before working backward to identify potential causes. This method has been started from standard fault tree(FT) and then extended to dynamic FT, repairable FT, fuzzy FT, etc. The three components of FTA include:

Fault tree diagram provides a visual framework of events leading to equipment breakdowns.

Events can refer to the causes of failure, contributors or failure itself.

Logic gates utilize a boolean “and/ or” sequence to connect related events.

As a brief, FT is a tree or more generally directed acyclic graph(DAG), where events model component failures and gates model rule of failures propagation. The probability of top event can be determined using FT according to the failure rate of basic events. Moreover, conventional FT method is not capable to consider some system behaviors, such as dependency between subsystems and components and ordering among the failure components occurrence.

Table 1. Levels for occurrence and severity numbers

Character	Level				
	1	2	3	4	5
Occurrence number	1	2,3	4,5,6	7,8,9	10
Severity number	1	2,3	4,5	6,7,8	9,10

Table 2. Ranks for occurrence and severity numbers

		Severity				
1			2	3	4	5
Occurrence	5	FL	FH	H	VH	VH
	4	L	M	FH	H	VH
	3	L	FL	M	FH	H
	2	VL	L	FL	M	FH
	1	VL	VL	L	L	M

Fuzzy set theory

The fuzzy set theory was introduced in 1965 by Lotfizadeh who exoressed that probability of conventional theories does not have sufficient ability for a variety of uncertainties; since they are unable to understand the human model and create perceptions that may exist in reality [18]. Accordingly, the fuzzy set theory is a suitable tool for ambiguous and uncertainty conditions and can convert possible qualitative expressions to numerical probabilities [17]. Following gives the steps required for the execution of this theory.

To quantify expert opinion regarding the failure rate of basic events, a 7-term linguistic scale is applied [12]. Table 3 provides fuzzy numbers associated with each linguistic term.

A number of different membership functions can be used for the fuzzification of linguistic terms, such as trapezoidal, triangular, gaussian or bell-shaped functions, depending on the real-world conditions of topic under study [9]. The current paper applies the trapezoidal fuzzy numbers.

Defuzzification of fuzzy numbers is an important step for decision making in fuzzy environment. For this purpose, the Center of Area defuzzification method was used. Equation 1 defuzzifies the trapezoidal fuzzy number $\tilde{A} = (a_1. a_2. a_3. a_4)$ to X^* as output [13].

$$X^* = \frac{1}{3} \times \frac{(a_4 - a_3)^2 - a_4 a_3 - (a_1 + a_2)^2 + a_1 a_2}{(a_4 + a_3 - a_1 - a_2)} \quad (1)$$

The results obtained in the previuos step is converted to a probability(FPB) from a possibility(FPS) via Equation 2 [11].

$$\overline{FPB(x)} = \begin{cases} k & FPS \neq 0 \\ i & 10^{\left(\frac{1}{FPS}\right)^{1/3}} \\ 0 & FPS = 0 \end{cases} \quad K = [1 - FPS)] \times 2.301 \quad (2)$$

Table 3. Fuzzy number associated with each linguistic term

Linguistic Term	Fuzzy Number
Very Low (VL)	(0,0,0.1,0.2)
Low (L)	(0.1,0.2,0.2,0.3)
Fairy Low (FL)	(0.2,0.3,0.4,0.5)
Medium (M)	(0.4,0.5,0.5,0.6)
Fairly High (FH)	(0.5,0.6,0.7,0.8)
High (H)	(0.7,0.8,0.8,0.9)
Very High (VH)	(0.8,0.9,1,1)

Bayesian networks

BNs are graphical probability models which can be built using available data or expert elicitation and have widespread application for qualitative and quantitative analysis in risk assessments. Principle of BNs is that they should satisfy the Markov condition. 'Parent' nodes impact their descendants, but parent nodes do not impact each other. A posterior probability, in Bayesian records, is the revised or updated probability of an event happening after taking into account new records. The posterior probability($\pi(x_i)$) is calculated by updating the prior probability($\theta(x_i)$) using Bayes' theorem. A BN is a DAG with assumption of conditional dependencies. Two aspects are concerned in BNs:

Qualitative: A dependency graph made by nodes and arcs:

Nodes are stochastic variables(X) that each variable has a set of states {x1,…,xn}.

Arcs are dependency between nodes, namely a dependency of X on its parents(P).

Quantitative: The distributions of a X given each combination of $p(x_i)$ of its parents.

When the FT is converted into a BN, each node in the BN corresponds to various events in the FT. The logical gate connecting the events in the FT is replaced by the conditional probability table of BN. The prior probability of the root node in BN corresponds to the occurrence probability of the bottom event in the FT.

Birnbaum firts introduced the importance of measures(BIM) as one criterion in reliability.Then criteria of risk reduction worth (RRW) and ratio of variation (ROV) were introduced based on FT. Following defines BIM, RRW and ROV [6].

$$BIM(x_i) = p(T = 1|x_i = 1) - p(T = 1|x_i = 0) \quad (3)$$

$$RRW(x_i) = \frac{p(T = 1)}{p(T = 1|x_i = 0)} \quad (4)$$

$$ROV(x_i) = \frac{\pi(x_i) - \theta(x_i)}{\theta(x)} \quad (5)$$

Approach framework

The current paper combines FMEA, FT, fuzzy set theory, and BNs to evaluate the reliability of one rotating machine. Figure 3 shows the flowchart of the methodology used in this study.These steps are:

Step1. FMEA and FTA

1.1. System is defined and all its constituents (subsystems, subassemblies and parts) are determined. Then relations between them are identified using block diagram, parameters diagram and matrix of interfaces.

Primary and secondary functions of system are defined and failure modes of every function of system are identified; Then SFME (FMEA in system level) table is filled.

Primary and secondary functions of subsystems are defined and failure modes of every function of subsystems are identified; Then DFME(FMEA in subsystem level) table is filled.

FT is drawn through events and their causes identified in 1.2 and 1.3.

Risk numbers are ranked and converted from numbers to linguistic terms. Step2. Fuzzy Theory

Linguistic terms related to the failure rate of basic events are quantified and fuzzy numbers are derived. In this study, fuzzy numbers are considered as fuzzy possibilities.

Defuzzification of fuzzy numbers is performed.

Results obtained in 2.2 are converted to fuzzy possibility. Step3. BNs

FT is converted to BN.

Probability of leave node (fault and health probabilities of rotating machine) is calculated. Also, posterior probabilities of all nodes (root and middle causes) are calculated.

Sensitivity analysis is conducted.

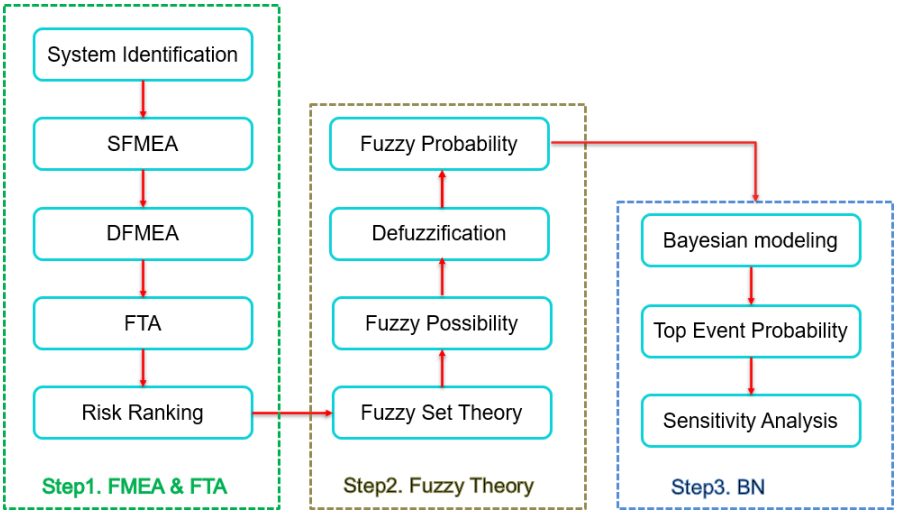

Fig. 3. Flowchart of the methodology applied in the paper

Calculations made in this study were coded by python language. Reliability calculations with BNs were done using pgmpy library [2].

Results

Target system as a rotating machine is an isotopic separator that rotates with very high speed and is used in nuclear industry. It has differnt models with different geometric features and operational conditions, but all models have the same subsystems. This machine comprises of 8 subsystems: 1) rotating parts as the main container for fluid processing called rotor, 2) fixed parts for feeding working fluid into the rotor and extracting processed fluid from it called gas-handling, 3) fixed parts for providing safe and vacuum domain for other parts calling casing, 4) fixed parts for damping vibrations of rotor and supporting the weight of it called suspension at the bottom side of the machine, 5) fixed parts for removing heat from system called cooling, 6) fixed parts for damping vibrations of rotor and supporting the weight of it called suspension at the top side of the machine, 7) fixed and rotary parts for providing driving force as motor, 8) fixed part for vacuuming space between rotor and casing called vacuum. This machine has more than 50 parts and Figure 4 shows its schematic in axisymmetric view.

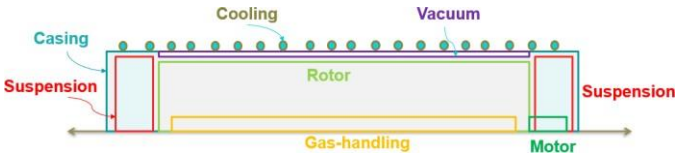

Fig. 4. Schematic of target system in axisymmetric view

524 root causes of failure(RCF) were identified using DFMEA. These causes are categorized as Geometry, Material, Assembly and Operation. Five levels are considered for FT. Transformation from fuzzy FT to BNs leads to 708 nodes(524 root and 184 intermediate nodes) with 791 arcs in the final model. Due to the large number of causes and relations mapped to the nodes and arcs, final BNs is too wide. The most important output of the calculations, is the system reliability. Based on the output demonstrated in the following, the system reliability is 0.3818.

```
from pgmpy.inference import VariableElimination
  inference = VariableElimination(model)
     leave_node = model.get_leaves()
   Top_event = inference.query([leave_node])
             print(Top_event)


+-----------------+-----------------+
| Rot_Mach        |   phi(Rot_Mach) |
+=================+=================+
| Rot_Mach(true)  |          0.3818 |
+-----------------+-----------------+
| Rot_Mach(false) |          0.6182 |
+-----------------+-----------------+
```

The reason why the value of reliability is such low should be found. The calculated RRW and BIM for all subsystems are plotted in bar charts, as shown in Figure 5. It shows that subsystems numbered "1 and 2" are more critical than the others. The calculated RRW and BIM for parts belong to the first subsystem are plotted in bar charts, as shown in Figure 6a. It shows that parts named T_T_01 and Blw_01 are more critical than the others. The calculated posterior probabilities for failure causes of part named "T_T_01" are plotted in bar charts, as shown in Figure 6b. It shows that designer should pay attention to modify geometry of this part.

The low value of system reliability should be improved by performing corrective actions on the parts in four categories(aspects): Geometry, Material, Assembly and Operation. The monotonic characteristics were investigated by reducing successively the value of occurrence for defects related to each aspect, whereas the value of other parameters were fixed. For example, the values in the second column of Table 4 indicate the system reliability when occurrence of all geometrical defects reduces in the order of 0, 25%, 50%, 75% and 95% respectively. Based on the results in this table, Maximum value for system reliability was derived 0.5292 .It seems that the major reason for low reliability is the high number of

defects in all subsystems. So to increase reliability, the number of defects was decreased in two stages. In the first stage, defects in the subsystems 5-8 were removed and the reliability reached to 50% from 38%. In the second stage, defects in the subsystems 1-4 were removed and then reliability reached to 78%.

Conclusions

This paper introduced an approach to evaluate the reliability of irreparable rotating machinery. It combined FMEA, fuzzy FT and BNs methods. This approach was applied to estimate the reliability of one rotating machine; Then the most critical subsystems and parts of the target system were identified by sensitivity analysis and effects of quality improvement on machine reliability were examined. There are some uncertainties in this study: Basic events are assumed independent; Its structure is static and has only single scenario for failure causes and their relations; Basic events and their probabilities have been derived only from expert opinions. In order to decrease uncertainties, application of dynamic BNs for including the dynamic fault process and the markov methods for modeling relationships between various faults can be recommended as topics for future studies.

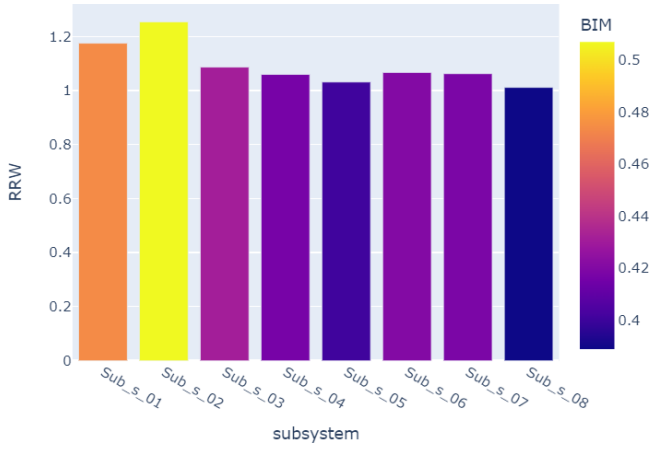

Fig. 5. Calculated RRW that colored by BIM for all subsystems

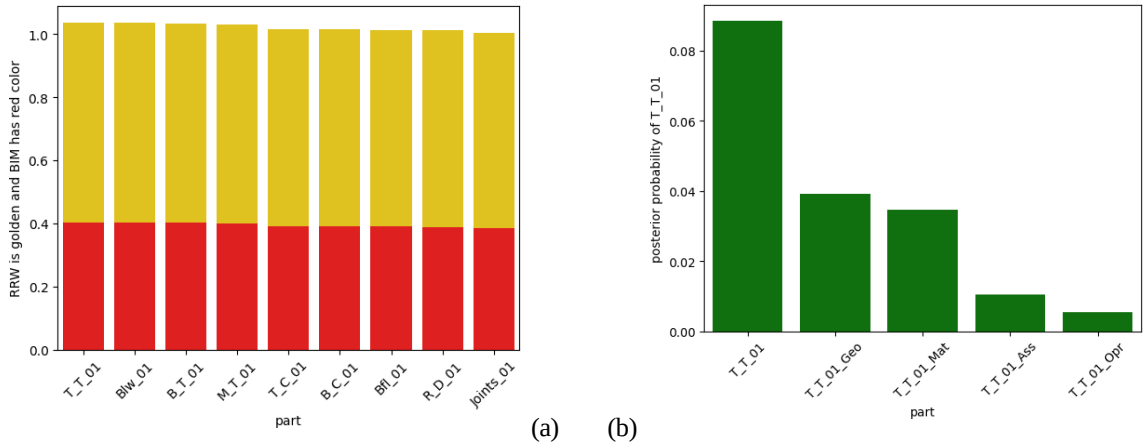

(a) (b)

Fig. 6. a) Calculated criteria for all parts in subsystem 8, b) Typical failure causes of T_T_01

Table 4. System reliability with reduction in the occurrence number for all defects in 4 aspects

Decrease percentage	Geometry	Material	Assembly	Operation
0	0/3818	0/3818	0/3818	0/3818
25	0/3876	0/4304	0/3841	0/3873
50	0/4007	0/4769	0/4453	0/4108
75	0/5248	0/4850	0/4621	0/4206
95	0/5292	0/4850	0/4621	0/4206

References

[1] Murthy, D. N., Rausand, M., & Østerås, T. (2008). *Product Reliability, Specification and Performance.* London: Springer .

[2] Ankan, A., & Panda, A. (2015). pgmpy: Probabilistic Graphical Models using Python. *PROC. OF THE 14th PYTHON IN SCIENCE CONF*.

[3] Bobbio, A., Portinale, L., Minichino, M., & Ciancamerla, E. (2001). Improving the analysis of dependable systems by mapping fault trees into Bayesian networks. . *Reliability Engineering & System Safety*, *71*(3), 249–260.

[4] Chen, Y., Wen, J., Tian, Y., Zheng, S., Zhong, Q., & Chai, X. (2023). Dynamic Reliability Assessment Method for a Pantograph System Based on a Multistate T-S Fault Tree, Dynamic Bayesian. *Applied Science, 13*.

[5] Chengshan, W., & Yinghua, X. (2004). Applying Bayesian network to distribution system reliability analysis. *IEEE Region 10 Conference, 100*, pp. 562-565. TENCON.

[6] Jafari, M. J., Pouyakian, M., khanteymoori, A., & Hanifi, S. M. (2020). Reliability evaluation of fire alarm systems using dynamic Bayesian networks and fuzzy fault tree analysis. *Journal of Loss Prevention in the Process Industries, 67*.

[7] Kabir, S., & Papadopoulos, Y. (2019). Applications of Bayesian networks and Petri nets in safety, reliability, and risk assessments: A review. *Safety Science, 115*, 154–175.

[8] Liu, H. C., You, J. X., Lin, Q. L., & Li, H. (2015). Risk assessment in system FMEA combining fuzzy weighted average with fuzzy decision-making trial and evaluation laboratory. *International Journal of Computer Integrated Manufacturing, 28*(7).

[9] Markowski, A. S., & Mannan, M. S. (2008). Fuzzy risk matrix. *J. Hazard Mater, 159.*

[10] Martins, M. R., & Maturana, M. C. (2013). Application of Bayesian Belief networks to the human reliability analysis of an oil tanker operation focusing on collision accidents. *Reliability Engineering & System Safety, 110*, 89-109.

[11] Onisawa, T. (1988). An approach to human reliability in man-machine systems using error possibility. . 27, 87–103. *Fuzzy Set Systems, 27*, 87-103.

[12] Saaty, T. L., & Ozdemir, M. S. (2003). Why the magic number seven plus or minus two.

[13] *Math.Comput. Model., 38*, 233-244.

[14] Sugeno, M., & Kang, G. (1986). Fuzzy modelling and control of multilayer incinerator. *Fuzzy Set Systems, 18*, 329-345.

[15] Xu, K., Tang, L., Xie, M., Ho, S., & Zhu, M. (2002). Fuzzy assessment of FMEA for engine systems. *Reliability Engineering & System Safety, 75*(1), 17-29.

[16] Yan, R., Jackson, L. M., & Dunnett, S. J. (2017). Automated guided vehicle mission reliability modelling using a combined fault tree and Petri net approach. *Int. J. Adv. Manuf.*, 1-13.

[17] Yang, Z., Bonsall, S., & Wang, J. (2008). Fuzzy rule-based Bayesian reasoning approach for prioritization of failures in FMEA. *IEEE Trans. Reliab., 57*(3), 517-528.

[18] Yazdi, M., & Kabir, S. (2020). Fuzzy evidence theory and Bayesian networks for process systems risk analysis. *Hum. Ecol. Risk Assess., 26*, 57–86.

[19] Zadeh, L. A. (1965). Fuzzy sets. *8*, 338–353.

ICNST 2024 International Conference on Nuclear Science and Technology
6 - 8 MAY 2024 | Isfahan, Iran

On the behavior of 238U and 234U isotopes in the natural analogue of Nb-Ta-Ti-oxide as a matrix of actinides at 200 ℃ (Paper ID : 1345)

Mohammad Hosseinpour Khanmiri [a,*], Elena V. Puchkova [b]

[a] *Central Laboratory, Nuclear Science and Technology Research Institute, AEOI, Tehran,14893-836, Iran*

[b] *Department of Radiochemistry, Institute of Chemistry, St. Petersburg State University, St. Petersburg, 199034, Russia*

Email: mhosseinpourkhanmiri@aeoi.org.ir

Abstract

By examining the behavior of uranium isotopes in metamict minerals, useful information is obtained for predicting the state of solidified forms of HLW (high-level radioactive waste) and the behavior of the actinides produced in the final stages of the nuclear fuel cycle under geological disposal conditions. In this research work, the behavior of ^{234}U and ^{238}U isotopes in radioactive Nb-Ta-Ti-oxide as a natural analog of actinides was studied at room temperature and 200 ℃. Radiochemical and alpha spectroscopic analyses showed that the secular equilibrium in the sample was violated, and 93% of the initial uranium isotopes were oxidized to hexavalent atoms during the geological history of Nb-Ta-Ti-oxide. The equal activity ratio obtained at room temperature between uranium isotopes in the U(IV) and U(VI) fractions was changed and increased in the tetravalent uranium fraction by heating Nb-Ta-Ti-oxide at 200 °C. Also, the amounts of U(IV) and U(VI) fractions changed from 7% to 30% and from 93% to 70%, respectively.

Keywords: Ion exchange chromatography, ^{238}U and ^{234}U isotopes, Alpha spectroscopy, High-level nuclear waste, Natural analogues of actinides

Introduction

It is quite obvious that metamict minerals are considered as natural analogues of the solid-form forms of HLW obtained at the final stage of the nuclear fuel cycle [1-7]. Due to the fact that nuclear decay can cause significant heating of the corresponding nuclear waste forms, a special look at thermochemical processes in metamict minerals is certainly worthwhile. Understanding the behavior of the oxidation state of uranium atoms in different stages of metamictization enables us to predict the behavior of actinides in mineral matrices used for the long-term disposal of HLW in underground reservoirs. Knowing the radioactivity ratio of AR($^{234}U/^{238}U$) in the natural radioactivity series of U-238 provides useful information about the behavior of uranium isotopes in the relevant minerals at the disposal of nuclear researchers whose main field of activity is related to the burial of heavy isotopes obtained in the

final stages of the nuclear fuel cycle. In the research work [8], a non-uniform thermochemical behavior of uranium isotopes in the britholite metamict mineral was observed. In this mineral, at room temperature, the radioactivity ratio of AR ($^{234}U/^{238}U$) in the U(IV) section is 0.875±0.014 and in the U(VI) section is 1.320±0.015. During the geological history of this mineral, 72 percent of the primary tetravalent uranium has been oxidized to a hexavalent state. At 650 ℃, the final equality of the radioactivity ratio AR ($^{234}U/^{238}U$) in tetravalent and hexavalent uranium parts is obtained. In fact, at the very beginning of the crystallization process restructuring of mineral metamict, by reducing U(VI), this equality of radioactivity ratio is obtained. At higher temperatures, the correlation between U(IV) and U(VI) contents changes, but the equilibrium ratios of $^{234}U/^{238}U$ in both U(IV) and U(VI) fractions remain constant.

In this research work, the thermochemical behavior of ^{234}U and ^{238}U isotopes in the radioactive Nb-Ta-Ti-oxide with laboratory code wk-8 as a natural analogue of nuclear fuel cycle actinides at room temperature and 200℃ (to see the experimental results at higher temperatures) has been studied.

Experimental

Note: It is worth noting that all the experiments (and results and data) given in this paper were carried out in the Radiochemistry Department of St. Petersburg State University (Russia) in 2019.

Reagents and chemicals

In this research, Dowex AB-8-17 anionic resin with 100 to 200 mesh size, nitric acid, hydrochloric acid, concentrated hydrofluoric acid, ascorbic acid, and isopropyl alcohol were used. Nb-Ta-Ti-oxide sample was obtained from the Faculty of Geology of St. Petersburg State University, Russia, and was crushed to a particle size of less than 120 mm for nuclear chemistry analysis, using ^{232}U as a tracer for control. The efficiency of uranium purification experiments and in order to calculate the registration coefficient of the alpha detector (θα), it was used from the standard source of ^{238}U with a specific radioactivity of 6.047 Bq.

Equipment and devices

For the separation and purification of U isotopes from Nb-Ta-Ti-oxide, two chromatographic columns were selected in large (100x10 mm) and small (75x6 mm) dimensions. In order to dissolve the Nb-Ta-Ti-oxide, a magnetic stirrer was used, an electrolytic deposition cell (made in Russia) was used to prepare U springs, and an alpha spectroscopic device (made in Russia) was used to measure the radioactivity of isotopes.

Dissolution of Nb-Ta-Ti-oxide in 23M fluoric acid

In a magnetic stirrer, a certain amount in mg of the crushed Nb-Ta-Ti-oxide sample was dissolved in 10 ml of concentrated 23M hydrofluoric acid for 80 min at laboratory temperature in Teflon containers. Simultaneously with the beginning of the digestion process, a certain amount of uranium-232 was added to the sample as a tracer.

The solution obtained from the complete dissolution of Nb-Ta-Ti-oxide, first to the semi-drying stage, and then to remove SiF4 gas three times in a row (3 ml each time) with 14 M concentrated nitric acid and to remove NO_2 gas three times with 12 M concentrated hydrochloric acid, was heated.

Finally, the semi-dry sample was heated three times with 6 M hydrochloric acid, and the studied sample was transferred to the ion exchange chromatography column after adding 2 ml of 6 M hydrochloric acid.

Anion-ion exchange chromatography

For the purification and separation of uranium isotopes, the anion exchange chromatography method was chosen with Dowex AB-8-17 anionic resin. The separation process was carried out at room temperature with a flow rate of 0.8–1 mL/min and a resin capacity of 25 mg U/g resin. Uranium forms complexes in hydrochloric acid solution, with increasing acid concentration, the rate of absorption of U into exchange resins also increases [9, 10]. Due to the fact that the rate of absorption of Fe^{+3} complexes into resin is the same as that of U, ascorbic acid was used to reduce Fe^{+3} to Fe^{+2}. After saturating both the large and small columns with 6 M chloric acid, the test solution was transferred to the large chromatographic column and washed twice with 6 M chloric acid. In this case, only uranium atoms are absorbed by the resin, and Th, Ra, rare earth elements, iron, and other elements are removed from the column. Then, uranium was separated from the column with 0.1 M hydrochloric acid, and after heating as in the previous method for more complete purification, the separation process was performed through a small column. Finally, the pure U was transferred to the electrolytic deposition cell.

Thermal annealing of the sample

A 150-mg sample of crushed Nb-Ta-Ti-oxide was placed in a quartz tube that was evacuated with a vacuum pump. The residual pressure obtained by the discharge was 0.1–1 mmHg. The sample was heated at 200°C for 10 minutes. Chromel-Copel and Chromel-Alumel thermocouples and the OVEN TRM-1 temperature regulator (Russia) were used to control the temperature.

Electrolytic deposition for the preparation of uranium isotope sources

The main and primary precision in preparing alpha sources from U isotopes is to coat their front faces with the thinnest and most uniform possible material layer of radioactive atoms. Therefore, the well-

known molecular plating method used in research [11, 12, 13] was utilized to prepare uranium sources. U-molecular plating was performed in isopropyl alcohol medium at a potential of 400 to 600 V with a current of 25 to 30 mA. The material of the anode was platinum, and the material of the cathode (source), on which the radioactive atoms of reduction are placed, was selected from nickel. Sedimentation was carried out for 70 to 100 minutes in a Teflon cell with a volume of 5 ml.

Alpha-spectroscopy

The sources containing U isotopes were placed in a vacuum chamber in the alpha spectrometer. The detector used is a surface barrier semiconductor type with an inherent resolving power of 25 to 35 keV, and according to the quality of the prepared sources and the duration of the measurement, the resolving power can be increased from 30 to 90 keV, and spectroscopy in the energy range of 3.6 Up to 9 MeV is possible. The active area of the detector is 2 cm^3, and alpha-spectrum analysis has been done with special computer software.

Results and discussion

According to secular equilibrium, the radioactivity ratio of daughter isotopes and mother isotopes in each radioactive decay series should be equal to 1. One of the important parameters regarding the durability and chemical strength of a mineral as a matrix for burying actinides obtained in the nuclear fuel cycle is the study and measurement of the radioactivity ratio of AR ($^{234}U/^{238}U$) in the corresponding mineral, because ores and minerals, during their geological history, are affected by natural chemical, physical, and biochemical factors. These effects sometimes cause major changes in the type of structure and chemical composition of the ore due to the leaching process. Therefore, first of all, it is necessary to check the state of secular equilibrium between U-238 and U-234 isotopes in the research sample. Also, the behavior of the mentioned isotopes as representatives of actinides at higher temperatures provides useful information. Table 1 shows the ratio of total radioactivity in the sample and the distribution of this radioactivity in tetravalent and hexavalent uranium parts at room temperature and at 200 ℃. As can be seen from Table 1, the total activity ratio of AR($^{234}U/^{238}U$) in the sample is equal to 0.972, which indicates the disturbance of the secular equilibrium in the ^{238}U radiation series. The share of tetravalent uranium in the sample is equal to 7%, which means that 93% of tetravalent uranium atoms have been oxidized to hexavalent atoms during the geological history of the mineral under the influence of environmental factors. It can also be concluded that the ^{234}U isotope has been more affected by natural factors compared to ^{238}U. The noteworthy point is that although the secular equilibrium in the mineral has been violated, an equal radioactivity ratio is maintained in the U(IV) and U(VI) fractions.

Heating the sample at 200 ℃ has caused changes in the ratio of activation in U(IV) and U(VI) fractions, and the amount of tetravalent uranium has increased from 7% to 30%. The reason for these changes is probably related to the mineral's attempt to crystallize. It seems that by increasing the temperature of the mineral, it is trying to recover its original crystal structure, which has become amorphous under the influence of natural factors. In the early stages of mineral formation, uranium atoms are placed in the crystal structure in a tetravalent form. The alpha spectroscopy of uranium isotopes in the U(IV) fraction at 200℃ is shown in Figure 1. The ambiguous and unexpected point about the research results is the behavior of uranium isotopes, because two isotopes of the same element have shown different oxidation behaviors. This non-identical behavior of uranium isotopes has also been observed in the metamict mineral britholite [8]. In this mineral the violated secular equilibrium was established at a temperature of 650 ℃ in both parts (U(IV) and (U(VI). But naturally, in the sample of our study, it is not possible to establish a secular equilibrium simultaneously in the U(IV) and U(VI) fractions because the total radioactivity ratio in the radioactive Nb-Ta-Ti-oxide is smaller than unity, but in britholite, secular equilibrium is established in the origenal fraction.

Table 1. Isotopic parameters in Nb-Ta-Ti-oxide at room temperature and 200℃

T (℃)	AR(^{234}U/^{238}U)			AR(^{232}U/^{234}U)		Content, %	
	U(IV)	U(VI)	U(Σ)	U(IV)	U(VI)	^{238}U (IV)	^{238}U (VI)
25	0.972 ± 0.031	0.972 ± 0.013	0.972 ± 0.011	2.295 ± 0.058	0.178 ± 0.004	7	93
200	0.997 ± 0.013	0.961 ± 0.021	0.972 ± 0.011	0.365 ± 0.006	0.227 ± 0.008	30	70

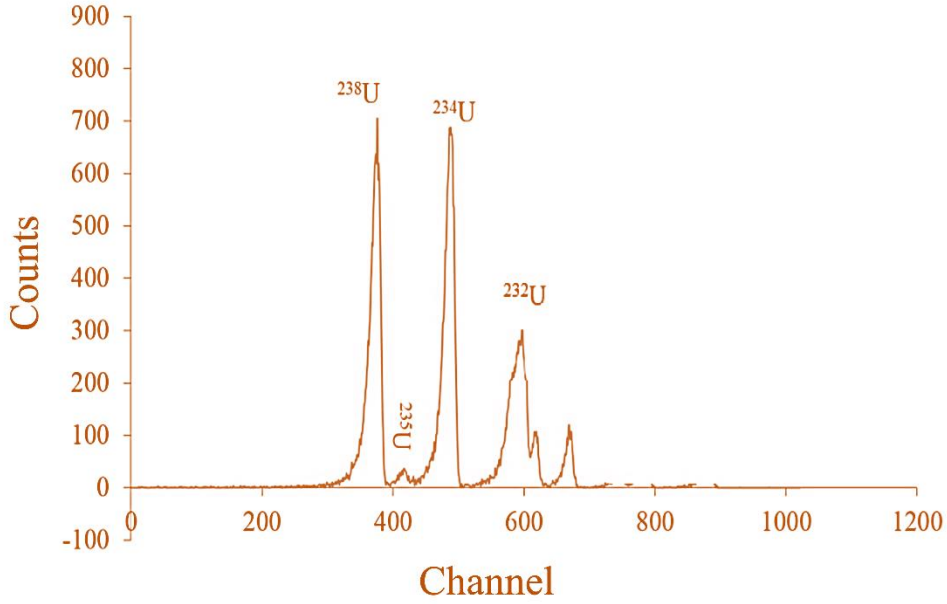

Fig. 1. Alpha spectrum of uranium isotopes in the U(IV) fraction at 200 ℃

Conclusion

Alpha spectroscopy of uranium isotopes at room temperature in radioactive Nb-Ta-Ti-oxide showed that only 7% of uranium isotopes remained in the tetravalent state throughout the geological history of the oxide, and despite the violation of the secular equilibrium in the sample, there is an equality of radioactivity ratio between the isotopes in the U(IV) and U(VI) sections. By heating the sample at 200 ℃, the non-uniform behavior of uranium isotopes was observed by changing the isotopic parameters. So that the amount of tetravalent uranium changed from 7% to 30% at high temperature, and the radioactivity ratio of AR($^{234}U/^{238}U$) in U(IV) and U(VI) sections increased and decreased, respectively.

References

[1] Deditius A. P., Smith, F. N., Utsunomiya, S. and Ewing, R. C. (2015). Role of veinphases in nanoscale sequestration of U, Nb, Ti, and Pb during the alteration of pyrochlore. Geochim Cosmochim Acta. 150: 226–252.

[2] Ewing, R. C., Weber, W. J. and Lian, J. (2004). Nuclear waste disposal—pyrochlore ($A_2B_2O_7$): nuclear waste form for the immobilization of plutonium and “minor” actinides. J. Appl. Phys. 95(11): 5949–5971.

[3] Lumpkin, G. R. (2012). Comprehensive Nuclear Materials. V.5: Material Performance and Corrosion. Waste Materials, pp. 563–600.

[4] Bogdanov, R. V., Skriplev, M. I., Petrunin, A. A. and Titov, A. V. (2013). The Thermochemistry of Uranium and Cerium in Native Britholite. J. Nucl. Mater. 440(1–3): 440–444.

[5] Hosseinpour Khanmiri, M. and Bogdanov, R. V. (2018). Nuclear chemical effects in the paragenetic mineral association based on polycrase. Radiochem. 60: 79–91.

[6] Hosseinpour Khanmiri, M., Goldwirt, D., Platonova, N., Janson, S., Polekhovsky, Yu. and Bogdanov, R. (2018). On the identification of Ti-Ta-Nb-oxides in "Wiikites" from Karelia. Mining of Mineral Deposits 12(1): 28–38.

[7] Hosseinpour Khanmiri, M., Yanson, S. Yu., Fomin, E. V., Titov, A. V., Grebeniuk, A. V., Polekhovsky, Yu. S. and Bogdanov, R. V. (2018). Uranium as a possible criterion for the hydro-chemical alteration of betafite. Phys. Chem. Miner. 45(5): 549–562.

[8] Skriplev, M. I., Bogdanov, R. V. and Schwink, L. R. (2017). Non-Identical thermochemical behavior of ^{234}U- and ^{238}U- isotopes in metamict britholite. Appl. Radiat. Isot. 119: 1–5.

[9] Marhol, M. (1982). Ion Exchangers in analytical chemistry: Their properties and use in inorganic chemistry, Amsterdam: Elsevier Scientific.

[10] О. Самуэльсон. Ионообменные разделения в аналитической химии. (1966). 288–301. (O.Samuelson. Ion exchange separation in analytical chemistry. (1966). 288–301) (in Russian).

[11] Bogdanov, R.V., Puchkova, E. V., Parnikov, N. G., Sergeev, A.S. (2011). Radiogenic uranium in paragenetic mineral associations, Radiochemistry. 53: 651–661.

[12] Hosseinpour Khanmiri, M. The modelling investigation of wiikit ore as radioactive waste matrices by studying behavior of its U and Th atoms. (2017). J. of Nuclear Sci. and Tech. 80: 44–52.

[13] Hosseinpour Khanmiri, M., Bogdanov, R., Titov, A., Fomin, E., Samadfam, M, Outokesh, M. The tendency towards equalization of the ^{234}U/^{238}U isotopic activity ratios in fractions of U(IV) and U(VI) during thermal annealing of metamict polycrase. (2024). Appl. Geochem. 161: 105881.

ICNST 2024 International Conference on Nuclear Science and Technology
6 - 8 MAY 2024 | Isfahan, Iran

Investigating the effective factors in the stability of emulsion liquid membrane used in uranium extraction in sulfuric acid media (Paper ID : 1371)

A.Heydari [a]*, M.R. Yaftian [a], J. Safdari [b], M. Raji[c]

[a] *Department of Chemistry, Faculty of Science, Zanjan University, Zanjan, 45371-38791, Iran.*

[b] *Nuclear Fuel Cycle Research School, Nuclear Science and Technology Research Institute*

[c] *Center for Separation Processes Modeling and Nano-Computations, School of Chemical Engineering, College of Engineering, University of Tehran, Tehran, Iran*

Email: amirheydari@znu.ac.ir

Abstract

In the present study, along with various influencing parameters in uranium extraction from aqueous solutions by using a water-in-oil (W/O) emulsion liquid membrane (ELM), effective factors in membrane stability, including breakage and swelling, were investigated. The ELM constitutes kerosene as an organic diluent, Di-(2-ethylhexyl) phosphoric acid (D2EHPA) as a carrier, sorbitan monooleate (Span-80) as a surfactant for stabilizing the emulsion phase, sulphuric acid as a stripping solution and potassium chloride (KCl) as a tracer. The study aims to give a comprehensive account of various parameters that affected the ELM formation and stability for increasing the extraction of U(VI).

Response surface methodology (RSM) based on central composite design (CCD) is carried out to explore the relationships between process variables namely initial pH of the donor phase, sulphuric acid concentration in the acceptor phase, surfactant concentration in the liquid membrane phase and mixing speed, and their interactions. The contours and 3D response surfaces of breakage and swelling of ELM were achieved.

The operational parameters mentioned above were optimized for achieving the minimum emulsion breakage and swelling and increasing the efficiency of the emulsion in order to increase the extraction.

The effect of the selected factors and the effect of their interactions were studied to obtain the optimal conditions. The optimized results are the Span 80 volume percentage 2% (V/V), sulfuric acid concentration 0.6 mol/L, pH of donor phase 3, and mixing speed 180 rpm.

With these conditions, the measured values of emulsion breakage and swelling were 0.39% and 3.50%, respectively.

Keywords: U(VI), emulsion liquid membrane, breakage, swelling, Response surface methodology

1. Introduction

Nuclear fuel is economically important compared to other fuels and the heavy metal uranium plays a significant role in this matter [1,2]. Uranium (VI), due to the radioactivity, long half-life, and chemical toxicity, is an important element in the radioactive wastes that must be removed [3].

Uranium enters the body causing kidney disease and toxicity to the bones. According to the law of the World Health Organization (WHO), the maximum contamination level (MCL) of U(VI) ions in drinking water is 30 μg L^{-1} as the permissible limit of uranium concentration. In addition to the importance of industrial wastewater treatment to protect the environment from the risk of emission of radioactive contaminants, uranium separation for reuse in the nuclear fuel cycle is an important and strategic issue [4]. Therefore, extraction, separation and recovery of this metal is very important. Several physical and chemical methods, including biological methods, liquid-liquid extraction, ion exchange, precipitation, resin extraction, electrolysis, etc., have been used and evaluated in this regard. Solvent extraction is the most well-known method for uranium recovery due to the specific formation of the metal-organic complex and the specific separation of the metal, as well as the recovery and reuse of the organic solvent in the process [4,5]. But if the uranium concentration is less than 1 $g.L^{-1}$, the mass transfer driving force for extraction is low, so this process is not an economical method, because a large solvent is required [6]. Therefore, a lot of research was done to replace other separation techniques [7]. One of these methods is the use of liquid membrane (LM). In the LM technique, generally two aqueous phases which is immiscible with the donor and receiving phases are kept in contact with each other via an organic phase consisting of an extractant and an appropriate solvent [3]. The LM techniques can be categorized as non-dispersion [bulk liquid membrane (BLM) and supported liquid membrane (SLM)] or dispersion [emulsion liquid membrane (ELM)] techniques. ELM that first invented by Li (1968) offers a promising technology for the separation of heavy metal ions from aqueous effluent streams [8].

ELM is a multiple water-in-oil-in-water (W/O/W) emulsion system which is prepared using three main phases of membrane, internal (receiving) phase, and external (donor) phase. The primary water-in-oil (W/O) emulsion was formed by homogenizing the internal phase into the membrane phase [9]. The membrane phase contains carrier and surfactant, dissolved in a diluent and the internal phase contains stripping agent. The existence of surfactant as an emulsifying agent is more important to have a stable emulsion. The prepared emulsion was then dispersed in the external phase which forms the W/O/W emulsion system [10,11]. By contacting feed phase and emulsion globules, solute is transported through

the membrane into the internal aqueous phase and is then concentrated. The transport of heavy metal ions from the external phase to the internal phase follows the facilitated transport mechanism. Figure 1 shows a schematic for the formation and phase separations of ELM system.

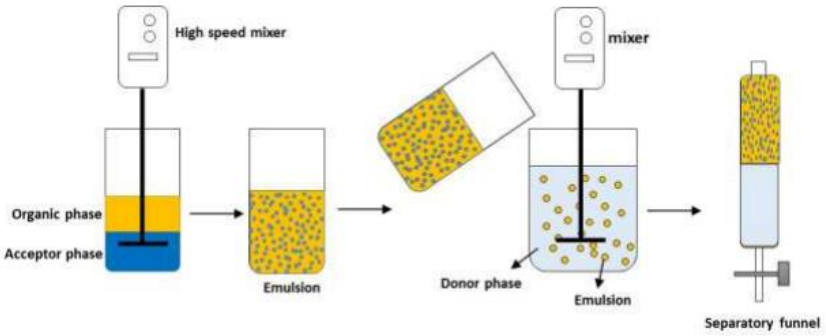

Figure 1: Schematic representation of the steps involving in an ELM process

The solute in the feed phase forms a complex with the carrier at the membrane and feed phase interface, the complex then diffuses through the membrane to reach the internal phase interface where a stripping reaction is occurred to prevent the solute from returning back to the external phase and also to regenerate the carrier molecules as well. The regenerated carrier then diffuses back to the membrane and external interface to extract the solutes again So, unlike the solvent extraction method, only a small amount of carrier is required in the liquid membrane system for separation processes [12]. Other advantages of ELM system are simplicity of the process, less energy consumption, less extractant consumption, considerable efficiency, combining extraction and stripping steps into a single step and larger interfacial area. ELM technology is an advanced separation method for recovery of elements [4,12].

Despite its high extraction rate and efficiency ELM industrial application is limited [13]. Controlling the emulsion's instability during the process is the most important challenge for commercializing this technology. Two major causes of the emulsion instability are emulsion swelling and emulsion breakage. Emulsion swelling refers to the case that the feed phase diffuses through the membrane into the stripping phase (internal phase) causing its dilution and hence decreasing the mass transfer driving force and extraction efficiency. With transporting water into the internal phase, the emulsion globule size increases causing a loss in mass transfer surface area as well as the extraction efficiency [12]. Swelling also increases the viscosity of the emulsion making it hard to handle and transport for demulsification [14]. The emulsion breakage is referred to the rupturing of the emulsion globules as a result of the shear forces entering the emulsion globule's surface. Breakage causes the leakage of the internal phase into the external phase resulting in loss of concentrated solute, reduction of driving force for mass transfer and

the extraction capacity of the emulsion, therefore nullifying the separation efficiency. After all, the emulsion instability is somehow inevitable but it can be reduced and controlled during the process. Generally, there can be two approaches for controlling the emulsion instability. The first approach is using proper operational parameters in order to minimize the instability. There are several parameters in the ELM process that can directly affect the emulsion stability. The most role-playing parameter is the surfactant type and its concentration, other parameters include the emulsion residence time, feed phase pH and concentration, stirring speed, extractant and stripping agent concentrations and the volume ratio of internal phase to membrane phase. The second approach for minimizing the ELM instability is application of other ingredients as stabilizers. This could be done either by adding water soluble surfactants to external or internal phases to encapsulate the emulsion globules, or by changing the membrane's rheological properties for further stabilization of the ELM. By adding a surfactant to an ELM system even at low concentration, the surface tension decreases and the average size of the globules decreases, therefore the coalescence decreases and the stability the emulsion improves [7,12,15].

2. Experimental

2.1. Materials and apparatus

All chemicals were of analytical grade and were used as received without further purification. Aqueous solutions were prepared with distilled water. Kerosene (reagent grade) as the diluent and sorbitan monooleate (Span-80) as the surfactant were procured from Sigma-Aldrich (Schnelldorf, Germany). The mobile carrier di-(2-ethylhexyl) phosphoric acid (D2EHPA) was purchased from Merck (Darmstadt, Germany). Uranyl nitrate ($UO_2(NO_3)_2.6H_2O$), sulfuric acid, nitric acid, potassium chloride, and sodium hydroxide were purchased from Merck.

A homogenizer, type Ultra-Turrax IKA T18 (Germany), was used for the emulsion preparation. For the pH measurement of aqueous solutions, a pH meter (Metrohm 780) was used. The concentrations of K(I) and U(VI) in aqueous solutions were measured by using inductivity coupled plasma-atomic emission spectrometry (ICP-AES, Optima 7300 DV, USA). A Labcon Incubator was used to break the emulsion into the primary organic and aqueous phases.

2.2. Experimental Procedure

2.2.1. Emulsion preparation

Emulsions were prepared by emulsifying an aqueous solution of the stripping phase with an organic phase. For preparing the ELM, firstly, the surfactant Span 80 (0.5-3.5 %v/v) was dissolved in kerosene. Then the carrier D2EHPA is added to the mixture with desired concentration to make the membrane phase. Then, the tracer K(I) with 1000 ppm concentration and sulfuric acid solution (0.1 to 2.1mol/l) were dissolved in distilled water to prepare the internal phase. To make a primary W/O emulsion, an equal volume of 30 ml portions of organic solution (membrane phase) and an aqueous acid solution (stripping phase) were emulsified using a homogenizer. The internal phase was added dropwise to the membrane phase. The mixture was stirred continuously at 12000 rpm for 15 min to obtain a milky-white stable emulsion. The fresh emulsion was prepared each time before performing the experiments.

2.2.2. Feed phase preparation

To prepare the feed solution, uranyl nitrate solution with uranium concentration of 50 ppm was prepared with dissolving into distilled water. For long-term storage of the stock solution, concentrated nitric acid was added to bring its pH to about 1. Nitric acid and caustic soda were used for further regulation of the feed phase solution's pH.

The prepared emulsion was smoothly dispersed into mixing chamber with feed phase solution. After that, the treated feed solution was separated from the emulsion and the concentrations of U(VI) and the tracer K^+ in the external and internal phases were analyzed.

After permeation, the emulsions are separated from the feed phase and their breakage (demulsification) is usually performed by thermal or electrical or other methods.

2.3. Experimental design

In order to uranium extraction by the emulsion method, the prepared emulsion should be stable and have good conditions and characteristics for extraction and stripping by using the optimization of effective factors.

In this study, CCD and RSM were applied to determine the optimum levels of the parameters affecting the presented ELM process. It was used to assess the significance of operating parameters on the system response and sets a correlation between them and the system response. Eventually, it was utilized to obtain optimum amounts of operating parameters on the system response. The design of experiments was performed with five responses, namely U(VI) extraction, breakage, swelling, stripping percents, and

distribution coefficient (Kd). An orthogonal 24 factorial central composites experimental design with eight-star points (α =2) and six replicates at the center point, all in duplicates, resulting in a total of 30 experiments were used to optimize the chosen key variables for ELM stability and extraction of U(VI). To describe the surfactant concentration (A), acceptor phase concentration (B), initial feed phase pH (C), and mixing speed (D) on the ELM stability and percentage of U(VI) extraction, batch experiments were conducted.

3. Result and Discussion

3.1. Effect of surfactant concentration

The success of the ELM process is determined by selecting the surfactant type and its concentration correctly. At lower surfactant concentrations, the surfactant content in the organic membrane is not enough to stabilize the emulsion. Hence, the emulsion is broken easily due to inadequate adsorption of surfactant on the organic–aqueous interface. The increase in surfactant concentration lowers the surface tension of the membrane and yields smaller globules which leads to a higher contact area. It can be seen that the extraction efficiency increases with increasing surfactant concentration up to certain level and decreases thereafter. high concentration of surfactant tends to hydrolysis of Span 80, aggregation of surfactant molecules and formation of reverse micelles, which led to transport of water molecules to internal phase called as osmotic swelling. Thus, the osmotic swelling ratio increased, and emulsion stability decreased. Accordingly, in all the following ELM extraction experiments, the applied surfactant level would be fixed at only 2 v/v% Span 80, as shown in Fig.2(a), (b), (c).

3.2. Effect of internal phase concentration

The stripping reaction in the acceptor phase plays a vital role in the transport of metal ions from the donor phase to the stripping phase. To investigate the effect of sulphuric acid concentration as the internal phase on the uranyl extraction, the concentration values were varied from 0.1 to 2.1 M. Increasing the internal phase concentration led to more efficient stripping of U(VI). Increase of ionic strength difference between internal and external phase led to swelling of the emulsion which caused dilution of the internal phase. Thus, the stripping of U(VI) abruptly decreases. The 0.6M sulphuric acid was selected as optimum internal phase agent as shown in Fig.3 (a), (b), (c).

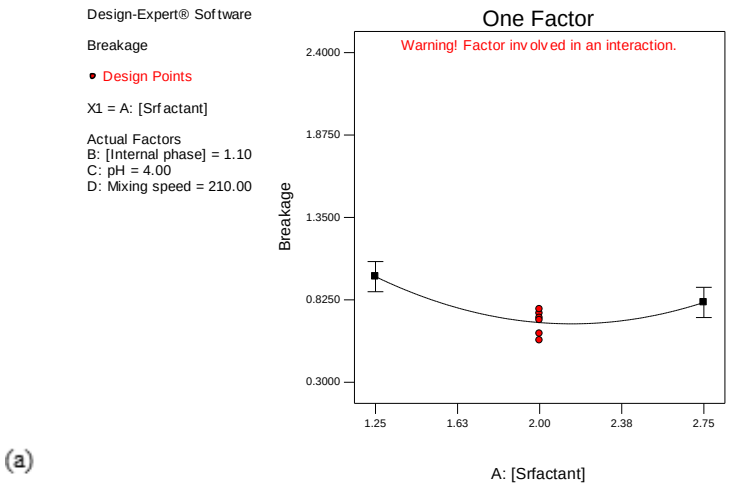

(a)

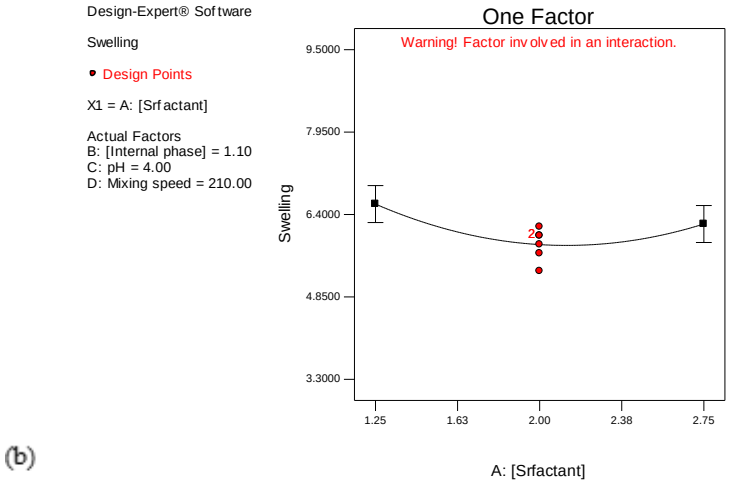

(b)

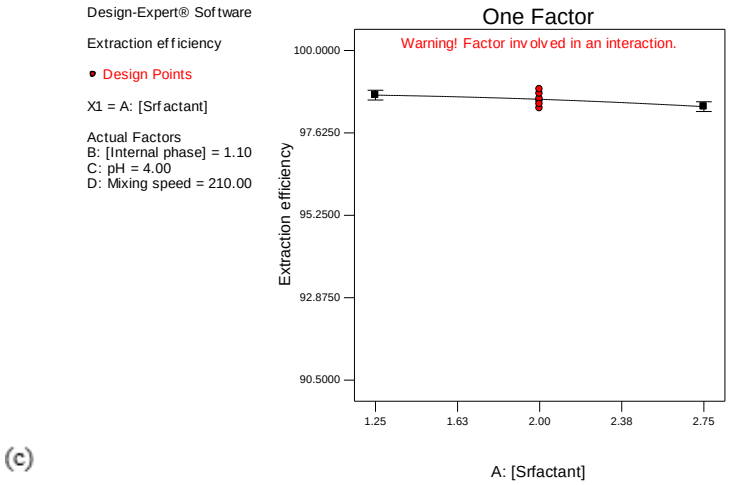

(c)

Figure 2 (a), (b), (c): Investigation of the surfactant concentration effect on ELM stability and extraction efficiency.

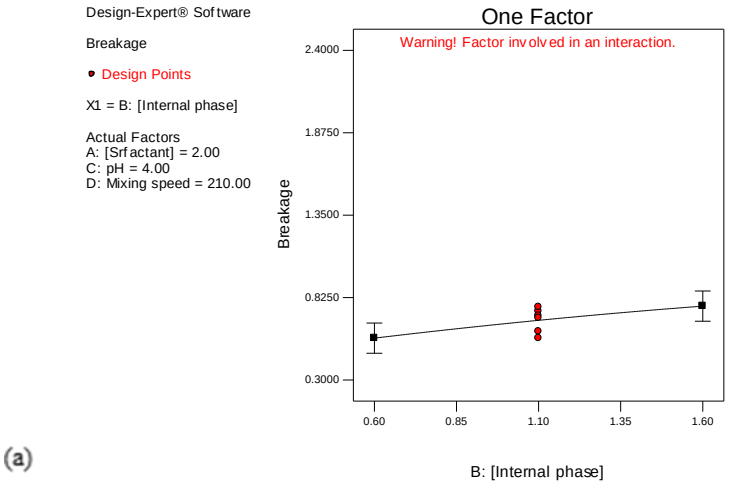

(a)

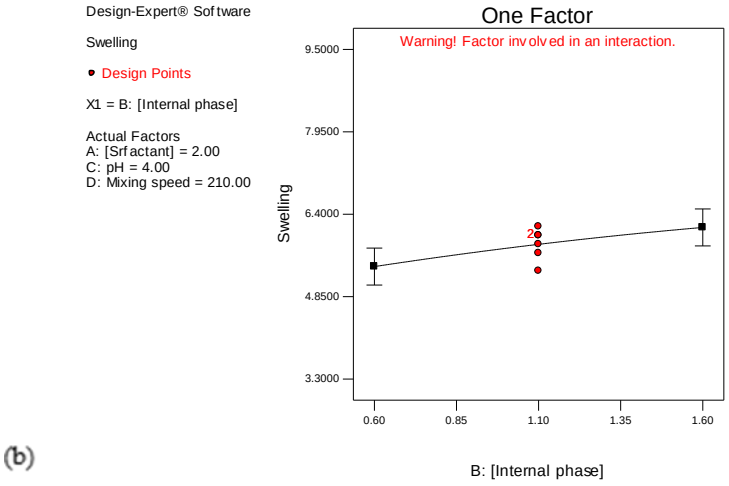

(b)

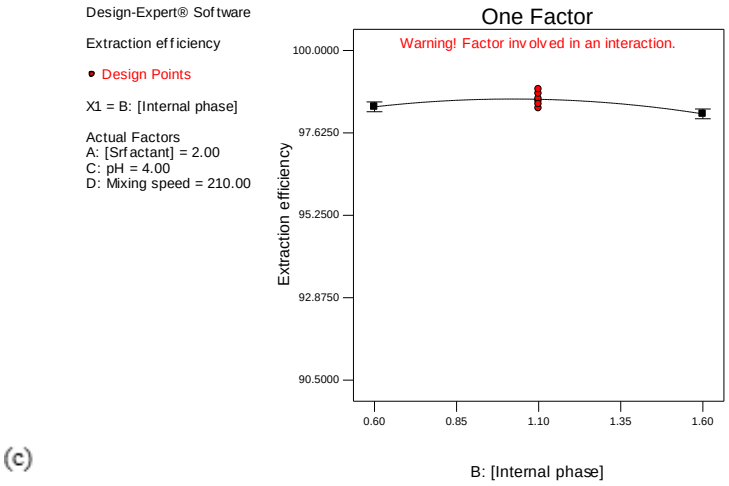

(c)

Figure 3(a), (b), (c): Investigation of the acceptor phase concentration effect on ELM stability and extraction efficiency.

3.3. Effect of initial pH of the feed phase

The extraction efficiency of U(VI) are strongly dependent on the acidity in the external phase solution. The extraction of U(VI) occurs by the replacement of hydrogen ions of the carrier. The effect of pH in the donor phase on transport of U was studied in a pH range of 2.0 to 6.0. It was found that by increasing pH of the feed phase from 2 to 3, percentage extraction as well as stripping of uranium is increased. Therefore, overall maximum extraction and stripping of uranium is found at pH 3, which is obviously attributed to less swelling and breakage of emulsion as shown in Fig.4 (a), (b), (c).

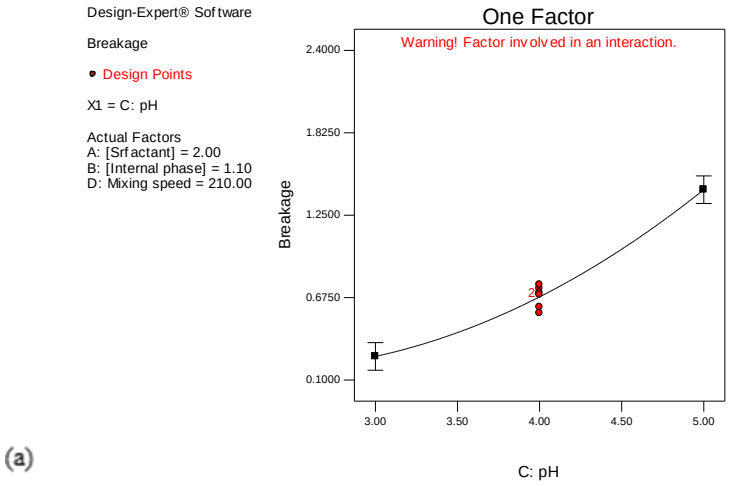

(a)

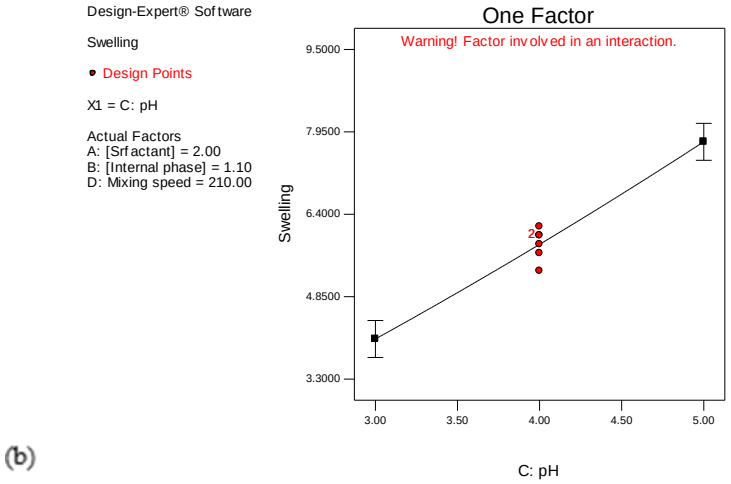

(b)

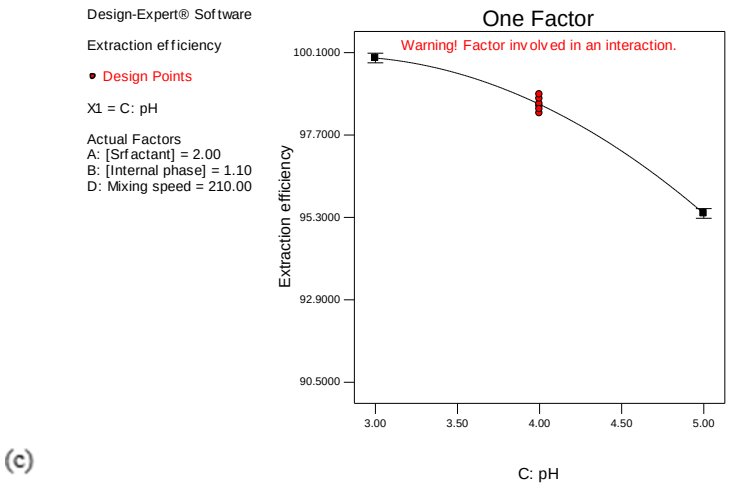

(c)

Figure 4(a), (b), (c): Investigation of the effect of pH of the feed phase on ELM stability and extraction efficiency.

3.4. Effect of mixing speed

The mixing speed is a key factor at membrane stability and in the mass transfer rate through ELM. With rising the stirring rate, the emulsion drop size becomes smaller and more surface area is available for mass transfer so more uranyl ions are extracted [12]. Meanwhile with further increasing the agitation speed, the emulsion swelling and breakage values intensify due to more entrainment and shear forces entering the globule's surface. Consequently, the extraction efficiency is adversely affected. From 150 rpm to 270 rpm, 6 levels selected and investigated for the effect of mixing speed behavior and finally 180 rpm was selected as optimum mixing speed as shown in Fig.5 (a), (b), (c).

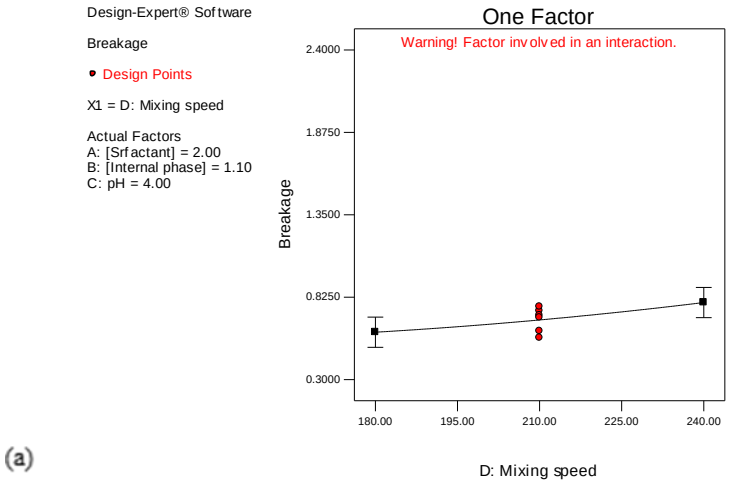

(a)

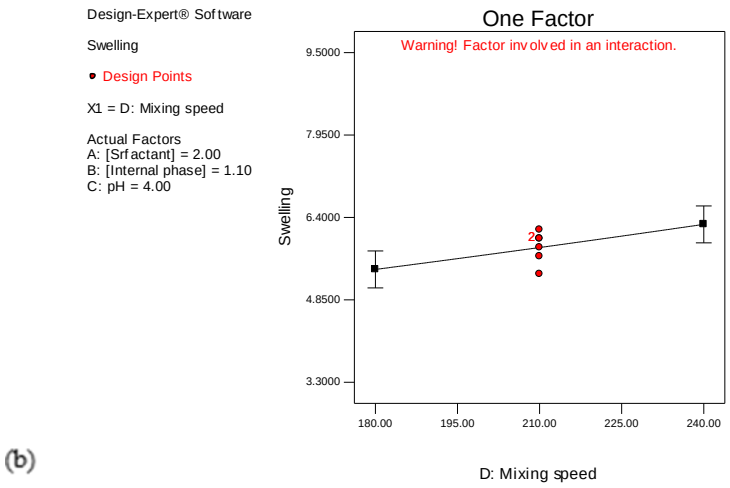

(b)

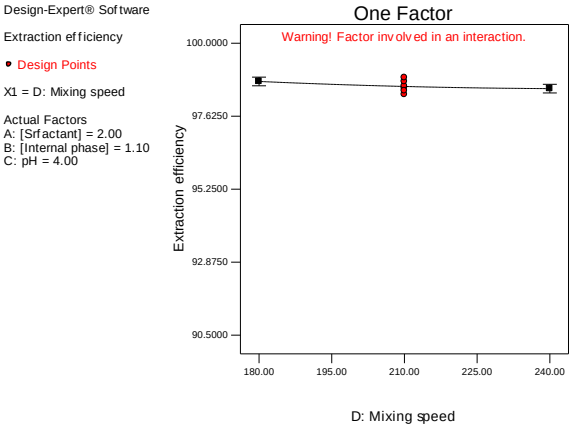

(c)

Figure 5 (a), (b), (c): Investigation of the stirring speed effect on ELM stability and extraction efficiency.

4. Conclusion and Recommendations

The objective of the proposed research is to evaluate the technical feasibility of pertraction of U(VI) from aqueous solution by ELM process consisting of kerosene as the organic diluent, Span 80 as the non-ionic surfactant, D2EHPA as the carrier and H2SO4 aqueous solution as the internal phase using RSM by CCD. Results indicated that the ELM stability is directly influenced by the surfactant concentration. Furthermore, under the optimum conditions from RSM and excess experiments, the extraction efficiency of 99.94% was obtained within 15 min, and the measured values of emulsion breakage and swelling were 0.3902% and 3.5%, respectively, at feed phase pH=3, surfactant concentration= 2 V/V%, acceptor phase concentration=0.6 mol/1 and mixing speed=180 rpm (table 1).

Table 1: The optimal results of the obtained factors and responses

Range of Operating parameters		Optimum value		Optimum Results	
[surfactant] (V/V %)	0.5, 1.25, 2, 2.75, 3.5	[surfactant]	2	Extraction	99.94%
[acceptor phase] (mol/L)	0.1, 0.6, 1.1, 1.6, 2.1	[acceptor phase]	0.6	Breakage	0.3902%
feed phase pH	1, 2, 3, 4, 5	pH	3	Swelling	3.5 %
mixing speed (rpm)	150, 180, 210, 240, 270	mixing speed	180	Stripping	87.99% - 99.67%

Referencess

1. Diehl P., (2011). Uranium mining and milling wastes: an introduction. World Information Service on Energy

2. Durazzo M., (2017). Manufacturing low enriched uranium metal by magnesiothermic reduction of UF4. Annals of Nuclear Energy, 07.033, 874–885.

3. Zaheri, P. and R. Davarkhah, (2017) Rapid removal of uranium from aqueous solution by emulsion liquid membrane containing thenoyltrifluoroacetone. Journal of environmental chemical engineering, 5(4): p. 4064-4068.

4. Beni, A.A., (2021). Design of a solar reactor for the removal of uranium from simulated nuclear wastewater with oil-apatite ELM system. Arabian Journal of Chemistry, 14(2): p. 102959.

5. Ghaemi, A. and A. Hemmati, (2021). Experimental investigation of uranium extraction from the industrial nuclear waste treatment plant by tri-butyl-phosphate. Journal of Radioanalytical and Nuclear Chemistry, 327(3): p. 1237-1249.

6. Davoodi-Nasab, P., (2018). Evaluation of the emulsion liquid membrane performance on the removal of gadolinium from acidic solutions. J. Mol. Liq. 262, 97–103.

7. Zereshki, S., (2018). Application of edible paraffin oil for cationic dye removal from water using emulsion liquid membrane. J. Hazard. Mater. 356, 1–8.

8. Zahakifar, F., (2018). Kinetic study of uranium transport via a bulk liquid membrane containing Alamine 336 as a carrier. Journal of Radioanalytical and Nuclear Chemistry, 316(1): p. 247-255.

9. Benderrag, A., (2019). Experimental and modeling studies on Cd (II) ions extraction by emulsion liquid membrane using Triton X-100 as biodegradable surfactant. J. Environ. Chem. Eng. 7, 103166.

10. Ferreira, L.C., (2019). Mn (II) removal from water using emulsion liquid membrane composed of chelating agents and biosurfactant produced in loco. J. Water Process Eng. 29, 100792.

11. Mhmmd, S., (2014). ChemInform abstract: phenol removal from industrial wastewaters: a short review. Desalin. Water, Treat. 53, 2215–2234.

12. Ardehali, B.A., (2020). The effect of operational conditions on the stability and efficiency of an emulsion liquid membrane system for removal of uranium. Progress in Nuclear Energy, 130: p. 103532.

13. Kohli, H.P., (2019). Stability and performance study of emulsion nanofluid membrane: A combined approach of adsorption and extraction of Ethylparaben. Colloids Surf., A 579, 123675.

14. Ahmad, A., (2011). Emulsion liquid membrane for heavy metal removal: An overview on emulsion stabilization and destabilization. Chem. Eng. J. 171, 870–882.

15. Davoodi-Nasab, P., (2019). Simultaneous effect of nanoparticles and surfactant on emulsion liquid membrane: Swelling, breakage and mean drop size. Sep. Purif. Technol. 219, 150–158.

ICNST 2024 International Conference on Nuclear Science and Technology
6- 8 MAY 2024 | Isfahan, Iran

Determination of the real drag force in a gas centrifuge machine using the DSMC method in three-dimensional conditions (Paper ID : 1442)

S. Basiri[1]*, J. Safdari[2], S. M. Ghoreishi[1], S. Yousefi-nasab[2]

Isfahan University of Technology (IUT), Department of Chemical Engineering, Isfahan, Iran.P.O.Box:8415683111.
Nuclear Science and Technology Research Institute, Nuclear Fuel cycle Research School, Atomic Energy Organization of Iran, P.O.Box:11365-08486, Tehran, Iran.

Abstract

In recent years, the demand for the production of stable isotopes with high richness has increased. One of the common industrial methods for isotope separation and increasing the richness of certain isotopes is the separation method using a gas centrifuge. It is common to use simulation tools in order to reduce the manufacturing costs of gas centrifuge machines. In this regard, simulating the centrifuge machine in axially symmetrical conditions is many uses in its optimization. But due to the three-dimensional geometry of the scoop inside the rotor, the modeling of this part is only possible by simulation in 3D conditions and considering the simplifying assumptions in the simulation of this piece in axially symmetrical conditions (considering the geometry of the scoop in the disk form), a considerable error enters the calculations. Because in the axially symmetric simulation, the drag force as the main factor in creating the axial flow and increasing the separation factor is determined based on the maximum separation power, the actual value of this parameter is not calculated. For this reason, in order to calculate the real value of this important parameter, in this article, the 3D simulation of the centrifuge machine has been discussed and by comparing its results with the axially symmetric simulation, it was determined that the difference between the actual drag force in the 3D mode and its hypothetical value in the axially symmetric simulation is 23% for the product scoop and 21% for the waste scoop.

Keywords: 3D simulation, Gas centrifuge, DSMC Method, Drag Force, Axially symmetric simulation

Introduction

Separation of multicomponent gases and their different isotopes from each other is one of the basic applications of gas centrifuge machine. Centrifuge machine uses the principle of centrifugal force to create a gradient in the physical properties of gas components, including molecular mass or density, and separates them according to the desired goals. One of the major applications of gas centrifuge in the industrial process is uranium enrichment. In this process, uranium hexafluoride gas is injected into a cylinder that rotates at high velocity inside a vacuum chamber. After the gas molecules are affected by the centrifugal force, particles with higher molecular mass accumulate near the rotor wall and particles

with lower molecular mass accumulate in the area of the rotor axis. In this way, the primary separation is done in the radial direction inside the rotor[1].

The separation coefficient in radial separation is very low; in order to increase this coefficient, axial flow should be created followed by axial separation. In order to increase the isotopic separation in the axial direction, a countercurrent flow is added to the overall flow inside the rotor. This countercurrent flow is created and controlled by the use of drives[2]. The drives inside the rotor include mechanical drives (scoop and baffle), thermal drives (the temperature difference of the caps and rotor wall temperature gradient) and sink and source drives (feed, product and waste scoop)[2, 3].

One of the most important drives is the mechanical drive of the scoop, which, in addition to harvesting enriched and depleted uranium inside the rotor, also increases the efficiency of isotope separation by creating a countercurrent flow. The rotating gas hits the scoop and loses its angular momentum. Then the gas moves along the rotor wall, and a countercurrent flow is created[4].

When the gas hits the body of the scoop, the drag force is applied to the gas in the opposite direction from the side of the scoop, and this force is the origin of the gas countercurrent flow. The geometry of the scoop inside the rotor is in the form of a curved tube, and for this reason its drag force can be accurately calculated using 3D simulation[5].The drag force directly affects the axial flow inside the rotor. Considering that in axially symmetric models, the geometry of the scoop is considered as a disk, the amount of drag force calculated from this simulation will not have an accurate value[6].

Sakurai in 1981 investigated a steady supersonic swirling flow of complete gas around thin scoops in an annular gas centrifuge. He solved the basic equations, boundary conditions and shock conditions for a weak supersonic flow by a linearized analytical method. This solution provided a simple summation theory for determining scoop drag force, which makes the resulting drag force of a multi-scoop system equal to the product of the number of scoops and the drag force of a standard single-scoop system. This solution, despite the above summation theory, determined that scoops interact in their effects on flow[7]. In 2000, Kai performed the separation efficiency of centrifuge machine with SF6 gas by numerical finite difference solution. In this study, compressible equations (in steady state and axially symmetric conditions) and diffusion equation were used. To determine the optimal value of separation efficiency; variations in feed flow rate, temperature difference between the end caps, drag force at the inlet of the product scoop, thickness of the scoop and the radius of the waste baffle holes were investigated[8]. In 2000, Borisevich simulated the flow of uranium isotopes in a supercritical gas centrifuge using a

numerical method in 2D conditions. He numerically solved the Navier-Stokes and diffusion equations using the finite difference method to study the effect of vacuum conditions on the flow and separation power of uranium isotopes in a supercritical gas centrifuge. He showed; the dependence of the separation power of the machine on the geometric parameters and the position of the bellows are as important as the drag force of the scoop and the feed flow[9].In 2016, Borman at al. did a 3D simulation of gas dynamics in a gas centrifuge machine using the CFD method. The results showed that the flow near the scoops creates strong shock waves. In this simulation and other 3D simulations done with the CFD method, the axis area has been ignored[10]. In 2018, Zhang and et al. investigated the effect of the scoop on the gas flow inside the rotor in an axially symmetric state using a numerical method. The scoop was modeled as a sink and source in one case and as a disk in another case and compared with each other[6].In 2019, Khaje Nouri and et al. simulated the feed flow and the flow around the scoops in the centrifuge using the DSMC method and in 2D conditions. They investigated the effect of feed and scoop drag force on each other[11].In 2021, Yousefinaseb et al. investigated the effect of the scoop drive and the polymer surface of the rotor on the separation power of a centrifuge machine using the combined simulation method of two MD-DSMC methods in 2D. Their results showed that for the rotational velocity reduction factor of 0.84, the amount of separation work unit reaches its maximum value and also the material of the rotor surface is also an influencing factor on the amount of separation power of a centrifuge machine[12].In 2022, Bogovalov and et al modeled the flow around the scoop of the Iguassu model gas centrifuge with ultra-fast rotation under optimal and 3D conditions. Their results showed that at the high velocity of the rotor (1500 m/s), the temperature of the shock wave gas (1356 K) increases to a significant amount, at which the uranium hexafluoride gas may be decomposed[13].

In this way, in centrifuge machines, the scoop drag force is one of the basic factors in creating axial flow. This force is basically created by a scoop inside the centrifuge, and according to its amount, the jump of particles after hitting the scoop will be variable. Increasing or decreasing the drag force of the scoop can lead to improved separation efficiency and reduced costs. The scoop drag force is considered as an important parameter in centrifuge design and performance. The centrifugal force of the centrifuge and the physical and geometric characteristics of the scoop directly affect the amount drag force of the scoop. The amount of drag force in a gas centrifuge depends on the following:

Centrifuge rotation velocity: higher rotation velocity increases the drag force and thus the axial flow is stronger.

Design of scoops: the geometrical shape, number and position of scoops inside the centrifuge also have a great effect on the drag force.

Density of materials: the density of materials inside the centrifuge also affects its drag force and axial flow.

One of the main factors affecting the amount of drag force is the geometric shape of the scoop. In this regard, it is common to use simulation tools in order to reduce the costs of manufacturing gas centrifuge machines. Simulating the flow inside the centrifuge machine in axially symmetrical conditions has many applications in parameter optimization. But due to the fact that in axially symmetric simulations, the geometry of the scoop is taken into account in the form of a disk, which is very far from its actual form, a considerable error enters the calculations. Since in the axially symmetric simulation, the drag force is determined as the main factor in creating the axial flow and increasing the separation coefficient based on the maximum separation power, the actual value of this parameter is not calculated. The geometry of the scoop is actually a bent tube. The gas molecules hit the scoop inlet in a rotational direction, and the scoop, in response to this collision, applies the drag force in the opposite direction to the gas molecules and throws the gas molecules in different directions. Applying the drag force of the scoop to the gas appears as shock waves around it.

For this reason, in order to calculate the real value of the drag force parameter, in this article, 3D simulation of the centrifuge machine was done using the DSMC method. By comparing the results of this research with the axially symmetric simulation, the difference between the real drag force in the 3D state and its hypothetical value in the axially symmetric simulation was obtained. The main target of this research is to determine the exact value of the drag force in order to use it in 2D simulations to optimize the geometric and operational parameters of the centrifuge machine.

DSMC method

Direct Simulation Monte Carlo is a molecular statistical simulation method that was introduced by Bird to solve the flow of dilute gases[14].

This method numerically solves dynamic equations for gas flow by using a large number of simulation molecules. Each simulation molecule is representative of a large number of real molecules. Assuming a dilute gas, only binary collisions should be considered, and as a result, if the computational time step is smaller than the physical collision time, motion and molecular collisions are considered separately. The

macroscopic characteristics of the flow are obtained statistically by sampling the molecular properties in each cell. At the beginning of the calculations, the simulated particles are uniformly distributed in the cells.

At each time step, all particles interact with the boundaries based on their velocity and then indexed. A certain number of collision pairs in each cell are selected using the No Time Counter (NTC) method to calculate the number of collisions. In order to increase the sample size, these steps are repeated until the statistical errors are sufficiently small[15-17].

The DSMC method uses probabilistic Monte Carlo simulation to solve the Boltzmann equation for fluid flow. The implementation of the DSMC method requires the decomposition of the computational domain into a set of grid cells[18]. In DSMC simulation, first, particles are uniformly dispersed in the system. The main algorithm of all DSMC solvers including dsmcFOAM for a time step ($t \rightarrow \Delta t$) is as follows[19]:

First stage: In this stage, the meshing and initialization of particles such as the number of particles, initial velocity, etc. are determined. First, the computational area is drawn and gridded in such a way that the direction of the particle placement, their movement and collisions are determined. Then, the initial values in the Cartesian coordinates is randomly placed in the calculation area. The position of all particles in the system is updated using the OpenFoam particle tracking algorithm. Also, the movement of particles across the mesh surfaces as well as the interaction with the boundaries is controlled.

Second step: The list of particles in each computational cell is updated to prepare for the collision step.

The third step: the number of collisions to be performed in each calculation cell is calculated and the collisions are performed according to the binary collision model defined by the user.

The fourth step: particle impact with the wall is checked based on the position of the particle and the boundary. In other words, due to the collision of the particle with the wall, its position and velocity are determined according to the type of boundary condition selected (diffusive, spectral and Cercignani-Lampis- Lord).

The fifth step: the particle positions, velocities, internal energies, etc., which are needed to calculate the macroscopic values, are sampled.

The sixth step: it returns to the first step where t=t+Δt and the steps are repeated until the end time of the simulation (tend) arrives.

3D simulation of the gas centrifuge machine

Geometry and meshing

The geometry and 3D grid of the centrifuge machine was drawn using Gambit software. In this work, two types of structured and unstructured meshes were used in combination. In order to reduce the error rate, the meshes next to the rotor wall were considered smaller than the average mean free path (less than

1.236 × 10−6(m)). After performing the mesh study test, the total number of meshes equal to 7375675 was chosen as the optimal number.

$$\lambda = \frac{K_B}{\sqrt{2}\pi d^2 p} = 1.236 \times 10^{-6}(m) \quad (1)$$

Where, K_B is Boltzmann's constant, T is the temperature, d is the diameter of the uranium hexafluoride molecule and p is the rotor wall pressure.

Determination of initial and boundary conditions

The velocity input boundary condition was set by applying "flowRateInletVelocity" as the feed input boundary condition into the rotor and the "flowRateOutletVelocity" boundary condition as the velocity output boundary condition, i.e. the output of the product and waste scoops. The velocity boundary condition for fixed surfaces was set as "fixedValue" and for rotating surfaces as "rotatingWallVelocity". "zeroGradient" boundary condition was also applied as velocity boundary condition for other unknown boundaries.

The temperature boundary condition was set by applying a linear temperature gradient on the rotor wall. For this purpose, the temperature on the rotor wall started from 300 K and increased linearly up to 325 K (according to Table 1). The boundary condition of the temperature at the entrance of the feed was considered constant.

Table 1. Temperature boundary conditions of the present problem

Boundary name	Temperature boundary conditions
Rotor wall	$\frac{\partial T}{\partial z} = 25$
Top cap	T=325 k (constant)
Bottom cap	T=300 k (constant)

Results and discussion

In order to determine the effect of the scoop on phenomena such as shock, the amount of drag force, pressure and velocity at the first moment and after the fluid hits the scoop and its influence on other parameters of the flow inside the rotor, 3D simulation of the entire rotor space with the presence of all its parts is is very important.For this purpose, in this article, the entire space inside the rotor of a gas centrifuge machine was investigated. The geometry inside the rotor examined in this study includes various components such as: bellows, rotor wall (side surface, top and bottom cap), baffle, parts of the gasification system (feed injection point, product scoop, waste scoop and gasification pipes).

As a result of the collision of gas molecules on the scoop inlet, variations are made in the flow parameters, including pressure and velocity. These variations indicate the occurrence of the shock phenomenon due to the application of the drag force by the scoop. That is why it is necessary to check them Figure 1 shows the velocity variations around the waste scoop (Z/ZH = 0.98) and the product scoop (Z/ZH = 0.011). As shown in this figure, due to the collision of gas molecules in the rotational direction with the scoop inlet, their velocity has decreased and reached zero in some places. In the time after the collision, the molecules around the scoop receive momentum through the molecules colliding with the rotor wall. In this way, after the collision, the velocity of the molecules around the scoop increases (Figure 1).

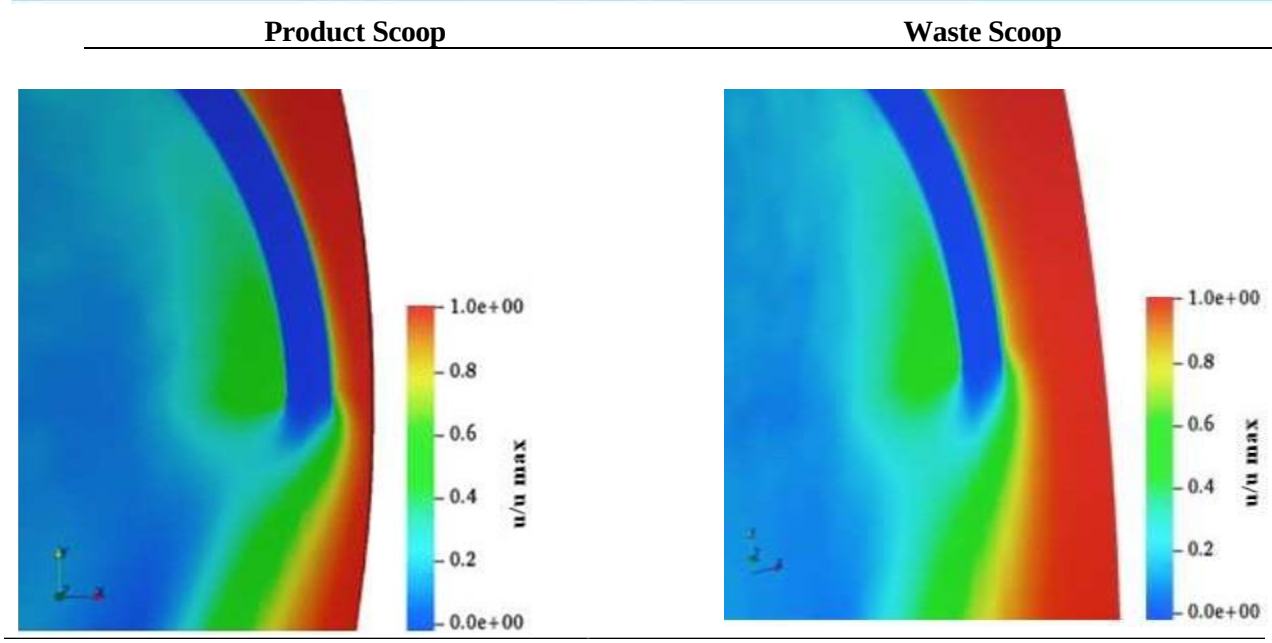

Fig. 1. Velocity variations around the waste scoop ($Z/Z_H = 0.98$) and the product scoop ($Z/Z_H = 0.011$)

Figure 2, shows the pressure variations around the waste scoop ($Z/Z_H = 0.98$) and the product scoop ($Z/Z_H = 0.011$). In this Figure, at the moment when the gas molecules collide with the scoop inlet and following the reduction of velocity by converting the kinetic energy of the molecules into internal energy, the pressure increases sharply. In the moments after the collision, the pressure has decreased in a stepwise manner.

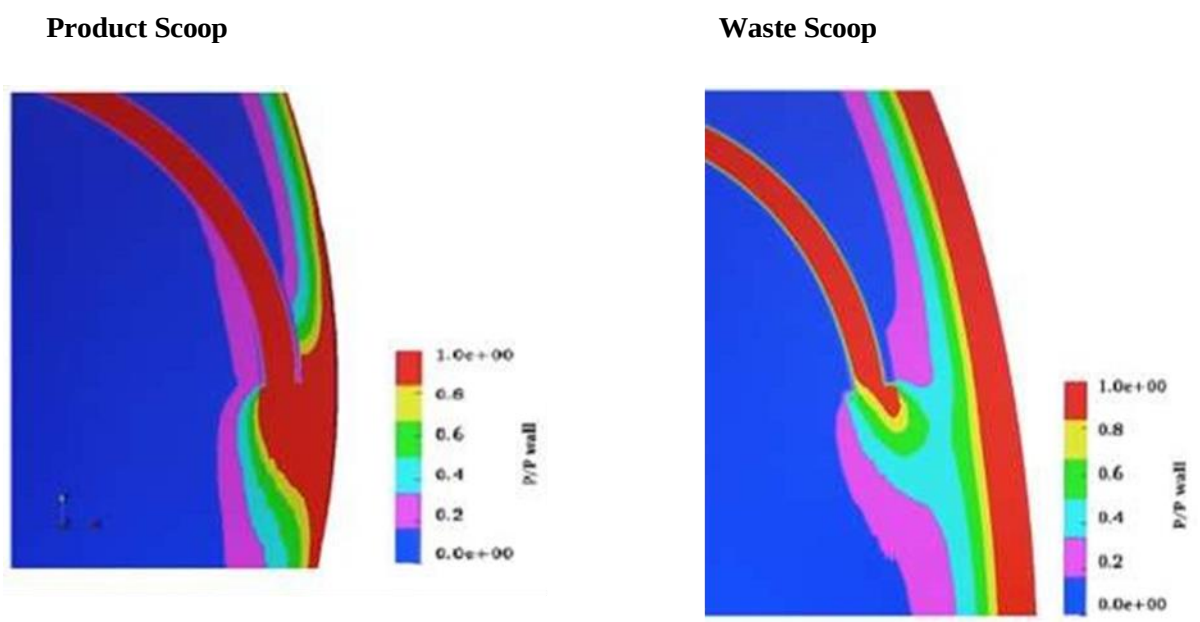

Fig. 2. Pressure variations around the waste scoop ($Z/Z_H = 0.98$) and the product scoop ($Z/Z_H = 0.011$).

Shock waves need two main characteristics:

Sudden variation of fluid properties: As it was investigated, from the inlet points of the scoop to after that (according to figures 1 and 2), a sudden variation in pressure and velocity has been created.

According to the definition of the shock phenomenon, as a result of a sudden variation in properties, especially pressure variations, there is an expectation of creating a cone wave (Mach cone) in a certain radius from the collision area. Due to the pressure and velocity gradients, the shock wave in the scoop area has caused a sudden jump of the fluid in this area in the form of a cone.

In Figure 3, the stream lines and the shock phenomenon around the waste scoop (parts b, Z/Z_H=0.98) and the product scoop (part a, Z/Z_H=0.011) are displayed. In addition, the conical lines created (Mach cone) due to the creation of shock waves and the sudden jump of the fluid due to the one-time gradients of the flow parameters are drawn in these two figures. Due to the high velocity of the rotor wall, the supersonic flow with high Mach hits the scoop and the shock phenomenon occurs around the scoop. Due to the occurrence of this shock phenomenon, at the moment the gas hits the scoop, the pressure increases and the velocity decreases. After the gas hits the scoop, the pressure drops and the rotational velocity of the gas molecules increases. The rotational velocity of the molecules, after hitting the thickness of the scoop inlet, decreases and approaches zero (this point is called the stagnation point). The rest of the molecules that hit the scoop inlet are also directed to the outside of the rotor through the scoop valve. Over time, other moving molecules collide with these stationary molecules, by transferring part of the kinetic energy, they will make them move. The geometric shape

and the radius of curvature of the scoop are important in the way of guiding the path of gas molecules in the axial flow. As a result, by jumping the current from the areas of the scoops, an axial flow is formed along the rotor. Considering that the distance between the product scoop and the rotor wall is considered to be about one third of the distance of the waste scoop, and as can be seen in the comparison of two parts (a) and (b) in Figure 3, due to the collision of the fluid with a stronger Mach to the

inlet of the product scoop, the axial flow formed around it also has a wider range than the waste scoop.

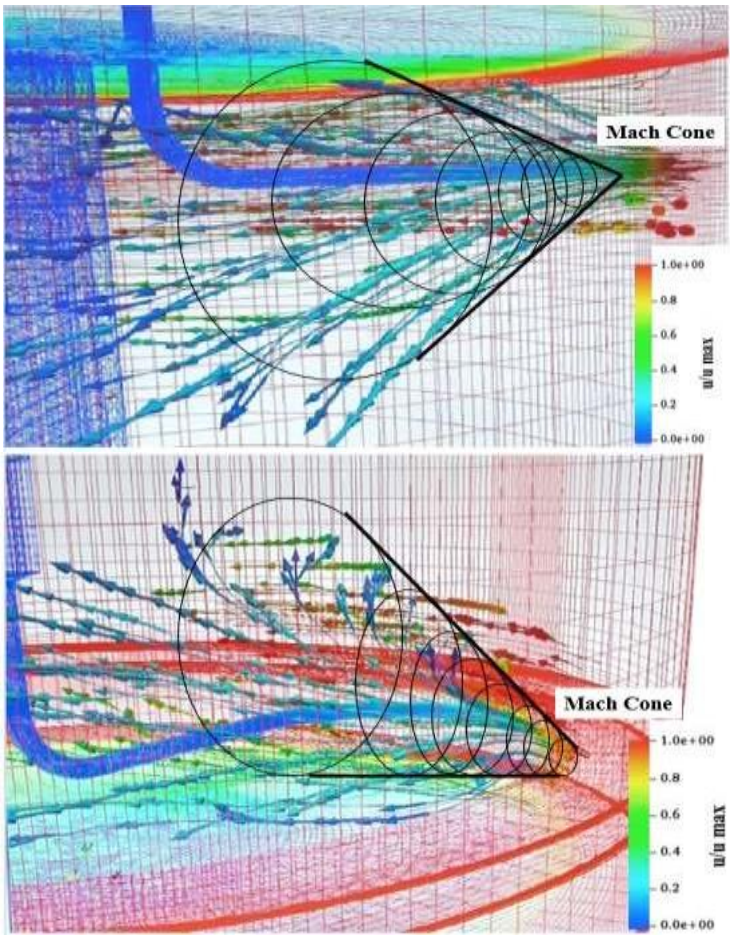

Fig. 3. Stream lines and shock waves around: a) the waste scoop (Z/ZH = 0.98) ,b) the product scoop (Z/ZH = 0.011)

In Figure 4, the diagram of the axial mass flux formed inside the rotor is drawn at two heights of the waste scoop and the middle height of the rotor. In the diagram related to the height of the rotor equal to Z/ZH = 0.98, it is clear that the waste scoop is the agent disturbing the flux. In other words, when the rotating molecules collide the inlet and the curvature of the scoop body, they deviate from their path and disrupt the axial flow behavior. In this way, several back and forth movements are formed around the scoop. By moving away from the scoop in the Z direction, the number of these back and forth movements decreases, and finally, due to the presence of centrifugal force, they turn into a countercurrent movement next to the rotor wall.

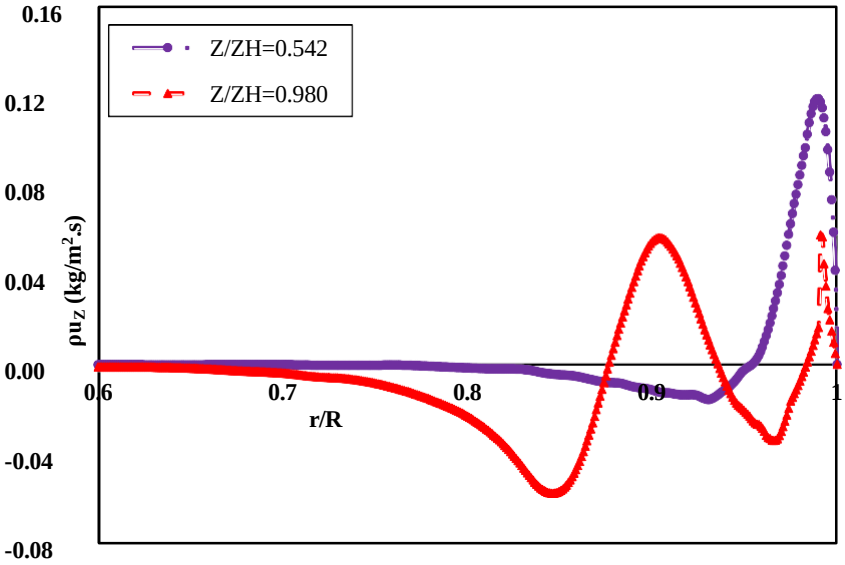

Fig. 4. Diagram of variations in axial mass flux at two heights of the waste scoop and the middle area of the rotor.

Finally, the total drag force was calculated by integrating the compressive and viscous drag forces on all surfaces of the scoop body in local, using the force function by the software. To use the force function, the necessary settings were made in the controlDict file. After applying the settings, when running the solution, the values related to the drag force appear in the terminal automatically based on the writeInterval settings, and all the desired outputs are printed in the postprocessing file. The amount of drag force provided in the output of the software; For the product scoop, it was determined equal to 1860 Dynes and for the waste scoop equal to 2140 Dynes. The difference between the actual drag force in the 3D mode and its hypothetical value in the axially symmetric simulation is 23% for the product scoop and 21% for the waste scoop.

Conclusions

In the simulation of the centrifuge machine, there is a shock phenomenon in the scoop areas. The shock phenomenon is used in these areas in order to create an axial flow and harvest the flow. The occurrence of

shock phenomenon is one of the design requirements of centrifuge machines. By creating this phenomenon and noticeable pressure variations in the inner and outer areas of the scoop by creating a mass sink, the necessary driving force is provided for the outflow of the flow and the non-return of the flow inside the scoop to the rotor. The certainty of the occurrence of this phenomenon in the design of centrifuge machines should be determined using simulation.

The results obtained from the pressure profiles in the scoop areas show that the local pressure in the inlet of the product scoop is higher than that of the waste scoop. Therefore, the product scoop should be the basis of the design and selection of materials for the scoops of the centrifuge machine.

3. The amount of the drag force for the product scoop was determined to be 2140 dynes and the drag force of the waste scoop was determined to be 1860 dynes. Due to the smaller distance between the product scoop and the rotor wall, stronger shock waves occur in its area with a wider current jump range. In the design of the scoop of the centrifuge machine, from the mechanical point of view, the drag force of the product scoop should be considered as the basis of the design. Also, the determined drag force should be used as an estimate in two-dimensional simulations.

The difference between the actual drag force in the 3D mode and its hypothetical value in the axially symmetric simulation is 23% for the product scoop and 21% for the waste scoop.

References

[1] H. G. Wood and J. B. Morton, “Onsager’s pancake approximation for the fluid dynamics of a gas centrifuge,” *J. Fluid Mech.*, vol. 101, no. 1, pp. 1–31, 1980, doi: 10.1017/S0022112080001504.

[2] P. Omnes, “Numerical and physical comparisons of two models of a gas centrifuge,” *Comput. Fluids*, vol. 36, no. 6, pp. 1028–1039, 2007, doi: 10.1016/j.compfluid.2006.05.006.

[3] P. J. Migliorini, “Modeling and Simulation of Gas Centrifuge Cascades for Enhancing the Efficiency of IAEA Safeguards,” University of Virginia., 2013.

[4] D. Jiang and S. Zeng, “CFD simulation of 3D flowfield in a gas centrifuge,” in *International Conference*

[5] *on Nuclear Engineering, Proceedings, ICONE*, 2006, pp. 403–408. doi: 10.1115/ICONE14-89783.

[6] H. Kulkarni, "CFD Simulation of Compressible Flow inside a Gas Centrifuge using OpenFOAM," *Int. J. Res. Appl. Sci. Eng. Technol.*, vol. 8, no. 12, pp. 444–449, 2020, doi: 10.22214/ijraset.2020.32496.

[7] Y. N. Zhang, S. Zeng, D. J. Jiang, and V. D. Borisevich, "On the scoop heating effect of a gas centrifuge in numerical simulation," in *Journal of Physics: Conference Series*, 2018. doi: 10.1088/1742- 6596/1099/1/012012.

[8] T. Sakurai, "Linearized thin-wing theory of gas-centrifuge scoops," *J. Fluid Mech.*, vol. 103, pp. 257–273, 1981, doi: 10.1017/S002211208100133X.

[9] T. Kai and K. Hasegawa, "Numerical calculation of flow and isotope separation for SF6 Gas centrifuge,"

[10] *J. Nucl. Sci. Technol.*, 2000, doi: 10.1080/18811248.2000.9714879.

[11] V. D. Borisevich, O. E. Morozov, and O. N. Godisov, "Numerical simulation of bellows effect on flow and separation of uranium isotopes in a supercritical gas centrifuge," *Nucl. Instruments Methods Phys. Res. Sect. A Accel. Spectrometers, Detect. Assoc. Equip.*, vol. 455, no. 2, pp. 487–494, 2000, doi: 10.1016/S0168-9002(00)00501-5.

[12] V. D. Borman, S. V. Bogovalov, V. D. Borisevich, I. V. Tronin, and V. N. Tronin, "The computer simulation of 3d gas dynamics in a gas centrifuge," in *Journal of Physics: Conference Series*, 2016. doi: 10.1088/1742-6596/751/1/012017.

[13] M. Khajenoori, A. Haghighi Asl, J. Safdari, and A. Norouzi, "Modeling and simulating of feed flow in a gas centrifuge using the Monte Carlo method to calculate the maximum separation power," *J. Mol. Model.*, vol. 25, no. 11, 2019, doi: 10.1007/s00894-019-4226-x.

[14] S. Yousefi-Nasab, J. Safdari, J. Karimi-Sabet, and A. Norouzi, "Study of scoop drive and polymeric surface effects on the separation factors for a gas centrifuge using MD-DSMC method," *J. Brazilian Soc. Mech. Sci. Eng.*, vol. 43, no. 7, 2021, doi: 10.1007/s40430-021-03067-5.

[15] S. V. Bogovalov, V. D. Borman, A. V. Vasilyev, I. V. Tronin, and V. N. Tronin, "Three-dimensional modeling of the flow around the gas scoop under optimal working regime of the Iguassu gas

[16] centrifuge at the hyper fast rotation," in *Journal of Physics: Conference Series*, 2022, p. 12003. doi: 10.1088/1742- 6596/2147/1/012003.

[17] G. A. Bird, *Molecular gas dynamics and the direct simulation of gas flows - 2nd edition*. 1994.

[18] M. Wang and Z. Li, "Similarity of ideal gas flow at different scales," *Sci. China, Ser. E Technol. Sci.*, vol. 46, no. 6, 2003, doi: 10.1360/02ye0072.

[19] M. Wang and Z. Li, "Nonideal gas flow and heat transfer in micro- and nanochannels using the direct simulation Monte Carlo method," *Phys. Rev. E - Stat. Nonlinear, Soft Matter Phys.*, vol. 68, no. 4 2, pp. 467041–467046, 2003.

[20] M. R. Wang and Z. X. Li, "Numerical simulations on performance of MEMS-based nozzles at moderate or low temperatures," *Microfluid. Nanofluidics*, vol. 1, no. 1, pp. 62–70, 2004, doi: 10.1007/s10404-004- 0008-5.

[21] E. Roohi and M. Darbandi, "Hybrid DSMC/Navier-Stokes solution of rarefied micro-nano flows," *Proc. 2nd GASMEMS Work. Embiez*, 2010.

[22] "www.OpenFOAM.org, [Online]."

ICNST 2024
International Conference on Nuclear Science and Technology
6- 8 MAY 2024 | Isfahan, Iran

Investigating the role of electron density change in estimating the separation factor of 10B and 11B isotopes by the complex of methoxybenzene and boron trifluoride (BF3): A theoretical study (Paper ID : 1454)

Masoud Arabieh[1*], Javad Fsishi[2], Hamid Sepehrian[1] and Mohammad-Reza Basaadat[1]
[1]Nuclear Science and Technology Research Institute (NSTRI), Tehran, Iran
[2]Iranian Research Organization for Science and Technology (IROST), Tehran, Iran

Abstract

In this research, based on the experimentally reported effective structures, a number of new compounds in the field of isotopic separation have been theoretically investigated for the separation of 10B and 11B isotopes. The interaction of these compounds with boron trifluoride (BF3) has been studied using the density functional theory approach to evaluate the role of structural changes in the estimation of the isotopic separation factor. Also, the vibration partition function of these structures has been calculated and the correlation between the charge exchange in the complexes and the separation ratio has been investigated. The results show that in all the proposed groups, there is a direct relationship between the amount of charge transferred to boron trifluoride and the separation ratios. In addition, the results of the electron substitution function on oxygen and nitrogen atoms shows the stronger bonding energy of NH2 groups with BF3. In conclusion, the findings of this research indicate the improvement of the isotope separation ratio by increasing the electron donating group of the compound to BF3. It is suggested to use some of structures proposed in this project in the separation process of the mentioned isotopes.

Keywords: BF3, separation factor, methoxybenzene, vibration frequency.

Introduction

Two stable isotopes can be found naturally (10B and 11B with natural abundances of 19.9% and 80.1%). Due to the remarkable neutron absorption capability of 10B (neutron absorption cross section 3837 barn) compared to 11B (0.005 barn), many efforts have been made to extract 10B from the natural mixture of boron isotopes. For example, various molecules have been investigated in isotope exchange reactions to separate the isotopes of this element [1]. Today, it is known that ethers that contain oxygen atoms, such as dimethyl ether [DME, O(CH3)2], diethyl ether [DEE, O(C2H5)2], and methyl phenyl ether [MPE, O(C10H12)], compared to thioethers (ethers containing Sulfur) and ethers containing nitrogen are more suitable compounds for the separation of boron isotopes [2]. Other compounds are often toxic, corrosive,

unstable, or have a small equilibrium constant (the equilibrium constant is considered as a measure of the separation factor).

One of the common methods for separating boron isotopes is the distillation method of complexes containing the BF3 structure. So far, many compounds containing BF3 have been investigated in this field[3]. The results have shown that the use of equilibrium distillation in such systems can be used as a suitable method for the separation of boron isotopes. For example, today it is known that the distillation of volatile boron compounds can be considered as one of the best methods for separating boron isotopes[4].

The distillation of complex formed between diethyl ether and BF3 differs from other cases. In other words, in the distillation of this complex, the mechanism of isotope exchange and complex decomposition, unlike the usual distillations, is proposed[4]. In this distillation, the separation factor increases significantly due to the isotope exchange mechanism. That is, the difference between the rate of decomposition of the complex containing 10B and 11B leads to the separation of boron isotopes.

Studies show that for the first time, the estimation of separation factor for isotope exchange reactions using vibrational frequencies was reported by Bigeleisen and Mayer[1]. They were able to estimate the separation factor of boron isotopes in BF3·O(CH3)2 and BF3·O(C2H5)2 systems using the frequency measured by infrared (IR) spectrum. The separation factors calculated using vibration frequencies were slightly higher than the experimental data. Nevertheless, the mentioned method has been used in calculating the separation factors of element isotopes such as: sulfur, boron, molybdenum, chlorine and etc. The progress of various methods in quantum calculations has made it possible to reproduce the vibrational spectra of chemical systems[5-7]. One of these methods is based on density functional theory (DFT). A research group in 2009 led by Takao compared the accuracy of frequency calculations based on the DFT and the perturbation method(MP2). They showed that the electron density method reproduces the frequency data at a suitable computational level in such a way that the isotope separation factor calculated for boron isotopes is very close to the experiment. In these reactions, the studied system includes methoxybenzene and BF3 (Fig.1).

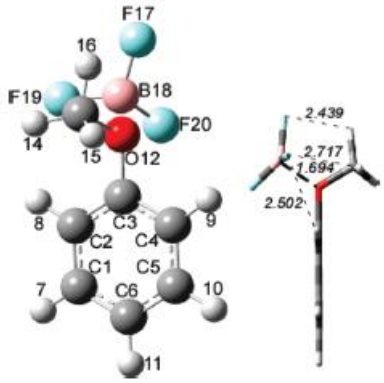

Fig1. The methoxybenzene and BF_3 complex. The distances are in angstrom. Atoms coloring: C, gray; H, white; O, red; B, pink and F,cyan.

The objective of this research is to investigate the impact of structural modifications and charge exchange on the isotopic separation of 10B and 11B isotopes using boron trifluoride (BF3) complexes. In this study, according to experimentally existing compounds, the interaction of selected compounds with boron trifluoride have been investigated by the density functional theory. In addition, the vibrational partition function has been calculated and the correlation function between this partition function and the transferred charge has also been investigated. According to calculations, it can be said that for all compounds the Pearson's coefficient should be positive. There is a direct relationship between the amount of transferred charge to boron trifluoride and the separation ratios.

Research Theories

A bunch of structures have studied in this research and the quantum calculations have run on the possible complex with BF_3 molecule. All the structures investigated in this study have been optimized at B3LYP/6-31+G** computational level by G09 code package. Also, frequency and thermochemical calculations have been done at the same level of calculation. For this group of calculations, the frequency correction factor mentioned in the references has been used. In other words, scale=1.0107 and scale=1.0123 were used for ^{10}B and ^{11}B isotopes, respectively. The charge densities were calculated by the Multiwfn. No condition or symmetry were considered for the systems in the optimization calculations.

In general, one way to obtain the separation factor is applying the reduced partition functions, The Born-Oppenheimer and harmonic oscillator approximation have used in the calculation of partition functions.

If the equilibrium reaction of isotope displacement is considered as eq.1 then the equilibrium constant of isotope displacement reaction can be estimated as eq.2 [2-7]:

$$AX + BX' \rightarrow AX' + BX \quad (1)$$

$$lnK = ln\left(\frac{S}{S'}\right) f_{BX} - ln\left(\frac{S}{S'}\right) f_{AX} \quad (2)$$

$$\left(\frac{S}{S'}\right) f = \prod_{i}^{f} u_i exp \frac{(-u_i/2)/1 - exp(-u_i)\}}{u_i' exp\,(-u_i'/2)/1 - exp(-u_i')\}} \quad (3)$$

Where X and X' represent lighter and heavier isotopes in molecular structures A and B, respectively. The expression ln(S/S') also shows the ratio of reduced partition functions for each molecular system, which requires the temperature and vibrational frequencies of the studied system. The selection of the studied structures in this project was based on several points: firstly, the structure to be studied for the formation of the complex with BF_3 should be commercially available. Secondly, the structures should be selected in such a way that the role of electron-donating/accepting functional groups and the spatial hindrance can be studied during the formation of the complex with BF_3. Based on these assumptions, some structures were selected (Fig. 2) to be considered in this interaction.

Results and discussion

At first, all the proposed structures and BF3 were optimized at B3LYP/6-31+G** computational level. Then, in order to check the stability of the resulting structures on the potential energy surface, Hessian matrix (frequency) calculations were performed. Next, the possible complexes between all the proposed structures and BF3 gas were optimized at B3LYP/6-31+G* computational level and their stability were also confirmed. The optimized structures of the mentioned complexes are shown in Fig. 3. In general, the amount of separation factor in these types of systems depends on the vibrational frequency of the bond formed between the boron atom of BF3 molecule and the oxygen atom of another molecule.

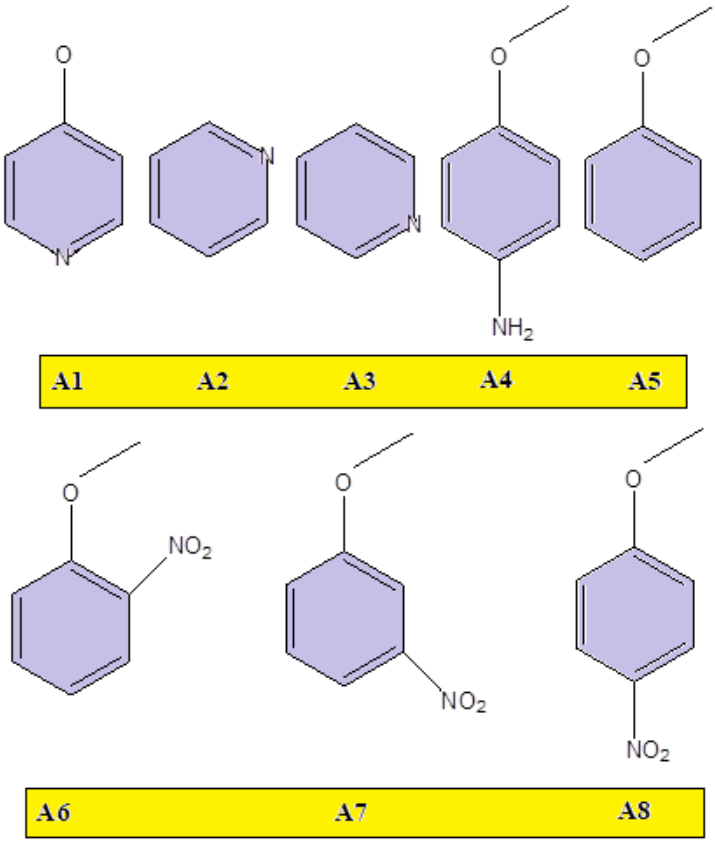

Fig. 2: Selected structures to investigate the interaction with BF3 molecule.

It can be seen that in these structures, the B-O bond lengths are in the range of 1.68-1.83 angstroms. On the other hand, the sum of the covalent radius of boron and oxygen atoms is 1.55 angstrom. Such values confirm the attraction interaction between the BF3 and other complexes.

Thermochemical and some structural data for each of the complexes and BF3 molecule have listed in table 1. In general, there are two possible sites for the formation of a complex between the BF3 molecule and the complex structures: the first is the oxygen of the methoxy group and the second is the nitrogen atom. The comparison of Gibbs free energy values shows that BF3 may have a strong interaction with NH2 group at the A4-NH2 and A5-NH2 structures. It can be stated that in the similar structures, the presence of N-atoms (individually or as NH2 group) may lead to a stronger bond between the BF3 gas and complex. According to table 1 for enthalpy changes, all interactions should be exothermic.

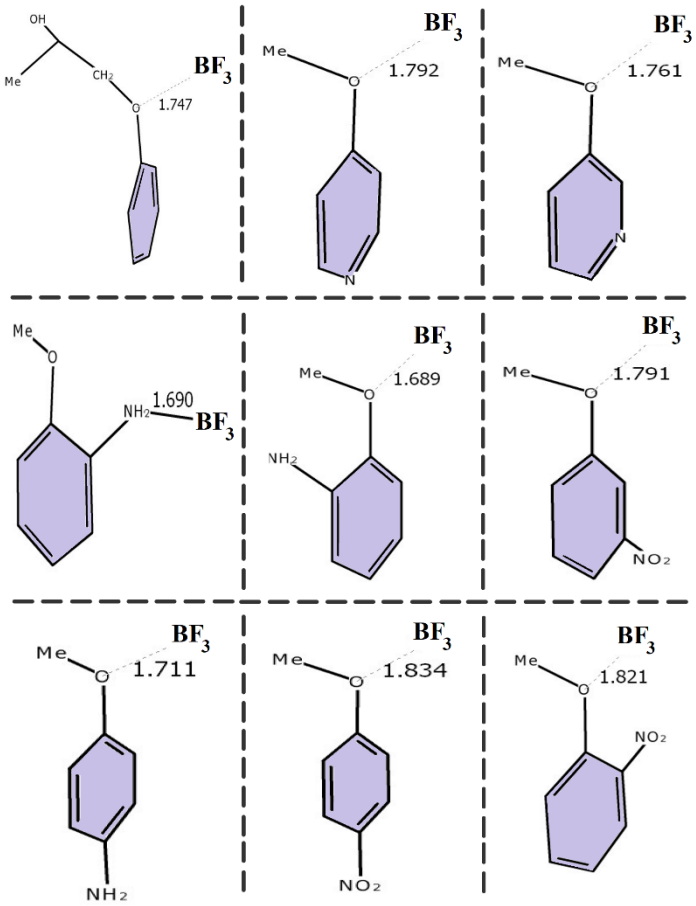

Fig. 3: The structure of the optimized complexes of BF3 molecule with complexes. The bond distance is reported in angstroms.

Table 1. Selected structural and thermochemical data. The bond lengths are in angstroms, angles in degrees and energies in kcal/mol.

system	D (B…O)	D (B…N)	X-O-X	ΔE_{com}	ΔH_{com}	ΔG_{com}
BF3-A1	1.79	-	114.9	-1.6	-1.3	8.0
BF3-A2	2.39	-	116.9	-3.3	-2.8	5.7
BF3-A3	1.76	-	114.8	-3.6	-3.4	6.8
BF3-A4-NH2	-	1.69	-	-16.3	-16.7	-5.8
BF3-A4-OMET	1.69	-	115.0	-7.1	-7.0	3.7
BF3-A5-NH2	-	1.69	-	-15.8	-16.0	-5.0
BF3-A5-OMET	1.69	-	115.0	-6.8	-6.9	4.3
BF3-A6	1.83	-	115.6	-0.8	-0.5	8.9
BF3-A7	1.82	-	115.7	-3.1	-2.8	7.7
BF3-A8	1.79	-	114.9	-1.7	-1.4	8.7

On the other hand, in these interactions, there should be some transferred charges between compounds and BF3 gas. Accordingly, the amount of charge transferring was calculated based on Hirschfeld's analysis and the theory of atoms in AIM molecules, and the results are declared in Table 2. In addition, the partition function corresponding to the vibration frequencies have been listed.

Table 2. The displaced charge based on Hirschfeld's analysis and the theory of atoms in AIM molecules, and the partition function (PF) corresponding to the vibrational frequency.

BF3/System	PF	AIM	Hirshfeld
A1	1.055927182	-0.127652	-0.188966
A2	1.04757881	-0.061182	-0.151223
A3	1.027334271	-0.127819	-0.190488
A4-NH2	0.99153085	-0.166787	-0.218684
A4-OMET	0.990922983	-0.134036	-0.207573
A5-NH2	0.990334584	-0.166168	-0.219555
A5-OMET	0.989301676	-0.126354	-0.197679
A6	1.013543732	-0.12452	-0.190815
A7	1.012944804	-0.122889	-0.179561
A8	1.012964359	-0.125874	-0.18859

Next, the correlation function between these values was calculated by Pearson's method, and then the Pearson correlation matrix between the displaced charges and the partition function was obtained. The results of these data for each system have been shown in Fig. 4. It is shown that there is a 95% correlation between Hirschfeld and AIM charges in the correlation matrix. This is an desired result because of the basic definitions of these quantities. But the remarkable point is the relatively high correlation between the above charge transferred and the calculated partition function. The 75% correlation between the amount of transferred charge and the partition function shows that there is a direct relationship between the amount of charge exchanged between the structure and the separation ratio of the BF3 molecule. In other words, the stronger the interaction between the molecule and BF3, the higher the separation constant. It is noted that the above result is limited to compounds that have similar groups in the vicinity of BF3, and by changing the group involved in the formation of the complex, the above rule may be violated. For example, despite the transfer of more constant charge, the A5 molecule-in which NH2 group (instead of oxygen) is interacted with BF3- shows a smaller separation. In order to have deeper

understanding, the electron localization function (ELF) for compounds A1 and A5 has been calculated and compared in Fig. 5. This comparison of the ELF distribution shows a serious difference in the orientation of non-bonding electron pairs in the case of A5 and A1 compounds. Since for the compound including nitrogen, the only available pair of electrons has a stronger orientation towards BF3, the resulting dative bond will be stronger.

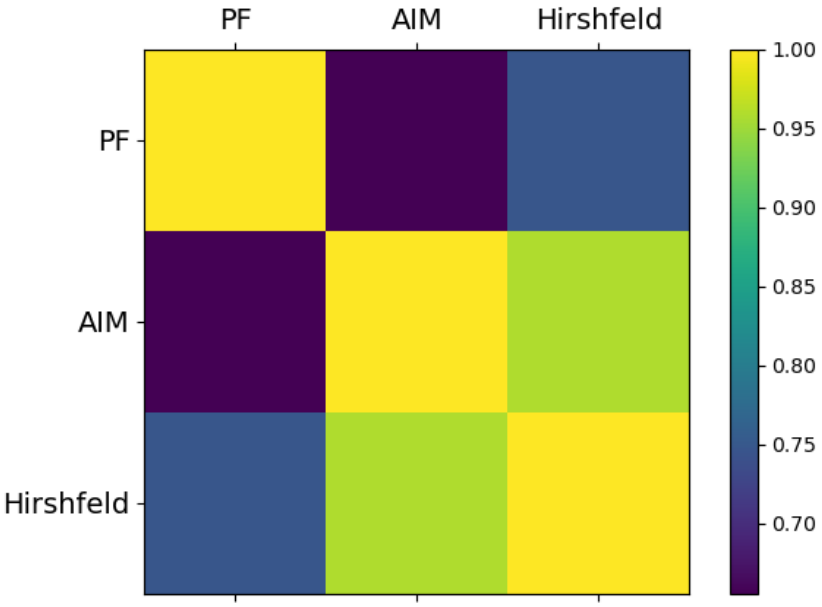

Fig. 4: Pearson's correlation matrix between the displaced charges and the partition function

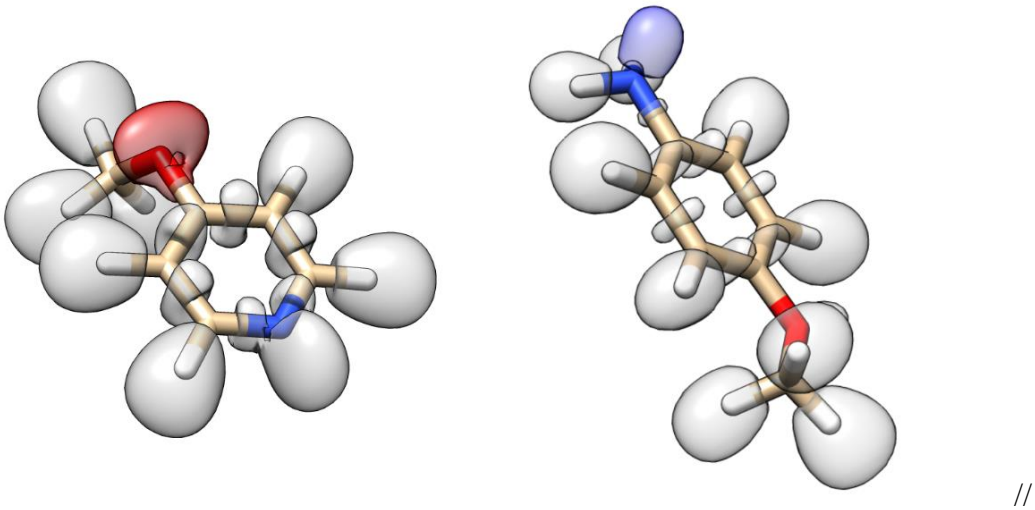

//

Fig. 5: The electron localization function (ELF) for compounds A1 and A5.

Conclusions

Due to the growing importance of boron isotopes in a wide range of new technologies, various mechanisms have been proposed for the separation of boron isotopes. Because of the relatively low cost and the impressive separation ratio, the use of the mechanism of exchange reactions for the extraction of boron isotopes has attracted the attention of researchers. The compound including methoxybenzene groups is a remarkable candidate to advance the mentioned reactions. Considering the upcoming problems in determining optimal combinations using experimental methods, simulation of separation process and theoretical calculation of separation constants are of great importance. In this research, based on the experimentally reported effective structures, a number of compounds have been proposed and the interaction of these compounds with boron trifluoride has been studied using density functional theory approach. Also, the vibrational scattering function of these structures has been calculated based on the thermal frequencies and the correlation between the charge exchange in the complex and the separation ratio has been investigated. The results show that in all mentioned compounds, there is a positive Pearson's coefficient and a direct relationship between the amount of transferred charge to boron trifluoride and the separation ratios. In addition, based on the investigation of the electron localization function on oxygen and nitrogen atoms, it explains the stronger bonding energy of NH2 groups with BF3. As stated above the most practical implications of the current research findings is suggesting new compounds for the isotopic separation of 10B and 11B isotopes. The results of this research indicate the improvement of the separation ratio by increasing the electron donating group of the introduced compound to BF3. For example, it was predicted that methoxy benzen substituted with NH2 in ortho-position could be suggested for increasing the isotopes boron separation. The most important challenge in this field could be constructing and tuning the distillation set-up which requires chemical engineering knowledge. It is worthy mention that from a chemical point of view, synthesizing the suggested compounds is straightforward and most of the reported compounds in this paper are commercially available. In conclusion, the findings of this research indicate the improvement of the separation ratio by increasing the electron donating group of the compound to BF3.

References

[1]Bigeleisen J, Mayer MG (1947) Calculation of equilibrium constants for isotopic exchange reactions. J Chem Phys 15:261–267.

[2]Urey H. C. and Greiff L. J. (1935) Isotopic exchange equilibria. J. Am. Chem. Soc. 57: 321.

[3]Wolfsberg M., Massa A. A. and Pyper J. W. (1970) Effect of vibrational anharmonicity on the isotopic self-exchange equilibria H2X+D2X = 2HDX. J. Chem. Phys. 12:408–412.

[4]Yanase S, Oi T (2001) Ab initio molecular orbital calculations of reduced partition function ratios of hydrated lithium ions in ion exchange systems. Z Naturforsch 56:297–306.

[5]Urey H. C. (1947) The thermodynamic properties of isotopic substances. J. Chem. Soc.

[6]Urey H. C. and Greiff L. J. (1935) Isotopic exchange equilibria. J. Am. Chem. Soc. 57:321.

[7]Urey H. C. and Rittenberg D. (1933) Some thermodynamic properties of the H1H2, H2H2 molecules and compounds containing the H2 atom. J. Chem. Phys. 1:137–143.

Leaching of lithium from coal gangue: the effect of acid type (Paper ID : 1506)

Ammari Allahyari S., Zaheri P.*, Zolfonoun E., Maleki F., Parvenus M., Charkhi A., Ahmadi S.J., Ghannadi Maragheh M.

Nuclear Fuel Cycle Research School, Nuclear Science and Technology Research Institute, P.O. Box: 11365-8486, Tehran, Iran

Abstract

Lithium is an important and practical strategic metal in nuclear industries. 6Li is used to produce tritium in deuterium-tritium fueled nuclear reactors; which is used as feed in fusion reactors. Due to its low thermal neutron absorption cross-section, 7Li is used in some light water-cooled reactors to adjust the alkalinity of the cooling fluid and also as an anti-corrosion compound in fission reactors. Recently, it has been found that in addition to extracting lithium from its mines, brines, and sea water, it is also possible to extract lithium from coal gangue. The coal gangue used in this experiment was roasted for two hours at 700 °C in order to burn and destroy the carbon therein. Afterwards, hydrochloric acid and sulfuric acid solutions were used to leach the lithium from the obtained coal ash. In contrast to 4 mol/l sulfuric acid solution, the observed findings indicated that employing 4 mol/l hydrochloric acid solution is an acceptable alternative for leaching of lithium.

Keywords: Lithium, Coal gangue, Coal ash, Roasting, Leaching

Introduction

As a strategic and vital metal, lithium is widely used in many industries such as aerospace, precision electronic industries such as chip manufacturing, computing components of supercomputers and high temperature industries. Lithium is also one of the useful and important elements in nuclear industries. 6Li is used to produce tritium in deuterium-tritium fueled nuclear reactors; which is used as feed in fusion reactors. Due to its low thermal neutron absorption cross-section, 7Li is used in some light water-cooled reactors to adjust the alkalinity of the cooling fluid and also as an anti-corrosion compound in fission reactors [1]. Three primary sources comprise lithium: brines, saltwater, and minerals like spodumene and lepidolite that contain lithium. The need for lithium resources is rising due to the new energy sector's explosive growth. The usage and development of lithium deposits of the brine and pegmatite types is restricted, though. Thus, it is now required to look for lithium in other places. It has recently been discovered that lithium can also be extracted from nontraditional sources, such as coal and

its byproducts, in addition to its mines. One of the biggest industrial solid wastes is now produced by the expansion of coal mining from mines, which causes several environmental issues. If coal can be used to produce lithium, this will encourage and expand the usage of coal and lessen associated environmental issues [2-4].

Xu et al. (2021) proposed a process for extracting lithium from coal fly ash by low temperature (125–160 oC) ammonium fluoride activation. The glass phase in coal fly ash was converted to water-soluble fluoride salts after the salt activation process, which was followed by the extraction of lithium from the glass phase via water leaching [5]. Zhang et al. investigated the Lithium extraction from the coal gangue via the integrated process of roasting and acid leaching. The majority (94%) of lithium was extracted when raw samples are roasted at 400°C for 20 min before 4 h leaching with 2 mol/L hydrochloric acid at 60°C [6]. A novel technique was also developed for the recovery of lithium and aluminum from coal fly ash using a combination of pre-desilication and an intensified acid leaching process. leaching efficiency of lithium was 82.23% with 6 mol/L HCl and solid to liquid ratio of 1:20 [7]. Rezaei et al. (2022) proposed an environmentally friendly process for recovering germanium, lithium, and vanadium from coal fly ash (CFA) using thermal pretreatment by sodium salts and hydrometallurgy. In this method, the highest recovery for lithium was reported 97.30% [8].

In this experimental work, the coal gangue was roasted for two hours at 700 °C in order to burn and destroy the carbon therein. Afterwards the effect of acid type and concentration was studied on the leaching of the lithium.

Experimental

Materials

Coal gangue samples (B1 and B2) used in this work were air-dried at 80 °C, and then grinded until the top particle size was 100 μm. The hydrochloric acid and sulfuric acid used in the acid leaching process was analytical grade and purchased from Merck company. Deionized water was used in all tests and experiments.

Roasting

During batch roasting, four square crucibles containing 15 g of sample were placed in the muffle furnace. Subsequently, the sample was heated to the specified temperature (٧٠٠ °C) from room temperature at a rate of 10°C/min and maintained for 120 min. After roasting, the sample was taken out and cooled naturally to room temperature, which could be used to study the leaching efficiency of lithium

Acid leaching

Acid leaching experiments were carried out to extract lithium from the roasted samples. A certain mass of the sample was put into a flask containing the diluted hydrochloric acid/ sulfuric acid solution with the target concentration, and then, the flask was placed in a temperature-controlled sheaker. During all leaching experiments, the liquid-solid ratio and stirring speed were fixed, respectively, at 50:1 mL/g and 300 rpm. The leaching temperature and time was 80°C, and 120 min, respectively. After the leaching process was done, the slurry was centrifuged and the concentration of lithium in the solution after dilution was measured by ICP-MS. The leaching efficiency of lithium was calculated according to Eq.1

$$S = \frac{VC_2}{mC_1} \times 100 \quad (1)$$

Where S represents the leaching efficiency of lithium; V is the volume of leachate, mL; m1 is the mass of sample, g; C1 is the content of lithium in the sample (μg/g); C2 is the content of lithium in the leachate (μg/mL).

Results And Disscusion

Mineral phase transformation during the roasting activation process is greatly influenced by the roasting temperature. In this experiment, the samples were heated to the target temperature and the ash percentage of the sample was 33.31. Figure 1 shows the sample before and after the roasting process. The obtained ash was subjected to acid leaching under the same conditions.

(a) (b)

Fig. 9. The coal gangue sample before and after the roasting process.

The acid type and concentration play a very crucial role in the acid leaching process. Setting the experimental conditions as leaching temperature of 80°C and leaching time of 120 min, the effect of HCl and H2SO4 concentration on lithium leaching rate was examined using the samples roasted at the suitable conditions as mentioned in the above section. The relationship between the leaching rate of lithium and HCl/H2SO4 concentration is presented in Fig. 1. For the sample B1, When the HCl concentration was 2 mol/L, the leaching rate of lithium is 77.3%, resulting from the lack of hydrochloric acid. With the increase in HCl concentration, the leaching rate of lithium rose up to 99.9% at 4 mol/l. It means that most the soluble lithium is leached out. The results also showed that 4 mol/L HCl is a more effective leaching agent of lithium from coal ash than 4 M H2SO4 solution. These results are also confirmed for sample B2.

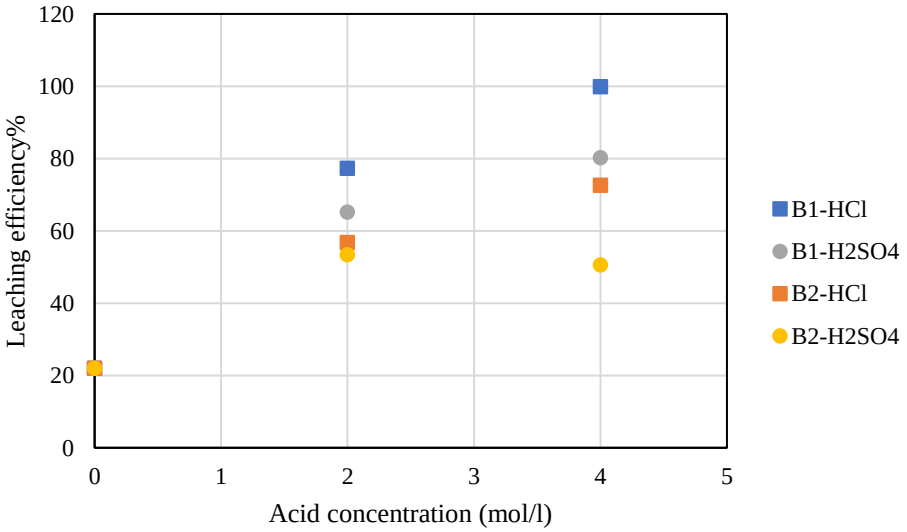

Fig. 10. The effect of acid type and concentration on the leaching efficiency (Leaching temperature: 80°C, leaching time: 120 min, liquid-solid ratio: 50:1 mL/g, stirring speed: 300 rpm).

Conclutions

It has recently been discovered that lithium can also be extracted from coal gangue, in addition to mines, brines, and sea water. To burn and eliminate the carbon in the coal gangue utilized in this experiment, it was roasted for two hours at 700 °C. After that, the lithium was extracted from the coal ash using solutions of sulfuric and hydrochloric acids. Compared to 4 mol/l sulfuric acid solution, the results showed that using 4 mol/l hydrochloric acid solution is a suitable substitute for lithium leaching from coal gangue.

References

[1] Wiśniewska, M., et al. (2018). Investigations of the possibility of lithium acquisition from geothermal water using natural and synthetic zeolites applying poly (acrylic acid). Journal of Cleaner Production, 195: p. 821-830.

[2] Li, X., et al. (2019). Efficient separation of silica and alumina in simulated CFB slag by reduction roasting-alkaline leaching process. Waste Management, 87: p. 798-804.

[3] Gao, H., et al. (2021). Explanation of heavy metal pollution in coal mines of china from the perspective of coal gangue geochemical characteristics. Environmental Science and Pollution Research, 28: p. 65363-65373.

[4] Dong, Y., et al. (2020). Repairing effects of sulfate-reducing bacteria on the dissolved pollutant of coal gangue based on leaching experiments. Energy Sources, Part A: Recovery, Utilization, and Environmental Effects, p. 1-14.

[5] Xu, H., et al. (2021). Extraction of lithium from coal fly ash by low-temperature ammonium fluoride activation-assisted leaching. Separation and Purification Technology, 279: p. 119757.

[6] Zhang, L., et al. (2023). Extraction of lithium from coal gangue by a roasting-leaching process. International Journal of Coal Preparation and Utilization, 43(5): p. 863-878.

[7] Li, S., et al. (2017). An efficient approach for lithium and aluminum recovery from coal fly ash by pre-desilication and intensified acid leaching processes. Metals, 7(7): p. 272.

[8] Rezaei, H., et al. (2022). A sustainable method for germanium, vanadium and lithium extraction from coal fly ash: Sodium salts roasting and organic acids leaching. Fuel, 312: p. 122844.

ICNST 2024
International Conference on Nuclear Science and Technology
6- 8 MAY 2024 | Isfahan, Iran

Characterization of coal gangue for lithium extraction (Paper ID : 1509)

Ammari Allahyari S[1], Zaheri P[1*], Ghannadi Maragheh M[1], Zolfonoun E[1], Forati Rad H[1], Maleki F[1], Parvenus M[1], Charkhi A[1], Ahmadi S J[1] ,

[1] Nuclear Fuel Cycle Research School, Nuclear Science and Technology Research Institute, P.O. Box: 11365-8486, Tehran, Iran

Abstract

Lithium is the lightest alkali metal with unique chemical properties, such as high electrochemical activity, high reduction potential, and high specific heat capacity. This element has a wide range of applications in various industries, including the nuclear industry. For instance, lithium-6 is a source of tritium for nuclear fusion fuel by absorbing neutrons. It comprises 7.5% of natural lithium. Lithium-7, with a notable isotopic abundance of 92.47%, is used as a coolant in nuclear reactors, in addition to controlling the pH level in the reactor water. Therefore, the separation of lithium from relevant sources is highly important. Since the separation of lithium from these resources is not possible without knowledge of its inventory, in this report, the characterization of the coal gangue is done using XRF and ICP-OES analysis for geochemical studies and measurement of major and minor oxides, as well as XRD analysis for determining the crystalline phases present in the samples.

Keywords: Lithium, Coal gangue, Characterization

Introduction

The need for specific materials with unique features and cutting-edge technologies in the current industry makes it clear that geological resources must be carefully evaluated while taking future technologies into account. Lithium is one of these elements that is used in cutting-edge technologies such as medical, pharmaceuticals, electronics, battery production, ceramics, glass, aerospace alloys, and nuclear industries. Lithium has two stable isotopes, 6Li and 7Li, which have abundances of 7.5% and 92.5%, respectively. The thermal neutron absorption cross-sections of lithium isotopes 6Li and 7Li are 940 and 0.037 barns, respectively. 6Li is used to produce tritium as a fuel for fusion reactors. Since 7Li has a lower thermal neutron absorption cross-section, is employed as an additive in PWR primary coolant, at about 2.2 ppm, for maintaining water chemistry, counteracting the corrosive effects of boric acid (used as neutron absorber) and minimizing corrosion in steam generators of PWRs [1,2].

Lithium is primarily found in three different sources: lithium-containing minerals such as spodumene and lepidolite, aqueous sources like brines and seawater, and ultimately in coal gangue. Lithium-bearing minerals can serve as a suitable extraction source for lithium, but increasing extraction of these resources leads to resource depletion. Seawater and brines account for over 60% of total lithium resources. Currently, lithium-rich resources are located in countries such as Chile, Bolivia, China, and the United States. The process of extracting lithium from aqueous solutions is relatively easier and less costly operationally than minerals. Today, the development of efficient technologies for extracting lithium from aqueous solutions is underway [3,4].

Another resource for lithium extraction is coal gangue and its by-products. For example, in coal basins such as Kirensk and Verkhne-Bikin in Russia, the inventory of lithium oxide ranges from 0.22 to 0.65%. Lithium predominantly exists in coal as aluminosilicate compounds and clay minerals. Currently, coal gangue is one of the most significant environmental challenges that can contaminate soil and water resources. If coal can be utilized as a source of rare metals such as lithium, many of these environmental problems can be mitigated. Additionally, it has been discovered that many coal fields are secondary resources for rare elements [5].

This article evaluates the lithium resource of coal gangue in a national mine to select an appropriate method for the separation and purification of lithium among the interfering elements. Identification of coal gangue was conducted through XRD, XRF and ICP analyses.

Experimental

Two representative samples were collected from different sections of the national coal mine. Characterization of the samples was performed before and after ashing. The most important analyses included XRF (OXFORD ED200, UK) and ICP-OES (Optima 7300 DV, USA) for geochemical studies and measurement of the main and secondary oxides in coal gangue samples, as well as XRD analysis (Philips PW 1800, USA) for determining the crystalline phases present in the samples. These analyses were carried out at the central laboratory of the Nuclear Science and Technology Research Institute.

Results and Discussion

The XRD results of coal samples B1 and B2 before ashing are presented in Fig. 1. The results show that the main mineral phases in the raw materials include quartz (SiO2, Ref. code : 083-0539), clay (kaolinite) (Al2Si2O5(OH)4), muscovite (KAl2[(OHF)2-AlSi3O10], Ref. Code: 007-0025), pyrite (FeS2, Ref. Code: 071-0053), albite (NiALSi3O8), and boehmite (AlOOH). Coal gangue mainly consists of kaolinite and quartz, along with small amounts of albite, boehmite, and other compounds. The kaolinite and quartz content in coal gangue is nearly 80%. In other words, the predominant mineral in coal samples is kaolinite. As seen in this figure, the most prominent peaks correspond to quartz and kaolinite. Additionally, identical peaks indicate that the compositions of samples B1 and B2 are the same. This conclusion aligns with reported studies [6-8].

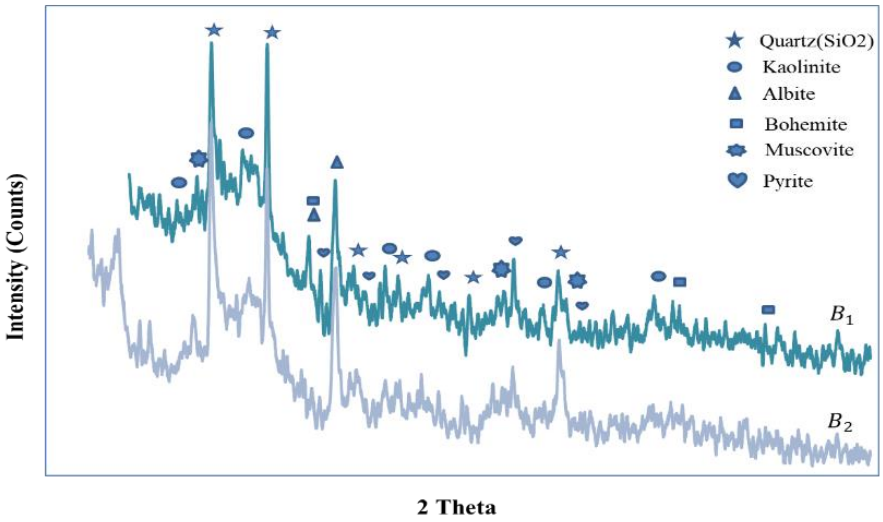

Fig. 1.XRD analysis of two coal samples B_1 and B_2 before ashing.

In the next stage, both coal samples B1 and B2 were ashed at temperatures of 700°C and 1000°C for four hours in a furnace (according to standard D 3174 - 11). The obtained results are presented in Table 1 [9].

Table 1.The ash percentage of B1 and B2 samples at different temperatures

Sample	Ash content	Temperature
B1	33.31	700
B2	50.94	700
B1	31.08	1000
B2	46.99	1000

After ashing the samples, XRD and XRF analyses were conducted on the samples. As shown in Fig. 2, the ashed coal samples B_1 and B_2 at a temperature of 700°C exhibit a 2θ peak corresponding to the mineral montmorillonite with the chemical formula $[(Na,Ca)0.33(Al,Mg)_2(Si_4O_{10})(OH)_2 \cdot nH_2O]$. Montmorillonite is a group of minerals that include illite, kaolinite, and halloysite. With the increase in temperature, the crystal structure of this mineral is destroyed, leading to its absence in the coal samples B_1 and B_2 ashed at 1000°C. Peaks at 2θ equal to 40, 26, 50, and 55 correspond to the mineral quartz seen in both coal samples B_1 and B_2 at both temperatures. Peaks at 2θ equal to 35 and 17 in coal samples B_1 and B_2 ashed at 700°C correspond to the mineral mullite with the chemical formula $3Al_2O_3.2SiO_2$. Additionally, at 1000°C, peaks at 2θ equal to 60, 33, and 65 correspond to mullite [10]. Furthermore, peaks appearing at 2θ 34 in coal samples B_1 and B_2 ashed at 700°C are attributed to the mineral hematite with the chemical formula Fe_2O_3. With the temperature increase, the intensity of these peaks decreases, and hematite transforms into magnetite, leading to new peaks at 2θ equal to 87.36. Muscovite, with the chemical formula KAl2(AlSi3O10)(F,OH)2, a group of minerals, appears at 2θ equal to 27, 18, 36, 65, and 77 in the samples.

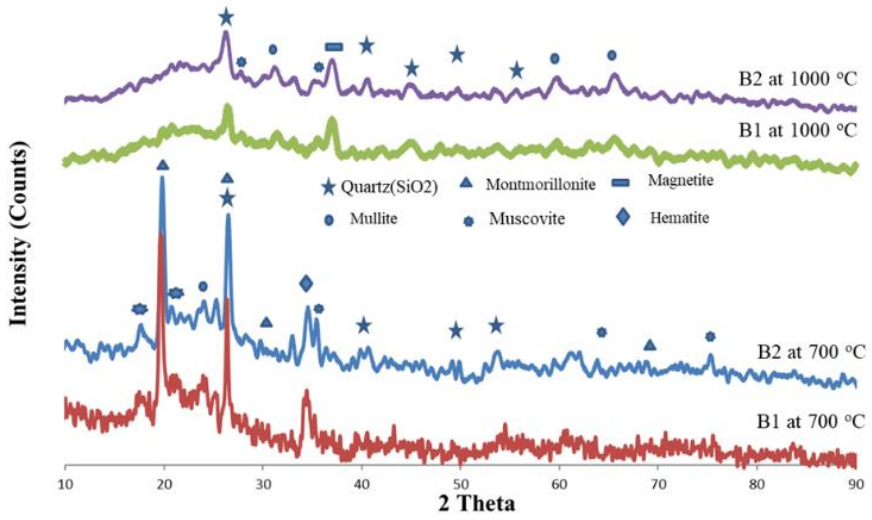

Fig. 2.XRD analysis of two coal samples B_1 and B_2 after ashing.

XRF analysis was also performed elementally on the ashes of samples B_1 and B_2, and the results are reported in weight percent in Table 2. The results indicate that the amount of lithium in coal sample B_1 is higher than in coal sample B_2. Additionally, the concentrations of other elements such as aluminum, calcium, iron, and magnesium are greater in coal sample B_1 compared to coal sample B_2. Therefore,

despite the identical mineral structures of the two coal samples, there is a difference in lithium concentration between the two samples.

Table 2. XRF analysis of ashed coal samples B1 and B2

Component wt%	B1 samples at 700 0C	B2 samples at 700 0C
Al2O3	13.21	15
SiO2	59.4	66.09
K2O	4.44	5.01
CaO	1.25	0.76
Fe2O3	10.28	7.1

In the next stage, a digestion test was conducted on the coal samples to determine the lithium content following the standard method (Standard D 6357 - 2011) [11]. The results of the lithium analysis are reported in the tables below:

Table 3. Results of ICP analysis for **B_1** ashed sample

Element	Content in ash(ppm)
Li	279
Al	131800
Ca	15763
Fe	51193
Mg	9788

Table 4. Results of ICP analysis for **B_2** ashed sample

Element	Content in ash(ppm)
Li	214
Al	12042
Ca	9690
Fe	12278
Mg	7980

According to the results, it can be seen that despite the same structure of the minerals in the samples B1 and B2, the amount of lithium and related elements in B1 sample is far more than B2 sample, which is due to taking samples from different parts of the coal gangue.

Conclusion

As mentioned, two representative samples labeled B1 and B2 were obtained from various sections of the coal gangue, and characterization tests were conducted on them. The XRD analysis results indicate

that both samples have similar structural minerals, with montmorillonite and quartz being the primary minerals. Montmorillonite is a group of minerals that include illite, kaolinite, and halloysite. Despite the structural similarity, the chemical compositions of these samples were different. According to the results, sample B1 had the highest lithium content at ppm 279, likely due to sampling from different sections of the coal gangue. Additionally, sample B2 has the highest ash content, reaching approximately 51% by weight, with a lithium content of around ppm 109. This makes lithium extraction from this sample challenging due to increased energy consumption, time, and costs associated with higher raw material consumption.

References

[1] Nemati M, Investigating the country's potential for exploration, extraction and recycling of lithium metal as the most important energy storage in the world. The study of infrastructure research and production affairs, Office of Energy, Industry and Mining Studies, 2017.

[2] Zhang, Y., et al., Systematic review of feldspar beneficiation and its comprehensive application. Minerals Engineering, 2018. 128: p. 141-152.

[3] Shao, L., & Jin, S. (2020). Resilience assessment of the lithium supply chain in China under impact of new energy vehicles and supply interruption. Journal of cleaner production, 252, 119624.

[4] Zhao, X., Feng, M., Jiao, Y., Zhang, Y., Wang, Y., & Sha, Z. (2020). Lithium extraction from brine in an ionic selective desalination battery. Desalination, 481, 114360.

[5] Zhang, W., Noble, A., Yang, X., & Honaker, R. (2020). Lithium leaching recovery and mechanisms from density fractions of an Illinois Basin bituminous coal. Fuel, 268, 117319.

[6] Chen, H., Zhang, L., Pan, J., Long, X., He, X., & Zhou, C. (2022). Study on modes of occurrence and enhanced leaching of critical metals (lithium, niobium, and rare earth elements) in coal gangue. Journal of Environmental Chemical Engineering, 10(6), 108818.

[7] Xie, Y., Ni, C., Wu, M., Han, Z., Liao, J., Nie, S., ... & Xie, W. (2023). Recycling Strategy toward Efficient and Green Lithium Leaching from Coal-Based Lithium Ores Enabled by Solubility Engineering and Reusable Solid Acid. ACS Sustainable Chemistry & Engineering, 11(7).

[8] Hu, P., Hou, X., Zhang, J., Li, S., Wu, H., Damø, A. J., ... & Xi, X. (2018). Distribution and occurrence of lithium in high-alumina-coal fly ash. International Journal of Coal Geology, 189.

[9]. ASTM, D., Standard Test Method for Ash in the Analysis Sample of Coal and Coke from Coal.

[10] Xu, H., Liu, C., Mi, X., Wang, Z., Han, J., Zeng, G., ... & Huang, S. (2021). Extraction of lithium from coal fly ash by low-temperature ammonium fluoride activation-assisted leaching. Separation and Purification Technology, 279, 119757.

[11] ASTM, D.-a., Standard Test Methods for Determination of Trace Elements in Coal, Coke, and Combustion Residues from Coal Utilization Processes by Inductively Coupled Plasma Atomic Emission Spectrometry, Inductively Coupled Plasma Mass Spectrometry, and Graphite Furnace Atomic Absorption Spectrometry1. 2000, American Society for the Testing of Materials Philadelphia, PA.

ICNST 2024
International Conference on Nuclear Science and Technology
6- 8 MAY 2024 | Isfahan, Iran

First-Principles Study of the Adsorption of Water Molecule on Zr Surface (Paper ID : 1529)

Basaadat M.R.*, Payami M., Sheykhi S.

Physics and Accelerators Research School, Nuclear Science and Technology Research Institute, AEOI, B. O. Box: 1439951113, Tehran, Iran.

Abstract

At working temperatures of the reactor, the water molecules interact with the Zr-based cladding which leads to Zr-H compounds that may degrade the heat transfer to the cooling water. Therefore, studying the interaction of water molecules with zirconium surface is one of the most important branches of research in nuclear materials field. In this study, using ab-initio molecular dynamics, which is based on the density functional theory, we have studied the dynamics of adsorption of a water molecule on Zr (0001)-surface. This study has been performed for two different initial distances of water molecule from the Zr surface: 1 Angstrom and 2.5 Angstrom. The results show that for closer distance, H2O molecule dissociates and each hydrogen atom makes a bond with a Zr atom on the surface to constitute the zirconium hydride composition. Actually, it has been shown that there are chemical interactions between the hydrogen and oxygen from the water molecule and zirconium atoms during the time for different distance of water molecule from the zirconium surface.

Keywords: water molecule, hydrogen adsorption, zirconium-based cladding, density functional theory, molecular dynamics

Introduction

Zirconium and its alloys are one of the most useful materials which are used in nuclear industry as structural materials [1-4]. As an example, it is used as fuel cladding in different forms such as: Zircaloy-2, Zircaloy-4, Zr-1%Nb [5] (with excellent ductility [6]) and so forth. There are three different phases for pure zirconium: alpha phase, beta phase and omega phase [7,8] which can be found in the literature. There are a huge number of theoretical and experimental studies in the zirconium based materials in different aspects. For example, phase transition and elastic properties of zirconium have been studied by Yan and coworkers [9]. The mechanical properties of zirconium alloys and zirconium hydrides have been explored by Weck [10]. Molecular dynamics (MD) simulation is a powerful instrument to study

different phenomenon of nuclear industrial materials in the working situation. Accordingly, there are a lot of studies in the literature which is increasing during the time. As an important phenomenon irradiation effects has been increasingly studied based on molecular dynamics. There are other hot topics in the nuclear industrial field which have simulated with MD. For instance, the elastic stiffness tensor of Zr-xNb alloy in presence of defects and the effect of point defects on mechanical properties of Zr and Zr-1%Nb structure have been studied by Basaadat [11,12] with molecular dynamics approaches. The effect of zirconium on the Ni nanocrystal have been studied by Pal [13]. There are also a lot of other studies on zirconium in the literature [16–24].

One of the most important phenomena which have been happening in the fuel cladding zirconium based materials is the interaction of water molecules with the zirconium at the PWR reactors. As it is known, the water molecules is the near clad as coolant. There are some hydrogen adsorptions in this process and this hydrogen can dissociate from H2O molecules and make a bond with zirconium. This process may lead to form zirconium hydride which degrades the corrosion behavior of Zr-based alloys.

In this study, the interaction of water molecule with the zirconium structure has been considered using the Ab-initio molecular dynamics. Since the molecules are in the different distance from the clad, two different distances were selected for starting simulations in the working situation of nuclear reactors. The results show that the hydrogen atom can dissociate from the water molecule near the surface and make bond with surface to make zirconium hydride.

Research Theories

A-zirconium (HCP) has been considered for simulation of the Zr-surface which is oriented in the (0001) direction. All of the optimizations and electronic structure calculations have been performed according to density functional theory which is implemented in the SIESTA [25] code package as a powerful and fast program with the basis set of strictly-localized atomic orbitals. The generalized gradient approximation (GGA) of Perdew, Burke and Ernzerhof (PBE) with double zeta polarization (DZP) basis set were used in all of the simulations [26].The supercell surface size optimization has been done to avoid the interaction of water elements with its periodic images and based on this, the surface with 4×4×1 unitcell with 32 zirconium atoms has been selected. The other optimizations which are related to calculations have been done and 38 kpoints have been considered for the Brilloun Zone sampling for

calculations. The cutoff energy was set to be 500 Ry. The convergency criterion for energy and density was chosen 1e-4 eV. The Nose-Car-Parrinello-Rahman MD method [27] have run for molecular dynamic simulations to obtain the atomic evolution at different time. Timestep for the simulations has 1 fs and the systems have been simulated for 300 steps. The temperature of the simulations was 600 K. The 15 angstroms of vacuum have been used for the calculations which is necessary for the surface calculations to prevent the interactions with periodic images.

Results and discussion

In this study we discuss about the interaction of water molecule near the zirconium surface. As it is mentioned, two different distances have chosen for these calculations: 1 angstrom and 2.5 angstrom between water molecule and the surface. This distance is actually between the hydrogen atom in the water molecule and the upper layer of the zirconium surface. The water molecule is oriented on the surface such that the hydrogen atoms are located under the oxygen atom and the molecule has been located on the hollow space of the zirconium atoms layer symmetrically (see Fig. 1).

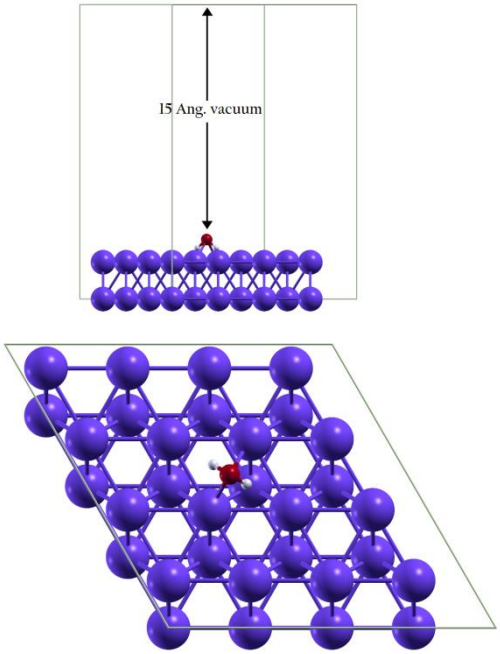

Fig1. The water molecule on the zirconium surface in two up and side view.

Since the water molecule can be on the different distance from the surface, we select two distances to see the interaction of it with the zirconium surface. The simulations have been performed for 300 time steps (equivalent to 0.3 picoseconds) and it has shown for both cases that the hydrogen atom can dissociate from the water molecules and make a bond with the surface to form zirconium hydride.

The time evolution of the bond of hydrogen atoms with oxygen in the water molecule have been presented in Fig.2 in the vicinity of the Zr-surface. It can be seen that in the 1 Ang. both of the hydrogen atoms has been dissociated of the water molecule from the beginning of the simulation in the 1 Ang. distance case. In the other case (2.5 Ang. distance), one of the hydrogen atoms has dissociated from the water molecule and make a bond with surface zirconium atom but the other hydrogen atom hasn't been dissociated.

In both cases, there are some maximum and minimum points on the bond length of H-O bond which is interpreted as the making chemical bonding (minimums) and cusp point from the surface (maximums).

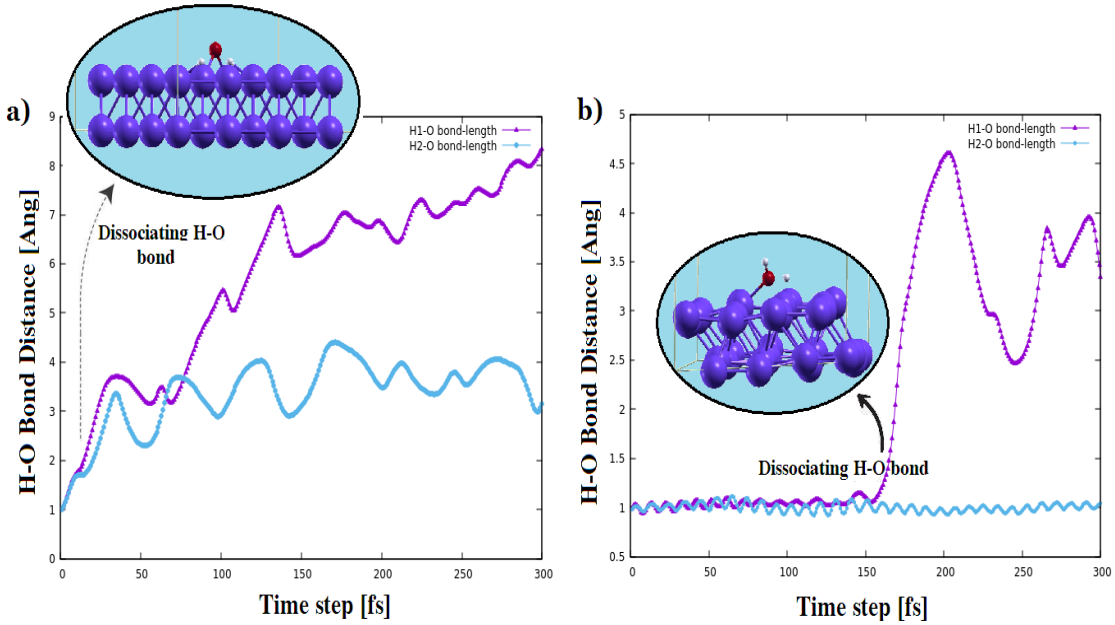

Fig 2. H-O bond length evolution during the interaction of water molecule with zirconium surface: a) Dist(Zr-H2O) = 1.0 Ang. b) Dist(Zr-H2O) = 2.5 Ang.

In the same way, it can be important to understand that the interaction of oxygen atom in this simulation. Accordingly, the time evolution of the relative oxygen atom is presented in the Fig.3. As it can be seen, the distance of the O atom from the Zr-surface relative to the first O distance is not change dramatically

for the case of 1 Ang distance. But in the other case, the oxygen atom goes nearer to the surface and making bond with the zirconium atoms to oxidize the surface. For the latter case, the position of oxygen atom in the [0001] direction is 1.5 Ang. less than the starting point approximately and it means that in this case the oxygen atom will be located at the 1 Ang. distances from the surface as the first case after the simulation!

The distance of nearest zirconium atom in the surface to the H and O atom in the water molecule have been listed in the table 1 for first and last time step of simulation. The 'i' and 'f' subscripts are denoted to initial and final step of the simulation. It is shown that the distance of both H and O atom with the Zr atom should be less after the simulation. The sum of the covalent radius of the H-Zr and O-Zr are 2.06 and 2.41 respectively and the distance of these atoms at the final of the simulation are less than this factor. Therefore, this can be the other evidence of the presence of the interaction between the element of the water and the zirconium surface atoms.

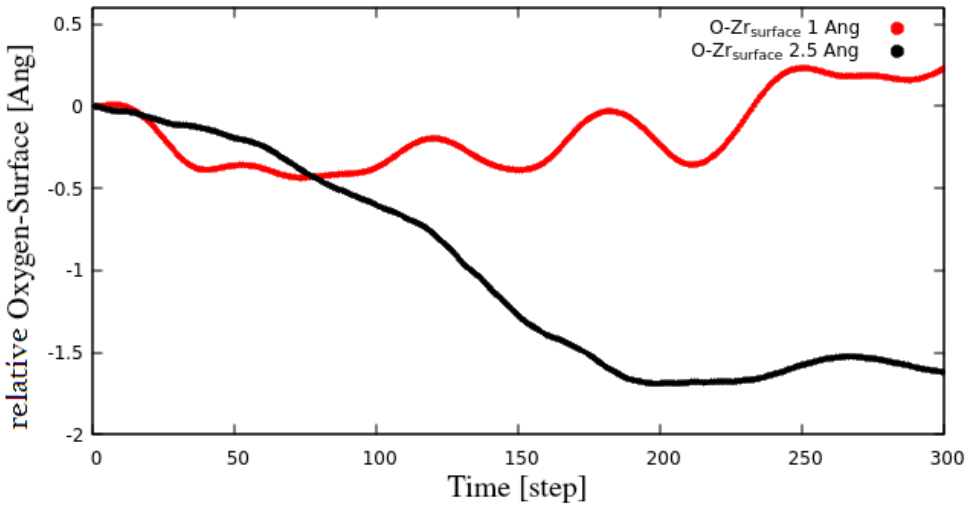

Fig 3. Relative oxygen distance evolution from the surface.

Table 1. The distance of nearest Zr atom to the H/O atom for the starting/ending simulation

	di(H-Zr)	df(H-Zr)	di(O-Zr)	df(O-Zr)
DH2O-Zr: 1 Ang	2.048	1.810	2.272	1.906
DH2O-Zr: 2.5 Ang	3.073	1.819	3.493	2.193

Conclusions

The interaction of H2O water molecule with the zirconium surface has been studied using the Ab-initio molecular dynamics simulation in the reactor working situation. The time evolutions of hydrogen and oxygen atoms in the simulation box have been monitored to have a deep insight of this interaction. Results show that there are chemical interactions between the H-Zr and also O-Zr during the time for different distance of water molecule from the zirconium surface. This is a remarkable result because this can make the zirconium hydrides/oxides while the water molecule goes near the zirconium-based alloys of the cladding materials in the reactor. It can be concluded that for the distances less than 2.5 angstroms there should be chemical interactions.

References

[1] Rickover H.G., Geiger L.D., and Lustman B., (1975) Energy Research and Development Administration, Washington, DC (USA). Div. of Naval Reactors.

[2] Lustman B. Et. al. (1957), Journal of The Electrochemical Society. 104,12:254ca.

[3] Cox B. Et. al. (2005) , Journal of Nuclear materials, 336(2-3), pp.331-368.

[4] Bell B.D.C., Murphy S.T., Burr P.A., Comstock R.J., Partezana J.M., Grimes R.W., and Wenman M.R. (2016), Corrosion Science, 105 , pp.36–43.

[5] Lemaignan C., and Motta A. T. (2006), Materials science and technology.

[6] Northwood D. O. (1985), Materials & design, 6(2) , pp.58–70.

[7] Kharchenko V. O., and Kharchenko D.O. (2012), arXiv preprint arXiv:1206.7035.

[8] Peng Q., Ji W., Lian J., Chen X. J., Huang H., Gao F., and De S. (2014), Scientific reports, 4(1), pp.1–7.

[9] Hao Y. J., Zhang L., Chen X. R., Li Y. H., and He H. L. (2008), Journal of Physics: Condensed Matter, 20(23), p.235230.

[10] Weck P. F., Kim E., Tikare V., and Mitchell J. A. (2015), Dalton Transactions, 44(43), pp.18769-18779.

[11] Basaadat M. R., and Payami M.(2020), International Journal of Modern Physics C, 31(02), p.2050028.

[12] Basaadat M. R. and Payami M. (2020), IRANIAN JOURNAL OF PHYSICS RESEARCH.

[13] Pal, S., Meraj, M. and Deng, C., (2017). Effect of Zr addition on creep properties of ultra-fine grained nanocrystalline Ni studied by molecular dynamics simulations. Computational Materials Science, 126, pp.382-392.

[16] Ashkenazi J., Dacorogna M., Peter M., Talmor Y., Walker E., and Steinemann S. (1978), Physical Review B, 18(8), p.4120.

[17] Bolef D.I. et. al. (1961) , Journal of Applied Physics, 32(1), pp.100–105.

[18] Hayes D. J., and Brotzen F. R. (1974), Journal of Applied Physics, 45(4), pp.1721–1725.

[19] Fast L., Wills J. M., Johansson B., and Eriksson O. (1995), Physical Review B, 51(24), p.17431.

[20] Al-Zoubi N., Sch¨onecker S., Li X., Li W., Johansson B., and Vitos L. (2019), Computational materials science, 159, pp.273–280.

[21] Pal S., Meraj M., Deng C. (2017), Computational Materials Science, 126, pp.382–392.

[22] Kaddour D., Frechinet S., Gourgues A. F., Brachet J. C., Portier L., and Pineau A. (2004), Scripta materialia, 51(6), pp.515–519.

[23] Adamson S., Adamson R., Garzarolli F., and Patterson C. (2009), Advanced Nuclear Technology International.

[24] Adamson R. B., Coleman C. E., and Griffiths M. (2019), Journal of Nuclear Materials, 521, pp.167–244.

[25] Soler, J.M., Artacho, E., Gale, J.D., García, A., Junquera, J., Ordejón, P. and Sánchez-Portal, D., (2002). The SIESTA method for ab initio order-N materials simulation. Journal of Physics: Condensed Matter, 14(11), p.2745.

[26] Perdew, J.P., Burke, K. and Ernzerhof, M., (1996). Generalized gradient approximation made simple. Physical review letters, 77(18), p.3865.

[27] Hutter, J. and Iannuzzi, M., (2005). CPMD: Car-Parrinello molecular dynamics. Zeitschrift für Kristallographie-Crystalline Materials, 220(5-6), pp.549-551.

Hubbard-corrected DFT study of UO2 : parameters tuning for correct lattice constant and electronic band-gap (Paper ID : 1543)

Payami Shabestar M.
School of Physics & Accelerators, Nuclear Science and Technology Research Institute, AEOI, P. O. Box 14395-836, Tehran, Iran

Abstract

Ordinary approximations in density-functional theory (DFT) such as local-density approximation (LDA) or semi-local approximations such as generalized gradient approximation (GGA) for the localized orbitals in strongly-correlated electron systems usually lead to incorrect metallic behavior. One workaround is to estimate the interactions of localized orbitals using the Hubbard model and add it to the DFT energy functional and then subtract the double-counting contributions from the DFT energy functional. UO2 is an example having O-2p, U-6d, and U-5f incomplete electronic shells. Usually, researchers apply the Hubbard correction only to the localized incomplete 5f electrons of U atoms and succeed to predict insulating property and good geometric properties by tweaking the Hubbard-U parameter. However, it turned out that in such a way it was impossible to obtain reasonable values for both geometry and electronic band-gap at the same time. In this work, we show that it is possible to reproduce good values at the same time for those properties just by applying and tuning the Hubbard corrections to all incomplete shells of O-2p, U-6d, and U-5f.

Keywords: Density-functional theory, Strongly-correlated electrons, Band-gap tuning, On-site repulsion, Occupation-matrix control.

Introduction

UO2, as a common fuel for nuclear power reactors, has attracted the interests of researchers for a better theoretical description within DFT+U approach [1-4]. Uranium dioxide has a 3D anti-ferromagnetic (AFM) crystal structure at temperatures less than 30 K [5, 6] but usually a simpler 1D-AFM model is used for the description. Recent XRD experiment [7] has shown that UO2 crystallizes with a cubic space group $Pa\bar{3}$ (No. 205). However, if the structure is modeled by a slightly different but more symmetric cubic space group $Fm\bar{3}m$ (No. 225) with experimental lattice constant of 5.47 Angstrom, which is shown in Fig. 1(a), then the structure can be represented by a simple tetragonal unit cell with 6 atoms as shown in Fig. 1(b).

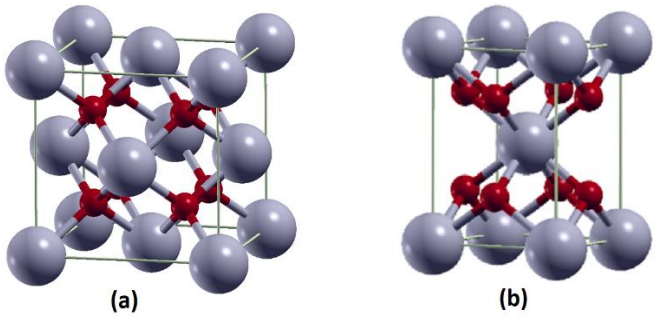

Fig. 1. (a)- UO_2 crystal structure with cubic space group $Fm\bar{3}m$ (No. 225) and lattice constant of 5.47 Angstrom; (b)- description by a simple tetragonal crystal structure with six atoms. Gray and small red balls represent uranium and oxygen atoms, respectively.

Experiment has shown [8] that UO_2 is electrically an insulator with a gap of 2.10 eV. Ordinary approximations in density-functional theory (DFT) such as local-density approximation (LDA) [9, 10] or semi-local approximations such as generalized gradient approximation (GGA) [11] for the localized orbitals usually lead to incorrect metallic behavior. One workaround is to estimate the interactions of localized orbitals using the Hubbard model and add it to the DFT energy functional and then subtract the double-counting contributions from the DFT energy functional [1, 12-14]:

$$E_{\mathrm{DFT+U}} = E_{\mathrm{DFT}} - E_{\mathrm{dc}} + E_{\mathrm{Hub}}. \qquad (1)$$

The interaction term in Hubbard model, when the Hamiltonian is represented in the basis of strongly localized Wannier functions, is written as:

$$E_{Hub} = U \sum_i n_{i\uparrow} n_{i\downarrow} \qquad (2)$$

where U is a real number, $n_{i\sigma}$ with $\sigma = \uparrow, \downarrow$ denote the particle number operators, and i specifies the lattice site $\vec{R}_i$. For positive values of U, the interaction behaves as on-site repulsion among the electrons, while on the other hand, negative values of U means that there exist on-site attraction among electrons.

In previous DFT+U calculations for UO2, the on-site Hubbard correction with positive interaction parameter U-5f was applied to only 5f electrons of uranium atoms which led to gap opening and thus

correct insulating behavior. However, the gap size and geometric properties such as lattice constant both depend on the value of interaction parameter. By tuning this on-site parameter, it is possible to reproduce only one of those properties: gap size or lattice constant. As is seen from Fig. 2, for the approximation used here, the correct band gap is reproduced by assuming UU-5f =3.2 eV while the correct lattice constant is reproduced by taking UU-5f =4.8 eV. In this work, we have extended the Hubbard correction to cover 6d orbitals of U atoms as well as 2p of O atoms, and determine the relevant interaction parameter values that reproduce both band-gap and lattice constant of the GS in very good agreement with experiment.

The organization of this paper is as follows. In Section 2, we explain the computational details; in Section 3 the calculated results are presented and discussed; and finally in Section 4 we concludes this work.

Computational Details

The DFT+U calculations are done by solution of the KS equations using the Quantum-ESPRESSO code package [15, 16]. Ultra-soft pseudo-potentials (USPP) are used for U and O atoms that has been generated by the atomic code, using the generation inputs (with small modifications for more desired results) from the pslibrary [17]. The valence configuration of U(6s2 6p6, 7s2, 7p0, 6d1, 5f3) and O(2s2, 2p4) were used in the generation. The relativistic effects were accounted at the level of scalar-relativistic (SR) approximation [18], which has been shown to give reasonable GS geometric results [4] for UU-5f =4.53 eV when the Perdew-Zunger [19] (PZ) LDA approximation was used for the exchange-correlation, and the projection on to Hubbard orbitals were chosen to be atomic ones that were not orthogonalized. The appropriate kinetic energy cutoffs for the plane-wave expansions were chosen as 90 and 720 Ry for the wavefunctions and densities, respectively. Also, the Methfessel-Paxton smearing method [20] for the occupations with a width of 0.01 Ry is used for better convergency process. For the Brillouin-zone integrations in geometry optimizations, a $8\times8\times6$ grid were used. All geometries were fully optimized for total residual pressures on unit cells to within 0.5 kbar, and residual forces on atoms to within 10^{-3} mRy/a.u. The occupation matrix control (OMC) [1] is used to avoid metastable states. The starting magnetization for oxygen atoms are set to zero values and for U atoms they are set as ±0.5 to make anti-ferromagnetic (AFM) configuration along the z direction. Since in the present work we apply

Hubbard corrections to 5f, 6d localized orbitals of U atoms and 2p orbitals of O atoms, we have occupation matrices of dimensions 7×7, 5×5, and 3×3, respectively. Applying the Hubbard correction for each of the orbitals U-5f, U-6d and O-2p separately one at a time showed that only the Hubbard corrections to U-5f orbitals lead to metastable states and the other two are insensitive to initial occupations. Since in the U-atom pseudo-potential the 5f orbital is occupied by 3 electrons, then we have $C_3^7 = 35$ different ways for occupying the diagonal elements of 7×7 matrix by 3 electrons: [1110000], [1101000], [1100100], … , [0001011], [0000111].

Results and Discussions

Examining Hubbard corrections for 5f, 6d of U-atom and 2p of O-atom separately one at a time shows that only correction on 5f is able to open an energy gap and give reasonable lattice constant. The situation is shown in Figs. 2-4.

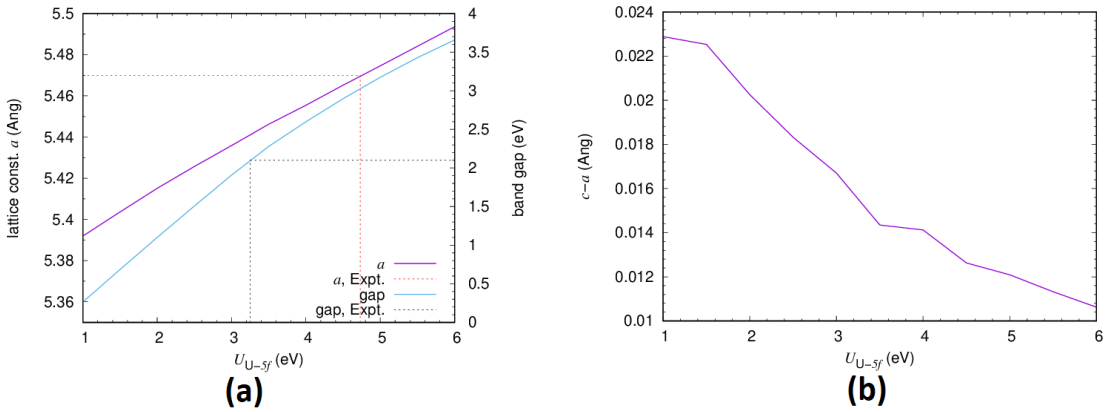

Fig. 2. (a)- Lattice constant a in Angstrom and band gap in eV as functions of Hubbard correction strength UU-5f ; (b)- Deviation form cubic geometry, (c-a), in Angstrom as function of Hubbard correction strength UU-5f of U-atom.

Inspecting Fig. 2(a), it is seen that the value for experimental lattice constant is reproduced around UU-5f ~ 4.8 eV while the correct band gap is reproduced by assuming UU-5f =3.2 eV. This implies that with only one correction parameter (i.e., UU-5f) one fails to reproduce reasonable values for both lattice constant and the band gap at the same time. In Fig. 2(b), the deviation from cubic geometry (c-a) is shown to be very small (~ 0.01 Angstrom) so that modeling the system by 1D-AFM (instead of 3D-AFM) does not cause any significant error in this study. On the other hand, Figs. 3 and 4 show that the

value of lattice constant is relatively insensitive to the values UU-6d and UO-2p . These results hint that one should do fine-tuning of UU-5f around the value of 4.0 eV. In addition, similar to the result in Fig. 2(b), the corresponding deviations from cubic geometries in Figs. 3-4 are negligible.

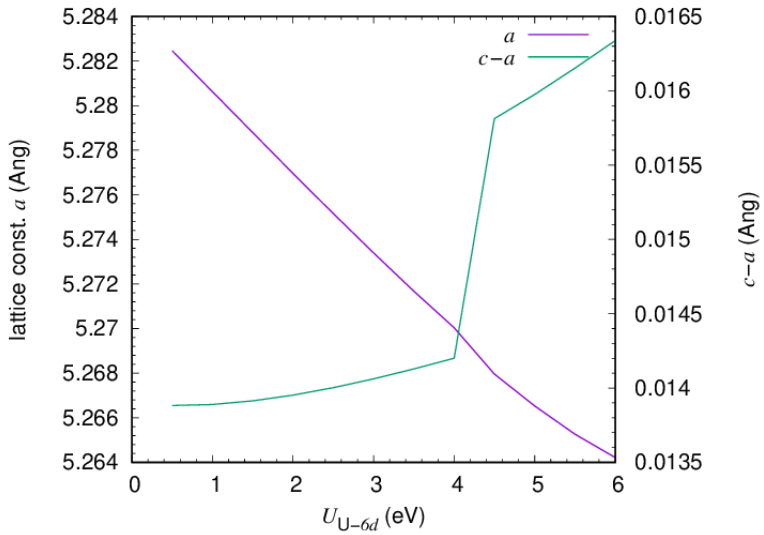

Fig. 3. Lattice constant a and deviation from cubic geometry (c-a) in Angstrom as functions of Hubbard correction strength UU-6d .

In the next step, we apply Hubbard corrections to two orbitals at a time. In above it was shown that the correct lattice constants were reproduced by applying the correction to only U-5f with the strength of ~ 4.00 eV. So, we consider the correction to U-5f with strength 4.00 eV as the main correction and add that for U-6d as a background one with different values. The result is shown in Fig. 5. As is seen from Fig. 5, adding the background correction for U-6d almost does not change the lattice constant for UU-6d < 3.0 eV and so we ignore the background correction for U-6d.

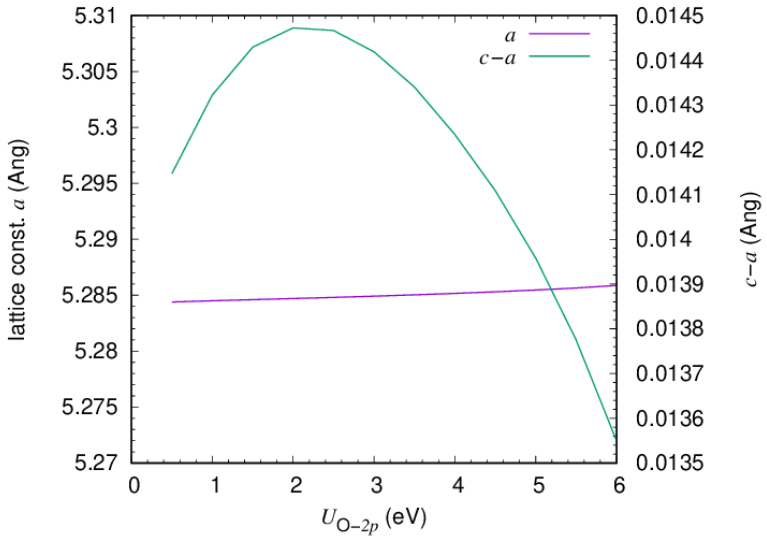

Fig. 4. The same as in Fig. 3 but for Hubbard correction strength $U_{O\text{-}2p}$.

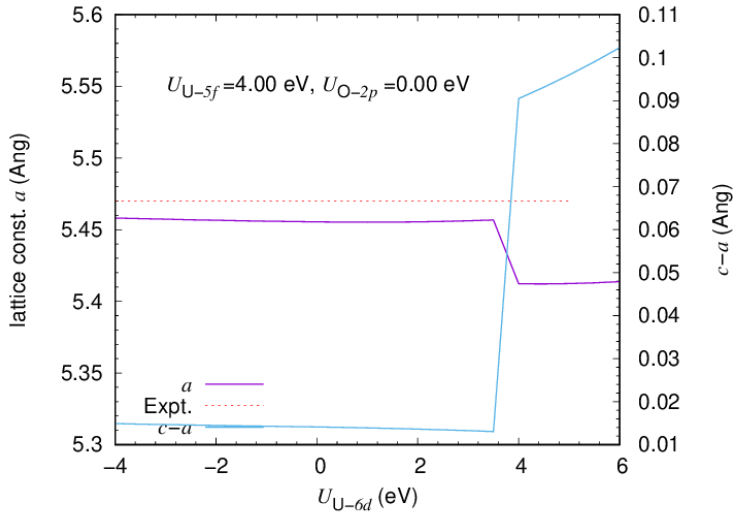

Fig. 5. The same as in Fig. 3 as functions of Hubbard correction strength $U_{U\text{-}6d}$ for fixed value of $U_{U\text{-}5f}$ =4.00 eV.

We now concentrate on adding the background correction of O-*2p* orbitals. As is seen from Fig. 6, in contrast to the case of U-*6d*, here the background correction to O-*2p* orbitals significantly modifies the results attained by the correction on U-*5f*. That is, in order to maintain the reasonable value for the lattice constant, one should use negative values for the Hubbard correction parameter for O-*2p* orbitals, meaning that the background correction is as an on-site attraction. To summarize, Fig. 6 indicates that

the combination of two simultaneous corrections with $U_{U\text{-}5f}$ =4.0 eV and $U_{O\text{-}2p}$ =-3.00 eV revives the reasonable value for the lattice constant. But now we expect that the electronic band gap is changed from the value 2.91 eV, obtained if only U-*5f* correction was applied [4]. Fig. 6 also indicates that the deviation from cubic geometry is still acceptable.

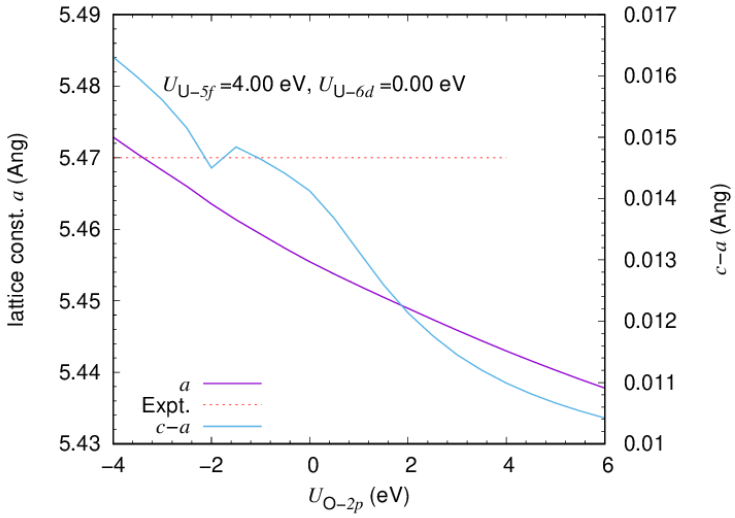

Fig. 6. The same as in Fig. 5 as functions of Hubbard correction strength $U_{O\text{-}2p}$ for fixed value of $U_{U\text{-}5f}$ =4.00 eV.

To have a closer inspection on the effect of negative values for UO-2p , we have calculated the GS lattice constants and electronic band gaps for different values of UU-5f , keeping UO-2p fixed at three values of -3.00, -3.50, and -4.00 eV. The results are presented in Table 1.

In order to estimate the proper combinations of Hubbard strengths for UU-5f and UO-2p for a desired value of band gap (2.00, 2.10, 2.20 eV), we have plotted the data of Table 1 in Fig. 7.

Table 1. Lattice constants in Angstrom and E_{gap} in eV as functions of $U_{U\text{-}5f}$ and fixed values of background correction $U_{O\text{-}2p}$ =-3.00, -3.50, and -4.00 eV.

U_O (eV)	U_U (eV)	a (c) ($\AA$)	E_{gap} (eV)
-3.00	3.00	5.4477 (5.4667)	1.7651
	3.10	5.4498 (5.4684)	1.8397
	3.20	5.4518 (5.4701)	1.9096
	3.30	5.45391(5.4718)	1.9706
	3.40	5.4559 (5.4734)	2.0308
	3.50	5.4579 (5.4751)	2.0900
	3.60	5.4599 (5.4767)	2.1484
	3.70	5.4619 (5.4784)	2.2059
	3.80	5.4644 (5.4795)	2.2623
	3.90	5.4666 (5.4817)	2.3180
	4.00	5.4682 (5.4838)	2.3731
-3.50	3.00	5.4499 (5.4693)	1.7387
	3.10	5.4520 (5.4710)	1.8125
	3.20	5.4541 (5.4727)	1.8789
	3.30	5.4561 (5.4744)	1.9387
	3.40	5.4581 (5.4759)	1.9977
	3.50	5.4601 (5.4776)	2.0556
	3.60	5.4622 (5.4794)	2.1129
	3.70	5.4642 (5.4812)	2.1691
	3.80	5.4665 (5.4830)	2.2245
	3.90	5.4685 (5.4847)	2.2789
	4.00	5.4705 (5.4864)	2.3320
-4.00	3.00	5.4522 (5.4720)	1.7112
	3.10	5.4543 (5.4737)	1.7842
	3.20	5.4564 (5.4754)	1.8472
	3.30	5.4584 (5.4769)	1.9057
	3.40	5.4604 (5.4786)	1.9636
	3.50	5.4626 (5.4805)	2.0206
	3.60	5.4648 (5.4823)	2.0765
	3.70	5.4669 (5.4841)	2.1315
	3.80	5.4689 (5.4858)	2.1855
	3.90	5.4708 (5.4874)	2.2383
	4.00	5.4728 (5.4891)	2.2902

As we see from Fig. 7, since here we have chosen three fixed values for $U_{O\text{-}2p}$, there exist three different combinations of the Hubbard strengths $U_{U\text{-}5f}$ and $U_{O\text{-}2p}$ for each desired value of band gap. To verify the validity of this guess, we have calculated the GS properties for nine combinations of Hubbard strengths hinted by plots of Fig. 7 and presented the results in Table 2.

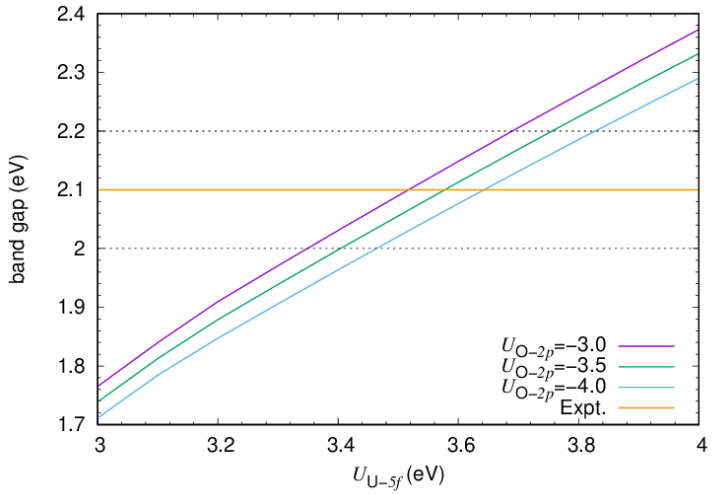

Fig. 7. Variation of band gap as function of $U_{U\text{-}5f}$ for different fixed values of $U_{O\text{-}2p}$. It is seen that, in this example, to obtain each desired values of E_{gap} =2.00, 2.10, and 2.20 eV one has three choices for the Hubbard strength combinations.

Table 2. Hubbard parameters U_U and U_O , in eV, needed to be used to obtain a desired band gap $\tilde{E}_{gap}$ along with the resulted lattice constants a (c) and band gap E_{gap} .

$\tilde{E}_{gap}$ (eV)	U_U, U_O (eV)	a (c) (Å)	E_{gap} (eV)
2.00	3.40, -3.00	5.4560 (5.4735)	2.03
	3.45, -3.50	5.4592 (5.4768)	2.03
	3.48, -4.00	5.4622 (5.4802)	2.01
2.10	3.50, -3.00	5.4579 (5.4751)	2.09
	3.60, -3.50	5.4623 (5.4795)	2.11
	3.65, -4.00	5.4658 (5.4832)	2.10
2.20	3.70, -3.00	5.4619 (5.4784)	2.21
	3.78, -3.50	5.4661 (5.4827)	2.21
	3.84, -4.00	5.4697 (5.4865)	2.21

From the data in Table 2, we see that applying simultaneous Hubbard on-site corrections on the U-5f and O-2p orbitals it is possible to tune both lattice constant and band gap to their experimental values.

Conclusions

In previous theoretical studies of UO2 crystal, in order to predict correct insulating behavior, researchers used Hubbard corrections for the U-5f localized orbitals in the DFT+U approach. It was already shown that depending on what XC functional is used and whether the projection on Hubbard orbitals were

orthogonalized or not, for a given Hubbard-U parameter (say 4.0 eV) different results were obtained for equilibrium lattice constant and the KS band gap. None of those results were satisfactory in predicting simultaneous reasonable values for the lattice constant and the size of band gap. In this work, employing the simplest LDA-PZ scheme for the XC energy functional, we have shown that applying the on-site Hubbard corrections simultaneously to U-5f and O-2p orbitals one can choose certain values to obtain results for both the lattice constant and energy band gap of the ground state in good agreement with experiment.

Acknowledgements

This work is part of research program in School of Physics and Accelerators, NSTRI, AEOI.

Data Availability

The raw or processed data required to reproduce these results can be shared with anybody interested upon sending an email to M. Payami.

References

[1] Dorado B., Amadon B., Freyss M., and Bertolus M. (2009). DFT+U calculations of the ground state and metastable states of uranium dioxide. Physical Review B 79 (23): 235125.
[2] Payami M. (2022). Spin-Symmetry Broken Ground-State of UO2 in DFT+U Approach: The SMC Method. Iranian Journal of Physics Research 22 (3): 175.
[3] Payami M. And Sheykhi S. (2024). Relativistic effects in the study of structure and electronic properties of UO2 within DFT+U method. Iranian Journal of Physics Research (In Press).
[4] Payami M. (2023). Comparison of SMC and OMC results in determining the ground-state and meta-stable states solutions for UO2 in DFT+U method. arXiv:2302.04231 .
[5] Amoretti G., Blaise A., Caciuffo R., Fournier J. M., Hutchings M. T., Osborn R., Taylor A. D. (1989). 5f-electron states in uranium dioxide investigated using high-resolution neutron spectroscopy. Physical Review B 40 (3): 1856.
[6] Faber J., Lander G. H., Cooper B. R. (1975). Neutron-diffraction study of UO2: Observation of an internal distortion. Physical Review Letter 35 (26): 1770.
[7] Desgranges L., Ma Y., Garcia Ph., Baldinozzi G., Simeone D., Fischer H. E. (2017). What is the actual local crystalline structure of uranium dioxide, UO2 : A new perspective for the most used nuclear fuel. Inorganic Chemistry 56 (1): 321.
[8] Schoenes J. (1978). Optical properties and electronic structure of UO2. *Journal of Applied Physics 49 (3).*
[9] Hohenberg P., Kohn W. (1964). Inhomogeneous electron gas. Physical Review 136 (3B): B864.

[10] Kohn W., Sham L. J. (1965). Self-consistent equations including exchange and correlation effects. Physical Review 140 (4A): A1133.
[11] Perdew J. P., Ruzsinszky A., Csonka G. I., Vydrov O. A., Scuseria G. E., Constantin L. A., Zhou X., Burke K. (2008). Restoring the density-gradient expansion for exchange in solids and surfaces. Physical Review Letter 100 (13): 136406.
[12] Cococcioni M., de Gironcoli S. (2005). Linear response approach to the calculation of the effective interaction parameters in the LDA+U method. Physical Review B 71 (3): 035105.
[13] Himmetoglu B., Floris A., de Gironcoli S., Cococcioni M. (2014). Hubbard-corrected DFT energy functionals: The LDA+U description of correlated systems. International Journal of Quantum Chemistry 114 (1): 14.
[14] Freyss M., Dorado B., Bertolus M., Jomard G., Vathonne E., Garcia Ph., Amadon B. (2012). First-principles DFT+U study of radiation damage in UO2: f-electron correlations and the local energy minima issue. ψ_k scientific highlight of the month. 113.
[15] Giannozzi P., Baroni S., Bonini N., Calandra M., Car R., Cavazzoni C., Ceresoli D., Chiarotti G. L., Cococcioni M., Dabo I., Dal Corso A., Gironcoli S., Fabris S., Fratesi G., Gebauer R., Gerstmann U., Gougoussis Ch., Kokalj A., Lazzeri M., Martin-Samos L., Marzari N., Mauri F., Mazzarello R., Paolini S., Pasquarello A., Paulatto L., Sbraccia C., Scandolo S., Sclauzero G., Seitsonen A. P., Smogunov A., Umari P., and Wentzcovitch R. M. (2009). QUANTUM ESPRESSO: a modular and open-source software project for quantum simulations of materials. Journal of Physics: Condensed Matter 21 (39): 395502.
[16] Giannozzi P., Baseggio O., Bonfa P., Brunato D., Car R., Carnimeo I., Cavazzoni C., de Gironcoli S., Delugas P., Ferrari Ruffino F., Ferretti A., Marzari N., Timrov I., Urru A., Baroni S. (2020). Quantum ESPRESSO toward the exascale. Journal of Chemical Physics 152 (15): 154105.
[17] Dal Corso A. (2014). Pseudopotentials periodic table: From H to Pu. *Computational Materials Science 95.*
[18] Koelling D. D., Harmon B. N. (1977). A technique for relativistic spin-polarised calculations. Journal of Physics C: Solid State Physics 10 (16): 3107.
[19] Perdew J. P., Zunger A. (1981). Self-interaction correction to density-functional approximations for many-electron systems. Physical Review B 23 (10): 5048.
[20] Methfessel M., Paxton A. T. (1989). High-precision sampling for Brillouin-zone integration in metals. Physical Review B 40 (6): 3616.

Self-consistent on-site and inter-site Hubbard parameters within DFT+U and DFT+U+V for UO2 using density-functional perturbation theory (Paper ID : 1545)

Payami Shabestar, M.*, Sheykhi, S. , and Basaadat, M. R.
Physics & Accelerators Research School, Nuclear Science & Technology Research Institute, AEOI, Tehran, Iran

Abstract

The local-density approximation and the generalized gradient approximation for the exchange-correlation in density-functional theory suffer from self-interaction errors, which limits their applicabilities to weakly-correlated electron materials bonded with s and p orbitals. In systems containing atoms with localized d and f orbitals, this error is significant and lead to incorrect prediction of metallic behavior for Mott insulators. One of the methods to cure this problem which is most popular and computationally very low-cost compared to other methods, is using Hubbard model to correct the correlation energy of localized orbitals in DFT energy-functional. The simplest such corrected method, called the DFT+U, adds only on-site corrections to the DFT energy functional. In the extended method called DFT+U+V, in addition to on-site corrections, the inter-site corrections, are also included. To apply the Hubbard-corrected density-functional theory for predicting some known materials' properties, the Hubbard parameters are usually so tuned that the calculations give results in agreement with some experimental data and then one uses the tuned model to predict unknown properties. However, in designing new unknown novel materials there is no data to fit the parameters and therefore self-consistent determination of these parameters is crucial. In this work, using the new method formulated by others, which is based on density-functional perturbation theory, we have calculated self-consistently the Hubbard parameters for UO2 crystal within different popular exchange-correlation approximations. The calculated ground-state lattice constants and electronic band-gaps are compared with experiment and shown that PBE-sol lead to results in best agreement with experiment.

Keywords: Uranium dioxide, Strongly-correlated electrons, Density-functional theory, Hubbard model.

Introduction

Uranium dioxide is a common fuel used in nuclear power reactors. It has a 3k-order anti-ferromagnetic (AFM) crystal structure at temperatures less than 30 K and para-magnetic structure at higher temperatures. Analysis of earlier experimental results showed that the uranium and oxygen atoms occupied respectively the octahedral (4a) and tetrahedral (8c) symmetry positions of cubic space group

$Fm\bar{3}m$ (No. 225) with lattice constant of 5.47 Angstrom. However, later XRD experiment indicated that UO2 crystallizes with a less symmetric cubic space group $Pa\bar{3}$ (No. 205) with oxygen atoms slightly displaced inside the cube. In applying the density-functional theory (DFT) [1, 2] to calculate a material's properties, practically one uses approximations for the exchange-correlation (XC) energy functional. Among the employed approximations, the most popular ones, i.e., local-density approximation (LDA) [2, 3] and the generalized gradient approximation (GGA) [4] suffer from self-interaction errors, which limits their applicabilities to weakly-correlated electron materials bonded with s and p orbitals. In systems containing atoms with localized d and f orbitals (such as UO2), this error is higher and lead to over-delocalization of their corresponding wave-functions which in turn lead to incorrect prediction of metallic behavior for Mott insulators. Different methods have been proposed to cure this problem. One of the methods, which is computationally very expensive, is using variants of hybrid orbital-dependent functionals among them HSE is computationally low-cost [5, 6]. Another method, which is most popular and computationally very low-cost compared to the latter method, is using Hubbard model to correct the correlation energy of localized orbitals in DFT energy-functional. The simplest such corrected method, called the DFT+U, adds only on-site corrections to the DFT energy functional [7]:

$$E_{DFT+U}[n(\vec{r})] = E_{DFT}[n(\vec{r})] + E_{Hub}[\{n_m^{I\sigma}\}] - E_{DC}[\{n^{I\sigma}\}] \quad (1)$$

in which $n(\vec{r})$ is electron density, $n_m^{I\sigma}$ are occupation numbers of orbitals of atom at lattice site R_I, and $n^{I\sigma} = \sum_m n_m^{I\sigma}$. The last term in right hand side of Eq. (1) is added to avoid double counting of interactions contained in the first and second terms.

The simplified rotationally invariant form [8] of the correction is given by [7]:

$$E_U[\{n_{mm'}^{I\sigma}\}] \equiv E_{Hub} - E_{DC} = \sum_{I,\sigma} \frac{U^I}{2} \mathrm{Tr}[\mathbf{n}^{I\sigma}(\mathbf{1} - \mathbf{n}^{I\sigma})], \quad (2)$$

in which $\mathbf{n}^{I\sigma}$ is the atomic occupation matrix. This correction, which is on-site correction, significantly corrects the incorrect prediction of metallic behavior of Mott insulators.

In the extended method called DFT+U+V, which in addition to on-site corrections, includes the inter-site corrections, the rotationally invariant correction to DFT energy functional becomes [9]:

$$E_{U+V} \equiv E_{Hub} - E_{DC} = \sum_{I,\sigma} \frac{U^I}{2} \mathrm{Tr}[\mathbf{n}^{II\sigma}(\mathbf{1} - \mathbf{n}^{II\sigma})] - \sum_{I,J,\sigma}^{*} \frac{V^{IJ}}{2} \mathrm{Tr}[\mathbf{n}^{IJ\sigma}\mathbf{n}^{JI\sigma}], \quad (3)$$

in which the asterisk * over the sum in second term indicates that the sum over J- index is sum over the atoms lying on the spherical concentric shells with atom I at the center. That is, the 1st shell contains the nearest neighbor atoms, the 2nd shell contains the next to nearest neighbor atoms, etc. The coefficients U^I and V^{IJ} are called Hubbard parameters. When we are dealing with a known material, these parameters may be empirically so tuned that the calculations give results in agreement with some experimental data and then employing the tuned model one is able to predict unknown properties of that material. In a new recent work [10] it was shown that taking into account only the on-site parameters for 5f orbital of uranium and 2p orbital of oxygen atoms in UO2, and tuning their values for the LDA approximation of XC and choosing projection operator onto non-orthogonalized Hubbard orbitals, it is possible to reproduce the experimental values of lattice constant as well as the electron band gap. It was also shown that this can happen for different pairs of parameter values indicating a degrees of freedom to select one that also lead to some third correct experimental data. However, in designing new unknown novel materials there is no data to fit the parameters. Additionally, it is advantageous to have a parameter-free theory and therefore self-consistent determination of these parameters is crucial.

In the earlier attempts to self-consistent determination of Hubbard parameters, linear-response constrained-DFT (LR-cDFT) was used within super-cell method [8,9]. The method was somewhat cumbersome and computationally expensive. The new method which was introduced in 2018, uses density-functional perturbation theory within the unit-cell, which is relatively fast and also feasible with low-memory computational facilities [11-13]. The self-consistent parameters are determined using HP code [13] included in the Quantum-ESPRESSO code package [14, 15]. In this work, using the HP code, we have performed a series of self-consistent calculation of Hubbard parameters in DFT+U and DFT+U+V schemes for UO2 crystal in the contexts of LDA [3] and gradient-corrected variants: PW91 [16], PBE [4], PBE-sol [17], and rev-PBE [18]. The calculations include results for both "atomic" and "ortho-atomic" types of projections.

This paper is organized as follows: Section 2 provides the computational details; in Section 3 the calculated results are presented and discussed; and Section 4 summarizes the conclusions of this research.

Computational Details

For the description of crystal structure we have used a simple tetragonal lattice with a six-atom basis, shown in Fig. 1. In addition, to setup anti-ferromagnetic (AFM) structure for U atoms, we used the simple model in which the planes of U atoms alternate their spins when moving in z direction, i.e., a 1-dimensional AFM.

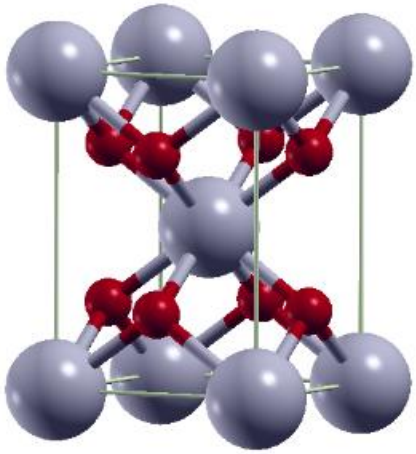

Fig. 1. UO_2 crystal structure as simple tetragonal with six atoms basis. Large gray and small red balls represent uranium and oxygen atoms, respectively.

Determined the Hubbard parameters using the HP code, all DFT, DFT+U, and DFT+U+V calculations were based on the solution of the KS equations using the Quantum-ESPRESSO code package [14,15]. For U and O atoms we have used scalar-relativistic ultra-soft pseudo-potentials (USPP) generated by the atomic code and generation inputs from the pslibrary [19]. The valence configurations U (6s2, 6p6, 7s2, 7p0, 6d1, 5f3) and O (2s2, 2p4) were used in the USPP generation. Different approximations for the XC interactions were used: LDA [3] and gradient-corrected variants: PW91 [16], PBE [4], PBE-sol [17], and rev-PBE [18]. The calculations include two cases when the Hubbard atomic orbitals were taken as orthogonalized or not. Kinetic energy cutoffs for the plane-wave expansions were chosen as 90 and 720 Ry for the wave-functions and densities, respectively. The smearing method of Marzari-Vanderbilt [20] for the occupations with a width of 0.01 Ry were used. For the Brillouin-zone integrations in geometry optimizations, a $8\times8\times6$ grid was used; All geometries were fully optimized for total residual pressures on unit cells to within 0.5 kbar, and residual forces on atoms to within 10-3 mRy/a.u. To self-

consistent determination of the Hubbard parameters we have employed the HP code [13] following the flowchart shown in Fig. 2.

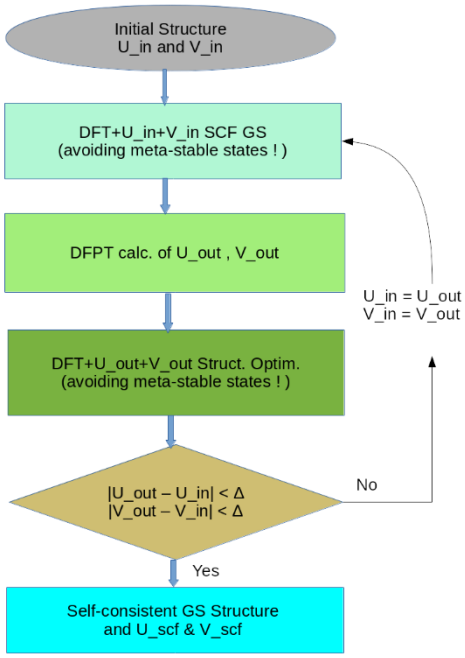

Fig. 2. Flowchart of SCF determination of Hubbard parameters. In the first-step SCF and last-step structure-optimization, the meta-stable states were avoided [21, 22].

To start the procedure for self-consistent determination of Hubbard parameters according to Fig. 2, we give initial values for Uin and Vin to open the electronic bang-gap; for the initial structure we choose simple tetragonal structure with appropriate lattice constants consistent with cubic structure of side 5.47 Angstrom. To avoid meta-stable states, we choose appropriate occupations of Hubbard orbitals 5f of uranium atoms [21, 22]. Our experience shows that starting from metallic ground state lead to divergence of some components of response function. For Hubbard-corrected DFT calculations, we consider on-site corrections for only 5f orbitals of uranium atoms, and the inter-site corrections between U-5f and O-2p orbitals of first nearest neighbor atoms. In the second step, we start the DFPT calculation and obtain new values for parameters named as Uout and Vout . In the third step, using the calculated parameters Uout and Vout , we optimize the geometry of the system taking care of meta-stable states. In each cycle we monitor the differences between input and output parameters to see if the self-

consistency is reached within Δ value. For this system the self-consistency is reached within 6 to 8 cycles in the flowchart.

Results and Discussions

The calculations were performed at three levels of approximations: i)-simple DFT with no Hubbard corrections, ii)-DFT with on-site Hubbard corrections (DFT+U), and iii)-DFT with on-site and inter-site corrections (DFT+U+V). For the simple DFT calculations incorrect metallic behavior is obtained, while for other two cases we get insulating behavior with different geometric and electronic properties. The results are presented in Table 1.

Table 1. Self-consistent Hubbard parameters in eV, equilibrium lattice constants in Angstroms, electronic band-gaps in eV for different XC approximations used for UO_2 crystal.

	DFT			DFT+U			DFT+U+V			
XC	$a\ (c)\ (\AA)$	$E_g\ (eV)$	U-proj	$U\ (eV)$	$a\ (c)\ (\AA)$	$E_g\ (eV)$	$U\ (eV)$	$V\ (eV)$	$a\ (c)\ (\AA)$	$E_g\ (eV)$
LDA	5.286 (5.300)	metal	atomic	2.14	5.414 (5.443)	1.18	2.22	0.37	5.406 (5.437)	1.18
			ortho	3.11	5.414 (5.431)	2.04	3.09	0.21	5.410 (5.430)	2.02
PW91	5.472 (5.487)	metal	atomic	1.98	5.517 (5.530)	1.61	2.01	0.32	5.509 (5.524)	1.59
			ortho	2.96	5.516 (5.517)	2.50	2.88	0.18	5.513 (5.515)	2.46
PBE	5.472 (5.450)	metal	atomic	1.99	5.519 (5.533)	1.57	2.02	0.32	5.512 (5.527)	1.56
			ortho	2.96	5.518 (5.520)	2.46	2.89	0.17	5.516 (5.518)	2.43
PBE-sol	5.337 (5.353)	metal	atomic	2.06	5.454 (5.476)	1.35	2.11	0.31	5.447 (5.471)	1.36
			ortho	**3.03**	**5.454 (5.463)**	**2.27**	**2.91**	**0.18**	**5.451 (5.460)**	**2.19**
rev-PBE	5.457 (5.463)	metal	atomic	1.99	5.550 (5.554)	1.63	2.01	0.32	5.543 (5.548)	1.62
			ortho	2.96	5.545 (5.546)	2.49	2.84	0.15	5.542 (5.543)	2.42

As is seen from Table 1, the DFT calculations for PW91, PBE, and rev-PBE give good lattice constants comparable with experiment but incorrect metallic properties. On the other hand, all Hubbard corrected results show correct insulating properties. Among all Hubbard-corrected calculations, the ones obtained using PBE-sol approximation for the XC are in good agreement with experiments. For both DFT+U and DFT+U+V, the non-orthogonalized Hubbard atomic orbitals lead to band gaps far from the experimental value. On the other hand, using the orthogonalized orbitals lead to band gaps of 2.27 eV for DFT+U and 2.19 eV for DFT+U+V in good agreement with experiment [23]. Taking into account the inter-site correction does not significantly modify the geometry, but lowers the band gap by 0.08 eV. In Table 1 the results for ortho-atomic PBE-sol are bolded.

Conclusions

In the study of strongly-correlated materials with some known experimental properties, it is not uncommon that the Hubbard parameters be chosen in such a way that lead to results consistent with known experimental properties and then continue the calculations with those tuned parameters to predict other unknown properties. However, the latter method is not applicable in designing new novel materials because of the lack of experimental investigations and one has to determine those Hubbard parameters self-consistently. In this work, using DFPT we have determined the self-consistent Hubbard parameters for different XC approximations and have shown that PBE-sol with ortho-atomic projection gives the best results.

Acknowledgements

This work is part of research program in School of Physics and Accelerators, NSTRI, AEOI.

Data Availability

The raw or processed data required to reproduce these results can be shared with anybody interested upon sending an email to M. Payami.

References

[1] Hohenberg P. and Kohn W. (1964). Inhomogeneous electron gas. Physical Review 136: B864.

[2] Kohn W. and Sham L. J. (1965). Self-consistent equations including exchange and correlation effects. Physical Review 140: A1133

[3] Perdew J. P. and Zunger A. (1981). Self-interaction correction to density-functional approximations for many-electron systems. Physical Review B 23: 5048.

[4] Perdew J. P., Burke K., and Ernzerhof M. (1996). Generalized gradient approximation made simple. Physical Review Letter 77 : 3865; Erratum (1997). Physical Review Letter 78 : 1396.

[5] Lin L. (2016). Adaptively compressed exchange operator. *Journal of Chemical Theory and Computation 12.*

[6] Sheykhi S. and Payami M. (2018). Electronic structure properties of UO2 as a Mott insulator. Physica C: Superconductivity and its Applications 549 : 93.

[7] Cococcioni M. and de Gironcoli S. (2005). Linear response approach to the calculation of the effective interaction parameters in the LDA+U method. Physical Review B 71 : 035105.

[8] Dudarev S. L., Botton G. A., Savrasov S. Y., Humphreys C. J., and Sutton A. P. (1998). Electron-energy-loss spectra and the structural stability of nickel oxide: An LSDA+U study. Physical Review.

[9] Campo Jr V. L. and Cococcioni M. (2010). Extended DFT+U+V method with on-site and inter-site electronic interactions. Journal of Physics: Condensed Matter 22 : 055602.

[10] Payami M. (2023). DFT+U study of UO2 : Correct lattice parameter and electronic band-gap. https://doi.org/10.48550/arXiv.2302.13381.

[11] Timrov I., Marzari N., and Cococcioni M. (2018). Hubbard parameters from density-functional perturbation theory. Physical Review B 98 : 085127.

[12] Timrov I., Marzari N., and Cococcioni M. (2021). Self-consistent Hubbard parameters from density-functional perturbation theory in the ultrasoft and projector-augmented wave formulations. Physical Review B 103 : 045141.

[13] Timrov I., Marzari N., and Cococcioni M. (2022). HP - A code for the calculation of Hubbard parameters using density-functional perturbation theory. Computational Physics Communications.

[14] Giannozzi P., Baroni S., Bonini N., Calandra M., Car R., Cavazzoni C., Ceresoli D., Chiarotti G. L., Cococcioni M., Dabo I., Dal Corso A., Gironcoli S., Fabris S., Fratesi G., Gebauer R., Gerstmann U., Gougoussis Ch., Kokalj A., Lazzeri M., Martin-Samos L., Marzari N., Mauri F., Mazzarello R., Paolini S., Pasquarello A., Paulatto L., Sbraccia C., Scandolo S., Sclauzero G., Seitsonen A. P., Smogunov A., Umari P., and Wentzcovitch R. M. (2009). QUANTUM ESPRESSO: a modular and open-source software project for quantum simulations of materials. Journal of Physics: Condensed Matter 21 (39): 395502.

[15] Giannozzi P., Baseggio O., Bonfa P., Brunato D., Car R., Carnimeo I., Cavazzoni C., de Gironcoli S., Delugas P., Ferrari Ruffino F., Ferretti A., Marzari N., Timrov I., Urru A., Baroni S. (2020). Quantum ESPRESSO toward the exascale. Journal of Chemical Physics 152 (15): 154105.

[16] Perdew J. P. and Wang Y. (1992). Accurate and simple analytic representation of the electron-gas correlation energy. Physical Review B 45 : 13244.

[17] Perdew J. P., et. al. (2008). Restoring the density-gradient expansion for exchange in solids and surfaces. Physical Review Letter 100 : 36406.

[18] Zhang Y. and Yang W. (1998). Comment on “Generalized gradient approximation made simple”. Physical Review Letter 80 : 890.

[19] Dal Corso A. (2014). Pseudopotentials periodic table: From H to Pu. Computational Materials Science 95 : 337.

[20] Marzari N., et. al. (1999). Thermal contraction and disordering of the Al (110) surface. Physical Review Letter 82 : 3296.

[21] Payami M. (2022). Spin-symmetry broken ground-state of UO2 in DFT+U approach: the SMC method. Iranian Journal of Physics Research 22 : 175.

[22] Payami M. (2023). Comparison of SMC and OMC results in determining the ground-state and meta-stable states solutions for UO2 in DFT+U method. https://doi.org/10.48550/arXiv.2302.04231.

[23] Schoenes J. (1978). Optical properties and electronic structure of UO2. Journal of Applied Physics 49 : 1463.

ICNST 2024
International Conference on Nuclear Science and Technology
6- 8 MAY 2024 | Isfahan, Iran

Investigation of Heat Transfer for Nuclear Fuel Storage Cask (Paper ID : 1584)

Hadipour A[1*], Hashemiyan M[2]

[1]National Center of Quality system and Atomic Standards of Iran, Tehran, Iran
[2]Faculty of Mechanical Engineering, Semnan University, Iran

Abstract

The purpose of this study is to perform thermal analysis for TN-24P cask in order to predict the maximum temperature of concrete cover, canister and fuel rod cover. Thermal analysis has been done for the intended cask in normal and accident conditions. The ambient temperature is considered to be 27°C in normal conditions and 47°C in abnormal conditions. Investigations have been performed for different geometries of inlet and outlet of air flow into the cask. Also, an accident is considered as the blockage of part of the air intake ducts around the cask, so that four of the eight air intake ducts are completely blocked. Thermal analysis is performed for both normal and accident conditions for natural and forced convection. Fluent software was used to perform thermal analysis. The results of this research show that increasing the number of air intake ducts has a noticeable effect on the heat transfer inside the cask. In addition, it was observed that changing the geometry of the air inlet and outlet ducts can have a significant effect on the heat transfer inside the cask.

Keywords: Thermal Analysis, Dry Storage Cask, Forced and Natural Convection, Incident Analysis

Introduction

Due to the widespread use of nuclear energy to generate electricity as a carbon-free energy source around the world, how to manage spent fuel and their storage issues are widely discussed in all countries that use nuclear energy. Therefore, the necessary measures for the storage of spent nuclear fuels are one of the most important things in the use of these fuels. Nuclear fuels used in nuclear reactors must be managed safely after exiting the reactor. Spent fuel pool are designed with the assumption that after a period of shutdown, spent nuclear fuel will be removed from the pool for reprocessing, disposal, or storage elsewhere. Therefore, the capacity of these pools is limited and it is necessary to remove the fuel from the pool and store it in another place after the required period of time. In order to store spent nuclear fuel after leaving the pool, single-purpose or dual-purpose casks are used. Single-purpose cask systems are only licensed to store spent fuel, while dual-purpose casks are licensed for storage and transportation.

The experiments showed that the TN-24P cask is suitable for storing spent fuel. It also shows excellent heat transfer performance, so that the temperature of the fuel rod remains below 380°C [1]. Manteufel [2]and Todreas [3] have used an analytical-numerical approach to derive models for calculating the effective thermal conductivity. While Bahney and Lotz, [4] used two-dimensional finite element solutions that include radiation and conduction effects. The thermal analysis of the ventilation system was performed to determine the size and shape of the optimal duct of the ventilation system by Lee et al [5]. Yoo et al simulated one-eighth of the TN-24P cask using the computational fluid dynamics method [6]. Wataru et al [7] investigated the flow and heat transfer inside the canister using the computational fluid dynamics method on a quarter of a concrete cask containing helium gas. Li and Liu [8] conducted a numerical study on a vertical single-purpose cusk model. Numerical simulation was performed by a 3D model by ANSYS Fluent software. Their results show that the use of materials with a higher heat capacity in the support network, increases the heat transfer inside the cage. Benavideset al. [9] also performed a two-stage simulation on a TN-24P cask. In the first stage, they include the simulation of the outer environment of cask and the border areas of cask. The second stage also includes the simulation inside the cask. In their paper, they investigated the effect of the distance between the internal components of the casing on heat transfer. Another thermal evaluation was done on TN-24P cask by Yun et al [10]. This evaluation has been simulated by the finite element method for three cases vacuum and filled with helium gas, nitrogen. The results in this article showed that the highest temperature is in the vacuum state and the lowest temperature is in the state filled with helium gas. Ji et al [11] investigated the effect of temperature distribution on the stress field created in a storage cask using a three-dimensional model and with the help of simulation. Also, the effect of the angle of the cask on the temperature distribution and thermal stresses created has been investigated.

In this research, a new effort has been performed to investigate the effect of the geometry and the number of flow inlet and outlet ducts and the ambient temperature on the heat transfer inside a TN-24P cask sample. The results of this study show that the number of flow inlet ducts and the geometry of the inlet and outlet ducts have a significant effect on the heat transfer inside the cask, while the decrease in ambient temperature does not have much effect on the temperature decrease inside the cask.

Specifications of Concrete Storage Cask

Figure 1 shows the types of casks of the TN family. These casks are being used in different countries. A spent nuclear fuel storage system consists of a concrete overpack and sealed canister (steel or copper) containing fuel baskets and a transport cask (Figure 2).

Fig. 1. The TN casks family

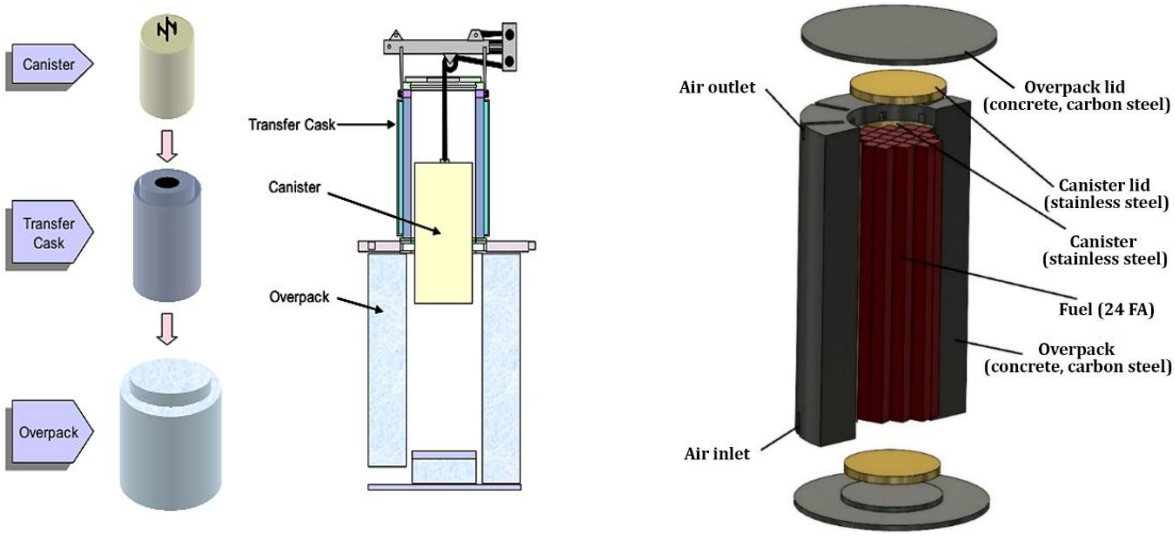

Fig. 2. Spent nuclear fuel storage system

In order to reduce the radiation around the cask and protect the environment from radiation, the spent fuel is first placed inside the canister. Figure 2 shows an overview of the storage cask. The investigated cask consists of structural materials, a concrete shield and a natural cooling system. Heat is transferred from the cask to the surrounding environment through air channels. Eight air inlet and outlet channels are created at the top and bottom of the case to create a natural cooling system (Figure 2). Table 1 shows

the description of the dry storage cask. The outer diameter of the storage cask is 3,550 mm and the overall height is 5,885 mm. The gross weight of the cask is approximately 135 tons. The storage cask is designed to store 24 PWR spent fuel assemblies with a burn-up of 55,000 MWD/MTU and a cooling time of 7 years. The decay heat load from the 24 PWR assemblies is 25.2 kW.

Table 1. Description of the Dry Storage Cask

Item	Description
Storage capacity	24 PWR assemblies
Component	- Sealed canister - Concrete overpack
Dimension	- Concrete overpack: O.D. 3,520 mm * 5,885 mm L - Canister: OD. 1,840 mm * 4,845 mm L
Weight	- Storage cask: 154.5 tons (loaded canister) - Canister: 38.2 tons (loaded fuels)
Material	- Overpack: Carbon steel, concrete - Canister: Stainless steel, boral (B4C + aluminum)
Design basis fuel	- Burn-up: 50,000 MWD/MTU - Cooling times: 7 years - Initial enrichment: 5.0 wt.% U235 - Decay heat: 25.2 kW / canister
Cooling system	- Natural cooling system: 8 air inlet and outlet ducts - Cavity: inert gas (helium)

Thermal Analysis Modelling For A Storage Cask

Thermal analyses have been carried out for a dry storage cask under normal and off-normal conditions. Generally, the annual average environmental temperature is applied to the thermal analysis for a normal condition. The ambient temperature is 27°C in the normal condition and in the environmental incident conditions, 47°C has been selected. Solar heat flux and maximum decay heat from the spent fuels are applied to all the analysis conditions. Decay heat from the 24 spent PWR fuel assemblies is 25.2 kW. FLUENT analysis models were performed for the three dimensional cylindrical quarter cask model. The thermal analyses were carried out in two stages to increase the computational speed substantially, as well as to reduce the requirements for the computer memory and space.

Solution Method

The aim of this study is to numerically investigate the heat of a used fuel storage cask in order to predict the maximum temperature of the concrete and fuel cover. For this purpose, a TN-24P PWR model in real dimensions has been considered. In order to analyze and validate the results, this study was conducted based on reference data [5] and the results were compared. The flow and thermal fields are predicted by the RNG (Renormalization Group) k–ε turbulent model34 with the enhanced wall treatment. Recent studies [11,12] have shown that the renormalization group (RNG) k–ε model offers superior performance to other turbulent models to predict hydrodynamic data in impinging jet flows over target surfaces with a higher convergence speed.

The numerical simulation is performed by solving the threedimensional governing equations including the following continuity, momentum, and energy conservation equations[15]:

$$\frac{\partial(\rho u_i)}{\partial x_i} = 0 \tag{1}$$

$$\frac{\partial(\rho u_i u_j)}{\partial x_j} = -\frac{\partial p}{\partial x_i} + \frac{\partial}{\partial x_j}\left(2\mu S_{ij} - \rho\overline{u_i' u_j'}\right) \tag{2}$$

$$\frac{\partial(\rho c_p u_i T)}{\partial x_i} = \frac{\partial}{\partial x_j}\left(K\frac{\partial T}{\partial x_i} - \rho C_p \overline{u_i' T'}\right) \tag{3}$$

where *ui* and *P* are the average velocity and static pressure, respectively. *u′ i* and *u′ j* represent fluctuating velocity components. In the following equation, *Sij* is the mean strain rate tensor

$$S_{ij} = \left[\frac{u_{i,j} + u_{j,i}}{2}\right] \tag{4}$$

The accuracy and high convergence speed of this model can come from some modifications including new constants and an additional term on the right-hand side of the ε equation compared to the standard *k*–ε model. It is noted that through an appropriate meshing near the wall regions, all advantages of the RNG k–ε model are achievable.

$$\frac{\partial(\rho k)}{\partial t} + \frac{\partial(\rho k u_i)}{\partial x_i} = \frac{\partial}{\partial x_i}\left\{\left(\mu + \frac{\mu_t}{\sigma_k}\right)\frac{\partial k}{\partial x_j}\right\} + p_k - \rho\varepsilon \tag{5}$$

$$\frac{\partial(\rho\varepsilon)}{\partial t} + \frac{\partial(\rho\varepsilon u_i)}{\partial x_i} = \frac{\partial}{\partial x_i}\left\{\left(\mu + \frac{\mu_t}{\sigma_\varepsilon}\right)\frac{\partial \varepsilon}{\partial x_i}\right\} + C_{1\varepsilon}\frac{\varepsilon}{k}p_k - C_{2\varepsilon}\rho\frac{\varepsilon^2}{k} - \frac{C_\mu \eta^3\left(1 - {}^{\eta}/_{\eta_0}\right)}{1+\beta\eta^3}\frac{\varepsilon^2}{k} \tag{6}$$

$$P_k = \left[2\mu_t S_{ij} - \frac{2}{3}\rho k S_{ij}\right]\frac{\partial u_j}{\partial x_i} \tag{7}$$

Table 2. Investigating the effect of the number computing cells on the results

The number of cells	198556	264112	310772	456021
max temperature of fuel rod (℃)	432	421	404	406
mean temperature of canister (℃)	390	379	372	373

Results and discussion

The effect of temperature and inlet flow velocity on heat transfer rate and fuel temperature is shown in Figure 3. As it can be seen from this figure, by decreasing the temperature of air inlet, the maximum temperature of the fuel also decreases by the same amount.

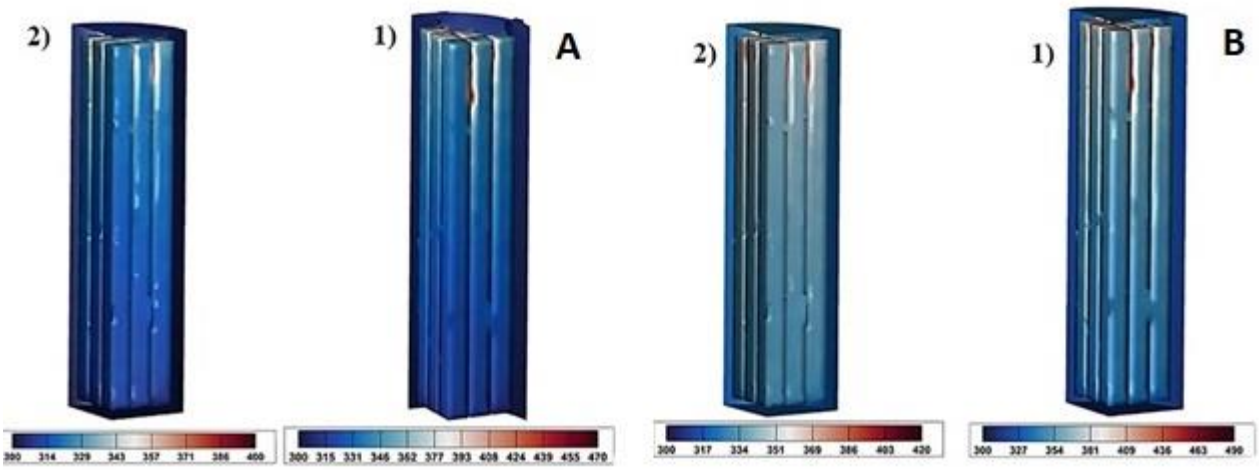

Fig. 3. The effect of the velocity and temperature of the air inlet inside the cask on heat transfer. ((A) inlet temperature 27℃, 1) natural air circulation, 2) inlet velocity m/s 20), ((B) inlet temperature 47℃, 1) natural air circulation, 2) inlet speed 20 m/s)

Figure 3 show that the effect of the inlet flow velocity on the temperature and heat transfer of fuel rods was greater than the changes in inlet air temperature. In other words, it can be said that inlet Reynolds has a greater effect on heat transfer than inlet air temperature. The main reason for this can be the high impact of flow turbulence on the heat transfer rate, which the results of the studies of Sharif and Mothe [12] also prove this claim.

Another investigation that has been done in this study is the investigation of the effect of the geometry of the inlet and outlet air flow on the distribution of flow and temperature inside the cask. In some models, the inlet and outlet of the flow are in the form of a vertical rectangle [5] and in other types of storage cask such as VSC-17, the inlet and outlet of the air flow are in the form of horizontal rectangles. For this purpose, to study the effect of the geometry of the inlet and outlet air flow on the value of heat transfer, the flow inlet with dimensions of 120 x 290 mm (horizontally and vertically) and outlet 105 x 425 mm (horizontally and vertically) have been investigated.

As can be seen in Figure 4, changes in the inlet and outlet flow geometry have a significant effect on the temperature distribution of the fuel rods and the canister. For example, the maximum temperature inside the cask decreases from 470 ℃ to 410 ℃, which shows the effect of the geometry of the inlet and outlet air flow on the amount of heat transfer inside the cask.

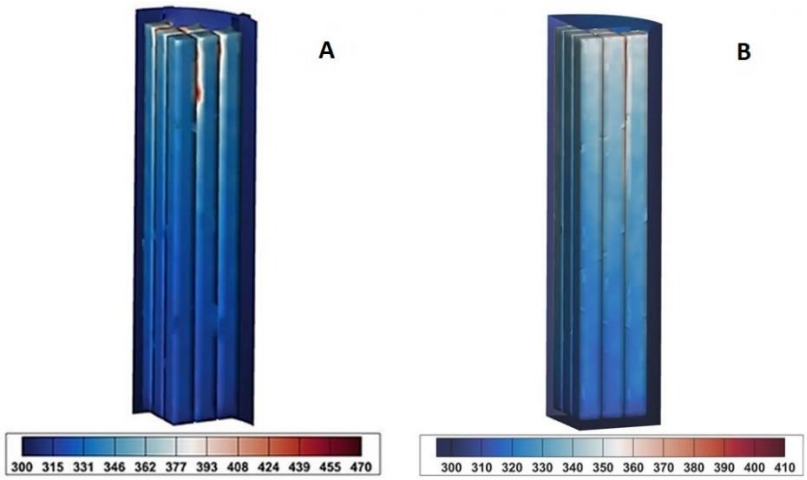

Fig. 4. Effect of inlet and outlet air flow geometry on heat transfer at ambient temperature of 27 ℃ and assuming natural circulation of air flow a) inlet and outlet geometry vertically b) inlet and outlet geometry horizontally

It should be noted that in the investigations carried out in this study, the inlet and outlet areas considered constant.

To better understand the effect of the mentioned parameters on heat transfer and temperature distribution inside the crucible, the fluid flow inside the crucible has also been studied. As shown in Figure 5, the air flow hits the canister wall at a significant velocity at the inlet and then flows inside the cask and

finally exits from the top of the chamber with a high temperature and a lower velocity than the inlet flow.

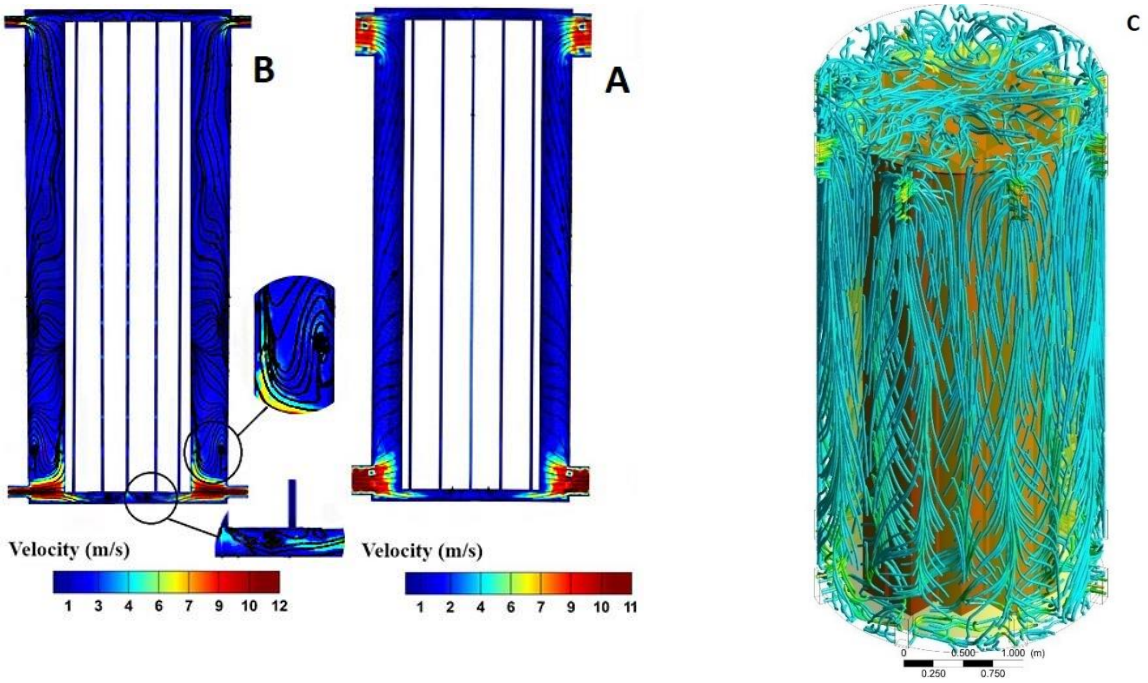

Fig. 4. Effect of inlet and outlet air flow geometry Velocity distribution inside the cask in a vertical sector, a) Vertical air inlet and outlet b) Horizontal air inlet and outlet c) Three-dimensional schematic of the flow lines between the concrete wall and the canister

Figure 5 shows the velocity contour with the flow lines for two different inlet and outlet geometries. According to the values of velocity and streamlines as shown in Figure 5, for the case where the inlet and outlet of the flow are horizontal, the turbulence of the flow and the effects of eddies inside the casing are higher and this increases the kinetic energy of the turbulence inside the casing. Hence the heat transfer for this state is higher than the state of vertical inlet and outlet flow.

Conclusions

In this study, the numerical simulation of the flow and heat transfer of a (concrete) storage cask for used nuclear fuels has been carried out in order to predict the maximum temperature of the concrete and fuel rods. The highlights obtained in this study are summarized as follows:

The most important factor to reduce the temperature inside the cask is the number of air flow inlets.

The results of this study show that changing the geometry of the flow inlet and outlet has a significant effect on the flow distribution and heat transfer inside the cask, and therefore, by changing the flow inlet and outlet geometry, it is possible to find the optimal state in heat transfer.

Increasing the veocity of the incoming air flow has a significant effect on reducing the temperature inside the casket. Therefore, it is suggested to use a flow mechanism such as a fan in the air inlet to create flow and heat transfer by forced displacement inside the casing.

References

J. M. Creer et al., The TN-24P PWR spent-fuel storage cask: Testing and analyses: Interim report., Pacific Northwest Lab., Richland, WA (USA); Virginia Electric and Power Co., Richmond (USA); Idaho National Engineering Lab., Idaho Falls (USA); Electric Power Research Inst., Palo Alto, CA (USA), 1987.

R.D Manteufel, Heat Transfer in an Enclosed Rod Array, .Ph.D Thesis, Massachusetts Institute of Technology, Cambridge, MA, USA, 1991.

R.D Manteufel, and N. E. Todreas, Effective Thermal Conductivity and Edge Conductance Model for a Spent Fuel Assembly, Nucl. Technology, 105, 421 (1994).

R.H. Bahney, and T.L.Lotz, Spent Nuclear Fuel Effective Thermal Conductivity Report, U.S. Department of Energy, BBA000000-017 17-5705-00010 REV 00 (1996).

J. C. Lee, D. H. Kim, K. S. Bang, K. S. Seo, B. I. Choi, and H. Y. Lee, Thermal analysis of a storage cask for 24 spent PWR fuel assemblies, Packag. Transp. Storage Secur. Radioact. Mater., 16.1, 19 (2005).

S. H. Yoo, H. C. No, H. M. Kim, and E. H. Lee, Full-scope simulation of a dry storage cask using computational fluid dynamics, Nuclear Engineering and Design, 240 (12), 4111 (2010).

M. Wataru et al., Thermal Hydraulic Analysis Compared with Tests of Full-Scale Concrete Casks, Nuclear Engineering and Design, 238, 1213 (2008).

Li, J. and Liu, Y.Y., Thermal modeling of a vertical dry storage cask for used nuclear fuel. Nuclear Engineering and Design, 301, 74-88, 2016.

Benavides, J., Jimenez, G., Galbán, M. and Lloret, M. Methodology for thermal analysis of spent nuclear fuel dry cask using CFD codes. Annals of Nuclear Energy, 133, 257-274, 2019.

Yun, H., Shin, J., Song, C. and Park, K., Thermal analyses of TN-24P dry storage cask with heterogeneous fuel assembly modeling. Progress in Nuclear Energy, 137, 10377, 2021.

Ji, W.H., Cheng, J.J., Tao, H.Z. and Li, W. Numerical simulation of coupling heat transfer and thermal stress for spent fuel dry storage cask with different power distribution and tilt angles. Nuclear Science and Techniques, 34(2), 26, 2023.

M.A.R. Sharif, and K.K. Mothe, Parametric study of turbulent slot-jet impingement heat transfer

ICNST 2024
International Conference on Nuclear Science and Technology
6- 8 MAY 2024 | Isfahan, Iran

Investigation of Heat Transfer for Nuclear Fuel Storage Cask (Paper ID : 1584)

Hadipour A[1*], Hashemiyan M[2]

[1]National Center of Quality system and Atomic Standards of Iran, Tehran, Iran
[2]Faculty of Mechanical Engineering, Semnan University, Iran

Abstract

The purpose of this study is to perform thermal analysis for TN-24P cask in order to predict the maximum temperature of concrete cover, canister and fuel rod cover. Thermal analysis has been done for the intended cask in normal and accident conditions. The ambient temperature is considered to be 27°C in normal conditions and 47°C in abnormal conditions. Investigations have been performed for different geometries of inlet and outlet of air flow into the cask. Also, an accident is considered as the blockage of part of the air intake ducts around the cask, so that four of the eight air intake ducts are completely blocked. Thermal analysis is performed for both normal and accident conditions for natural and forced convection. Fluent software was used to perform thermal analysis. The results of this research show that increasing the number of air intake ducts has a noticeable effect on the heat transfer inside the cask. In addition, it was observed that changing the geometry of the air inlet and outlet ducts can have a significant effect on the heat transfer inside the cask.

Keywords: Thermal Analysis, Dry Storage Cask, Forced and Natural Convection, Incident Analysis

Introduction

Due to the widespread use of nuclear energy to generate electricity as a carbon-free energy source around the world, how to manage spent fuel and their storage issues are widely discussed in all countries that use nuclear energy. Therefore, the necessary measures for the storage of spent nuclear fuels are one of the most important things in the use of these fuels. Nuclear fuels used in nuclear reactors must be managed safely after exiting the reactor. Spent fuel pool are designed with the assumption that after a period of shutdown, spent nuclear fuel will be removed from the pool for reprocessing, disposal, or storage elsewhere. Therefore, the capacity of these pools is limited and it is necessary to remove the fuel from the pool and store it in another place after the required period of time. In order to store spent nuclear fuel after leaving the pool, single-purpose or dual-purpose casks are used. Single-purpose cask systems are only licensed to store spent fuel, while dual-purpose casks are licensed for storage and transportation.

different artificial radionuclides of SNF may significantly speed up the chemical alteration of uranium oxides. Spontaneous formation of uranyl-phases was surprisingly observed in 2011 [4] in local areas of Chernobyl "lava" fragment collected in 1990 and then stored in radiochemical laboratory under room temperature but without humidity control (Fig.3). Also, examination of some Chernobyl samples in UV-light allowed observing the presence of uranyl phases, which are almost invisible by eyes (Fig.4).

Fig.1 New formed uranyl phases (bright yellow aggregates) discovered on the surface of Chernobyl "lava" in steam-discharge corridor. Photo by scientists of Kurchatov Institute (1990).

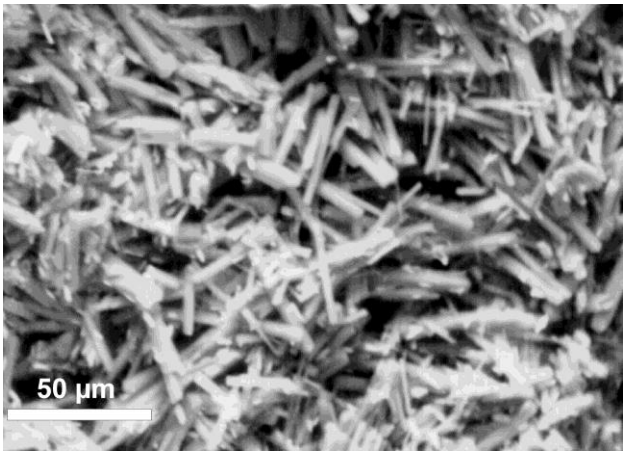

Fig.2 Back-scattered electron image of secondary uranium minerals formed at the surface of Chernobyl "lava" in steam-discharge corridor. Photo by B. Burakov (1990).

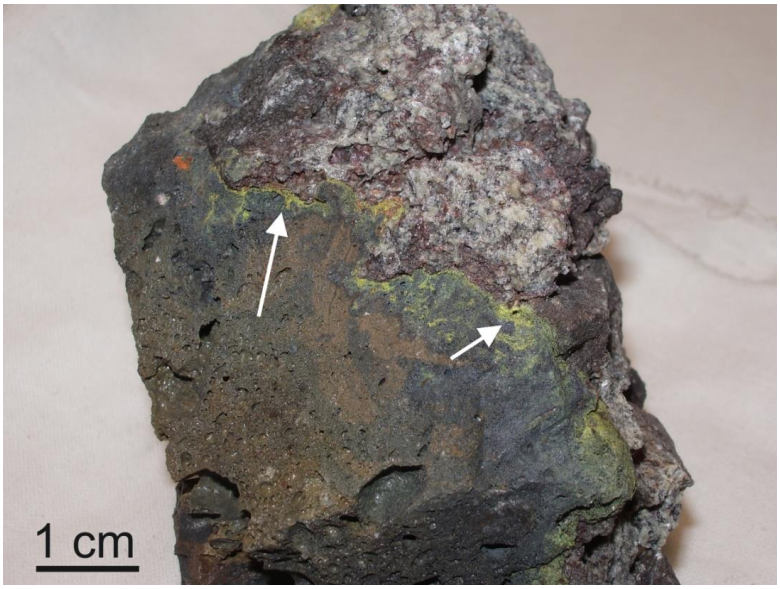

Fig. 3 Uranyl-phases (marked by arrays), which spontaneously formed on the surface of highly radioactive Chernobyl "lava" sample collected in 1990 and then stored over 20 years in a laboratory in air without humidity control. Photo by V. Zirlin and B. Burakov, 2011.

Fig. 4 Highly radioactive Chernobyl sample (placed on aluminum foil), which was formed as a result of corium-steel interaction (Zr-U-O + Fe-Cr-Ni), melting and oxidation: general image (left) and UV-luminescence of uranyl-phases on the sample surface. Sample size is approximately 5 x 3 cm. Photo by B. Burakov and Yu. Petrov, 2018.

Safe geological disposal of SNF and any other actinide-bearing highly radioactive materials is related to many uncertainties [2,5]. Modeling of corrosion of host matrix and further radionuclide migration into underground water should cover extremely long period of time – at least dozens thousands of years. Study of natural uranium minerals and their chemical alteration products forming during millions of years may provide valuable information however it is not enough yet in order to justify long-term safety of geological disposal. Laboratory-scale experiments using real highly radioactive samples are needed

as well. Moreover, such laboratory experiments should be carried out under so called “accelerated” conditions to speed up multi-scale corrosion effects.

This paper considers some experimental results obtained recently from the study of accelerated chemical alteration of highly radioactive Chernobyl samples: “lava” and oxidized corium-steel material (Zr-U-O + Fe-Cr-Ni). Basic properties of these Chernobyl samples have been reported before [6-9]. Main target is to demonstrate the complexity of corrosion and the contribution of secondary uranium minerals into processes of radionuclide redistribution and migration.

Experimental

The following Chernobyl highly radioactive samples of two types have been applied for alteration experiments: 1) brown “lava” (with bulk U-content 7-8 wt.%); and 2) corium-steel interaction material (with bulk U-content less than 1 wt. %). “Lava” sample consists of aluminum-silicate glass dissolved in its matrix almost 50 % of total uranium, and other part of uranium is related to crystalline inclusions of solid-solutions “ZrO2-UO2” with a broad range Zr/U ratio, and U-bearing zircon (Zr,U)SiO4. Chemical durability of zircon is very high, but chemical durability of solid-solutions “ZrO2-UO2” increases depending on Zr-content. Corium-containing sample consists of mainly Fe3O4 and similar inclusions of solid-solutions “ZrO2-UO2” with a broad range Zr/U ratio. It is assumed that similar materials can be discovered in the near future at Units #1, 2 and 3 of Fukushima-1 NPP.

Small fragments of both samples have been placed separately in Teflon vessels in distilled water at 150 ◦C for one year. Some details of these experiments and data obtained on leaching of isotopes of Pu and Am, Cs-137, Eu-154 have been repoted before [4,7,8]. New-formed phases were characterized using Single-Crystal X-ray Diffraction Analysis (SCXRD) and optical microscopy. Detailed study has not been completed yet and our research is going on now.

Results and discussion

Intensive corrosion accompanied with formation of secondary uranium minerals have been confirmed for both samples (Fig.5,6). Chemical alteration of silicate matrix of Chernobyl “lava” on the sample surface caused formation of silicate gel (Fig.5). Both samples despite their very different chemical and phase compositions demonstrated similar formation of artificial secondary uranium minerals. For “lava”

sample these uranyl-phases are still under examination. For corium-steel sample two analogues of natural minerals have been identified: isometric crystals of becquerelite: (Ca[(UO2)6O4(OH)6]·8H2O) and elongated crystals of phurcalite: (Ca2[(UO2)3O2(PO4)2]·7H2O) (Fig.6). It is interesting to notice that phurcalite phase contains phosphor, which occurs in initial matrix of corium-steel sample in quite insignificant amount and it is detectable by microprobe analysis in some rare points only. The results obtained are important not only for predicting aging of uranium-SNF (in contact with air and water) including one, which was mechanically destroyed, burned or melted under severe accidents, but also for evaluating the stability of SNF and cemented U-bearing wastes under temporary long-term storage and final repository conditions.

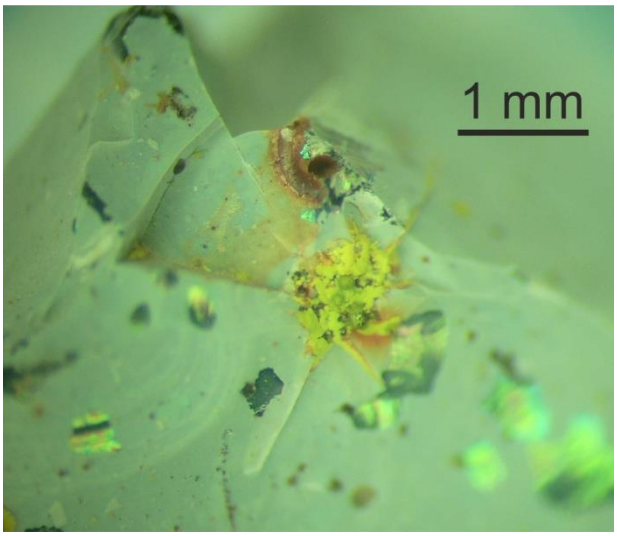

Fig. 5 Formation of silicate gel (grey color) and secondary uranium minerals (bright yellow inclusions) on the surface of Chernobyl brown “lava” sample as a result of alteration test in distilled water at 150 °C for one year. Photo by B. Burakov and B. Zubekhina, 2020.

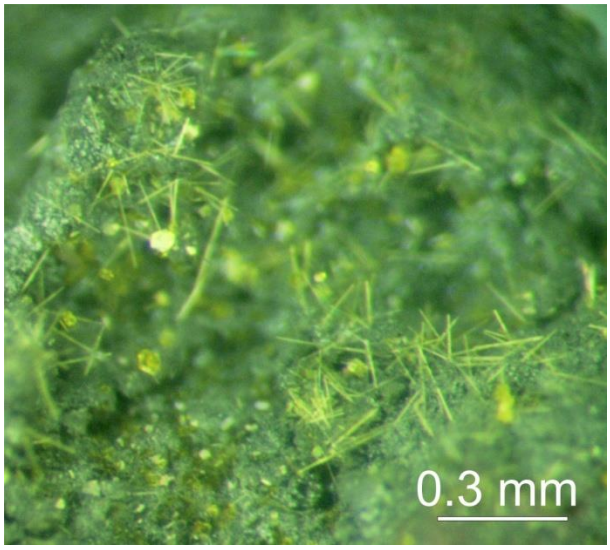

Fig. 6 Formation of secondary uranium minerals: isometric crystals of becquerelite (Ca[(UO2)6O4 (OH)6]·8H2O) and elongated crystals of phurcalite (Ca2[(UO2)3O2(PO4)2]·7H2O) on the surface of Chernobyl corium-steel interaction sample as a result of alteration test in distilled water at 150 °C for one year. Photo by B. Burakov and B. Zubekhina, 2020.

Conclusions

The following preliminary conclusions are proposed:

Chemical alteration of SNF in contact with water and air is much more complicated process than just matrix dissolution and radionuclide leaching. It is accompanied with formation of crystalline uranyl-phases, which are analogues of natural secondary uranium minerals. Formation of such phases affects significantly the radionuclide redistribution and migration. It must be taken into consideration for modeling of long-term environmental behavior of SNF and final geological disposal.

Modeling of SNF aging and alteration requires not only the study of natural uranium minerals but investigation of real highly radioactive samples (SNF and damaged SNF) as well.

The results obtained indirectly support the alternative option of SNF reprocessing (instead of direct SNF disposal) and development of separate durable waste forms for different groups of artificial radionuclides in particular for the most dangerous long-lived actinides [5].

Acknowledgements

This research was supported was supported by the Russian Science Foundation (grant No. 23-17-00080). The authors would like to thank personally Vladimir Zirlin and Larisa Nikolaeva (of the V.G. Khlopin Radium Institute, Russia), who have collected manually the highly radioactive samples under extremely dangerous conditions inside Chernobyl "Shelter" in 1990. The XRD and optical microscopy studies have been performed at the X-ray Diffraction Centre of St. Petersburg State University.

The authors would like to express special thanks to Prof. Javad Karimi-Sabet, Chemical Engineering Head of NSI, for inviting presentation of this paper at International Conference on Nuclear Science and Technology (ICNST2024).

References

[1] Soboleva, M.V. and Pudovkina I.A. (1957) Minerals of uranium, Moscow, 408 p. (in Russian).

[2] Lutze, W. and Ewing, R.C. (1988) Radioactive waste forms for the future, North-Holland Physics Publishing, the Netherlands, 778 p.

[3] Burakov, B.E.; Anderson, E.B. and Strykanova, E.E. (1997) Secondary uranium minerals on the surface of Chernobyl "lava". Materials Research Society Symposium Proceedings, Scientific Basis for Nuclear Waste Management XX, 465: 1309–311.

[4] Zubekhina, B.Yu. and Burakov, B.E. (2017) Leaching of actinides and other radionuclides from matrices of Chernobyl "lava" as analogues of vitrified HLW. J. Chem. Thermodynamics, 114: 25-29.

[5] Burakov, B.E.; Ojovan, M.I. and Lee, W.E. (2010) Crystalline materials for actinide immobilization. Imperial College Press, Materials for Engineering, Vol.1. 197 p.

[6] Burakov, B.E. (2020) Lava-like materials formed and solidified during Chernobyl accident. In: Konings, Rudy JM and Stoller Roger E (eds.) Comprehensive Nuclear Materials 2nd edition, 2: 525–540.

[7] Zubekhina, B.; Burakov, B.; Silanteva E.; Petrov Yu.,; Yapaskurt, V.; Danilovich, D. (2021) Long-term aging of Chernobyl fuel debris: corium and "lava". Sustainability, 13: 1073.

[8] Shiryaev, A.A.; Burakov, B.E.; Yapaskurt, V.O.; Zubekhina, B.Yu.; Averin, A.A.; Petrov, Yu.; Orlova V.; Silantyeva E.; Nickolsky M.S.; Zirlin, V.A.; Nikolaeva, L.D. (2022) Products of molten corium-metal interaction in Chernobyl accident: Composition and leaching of radionuclides. Progress in Nuclear Energy, 152:1104373.

[9] Lonartz, M.I.; Poml, P.; Colle, J.Y.; Manara, D.; Burakov, B.E. (2023) Characterization of black and brown Chernobyl “lava” matrices: The formation process reviewed. Prog. Nucl. Energy, 163: ArtNo: #10479

[10] Gurzhiy, V.V.; Burakov, B.E.; Zubekhina, B.Yu.; Kasatkin, A.V. (2023) Evolution of Chernobyl corium in water: formation of secondary uranyl phases. Materials, 16: 4533.

ICNST 2024
International Conference on Nuclear Science and Technology
6- 8 MAY 2024 | Isfahan, Iran

Fracture toughness of epoxy resin/functionalized MWCNTs nanocomposites: Fabrication, characterization, and simulation (Paper ID : 1685)

Araghchi M. Correspondent*, Daneshmand H. Co-Author
[1] *Nuclear Science and Technology Research Institute (NSTRI), P.O. Box 11365-8486, Tehran, Iran*

Abstract

The supreme features and functions of multi-walled carbon nanotube (MWCNTs) in composite materials have made them used as unique reinforcements for polymeric composites. The interfacial interactions between MWCNTs and polymeric materials have a significant relationship with the mechanical properties of polymer/MWCNTs composites. Functionalization of MWCNTs had been introduced as an excellent method for increasing the interfacial and mechanical features in nanoscale of polymer/MWCNTs nanocomposites. In this investigation, 5052-epoxy resin/0.5 wt% of non-functionalized MWCNTs, OH-functionalized MWCNTs, COOH-functionalized MWCNTs, and NH2-functionalized MWCNTs nanocomposites were fabricated and characterized. The pull-out process was simulated by molecular dynamics (MD) simulations to study the fracture toughness and the interfacial features between functionalized MWCNTs and epoxy resin just considering van der Waals interactions in nanocomposites. The results of the pull-out functionalized MWCNTs on the fracture surface of the nanocomposites represented the crack bridging pull-out as the prevailing mechanism in the fracture toughness process, which was also corroborated using MD simulations. In addition, NH2-functionalized MWCNTs had the most fracture toughness value and interfacial adhesion to the epoxy resin than non-functionalized MWCNTs using the mechanical interlocking mechanism from the atomistic scale.

Keywords: Polymer-matrix composites; Fracture toughness; Functionalized MWCNT; Molecular dynamics simulation.

Introduction

Polymeric materials have been wieldy used in different applications due to their proper properties [1]. Among the polymeric materials, epoxy resins due to their features have received attention [2]. However, epoxy resins are classifyed in the brittle polymeric martials recodnized by low resistance to crack propagate and fracture toughness factors. Therefore, study of the fracture toughness and their involved mechanisms is an important topic in polymeric industry.

Recently, various fillers such as carbon nanotubes [3], graphene [4], and micro/nanoparticles [5] have been used to improve the fracture toughness of epoxy resin. MWCNTs are one of the most important filler have been used in epoxy resin composites. MWCNTs were reinforced polymeric nanocomposites as appropriate filler, but their aptitude to produce clusters decrease of the prognosticated properties. The investigate of the fracture toughness MWCNTs/epoxy nanocomposites was performed using the analysis of the fracture surface [6-9].

The use of the functionalized MWCNTs inside polymeric matrix is one of the modification methods and increase the interfacial features of the MWCNTs in their compounds in polymeric composites [10]. Covalent functionalization of the MWCNTs for increasing the load transfer efficiency is considered as a significant method in MWCNTs/polymer composites, which is attained by chemical methods [11]. Different functional groups such as amine, carboxyl, and hydroxyl can be used to the MWCNTs/epoxy nanocomposites [12]. These are prevalent functional groups collaborate in cross-linking process and fabricate effective reactions with the epoxy matrix. This surface modification process has impressive role in dispersion of MWCNTs in the epoxy matrix and barricade from agglomerating of them [13]. The mechanical features of MWCNTs/epoxy nanocomposites used functionalized MWCNTs with the amine, carboxyl, and hydroxyl functional groups have been significantly improved [10-13].

However, the effects of various functionalized groups on the MWCNTs/epoxy nanocomposites through the mechanical deformations have not been completely investigated especially in experimental investigations. Recently, few investigations have been reported the effects of various functionalization groups on the physical and mechanical properties of the MWCNTs/epoxy nanocomposites. Therefore, the effects of various functional groups on the interfacial properties of nanocomposites and their comparison at the atomistic scale is an important subject to consider.

Jian et al. [14] investigated the impacts of the surface interactions between the amine-functionalized and epoxy resin matrix and pull-out process using MD simulations. Their results demonstrated that surface interactions and the Young's modulus of the functionalized CNT were 68% and 31% more than that of the non-functionalized CNTs in nanocomposite. Chai et al. [15] studied the effects of the surface interactions between the unfunctionalized, hydroxyl-functionalized, and carboxy-functionalized CNTs and epoxy resin matrix and pull-out process using MD simulations. The results of the pull-out process

indicated that functional groups increased the surface interactions between the CNTs and epoxy resin matrix. The carboxyl functionalized CNTs improved bonding features in nanocomposite compared to the hydroxyl-functionalized CNTs.

However, the reinforcing effects of the MWCNTs into polymeric materials have been widely reported in the many investigations, the prevailing mechanisms of the fracture toughness using experimental and simulation methods have not been comprehensively studied. According to the literature review, it seems that the effect of different types of functional groups on the interfacial properties of MWCNTs and epoxy resin and their comparison with each other has not been investigated so far in order to choose the best functional groups.

The aim of this investigation was the study the mode I fracture toughness of 5052-epoxy resins reinforced by the addition non-functionalized MWCNTs, CNOH-functionalized MWCNTs, COOH-functionalized MWCNTs, and NH2-functionalized MWCNTs in 0.5 wt%. To study the morphology of the fracture surface field emission scanning electron microscopy (FESEM) was applied. In addition, the fracture toughness values were msueared by mechanical tests. The involved mechanisms of the pull-out process were studied. The pull-out process by MD simulation was done to investigate the fracture surface of the epoxy resin/MWCNTs nanocomposites.

Experimental

Materials

The 5052-epoxy resin (Araldite LY 5052, Huntsman) and a hardener (Aradur HY 5052, Huntsman) supplied in the form of liquid. The 5052-epoxy resin/functionalized MWCNTs nanocomposites for the fracture toughness test were fabricated using injection molding method. The non-functionalized MWCNTs, CNOH-functionalized MWCNTs, COOH-functionalized MWCNTs, and NH2-functionalized MWCNTs in experimental grade were supplied from US research nanomaterials, Inc.

Sample preparation

The following steps were done for the producing of epoxy resin/0.5 wt% of non-functionalized MWCNTs, CNOH-functionalized MWCNTs, COOH-functionalized MWCNTs, and NH2-

functionalized MWCNTs nanocomposites. The details of the sample preparation of the nanocomposites according to the previous work were followed.

Simulation

An epoxy resin (Araldite LY 5052, Huntsman) and a hardener (Aradur HY 5052, Huntsman) reinforced with MWCNTs are used in this simulation. MD simulations were carried out using Materials Studio V8.0 software with the COMPASS II force field on the atomic/molecular scale. In this simulation, the van der Waals and the Coulombic interactions with a cutoff distance of 10 Å were applied for the epoxy resin/MWCNTs nanocomposites. The components of Araldite LY 5052 resin are epoxy phenol novolac and 1, 4-butanediol diglycidyl ether, and the components of Aradur HY 5052 hardener are IPDA and cycloaliphatic diamine, as can be seen in Fig. 1. The epoxide functional groups exist in two components of the resin and two nitride functional groups in two components of the hardener. The cross-linked polymer chains are fabricated by the reaction between the nitride functional groups of aradur and epoxide groups of araldites. The fracture toughness of polymers depends on the density of the cross-linking process. The positions of the CH2 and N are activated with the breaking of the CH2–O and N–H bonds in the cross-linking process.

Nanocomposite fabrication method

At first, phenol novolac, 1, 4-butanediol diglycidyl ether, IPDA, and cycloaliphatic diamine were added into the MWCNT cell by amorphous cell packing with an initial density of 0.5 g/cm3. Conjugate gradient algorithm for geometrical optimization was used to obtain a stable structure with minimum energy. Then, NVT and NPT ensembles were run for 500 ps at 300 K to acquire a generally stable state. Finally, the annealing simulation was done in the NVT and NPT ensembles at a temperature of 373 K for 500 ps.

Pull-out simulation

The geometry of the simulation was optimized and a dynamic simulation via the NVT ensemble was done to form a steady crystal structure with minimum energy. The pull-out process was carried out in eight steps and MWCNT evacuated from the epoxy resin at a distance of 10 Å in each step. Finally, MWCNT completely disconnected from the epoxy resin after 80 Å.

Results and discussion

Fig. 1 demonstrates FESEM images of the nanocomposites of (a), (b) epoxy resin/0.5 wt% non-functionalized MWCNTs, (c), (d) epoxy resin/0.5 wt% CNOH-functionalized MWCNTs, (e), (f) epoxy resin/0.5 wt% COOH-functionalized MWCNTs, and (g), (h) epoxy resin/0.5 wt% NH2-functionalized MWCNTs samples, respectively. Generally, the pull-out process happened in regions where the cluster of MWCNTs with high density exists inside a polymer matrix, as shown in Fig. 1. This process is confirmed by several investigations with a similar composite (epoxy resin/MWCNTs composites), using the FESEM analysis. The pulled-out MWCNTs in various magnifications were observed using FESEM images of the fracture surfaces of epoxy resin/0.5 wt% non-functionalized MWCNTs (Fig. 1(a), (b)), poxy resin/0.5 wt% CNOH-functionalized MWCNTs (Fig. 1(c), (d)), epoxy resin/0.5 wt% COOH-functionalized MWCNTs (Fig. 1(e), (f)), and epoxy resin/0.5 wt% NH2-functionalized MWCNTs (Fig. 1(g), (h)) samples. Pulled-out MWCNTs in fracture surfaces were created in all samples with different functional groups of the MWCNTs inside the polymer matrix in the fracture toughness test.

The pull-out process is basically depended on the size of the MWCNTs and the adhesion between the MWCNTs and polymer matrix. In addition, while the length of the MWCNTs was larger than the critical length, the stress transition propagated entirely, and consequently, the MWCNTs would be ruptured from each other. On the other hand, while the length off the MWCNTs was smaller than the critical length, the stresses transmitted to the MWCNTs were not adequate to break of the MWCNTs. Therefore, the polymer matrix separated from the MWCNTs and the pull-out process would happen. The ruptured and pulled-out MWCNTs on the fracture surface of the nanocomposites represented the sliding fracture mechanism. The length and the thickness of the pulled out MWCNTs in the fracture surfaces of the samples were non-functionalized MWCNTs < CNOH-functionalized MWCNTs < COOH-functionalized MWCNTs < NH2-functionalized MWCNTs, respectively (Fig. 1(b), (d), (f), and (h)). Therefore, the minimum and maximum adhesion between the MWCNTs and polymer matrix were belonged to the non-functionalized MWCNTs and NH2-functionalized MWCNTs, respectively [21, 22]. The thickness of the pulled out functionalized MWCNTs in the fracture surfaces of the samples was more than of the non-functionalized MWCNTs, as shown in Fig. 1(b), (d), (f), and (h).

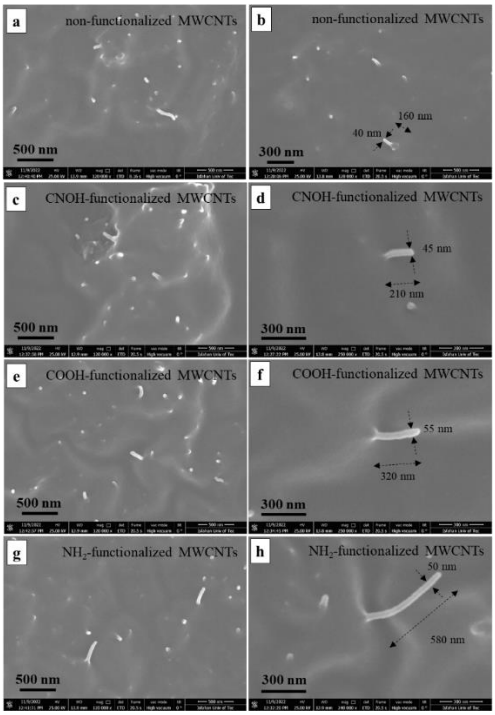

Fig. 1. FESEM images of the fracture surfaces of (a), (b) epoxy resin/0.5 wt% non-functionalized MWCNTs, (c), (d) epoxy resin/0.5 wt% CNOH-functionalized MWCNTs, (e), (f) epoxy resin/0.5 wt% COOH-functionalized MWCNTs, and (g), (h) epoxy resin/0.5 wt% NH2-functionalized MWCNTs samples.

Indeed, the bridge effect happens in the epoxy resin/MWCNTs composite, which prevents crack propagation and opening, and consequently, the fracture toughness parameter would be increased. The diminished fracture line size and the increased surface roughness infer the distortion of the crack path. Therefore, the growth and propagation of the crack inside an epoxy resin/MWCNTs composite would be difficult owing to the MWCNTs. The roughness of the fracture surface was raised by adding the MWCNTs in the polymeric matrix. In fact, the roughness of the fracture surface can be apprised by the distribution of MWCNTs inside the matrix.The pull-out mechanism is basically attributed to the physical features of the MWCNTs and the adhesion between the polymer/MWCNTs. MWCNTs play the role of a barrier on the nano-scale during crack growth and propagation. In the pull-out process, a large number of the MWCNTs were egressed on the fracture surface according to obtained results in similar investigations.

For further study of the pull-out mechanism MWCNT, the MD simulation was applied. Fig. 2 demonstrates the snapshots of MWCNT pulling out from 5052-epoxy resin. Non-bonded interactions

occurred between the carbon atoms of MWCNT and the epoxy resin. In addition, the proportion of electrostatic interactions between MWCNT and epoxy resin on the surface is negligible. Indeed, van der Waals interactions are the source of the nonbonded interactions between MWCNT and epoxy resin. The prior investigations have indicated that the interactions of the van der Waals can be principally ascribed to the π-π pile-up between carbon atoms of MWCNT and the aromatic ring of epoxy resin chain for the surface connections of the epoxy resin chains on the MWCNT in atomic scale. The effect of the load transfer from epoxy resin to MWCNTs has a major share in their interfacial interactions such as the van der Waals, the covalent bonding, and the mechanical interactions. The surface adhesion originating from the non-bonded interactions leads to an ineffective load transfer. Furthermore, type of the dispersion of MWCNTs and their orientations inside the matrix are the main factors in determining the reinforcement process of the nanocomposites.

It was observed in the FESEM images that the thickness of the MWCNT in the fracture cross-section has increased, which indicates the presence of the resin layer and the proper wetting of the MWCNT with the 5052-epoxy resin. The study of MD simulation showed that the reason for this is due to interface interactions of MWCNT by epoxy phenol novolac and cycloaliphatic diamine of 5052-epoxy resin that causes interlocking processes. As a result, the addition of MWCNTs has improved the fracture toughness of the resin.The pulling-out simulations of MWCNTs with various functional groups from the 5052-epoxy resin matrix was done to determine the interfacial properties of the nanocomposite. Snapshots of the pull-out simulations are shown in Fig. 2. It has been determined that due to the uniform charge distribution on the surface of MWCNTs, the interaction of MWCNTs with epoxy resin matrix is non-reactive and van der Waals based on π-π stacking of the carbon atom of MWCNT with the aromatic ring of the resin chain. However, the addition of functional groups has increased the van der Waals force. As shown in Fig. 2, the addition of a functional group on the surface of the MWCNTs increased the energy of pulling-out the MWCNTs from the epoxy resin matrix. In other words, for the non-functionalized MWCNTs, there was weak interaction between the MWCNTs and the epoxy resin when the MWCNTs was completely pulled-out from the epoxy resin matrix compared to the functionalized MWCNTs. However, due to the presence of functional groups on the surface of MWCNTs and the increase of van der Waals interaction, the matrix adheres to the MWCNTs when the MWCNTs was completely removed from the surface. In addition, the presence of the functional group caused the activation of the

interlocking mechanism, which increased the adhesion at the MWCNTs/epoxy resin interface and increased the pull-out energy.

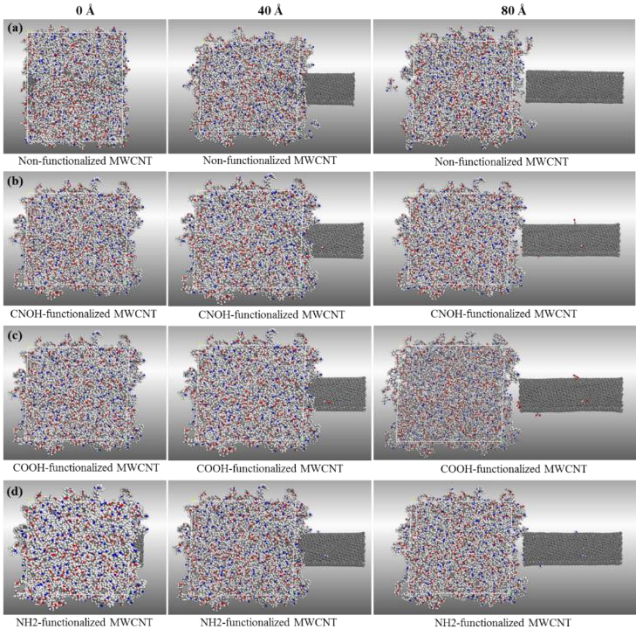

Fig. 2. Snapshots of pull-out simulation of non-functionalized MWCNTs, CNOH-functionalized MWCNTs, COOH-functionalized MWCNTs, and NH2-functionalized MWCNTs inside epoxy resin in three steps.

Therefore, both of the form components of the 5052-epoxy resin interacted with MWCNT and this issue led to interface interactions and interlocking processes. Consequently, mechanical properties especially fracture toughness parameters would be improved. A diagram of the pull-out energy vs. displacement of an MWCNT inside epoxy resin of non-functionalized MWCNTs, CNOH-functionalized MWCNTs, COOH-functionalized MWCNTs, NH2-functionalized MWCNTs is shown in Fig. 3. The obtained results demonstrate that the energies of the pull-out process enhance approximately linearly with the displacement variations ranging from 10 Å to 70 Å, and subsequently, approached a steady state after the pulling out process of the MWCNT from the epoxy resin. These obtained results were in perfect accordance with the reported investigations by other researchers. It is obvious that the highest energy was for amino functional group, followed by carboxyl and finally hydroxyl functional group.

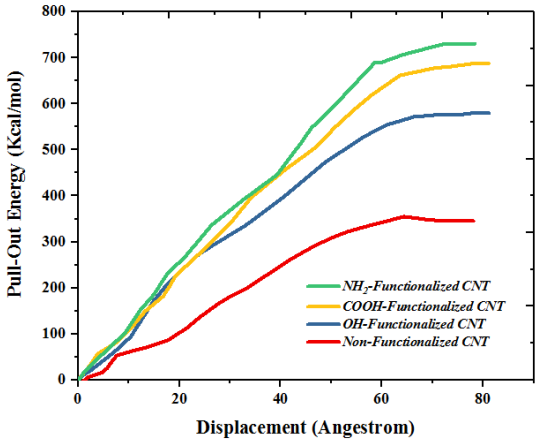

Fig. 3. Pull-out energy vs. displacement of non-functionalized MWCNTs, CNOH-functionalized MWCNTs, COOH-functionalized MWCNTs, and NH2-functionalized MWCNTs inside epoxy resin.

Conclusions

In summary, 5052-epoxy resin/0.5 wt% of non-functionalized MWCNTs, OH-functionalized MWCNTs, COOH-functionalized MWCNTs, and NH2-functionalized MWCNTs nanocomposites were experimentally produced. The fracture interfacial and mechanical features in nanoscale using functionalized MWCNTs by carboxyl, hydroxyl, and amino functional groups of 5052-epoxy resin/0.5 wt% MWCNTs nanocomposites were studied. A series of pull-out processes of non-functionalized MWCNTs and functionalized MWCNTs with various functional groups from epoxy resin/0.5 wt% MWCNTs nanocomposites were simulated using MD simulation. The pull-out process of the functionalized MWCNTs is investigated using MD simulations. The results of the MD simulation demonstrated that the functionalized MWCNTs-epoxy with amino functional group had the highest energy compared to that of non-functionalized MWCNTs, the functionalized MWCNTs-epoxy with carboxyl and hydroxyl functional groups during the pull-out process. These functional groups caused to MWCNTs had significant surface interactions with epoxy resin, and subsequently intense deformations was observed on their fracture surface of the nanocomposites after the pull-out process. The results of the fracture toughness values of various functionalized MWCNTs-epoxy resin nanocomposite were NH2-functionalized MWCNTs<COOH-functionalized MWCNTs<CNOH-functionalized MWCNTs<non-functionalized MWCNTs. The involving mechanism of various functionalized MWCNTs was extra mechanical interlocking during the pull-out process which was also confirmed via

MD simulations. The functionalization process was increased the surface interactions of the MWCNTs with epoxy resin and consequently the pull-out energy in nanocomposite.

References

1. Brown N 2007 Intrinsic lifetime of polyethylene pipelines Polymer Engineering & Science 47.

2. P. M. Ajayan, L.S. Schadler, P.V. Braun, Nanocomposite Science and Technology, first ed., Wiley, Weinheim, 2003.

3. J. Bai, Evidence of the reinforcement role of chemical vapour deposition multi-walled carbon nanotubes in a polymer matrix, Carbon 41 (6) (2003) 1325–1328.

4. M. Rafiee, J. Rafiee, I. Srivastava, Z. Wang, H. Song, Z. Yu, et al., Fracture and fatigue in graphene nanocomposites. Small 6 (2) (2009) 179–183

5. S. Zunjarrao, R. Singh, Characterization of the fracture behavior of epoxy reinforced with nanometer and micrometer sized aluminum particles, Compos. Sci. Technol. 66(13) (2006) 2296.

6. Z. Spitalsky, D. Tasis, K. Papagelis, C. Galiotis, Carbon nanotube-polymer composites: Chemistry, processing, mechanical and electrical properties, Prog. Polym. Sci. 35 (3) 2010) 357.

7. P. Ma, N. Siddiqui, G. Marom, J. Kim, Dispersion and functionalization of carbon nanotubes for polymer-based nanocomposites: A review. Compos. - A: Appl. Sci. Manuf. 41(10) (2010) 1345.

8. B. Fiedler, F. Gojny, M. Wichmann, M. Nolte, K. Schulte, Fundamental aspects of nanoreinforced composites, Compos. Sci. Technol. 66 (16) (2006) 3115–3125.

9. D. Ke, L. Li, W. Fei, L. Sihan, H. Yujin, W. Xuelin. New insights into interface interactions of CNT-reinforced epoxy nanocomposites, Compos. Sci. Technol. 204 (2021) 108638.

10.Z. Abousalman-Rezvani, P. Eskandari, H. Roghani-Mamaqani, M. Salami-Kalajahi, Functionalization of carbon nanotubes by combination of controlled radical polymerization and “grafting to” method, Adv. Colloid Interface Sci. 278, (2020) 102126.

11. M. Liebscher, T. Gärtner, L. Tzounis, M. Mičušík, P. Pötschke, M. Stamm, G. Heinrich, B. Voit, Influence of the MWCNT surface functionalization on the thermoelectric properties of melt-mixed polycarbonate composites, Compos. Sci. Technol. 101 (2014) 133–138.

12. N.Tz. Dintcheva, R. Arrigo, E. Morici, C. Gambarotti, S. Carroccio, F. Cicogna, G. Filippone, Multi-functional hindered amine light stabilizers-functionalized carbon nanotubes for advanced ultra-high molecular weight Polyethylene-based nanocomposites, Compos. B Eng. 82 (2015) 196.

13. N. Gopal Sahoo, S. Rana, J. Whan Cho, L. Li, S. Hwa Chan, Polymer nanocomposites based on functionalized carbon nanotubes, Prog. Polym. Sci. 35:7 (2010) 837–867.

14. W. Jian, D. Lau, Understanding the effect of functionalization in CNT-epoxy nanocomposite from molecular level, Compos. Sci. Technol. 191 (3) (2020) 108076.

15. S. Chai, J. Liu, D. Hou, P. Wang, Molecular insights into the interfacial adhesion mechanism between carbon nanotubes and epoxy resin, RSC Adv. 13(2023) 30915-30924.

16. M. Jafari Eskandari, M. Araghchi, H. Daneshmand, A. Hadipour, Repeatable and controllable notch and pre-crack sharpening via continuous-wave laser for fracture toughness of epoxy resin/MWCNTs nanocomposites: Fabrication, preparation, and characterization. Opt. Laser Technol. 170 (2024) 110272.